University of Alberta

Particle Image Velocimetry Applied to a Deflected Wall Jet

by

©

Peter Onyshko

A thesis submitted to the Faculty of Graduate Studies and Research in

partial fulfillment of the requirements for the degree of Master of Science

in

Water Resources Engineering

Department of Civil and Environmental Engineering

Edmonton, Alberta

Spring 2002

National Library of Canada

Acquisitions and Bibliographic Services

395 Wellington Street
Ottawa ON K1A 0N4
Canada

Bibliothèque nationale du Canada

Acquisitions et services bibliographiques

395, rue Wellington
Ottawa ON K1A 0N4
Canada

Your file Votre référence

Our file Notre référence

The author has granted a non-exclusive licence allowing the National Library of Canada to reproduce, loan, distribute or sell copies of this thesis in microform, paper or electronic formats.

L'auteur a accordé une licence non exclusive permettant à la Bibliothèque nationale du Canada de reproduire, prêter, distribuer ou vendre des copies de cette thèse sous la forme de microfiche/film, de reproduction sur papier ou sur format électronique.

The author retains ownership of the copyright in this thesis. Neither the thesis nor substantial extracts from it may be printed or otherwise reproduced without the author's permission.

L'auteur conserve la propriété du droit d'auteur qui protège cette thèse. Ni la thèse ni des extraits substantiels de celle-ci ne doivent être imprimés ou autrement reproduits sans son autorisation.

0-612-69746-0

Canada

University of Alberta

Library Release Form

Name of Author: Peter Onyshko

Title of Thesis: Particle Image Velocimetry Applied to a Deflected Wall Jet

Degree: Master of Science

Year this Degree Granted: 2002

Permission is hereby granted to the University of Alberta Library to reproduce single copies of this thesis and to lend or sell such copies for private, scholarly or scientific research purposes only.

The author reserves all other publication and other rights in association with the copyright in the thesis, and except as herein provided, neither the thesis nor any substantial portion thereof may be printed or otherwise reproduced in any material form whatever without the author's prior written permission.

Peter Onyshko.

8307 - 44 Avenue, Edmonton, Alberta

15 april 2002

University of Alberta

Faculty of Graduate Studies and Research

The undersigned certify that they have read, and recommended to the Faculty of Graduate Studies and Research for acceptance, a thesis entitled Particle Image Velocimetry Applied to a Deflected Wall Jet submitted by Peter Onyshko in partial fulfillment of the requirements for the degree of Master of Science in Water Resources Engineering.

Mark Loewen

Dr. M.R. Loewen

Dr. N. Rajaratnam

Dr. S.M. Kresta

12 april 2002

Abstract

This thesis presents the results of an experimental study of a deflected wall jet using particle image velocimetry (PIV). A wall jet was formed in a rectangular flume and deflected upwards to the water surface by a baffle affixed across the width of the flume. A square data mosaic was assembled from fourteen tesserae, each with 15 cm square fields of view. The velocity data was decomposed and the following flow parameters were calculated: u and v velocities, kinetic energy, Reynolds stress, turbulent kinetic energy, dissipation rate, vorticity, strain and Kolmogorov length and velocity scales. Profiles along the curved jet trajectory were extracted and similarity analyses were performed. Wall jet-like, plane jet-like and surface jet-like regions of flow were identified. Results consistent with those of Wu and Rajaratnam (1995a) were observed for the mean flow. Turbulence was concentrated in the body of the jet and decayed with distance along the trajectory.

Acknowledgements

My sincere gratitude is extended to Dr. M.R. Loewen and Dr. N. Rajaratnam for their support, guidance and indulgence throughout the course of my research. I would also like to thank Perry Fedun for his assistance with my experimental arrangement.

I gratefully acknowledge the help provided by both my brother and my colleagues at the T. Blench Hydraulics Laboratory in the collection and analysis of data. My heartfelt appreciation is also extended to my immediate family and close friends for their continued encouragement and support.

Funding for this research was provided by the National Science and Engineering Research Council in the form of a postgraduate scholarship.

Table of Contents

1 Introduction 1

2 Literature Review 4
    2.1 Plane Turbulent Jets 4
        2.1.1 Classic Plane Jet 4
        2.1.2 Plane Jet in a Crossflow 8
    2.2 Plane Turbulent Wall Jets 9
    2.3 Plane Turbulent Surface Jets 11
    2.4 Plane Turbulent Deflected Wall Jets 12

3 Experimental Methods 20
    3.1 PIV Methodology 20
    3.2 Flume Arrangement 21
    3.3 PIV Setup 22
        3.3.1 Illumination Sub-System 22
        3.3.2 Timing Sub-System 23
        3.3.3 Imaging Sub-System 24
    3.4 Measurement Programme 25

4 Data Processing 42
    4.1 Image Pre-Processing 42
    4.2 Primary PIV Processing 43
    4.3 Corrective Post-Processing 44
    4.4 Supplementary Processing 46
    4.5 Error Consideration 48
        4.5.1 Out-of-Plane Motion 48
        4.5.2 Standard PIV Errors 49
        4.5.3 Misalignment Errors 51

5 Data Analysis 68
    5.1 Whole-Field Flow Properties 68
        5.1.1 Mean Velocity 69
        5.1.2 Mean Kinetic Energy 70
        5.1.3 Mean Reynolds Stress 71
        5.1.4 Mean Turbulent Kinetic Energy 73
        5.1.5 Mean Dissipation 74
        5.1.6 Vorticity 75
            5.1.6.1 Mean Vorticity 75
            5.1.6.2 Mean Circulation 77
            5.1.6.3 Instantaneous Vorticity 78
        5.1.7 Mean Strain 80
        5.1.8 Mean Kolmogorov Scales 81

5.2 Jet Flow and Development 81
  5.2.1 Trajectory Identification 82
  5.2.2 Centreline Velocity Decay 85
  5.2.3 Centreline Velocity Angles 87
  5.2.4 Profile Extraction 88
  5.2.5 Characteristic Length Scales 89
  5.2.6 Nondimensional Similarity 92
    5.2.6.1 Wall Jet-Like Flow 93
    5.2.6.2 Plane Jet-Like Flow 94
    5.2.6.3 Surface Jet-Like Flow 95
    5.2.6.4 Return Surface Jet-Like Flow 96
    5.2.6.5 Transition Flows 97
  5.2.7 Discharge Intensity Variation 97
  5.2.8 Momentum Flux Variation 100
  5.2.9 Entrainment Velocities 101

6 Conclusion 216
  6.1 Experimental Observations 216
  6.2 Future Considerations 218

7 References 219

8 Appendix 223

List of Tables

Table 3.1: Global coordinate tesserae positions and extents. 27

Table 3.2: Mean water surface profile coordinates. 28

Table 3.3: Environmental parameters. 29

Table 3.4: Experimental timing delays and separations. 30

Table 4.1: Spurious vector statistics arranged by tessera and iteration. 53

Table 4.2: Maximum displacement and velocity resolutions for all tesserae. 54

Table 4.3: Estimates of out-of-plane displacement (d_{pxz}) for all tesserae. 55

Table 4.4: Peak locking error percentages (I_{plu} and I_{plv}) for all tesserae. 56

Table 4.5: Errors in velocity (e_u and e_v) for all tesserae. 57

Table 4.6: Errors in vorticity (e_ω) for all tesserae. 58

Table 5.1: Minimum and maximum mean velocities in each tessera. 102

Table 5.2: Minimum and maximum mean flow properties in the full data mosaic. 103

Table 5.3: Minimum and maximum mean flow properties in each tessera. 104

Table 5.4: Flow regime extents and boundary ordinates for the main jet flow. 108

Table 5.5: Flow regime extents and boundary ordinates for the return jet flow. 109

Table 5.6: Variation of the C_1 coefficient along the full jet trajectory. 110

Table 5.7: Variation of the C_2 coefficient for the negative profile stem (δ_{1-}) along the full jet trajectory. 111

Table 5.8: Variation of the C_2 coefficient for the positive profile stem (δ_{1+}) along the full jet trajectory. 112

Table 5.9: Variation of the C_3 coefficient along the full jet trajectory. 113

Table 8.1: Contents of accompanying compact disc. 224

List of Figures

Figure 1.1: Dye visualization still of the plane deflected wall jet. 3
Figure 2.1: Plane turbulent jet definition sketch. 14
Figure 2.2: Plane turbulent jet potential core and development sketch. 15
Figure 2.3: Plane turbulent jet in a crossflow definition sketch. 16
Figure 2.4: Plane turbulent wall jet definition sketch. 17
Figure 2.5: Plane turbulent surface jet definition sketch. 18
Figure 2.6: Plane turbulent deflected wall jet definition sketch. 19
Figure 3.1: Flume arrangement diagram. 31
Figure 3.2: Channel measured drawing. 32
Figure 3.3: (a) General PIV setup layout and (b) broad laser timing structure. 33
Figure 3.4: PIV illumination sub-system diagram. 34
Figure 3.5: (a) PIV timing sub-system signal flow and (b) detailed timing scheme. 35
Figure 3.6: PIV imaging sub-system target apparatus measured drawing. 36
Figure 3.7: T. Blench Hydraulics Laboratory experimental area. 37
Figure 3.8: Flume arrangement and PIV setup. 37
Figure 3.9: Flume arrangement pump and magnetic flowmeter. 38
Figure 3.10 :Flume arrangement water reservoir. 38
Figure 3.11: PIV illumination sub-system optical rail, lens and mirror. 39
Figure 3.12: PIV timing sub-system sync stripper and delay generator. 39
Figure 3.13: PIV imaging sub-system. 40
Figure 3.14: Submerged targeting apparatus and CDD camera. 40
Figure 3.15: Target images taken of (a) tessera 12 and (b) tessera 13. 41
Figure 4.1: Baffle shadow and edge reflection defects visible in (a) tessera 2 and (b) tessera 3 raw PIV images. 59
Figure 4.2: Water surface reflection defects visible in (a) tessera 6 and (b) tessera 7 raw PIV images. 60
Figure 4.3: Interrogation window grid superposed on a tessera 4 PIV image. 61
Figure 4.4: PIV methodology schematic showing (a) interrogation and search windows, (b) the correlation field and (c) identified pixel displacements. 62
Figure 4.5: Representative instantaneous raw pixel displacement vector fields for (a) tessera 4 and (b) tessera 7. 63
Figure 4.6:Exclusion zones in the assembled mosaic. 64
Figure 4.7: Representative instantaneous corrected and interpolated pixel displacement vector fields for (a) tessera 4 and (b) tessera 7. 65

Figure 4.8: Peak locking error in tessera 1 raw pixel displacement data........................ 66
Figure 4.9: Example of edge dislocation in the upper-left corner of tessera 10............ 67
Figure 5.1: Full mean velocity vector field with additional superposed field showing every tenth vector at a larger scale. 114
Figure 5.2: Mean velocity vector field for full mosaic showing every tenth vector at scale and jet centreline trajectory... 115
Figure 5.3: Mean velocity vector field of the area encompassing the small eddy of clockwise rotation. 116
Figure 5.4: (a-b) Mean kinetic energy per unit mass (KE) contour maps describing full data mosaic with jet centreline trajectory. 117
Figure 5.5: Mean kinetic energy per unit mass (KE) contour map for tessera 3 with jet centreline trajectory.. 118
Figure 5.6: (a-b) Mean Reynolds stress per unit mass (τ/ρ) contour maps describing full data mosaic with jet centreline trajectory. 119
Figure 5.7: Mean Reynolds stress per unit mass (τ/ρ) contour map for tessera 3 with jet centreline trajectory. 120
Figure 5.8: (a-b) Mean turbulent kinetic energy per unit mass (k) contour maps describing full data mosaic with jet centreline trajectory. 121
Figure 5.9: Mean turbulent kinetic energy per unit mass (k) contour map for tessera 3 with jet centreline trajectory. 122
Figure 5.10: The cumulative average, plotted over increasing periods of time and averaging larger batches of PIV data files, of the sum of all turbulent kinetic energy (k) measurements in a tessera, presented for (a) tessera 2 and (b) tessera 4; showing that a sufficient amount of data was collected at each tessera for representative mean turbulent flow characteristics to be calculated. Note the stabilization by 2.5 minutes. 123
Figure 5.11: (a-b) Mean dissipation per unit mass (d) contour maps describing full data mosaic with jet centreline trajectory... 124
Figure 5.12: Mean dissipation per unit mass (d) contour map for tessera 3 with jet centreline trajectory.. 125
Figure 5.13: (a-d) Mean vorticity (ω) contour maps describing full data mosaic with jet centreline trajectory. 126
Figure 5.14: Mean vorticity (ω) contour map of mosaic area surrounding the baffle. 128
Figure 5.15: Velocity, vorticity and circulation in the large elliptical eddy found on the inbound side of the jet centreline trajectory. 129

Figure 5.16: Vorticity distribution along the radius of the large elliptical eddy found on the inbound side of the jet centreline trajectory. 130

Figure 5.17: Instantaneous vorticity (ω_i) contour map for tessera 2; consecutive 15 Hz frames with the background vorticity plotted in white to accentuate the coherent vortical structures and with the jet centreline trajectory as reference.... 131

Figure 5.18: Instantaneous vorticity (ω_i) contour map for tessera 3; consecutive 15 Hz frames with the background vorticity plotted in white to accentuate the coherent vortical structures and with the jet centreline trajectory as reference.... 133

Figure 5.19: Instantaneous vorticity (ω_i) contour map for tessera 1; consecutive 15 Hz frames with the background vorticity plotted in white to accentuate the coherent vortical structures. 135

Figure 5.20: Instantaneous vorticity (ω_i) contour map for tessera 11; consecutive 15 Hz frames with the background vorticity plotted in white to accentuate the coherent vortical structures. 137

Figure 5.21: (a-b) Mean strain (ε) contour maps describing full data mosaic with jet centreline trajectory. 139

Figure 5.22: Mean strain (ε) contour map for tessera 3 with jet centreline trajectory. 140

Figure 5.23: Mean Kolmogorov (a) length scale (l_k) and (b) velocity scale (v_k) contour maps describing full data mosaic with jet centreline trajectory. 141

Figure 5.24: Mean Kolmogorov (a) length scale (l_k) and (b) velocity scale (v_k) contour maps for tessera 3 with jet centreline trajectory. 142

Figure 5.25: Replacement of mean velocity vectors in water surface reflection defect exclusion zone with raw mean corrected and scaled velocity vectors. 143

Figure 5.26: Interpolated mean velocity vectors in baffle reflection and baffle shadow defect exclusion zone. 144

Figure 5.27: Locations of the maximum mean velocity magnitudes found in each column and each row of the full data mosaic. 145

Figure 5.28: The contour line showing where the mean vorticity (ω) is equal to zero in the full data mosaic, including the replacement vectors in the water surface reflection defect exclusion zone. 146

Figure 5.29: Final deflected wall jet trajectory for both the main jet and the return flow section. 147

Figure 5.30: Flow regimes within the plane deflected wall jet. 148

Figure 5.31: Variation of U_m with s over (a) the full jet trajectory and over (b-d) the sections upstream of the baffle, between the baffle and the point of impingement and downstream of the point of impingement, respectively. 149

Figure 5.32: Variation of U_m/U_o with $\xi^{-0.5}$ over (a) the full jet trajectory and over (b-d) the sections upstream of the baffle, between the baffle and the point of impingement and downstream of the point of impingement, respectively. 151

Figure 5.33: Variation of the C_1 coefficient along the full jet centreline trajectory. 153

Figure 5.34: Variation of (a) U_m with s and of (b) U_m/U_o with $\xi^{-0.5}$ along the full return flow jet trajectory. 154

Figure 5.35: Variation of θ_c with s over (a) the full jet trajectory and over (b-d) the sections upstream of the baffle, between the baffle and the point of impingement and downstream of the point of impingement, respectively. 155

Figure 5.36: Variation of θ_c with s along the full return flow jet trajectory. 157

Figure 5.37: Select mean velocity vector profiles showing the development of the plane deflected wall jet with a provided velocity scale; only every tenth mean velocity data point along each profile section is plotted for clarity. 158

Figure 5.38: Select mean velocity profiles showing the development of the plane deflected wall jet in the wall jet-like (WJL) region of flow. 159

Figure 5.39: Select mean velocity profiles showing the development of the plane deflected wall jet in the plane jet-like (PJL) region of flow. 160

Figure 5.40: Select mean velocity profiles showing the development of the plane deflected wall jet in the surface jet-like (SJL) region of flow. 161

Figure 5.41: Select mean velocity profiles showing the development of the plane deflected wall jet in the return flow surface jet-like (SJL) region; only every sixth mean velocity data point along each profile section is plotted for clarity. ... 162

Figure 5.42: Loci of the jet centreline trajectory, the jet half-width (δ_1), the jet width (δ_2) and the water surface in the global Cartesian coordinate system. 163

Figure 5.43: Loci of the return flow jet centreline trajectory, the jet half-width (δ_1), the jet width (δ_2) and the water surface in the global Cartesian coordinate system. 164

Figure 5.44: Variation of δ_1 with s over the full jet trajectory. 165

Figure 5.45: Variation of δ_1/b_o with ξ over (a) the full jet trajectory and over (b-d) the sections upstream of the baffle, between the baffle and the point of impingement and downstream of the point of impingement, respectively. 166

Figure 5.46: Variation of the C_2 coefficients for both δ_{1-} and δ_{1+} along the full jet centreline trajectory. 168

Figure 5.47: Variation of(a) δ_1 with s and of (b) δ_1/b_o with ξ along the full return flow jet trajectory. 169

Figure 5.48: Variation of δ_2 with s over the full jet trajectory. 170

Figure 5.49: Variation of δ_2/b_0 with ξ over (a) the full jet trajectory and over (b-d) the sections upstream of the baffle, between the baffle and the point of impingement and downstream of the point of impingement, respectively. 171

Figure 5.50: Variation of (a) δ_2 with s and of (b) δ_2/b_0 with ξ along the full return flow jet trajectory. 173

Figure 5.51: (a) Dimensional and (b) nondimensional u mean velocities for wall jet-like (WJL) profiles. 174

Figure 5.52: Comparison of theoretical curves describing the variation of u/U_m with η for wall jet-like (WJL) profiles using (a) classical wall jet and (b) free mixing region definitions. 175

Figure 5.53: (a) Dimensional and (b) nondimensional v mean velocities for wall jet-like (WJL) profiles. 176

Figure 5.54: (a) Dimensional and (b) nondimensional mean Reynolds stress per unit mass (τ/ρ) for wall jet-like (WJL) profiles. 177

Figure 5.55: (a) Dimensional and (b) nondimensional mean kinetic energy per unit mass (KE) for wall jet-like (WJL) profiles. 178

Figure 5.56: (a) Dimensional and (b) nondimensional mean turbulent kinetic energy per unit mass (k) for wall jet-like (WJL) profiles. 179

Figure 5.57: Mean dissipation per unit mass (d) for wall jet-like (WJL) profiles. 180

Figure 5.58: Mean (a) vorticity (ω) and (b) strain (ε) for wall jet-like (WJL) profiles. 181

Figure 5.59: Mean Kolmogorov (a) length scales (l_k) and (b) velocity scales (v_k) for wall jet-like (WJL) profiles. 182

Figure 5.60: (a) Dimensional and (b) nondimensional u mean velocities for plane jet-like (PJL) profiles. 183

Figure 5.61: Variation of u/U_m with η for plane jet-like (PJL) profiles with equation [2.9] plotted for reference. 184

Figure 5.62: (a) Dimensional and (b) nondimensional v mean velocities for plane jet-like (PJL) profiles. 185

Figure 5.63: (a) Dimensional and (b) nondimensional mean Reynolds stress per unit mass (τ/ρ) for plane jet-like (PJL) profiles. 186

Figure 5.64: (a) Dimensional and (b) nondimensional mean kinetic energy per unit mass (KE) for plane jet-like (PJL) profiles. 187

Figure 5.65: (a) Dimensional and (b) nondimensional mean turbulent kinetic energy per unit mass (k) for plane jet-like (PJL) profiles. 188

Figure 5.66: Mean dissipation per unit mass (d) for plane jet-like (PJL) profiles. 189

Figure 5.67: Mean (a) vorticity (ω) and (b) strain (ε) for plane jet-like (PJL) profiles. 190
Figure 5.68: Mean Kolmogorov (a) length scales (l_k) and (b) velocity scales (v_k) for plane jet-like (PJL) profiles. 191
Figure 5.69: (a) Dimensional and (b) nondimensional u mean velocities for surface jet-like (SJL) profiles. 192
Figure 5.70: Variation of u/U_m with η for surface jet-like (SJL) profiles with equation [2.9] plotted for reference. 193
Figure 5.71: (a) Dimensional and (b) nondimensional v mean velocities for surface jet-like (SJL) profiles. 194
Figure 5.72: (a) Dimensional and (b) nondimensional mean Reynolds stress per unit mass (τ/ρ) for surface jet-like (SJL) profiles. 195
Figure 5.73: (a) Dimensional and (b) nondimensional mean kinetic energy per unit mass (KE) for surface jet-like (SJL) profiles. 196
Figure 5.74: Mean (a) turbulent kinetic energy per unit mass (k) and (b) dissipation per unit mass (d) for surface jet-like (SJL) profiles. 197
Figure 5.75: Mean (a) vorticity (ω) and (b) strain (ε) for surface jet-like (SJL) profiles. 198
Figure 5.76: Mean Kolmogorov (a) length scales (l_k) and (b) velocity scales (v_k) for surface jet-like (SJL) profiles. 199
Figure 5.77: (a) Dimensional and (b) nondimensional u mean velocities for return surface jet-like (SJL) profiles. 200
Figure 5.78: Variation of u/U_m with η for return surface jet-like (SJL) profiles with equation [2.9] plotted for reference. 201
Figure 5.79: (a) Dimensional and (b) nondimensional u mean velocities for the first transition zone (TZ1) profiles. 202
Figure 5.80: (a) Dimensional and (b) nondimensional u mean velocities for the second transition zone (TZ2) profiles. 203
Figure 5.81: (a) Dimensional and (b) nondimensional u mean velocities for the return flow second transition zone (TZ2) profiles. 204
Figure 5.82: Variation of q with s over (a) the full jet trajectory and over (b-d) the sections upstream of the baffle, between the baffle and the point of impingement and downstream of the point of impingement, respectively. 205
Figure 5.83: Variation of (a) q/q_o with ξ and of (b) q/q_o with $\xi^{0.5}$ along the full jet trajectory. 207
Figure 5.84: Variation of (a) q with s and of (b) q/q_o with ξ along the full return flow jet trajectory. 208

Figure 5.85: Variation of (a) q with s and of (b) q/q_o with ξ along the full trajectory for both the main flow and the return flow components of the jet. 209

Figure 5.86: Variation of m with s over (a) the full jet trajectory and over (b-d) the sections upstream of the baffle, between the baffle and the point of impingement and downstream of the point of impingement, respectively. 210

Figure 5.87: Variation of (a) m/m_o with ξ and of (b) m/m_o with $\xi^{0.5}$ along the full jet trajectory. 212

Figure 5.88: Variation of (a) m with s and of (b) m/m_o with ξ along the full return flow jet trajectory. 213

Figure 5.89: Variation of (a) m with s and of (b) m/m_o with ξ along the full trajectory for both the main flow and the return flow components of the jet. 214

Figure 5.90: Variation of (a) v_c with s and of (b) v_c/U_m with ξ along the full jet trajectory. 215

Figure 8.1: Sample instantaneous (a) raw and (b) corrected and interpolated pixel displacement vector fields for tessera 14. 225

Figure 8.2: Sample instantaneous (a) raw and (b) corrected and interpolated pixel displacement vector fields for tessera 1. 226

Figure 8.3: Sample instantaneous (a) raw and (b) corrected and interpolated pixel displacement vector fields for tessera 2. 227

Figure 8.4: Sample instantaneous (a) raw and (b) corrected and interpolated pixel displacement vector fields for tessera 3. 228

Figure 8.5: Sample instantaneous (a) raw and (b) corrected and interpolated pixel displacement vector fields for tessera 4. 229

Figure 8.6: Sample instantaneous (a) raw and (b) corrected and interpolated pixel displacement vector fields for tessera 5. 230

Figure 8.7: Sample instantaneous (a) raw and (b) corrected and interpolated pixel displacement vector fields for tessera 6. 231

Figure 8.8: Sample instantaneous (a) raw and (b) corrected and interpolated pixel displacement vector fields for tessera 7. 232

Figure 8.9: Sample instantaneous (a) raw and (b) corrected and interpolated pixel displacement vector fields for tessera 8. 233

Figure 8.10: Sample instantaneous (a) raw and (b) corrected and interpolated pixel displacement vector fields for tessera 9. 234

Figure 8.11: Sample instantaneous (a) raw and (b) corrected and interpolated pixel displacement vector fields for tessera 10. 235

Figure 8.12: Sample instantaneous (a) raw and (b) corrected and interpolated pixel displacement vector fields for tessera 11. 236

Figure 8.13: Sample instantaneous (a) raw and (b) corrected and interpolated pixel displacement vector fields for tessera 12. 237
Figure 8.14: Sample instantaneous (a) raw and (b) corrected and interpolated pixel displacement vector fields for tessera 13. 238
Figure 8.15: Mean velocity vector fields for (a) tessera 14 and (b) tessera 1; individual scale. 239
Figure 8.16: Mean velocity vector fields for (a) tessera 2 and (b) tessera 3; individual scale. 240
Figure 8.17: Mean velocity vector fields for (a) tessera 4 and (b) tessera 5; individual scale. 241
Figure 8.18: Mean velocity vector fields for (a) tessera 6 and (b) tessera 7; individual scale. 242
Figure 8.19: Mean velocity vector fields for (a) tessera 8 and (b) tessera 9; individual scale. 243
Figure 8.20: Mean velocity vector fields for (a) tessera 10 and (b) tessera 11; individual scale. 244
Figure 8.21: Mean velocity vector fields for (a) tessera 12 and (b) tessera 13; individual scale. 245
Figure 8.22: Tessera 14 component of assembled mean velocity vector field mosaic. 246
Figure 8.23: Tessera 1 component of assembled mean velocity vector field mosaic... 247
Figure 8.24: Tessera 2 component of assembled mean velocity vector field mosaic... 248
Figure 8.25: Tessera 3 component of assembled mean velocity vector field mosaic... 249
Figure 8.26: Tessera 4 component of assembled mean velocity vector field mosaic... 250
Figure 8.27: Tessera 5 component of assembled mean velocity vector field mosaic... 251
Figure 8.28: Tessera 6 component of assembled mean velocity vector field mosaic... 252
Figure 8.29: Tessera 7 component of assembled mean velocity vector field mosaic... 253
Figure 8.30: Tessera 8 component of assembled mean velocity vector field mosaic... 254
Figure 8.31: Tessera 9 component of assembled mean velocity vector field mosaic... 255
Figure 8.32: Tessera 10 component of assembled mean velocity vector field mosaic. 256
Figure 8.33: Tessera 11 component of assembled mean velocity vector field mosaic. 257
Figure 8.34: Tessera 12 component of assembled mean velocity vector field mosaic. 258
Figure 8.35: Tessera 13 component of assembled mean velocity vector field mosaic. 259
Figure 8.36: Peak locking error in tessera 1 raw pixel displacement data.......... 260
Figure 8.37: Peak locking error in tessera 2 raw pixel displacement data.......... 261
Figure 8.38: Peak locking error in tessera 3 raw pixel displacement data.......... 262
Figure 8.39: Peak locking error in tessera 4 raw pixel displacement data.......... 263

Figure 8.40: Peak locking error in tessera 5 raw pixel displacement data.......... 264

Figure 8.41: Peak locking error in tessera 6 raw pixel displacement data.......... 265

Figure 8.42: Peak locking error in tessera 7 raw pixel displacement data.......... 266

Figure 8.43: Peak locking error in tessera 8 raw pixel displacement data.......... 267

Figure 8.44: Peak locking error in tessera 9 raw pixel displacement data.......... 268

Figure 8.45 Peak locking error in tessera 10 raw pixel displacement data.......... 269

Figure 8.46: Peak locking error in tessera 11 raw pixel displacement data.......... 270

Figure 8.47: Peak locking error in tessera 12 raw pixel displacement data.......... 271

Figure 8.48: Peak locking error in tessera 13 raw pixel displacement data.......... 272

Figure 8.49: Peak locking error in tessera 14 raw pixel displacement data.......... 273

Figure 8.50: (a-n) The cumulative average, plotted over increasing periods of time and averaging larger batches of PIV data files, of the sum of all turbulent kinetic energy (k) measurements in a tessera, presented for (a) tessera 1 through (n) tessera 14; showing that a sufficient amount of data was collected at each tessera for representative mean turbulent flow characteristics to be calculated.......... 274

Figure 8.51: (a) Dimensional and (b) nondimensional u mean velocities for return surface jet-like (SJL) profiles.......... 279

Figure 8.52: (a) Dimensional and (b) nondimensional v mean velocities for return surface jet-like (SJL) profiles.......... 280

Figure 8.53: (a) Dimensional and (b) nondimensional mean Reynolds stress per unit mass (τ/ρ) for return surface jet-like (SJL) profiles.......... 281

Figure 8.54: (a) Dimensional and (b) nondimensional mean kinetic energy per unit mass (KE) for return surface jet-like (SJL) profiles.......... 282

Figure 8.55: Mean (a) turbulent kinetic energy per unit mass (k) and (b) dissipation per unit mass (d) for return surface jet-like (SJL) profiles.......... 283

Figure 8.56: Mean (a) vorticity (ω) and (b) strain (ε) for return surface jet-like (SJL) profiles.......... 284

Figure 8.57: Mean Kolmogorov (a) length scales (l_k) and (b) velocity scales (v_k) for return surface jet-like (SJL) profiles.......... 285

Figure 8.58: (a) Dimensional and (b) nondimensional u mean velocities for the first transition zone (TZ1) profiles.......... 286

Figure 8.59: (a) Dimensional and (b) nondimensional v mean velocities for the first transition zone (TZ1) profiles.......... 287

Figure 8.60: (a) Dimensional and (b) nondimensional mean Reynolds stress per unit mass (τ/ρ) for the first transition zone (TZ1) profiles.......... 288

Figure 8.61: (a) Dimensional and (b) nondimensional mean kinetic energy per unit mass (KE) for the first transition zone (TZ1) profiles. 289

Figure 8.62: Mean (a) turbulent kinetic energy per unit mass (k) and (b) dissipation per unit mass (d) for the first transition zone (TZ1) profiles. 290

Figure 8.63: Mean (a) vorticity (ω) and (b) strain (ε) for the first transition zone (TZ1) profiles. 291

Figure 8.64: Mean Kolmogorov (a) length scales (l_k) and (b) velocity scales (v_k) for the first transition zone (TZ1) profiles. 292

Figure 8.65: (a) Dimensional and (b) nondimensional u mean velocities for the second transition zone (TZ2) profiles. 293

Figure 8.66: (a) Dimensional and (b) nondimensional v mean velocities for the second transition zone (TZ2) profiles. 294

Figure 8.67: (a) Dimensional and (b) nondimensional mean Reynolds stress per unit mass (τ/ρ) for the second transition zone (TZ2) profiles. 295

Figure 8.68: (a) Dimensional and (b) nondimensional mean kinetic energy per unit mass (KE) for the second transition zone (TZ2) profiles. 296

Figure 8.69: Mean (a) turbulent kinetic energy per unit mass (k) and (b) dissipation per unit mass (d) for the second transition zone (TZ2) profiles. 297

Figure 8.70: Mean (a) vorticity (ω) and (b) strain (ε) for the second transition zone (TZ2) profiles. 298

Figure 8.71: Mean Kolmogorov (a) length scales (l_k) and (b) velocity scales (v_k) for the second transition zone (TZ2) profiles. 299

Figure 8.72: (a) Dimensional and (b) nondimensional u mean velocities for the return flow second transition zone (TZ2) profiles. 300

Figure 5.73: (a) Dimensional and (b) nondimensional v mean velocities for the return flow second transition zone (TZ2) profiles. 301

Figure 8.74: (a) Dimensional and (b) nondimensional mean Reynolds stress per unit mass (τ/ρ) for the return flow second transition zone (TZ2) profiles. 302

Figure 8.75: (a) Dimensional and (b) nondimensional mean kinetic energy per unit mass (KE) for the return flow second transition zone (TZ2) profiles. 303

Figure 8.76: Mean (a) turbulent kinetic energy per unit mass (k) and (b) dissipation per unit mass (d) for the return flow second transition zone (TZ2) profiles. 304

Figure 8.77: Mean (a) vorticity (ω) and (b) strain (ε) for the return flow second transition zone (TZ2) profiles. 305

Figure 8.78: Mean Kolmogorov (a) length scales (l_k) and (b) velocity scales (v_k) for the return flow second transition zone (TZ2) profiles. 306

Nomenclature

A	solid body rotation eddy area
b_o	slot width at gate
d	mean dissipation rate per unit mass
d_{px}	PIV pixel displacement vector
d_{pxx}	x-component PIV pixel displacement
d_{pxy}	y-component PIV pixel displacement
d_{pxz}	z-component pixel displacement (out-of-plane displacement)
e_u	error in x- or y-component velocity
e_V	error in total velocity
e_ω	error in vorticity
F	Froude number, $F = U_o / \sqrt{gb_o}$
g	acceleration due to gravity
h	baffle height
I_{plu}	peak locking intensity of d_{pxx}
I_{plv}	peak locking intensity of d_{pxy}
k	mean turbulent kinetic energy per unit mass
k_i	instantaneous turbulent kinetic energy per unit mass
KE	mean kinetic energy per unit mass
KE_i	instantaneous kinetic energy per unit mass
l_k	mean Kolmogorov length scale
m	mean momentum flux per unit mass, $m = \int_{n=\delta_{2-}}^{n=\delta_{+}} u^2 dn$
m_o	mean momentum flux per unit mass at gate
M_o	momentum flux at the outlet for a plane turbulent jet, $M_o = 2\rho b_o U_o^2$
n	sectional coordinate normal to θ_c measured from local jet centreline in the outbound direction
p	mean pressure
p_i	instantaneous pressure
q	mean discharge intensity, $q = \int_{n=\delta_{2-}}^{n=\delta_{+}} u \, dn$
q_e	entrainment intensity
q_o	discharge intensity at gate
Q_o	mean discharge at gate
r	solid body rotation eddy radius
R	Reynolds number, $R = b_o U_o / \nu$

s	axial coordinate along jet centreline trajectory measured from slot
S_{FOV}	image scale
t	time
t_k	mean Kolmogorov time scale
u_i	instantaneous x- and s-component velocities
u	mean x- and s-component velocities
u'	turbulent x- and s-component velocities
U_o	mean jet exit velocity
U_m	maximum mean axial velocity at jet section
v_i	instantaneous y- and n-component velocities
v	mean y- and n-component velocities
v'	turbulent y- and n-component velocities
v_e	mean entrainment velocity component
v_k	mean Kolmogorov velocity scale
V	voltage
$V_{i\,max}$	maximum instantaneous velocity magnitude
V_{max}	maximum mean velocity magnitude
V_{min}	minimum mean velocity magnitude
w_i	instantaneous z-component velocity
w	mean z-component velocity
w'	turbulent z-component velocity
x	global Cartesian longitudinal coordinate measured from gate
x_o	longitudinal position of the baffle, measured from gate
y	global Cartesian normal coordinate measured from bed
y_1	depth upstream of gate in head tank
y_2	depth immediately downstream of gate
y_t	tailwater depth
z	global Cartesian orthogonal to x and y
α_e	entrainment coefficient
δ_{1+}	jet half-width along positive section n-stem, where $u = 0.5U_m$
δ_{1-}	jet half-width along negative section n-stem, where $u = 0.5U_m$
δ_{2+}	distance from local jet centreline to jet boundary along positive section n-stem, where $u = 0$

δ_{2-}	distance from local jet centreline to jet boundary along negative section n-stem, where $u = 0$
Δt	time separation
ΔH	driving head of the jet, $\Delta H = y_1 - y_2$
ε	mean strain
ε_i	instantaneous strain
γ	specific weight of water
Γ	mean circulation, $\Gamma = \int \omega \, dA$
η	nondimensional jet section ordinate, $\eta = n/\delta_1$
μ	viscosity of water
ν	kinematic viscosity of water, $\nu = \mu/\rho$
ξ	nondimensional jet centreline trajectory ordinate, $\xi = s/b_o$
ω	mean vorticity in the x-y plane, counter-clockwise considered positive
ω_i	instantaneous vorticity in the x-y plane, counter-clockwise considered positive
θ	displacement or velocity vector angle
θ_c	angle of mean velocity vector at jet centreline
ρ	mass density of water
σ_{pxx}	standard deviation of d_{pxx}
σ_{pxy}	standard deviation of d_{pxy}
τ	mean Reynolds shear stress, $\tau = \tau_{xy} = -\rho \overline{u'v'}$
τ_i	instantaneous Reynolds shear stress
τ_o	wall shear stress

1 Introduction

The topic of this current work is motivated by the study of Wu and Rajaratnam (1995a) on the effect of baffles on submerged flows. Therein, the authors conceptualize the submerged hydraulic jump as an energy dissipator and describe the limitations encountered when tailwater depths are larger than subcritical sequent depths in such flows. It is suggested that the employment of submerged jet flows as energy dissipators is generally avoided in civil engineering practice; attributed to the concern that high-velocity streams may continue for relatively large distances along a riverbed without appreciable dissipation and thereby cause serious downstream erosion. This erosion can damage native fish and wildlife river ecosystems as well as endanger the foundations of hydraulic structures and adjacent public works.

It is also suggested that the provision of baffle walls in these types of submerged flows may attenuate the risk of bed degradation and erosion. Introduced by Wu and Rajaratnam is the instance of the deflected wall jet, the flow structure in which a baffle wall is employed to deflect a plane wall jet in such a way that it travels upward as a plane turbulent jet to eventually become a plane surface jet at the free surface. Wu and Rajaratnam propose that such a deflected wall jet can dissipate energy similarly to a deeply submerged hydraulic jumps without the associated erosion risks under certain conditions. A video still obtained from a dye visualization test of the plane deflected wall jet is shown in Figure 1.1. It is this flow that is presently studied.

The velocity and pressure data assembled by Wu and Rajaratnam is time averaged in nature and was collected using standard Prandtl tube point measurement techniques. Although a wealth of information concerning both the mean flow structure and velocity similarity configurations are presented by the authours, there currently exists no detailed mean or turbulent data set describing the whole flow field of the deflected wall jet.

This study aims to remedy the deficiency by employing the particle image velocimetry (PIV) technique in a limited experimental investigation of the phenomenon. The specific PIV arrangement is quite non-standard. It divides a large flow field in to individual tesserae, which are imaged and processed separately. The resulting data sets are then assembled into a final mosaic fully describing the experimental area of interest, providing greater spatial and velocity resolution than could be achieved by studying the mosaic as a whole. The measurement programme and analyses presented in the current work provide original instantaneous, mean and turbulent data including but not limited to: velocity, Reynolds stress, vorticity and turbulent kinetic energy.

The structure of this thesis follows the progression of the theoretical investigation, the experimental programme and the analysis of resultant data. A detailed literature review is found in §2 that considers the theory of plane turbulent jets. It focuses, in particular, on the classic plane jet, but considers also the plane jet in a crossflow, the plane wall jet and the plane surface jet, as these are the constitutive elements of the deflected plane wall jet, as outlined by Wu and Rajaratnam (1995a). The experimental methods of the investigation are outlined in §3. This includes a brief outline of PIV methodology and follows with a description of the flume arrangement, the PIV instrumentation setup and the measurement programme. Details of the primary PIV processing and supplementary computations are presented in §4, along with sources of error. Analysis of the resultant data is presented in §5, as well as concurrent discussions regarding the findings of this research and its relationship to the current state of knowledge on the subject. Conclusions and recommendations for future work are given in §6. References are provided in §7 and the appendix is §8.

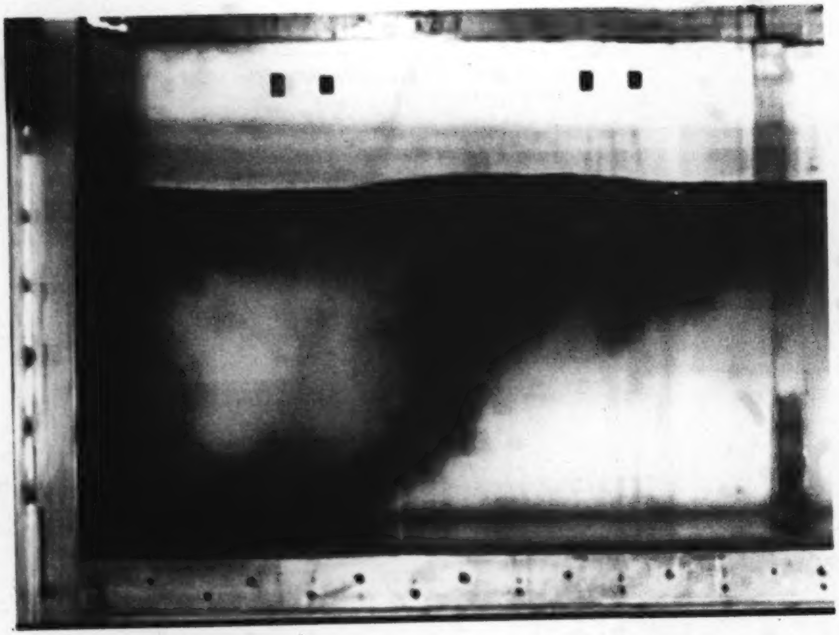

Figure 1.1: Dye visualization still of the plane deflected wall jet.

2 Literature Review

Because the plane turbulent deflected wall jet has plane jet-like, wall jet-like and surface jet-like constitutive elements, condensed reviews of the current states of knowledge on these subjects are presented below. More consideration will be given to the plane jet as the other cases may be considered as special cases of the plane jet, and analyses are similar. An excellent review of jet theory, and especially that of a plane and wall jets, is presented by Rajaratnam in the book *Turbulent Jets* (1976), and it is from this volume that a great portion of the following discussion is derived.

2.1 Plane Turbulent Jets

2.1.1 Classic Plane Jet

The classic plane turbulent jet (also called simply the plane jet) can be considered as a jet of either water or air issuing from a plane nozzle into a large body of an identical fluid, with the slot width at the upstream gate defined as $2b_0$, the mean jet exit velocity defined as U_0 and the mean jet discharge defined as Q_0. In such a configuration, the origin of the Cartesian coordinate system is located at the centreline of the issuing jet and at the downstream edge of the slot, with x being the coordinate measured from the gate in the direction of the jet axis, y being the coordinate measured normal to x in the direction of the plane surface and z being the third axis of the coordinate system orthogonal to the others. The two-dimensionality of the plane jet results in a plane of symmetry coincident with the x-z plane and hence normal to the slot at the upstream gate. Figure 2.1 shows the definition sketch of this type of plane turbulent jet.

The fluid discharged from the gate opening may be assumed to be of relatively constant mean velocity, with a pronounced velocity discontinuity between the jet and the surrounding fluid both above and below the body of the jet (Albertson *et al.* 1950). The eddies generated in this region of high shear will immediately result in a lateral mixing process whereby the kinetic energy of the oncoming flow is steadily converted into turbulence, with the latter steadily decaying through viscous shear. Due to the turbulent nature of the mixing region, the fluid within the jet undergoes both lateral diffusion and deceleration, with fluid from the surrounding area being brought into motion or entrained into the body of the jet. Thus the deceleration of the fluid in the jet is accompanied by a simultaneous acceleration of the surrounding fluid, resulting in both an increase in jet width and discharge intensity (q) at successive sections of the jet with distance from the efflux section and origin.

The mean flow of the plane jet can be divided into two distinct regions of developmental stability: the developing flow region and the fully developed flow region. In the first region, nearest to the efflux section, the jet begins with a near-uniform velocity distribution of $u = U_0$. Turbulence generated by each of the shear layers bounding the plane jet penetrate both outwards and inwards, both away from and toward the plane of symmetry of the jet. A wedge-like region of undiminished mean velocity equal to U_0 can be found between the successively closer turbulent fronts propagating towards the plane of symmetry, as shown in Figure 2.2. This zone is called the potential core and has a length of approximately $12b_o$ measured from the origin (Rajaratnam 1976). Its presence defines the developing flow region; that is, the limit of this zone of flow establishment is reached when the mixing region has penetrated to the centreline of the jet and there is no longer any province where U_o exists unchanged.

The second region is characterized by the lack of a potential core and by the establishment of dynamic similarity whereby the diffusion process and the growth of the jet continue without essential change in character. In this fully developed flow region, further entrainment of the surrounding fluid by the expanding eddy region is balanced inertially by a continuous reduction in the velocity of the entire body region (Albertson *et al.* 1950) of the jet. It is here that the most interesting relationships between the various parameters of the plane turbulent jet can be and historically have been identified and compared. In this region it is noted that at each section taken along the trajectory, the axial component velocity u decreases continuously from a maximum U_m at the jet centreline to a zero value with distance away from the central axis. Two points of interest are defined in such velocity profiles: the point at which the mean velocity is equal to half of the maximum velocity, where $u = 0.5U_m$, and the point at which the velocity is equal to zero, where $u = 0$. The first location is defined as the jet half-width δ_1 and the second is defined as the jet width δ_2.

The similarity of the u profiles at various longitudinal sections on the x-axis when the flow is completely established can best be observed when the profiles are non-dimensionalized and collapsed onto each other. The standard non-dimensionalizing quantities are called the velocity scale and the length scale, and are defined respectively as U_m and δ_1. Plotting u/U_m against $\eta = y/\delta_1$ for different longitudinal sections yields velocity distributions that fall on one common geometric curve. They are thus said to be similar, exhibiting a strong relationship of the form $u/U_m = f(\eta)$.

In order to study the similar velocity distributions found in the fully developed region, it is advantageous to investigate the phenomenon from an analytical standpoint and develop the equations of motion for the plane turbulent jet. Following the procedure and logic outlined by Rajaratnam (1976), one accepts the decomposition of velocity and pressure terms into mean and fluctuating components and begins with the three dimensional Reynolds equations and the continuity equation for incompressible flow. Presuming the flow to be both steady and completely two dimensional, terms including time derivatives or w-component velocities and derivatives are dropped from the equations. Further reductions to the equations are made following the observation that u is generally much larger than v in a large portion of the jet and that both the velocity and pressure gradients are much smaller in the x-coordinate direction that the y-coordinate direction. After equation rearrangement, a final assumption of the pressure gradient in the axial direction being negligibly small is made (assuming a simple hydrostatic pressure distribution), resulting in the well-known equations of motion for the plane jet:

$$u\frac{\partial u}{\partial x}+v\frac{\partial u}{\partial y}=\frac{1}{\rho}\frac{\partial \tau}{\partial y} \qquad [2.1]$$

$$\frac{\partial u}{\partial x}+\frac{\partial v}{\partial y}=0 \qquad [2.2]$$

where u, v and w are the mean component velocities in the x-, y- and z-directions, respectivey, and τ is the mean Reynolds shear stress.

Further theoretical analyses can be performed with the above equations in order to better understand the mean flow of the plane jet. Approaches have been developed in which the equations of motion are integrated across the jet and conservation integrals for momentum, energy and volume derived (Kotsovinos 1975). Rajaratnam derives the integral momentum equation by multiplying equation [2.1] by ρ and integrating across y. Employing our assumption on the nature of the velocity distribution at different jet sections and from considerations of symmetry, the remaining equation can be expressed as:

$$\frac{d}{dx}\int_0^\infty \rho u^2 dy=0 \qquad [2.3]$$

This equation indicates that the rate of change of momentum flux in the x-direction is zero and that therefore the momentum flux, $M_o = 2\rho b_o U_o^2$, should be conserved. The momentum flux is an important physical quantity controlling the behaviour of the plane jet. It effectively replaces the individual values of b_o and U_o in any similarity analysis and indicates that, for a given value of M_o, the same jet behaviour is obtained for different combinations of b_o and U_o (Rajaratnam 1976). A parallel analysis of the energy flux, performed by multiplying equation [2.1] by ρu and integrating over y yields the following equation, indicates that the rate of decrease of the kinetic energy flux is equal to the rate at which turbulence is produced, supporting the assertion that the mixing action of the jet converts kinetic energy into turbulence which is ultimately dissipated:

$$\frac{d}{dx}\int_0^\infty \frac{\rho u^2}{2} u\,dy=-\int_0^\infty \tau\frac{\partial u}{\partial y}dy \qquad [2.4]$$

Rajaratnam (1976) also derives the volume flux integral equation and discusses the entrainment hypothesis originally introduced by Morton *et al.* (1956) relating to the plane turbulent jet. Here, the discharge intensity at any section of the jet is defined as twice the integral of u from $y=0$ to $y=\infty$ and the rate of change of q with longitudinal distance from the gate can be obtained from integration of equation [2.2] and finally written as:

$$\frac{dq}{dx} = \frac{d}{dx}\int_{-\infty}^{\infty} u\,dy = -v_e \qquad [2.5]$$

where v_e is the entrainment velocity magnitude component, representing the velocity magnitude of the fluid being brought into the jet. The entrainment velocity could also be expressed as $-v_e = \alpha_e U_m$, with α_e representing the entrainment coefficient. As explained earlier, the jet entrains a considerable amount of the surrounding fluid as it moves forward. If momentum is considered to be conserved, it would follow that there should be no axial component to the entrainment velocity, however, Heskestad (1965) has reported that the flow near the edge of the jet enters the jet at angles in excess of normal to the x-axis. This indicates that momentum is not actually conserved and that the assumptions used in the determination of equation [2.3] are imperfect. Kotsovinos (1978) notes a loss of $0.2M_o$ in the momentum flux of a plane jet approximately $100b_o$ downstream of the origin and presents an equation describing the variation.

Regardless, from dimensional considerations of the three flux integrals and the Reynolds and continuity equations it is possible to present general proportionalities describing the decay of the maximum mean centreline velocity, the jet growth rate, and the increase of the jet discharge intensity in the context of the velocity distribution relationship $u/U_m = f(\eta)$ noted earlier. Substitution and rearrangement suggest that $U_m \propto 1/\sqrt{x}$, that $\delta_1 \propto x$ and that $v_e \propto U_m$. Further dimensional analysis (Rajaratnam 1976) produces the following three semi-empirical equations with the coefficients C_1, C_2 and C_3 requiring evaluation with experimental data:

$$\frac{U_m}{U_o} = \frac{C_1}{\sqrt{x/b_o}} \qquad [2.6]$$

$$\delta_1/b_o = C_2\left(x/b_o\right) \qquad [2.7]$$

$$q/q_o = C_3\sqrt{x/b_o} \qquad [2.8]$$

There exists a long history of experimental and mathematical studies performed to give explanation and prediction to the velocity distribution in the plane turbulent jet. Tollmien (1926) and Görtler (1942) each produced theoretical approximations to the similarity curve by substituting varying hypothetical relations between shear stress and velocity gradients based on the equations of Prandtl (concepts such as mixing length and eddy viscosity) in the simplified equations of motion. Förthmann (1934) and Reichardt (1941) both collected extensive data sets of mean flow properties that adequately validated the previous semi-empirical solutions. Reichardt derived a solution similar to those of Tollmien and Görtler by instead using a thermal conduction analogy as the shear stress substitution in the equations of motion while Zijnen (1958) showed that the velocity distribution could be satisfactorily represented by a Gaussian curve. Corrsin (1943) noted certain shortcomings of the hypotheses used by Tollmien and Görtler (reported by Albertson *et al.* 1950 and by Miller and Comings 1957) and confirmed the insensitivity of their velocity functions to their employed closure relationships when he conducted detailed measurements of the turbulence within two dimensional jets. Additional detailed mean and turbulent data was collected by Albertson *et al.* (1950), Miller and Comings (1957), Zijnen (1958), Heskestad (1965) and Goldshmidt and Eskinazi (1966) and supplementary solutions were presented by them.

The resulting wealth of theoretical arguments, experimental data and semi-empirical solutions have lead to a refined set of functions which describe most of the experimenta data accurately. It can be noted that Tollmein's solution appears to provide a better fit in the outer region of the velocity profile while Görtler's solution appears superior near the jet axis. The following solution of Reichardt provides a good general fit (Goldshmidt and Eskinazi 1966) and is considered a suitable $f(\eta)$ approximation:

$$u/U_m = e^{-0.693\eta^2} \tag{2.9}$$

Rajaratnam (1976) reports that due to the imprecise methods of locating the virtual origin of plane jets, it can be taken as coincident with the origin described earlier. In fact, most of the solutions historically presented can be reworked in forms of equations [2.6], [2.7] and [2.8] and coefficients compared. The following are accepted coefficient values: $C_1 = 3.50$, $C_2 = 0.1$ and $C_3 = 0.44$, with $\alpha_e = 0.053$ obtained from equation [2.5], as reported by Rajaratnam. They result in the following formulae:

$$\frac{U_m}{U_o} = \frac{3.50}{\sqrt{x/b_o}} \tag{2.10}$$

$$\delta_1 = 0.1x \tag{2.11}$$

$$q/q_o = 0.44\sqrt{x/b_o} \tag{2.12}$$

$$v_e = -0.053U_m \tag{2.13}$$

2.1.2 Plane Jet in a Crossflow

Consider a plane turbulent jet issuing into a body of fluid which has a uniform velocity, and orient the jet and slot so that the jet exit velocity is normal to the uniform velocity. This flow is shown in Figure 2.3 and describes the case of a plane turbulent jet in a crossflow. The initial characteristics of the such a jet are identical to those of the plane jet: the slot width is defined as $2b_o$, the mean jet exit velocity as U_o and the mean jet discharge as Q_o. The origin of the global Cartesian coordinate system is located at the centreline of the jet at efflux section, with x measured from and normal to the gate, y measured normal to x and in the direction of flow in the surrounding fluid body, and x orthogonal to both the x- and y-coordinate axes. There is, however, no plane of symmetry. The trajectory of the jet centreline is curved in nature and therefore not coincident with the x-axis; it defines the local coordinate system through which the plane jet in a crossflow can be studied and is defined by the locus along which the maximum mean axial jet velocity U_m exists. This frame of reference shares its origin with the global frame, but considers the s-coordinate axis (defined by the trajectory), θ_c (defined as the angle between U_m and the x-axis) and the n-coordinate axis (defined as normal to θ_c in the outbound direction) as seen in the provided figure.

For reasons which will be obvious in §2.4, it becomes convenient to neglect a detailed fluid mechanical analysis of the plane jet in a crossflow. The significant observation taken from the current literature is that there exists a similarity in velocity profiles taken at different sections along the s-axis in the developed flow region that can be approached in a manner comparable to that in §2.1 and that growth rate of the jet is non-symmetrical (Yu-Leuk and Wood 1966). As such, let δ_{1+} and δ_{2+} define the jet half-width and jet width along the positive (outbound) section n-stem, where $u = 0.5U_m$ and $u = 0$ respectively, and let δ_{1-} and δ_{2-} define the same values along the negative (inbound) section n-stem. Likewise, the dual length scales are defined as δ_{1+} and δ_{2+} with the velocity scale as U_m.

2.2 Plane Turbulent Wall Jets

The classic plane turbulent wall jet (also called simply the wall jet) can be considered as a jet of either water or air issuing from a plane nozzle tangentially onto a flat plate or bed that is submerged in a semi-infinite body of an identical fluid. The slot width at the upstream gate is defined as b_o, the mean jet exit velocity defined as U_o and the mean jet discharge defined as Q_o, much like the definitions applied to a plane jet. In such a configuration, the origin of the Cartesian coordinate system framing the flow is located on the bed and at the downstream edge of the slot. The x-coordinate is measured from the gate in the direction of the jet axis, with the y-axis taken normal to the x-axis towards the free surface and with the z-axis of the coordinate system orthogonal to both the x- and y-coordinate axes. Figure 2.4 shows the definition sketch of plane turbulent wall jet.

The behaviour of the fluid and the mean characteristics of the jet as it exits the outlet closely resemble those of the plane jet. In both cases a shear layer is formed where the velocity discontinuity exists, there is the presence of a potential core and therefore there is both a developing and a fully developed flow region to the body of the jet. The surrounding fluid is likewise also entrained into the mixing region of the wall jet. Like the plane jet, the length of the developing region of a plane wall jet is also equal to approximately $12b_o$, as measured from the coordinate system origin (Rajaratnam 1965a). However, unlike the former, this flow is not symmetrical about the x-z plane, nor can its virtual origin be considered coincident with the coordinate system origin. It is, in fact, located approximately $10b_o$ upstream of the global origin (Rajaratnam 1976). The reason for the differences is obvious: the presence of the bed. Instead of two shear layers propagating both toward and way from each other in an axisymmetrical manner, there is a growing free-mixing region on one side and a boundary layer of thickness δ on the other.

Overlooking the boundary layer and the slightly different mechanisms by which the potential core of the plane turbulent wall jet is consumed, the wall jet presents itself surprisingly similar to the upper half of the plane turbulent jet. It is defined with via a corresponding logic. In the fully developed flow region, it is noted that at each section taken along the trajectory, the axial component velocity u decreases continuously from a maximum U_m where $y = \delta$ to a zero value some distance above the bed. The two main locations of interest in such velocity profiles are defined like those in the plane jet: the point at which the mean velocity is equal to half of the maximum velocity, where $u = 0.5\,U_m$ with the caveat $\partial u/\partial y < 0$, and the point at which the velocity is equal to zero, where $u = 0$ with that same caveat. The first location is defined as the jet half-width δ_1 and the second is defined as the jet width δ_2.

Similarity of the u profiles at various sections along the x-axis (when the flow is completely established) is observed when the profiles are non-dimensionalized and superposed. The velocity scale and length scales are taken as U_m and δ_1, respectively. Plotting u/U_m against $\eta = y/\delta_1$ for different longitudinal sections yields a common similarity curve of the form $u/U_m = g(\eta)$.

Following closely the arguments presented in §2.1 and again neglecting the effects of any longitudinal pressure gradient, it can be shown that the simplified equations of motion for the plane turbulent wall jet are as follows:

$$u\frac{\partial u}{\partial x} + v\frac{\partial u}{\partial y} = \nu\frac{\partial^2 u}{\partial y^2} + \frac{1}{\rho}\frac{\partial \tau}{\partial y} \qquad [2.14]$$

$$\frac{\partial u}{\partial x} + \frac{\partial v}{\partial y} = 0 \qquad [2.15]$$

The momentum, energy and volume fluxes can be similarly produced, integrated and manipulated. This process introduces the wall shear stress τ_o as an important term, and it becomes clear that the friction at the wall is a decisive agency that must be given a prominent place in any theory of the turbulent plane wall jet (Glauert 1956). Coupled with the same type of dimensional analysis used in the analysis of the plane jet, the relationships $U_m \propto 1/\sqrt{x}$, that $\delta_1 \propto x$, $\tau_o \propto 1/x$ and $v_e \propto U_m$ are suggested Rajaratnam (1976). Theoretical arguments and experimental observations have been given by Förthmann (1934), Glauert (1956), Sigalla (1958), Schwartz and Cosart (1961), Myers *et al.* (1963), Verhoff (1963), Rajaratnam (1965a-c), Rajaratnam and Subramanya (1967 and 1968) and Wu and Rajaratnam (1995b). In his summary of the works completed previous to 1976, Rajaratnam reports the following formulae as describing the turbulent plane wall jet:

$$u/U_m = 1.48\eta^{1/7}\left[1 - \mathrm{erf}(0.68\eta)\right] \qquad [2.16]$$

$$\frac{U_m}{U_o} = \frac{3.50}{\sqrt{x/b_o}} \qquad [2.17]$$

$$\delta_1 = 0.068x \qquad [2.18]$$

$$q/q_o = 0.248(x/b_o) \qquad [2.19]$$

$$v_e = -0.035U_m \qquad [2.20]$$

2.3 Plane Turbulent Surface Jets

A plane turbulent surface jet can be observed as a fluid jet of thickness b_o issuing from a slot into a semi-infinite body or large channel of an identical stagnant fluid, where the jet enters tangentially to the free surface and the bed of the channel is at such a depth as to hold no influence over the behaviour of the jet. There exists a near-uniform mean velocity as the jet issues into the body of fluid defined as U_o and a mean discharge defined as Q_o. This describes the plane turbulent surface jet. In such a configuration, the origin of the Cartesian coordinate system framing the flow is located at the water surface and at the downstream edge of the slot. The x-coordinate axis is measured from the gate in the direction of the plane surface jet flow, with the y-coordinate axis taken normal to the x-axis toward the bed and with the z-coordinate axis orthogonal to both the x- and y-coordinate axes. Figure 2.5 shows the definition sketch of the plane turbulent surface jet.

If one were to mirror this two-dimensional flow about its x-axis, it would very closely resemble to upper half of the plane jet of §2.1 or the plane wall jet of §2.2. A number of parallels can be drawn from the previous reviews. On the underside of the surface jet a shear layer is formed due to the velocity discontinuity between the jet and the ambient into which it enters. Surrounding fluid is entrained into the body of the jet. There exists a potential core that is consumed when the mixing region of the shear layer eventually reaches the surface, as well as developing (approximately $12b_o$ in length measured from the origin) and fully developed flow regions. As is the case for the plane wall jet, the virtual origin of the plane turbulent surface jet is located approximately $10b_o$ behind the global Cartesian origin.

In the fully developed flow region, the axial component velocity u is at its maximum U_m very near to the water surface and smoothly decreases to zero at some distance below. Important characteristic locations and scales along velocity profiles taken at various sections on the x-axis are defined as those of the plane jet. The jet half-width δ_1 is defined where the mean velocity is equal to half of the maximum velocity and the jet width is defined where the velocity is equal to zero. Similarity of the u profiles at various sections along the x-axis is observed when u/U_m is plotted against $\eta = y/\delta_1$ for different longitudinal sections, with the mean velocity relationship expressed in the form $u/U_m = h(\eta)$. Rajaratnam and Humphries (1984) report that equation [2.9], $u/U_m = e^{-0.693\eta^2}$, adequately describes both their own data and that of Vanvari and Chu (1974) for $\eta < 1.4$. Following closely the arguments and assumptions presented in §2.1, it can be shown that the simplified equations of motion for the plane turbulent surface jet are equations [2.1] and [2.2] and that the relationships $U_m \propto 1/\sqrt{x}$, $\delta_1 \propto x$ and $v_e \propto U_m$ are valid through flux integral analysis and dimensional considerations. The following equations describing the mean flow of the plane turbulent surface jet are reported by Rajaratnam and Humphries (1984):

$$\frac{U_m}{U_o} = \frac{3.10}{\sqrt{x/b_o}} \qquad [2.21]$$

$$\delta_1 = 0.09x \qquad [2.22]$$

$$v_e = -0.037U_m \qquad [2.23]$$

More recent studies, including those by Swean *et al.* (1989) and Ead and Rajaratnam (2001), provide additional experimental data of more jets with finite depths of tailwater and adverse pressure gradients, and analyses attacking the acknowledged decay of momentum flux in jets which entrain fluid.

2.4 Plane Turbulent Deflected Wall Jets

Consider a supercritical plane jet of water issuing into a rectangular channel filled with a identical fluid, where the jet nozzle is set tangentially to the flume bed and a baffle of height h is placed on the bed at a distance of x_o from the outlet. The baffle extends across the entire width of the channel and is oriented perpendicular to the channel side walls. The slot width at the upstream gate is defined as b_o and the mean jet exit velocity is defined as U_o. The jet discharge is defined as Q_o. Consider the origin of the coordinate system as located on the bed and at the downstream edge of the slot. The x-axis is measured from the gate in the downstream direction, the y-axis is taken normal to the x-axis towards the water surface and the z-axis is orthogonal to both x and y. The water level upstream of the gate is called y_1 and the level immediately downstream is called y_2, with the tailwater called y_t. The driving head of the jet is expressed as $\Delta H = y_1 - y_2$.

The plane deflected wall jet is observed if the jet behaves like a plane wall jet upstream of the baffle, where it is deflected and travels upward, behaving as a curved plane turbulent jet, with a return flow between the inbound face of the jet and the gate, and eventually behaves like a plane surface jet at the water surface. This return flow is defined by the axial velocity profiles passing through zero at some sectional ordinate and having negative axial velocities past that ordinate, and occurs as a result of the effective jet confinement. It is similar to actual experimental data, such as in the submerged flow in a sluice way (Rajaratnam 1965a) or in the flow of a plane surface jet in shallow tailwater (Ead and Rajaratnam 2001). Figure 2.6 shows both the mean flow pattern of and the definition sketch for the plane turbulent wall jet.

It is mentioned in §1 that Wu and Rajaratnam (1995a) discuss the submerged hydraulic jump as an energy dissipator. The authors note that although submerged jumps are well understood phenomena, they are not commonly used in practice, for fear of serious bed erosion under sub-optimal tailwater level conditions. As an alternative, Wu and Rajaratnam employ a baffle wall in a configuration physically identical to the one described above, and study the effects of the baffle on the submerged plane jet flow. Their experiments were performed in a flume 7.60 m long, 0.466 m wide and 0.60 m deep with varying baffle heights, baffle positions, tailwater levels, and Froude numbers. Wu and Rajaratnam measured time-averaged velocities and pressures using both pitch probes and Prandtl tubes connected to either transducers or manometer boards.

Their experiments identify two possible flow states: the first being that described earlier, of a plane turbulent deflected wall jet (defined by Wu and Rajaratnam as the deflected surface jet) having wall jet-like (WJL), plane jet-like (PJL) and surface jet-like (SJL) constitutive elements; and the second being that of a stable reattached wall jet, where the main flow passes over the baffle and reattaches to the bed of the flume. In the case of the deflected wall jet, three eddies are observed. They are positioned in relation to the centreline of the jet (defined by the locus of the maximum velocity filament) and the baffle. There first exists a large eddy of clockwise rotation on the outbound side of the curved jet extending to the downstream end of the flume. Second is an eddy of counter-clockwise rotation and significant circulation (Wu and Rajaratnam 1995a) bounded by the upstream flume gate and the jet centreline. There thirdly exists a small eddy of clockwise rotation upstream of the baffle and below the jet centreline, with a diameter of the same order as h. A reference curve was produced by plotting x_o/y_t against h/y_t which identifies the stable reattaching and stable deflected wall jet regimes as well as a transition region where the jet oscillates between the two stable patterns.

Further experiments were conducted by Wu and Rajaratnam on the deflected wall jet case with mean u and v velocity profiles taken at various stations along the length and height of the flow. Analysis was performed parallel to either wall jet or surface jet theory, with no distinction made when the jet is plane jet-like. In the main flow region before the baffle (wall jet-like) it was found that the velocity profiles are similar and well represented by the equations of §2.2. It is reported that the growth rate of the length scale δ_1 is not greatly affected by the presence of the baffle until the jet gets very close to the baffle and that the velocity scale U_m decays in the familiar manner. The curved plane jet-like region begins approximately at $x = x_o$ and it is here that deviation is noted: there is a rapid decrease in U_m that reaches a minimum near where the jet trajectory approaches the free surface and there is enhanced entrainment due to the curved nature of the jet in this region. In the main flow region downstream of the point where the jet centreline reaches the free surface (plane jet-like) Wu and Rajaratnam observe that velocity profiles are similar but somewhat different than given in §2.3. The length scale has a growth rate smaller than for the classic plane surface jet and is approximately $2b_o$ at the upstream limit of the region. Maximum velocity decay occurs as it would for a surface jet that is located upstream of the gate.

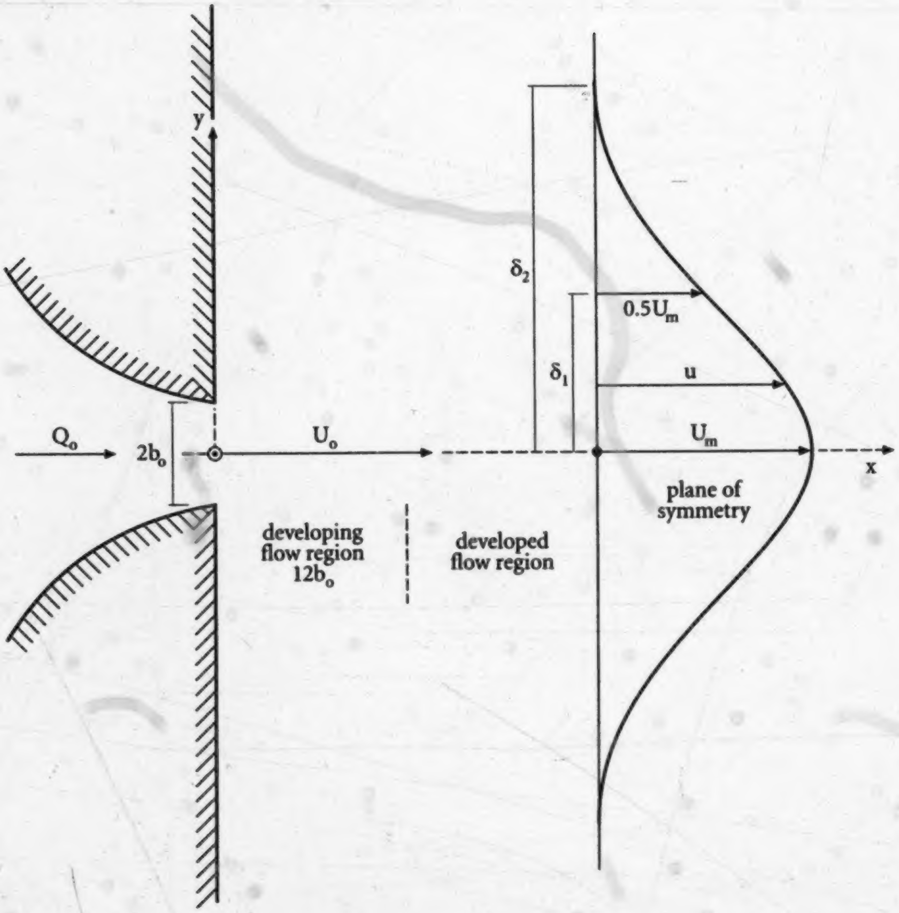
y
δ_2
0.5U$_m$
δ_1
u
Q$_o$
2b$_o$
U$_o$
U$_m$
x
plane of symmetry
developing flow region 12b$_o$
developed flow region

Figure 2.1: Plane turbulent jet definition sketch.

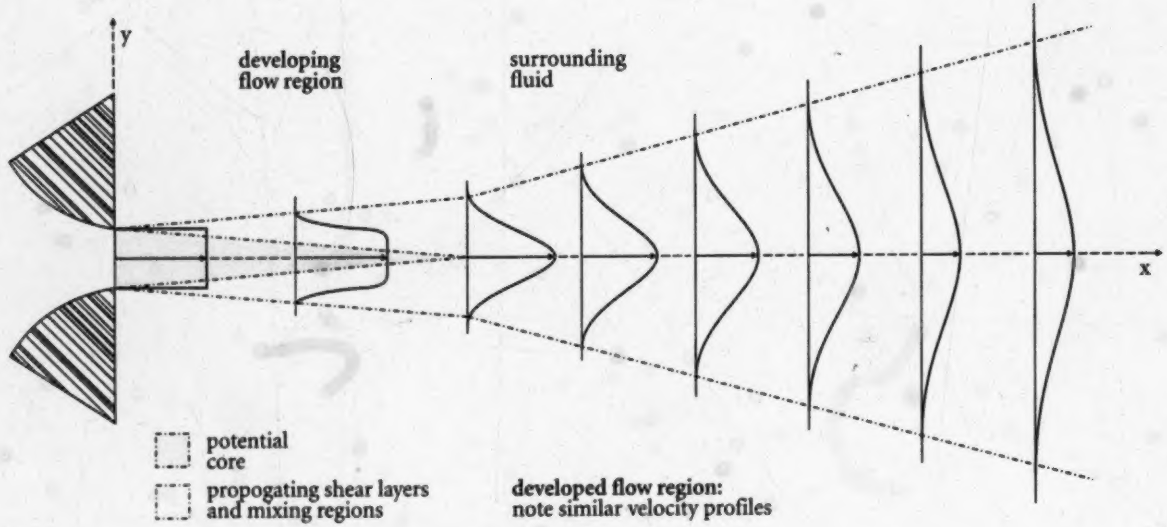
y
developing
flow region
surrounding
fluid
x
potential
core
propogating shear layers
and mixing regions
developed flow region:
note similar velocity profiles

Figure 2.2: Plane turbulent jet potential core and development sketch.

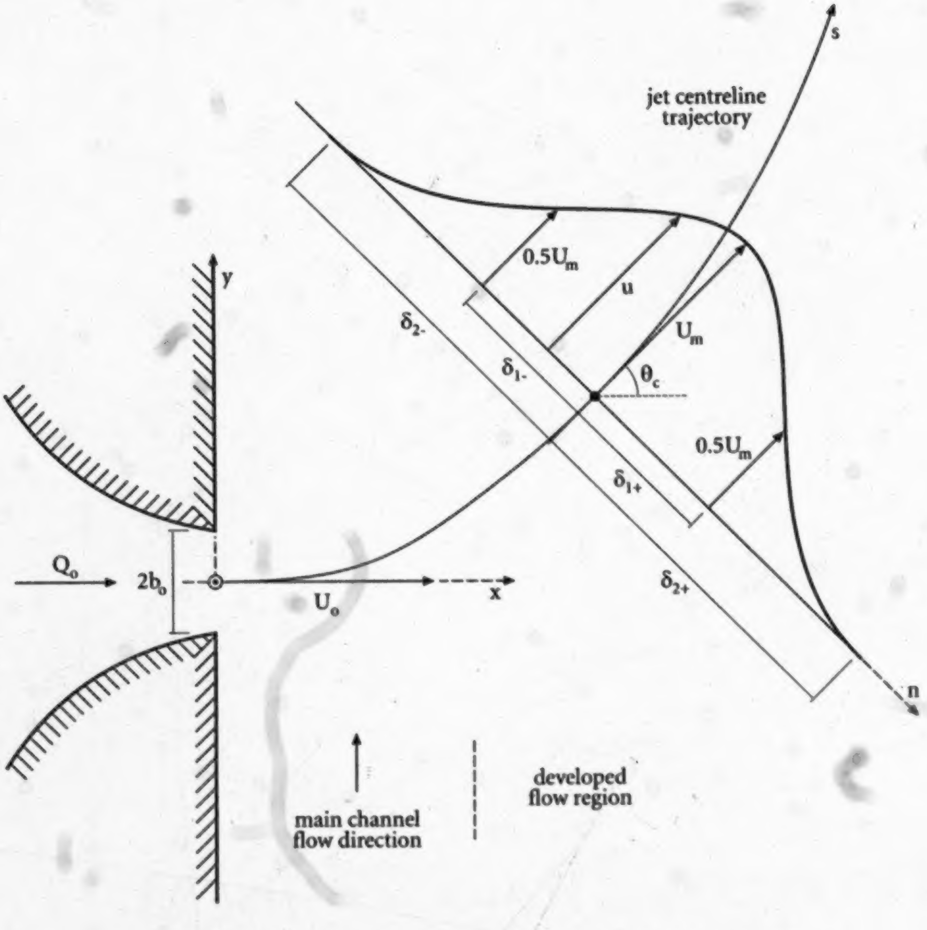
s
jet centreline trajectory
0.5U_m
u
U_m
θ_c
δ_2-
δ_1-
δ_1+
δ_2+
0.5U_m
n
y
Q_o
2b_o
U_o
x
main channel flow direction
developed flow region

Figure 2.3: Plane turbulent jet in a crossflow definition sketch.

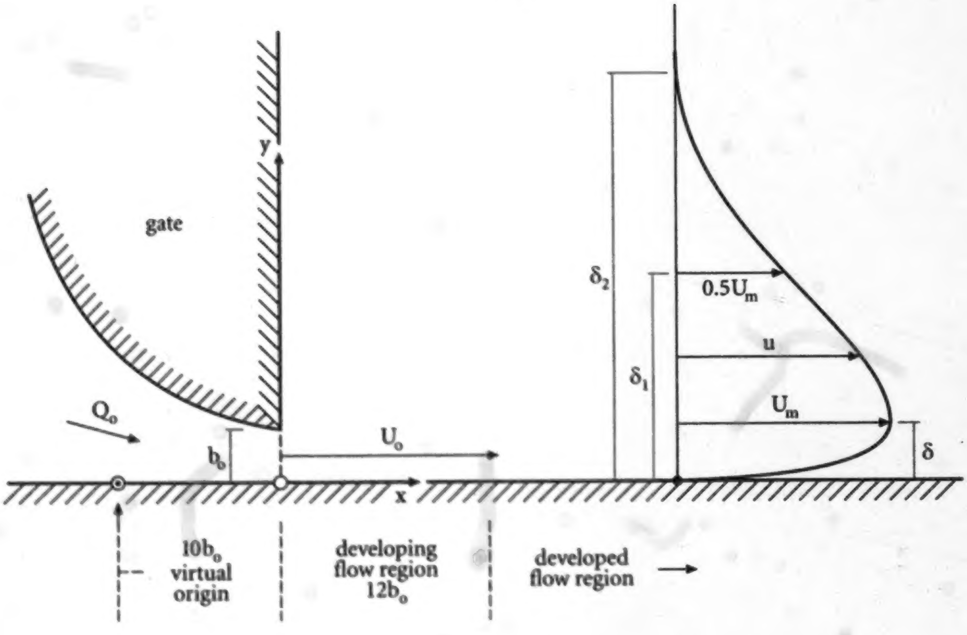
gate
y
Q_o
b_o
U_o
x
$10b_o$
virtual
origin
developing
flow region
$12b_o$
developed
flow region
δ_2
δ_1
$0.5U_m$
u
U_m
δ

Figure 2.4: Plane turbulent wall jet definition sketch.

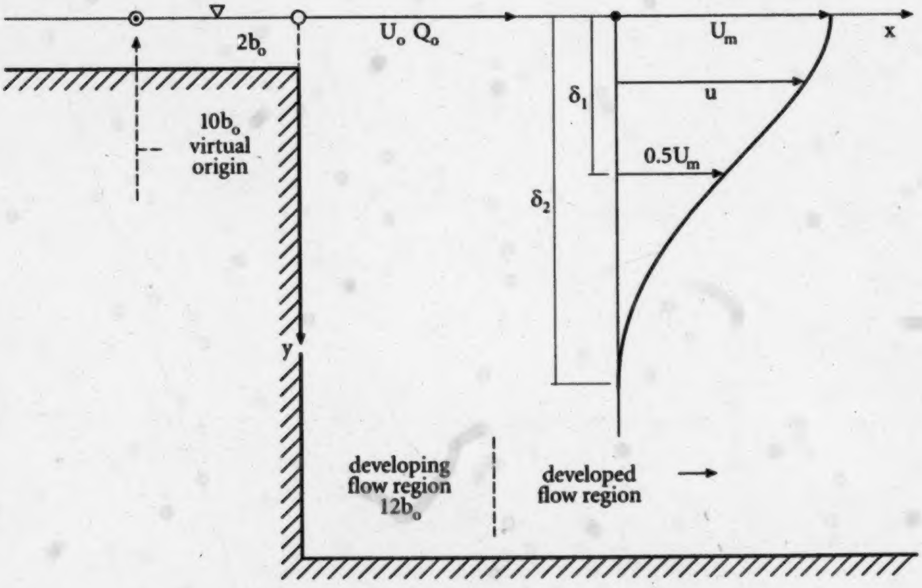
2b$_o$
U$_o$ Q$_o$
U$_m$
x
δ$_1$
u
10b$_o$
virtual
origin
0.5U$_m$
δ$_2$
y
developing
flow region
12b$_o$
developed
flow region

Figure 2.5: Plane turbulent surface jet definition sketch.

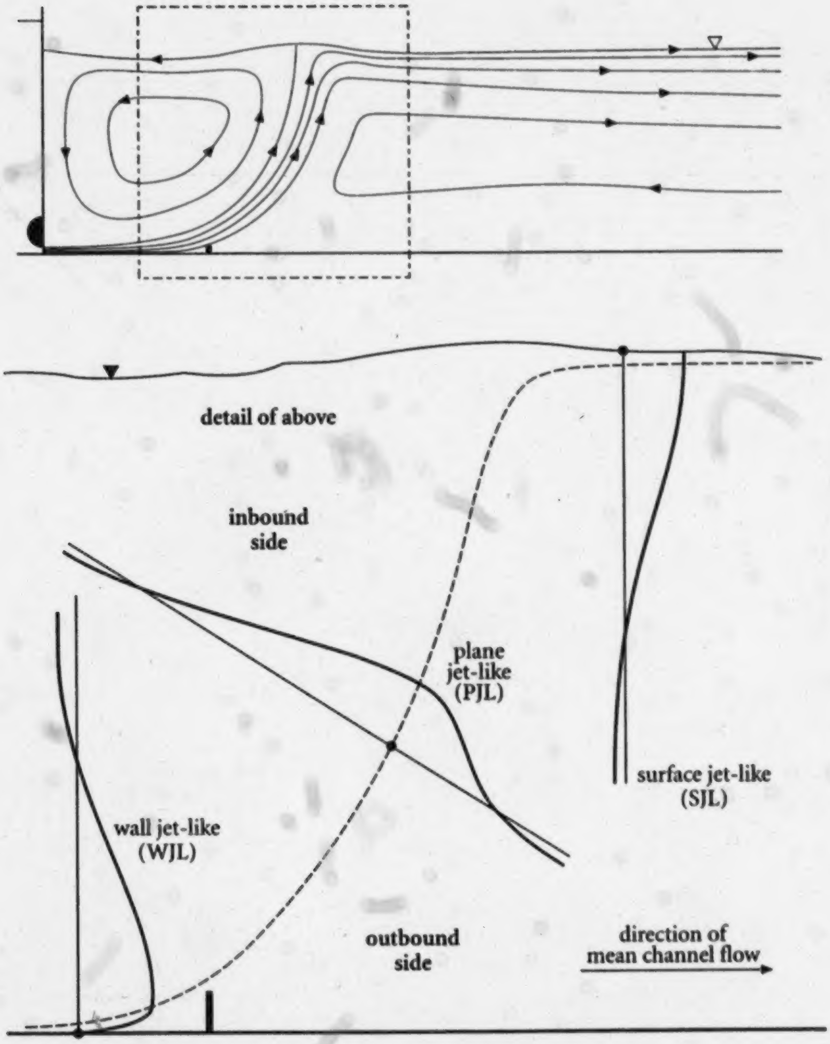
detail of above
inbound side
plane jet-like (PJL)
surface jet-like (SJL)
wall jet-like (WJL)
outbound side
direction of mean channel flow

Figure 2.6: Plane deflected wall jet definition sketch.

3 Experimental Methods

The particle image velocimetry (PIV) technique used in this experimental work requires a complex instrumentation arrangement and data analysis programme in addition to a modified physical flow setup. This section is divided into four main subsections: §3.1 outlines basic PIV methodology, §3.2 describes the flume arrangement, §3.3 presents the PIV setup assembly and §3.4 describes the measurement programme.

3.1 PIV Methodology

Particle image velocimetry is a technique which employs tracer particles suspended in a flow to provide a quantitative measure of the instantaneous velocity field of the flow (Prasad *et al.* 1992). Generally, a plane section of a flow is illuminated by a light source and a sequence of images is recorded with a specified time interval between images. The resulting image sequence captures specular reflections from the seeded particles as they travel in the illuminated flow plane. If the timing sequence of the illumination and recording processes are synchronized correctly, and if the majority of particles remain in the illuminated field of view (FOV) without appreciable out-of plane-motion particle loss, individual particles or patterns of particles can be tracked between images. With knowledge of the time separation between the images, correlations, displacements and hence velocities can then be computed for either individual particles or for regions encompassing groups of particles.

In the earliest PIV methods, particles carried by a flow were imaged under natural light onto photographic film and velocity data extracted through manual displacement measurement. Artificial, and strobing illumination devices were later introduced to increase image quality and decrease minimum time separations, including illumination by laser light. Variations on the classic photographic PIV method, including double exposures within single images, were used in order to reduce both the number of images analyzed and the cost associated with photo development. Computers aided in the analysis if images were digitized and processed. As charge-coupled device (CCD) camera technology matured and powerful computers became more readily available, completely digital PIV analysis methods followed. An excellent review of PIV theory and history is presented by Raffel *et al.* in the book *Particle Image Velocimetry: A Practical Guide* (1998) and by Lourenço (1996).

The PIV technique implemented in this current work employs reflective tracer particles, a pulsing laser sheet and various digital devices to produce, store and process image sequences. These sequences are separated into image pairs which are then processed by computer to obtain cross-correlation fields and ultimately, instantaneous velocity fields. A detailed description of the actual PIV computational process which extracts the velocity data from the images is presented in §4.

3.2 Flume Arrangement

The experiments presented in this study were conducted in the T. Blench Hydraulics Laboratory, at the University of Alberta in Edmonton, Canada. A relatively large rectangular flume with a self-contained water supply, as shown in Figure 3.1, was employed. The horizontal under-bed of the flume was constructed of aluminium, topped with either Plexiglas or glass, and the sidewalls were also either Plexiglas or glass. An aluminium baffle was located downstream of the channel gate and placed across the width of the flume and perpendicular to the centreline. There was a rectangular opening in the aluminium under-bed, aligned with the centreline axis of the flume, situated to allow unobstructed transmission of the laser sheet through the channel bed and into the flow. Due to the scratched and clouded condition of the Plexiglas sidewalls, glass was installed where greater clarity and transparency was required for both image capture and laser transmission. Flume covers and sidewall shrouds were employed to eliminate ambient light pollution of the PIV imaging area. Water was pumped from the downstream reservoir into the upstream head tank with discharge measured by a magnetic flowmeter located in the supply line.

The global Cartesian coordinate system of the flume assembly has an origin defined at the downstream gate section, at the flume bed and in the centre of the channel width. The definition and direction of the coordinate axes are identical to those of the classical plane turbulent wall jet, i.e. x was the longitudinal coordinate, y was the vertical coordinate and z was the transverse coordinate.

The channel itself measured 45.7 cm wide, 450.0 cm long and 90.2 cm tall and was raised 95.3 cm above the floor, allowing for piping and PIV equipment to be placed under the channel bed. Figure 3.2 is a dimensioned drawing of the channel. Water enters the flume from the head tank under a sluice gate with a streamlined lip, and produces a supercritical stream of thickness equal to the slot width of the gate opening. Both the slot width b_o and the baffle height h_o were set at 2.54 cm for the experiments discussed in this work. The tailwater level was controlled via an adjustable weir located at the downstream end of the flume. The baffle consists of a 3.175 mm thick aluminium angle (painted black to eliminate reflections), affixed to the bed at $x_o = 50.0$ cm downstream of the sluice gate opening, with the vertical face of the angle facing upstream. A section of the angle bottom at the centreline of the flume was removed so that the baffle provided the least possible obstruction to the laser illumination sheet. When the pump was in operation and the reservoir fully filled, the flume arrangement held approximately 8 m^3 of water. This water was seeded with approximately 30 g of silver-coated glass sphere tracer particles (Potter Industries, Valley Forge, Pennsylvania) with a 15 μm nominal diameter and a mean specific gravity of 2.6.

3.3 PIV Setup

The PIV instrumentation used in this study of the plane deflected wall jet was comprised of three main sub-systems: the illumination system, consisting of a laser and optics; the timing system, consisting of a signal sync stripper and a delay generator; and the imaging system, consisting of a CCD camera, a computer equipped with a frame-grabber and a positioning and targeting apparatus. The three sub-systems were configured to sample sequential digital images of the seeded flow, capturing pairs separated by small Δt values at an ultimate rate of 15 Hz. Figure 3.3 shows (a) the general layout of the PIV setup and (b) laser timing structure.

3.3.1 Illumination Sub-System

The central element of the illumination sub-system was the laser. It was used to produce a beam of light that, when directed through a plano-cylindrical lens, was spread into a sheet of light the same thickness as the beam. The laser was fastened to a mobile table equipped with an optical rail; the laser was fixed so that the axis of the beam follows the rail and was perpendicular to the flume. The plano-cylindrical lens was attached to the rail and aligned such that the beam passed through the lens centre to produce a plane of light parallel to the flume bed. The mobile table height was adjusted so the horizontal light sheet passed under the lower edge of the flume and a mirror angled at 45 degrees was used to reflect it vertically upwards through the glass bed and into the channel. This sheet illuminates a plane in the flow along the centreline of the channel, coincident with the x-y plane of the flume. Figure 3.4 shows a diagrammatic representation of the illumination sub-system.

The specific laser used in this study was a dual-cavity Minilite PIV model q-switched Nd:YAG laser (Continuum Electro-Optics, Santa Clara, California). Along with internal optics, electrical components and a distilled-water cooling system, each laser cavity contains a flashlamp and a solid-state lasing-medium rod. The two rods are called laser A and laser B for convenience. Both lasers are housed in a single laser head, and beams from each cavity are tuned to be co-incident upon emission. When electrically stimulated by the power supply, the flashlamp emits a non-polarized light which excites the Neodymium atoms in the rod. These atoms absorb and effectively store the flashlamp's optical energy until the rod is allowed to release the energy. The release of the laser energy, expressed as a highly coherent laser-light beam, occurs a short time (defined as the build-up time) after the q-switch component of the laser is triggered and opened. Thus the beam generation and emission of each Minilite PIV laser cavity is controlled via two different signals: the flashlamp delay and the q-switch delay. The sequence and cycle pattern of the resulting four delay signals directly controls the timing and strength of the dual laser pulses.

The Nd:YAG laser produces horizontally polarized infrared light at a wavelength of 1064 nm by default, but with the installation of non-linear crystals and dichroics, wavelengths of 532 nm, 355 nm, and 266 nm can also be produced. In this experiment, the laser operated at the visible wavelength of 532 nm to produce a circularly polarized beam of 3 mm nominal diameter. Under such operating conditions, the lasers each achieve 28 mJ per pulse, resulting in an average power level of 0.42 W per laser rod. The combined energy was 56 mJ per each dual-pulse, resulting in a total power level of 0.84 W. Separation time (Δt) between pulses could vary between 40 ns and 100 ms. The rated build-up time was 60 ns and the rated pulse width was approximately 5 ns. Factory calibrations indicated that to achieve optimal power in each laser, the q-switch delay should be set to 148 μs, however it was found that lasers A and B required individual and unique q-switch delays to produce pulses of equal intensity.

The plano-cylindrical glass lens (Melles-Griot, Nepean, Ontario) had a focal length of −12.7 mm and a design wavelength of 587.6 nm. The flat surface mirror (Edmund Industrial Optics, Barrington, New Jersey) was 200 mm by 235 mm in size and was comprised of a fine annealed Pyrex substrate coated with enhanced aluminium as protection and to increase reflectance in the 200 nm to 650 nm range. These optics produced a pulsed 3 mm thick light sheet that can be directed upwards, perpendicular to the flume bed, and positioned perfectly along the centreplane of the flow.

3.3.2 Timing Sub-System

In order to synchronize the laser pulses with the imaging system, and to enable use of the PIV technique, the laser pulses must be accurately controlled. This is accomplished by the timing sub-system. The purpose of the timing sub-system is to produce pulses of illumination very close to the end of the first frame of an image pair and very close to the beginning of the second frame of the same pair. It must do this repeatedly, as long as images are being acquired by the imaging sub-system. In this way high-velocity flows can be resolved using standard 30 Hz digital video equipment. The main timing component was a model 500A (Berkeley Nucleonics, San Rafael, California) pulse generator. It has one input BNC connection and four BNC output connections.

Using an external input signal as a trigger, it generates four separate output signals with user-programmable delays, pulse widths and polarities. The delays generated by the four outputs are called T1, T2, T3 and T4 respectively. They correspond to the laser A flashlamp and q-switch delays (T1 and T2) and the laser B and flashlamp and q-switch delays (T3 and T4) previously discussed. With the exception of the T2 delay, each is triggered by the same rising edge in the input signal. T2 is triggered at the end of the T1 signal. The input signal to the delay generator was a 15 Hz square signal describing the occurrence rate of image pairs. This signal was derived from the 30 Hz odd-even signal stripped from the analog video output of the CCD camera using a video signal sync stripper circuit assembled at the University of Alberta. The sync stripper produces a signal with a rising edge at the beginning of every second frame taken by the imaging system. Figure 3.5 (a) presents a schematic diagram of the timing sub-system connection and signal flow and Figure 3.5 (b) illustrates the detailed timing scheme.

3.3.3 Imaging Sub-System

The imaging sub-system is responsible for the storage and acquisition of the digital PIV images. It is comprised of a digital CCD camera, a desktop computer equipped with a digital frame-grabber, image acquisition software and a positioning and targeting apparatus. The camera signal drives the PIV imaging as well as provides the necessary input to the timing sub-system. The camera used for imaging was a model TM-1040 progressive scanning high resolution monochrome CCD camera (Pulnix, Sunnyvale, California) with a 30 fps output rate. It captures 10-bit grayscale images 1 008 px by 1 008 px in size and has an adjustable manual gain control. Both digital and analog output is provided. Equipped with a 25 mm 1:1.4 camera lens (Fujinon, Deerfield, Illinois) and set at an aperture of 2.8, the camera has a approximate minimum 9 cm FOV length.

Digital images were recorded using a single 733 MHz Pentium III-class personal computer running Windows NT 4, equipped with 256 MB of RAM memory and a striped-set array of four high-speed SCSI 9.1 GB (unformatted) hard drives as well as a removable hard drive bay. The frame-grabbing software package Video Savant (IO Industries, London, Ontario) and Road Runner digital camera interface hardware (BitFlow, Woburn, Massachusetts) permitted real-time image acquisition to the computer and subsequent export of individual image frames in an 8-bit tagged image file format (TIFF) for further analysis. A maximum of approximately 34 000 frames could be captured to the striped-set array before export to the removable hard drive was required.

Through early experimental investigation using acoustic Doppler velocimetry (ADV), it was decided that the complete field of interest of the plane deflected wall jet phenomenon began approximately 35 cm downstream of the gate and extended approximately 60 cm further downstream. Because actual pixel (px) resolution is reduced when larger fields of view are employed (i.e. each pixel element represents and reduces to a single grayscale value a larger physical area), the area was divided into tesserae which could be imaged separately and later combined into one complete mosaic. This led to the need for accurate positioning of the camera in the global coordinate system. Such a system was provided through use of a positioning stage for the camera and a corresponding target apparatus placed in the flume at the location of the particular tessera FOV. The camera was attached to a set of precision scissor-jacks which controlled the vertical height of the camera. A small two-dimensional stage was installed between the upper jack and the camera to provide accurate positioning in the horizontal plane. This entire assembly was supported by a table constructed so as not to interrupt the path of the laser.

The target apparatus consisted of rigid 75 cm by 100 cm Lexan sheet placed into the operating flume and locked into position through the use of spacer bars, clamps and wedges. The target apparatus was placed on the flume bed at the [illegible] the grid plane was coincident with both the laser sheet and the [illegible] camera. During the course of the experiment, the target would be lowered into the flow, and the laser and camera positioned to provide illumination and imaging for the tessera of interest before data was collected. A laminated 1-cm grid was created and adhered to the rigid sheet to provide tesserae reference points. Sixteen overlapping square tesserae formed the single square mosaic: each tessera 15.75 cm by 15.75 cm in size, with 0.75 cm overlaps, resulting in a mosaic 60.75 cm by 60.75 cm in size. Tesserae centres, edges and numbers were visible during setup and allowed the camera to be consistently positioned in the global coordinate system via optical adjustment. Figure 3.6 shows a dimensioned drawing of the target apparatus in relation to the flume and baffle.

Figures 3.7 through 3.14 show photographs taken of the complete experimental area, including the flume arrangement and the PIV setup sub-systems.

3.4 Measurement Programme

Fourteen of the available sixteen tesserae were chosen to adequately describe the plane deflected wall jet and the follow the jet centreline trajectory and are shown in Figure 3.6 as the numbered tesserae. The data collection programme began at the fourteenth tessera and then proceeded in an order chosen to reduce equipment movement and repositioning. The exact location of the target and alignment apparatus was set so the baffle was always centered in the overlap region between the second and third tesserae. This minimized the manifestation of a baffle shadow in the captured images to a thin wedge-like region above the baffle. Table 3.1 presents the global coordinate centres and extents of the individual tesserae FOV areas. The lowest image edge is not found at the bed due to the visible presence of silicon caulking at the flume seams and because of reflections at the glass bed boundary. The image scale is $S_{FOV} = 156.25\ \mu m/px$.

The flow rate in the flume was measured by a voltmeter connected to the magnetic flowmeter; the average reading was 30.6 volts, corresponding to an average volumetric flow rate of $Q = 0.0153\ m^3/s$, a discharge intensity of $q = 0.0335\ m^2/s$, and a mean uniform jet exit velocity of $U_o = 1.32\ m/s$. The resulting average Reynolds and Froude numbers were $R = 28\,400$ and $F = 2.64$, respectively. The average tailwater depth y_t and depth immediately downstream of the gate y_2 were both 55.0 cm while the average depth immediately upstream of the gate in the head tank was $y_1 = 64.0$ cm. The U_o measurement from the flowmeter was confirmed using the relation $U_o = \sqrt{2g\Delta H} = 1.33\ m/s$. A mean water surface profile was taken through direct measurement of the water level at the flume sidewall; profile data is presented in Table 3.2. The experimental work was completed over an approximate ten-hour period over which the average measured water temperature was 13.8 °C, yielding a mean kinematic viscosity of $\nu = 0.0118\ cm^2/s$. The electronic thermometer used in temperature measurement broke after the tessera 8 data collection process. [illegible] the temperatures from tesserae 4 through 8 experiments. The water temperature while collecting data for tessera 14 was 10.8 °C and it stabilized at approximately 14.0 °C by the tessera 4 experiment. Only actually measured temperatures were included in the average calculation. The full set of environmental data is provided in Table 3.3.

The laser timing and delays for each tessera were programmed individually and recalled from the delay generator memory before data collection commenced at each section. The Δt pulse separations were chosen based on a maximum allowable particle pixel shift of 16 px in either the x- or y-direction and a maximum expected instantaneous velocity for the individual tesserae as measured in both the investigatory ADV study and preliminary PIV measurements. The need for this limitation is made clear in §4 and is related to the size of the chosen interrogation window in the PIV analysis. The minimum pulse separation was 1.3 ms, corresponding to a maximum instantaneous velocity resolution of 192 cm/s; the maximum pulse separation was 4.0 ms, corresponding to a minimum instantaneous velocity resolution of 63 cm/s. The full set of delays and pulse separations are presented in Table 3.4 with a sample calculation provided in §8.

A total of 180.2 seconds of 30 frames per second (fps) video data was recorded for each of the tesserae. This corresponds to 5 400 TIFF flawless images per tessera and 76 600 flawless images for the complete experimental mosaic. In addition, images were taken of the target apparatus to confirm location and scale accuracy. Figure 3.15 shows the target images for tesserae (a) twelve and (b) thirteen; note the centre point, the cm-grid, the FOV edges and the water surface. Each TIFF image is approximately 0.97 MB in size; this necessitated periodic export of image data from the main PIV hard drive to one of three 60 GB (unformatted) removable hard drives. The first hard drive stored the images of tesserae 14, 1, 2 and 3; the second hard drive stored the images of tesserae 4, 5, 6, 7 and 8; and the third hard drive stored the images of tesserae 9, 10, 11, 12 and 13. The average time to export the images of one tessera to the removable media was approximately 25 minutes. All three drives were less than half full in anticipation of further processing and data-file creation.

[illegible]	x-centre (cm)	y-centre (cm)	top (cm)	bottom (cm)	left (cm)	right (cm)
[illegible]	42.625	23.125	31.00	15.25	34.75	50.50
[illegible]	42.625	8.125	16.00	0.25	34.75	50.50
[illegible]	57.625	8.125	16.00	0.25	49.75	65.50
[illegible]	57.625	23.125	31.00	15.25	49.75	65.50
[illegible]	57.625	38.125	46.00	30.25	49.75	65.50
[illegible]	57.625	53.125	61.00	45.25	49.75	65.50
[illegible]	72.625	53.125	61.00	45.25	64.75	80.50
[illegible]	72.625	38.125	46.00	30.25	64.75	80.50
[illegible]	72.625	23.125	31.00	15.25	64.75	80.50
[illegible]	72.625	8.125	16.00	0.25	64.75	80.50
[illegible]	87.625	23.125	31.00	15.25	79.75	95.50
[illegible]	87.625	38.125	46.00	30.25	79.75	95.50
[illegible]	87.625	53.125	61.00	45.25	79.75	95.50
[illegible]	42.625	38.125	46.00	30.25	34.75	50.50

Table 3.1: Global coordinate tesserae positions and extents.

x (cm)	y (cm)	x (cm)	y (cm)	x (cm)	y (cm)
10.0	54.1	48.0	52.5	86.0	54.3
11.0	54.1	49.0	52.4	87.0	54.3
12.0	54.1	50.0	52.5	88.0	54.1
13.0	54.1	51.0	52.6	89.0	54.1
14.0	54.2	52.0	52.9	90.0	54.0
15.0	54.0	53.0	53.1	91.0	54.0
16.0	53.9	54.0	53.3	92.0	53.9
17.0	53.9	55.0	53.2	93.0	53.9
18.0	53.7	56.0	53.3	94.0	53.9
19.0	53.5	57.0	53.3	95.0	53.8
20.0	53.3	58.0	53.5	96.0	53.7
21.0	53.3	59.0	53.9	97.0	53.7
22.0	53.1	60.0	54.0	98.0	53.6
23.0	52.9	61.0	53.9	99.0	53.6
24.0	52.9	62.0	54.0	100.0	53.6
25.0	52.9	63.0	54.1	101.0	53.5
26.0	52.8	64.0	54.3	102.0	53.5
27.0	52.8	65.0	54.5	103.0	53.5
28.0	52.7	66.0	54.5	104.0	53.5
29.0	52.7	67.0	54.7	105.0	53.5
30.0	52.6	68.0	54.9	106.0	53.4
31.0	52.6	69.0	55.0	107.0	53.5
32.0	52.6	70.0	55.1	108.0	53.3
33.0	52.7	71.0	55.0	109.0	53.3
34.0	52.8	72.0	54.9	110.0	53.4
35.0	52.7	73.0	54.9	111.0	53.5
36.0	52.6	74.0	54.8	112.0	53.5
37.0	52.7	75.0	54.7	113.0	53.5
38.0	52.5	76.0	54.7	114.0	53.6
39.0	52.5	77.0	54.7	115.0	53.6
40.0	52.4	78.0	54.6	116.0	53.7
41.0	52.3	79.0	54.6	117.0	53.6
42.0	52.3	80.0	54.8	118.0	53.8
43.0	52.3	81.0	54.7	119.0	53.9
44.0	52.5	82.0	54.7	120.0	54.0
45.0	52.7	83.0	54.6	-	-
46.0	52.7	84.0	54.6	-	-
47.0	52.7	85.0	54.5	-	-

Table 3.2: Mean water surface profile coordinates.

tessera	V (volts)	Q (m^3/s)	U_o (cm/s)	T (°C)	ν (cm^2/s)	y_1 (cm)	y_2 (cm)	y_t (cm)
1	30.8	0.0154	132.6	11.8	0.0125	64.0	55.0	55.0
2	30.8	0.0154	132.6	12.1	0.0124	64.0	55.0	55.0
3	30.6	0.0153	131.8	12.4	0.0123	64.0	55.0	55.0
4	30.8	0.0154	132.6	14.0	0.0117	64.0	55.0	55.0
5	30.3	0.0152	130.5	16.0	0.0111	64.0	55.0	55.0
6	30.5	0.0153	131.3	14.6	0.0115	64.0	55.0	55.0
7	30.6	0.0153	131.8	14.3	0.0116	64.0	55.0	55.0
8	30.9	0.0155	133.0	14.2	0.0117	64.0	55.0	55.0
9	30.3	0.0152	130.5	14.6 *	0.0115	64.0	55.0	55.0
10	30.6	0.0153	131.8	14.6 *	0.0115	64.0	55.0	55.0
11	30.6	0.0153	131.8	14.6 *	0.0115	64.0	55.0	55.0
12	30.5	0.0153	131.3	14.6 *	0.0115	64.0	55.0	55.0
13	30.6	0.0153	131.8	14.6 *	0.0115	64.0	55.0	55.0
14	30.8	0.0154	132.6	10.8	0.0128	64.0	55.0	55.0
average	30.6	0.0153	131.8	13.8	0.0118	64.0	55.0	55.0

notes: laser A flashlamp delay = 148 µs and laser B flashlamp delay = 228 µs
laser A and laser B q-switch delay = 63 ns
* indicates interpolated temperature data not use in average

Table 3.3: Environmental parameters.

tessera	Δt (ms)	T1 delay (s)	T2 delay (s)	laser A pulse (s)	T3 delay (s)	T4 delay (s)	laser B pulse (s)
1	3.0	0.0151666	0.0001480	0.0153147	0.0180866	0.0183146	0.0183147
2	1.3	0.0160166	0.0001480	0.0161647	0.0172366	0.0174646	0.0174647
3	1.6	0.0158666	0.0001480	0.0160147	0.0173866	0.0176146	0.0176147
4	1.7	0.0158166	0.0001480	0.0159647	0.0174366	0.0176646	0.0176647
5	2.0	0.0156666	0.0001480	0.0158147	0.0175866	0.0178146	0.0178147
6	2.0	0.0156666	0.0001480	0.0158147	0.0175866	0.0178146	0.0178147
7	2.0	0.0156666	0.0001480	0.0158147	0.0175866	0.0178146	0.0178147
8	1.8	0.0157666	0.0001480	0.0159147	0.0174866	0.0177146	0.0177147
9	1.7	0.0158166	0.0001480	0.0159647	0.0174366	0.0176646	0.0176647
10	3.0	0.0151666	0.0001480	0.0153147	0.0180866	0.0183146	0.0183147
11	4.0	0.0146666	0.0001480	0.0148147	0.0185866	0.0188146	0.0188147
12	2.6	0.0153666	0.0001480	0.0155147	0.0178866	0.0181146	0.0181147
13	2.0	0.0156666	0.0001480	0.0158147	0.0175866	0.0178146	0.0178147
14	2.6	0.0153666	0.0001480	0.0155147	0.0178866	0.0181146	0.0181147

notes: laser A flashlamp delay = 148 μs and laser B flashlamp delay = 228 μs
laser A and laser B q-switch delay = 63 ns

Table 3.4: Experimental timing delays and separations.

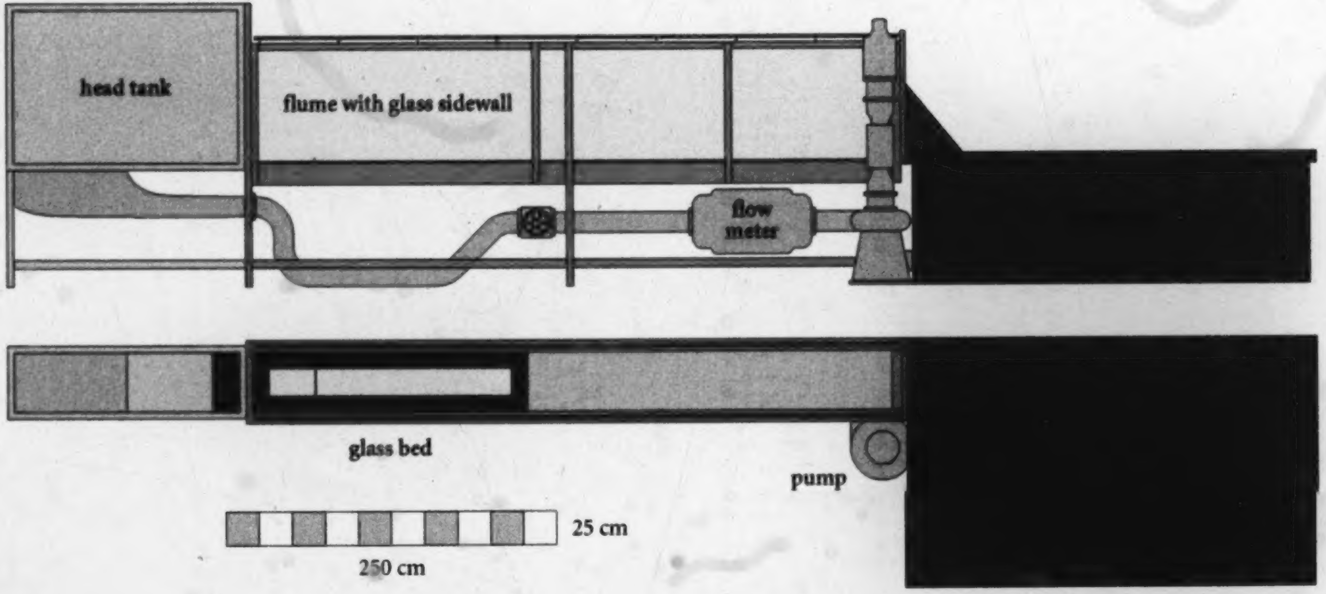
head tank
flume with glass sidewall
flow meter
glass bed
pump
25 cm
250 cm

Figure 3.1: Flume arrangement diagram.

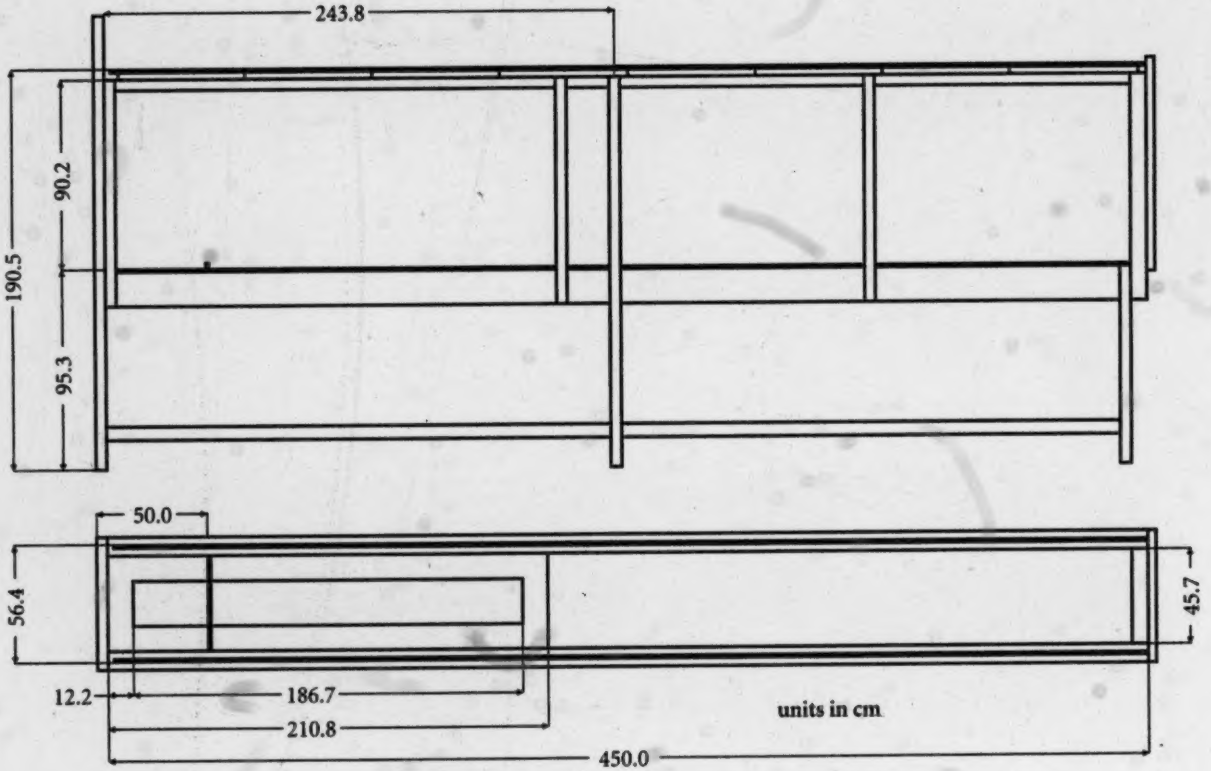
243.8
190.5
90.2
95.3
50.0
56.4
45.7
12.2
186.7
210.8
450.0
units in cm

Figure 3.2: Channel measured drawing.

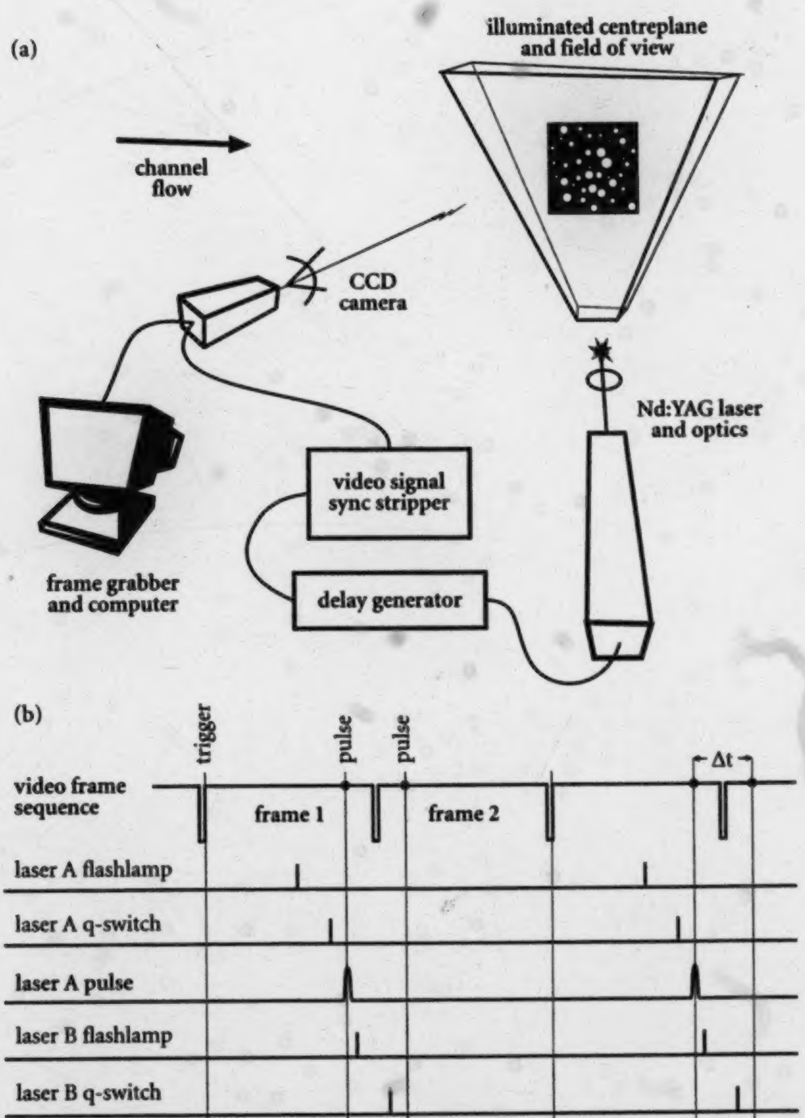
(a)
illuminated centreplane and field of view
channel flow
CCD camera
Nd:YAG laser and optics
video signal sync stripper
delay generator
frame grabber and computer
(b)
trigger
pulse
pulse
Δt
video frame sequence
frame 1
frame 2
laser A flashlamp
laser A q-switch
laser A pulse
laser B flashlamp
laser B q-switch
laser B pulse

Figure 3.3: (a) General PIV setup layout and (b) broad laser timing structure.

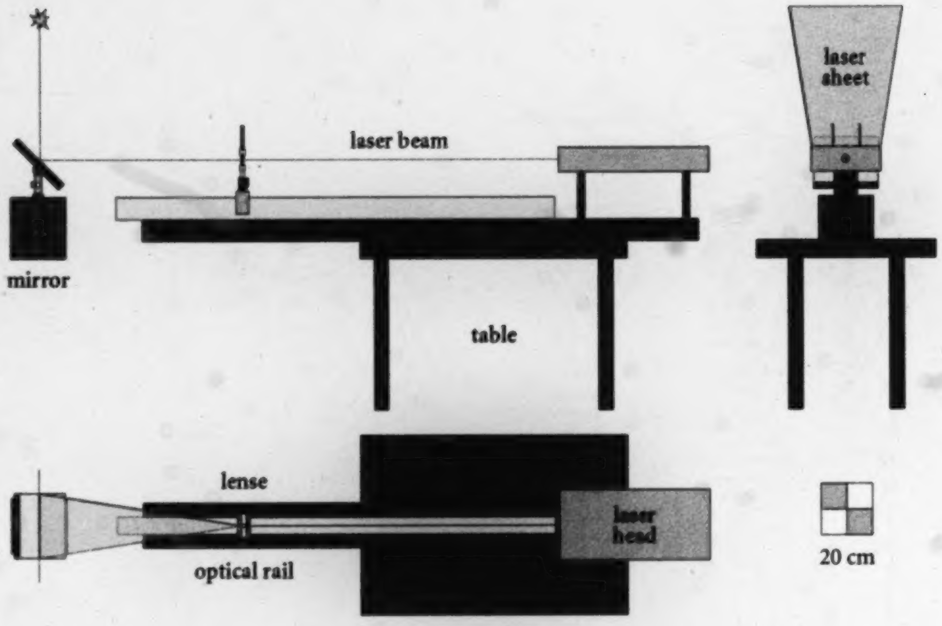
laser sheet
laser beam
mirror
table
lense
optical rail
laser head
20 cm

Figure 3.4: PIV illumination sub-system diagram.

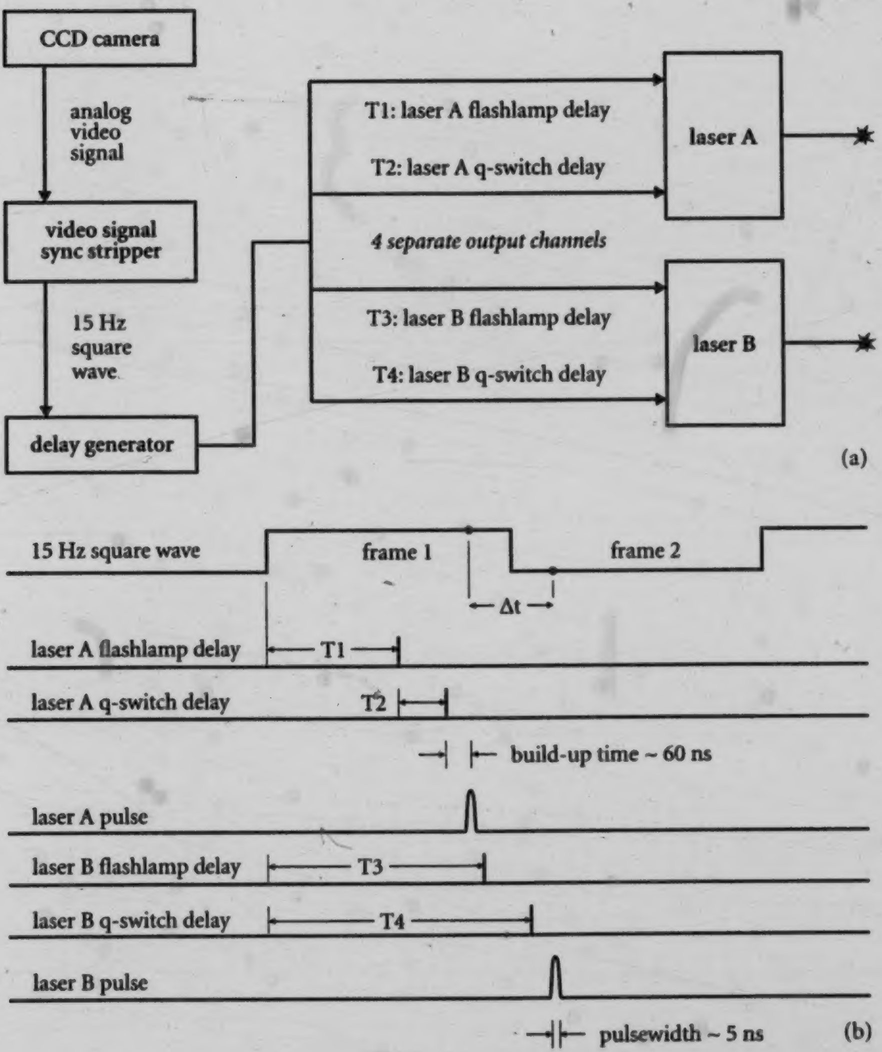
CCD camera
analog video signal
video signal sync stripper
15 Hz square wave
delay generator
T1: laser A flashlamp delay
T2: laser A q-switch delay
4 separate output channels
T3: laser B flashlamp delay
T4: laser B q-switch delay
laser A
laser B
(a)
15 Hz square wave
frame 1
frame 2
Δt
laser A flashlamp delay
T1
laser A q-switch delay
T2
build-up time ~ 60 ns
laser A pulse
laser B flashlamp delay
T3
laser B q-switch delay
T4
laser B pulse
pulsewidth ~ 5 ns
(b)

Figure 3.5: (a) PIV timing sub-system signal flow and (b) detailed timing scheme.

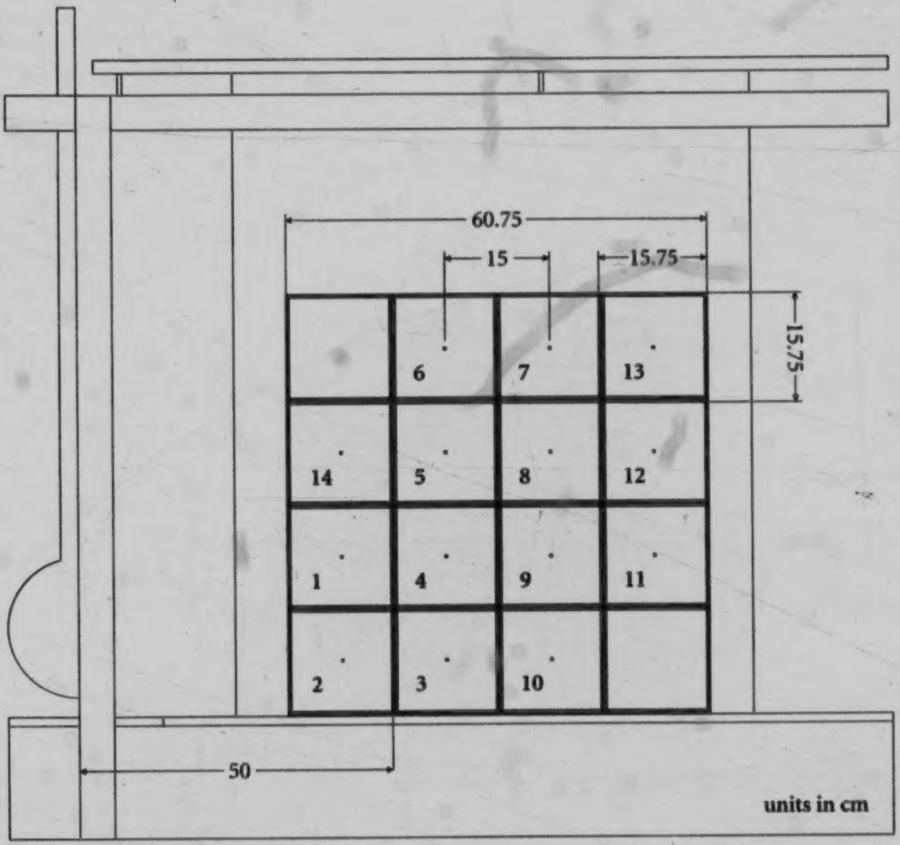
60.75
15
15.75
15.75
6
7
13
14
5
8
12
1
4
9
11
2
3
10
50
units in cm

Figure 3.6: PIV imaging sub-system target apparatus measured drawing.

Figure 3.7: T. Blench Hydraulics Laboratory experimental area.

Figure 3.8: Flume arrangement and PIV setup.

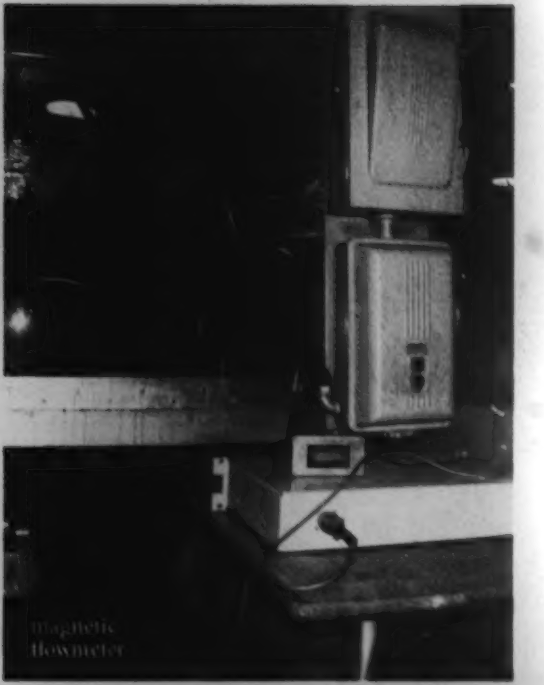
magnetic
flowmeter

**Figure
Flum
pum
flow**

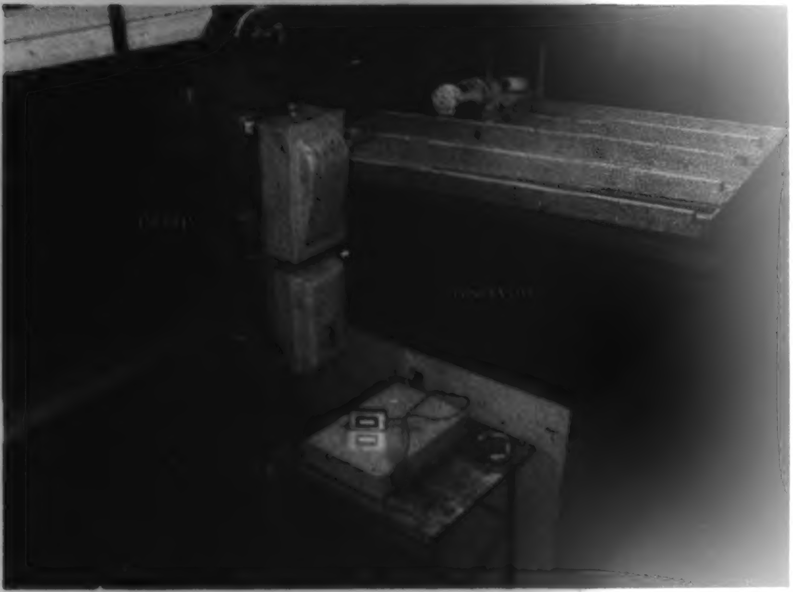
pump
reservoir

Figure 3.10: Flume arrangement water reservoir.

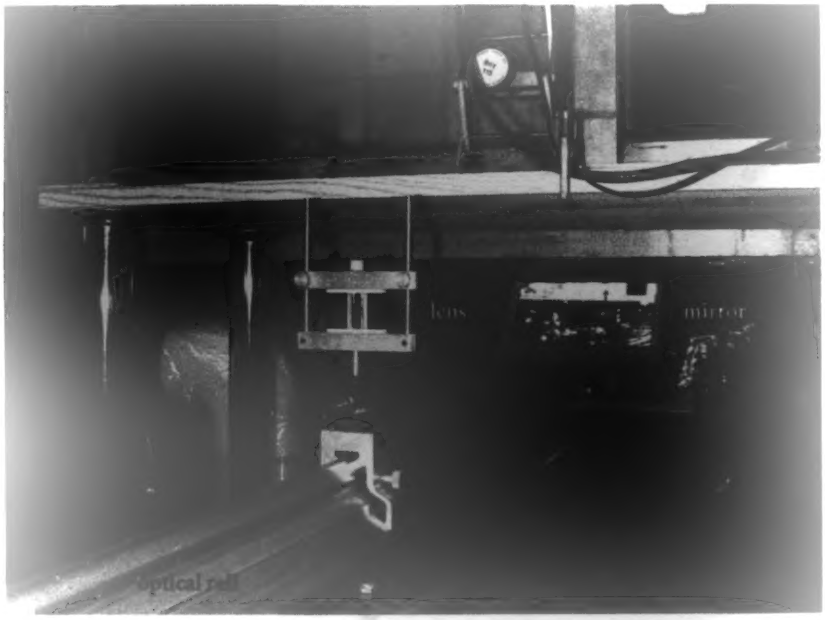
lens
mirror
optical rail

Figure 3.11: PIV illumination sub-system optical rail, lens and mirror.

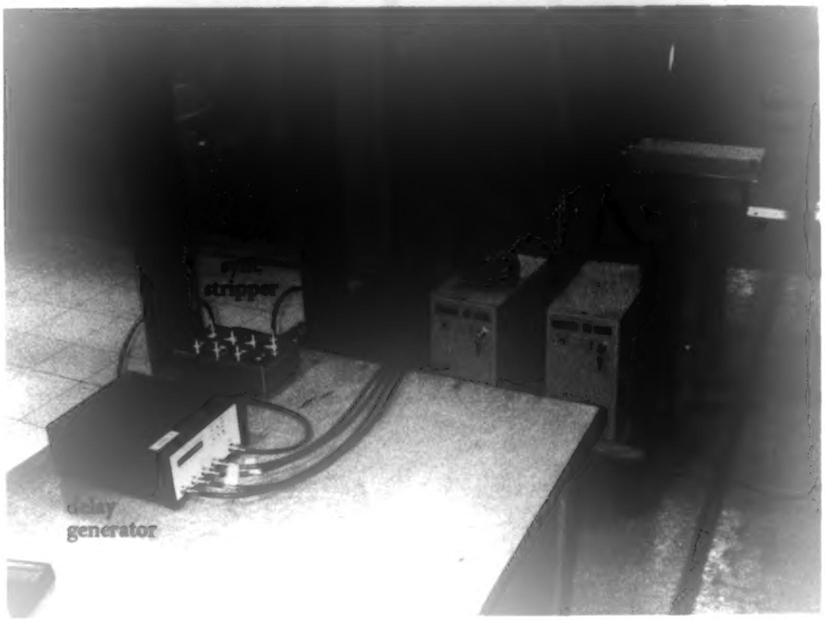
sync stripper
delay generator

Figure 3.12: PIV illumination sub-system sync stripper and delay generator

imaging
apparatus

Figure 3.13: PIV imaging sub-system.

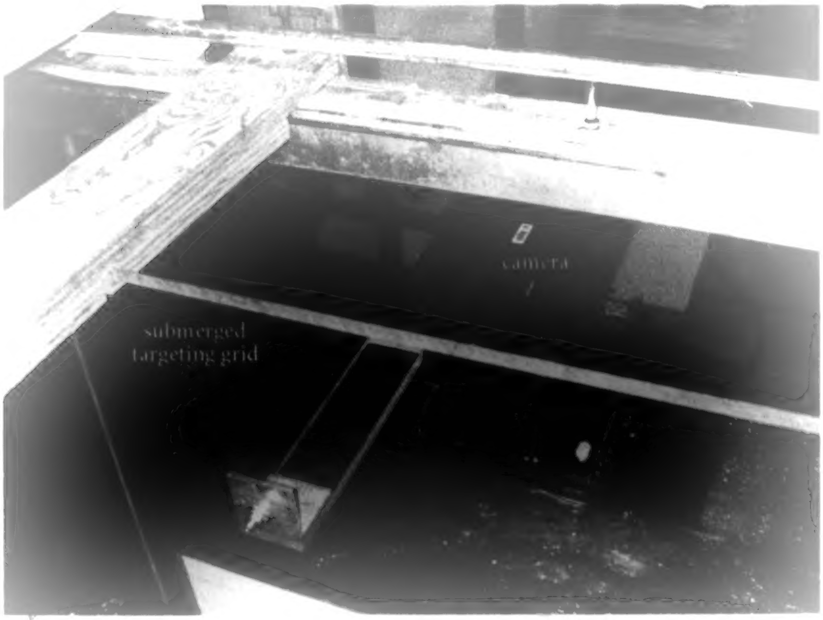
camera
submerged
targeting grid

Figure 3.14: Submerged targeting apparatus and CCD camera.

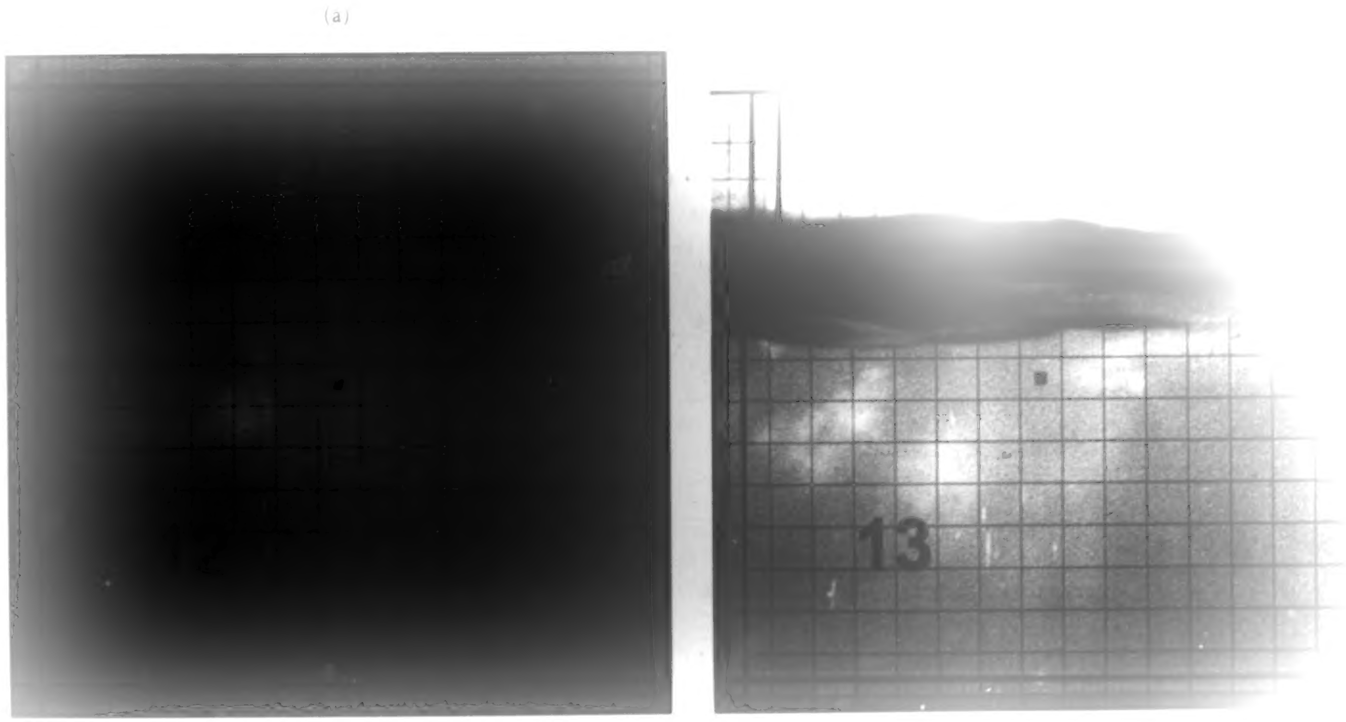

Figure 3.15: Target images of (a) [illegible]

4 Data Processing

§4 describes the unique PIV data processing technique employed in this investigation and details the specific steps required to extract flow data from the images collected in the experimental programme. Prior to any significant flow analysis, it was necessary to process the raw images yielded by the experimental programme. Depending on the quality of the images and the area of flow imaged, the actual PIV procedure required up to three distinct steps: preliminary image pre-processing, primary PIV processing and corrective post-processing. Image pre-processing ensured that poor image quality and obvious defects did not manifest themselves in the primary PIV processing while post-processing removed a majority of the spurious vectors which contaminated the PIV data sets. Although the general methodology of the PIV technique was presented in §3.2, the non-ideal data collected in this study required both pre- and post-processing in addition to the primary PIV processing. Supplementary processing was also performed to compute instantaneous, mean and turbulent flow data from the final instantaneous PIV data. The complete processing of all tessera required approximately 50 computer-days of computation time.

4.1 Image Pre-Processing

Image defects were present in those tesserae whose fields of view encompassed either the baffle or the water surface. As already described in §3.4, a thin wedge-like shadow is visible above the baffle in tessera 2 and tessera 3 images. The non-reflective paint applied to the baffle deteriorated through jet attack and delaminated from the baffle in many areas. Consequently a static, bright baffle edge reflection is also visible in the images of those tesserae. Both the shadow and the reflection are shown in Figure 4.1. In addition, the water surface in the area of the deflected wall jet is rather violent, especially at the location of jet impingement. Under laser sheet illumination, the churning water surface produced transient, dramatically bright reflections which rendered the tracer particles effectively invisible. This water surface reflection defect is consistently visible in the images collected from tesserae 6, 7 and 13 and is shown in Figure 4.2.

Because the baffle reflection defects present in tesserae 2 and 3 were persistent between images, any cross-correlation of regions including it would have yielded an inaccurately strong displacement at the location of the reflection. The PIV processing routine would, in effect, interpret the reflection as a perfectly static particle and assign a false displacement of zero to the region. To prevent this from occurring, the reflections and small surrounding areas affected by the reflections, in each image had their pixel values set to the mean background level. Much like a shadow, the area would not exhibit any appreciable correlation, and at worst, limit the ability of the PIV routine in finding a significant displacement. A combined total of 10 800 images (the full three minutes for both tesserae) containing the baffle defect were pre-processed over a two-hour period.

Although the reflections caused by the water surface would likewise ultimately yield spurious displacements, the nature of the defect is both temporally transient and spatially dynamic. Elimination of the defect would necessitate exclusion of any part of an image affected by the individual reflections. Because the surface changes with time it would require complicated reflection identification as well as pre-processing schemes to be effective. Even then, displacement vectors could only be computed randomly at locations with the reflections. The usefulness of the resulting data would not offset the computational cost of pre-processing; it was decided that the water surface defect could be more easily corrected by post-processing.

4.2 Primary PIV Processing

The basics of the PIV methodology were outlined in §3.1 and the PIV setup used in the experimental programme was detailed in §3.3. It has already been noted that the PIV technique requires image sets separated into a sequence of image pairs, and that the fundamental processing essentially defines regions of particles in one image and attempts to identify the locations of those same particles in another image though correlation. However, the specifics of the process require further description. The details are more easily understood if one considers a single image pair and follows the steps required to obtain a single instantaneous displacement field.

The first image is divided into regularly sized regions, each small enough that the motion within is approximately uniform, called interrogation windows (Figure 4.3). For each interrogation window there exists a larger corresponding search window in the second image, which is typically twice as large as the interrogation window. The centres of the windows are spatially coincident, however, the content of the image regions they encompass are separated in time by Δt, the laser pulse separation time. A cross-correlation algorithm is applied to the interrogation window and various equally sized sub-regions within the search widow. Produced is a correlation field and the position of the correlation peak in the field is ascertained. The location of the peak defines the most likely location, in the search window of the second image, of the particle pattern bounded by the interrogation window of the first image. Pixel displacements in the x- and y-directions are calculated (from the centre of the interrogation window to the correlation peak location) and defined as d_{pxx} and d_{pxx} respectively. The resultant pixel displacement vector is assigned to the relevant interrogation region. The process is repeated at all interrogation regions and results in an instantaneous two-dimensional pixel displacement field describing the FOV of the image pair. This correlation process is illustrated in Figure 4.4.

The raw displacements are initially correlated to a single-pixel resolution scale; the images only have pixel brightness data for each distinct pixel and the correlated displacements are from pixel centre to pixel centre. This resolution is unacceptably low, considering that the actual size of the seeded tracer particles is an order of magnitude smaller. Sub-pixel resolution was achieved via a three-point Gaussian peak fitting scheme. Siddiqui (2002) conducted tests on the accuracy of several peak fitting estimators, including the three-point Gaussian, parabolic and centre-of-mass schema, and corroborated the assertion of Cowen and Monismith (1997) that the three-point Gaussian performs the best. The error associated with sub-pixel estimation (along with other error) is further discussed in §4.5.2.

In the present study, the raw displacement fields were computed using a standard cross-correlation algorithm written by Marxen (1998), that utilizes Heurisko (AEON Verlag & Studio, Hanau, Germany) image processing software. The processing was similar to that used by Siddiqui (2002). Interrogation windows were 32 px by 32 px in size and were overlapped by 50% to increase the nominal resolution of the resultant pixel displacement grid to 16 px by 16 px. The search windows were 64 px by 64 px in size to ensure that all the particles in the interrogation window remained in the search window (Keane and Adrian 1992). As noted in §3.4, the sizes of the interrogation and search windows limited the maximum displacement component resolution to ±16 px, the distance from any interrogation window centre to the centre of a sub-region located at an extreme corner of the corresponding search window.

2 700 image pairs were processed for each of the fourteen tesserae, resulting in a total of 37 800 displacement fields divided equally between the tesserae. Over 110 computer-hours were required to complete this primary PIV processing. Each displacement field contained 3 600 raw vectors distributed irregularly within a regularly spaced interrogation window grid. The interrogation grid has a nominal spatial resolution of 16 px or 2.5 mm. Because each interrogation window required a larger search window in which to detect displacement, no displacements could be calculated in the border region of the images; the edge of the interrogation window grid was located 16 px or 2.5 mm inside of the FOV edge of its tessera. If the tesserae had been structured in an edge to edge fashion, instead of overlapped, effective data-gaps would have been created at all edges when the tesserae were assembled into the full mosaic. The 7.5 mm overlap of tesserae in the experimental programme yielded an uninterrupted and regular mosaic of interrogation windows when tesserae were combined, with each tessera contributing a 60 by 60 displacement vector field. Figure 4.5 presents representative instantaneous raw displacement vector fields from (a) tessera 4 and (b) tessera 7. A complete set of instantaneous raw pixel displacement fields for all tesserae can be found in §8.

4.3 Corrective Post-Processing

Corrective post-processing was performed using the Matlab 5.3 (Mathworks, Natick, Massachusetts) data analysis software package. The first step of the post-processing involved identification and adjustment of spurious displacement vectors, including the displacements derived from images with either baffle shadow or water surface reflection defects; the second step involved conversion of the all displacements into velocities using the individual tessera pulse separation times and the interpolation of these velocities onto a regular 2.5 mm grid. The complete post-processing of each tessera took approximately 48 computer-hours and was performed concurrently on both computers.

As previously mentioned, the PIV technique essentially tracks particles as they move through an illumination plane. Ideally, the quality of the collected images would be flawless and the raw PIV displacements described above would be consistently accurate. However, experimental data is unfortunately quite non-ideal. There are variations in illumination intensity and particle density; there are systemic and random flaws in image quality as well as variations in focus between tesserae; there are unpredictable out-of-plane particle losses due to the actual three-dimensionality of the flow. The raw displacement vectors computed by Heurisko contain a varying number of spurious or improbable displacement vectors, as evident in Figure 4.5 and Figure 4.6.

As previously indicated, a static shadow was visible in images containing the baffle, and bright reflections occurred in and polluted a significant area of the fields of view of those tesserae imaging the water surface. Before random spurious vector data was corrected, the spurious vectors produced by those phenomena were removed from the data sets. Matlab was instructed to zero, and then computationally ignore, the displacement vectors within certain defined exclusion zones. In tesserae 2 and 3 PIV files, the region where the baffle or baffle shadow consistently and significantly affected raw displacements was ignored. The baffle exclusion zone comprised a 0.5 cm by 9.0 cm data-free area (a 36 displacement vector column in each tessera) centered around the baffle and adjacent to the bed. The upper 9.5 cm of tesserae 6, 7 and 13 PIV files were also computationally ignored, excluding 2 280 displacement vectors in each tessera file. Figure 4.6 shows the exclusion zones in relation to the tesserae boundaries of the assembled mosaic, the mean water surface and the baffle. Effectively, tesserae 2 and 3 each contained 3 564 displacement vectors and tesserae 6, 7 and 13 each contained 1 320 in further post-processing. All other tesserae preserved the full 3 600 raw displacement vectors.

Following the elimination of the obviously flawed displacements found in the exclusion zones, all of the remaining random spurious vectors required identification and correction. Identification was accomplished with a local-median test scheme identical to that used by Siddiqui *et al.* (2001). The ratios of the component pixel displacements d_{pxx} and d_{pxx} and the displacement vector angle θ at a point, to the median of the same values for all the available neighbours to that point, were calculated for all points in the displacement field. If the ratios exceeded a specified limit, the displacement vector was considered spurious. Westerweel (1994) showed that this type of local median test is more robust for detecting spurious vectors than a local mean test. Once identified as spurious, vectors were replaced with the previously calculated median vector and considered corrected.

This identification and correction scheme was iterated four times for every raw PIV displacement field. The spurious detection limit was designed such that the maximum allowable velocity gradient between the point in question and its neighbours was ≤ 7% (Siddiqui 2002). In the first iteration, approximately 2% of the total 43 488 vectors were identified as spurious; after the fourth iteration, only approximately 0.1% retained the designation. A consistent source of spurious vectors was an area of the camera FOV which contained several burnt pixels. These burnt pixels manifest as pixel-sized white points in the PIV images and as zero-displacements following primary PIV processing. The spurious displacements were corrected in post-processing. A complete breakdown of identified spurious vector statistics, organized both by tessera and by iteration, is presented in Table 4.1.

The corrected vectors were then interpolated onto a regular grid, with grid points at the centre of the interrogation windows, using an adaptive Gaussian window interpolator (AGW) scheme (Agüí and Jiménez 1987). Cowen and Monismith (1997) as well as Spedding and Rignot (1993) have shown that this type of interpolation induces certain errors into the displacement and final velocity data; this source of error is further discussed in §4.5. The regular spacing of the interpolated vectors allow for further processing using various central difference schema and straightforward analyses of the resulting data. Sample corrected and interpolated pixel displacement vector fields for (a) tessera 4 and (b) tessera 7 are presented in Figure 4.7.

4.4 Supplementary Processing

For the PIV data to provide more than simple velocity data in this analysis of the plane deflected wall jet, instantaneous, mean and turbulent flow variables require computation. Instantaneous, mean and turbulent velocity, Reynolds stress, vorticity and turbulent kinetic energy were obtained from the instantaneous corrected and interpolated pixel displacement vector data-cloud through supplementary processing.

Instantaneous velocity vector components were first calculated from the corrected and interpolated displacement fields for each PIV file using the following relations:

$$u_i = S_{FOV} d_{pxx} \Delta t \qquad [4.1]$$

$$v_i = S_{FOV} d_{pxy} \Delta t \qquad [4.2]$$

Due to the various pulse separation times, each tessera had different ranges of maximum achievable velocity. Table 4.2 presents the maximum displacement and velocity resolutions for all tesserae.

Using these instantaneous velocities, instantaneous kinetic energy per unit mass (KE_i) was computed for each point in every tessera field. Employing the assumption that the velocity component in the z-direction was insignificant compared to the x- and y-directions (a valid assumption for plane jets and a necessary one for employment of the PIV technique), the following equation was used:

$$KE_i = 0.5\left(u_i^2 + v_i^2\right) \qquad [4.3]$$

In order to calculate the various turbulent flow properties, average velocity values were first required. They were calculated for each grid point by averaging each of the 2 700 instantaneous velocity components acquired through the measurement programme and previously computed. The resultant average velocities were then subtracted from the instantaneous velocities to obtain turbulent velocities, using Reynolds decomposition:

$$u_i = u + u' \qquad [4.4]$$

$$v_i = v + v' \qquad [4.5]$$

Values of both the instantaneous Reynolds stress per unit mass (τ_i/ρ)and turbulent kinetic energy per unit mass (k_i) were then computed for each grid point in the field using the following relations:

$$\tau_i/\rho = -\overline{u'v'} \qquad [4.6]$$

$$k_i = 0.75\left(u'^2 + v'^2\right) \qquad [4.7]$$

The z-direction turbulent velocity component is not negligible, and as such it cannot be omitted from the turbulent kinetic energy calculation as it was in the formulation of equation [4.3]. Because the PIV technique only generates velocity data in the x-y plane, neither w nor w' data exists. To compensate in equation [4.7], all three turbulent velocity components were considered to be approximately of the same order, with $w'^2 = 0.5\left(u'^2 + v'^2\right)$.

A standard central difference scheme was implemented to calculate instantaneous velocity gradients for all grid points. For those points at the edge of a tessera data field or adjacent to an exclusion zone, the gradient calculation only considered the differences in velocity between the two valid grid points, to avoid erroneous gradients at those locations. These gradients were then used to compute instantaneous vorticity (ω_i) and strain rate (ε_i)using the following relations:

$$\omega_i = \frac{\partial v_i}{\partial x} - \frac{\partial u_i}{\partial y} \qquad [4.8]$$

$$\varepsilon_i = \frac{1}{2}\left[\frac{\partial v_i}{\partial x} + \frac{\partial u_i}{\partial y}\right] \qquad [4.9]$$

The gradients were averaged and then subtracted from the instantaneous gradients to produce gradients of the fluctuating turbulent velocities. These fluctuating gradients were used to estimate the mean dissipation rate (d). It is recognized that the calculated d values are simply estimates and may not represent the full and total energy dissipation. Using the method of Doron *et al.* (2001), the following equation was employed:

$$d = 3\nu\left[\overline{\left(\frac{\partial u'}{\partial x}\right)^2} + \overline{\left(\frac{\partial v'}{\partial x}\right)^2} + \overline{\left(\frac{\partial u'}{\partial y}\right)^2} + \overline{\left(\frac{\partial v'}{\partial y}\right)^2} + 2\overline{\left(\frac{\partial u'}{\partial y}\frac{\partial v'}{\partial x}\right)} + \frac{2}{3}\overline{\left(\frac{\partial u'}{\partial x}\frac{\partial v'}{\partial y}\right)}\right] \qquad [4.10]$$

Using the measured temperatures and calculated kinematic viscosity values for each tessera, mean Kolmogorov length scales (l_k), velocity scales (v_k) and time scales (t_k) were computed at each point in each tessera. The following equations were used, following Tennekes and Lumley (1972):

$$l_k = \nu^{0.75} d^{-0.25} \qquad [4.11]$$

$$v_k = (\nu d)^{0.25} \qquad [4.12]$$

$$t_k = l_k / v_k \qquad [4.13]$$

Time averages were also calculated for all of the flow parameters presented in equations [4.1] to [4.9], over the full three minutes of PIV data recorded at each tessera. This supplementary processing took approximately 24 computer hours of computation time for each tessera. The calculations were performed for every point in every PIV data file, for every tessera. Further processing was performed in §5 on select data for specific profile related analyses and will be discussed in that section.

4.5 Error Consideration

This section presents an approximation of the errors contained in the PIV data. Generally, the total error associated in PIV data is a function of out-of-plane particle motion, both the particle size and particle density, peak locking, the dynamic range of measured pixel displacements, and the sub-pixel interpolation scheme employed (Cowen and Monismith 1997). §4.5.1 discusses the effects of out-of-plane particle motion while §4.5.2 discusses the standard PIV errors of peak locking, particle displacement and velocity gradients. §4.5.3 presents the special errors associated with this experiment; namely errors introduced by the imaging sub-system, including those introduced by the camera optics and produced through tessera misalignment.

4.5.1 Out-of-Plane Motion

Employment of PIV relies on the assumption that the out-of-plane motion of the tracer particles is negligible, and that the z-component of the flow is small. This assumption must be validated if the PIV data is to be accepted as representative of the flow field, as error increases with increasing out-of-plane motion. To estimate the out-of-plane motion, the mean pixel displacements (d_{px} and d_{py}) and the associated standard deviations (σ_{px} and σ_{py}) were calculated for each tessera. Following the analysis of Siddiqui (2002), the out-of-plane pixel displacements were expected to be less than or equal to the smallest x-y plane displacement, and were estimated as the sum of d_{px} and σ_{px} for the smaller of either the x- or y-component displacements. The results of this analysis are presented in Table 4.3 and $(d+\sigma)_z$ ranges from 105 μm to 817 μm. Out-of plane motion would be considered significant if the average z-direction displacement was larger that the laser sheet thickness, however it is clear that all values are less than 3 000 μm. As such, the errors associated by the out-of-plane motion can be considered negligible in the present study.

4.5.2 Standard PIV Errors

Peak locking refers to the bias that occurs when the estimated location of the correlation peak detected by the PIV routine is shifted towards an integer value. According to Fincham and Spedding (1997), this peak locking bias error will occur in any image velocimetry technique that uses sub-pixel correlation peak interpolation. Siddiqui *et al.* (2001) demonstated that the three-point Gaussian estimator peak fitting scheme produced the least peak locking error, and this is the scheme which was used in this study.

The effects of peak locking in this study were determined using the method of Fincham and Delerce (2000). Using all of the raw pixel displacements produced for a single tessera by primary PIV processing over the full three minutes of experimental data, histograms of d_{pxx} and d_{pxy} were plotted for each individual tessera. Bin sizes of 1.0 px and 0.1 px were employed and the resulting histograms superposed and compared. Figure 4.8 presents the set of histograms of d_{pxx} and d_{pxy} for tessera 1 as an example. The peak locking error (I_{plu} and I_{plv}) is defined as a percentage, and reflects the total number displacements, using the 0.1 px bin size and within ±0.5 px ranges of integer pixel displacements, which exceed the number of displacements that fall within the same range using a 1.0 px bin size. The peaks formed by the 0.1 px bin size histogram are clearly visible in Figure 4.8 and show the bias towards integer pixel displacements. Similar figure for all tesserae can be found in §8.

Table 4.4 presents the peak locking error percentages for all tesserae. The average values of I_{plu} and I_{plv} are 14.8% and 12.8%, respectively, and are consistent with the peaklocking values of Fincham and Spedding (1997) and Siddiqui *et al.* (2001). I_{plu} varied from a minimum value of 11.1% in tessera 11 to a maximum value of 17.6% in tessera 10, while I_{plv} varied from a minimum value of 8.4% in tessera 5 to a maximum value of 17.7% in tessera 10. The variation in peak locking between tesserae seems to be related to the dynamic range of pixel displacement, with increased peak locking present in those tesserae whose dynamic range is either more limited or somewhat skewed in distribution.

The errors in both velocity (e_v) and vorticity (e_ω) for each tessera were calculated following the method of Siddiqui (2002), using the results of Cowen and Monismith (1997) and Prasad *et al.* (1992). Time averaged values in time for all four of the displacement gradients were calculated for each tessera and the largest gradient was identified. So as to consider the worst-case scenario, errors were estimated for both the u and v velocities on the basis of this gradient value. The maximum averaged gradients ranged from 0% to 1%. Figure 5 (e) of Cowen and Monismith (1997) plots the peaklocking and the root-mean-square error in pixel displacement (the sum of which are defined as e_u) as a function of the nondimensional mean velocity gradient using a particle size of 2.0 px/px. Preliminary e_u estimates for each of the tesserae were obtained from this figure.

However, as the nondimensional tracer particle size in this study was approximately 0.1 px/px, the difference in particle sizes obliged a correction of the preliminary error estimates. Using Figure 5 (a) of Cowen and Monismith (1997), it was ascertained that a decrease in particle size from 2.0 px/px to 1.0 px/px (the samllest size considered by Cowen and Monismith) resulted in an increase to e_u of 0.02 px. Using Figure 13 of Prasad *et al.* (1992), which shows the variation of e_u as a function of particle diameter, it was estimated that the errors associated with a particle size of 0.1 px/px would be approximately 50% greater than those of a 1.0 px/px particle size. The results of Prasad *et al.* (1992), however, were based on a centre-of-mass peak fitting scheme, which is a scheme particularly susceptible to peak locking error (Fincham and Spedding 1997). Because the present study employed a three-point Gaussian estimator peak fitting scheme, it was estimated that a more realistic estimate of the increase in error due to the particle size would be 25% (Siddiqui 2002).

As argued in §4.5.1, the error associated with out-of-plane motion can be considered negligible. The constant error associated with the AGW interpolation of the displacement vectors onto a regular grid was estimated to be 0.08 px from Figure 5 (f) of Cowen and Monismith (1997). The sum of the combined errors due to the gradients, the particle size and the AGW interpolation formed the final e_u estimates for each tessera. Table 4.5 presents the root-mean-square errors in u and v velocity components for each tessera, both in terms of pixel displacement units and actual velocity units. The error in velocity (e_V) was calculated as $e_V = \sqrt{2e_u^2}$ using the assumption that the u and v velocity component error are approximately equal. Table 4.5 also presents the final e_V values; e_V ranges from 0.6 cm/s to 2.6 cm/s.

Because the error in velocity was based on the displacement gradients, it is larger in those tesserae that image areas of flow containing large gradients in velocity. Tesserae 2, 3, 4, 5. 8 and 9 each image areas of the FOV containing the main deflected wall jet body, and naturally have larger e_V values. Fortunately, the maximum velocity resolutions in those tesserae are also larger, so the error as a percent of the maximum achievable instantaneous velocity ($V_{i\,max}$) is not dramatically larger as well. Unfortunately, the measured velocities near the lowest end of the dynamic ranges (i.e. the smallest velocities in tesserae that needed to be able to capture relatively large velocities) in all tesserae, may be subjected to errors larger than the measured velocities themselves.

The error in vorticity (e_ω) for each tessera was estimated from the e_V errors using the method of Siddiqui (2002). The two gradients used in equation [4.8] can be considered in the form $\Delta u/\Delta x$, where Δu is the difference in either the u or v velocity between two grid points and Δx is either to x- or y-distance between the same two grid points. A central difference scheme was used in the computation of the gradients, therefore Δx in the present case is equal to 0.5 cm. The variance of the error of the gradients can then be estimated as $e_u^2/\Delta x$ for both gradients in equation [2.8]. Using the assumption that the error in both u and v are equal and based upon the largest gradients, the root-mean-square error in vorticity can be expressed as $e_\omega = \sqrt{e_u^2/\Delta x}$. Table 4.6 presents e_ω for all tesserae; the minimum error in vorticity is 1.3 s^{-1} and the maximum is 5.3 s^{-1}.

4.5.3 Misalignment Errors

The PIV implementation employed in this experiment is unique in that it uses a number of tesserae whose PIV data sets are assembled into a single mosaic to describe the entire flow structure of the plane deflected wall jet. The unique nature of the experiment presented equally unique error associated with the boundaries and edges of the individual tesserae.

When PIV is traditionally used, the edges of the images do not usually contain the focus of the experiment; the area of greatest interest is normally centered in the FOV where the quality of both the illumination sheet and the images are most consistent. In this study, the cylindrical lens used in laser sheet generation produced a plane of illumination exhibiting a Gaussian intensity profile. The intensity of the light was reduced at the edges of the sheet and therefore at the edges of the images, resulting in weak particle reflections. This was especially noticeable in tesserae adjacent to the glass bed, as the sheet was only slightly wider that the FOV of the camera. The effects of this variation were minimized as much as possible through positioning the lens along the rail; however, it was always present in some degree.

In addition, the camera lens used in this study produced images which were not always focused at the corners and edges, even when the majority of the FOV was in focus. Although great care was taken to position the camera fields of view coincident with the predetermined tesserae positions, the alignment was not always ideal. Occasionally, all four of the FOV edges could not be made perfectly coincident with the orthogonal alignment grid markings, and sometimes the fields of view were not perfectly square (a further limitation of the camera lens). The tessera edges were within 1.0 mm of the predetermined alignment grid markings and the centres were perfectly aligned with the registration marks.

The combination of the optical distortion and positioning limitations resulted in vectors along the edges of each tessera being somewhat flawed. The flaws became important when the tesserae were assembled into the full mosaic. Figure 4.9 shows the edge dislocations present in the mean corrected and interpolated velocity vector field, in the region around the upper-left corner of tessera 10. The vectors in this corner of tessera 10 are noticeably smaller than those in the adjacent tesserae. In addition, it has already been stated that gradients were not calculated across tessera boundaries; as a result, those parameters based on both the velocities and gradients of data point along the edges of the tesserae are susceptible to edge dislocation flaws, which will be noticeable in some of the figures in §5. Hasselbrink and Mungal (2001a-b) employed a similar PIV mosaic assembly method in their study of a circular jet in a crossflow, and also report flawed data at the edges of their individual tesserae fields of view. The potential error associated with the misalignment and out-of-focus corners is estimated to be on the same order of e_v, but localized at tessera edges and corners.

tessera	total vectors	percentage of total vectors identifed as spurious per iteration			
		1	2	3	4
1	3600	0.42	0.16	0.08	0.04
2	3564	0.58	0.13	0.05	0.03
3	3564	5.90	1.84	0.71	0.31
4	3600	0.86	0.16	0.04	0.02
5	3600	0.25	0.05	0.02	0.01
6	1320	1.15	0.22	0.07	0.03
7	1320	3.50	0.99	0.41	0.20
8	3600	2.27	0.47	0.17	0.08
9	3600	3.38	0.95	0.39	0.19
10	3600	1.63	0.68	0.31	0.15
11	3600	1.82	0.73	0.34	0.18
12	3600	4.51	1.31	0.55	0.27
13	1320	1.84	0.28	0.08	0.03
14	3600	0.28	0.07	0.03	0.01
average	-	2.03	0.58	0.23	0.11

Table 4.1: Spurious vector statistics arranged by tessera and iteration.

tessera	FOV (cm)	FOV (px)	S_{FOV} (μm/px)	Δt (ms)	$d_{px\,max}$ (px)	$u_{i\,max}$ (cm/s)	$v_{i\,max}$ (cm/s)	$V_{i\,max}$ (cm/s)
1	15.75	1008	156.25	3.0	16	83.3	83.3	117.9
2	15.75	1008	156.25	1.3	16	192.3	192.3	272.0
3	15.75	1008	156.25	1.6	16	156.3	156.3	221.0
4	15.75	1008	156.25	1.7	16	147.1	147.1	208.0
5	15.75	1008	156.25	2.0	16	125.0	125.0	176.8
6	15.75	1008	156.25	2.0	16	125.0	125.0	176.8
7	15.75	1008	156.25	2.0	16	125.0	125.0	176.8
8	15.75	1008	156.25	1.8	16	138.9	138.9	196.4
9	15.75	1008	156.25	1.7	16	147.1	147.1	208.0
10	15.75	1008	156.25	3.0	16	83.3	83.3	117.9
11	15.75	1008	156.25	4.0	16	62.5	62.5	88.4
12	15.75	1008	156.25	2.6	16	96.2	96.2	136.0
13	15.75	1008	156.25	2.0	16	125.0	125.0	176.8
14	15.75	1008	156.25	2.6	16	96.2	96.2	136.0

Table 4.2: Maximum displacement and velocity resolutions for all tesserae.

tessera	mean d_{pxx}	σ_{pxx}	$(d+\sigma)_{pxx}$	mean d_{pxy}	σ_{pxy}	$(d+\sigma)_{pxy}$	$(d+\sigma)_{pxz}$	$(d+\sigma)_z$ (μm)
1	2.8	1.9	4.7	-2.6	1.3	3.9	3.9	609
2	4.2	1.9	6.1	-1.3	1.0	2.3	2.3	362
3	2.1	3.1	5.2	-2.6	2.6	5.2	5.2	817
4	2.7	1.2	3.9	-4.6	1.5	6.1	3.9	614
5	-0.6	1.4	2.0	-3.0	1.3	4.3	2.0	311
6	-1.5	2.1	3.6	-0.4	0.7	1.1	1.1	170
7	0.4	1.2	1.5	-1.0	1.4	2.5	1.5	242
8	1.7	0.7	2.4	-4.6	1.3	5.9	2.4	372
9	0.9	1.5	2.5	-2.7	2.2	4.9	2.5	388
10	-2.0	0.6	2.6	-0.3	0.4	0.7	0.7	105
11	-2.3	0.7	3.0	-1.2	0.2	1.5	1.5	228
12	2.0	1.8	3.8	-1.2	0.9	2.1	2.1	324
13	1.8	2.4	4.1	-0.3	0.5	0.8	0.8	131
14	-3.7	1.8	5.5	-1.2	0.8	2.0	2.0	316

Table 4.3: Estimates of out-of-plane displacement (d_{pzz}) for all tesserae.

tessera	I_{plu} (%)	I_{plv} (%)
1	11.1	12.9
2	14.4	14.5
3	14.5	15.4
4	14.0	14.0
5	15.1	8.4
6	16.8	11.1
7	15.8	10.6
8	16.1	12.4
9	15.0	13.4
10	17.6	17.7
11	11.6	13.0
12	13.3	11.5
13	17.5	12.0
14	11.6	12.1
average	14.6	12.8

Table 4.4: Peak locking percentages (I_{plu} and I_{plv}) for all tesserae.

tessera	du/dx (px/px)	du/dy (px/px)	dv/dx (px/px)	dv/dy (px/px)	maximum gradient	e_u (px)	e_u (cm/s)	e_V (cm/s)
1	0.001	0.013	-0.009	-0.002	0.01	0.155	0.8	1.1
2	-0.002	0.010	-0.006	0.002	0.01	0.155	1.9	2.6
3	-0.010	-0.009	0.006	0.010	0.01	0.155	1.5	2.1
4	0.003	0.007	-0.007	-0.003	0.01	0.155	1.4	2.0
5	0.006	0.009	-0.008	-0.005	0.01	0.155	1.2	1.7
6	0.003	0.005	-0.002	-0.003	0.00	0.118	0.9	1.3
7	0.004	0.002	0.000	-0.004	0.00	0.118	0.9	1.3
8	0.002	0.001	0.006	-0.002	0.01	0.155	1.3	1.9
9	-0.009	-0.005	0.011	0.008	0.01	0.155	1.4	2.0
10	-0.002	-0.001	0.001	0.002	0.00	0.118	0.6	0.9
11	-0.002	-0.004	0.000	0.001	0.00	0.118	0.5	0.6
12	0.000	-0.012	0.006	0.000	0.01	0.155	0.9	1.3
13	0.001	-0.003	0.001	-0.001	0.00	0.118	0.9	1.3
14	0.004	0.013	-0.005	-0.003	0.01	0.155	0.9	1.3

Table 4.5: Errors in velocity (e_u and e_V) for all tesserae.

tessera	e_u (cm/s)	$2(e_u)^2$ (cm^2/s^2)	$2(e_u)^2/\Delta x$ (s^{-2})	e_ω (s^{-1})
1	0.8	1.3	2.6	2.3
2	1.9	6.9	13.9	5.3
3	1.5	4.6	9.2	4.3
4	1.4	4.1	8.1	4.0
5	1.2	2.9	5.9	3.4
6	0.9	1.7	3.4	2.6
7	0.9	1.7	3.4	2.6
8	1.3	3.6	7.2	3.8
9	1.4	4.1	8.1	4.0
10	0.6	0.7	1.5	1.7
11	0.5	0.4	0.8	1.3
12	0.9	1.7	3.5	2.6
13	0.9	1.7	3.4	2.6
14	0.9	1.7	3.5	2.6

Table 4.6: Errors in vorticity (e_ω) for all tesserae.

(a)

(b)

Figure 4.1: Baffle shadow and edge reflection defects visible in raw (a) tessera 2 and (b) tessera 3 PIV images.

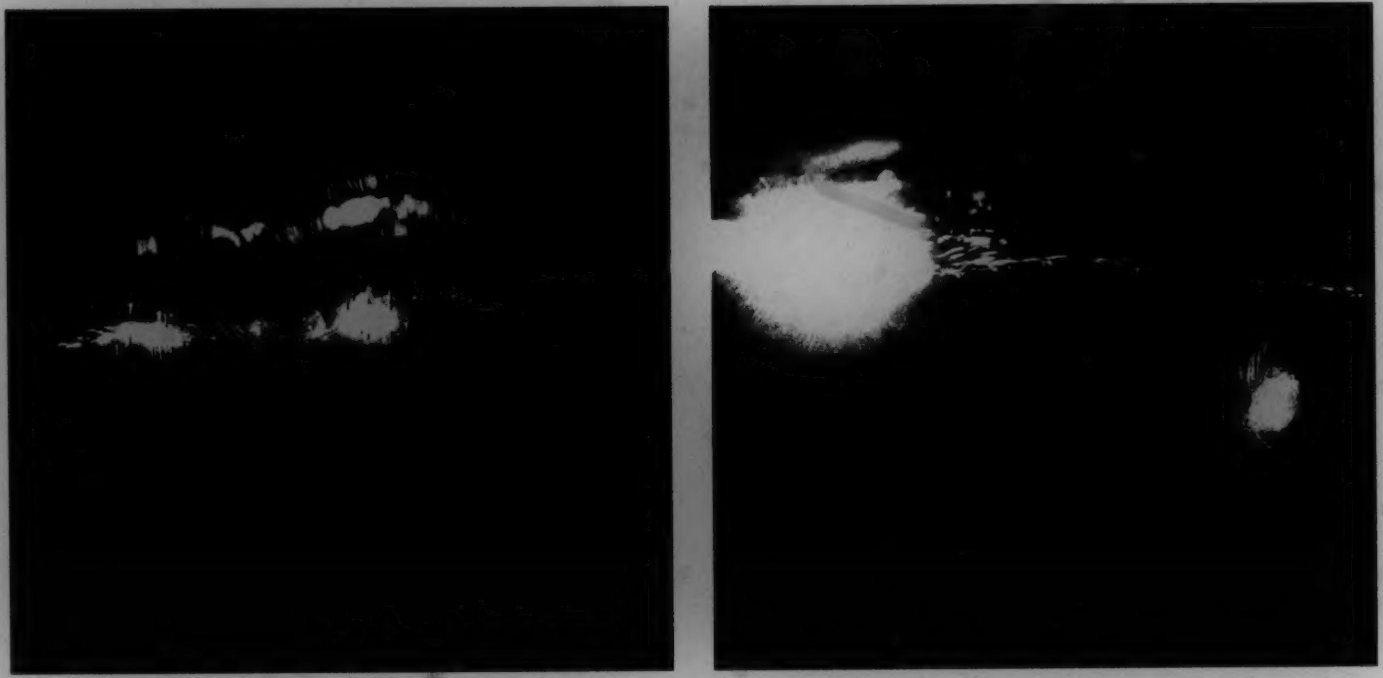

(a)

(b)

Figure 4.2: Water surface reflection defects visible in (a) tessera 6 and (b) tessera 7 raw PIV images.

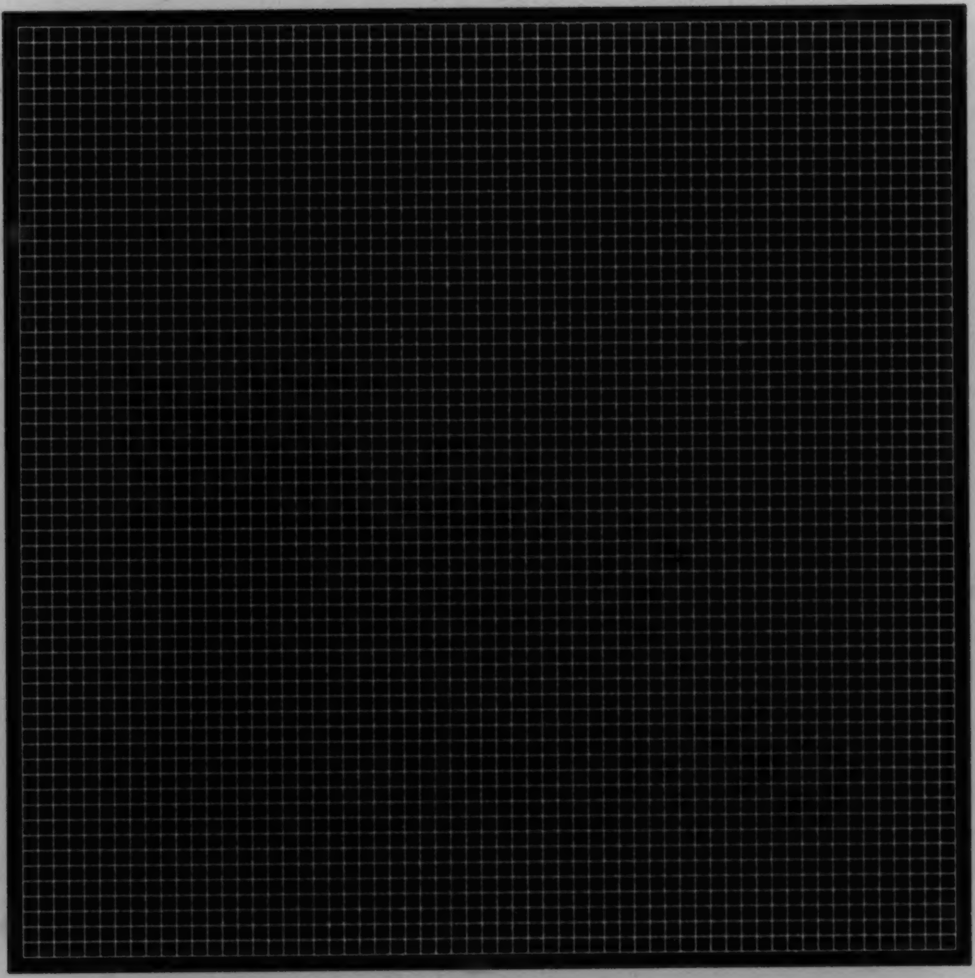

Figure 4.3: Interrogation window grid superposed on a tessera 4 PIV image.

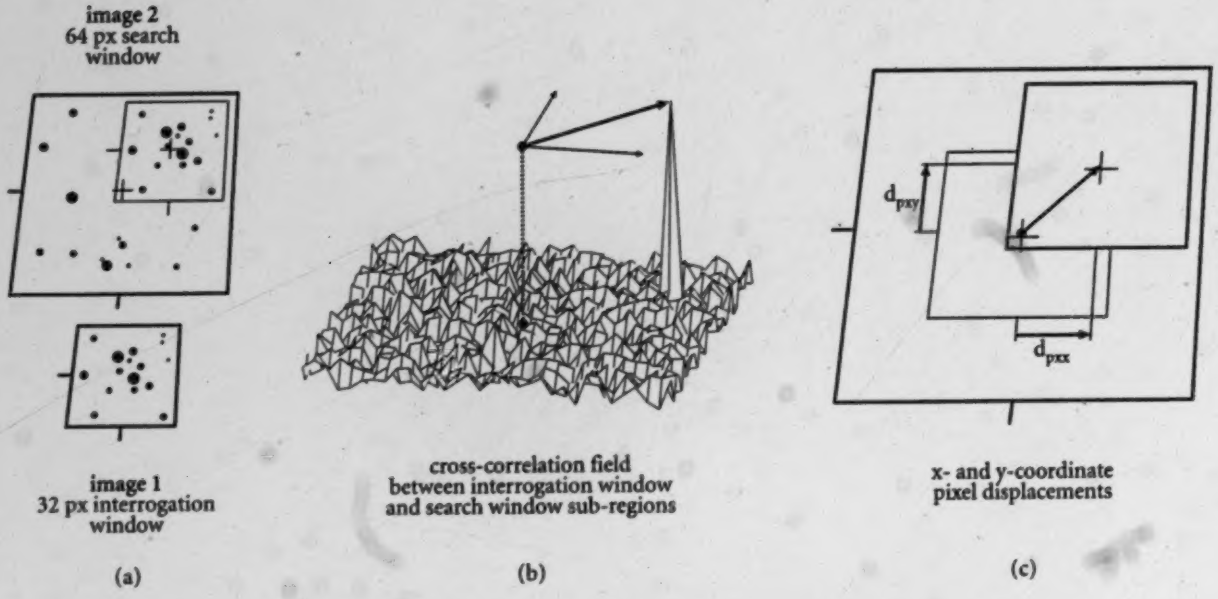
image 2
64 px search
window
image 1
32 px interrogation
window
(a)
cross-correlation field
between interrogation window
and search window sub-regions
(b)
d_{pxy}
d_{pxx}
x- and y-coordinate
pixel displacements
(c)

Figure 4.4: PIV methodology schematic showing (a) interrogation and search windows, (b) the correlation field and (c) identified pixel displacements.

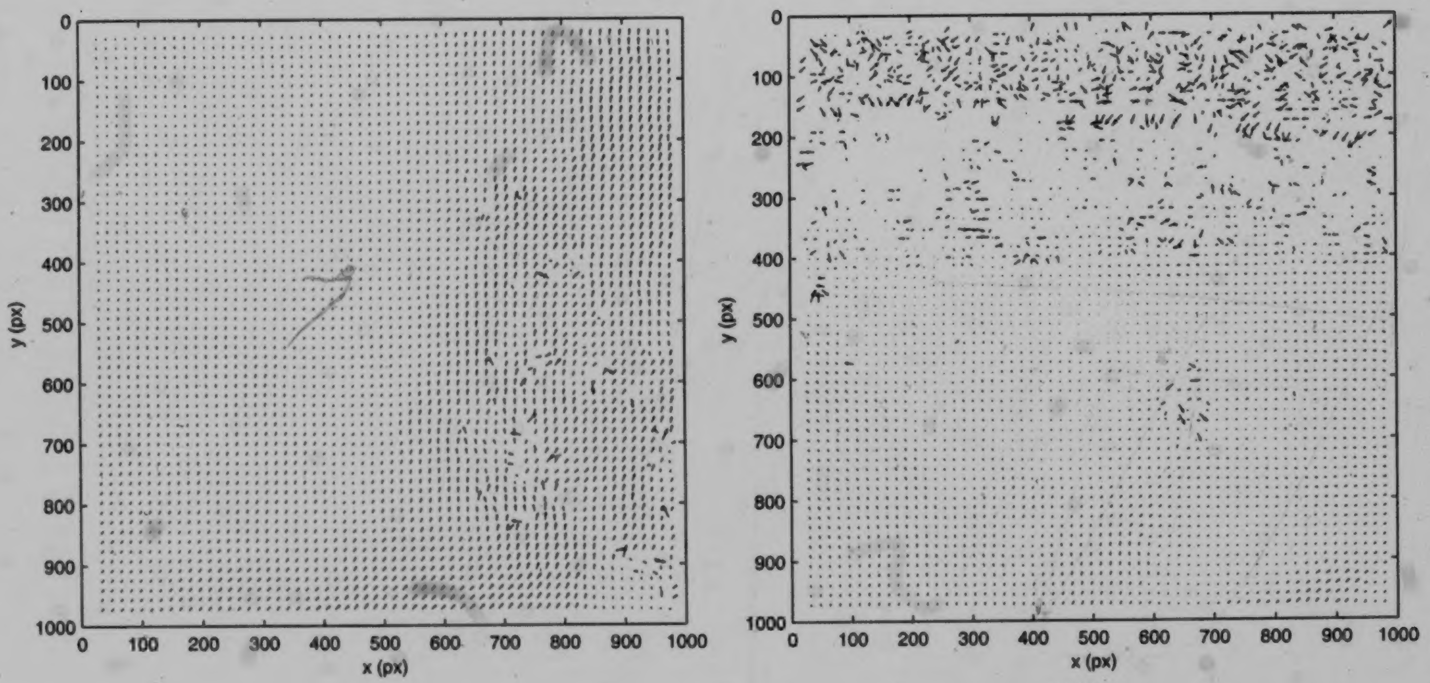

(a)

(b)

Figure 4.5: Representative instantaneous raw pixel displacement vector fields for (a) tessera 4 and (b) tessera 7.

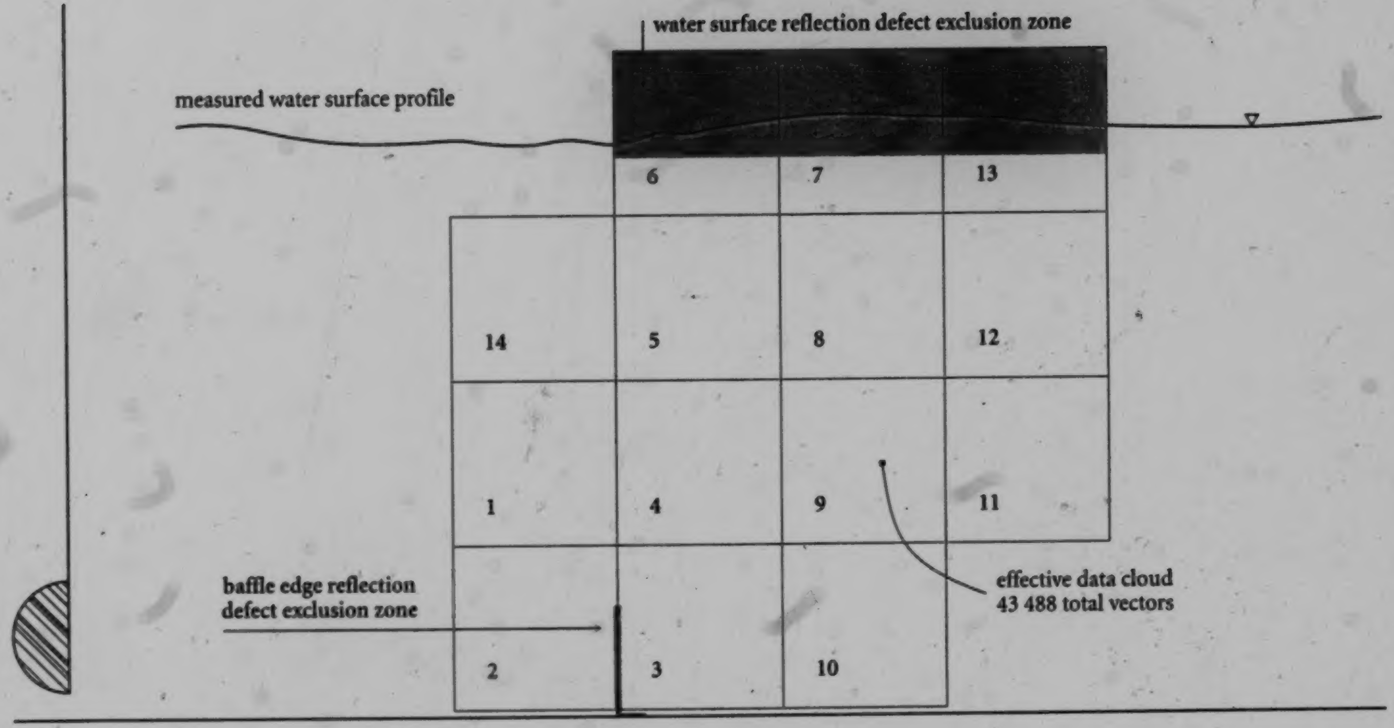
water surface reflection defect exclusion zone
measured water surface profile
6
7
13
14
5
8
12
1
4
9
11
baffle edge reflection
defect exclusion zone
2
3
10
effective data cloud
43 488 total vectors

Figure 4.6: Exclusion zones in the assembled mosaic.

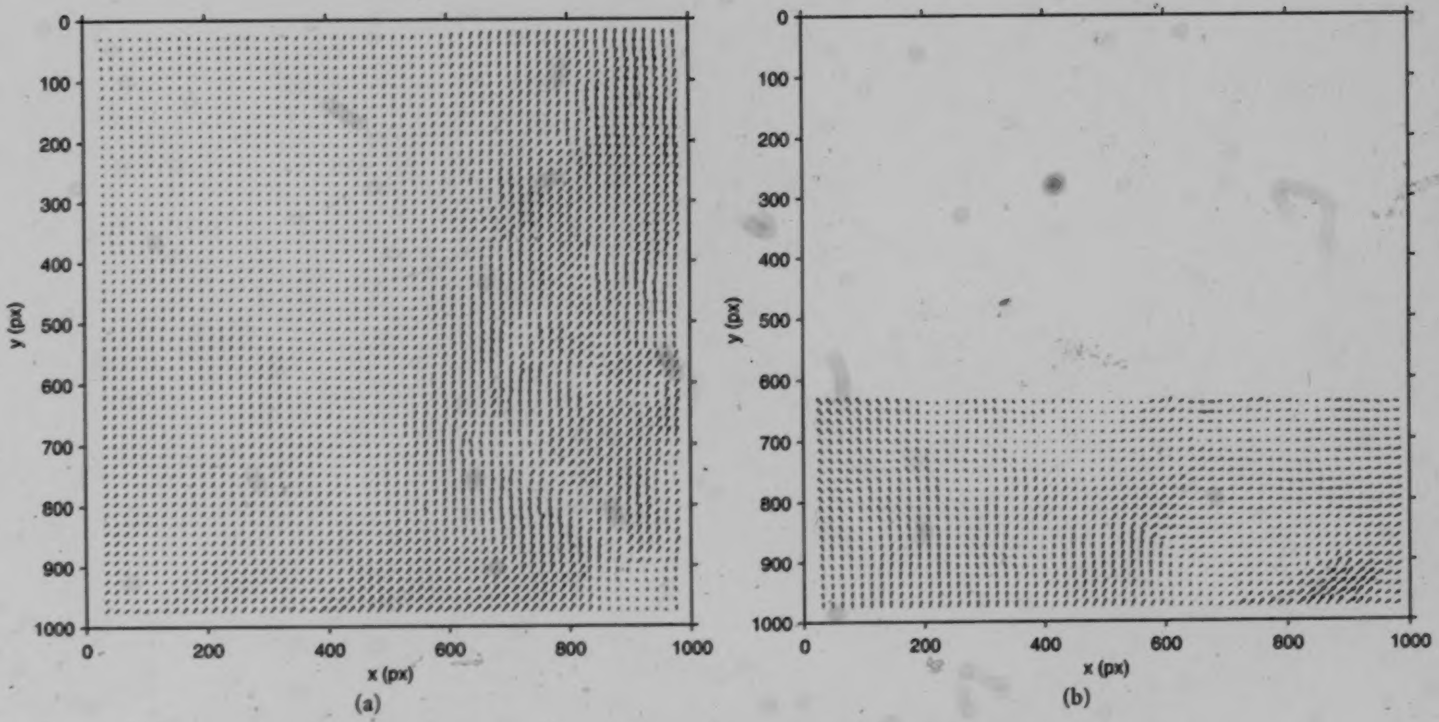

Figure 4.7: Representative instantaneous corrected and interpolated pixel displacement vector fields for (a) tessera 4 and (b) tessera 7.

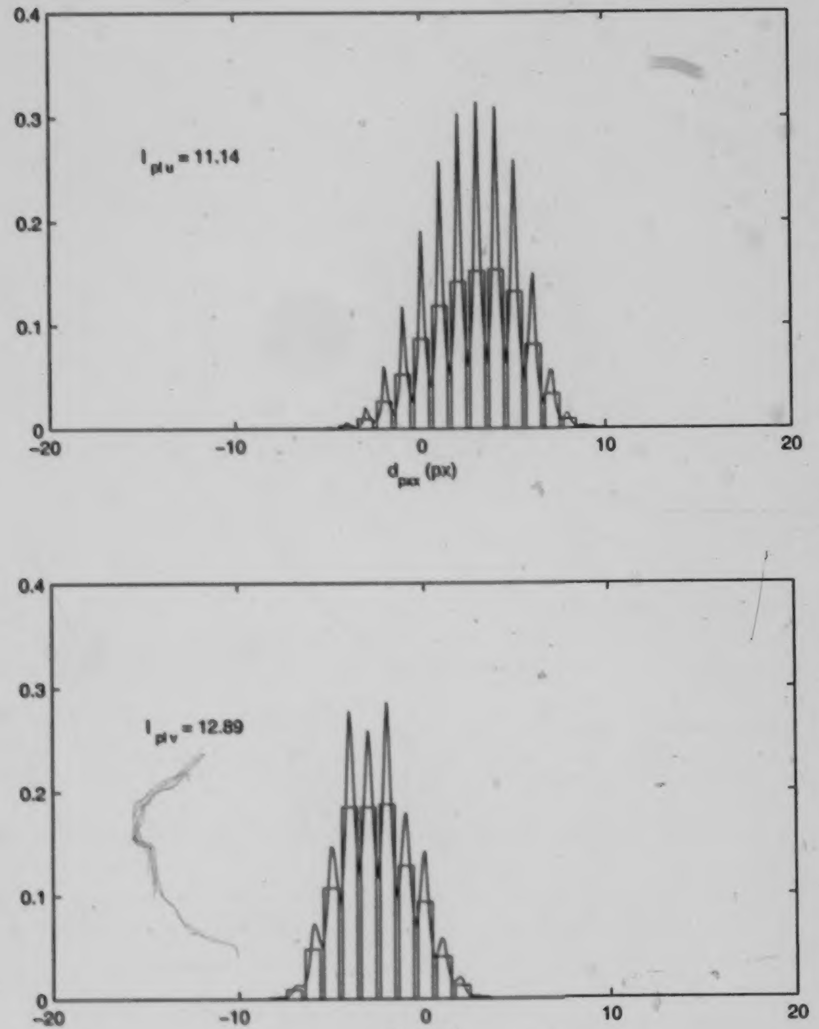

Figure 4.8: Peak locking error in tessera 1 raw displacement data.

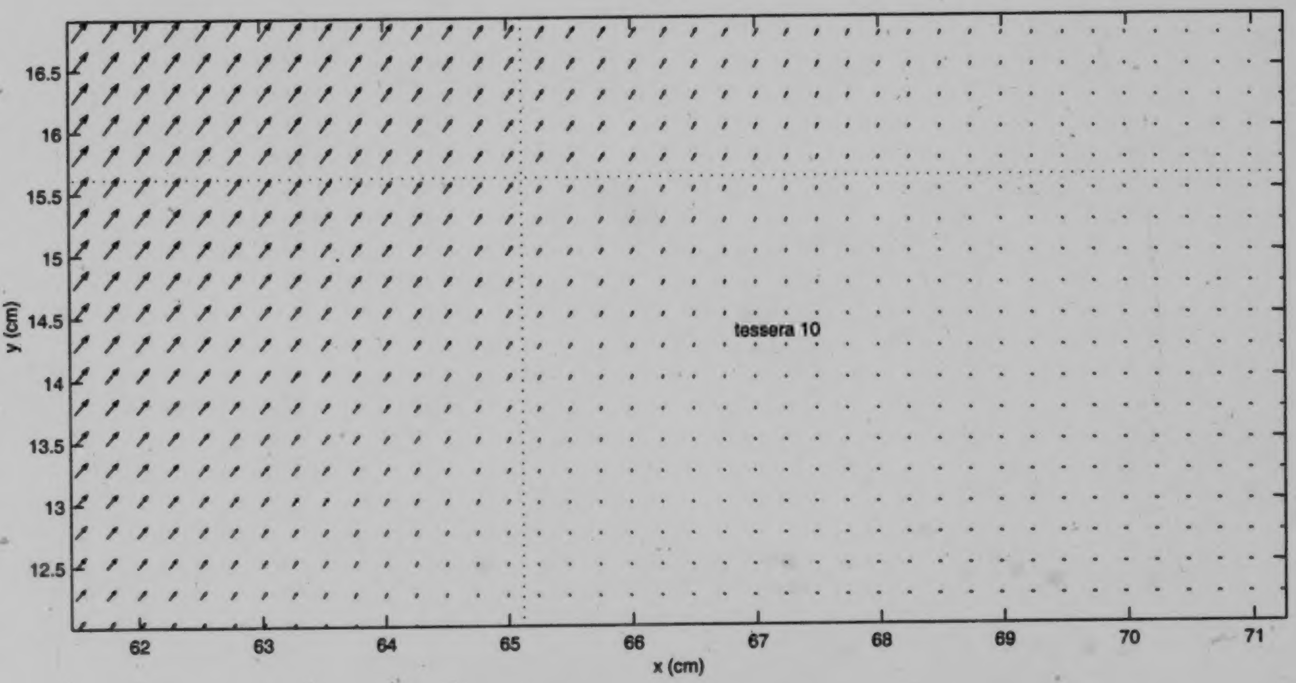

Figure 4.9: Example of edge dislocation in the upper-left corner of tessera 10.

5 Data Analysis

The most significant benefit of using the particle image velocimetry technique over other techniques is that it provides whole-field experimental data. Unlike standard point measurement techniques, such as those using Prandtl tubes and manometer boards or even acoustic or laser Doppler anemometers, PIV yields a large number of instantaneous velocity measurements characterizing an entire area of flow as opposed to a single point in a flow. Because the PIV technique is completely non-invasive (i.e. there exist no immersed probes or instrumentation to affect the flow being investigated), the resultant data sets are very robust and descriptive. The instantaneous velocities can be computationally manipulated to provide a variety of instantaneous, mean and turbulent flow properties, such as those discussed in §4.4.

It can be advantageous to observe flow patterns and coherent structures as whole-field phenomena rather than to interpret them from numerous point measurements. Features and trends which may otherwise be either indiscernible or overlooked become recognizable and sometimes even obvious. PIV provides data ideal for this approach, because all points in a field of view are temporally coincident as well as spatially distributed. Not only do PIV data sets lend themselves to such whole-field analysis, but point measurement analytical approaches can also be employed. It is entirely possible to consider specific locations in the FOV and observe the variation of flow properties as a function of time at those locations only, as is done with data provided by standard techniques. Fluctuations at a point or mean profiles can be extracted from a PIV data-cloud. The following sections provide analyses using both approaches and present the error associated with the PIV technique used in this study.

5.1 Whole-Field Flow Properties

As previously discussed, PIV data was processed and instantaneous, mean and turbulent flow properties extracted for each of the fourteen tesserae that make up the complete experimental FOV. Both the size and position of the tesserae made it possible to assemble the individual fields into a large contiguous mosaic containing a dense array of points spaced in a regular 2.5 mm grid. The full mosaic encompasses an area beginning approximately 35.1 cm downstream of the gate to approximately 95.1 cm downstream of the gate, with a bottom edge located approximately 0.6 cm above the flume bed and an upper edge located approximately 50.1 cm above the bed. This type of mosaic approach is similar to that used by Hasselbrink and Mungal (2001a-b) in their investigation of a circular jet in a crossflow.

Not only does the approach allow for large fields of view to be considered with greater spatial resolution than would be possible through the use of a single large FOV (imaged with the same camera and the same number of pixels), but it allows for more accurate velocity resolution. The employment of different timing sequences at different tesserae allows for the dynamic range of the velocity measurements at an individual tessera to be matched to the actual velocity range found in the flow encompassed by that tessera. Although the time series data for all points in a single tessera is continuous over a full three minutes, the time series' of each of the individual tesserae are separated from each other and neither temporally coincident nor continuous. This is due to the time required to move and prepare the instrumentation prior to data collection at each tessera as well as the time required to export captured images to the removable media when the computer hard drives were filled to capacity. As such, the full experimental mosaic can only present mean flow properties; instantaneous properties are temporally coherent within each tessera at any time, but because the data presented in all neighbouring tesserae were collected at a different actual times, there exists no true temporal connection across tessera boundaries.

The figures introduced in this section present various whole-field mean flow properties for the assembled experimental mosaic, omitting data from the exclusion zones. When considering these figures, it is helpful to maintain awareness of two important physical references: the baffle and the jet centreline trajectory. The baffle is located at $x_0 = 50$ cm and is generally not shown in the figures. It is important not to confuse the exclusion zone surrounding the baffle with the baffle itself; the exclusion zone is approximately 9.0 cm tall while the baffle is only 2.54 cm tall. The jet centreline trajectory is generally shown in the figures, as either a solid black line or as a dashed grey line. The method used to obtain the trajectory is further explored in §5.2.1 and is based on the locus of zero vorticity; the jet centreline itself aids greatly in the description of whole-field data by provideing a convenient reference for description.

5.1.1 Mean Velocity

The general mean flow pattern of the mosaic is presented in Figure 5.1 as a vector field containing all 43 488 processed velocities. The vectors are scaled so that smaller velocities are represented by proportionally smaller arrows. The field is so dense and the plotted vectors so small that it appears almost as a concentration map, with darker areas representing larger velocities. Superposed onto this complete vector field is another field consisting of every tenth point velocity along with a velocity scale; the superposed field provides a measure of scale and clarity to the data. Figure 5.2 presents only the vector field of every tenth velocity point with a velocity scale; the jet centreline trajectory, the water surface, the baffle as well as the tesserae boundaries are plotted for convenience.

The description of the mean flow pattern of the deflected wall jet provided by Wu and Rajaratnam (1995a) is confirmed by Figures 5.1 through 5.3. Visible is a strong jet that closely follows the wall before reaching the baffle. This jet is then deflected along a curved trajectory toward the water surface and ultimately impinges upon the water surface at approximately $x = 75$ cm. At the surface, the jet effectively separates into two different flows: one that continues along the water surface downstream and one that returns upstream.

Three eddies are also clearly extant. An upstream portion of the first eddy is observed on the outbound side of the jet trajectory, between the strong downstream jet flow at the surface and the flume bed. It is assumed to persist until the downstream end of the flume as reported by Wu and Rajaratnam. It has a general clockwise rotation. The second and most dominant eddy appears centered at approximately x = 35 cm and y = 28 cm and rotates counter-clockwise. It is fully contained on the inbound side of the jet and is assumed to persist upstream until the gate with a generally elliptical shape. The third eddy is smaller, with a diameter approximately equal to the baffle height (h) and a clockwise rotation. It is found immediately upstream of the baffle and on the outbound side of the jet trajectory and is shown in Figure 5.3.

Generalizations on the nature of the jet, and its development from plane wall jet-like (WJL) flow to plane jet-like (PJL) flow and ultimately to plane surface jet-like (SJL) flow, is further explored in §5.2. However, the whole-field velocities appear to support the observation of Wu and Rajaratnam. Even a simple visual inspection of the magnitude and direction of the velocities as they follow the jet centreline trajectory downstream indicate that the observed flow is comprised of at least those three distinct jet regimes The maximum velocity in the jet appears to decay along the trajectory and the width of the jet (i.e. the body or general mixing region) appears to increase. The minimum and maximum u and v velocity components as well as the minimum and maximum velocity magnitudes (V_{min} and V_{max}) for all tesserae are presented in Table 5.1. Individual mean velocity vector fields for each of the tesserae are presented at a much larger scale in §8 if one wishes to observe them in greater detail.

5.1.2 Mean Kinetic Energy

Figure 5.4 presents two colour contour maps of mean kinetic energy (KE) for the entire experimental data mosaic, with different scales of interest and the jet centreline trajectory plotted in gray. The first contour map (a) is scaled to show the maximum range of data, from KE = 0 cm^2/s^2 to KE = 7 000 cm^2/s^2, and the second (b) is scaled to provide more detail in the KE = 0 cm^2/s^2 to KE = 1 000 cm^2/s^2 range. The minimum mean kinetic energy for the full mosaic is 0.1 cm^2/s^2 and the maximum is 7 445.6 cm^2/s^2. Table 5.2 presents the extreme values of mean flow parameters for the full mosaic and Table 5.3 provides the extreme values on a tessera basis.

The first map clearly shows that the bulk of the KE of the flow is contained directly in the jet body region. Maximum KE values are found in the region before the baffle, along the flume bed. Except for a small area coincident with the location of the baffle eddy, locus of the KE_{max} follows that of the trajectory closely. The kinetic energy is proportional to the square of the total velocity magnitude, and therefore this figure correlates well with the velocity vector fields introduced in §5.1.1. In the region before the baffle, the KE rapidly decreases in the upwards direction and along the jet centreline in the curved trajectory region. KE decreases with distance from the centreline trajectory on both sides. The scale of this figure indicates that at some point before the jet reaches the water surface, the KE approaches a general background level of between 0 cm^2/s^2 and 2 000 cm^2/s^2. The position and distribution of the KE contours support the generalizations of a wall jet-like region before the baffle and plane jet-like region after the baffle region.

Figure 5.4 (b) further supports the supposition that different jet regimes and eddy patterns characterize and dominate the flow of the deflected wall jet. In this figure, all values greater than the maximum extreme of the scale are assigned the colour of the maximum. Figure 5.4 (a) has already qualitatively corroborated the existence of wall jet- and plane jet-like elements with those regions shown in Figure 5.4 (b) as a monolithic dark-red zone. But the second figure also supports the concept that near point of impingement the jet separates into two weaker secondary jets both located at the water surface: a main flow jet that continues downstream and a return flow jet that is driven upstream. These surface jet-like flow elements are suggested in the figure by areas of high KE near the upper edge of the mosaic that decrease in the downwards direction. A large elliptical eddy is also clearly visible on the inbound side of the jet centreline trajectory.

Because the baffle plays such a dominant role in the flow pattern of the deflected wall jet, it is interesting to observe the effects immediately downstream of the baffle. As shown in Figure 5.4 (a), the mean kinetic energy of the jet increases in magnitude after the baffle. Figure 5.5 presents the colour contour map of KE for tessera 3 (the tessera adjacent to the downstream baffle edge), along with the jet centreline trajectory plotted in gray. Although the maximum KE occurs upstream of the baffle and near the bed, Figure 5.5 shows in greater detail a small core of high KE directly downstream of and approximately 2 cm above the baffle tip, centered about the jet centreline. The interaction of the baffle and the jet therefore directly induces increased velocities in the jet body. This phenomena as well as other matters relating to the development of the jet will be further discussed in §5.2.

5.1.3 Mean Reynolds Stress

Figure 5.6 presents two colour contour maps of mean Reynolds stress per unit mass (τ/ρ) for the entire experimental data mosaic, with different scales of interest and the jet centreline trajectory plotted in gray. The first contour map (a) is scaled to show the maximum range of data, from $\tau/\rho = -390\ cm^2/s^2$ to $\tau/\rho = 0\ cm^2/s^2$, and the second (b) is scaled to provide more detail in the $-50\ cm^2/s^2$ to $15\ cm^2/s^2$ range. The minimum mean Reynolds stress per unit mass for the full mosaic is $\tau/\rho = -392.2\ cm^2/s^2$ and the maximum is $\tau/\rho = 49.2\ cm^2/s^2$. Values larger than the maximum of the range are assigned the colour of the extreme and values smaller than the minimum of the range are assigned no colour and appear as monolithic white zones. Figure 5.7 presents the τ/ρ contour map for tessera 3, showing the FOV directly downstream of the baffle. As mentioned earlier, Table 5.2 presents the extreme values of mean flow parameters for the full mosaic and Table 5.3 provides them on a tessera basis.

The pattern of mean Reynolds stress is superficially similar to that of mean kinetic energy in that it decays along the jet trajectory, especially after the jet is deflected by the baffle. However, the distribution is actually quite different. The locus of greatest Reynolds stress (the most negative) is not coincident with the jet centreline trajectory; although the two are generally parallel, the $(\tau/\rho)_{max}$ locus is found on the outbound side of the trajectory. As shown in Figure 5.6 (a), there exists band of highly negative τ/ρ on the outbound side of the jet centreline which grows in width along the trajectory. The distribution of τ/ρ in this region is such that Reynolds stress first increases to some negative maximum and then decreases to some smaller negative value with perpendicular distance taken in the outbound direction of the jet centreline trajectory. This is also clearly shown in Figure 5.7.

The region upstream of the jet centreline trajectory, in the inbound direction, is one of generally small negative mean Reynolds stress and the region downstream of the highly negative τ/ρ band is one of generally small positive mean Reynolds stress. It is interesting to note that the most positive τ/ρ values can be found in four concentrated pockets, located where the deflected jet transitions between constitutive jet flow regimes (i.e. from WJL to PJL to SJL). These are most visible in Figure 5.6 (b) and are described below.

The area surrounding the baffle is the transition region between the wall jet-like regime and the plane jet-like regime. In this transition region, two of the pockets are noticeable: the first along the inbound edge of the jet centreline and the second coincident with the small eddy of clockwise rotation upstream of the baffle and on the outbound side of the jet centreline. In this limited area directly around the baffle, the most dramatic range of τ/ρ is found, from the minimum extremes in the slightly positive pockets to the maximum extreme in the highly negative zone near the baffle tip. The other two pockets are found in the transition region between plane jet-like flow to surface jet-like flow, on both sides of the jet centreline trajectory as the jet reaches the water surface. They both appear to follow the general curves of the maximum velocity as the main jet divides into the return flow surface jet and the main flow surface jet.

Several tessera edge and corner dislocation defects are visible in Figure 5.6 (b) and will also be visible in a number of other contour maps introduced in the section. As mentioned in §4.5.3, they are most likely caused by misalignment of the individual tesserae fields of view in the measurement programme as well as poor focus at the edges of tesserae. These dislocations do not significantly affect the whole-field patterns or the basic trend of the mean flow parameters.

5.1.4 Mean Turbulent Kinetic Energy

Figure 5.8 presents two colour contour maps of mean turbulent kinetic energy per unit mass (k) for the entire experimental data mosaic, with different scales of interest and the jet centreline trajectory plotted in gray. The first contour map (a) is scaled to show the maximum range of data, from $k = 0\ cm^2/s^2$ to $k = 900\ cm^2/s^2$, and the second (b) is scaled to provide more detail in the $0\ cm^2/s^2$ to $100\ cm^2/s^2$ range. The minimum mean turbulent kinetic energy per unit mass for the full mosaic is $k = 5.6\ cm^2/s^2$ and the maximum is $k = 990.5\ cm^2/s^2$. Again, values larger than the maximum extreme are assigned the colour of the extreme and appear as monolithic dark-red zones. Table 5.2 presents the extreme values of mean flow parameters for the full mosaic and Table 5.3 provides the extreme values on a tessera basis.

Much like the mean kinetic energy, the magnitude of the mean turbulent kinetic generally decreases as the jet progresses downstream. Unlike KE however, the location of maximum k occurs not upstream of the baffle and along the flume bed, but directly downstream of the baffle tip. In fact, the great bulk of k is found on the outbound side of the jet trajectory where the locus of k_{max} is parallel to the trajectory. This is similar to the distribution of mean Reynolds stress. As was the case in Figure 5.6, tessera edge and corner dislocations are clearly visible in Figure 5.8: most obviously at the upper-right corner of tessera 3 and the upper-left corner of tessera 10.

Even without a deeper quantitative understanding of the geometry of the curved plane jet-like section of flow, it can be noted that the turbulent kinetic energy increases relatively quickly to some maximum value and then more slowly decreases to a background value with increasing distance from the centreline in the outbound direction. As previously mentioned, k_{max} is found directly downstream of and slightly higher than the baffle tip. This is clearly shown in Figure 5.9. The value of k rapidly decreases to approximately zero only millimeters below the core of maximum turbulent kinetic energy. The turbulent kinetic energy decreases more slowly with distance from the centreline in the inbound direction.

Because turbulent kinetic energy, like Reynolds stress, is a turbulent property that is dependent on instantaneous velocity data, the question arises whether or not the acquired PIV data set is large enough to provide an adequate and representational mean estimate. Three minutes of data was collected at each tessera at a rate of 15 Hz, corresponding to a total of 2 700 velocity fields sampled during the experimental period. To determine if this was a sufficient sample duration, the total k was computed for each field (i.e. the sum of the all the k values for each of the 2 700 fields), resulting in a single sum value for each of the 2 700 data sets from t = 0 seconds to t = 180 seconds. Average values of the total k were calculated for increasingly larger time series'. That is, the average of the first 100 sum of k values was computed, followed by the average of the first 200 sum of k values, followed by the first 300, and so on, until the average of all 2 700 sum of k values was computed. This cumulative averaging procedure was performed on the data sets of each of the fourteen tesserae.

The cumulative average of the total k values should approach an asymptotic value (i.e. become stable) when the time series is sufficiently long and when enough data has been sampled to provide a representative mean for turbulent flow parameters. The actual magnitudes of the sum of k values are somewhat meaningless, and not as important as the trend they exhibit. Figure 5.10 plots the resulting cumulative averages of k values for (a) tessera 2 and (b) tessera 4 against time. The scale of the y-axis is such that the data appear to be somewhat erratic and was chosen to show the range in greater detail; however, the data in the last minute suggest stabilization. The variations decrease with time and all approach and asymptotic values at approximately 2.5 minutes. For example, in Figure 5.10 (a) the variation is approximately 10% in the first 30 seconds, and decreases to less than 2% in the last 60 seconds.

Individual dimensional plots of the raw sum of k values for all tesserae can be found in §8. It is interesting to note that the tesserae around the baffle and those which describe the jet as it transitions from wall jet-like to plane jet-like achieve stabilization earlier than other tesserae. This may be because of the strong and persistent turbulence inherent to the mixing region of the jet body. The jet weakens as it travels downstream and it becomes somewhat oscillatory about its own centreline (further discussed in §5.1.6). In this area, and in areas where the background energy is generally lower than in the jet body, such as the weak but large eddy on the outbound side of the trajectory, random and transient turbulence manifests itself as greater variation in the average sum of turbulent kinetic energy. To attain representative time averaged flow parameters in these tesserae, a larger data is required, and hence stabilization times are greater.

5.1.5 Mean Dissipation

Figure 5.11 presents two colour contour maps of mean dissipation rate per unit mass (d) of k for the entire experimental data mosaic, with different scales of interest and the jet centreline trajectory plotted in gray. The first contour map (a) is scaled to adequately show the range of data from d = 0 cm^2/s^3 to d = 135 cm^2/s^3, and the second (b) is scaled to provide more detail in the 0 cm^2/s^3 to 5 cm^2/s^3 range. The minimum mean dissipation per unit mass for the full mosaic is d = 0 cm^2/s^2 and the maximum is d = 229.4 cm^2/s^3. Values larger than the maximum extreme are assigned the colour of the extreme. Figure 5.12 presents the d contour map for tessera 3 and is able to show a complete range of mean dissipation extremes. Again, Table 5.2 presents the extreme values of mean flow parameters for the full mosaic and Table 5.3 provides the extreme values on a tessera basis.

Similar to the figures introduced in §5.1.4 for the mean turbulent kinetic energy, Figure 5.11 (a) indicates that the bulk of mean dissipation occurs on the outbound side of the jet centreline trajectory, mostly in the curved plane jet-like region of flow. There is also significant dissipation visible in the wall-jet-like region of flow upstream of the baffle. However, the dissipation is most definitely concentrated in the section around the baffle; in fact, almost all of the dissipation occurs within the first transition region, between the jet centreline trajectory and the baffle and in the small eddy region in the bottom right corner of tessera 2. Figure 5.12 clearly shows that d decays from $d_{max} = 229.4\ cm^2/s^3$ to approximately $100\ cm^2/s^3$ only 4 cm downstream of the baffle.

Outside of the band of noticeably high dissipation, the values of d are generally of the same low order. Figure 5.11 (b) provides a good view of this area. On the inbound side of the trajectory, in the area of the large eddy of counter-clockwise rotation, the dissipation is slightly positive and increases in magnitude with distance from the eddy centre. On the outbound side of the jet trajectory, the dissipation is lower and increases as the jet progresses downstream. Mirroring the eddy found directly upstream of the baffle is a small zone of slightly positive mean dissipation directly downstream of the baffle. This zone is roughly circular in size and has a diameter on the same order as the small eddy.

5.1.6 Vorticity

The plane jet definitions introduced in §2 describe the jet as being bound on either side by shear layers which propagate away from the jet centreline. The area inside the shear layers (generally where the axial velocity component is zero) constitutes the body and mixing region of the jet and separates the jet from the surrounding ambient fluid. In terms of velocity, the difference between the jet and the ambient can considered one of velocity gradients. That is, the axial component velocity (u) decreases continuously from a maximum U_m at the jet centreline to a smaller values with distance away from the central axis on both sides. However, instead of looking at the jet in terms of velocity gradients, it is entirely possible to employ an analysis using the concept of vorticity, where vorticity is defined as twice the angular velocity of a fluid parcel. In fact, a whole-field analysis of the mean vorticity in the flow of the deflected plane wall jet is very illuminating and productive. A vortical analysis can yield succinct information regarding eddies and their circulation as well as greatly aid in the visualization of the jet geometry and the mean and instantaneous flow patterns.

5.1.6.1 Mean Vorticity

Figure 5.13 presents four colour contour maps of mean vorticity (ω) for the entire experimental data mosaic, with different scales of interest and counter-clockwise rotation defined as positive. The jet centreline trajectory is shown in gray The first contour map (a) is scaled to show the maximum range of data and the other three are scaled to provide more detail in specific ranges (b-d). The minimum mean vorticity for the full mosaic is $\omega = -157.8\ s^{-1}$ and the maximum is $\omega = 19.2\ s^{-1}$. Values larger than the maximum extreme are assigned the colour of the extreme and values smaller than the minimum extreme are assigned no colour and appear as monolithic white zones. As mentioned earlier, Table 5.2 presents the extreme values of mean flow parameters for the full mosaic and Table 5.3 provides the extreme values on a tessera basis.

Figures 5.13 (a) and (b) dramatically illustrate one of the major differences between the inbound and outbound sections of the deflected wall jet flow pattern suggested by the velocity vector fields shown in Figures 5.1 though 5.3. It was noted in §5.1.1 that a large counter-clockwise eddy was extant in the region bounded by the jet centreline trajectory, the water surface and the upstream flume gate. A second large eddy of clockwise rotation was also observed on the outbound side of the jet axis, along with a smaller eddy upstream of the baffle but also on the outbound side of the centreline trajectory. The two regions of generally opposite fluid rotation are clearly visible as regions of positive and negative mean vorticity.

The range of data mapped in Figure 5.13 (a) would indicate that the entire inbound region has a relatively constant and small counter-clockwise rotation and (b) confirms that the mean vorticity there ranges from $\omega = 0\ s^{-1}$ to $\omega = 19.2\ s^{-1}$. The most intense zone of positive mean vorticity lies along the jet trajectory in the wall jet-like region and the adjacent transition region. The large velocity gradient between the strong flow of the wall and the slower flow of the eddy and the surrounding fluid is responsible for a constant production of counter-clockwise vorticity, which convects away from the jet axis towards the centre of the eddy. Obviously, the ω production would be concentrated in the jet body region, and as such the width of the highly positive band visible in Figure 5.13 (b) can be considered as a crude jet width. The distribution of vorticity shows that $\omega = 0\ s^{-1}$ at the jet centreline and that with distance away from the jet centreline, the mean vorticity first increases to some local maximum value and then decreases again. The locus of ω_{max} follows the location where the velocity gradient is largest. It is very interesting to note that the mean vorticity in the eddy itself is limited to a very narrow magnitude of approximately to $\omega = 4\ s^{-1}$; the distribution of vorticity in this region will be assessed in greater detail when the circulation is calculated.

Figure 5.13 (a) also shows a similar type of vorticity distribution on the outbound side of the jet axis. Vorticity is zero at the centreline, and then increases to some local maximum negative value with distance in the outbound direction. After the local maximum is reached, the vorticity decreases again to a lower negative background value. The two main differences are that the mean rotation is clockwise (and the mean vorticity is negative) and that the absolute magnitude of the generated vorticity is two orders larger ($\omega_{min} = -157.8\ s^{-1}$). Almost all of the highly negative vorticity is generated directly at the tip of the baffle. As the jet flows over the baffle and is deflected upwards, the velocity gradient between the jet and the almost-still fluid on the downstream side of the baffle is largest. The baffle effective creates all of the negative vorticity in the flow, either directly (as is the case downstream of the baffle tip) or indirectly (as is the case with the small eddy induced directly upstream of the baffle). Figure 5.14 presents the mean vorticity contour map of the mosaic area surrounding the baffle at a larger scale, and the concentrated zone of negative vorticity generation is clearly visible.

Figures 5.13 (c) and (d) provide deeper insight into the vorticity distribution in the transition region where the flow pattern changes from plane jet-like to surface jet-like. The contour range is more limited in these figures, as further downstream and near the water surface, the jet splits and there exists a stagnation-like region. Part of the jet flow returns upstream and part continues downstream; in between the two resultant surface-like jets, the velocity is quite small, and theoretically zero where the jet impinges upon the water surface. The mean vorticity of deflected wall jet seems to collapse into incoherence here, and is highly unstable and erratic; the contours appear almost Medusa-like. The range of variation is within the range of e_ω and can be considered as manifestations of the vorticity error. However, they make for compelling and beautiful figures!

5.1.6.2 Mean Circulation

The inbound eddy of positive vorticity and counter-clockwise rotation is a dominating feature of the flow. In fact, it may affect the trajectory and nature of the jet as much as the baffle does. The eddy provides a stable region of circulation and can be considered a zone of solid-body rotation that both feeds and starves the deflected wall jet of flow. As the wall jet progresses downstream from the gate and as it is deflected upwards, the flow in the bottom half of the eddy is in the same direction as the jet flow. As the plane jet-like section transitions and divides into two surface jet-like flows, the top half of the inbound eddy has a general upstream flow. This is opposite to the main WJL and PJL flows on the inbound side of the centreline, and contributes to the division of flow between the return flow surface jet and the main downstream flow surface jet. The contribution of the eddy to the flow rate in the jet can be quantified Stokes theorem:

$$\Gamma = \int_A \omega \cdot dA \qquad [5.1]$$

where Γ is the mean circulation in the region defined by a constant mean vorticity (ω) and bounded inside an area (A) of solid-body rotation.

Figure 5.15 presents the general velocity, vorticity and circulation in the large elliptical eddy found on the inbound side of the jet centreline trajectory. With the assumption that the mean vorticity in the eddy is generally constant, the $\omega = 4\ s^{-1}$ contour of is plotted, and then extrapolated outside of the full mosaic to form a closed circuit. This circuit approximates the boundary of the solid-body rotation core, shown in gray. Superposed on to the mean vorticity contour is the observed eddy centre. Five radial mean velocity profiles are then plotted using the centre, from 90 degrees to –90 degrees with 45 degree increments. The mean velocity distribution inside of the eddy boundary is clearly linear and passes through zero at the eddy centre, indicating that the assumption that the eddy can be approximated by solid-body rotation is valid.

Figure 5.16 plots the vorticity along the five rays and confirms that the vorticity is approximately constant within the eddy, at $\omega = 3.7\ s^{-1}$. With radial distance (r) away from the eddy centre the vorticity remains constant until some characteristic radius, at which point the vorticity begins to increase. This increase is consistent with the earlier observation of the vorticity distribution inside of the body of the jet and generally occurs where the velocity distribution diverges from linearity. The area of solid-body rotation is elliptical in shape rather than circular, and thus the characteristic radius is larger in the upper-right quadrant of the eddy.

Computation of the mean circulation generated by the eddy requires knowledge of its area. Although it is not exactly circular, it can be reasonably approximated as a circular area. Using a radius of $r = 20$ cm (an average value taken from Figure 5.16) an area of 0.13 m^2 is computed. This approximation is very loose, as neither the existence nor the shape of the upstream half of the eddy is actually known because it lies outside of the combined field of view of the assembled mosaic. Equation [5.1] then gives an approximate mean circulation of $\Gamma = 0.48$ m^2/s. This value will be considered in relation to the flow of the deflected wall jet in §5.2, along with the effects of the solid-body rotation on the velocity distributions.

5.1.6.3 Instantaneous Vorticity

As stated at the beginning of this section, a vortical analysis can also provide insight into the instantaneous flow pattern of the plane deflected wall jet. Although only contour maps of the mean flow properties have been introduced thus far, full sets of instantaneous data are available. Because the measurements at each tessera are temporally isolated from one another, they must also be presented individually. Instantaneous vorticity contour maps were plotted for all of the data files (all instants in the 15 Hz time series) for each tessera and then movies created, by organizing successive maps as individual video frames. Observation of the resulting movies revealed how individual coherent vortical structures behaved in and advected through the flow. It was possible to track the individual vortices as they move inside of the tesserae fields of view; they act as crude tracers of the instantaneous flow pattern. Although they cannot be observed across tessera boundaries, the movies allowed for observation of vortex creation, interaction, evolution and decay within a single FOV through time.

Following are several observations of the general behaviour of the instantaneous vorticity, accompanied by sample frames taken from the movies where interesting activity was noted. Figures presenting the instantaneous vorticity (ω_i) fields in tesserae 2, 3, 1 and 11 are presented, to illustrate the vorticity in the transition regions surrounding the baffle, in the region of the large upstream eddy and in the region of the elongated downstream eddy, respectively. The figures each show 28 consecutive contour maps from the 15 Hz data sets of the three tesserae (1.87 seconds in total). In order to accentuate the coherent structures in the contour maps, ranges of vorticity that were considered to include the background vorticity have been plotted in white and omitted from the colour map scales.

Figure 5.17 presents ω_i for tessera 2 and includes the jet centreline trajectory to provide reference. The baffle would be located at the bottom-right corner of each sub-figure. As is the case for all tesserae which imaged the main jet, the individual vortices do not remain in the FOV for more than three or four frames. Significant generation of positive vorticity can be observed near the wall and is due to the strong velocity gradient between the wall jet-like flow and the no-slip wall boundary. It is assumed that much of the existing positive vorticity in the region was created at the upper boundary of the gate slot, as there is also a dramatic velocity gradient at that location (Figure 2.2) Individual vortices rotate in a counter-clockwise direction and are advected away from the wall source: mostly along the centreline, but to a lesser extent into to the large elliptical eddy above. Decay of the ω_i magnitude of these structures is observed. Also observed is the persistent negative ω_i core directly upstream of the baffle and on the outbound side of the jet centreline. This is the small eddy of clockwise rotation upstream of the baffle described earlier.

Figure 5.18 presents ω_i for tessera 3 and also includes the jet centreline trajectory. In this figure, the baffle would be located at the bottom-left corner of each sub-figure. The first and most obvious feature visible in this figure is the persistent and concentrated generation of strongly negative vorticity at the baffle tip. These negative vortices are constantly being shed downstream and remain on the outbound side of the jet centreline. The large velocity and pressure gradients the baffle tip, as discussed earlier in this section, is directly responsible for the creation of the vorticity, much like in flow over any bluff body edge. The ω_i strength does not appear to decay significantly in this FOV and persists as highly negative ω_i pockets below the jet trajectory. Their downstream advection is rapid and most of the structures remain in the FOV for only two or three frames. Positive vorticity is also visible on the inbound side of the jet trajectory, however its absolute ω_i magnitude is smaller. Figure 5.18 clearly shows how the jet centreline trajectory divides the flow region into zones of general positive and negative vorticity, and indicates the source most of the negative ω_i in the full mean vorticity mosaic.

Figure 5.19 presents ω_i contour maps for tessera 1. As indicated earlier, the large elliptical eddy of counter-clockwise rotation has its centre in this FOV. The eddy region has a slightly positive mean vorticity and exhibits general solid-body rotation. The advection of the vortices in this region is more gentle and slow than in those zones which contain the deflected wall jet proper, and here they travel around the eddy centre. Because the structures remain in the FOV for longer periods of time, the figure shows their interaction and evolution much more clearly. Although they are in a state of constant strength decay, individual vortices can be observed to rotate about each other as well as pair together. Coupled with the constant introduction of additional positive ω_i from the gate and wall sources, this provides a plausible explanation for the stable (and less ordered) mean vorticity found inside the eddy region.

Figure 5.20 presents ω_i contour maps for tessera 11 with the background instantaneous vorticity plotted in white to accentuate the coherent structures. Tessera 11 images the area of flow at the boundary between the curved plane jet-like flow and the elongated eddy of clockwise rotation and relative slow velocity on the outbound side of the jet centreline trajectory. Its FOV is somewhat below the transition region between plane jet-like flow regime and the surface jet-like flow regime. Figures 5.13 (c) and (d) show this tessera to contain a region of unstable mean vorticity, and Figure 5.20 corroborates this observation. Both positive and negative ω_i are clearly visible, scattered throughout the field of view. A strong vortex of negative ω_i can be seen to advect through the upper-left corner of the tessera. Near the water surface transition region, the jet becomes somewhat oscillatory in nature; although the mean velocity pattern is still strongly centered about the trajectory, the instantaneous vorticity movie created shows how the jet body sways back and forth. The strongly negative individual vortex observed in Figure 5.20 is a manifestation of this oscillation. Most of the other individual vortices (which only appear to be small in size because they are close in magnitude to the background vorticity, and thus only represent the inner cores of the structures) remain in the FOV for relatively long periods of time (on the order of seconds) and show the relative weakness of the flow in this eddy region.

It is unfortunate that the movies of instantaneous vorticity cannot be presented as stills in this thesis in their entirety due to the large number of individual images. However, all the movies were saved as Quicktime AVI (Apple Computer, Cupertino, California) movie files and are provided on the compact disc accompanying this thesis. They can be viewed on any personal computer capable of playing AVI media files.

5.1.7 Mean Strain

Figure 5.21 presents two colour contour maps of mean strain rate (ε) for the entire experimental data mosaic, with different scales of interest and the jet centreline trajectory plotted in gray. The first contour map (a) is scaled to show the maximum range of data, from $\varepsilon = -55\ s^{-1}$ to $\varepsilon = 0\ s^{-1}$ and the second (b) is scaled to provide more detail in the $-6\ s^{-1}$ to $5\ s^{-1}$ range. The minimum mean strain value for the full mosaic is $\varepsilon = -53.8\ s^{-1}$ and the maximum is $\varepsilon = 9.3\ s^{-1}$. Values larger than the maximum extreme are assigned the colour of the extreme and values smaller than the minimum extreme are assigned no colour and appear as monolithic white zones. Figure 5.22 presents the mean strain contour map for tessera 3. As mentioned earlier, Table 5.2 contains the extreme values of mean flow parameters for the full mosaic and Table 5.3 provides the extreme values on a tessera basis.

The highest mean strain is concentrated around the shear layers bounding the deflected wall jet mixing region. In those areas where positive vorticity is generated, the strain is at a positive maximum, and in those areas where negative vorticity is generated, the strain is at a negative maximum. This is especially evident in Figure 5.21 (b) and Figure 5.22. Where the vorticity is relatively constant, in the two large eddies on either side of the jet centreline trajectory, the mean strain is approximately $\varepsilon = 0\ s^{-1}$. Increased ε is also observed beneath the surface jet-like main flow in the upper-right corner of the full assembled mosaic.

5.1.8 Mean Kolmogorov Scales

Figure 5.23 presents colour contour maps of (a) the mean Kolmogorov length scale (l_k) and (b) the mean Kolmogorov velocity scale (v_k) for the entire experimental data mosaic. Figure 5.24 presents the same data for tessera 3. The jet centreline trajectory is shown in gray and both contour maps are scaled to show the full ranges of data The mean Kolmogorov length scales range from $l_k = 0.009$ cm to $l_k = 0.036$ cm and mean Kolmogorov velocity scales range from $v_k = 0$ cm/s to $v_k = 1.3$ cm/s. Again, values larger than the maximum extreme are assigned the colour of the extreme and values smaller than the minimum extreme are assigned no colour and appear as monolithic white zones. Although the Kolmogorov time scales were also calculated, they are not presented in contour maps. As mentioned earlier, Table 5.2 presents the extreme values of mean flow parameters for the full mosaic and Table 5.3 provides the extreme values on a tessera basis. Extreme mean data for all three Kolmogorov scales are presented in the tables.

The Kolmogorov scales describe the characteristic sizes and velocities of the smallest dissipative turbulent structures which break down the energy of a flow. It has already been shown in §5.1.6 that the vortices present in this flow exhibit growth by pairing after creation. They are smallest in size, but greatest in strength, along the flume bed upstream of the baffle and downstream of the baffle tip. The values of l_k are generally inversely proportional to the magnitude of ω_i and proportional to the size of the vortices. The values of v_k exhibit the opposite relationship. The mean Kolmogorov length scales are smallest at the baffle tip and either above the wall jet-like flow or on the outbound side of the jet centreline trajectory, and the mean Kolmogorov velocity scales are largest in the same regions.

5.2 Jet Flow and Development

In the study of Wu and Rajaratnam (1995a), a Prandtl tube measurement system in combination with either a manometer board or pressure transducers were used to sample time averaged mean velocity and pressure data in a plane deflected wall jet. By taking point measurements at many select locations in the flow, they were able to define the boundaries of the jet as it developed from the gate, over the baffle, to the water surface and then downstream. They identified three separate regimes in the flow: a zone of wall jet-like (WJL) flow before the baffle, a zone of plane jet-like (PJL) flow after the baffle and before impingement upon the water surface and a zone of surface jet-like (SJL) flow after impingement upon the water surface. The locations of the point measurements were chosen to provide velocity profiles across the width of the jet flow at different stations along the jet centreline axis.

The mean data set yielded by the PIV analysis of the present study provides a dense array of velocity data as well as other flow parameters, spatially distributed in a regular 2.5 mm grid. As previously mentioned, analyses of such rich data sets can follow either whole-field or point measurement paradigms. §5.1 presented the results of the whole-field approach; this section presents the analysis using the point measurement approach. After the jet centreline trajectory is identified, the variation of the centreline velocity is studied. The jet geometry is defined along the trajectory and then profiles across the width of the jet are extracted from the full PIV data mosaic. Development of the deflected wall jet is studied by non-dimensionalizing and then comparing the flow properties along the profiles for different stations with jet theory and other experimental results. The transition regions between the three classical plane jet flow regime states (between the WJL, PJL and SJL states) are refined and more thoroughly described. Finally, the mean discharge intensity, mean momentum flux, and mean entrainment at stations along the trajectory are presented and compared to theoretical values.

5.2.1 Trajectory Identification

The theoretical definitions used in classical jet theory and described in §2 rely on very rigid analyses of ideal jets under ideal conditions. When applying the theory to actual experimental data, the centreline axis of a real jet is first defined by the locus of the maximum velocity filament and then profile data across the width of the jet body is measured. Mean properties such as velocity and pressure, and turbulent properties such as Reynolds stress and turbulent kinetic energy, are often assessed. The data is usually non-dimensionalized with characteristic length and velocity scales, such as b_o and U_o or U_m, and then compared for similarity. Because the classical definitions of simple plane jets generally consider jets in either infinite or semi-infinite ambients, identification of the centreline trajectory is relatively simple. In these cases, the centreline is usually straight and completely parallel to the main flow direction. Profiles are taken perpendicular to the trajectory and are thus often essentially vertical.

The deflected plane wall jet studied in this thesis is most definitely not an ideal jet under ideal conditions. The analysis of the whole-field properties of the mean and instantaneous flow pattern presented in §5.1 corroborates the findings of Wu and Rajaratnam (1995a), that the phenomena can be divided into wall jet-like, plane jet-like and surface jet-like flow section, with transition regions first near the baffle and second near the point of jet impingement upon the water surface. The jet trajectory is curved and the angle of curvature varies along the jet axis, as shown in both Figure 1.1 and in the full mosaic contour map figures already introduced. As a result, the analysis is more complicated.

Wu and Rajaratnam defined the jet trajectory by the locus of the maximum velocity filament. Their measurements were concentrated in the region of flow downstream of jet impingement upon the surface; in fact, less than ten u and v velocity pair measurements were taken upstream of the surface jet-like flow zone. Because their analysis also focused on the surface jet-like flow, whose trajectory was generally parallel to and slightly below the almost horizontal water surface, a more precise trajectory was neither required nor defined. For all intents and purposes, it was the water surface.

This present study can utilize the dense PIV data set to describe the flow pattern of the entire mosaic in greater inherent detail, and a more refined and accurate method of trajectory identification is possible. It was realized that at some point the jet would impinge upon the water surface and then continue downstream as a surface jet-like flow. It became obvious that the jet centreline trajectory would lie very close to the water surface in this region; however, a large portion of the raw PIV data below the water surface had already been disregarded as the water surface reflection defect zone (as discussed in §4).

To adequately locate the trajectory, those previously disregarded vectors required replacement. Although many of the instantaneous velocities were considered to be corrupt due to transient reflections and false correlation, it was postulated that the mean velocities would still be representative of the true flow pattern. The original raw displacements below the measured mean water surface were therefore averaged and then subjected to both the correction and interpolation scheme outlined in §5.1. and the gradient and vorticity post-processing schemes of §5.2. The resultant mean velocity vectors were added to the full mosaic velocity vector and vorticity fields. In addition, the two columns of grid points located inside of the baffle shadow defect exclusion zone had their u and v velocities bi-linearly interpolated using the surrounding velocity components to provide a complete vector field for the entire mosaic. Those grid points located directly on the baffle retained their zero velocity designation. As final preparation for trajectory location, and in anticipation on further analysis, a boundary condition of zero velocity at the flume bed ($x = 0$ cm) was enforced, with the two row data gap between the bottom-most row of vectors and the bed linearly interpolated. Figures 5.25 and 5.26 present the replacement of the vectors in the surface reflection defect zone and the interpolation of vectors in both the baffle shadow defect and flume bed gap zones. Close inspection of the replacement mean velocities at the interface between the previously computed and the replacement zones confirmed that the vectors were physically valid in direction and magnitude.

Following the logic of Wu and Rajaratnam, a first attempt was made to locate the jet centreline trajectory. The locus of V_{max} was obtained using two methods: searching for the maximum velocity magnitude in each column as well as in each row of the full velocity field matrix. Figure 5.27 presents the results of this attempt. To be considered successful, one would expect both routines to identify the same trajectory. They clearly do not. Although the two methods produce similar trajectories between $x = 50$ cm and $x = 65$ cm , the trajectories are significantly different in other regions. Where the trajectory of the jet would be expected to be more horizontal, the column method produced a more plausible centreline; and where the trajectory would be expected to be more vertical, the row method produced a more plausible centreline. The divergence is most prominent downstream of $x = 65$ cm. The trajectory is curved, and the flow pattern in the surrounding fluid is not simple. The maximum velocity vector in a column or row would not necessarily be physically connected to the main flow region of a curved jet. It was surmised that the true trajectory would most likely be bounded by the results of the first attempt.

A second trajectory analysis was then conducted. The trajectory of the deflected wall jet is curved, and therefore it was decided that a trajectory analysis similar to that used for plane jets in a crossflow was most physically appropriate. If one accepts the postulate that the centreline of a jet constitutes a streamline across which there is no perpendicular flow, it follows that the gradient across the centreline is zero. This suggests that the mean vorticity at the jet centreline would also be zero. Figure 5.28 presents the $\omega = 0\ s^{-1}$ contour line, interpolated using all available vorticity values in the full data mosaic. Not only does the contour fall either directly on the V_{max} loci common to both the column and row methods previously outlined, but it falls directly between the two after they diverge. The contour also provides a centreline trajectory for both the surface jet-like return jet and main jet flows. This contour constitutes a very plausible and theoretically defensible jet centreline.

The mosaic grid points closest to the $\omega = 0\ s^{-1}$ contour line were selected to form the continuous final deflected wall jet centreline trajectory as well as the trajectory of the return flow surface jet. Figure 5.29 presents these final trajectories. 322 discrete grid points form the main flow trajectory and 70 discrete grid points form the return flow trajectory. Although the selected grid points do not constitute a perfectly smooth trajectory curve, calculated flow parameters are available at all the defined locations (with only mean velocity and vorticity at those points in the upper exclusions zone). The zero vorticity contour is somewhat erratic in the zone where the velocity begins to stagnate; the trajectory points in this region were located in the centres of the zero vorticity pockets and form as smooth a curve as possible. The general low ω levels in the region limited the accuracy of the trajectory here, but in the absence of any superior identification scheme, it was considered adequate. No attempt was made to connect the return flow trajectory to the main trajectory because the $\omega = 0\ s^{-1}$ contour is not continuous between the two sections.

Consistent with the definition provided for a plane jet in a crossflow by Yu-Leuk and Wood (1966), the ordinate s is defined as the axial distance along the jet centreline trajectory, measured from jet exit at the slot. Because the first trajectory point is so close to the bed, it is designated as $s = 35.50$ cm, the straight-line distance from the Cartesian jet origin at the flume bed ($y = 0$ cm) and the gate ($x = 0$ cm) to the first grid point. In this axial frame of reference, the baffle is located between $s = 51.80$ cm and $s = 52.16$ cm. The point of jet impingement with the water surface (where the jet begins being more surface jet-like in nature) is located at $s = 109.87$ cm. The furthest downstream point of the main flow trajectory is at $s = 128.90$ cm. The first point in the return flow trajectory is given an starting value of $s = 109.87$ cm and is the point located furthest downstream, nearest the rise (or hump) in the water surface caused by jet impingement; it is given this value so that the two surface jet-like regions can be compared directly. The final upstream point of the return flow section trajectory is at $s = 127.95$ cm.

At this point, it becomes convenient to divide the trajectory into defined regions which can be analyzed together. Although the designations of wall jet-like (WJL), plane jet-like (PJL) and surface jet-like (SJL) flow have already been introduced in §2.4 and §5.1, the discussions were rather qualitative and the descriptions somewhat conceptual in nature. Following trajectory identification and definition, and using the results of the analyses of §5.2, the s-coordinate locations of the regime boundaries become tangible. Figure 5.30 presents a schematic of the breakdown of the full plane deflected wall jet trajectory and the return flow trajectory into their constitutive flow regimes. Tables 5.4 and 5.5 provide specific data describing the extents of the regimes relative to the number of trajectory data points for both the main and the return flows, and present dimensional as well as nondimensional axial regime boundary ordinates along the jet centreline trajectory. The nondimensional jet centreline trajectory ordinate is defined as $\xi = s/b_o$ with b_o being the slot width of 2.54 cm.

The centreline trajectories for both the main flow and the return flow plotted in Figure 5.30 represent all available trajectory points; the discrete circles or squares show each tenth data point for clarity. The first 30 points along the main flow trajectory form the wall jet-like flow region. The next 40 points form the transition zone between the WJL and the PJL flow regimes, called TZ1, and it is here that the baffle is located. The plane jet-like flow region begins at trajectory point 71 and extends to trajectory point 200. The next 80 points form the transition zone between the PJL and the SJL flow regimes, called TZ2, and it is here that the point of impingement is located. Trajectory point 281 marks the beginning of the surface jet-like flow region, which extends to the end of the available data points and thus contains 52 data points. The WJL region is approximately 7.2 cm in length, the TZ1 region approximately 12.2 cm, the PJL region approximately 39.5 cm, the TZ2 region approximately 22.9 cm and the SJL region approximately 10.5 cm. In this nondimensional frame of reference, the baffle is located at approximately $\xi = 20.39$ and the point of jet impingement is located at approximately $\xi = 43.26$. The first point in the trajectory is $\xi = 13.98$ and the last point is $\xi = 50.75$.

5.2.2 Centreline Velocity Decay

The mean velocity along the centreline is defined as U_m, and is assumed to be the maximum mean velocity in the jet at that location along its trajectory. Figure 5.31 (a) presents U_m plotted against axial distance (s) and (b-d) present the sections upstream of the baffle, between the baffle and the point of impingement and downstream of the point of impingement, respectively, in greater detail. Following the standard jet analysis practice of non-dimensionalization using characteristic velocity and length scales, U_m is non-dimensionalized by the mean velocity at the gate (U_o). Figure 5.32 (a) presents the plot of U_m/U_o against $\xi^{-0.5}$. The nondimensional maximum mean velocity plots in the three regions upstream of the baffle, between the baffle and the point of impingement and downstream of the point of impingement, are presented in Figures 5.32 (b-d), respectively.

The figures indicate that the at the mean centreline velocity had decayed to 0.92 of the mean gate velocity at s = 35.50 cm and continues to decay, albeit at an increasing rate, throughout the WJL region. In the TZ1 region, as the jet begins to diverge from the bed and the trajectory deviates from horizontal, U_m continues to decay. As the trajectory passes over the small eddy upstream of the baffle, the mean centreline velocity reaches a local minimum value of $U_m/U_o = 0.64$ at s = 48.37 cm. It then begins to increase and reaches a local maximum of 0.78 slightly downstream of the baffle at s = 55.24 cm, at the end of the TZ1 region. As the jet approaches the baffle, the effect of the re-circulation zone is reduced and both the pressure and the velocity recover. Figures 5.31 (b) 5.32 (b) clearly show that the mean velocity deficit caused by the eddy inside the transition region is fully recovered at the downstream boundary of the eddy (the baffle).

The figures also show that U_m decays again in the PJL region, and in fact, Figures 5.31 (c) and 5.32 (c) indicate that the decay is quite linear. U_m/U_o decays by almost half in the region, from approximately 0.78 at s = 55.59 cm to approximately 0.40 at s =95.09 cm. The rate of decay increases in the TZ2 region and U_m/U_o reaches a global minimum value of approximately 0.08 at the point of impingement (s = 109.87 cm). Downstream of the point of impingement, through the remainder of the transition region and through the SJL region, U_m increases. The recovery is quite linear in these regions, as shown in Figures 5.31 (d) and 5.32 (d) and U_m/U_o increases from approximately 0.08 at s = 109.87 cm to approximately 0.40 at s =128.90 cm. Again, the U_m deficit evident in the TZ2 region before the point of impingement is completely recovered at the end of the SJL region. It is postulated that the decay and recovery of U_m in this region is most likely due to the curvature of the jet around the large elliptical eddy on the outbound side of the trajectory. However, it may also be due to a poor choice of trajectory thorough the TZ2 region, resulting in a flawed definition of the jet centreline and erroneous U_m velocities.

The decay of U_m in plane jets has been studied in great detail and equations have been fit to the experimental data of a number of investigators. §2 presented an overview of the available literature, and presented a number of equations ([2.10], [2.17] and [2.21]) to describe the decay. All three are variations on a single equation ([2.6]) which relates U_m/U_o to the nondimensional parameter $\xi^{-0.5}$. When presented in this form, classical plane jets, wall jets and surface jets exhibit linear decay rates, described by the coefficient C_1 in equation [2.6]. The trajectory was divided into nine regions of general linearity and the value of C_1 was computed in each region assuming equation [2.6] could be applied locally in each region. Figure 5.33 presents both the regions and the variation of the C_1 coefficient along the full jet centreline. In Table 5.6 the values of C_1 are listed. It is evident that C_1 changes radically along the trajectory of the jet. In the first half of the WJL region the coefficient is approximately 3.26, which compares well with the accepted value of $C_1 = 3.50$ for plane wall jets. However, the coefficient then increases to a maximum of 12.77 and then decreases to a minimum of –0.72 at the end of the TZ1 region. C_1 remains constant at 7.46 through the entire PJL region; this value is approximately twice of $C_1 = 3.10$, the value expected for a classic plane turbulent jet. In the TZ2 region, the coefficient increases to a maximum value of 21.84 before the point of impingement. U_m then begins to increase, and the coefficient is approximately –20.93 through the remainder of the TZ2 region and the SJL region. Wu and Rajaratnam (1995a) and Ead and Rajaratnam (2001) both note that U_m/U_o decreases linearly for plane surface jets. The discrepancy is not fully understood; however, it may be due to a flawed trajectory (further discussed in §5.2.5), interaction between the curved jet and the outbound eddy of clockwise rotation or an inadequate length of surface jet (resulting in analysis of a non-fully developed flow region).

Figure 5.34 presents the variation of U_m along the trajectory of the return flow surface jet, both in (a) dimensional and (b) nondimensional form. U_m in the return flow TZ2 and SJL regions increases, similar to the same regions in the main flow except at a slightly greater rate. At s = 109.87 cm, U_m/U_o is approximately equal to 0.12 and by s = 127.95 cm, U_m/U_o has increased to approximately 0.41. This behaviour, again, does not agree with classic surface jet theory or experimental data, and may be attributed to interaction with the large inbound eddy of counter-clockwise rotation. With distance upstream of the point of impingement, through the region where the PJL main flow splits into the two SJL flows, the flow of the eddy increasingly affects the return flow. This may explain the increase in U_m in this region.

5.2.3 Centreline Velocity Angles

The angle from horizontal of any velocity along the axis of the jet is defined as θ_c. Figure 5.35 (a) presents θ_c plotted against s along the full jet trajectory and (b-d) present the sections upstream of the baffle, between the baffle and the point of impingement and downstream of the point of impingement, respectively, in greater detail. Figure 5.36 presents the variation of θ_c with s along the full return flow jet trajectory.

θ_c remains relatively constant and horizontal in the WJL region, and varies from approximately 0 to 3 degrees from the horizontal. In the TZ1 region, the angle rises rapidly to approximately 40 degrees from the horizontal at the baffle. This quick rise occurs as the jet flows over the small eddy of clockwise rotation upstream of the baffle. It is interesting to note that while θ_c increases dramatically, the trajectory itself is smooth and appears to diverge gently from the flume bed. One might assume that the jet trajectory would be coincident with a locus taken tangential to the θ_c values of the trajectory point. This is not the case, and the discrepancy may be due to a trajectory which is not truly representative of the jet centreline in the transition region. As the jet flows directly over the tip of the baffle, the angle of the centreline velocity becomes horizontal again for a short distance.

Throughout the remainder of the TZ2 region, and through the entire PJL region, θ_c increases at a generally constant rate. The angle peaks at approximately 75 degrees from the horizontal before beginning to decrease in the TZ2 region. It is interesting to note that the rate of decrease is maximum at the point of impingement; in fact, the point of impingement represents the point of inflection of the θ_c curve. After the point of impingement, the rate of θ_c. decrease slows and at the end of the TZ2 region, $\theta_c = 4$ degrees. In the SJL region, the angle decreases to approximately zero and the jet is parallel to the water surface. In the return flow SJL region, θ_c varies in much the same way as the main flow SJL region. The angle flattens from approximately 157 degrees at the beginning of the return flow TZ2 region to approximately 180 degrees (parallel to the water surface upstream of the point of impingement) at the end of the return flow SJL region.

5.2.4 Profile Extraction

As previously mentioned, profiles across the width of a plane jet are often taken along the trajectory of the jet, in order to better understand its development. Often such profile data is non-dimensionalized and similarity arguments are presented. The PIV technique used in this investigation provided such a spatially dense set of data that profile analysis becomes relatively simple to perform. The deflected wall jet has already been described by Wu and Rajaratnam (1995a) as being comprised of different classical plane jet-like flow regimes: wall jet-like, plane jet-like and surface jet-like. The whole-field analysis presented in §5.1 supported this assertion; however, the descriptions were somewhat qualitative.

In order to use the same set of definitions in all of the constituent regions of the flow, it is most convenient to apply the structural definitions of the plane jet in a crossflow to all sections. As discussed in §2.2, and using the set of definitions outlined in Yu-Leuk and Wood (1966) and Hasselbrink and Mungal (2001), the variable n is defined as the transverse coordinate normal to θ_c, and measured from the local jet centreline. The variable s is the ordinate taken along the trajectory. In the main jet flow, the outbound side is defined as positive and the inbound direction is defined as negative. For the return flow jet, to aid in the comparison of both SJL regions, the inbound direction (towards the flume bed) is defined as positive.

A profile was extracted for each grid point defined in the jet trajectory. Each profile was taken perpendicular to θ_c in both the positive and negative n-directions. Positions were defined every 0.05 cm, and a bi-linear interpolation scheme using all grid points surrounding the profile points was employed to obtain continuous data sets for all previously calculated mean parameters. The profile lines pass through the array of grid points, but the n-axes do not necessarily intersect with them. The interpolation was necessary; without it profiles would be limited in location and angle. Following the extraction of profile data sets, both the u and v velocity components were transformed to the local s-n coordinate system. Obviously, the centreline velocity for each profile was not transformed, as its direction defines the local coordinate system. Figure 5.37 presents 21 mean velocity profiles out of the 322 total profiles to clearly show the development of the plane deflected wall jet. Only every tenth point along each profile section was plotted for clarity. Figures 5.38 through 5.41 present mean velocity profiles for the WJL, PJL, SJL and return flow SJL regions separately.

Because individual θ_c values were not uniformly tangential to the jet trajectory, the resulting profiles are not uniformly perpendicular to the trajectory either. The variation is most noticeable in the transition regions. For example, in the TZ1 region, where the eddy of counter-clockwise rotation dominates the flow field, one might assume that that the profiles would share the eddy centre as a common point through which all the profiles would fall. Figure 5.37 shows this not to the case; the profiles of the WJL region are uniformly horizontal and the location where u = 0 moves horizontally downstream with s, even when s is curved. In the TZ1 region, where the trajectory curves gently upwards, the profiles begin to rotate counter-clockwise. However, the rotation is excessive, with the location of u = 0 below the eddy centre, and sometimes out of the assembled mosaic FOV, further upstream. Similar unrealistic and improbable profile behaviour is found in the TZ2 region. The definition of the profile angle by θ_c and the subsequent awkward profiles in the transition regions expose the challenge in identifying the jet trajectory.

5.2.5 Characteristic Length Scales

An extraordinary amount of information can be taken from the profiles. Figure 5.39, for example, clearly shows the decay of the centreline velocity along s as well as the general entrainment of surrounding fluid and asymmetrical growth of the jet width. However, the analysis need not be so qualitative. Applying the definitions introduced for a plane jet in a crossflow one can quantify the variation of both the jet width and half-width along the centreline.

As previously introduced, δ_{1+} and δ_{1-} define the jet half-widths (and consequently the characteristic length scales) for both the positive and negative section n-stems, to points where $u = 0.5U_m$. Similarly, δ_{2+} and δ_{2-} define the jet dual widths, to points where $u = 0$. Figure 5.42 presents the loci of the jet centreline trajectory, the jet half-width (δ_1), the jet width (δ_2) and the water surface in the global Cartesian coordinate system, while Figure 5.43 presents the same for the return flow region. The growth rates of δ_1 and δ_2 are visible, with the rate on the inbound side clearly suppressed (but still growing) by the inbound eddy, and the rate on the outbound side clearly expanding freely after passing by the baffle.

Two flaws are immediately evident in Figure 5.42: the loci of both δ_{1+} and δ_{2+} become erratic downstream of approximately x = 80 cm. In the case of δ_{1+} this is due to the curve of the trajectory in the TZ2 region (discussed in §5.2.4). In the case of δ_{2+} it is due to the algorithm used to identify the location where u = 0. The computer was instructed to locate the position along the profile where the u-component of velocity (transformed into the local coordinate system) first changed from positive to negative. This position was defined as δ_2. The velocities in the region outside of the jet body, on the outbound side of the trajectory and in the large eddy of clockwise rotation, are generally very small. They are also in the same direction as the main jet near the water surface. In some cases u did not pass through zero and simply became small: resulting in δ_2 values that are too large and not representative of the true jet width. This can be seen in Figure 5.39, where the jet width rapidly increases, and much of the increase is comprised of extremely small velocities of the same order and direction. It is recognized that the criteria defining δ_2 was rigid and simplistic. A better criteria might have defined δ_2 as the position where u was equal to some small fraction of U_m. However, because the flaw is limited to a small section of the PJL and TZ2 regions, and because the TZ2 region is not the focus of this investigation, the current definition of δ_2 is considered acceptable.

Figure 5.44 presents the variation of δ_1 with s over the full jet trajectory, while Figure 5.45 (a-d) present the variation of the nondimensional δ_1/b_o parameter with ξ over (a) the full jet trajectory and (b-d) the sections upstream of the baffle, between the baffle and the point of impingement and downstream of the point of impingement, respectively, in greater detail.

Consider first the variation of δ_{1-}. In the WJL region of flow, the jet half-width on the inbound side of the trajectory increases from approximately –4.0 cm to approximately –5.0 cm (see Figure 5.44). Please note that although the values are negative, the sign only reflects that δ_{1-} is measured along the negative n-axis. Then δ_{1-} decreases in the TZ1 region upstream of the baffle, before stabilizing at approximately $\delta_{1-} = -4.5$ cm. This local decrease in half-width is coincident with the local decrease in U_m noted in §5.2.2. In the PJL region, the growth of δ_{1-} is limited by the eddy of counter-clockwise rotation, and slowly increases to approximately –8.0 cm at the end of the region. Through the TZ2 region, δ_{1-} decreases steadily to approximately –1.0 cm. In the SJL region, δ_{1-} remains constant. The jet centreline is parallel with and close to the water surface; the inbound jet half-width in this region is simply the distance between the water surface and the centreline.

Consider second the variation of δ_{1+}. In the region upstream of the baffle, and especially in the WJL region of flow, δ_{1+} is less than approximately 1 cm; the centreline of the wall jet-like flow is very close to the bed, with the outbound half-width defined as, and approximately equal to, the turbulent boundary layer thickness. As the jet lifts away from the flume bed and is deflected over the small eddy of clockwise rotation and the baffle, δ_{1+} increases slightly before decreasing again at the baffle tip. In the PJL region, δ_{1+} increases almost linearly, from approximately 1.0 cm at s = 51.80 cm to approximately 9.5 cm at s = 95.09 cm. From the beginning of the TZ2 region to the point of impingement, δ_{1+} increases more rapidly and reaches a maximum of approximately 17.0 cm before falling again to approximately 9.5 cm at the end of the SJL region.

Like the decay rate of U_m, the growth rate of δ_1 has been studied by many investigators. §2 presented number of equations that describe the relationship: equations [2.11] and [2.18] and [2.22], for plane jets, plane wall jets and plane surface jets respectively. They all take the form of equation [2.7], which relates δ_1/b_o linearly to ξ via a coefficient called C_2. As in the analysis of C_1, the C_2 coefficient was computed for both δ_{1+} and δ_{1-} over sections where it appeared to vary linearly with ξ. Figure 5.46 plots the variation of C_2 along the full jet centreline trajectory, and Tables 5.7 and 5.8 present the numerical values of C_2 for both the inbound and outbound half-widths.

It is evident that C_2 varies greatly both along the trajectory of the jet and between the inbound and outbound jet half-widths. In the WJL region the growth rate of δ_{1-} increases from –0.08 to –0.20, designating growth in the negative n-direction. It is interesting to note that C_2 for a classical plane wall jet is 0.08. In the TZ1 region, C_2 continues to increase until $\xi = 18.33$. There is effectively no δ_{1-} growth until $\xi = 19.04$, where C_2 changes to 0.51, designating a constant decay rate of jet half-width. At the baffle, C_2 decreases to 0.00 and is constant until slightly into the PJL region. From $\xi = 23.10$ to $\xi = 33.92$, $C_2 = -0.12$. This compares to the C_2 coefficient for a classical plane jet of approximately 0.10. At the end of the PJL region, there again is no jet half-width growth: $C_2 = 0.00$ in this region. In the TZ2 region, the growth rate of δ_{1-} is equal to 0.32, designating half-width decay until the jet becomes surface jet-like, where there is no need to track C_2 any longer. The growth rate of δ_{1+} in the PJL region is constant at 0.19. This rate is approximately double that for a classical plane jet. C_2 for δ_{1+} increases to 0.70 on the TZ2 region, and then decreases to –0.54 after the point of impingement. It is odd to note that C_2 remains negative in the SJL region (designating a decay of jet half-width), where it is equal to –0.21. This may indicate that the flow has not really finished impinging.

Figure 5.47 presents (a) the variation of δ_1 with s and (b) the variation of δ_1/b_o with ξ over the full return flow jet trajectory. Unlike the odd half-width decay relationship noted in the SJL region of the main flow, the relationship in the SJL region in the return is more consistent with surface jet theory.

Figure 5.48 presents the variation of δ_2 with s over the full jet trajectory. Figure 5.49 presents the variation of (a) δ_2/b_o with ξ over (a) the full jet trajectory and over (b-d) the sections upstream of the baffle, between the baffle and the point of impingement and downstream of the point of impingement, respectively. Figure 5.50 (a-b) presents the same jet width parameters for the full return flow jet trajectory. The jet width is not usually reported in studies of plane jets, as the half-width appears to constitute a much better scale and nondimensional parameter. However, in the case of the plane deflected wall jet, it is interesting to note that the growth of δ_{2-} is much more limited than that of δ_{2+}. This results directly from the influence of the inbound eddy of counter-clockwise rotation, which dominates the flow pattern on the inbound side of the deflected jet. As noted earlier in Figure 5.42, the flaw in the delineation of the jet width on the outbound side of the trajectory at the end of the PJL region and in the TZ2 region is clearly visible. The variation in the earlier and later region is more realistic. The imprecise and sensitive methods used to define the extreme ends of the jet body reinforces the utilization of δ_1 as the characteristic length scale. That said, the calculation of δ_2 remains important for the computation of integrals across the width of the jet; the values will be employed in §5.2.7 though §5.2.9.

5.2.6 Nondimensional Similarity

It was noted in § 2 that there exists similarity of the u velocity profiles at various longitudinal sections along the axis of the jet when the flow is completely established. It is observed when the profiles are non-dimensionalized and collapsed onto each other. This section presents such profile plots, separated into the previously described WJL, PJL,, SJL, return flow SJL, and transition regions: of the u and v profile mean velocities as well as of the other mean calculated flow parameters introduced in §5.1. They are always presented in dimensional form, and often presented in nondimensional form. The standard non-dimensionalizing quantity is U_m. The profile ordinate n is non-dimensionalized by δ_1 to give the ordinate $\eta = y/\delta_1$. Note that data on the negative n-stem is non-dimensionalized by δ_{1-}, while data on the positive n-stem is non-dimensionalized by δ_{1+}.

Wu and Rajaratnam (1995a) analyzed the plane deflected wall jet entirely in terms of classic plane jet theory. The major concentration was on the SJL region, with only general vertical and horizontal mean velocity profiles presented for both the WJL and SJL regions. Although all regions of flow are analyzed in detail herein, the same approach is taken in this work. That is, the entire deflected wall jet is conceptualized as a plane jet. Where there do not exist two profile stems (in the WJL and SJL regions, for example), the free mixing regions (the inbound side of the WJL region and the outbound side of the SJL region) are treated as one half of an imaginary plane jet.

Due to the large number of plots generated for this section, the full set of plots is presented only in §5.2.6.1 to §5.2.6.3, as the data in the WJL, PJL, and SJL flow sections are the most illuminating. §5.2.6.4 and §5.2.6.5 present abridged sets for the return flow SJL and transition sections, with the full sets presented in §8. To avoid needless repetition, the format is described herein.

The first set of figures presents the dimensional and nondimensional u mean velocities, against either n or η. While the entire dimensional data set is plotted, the nondimensional set is only plotted across $-2.5 \leq \eta \leq 2.5$, (or from zero for the WJL and SJL regions) as this range fully contains the theoretical similarity equations [2.9] and [2.16]. The next figure plots u/U_m against η, with either equation [2.9] or [2.16] for comparison with theory and other data. The next figures are of the same form and plot: v and v/U_m; τ/ρ and $-\tau/\rho U_m^2 \times 100$; and KE and KE/U_m^2. The next plots present mean k, d, ω, ε, l_k and v_k, each in dimensional form. Deviations from this format will be noted and explained in the relevant sections. Although it may appear that the plots consist simply of solid gray areas, all the data points for all the available profiles have been plotted; the appearance is only a manifestation of the immense number of individual points. For clarity and to show the variation of the parameters with s, the first profile of the plotted set is plotted with an open circle and the last with an open square. Furthermore, dark lines are plotted at intervals along s.

5.2.6.1 Wall Jet-Like Flow

Figure 5.51 shows that the axial u velocities in the WJL region collapse well and exhibit a good degree of similarity, even in dimensional form. The linear section of u is clearly visible in Figure 5.51 (a), with u passing through zero between –27 cm and –29 cm. The decay of U_m is also evident at n = 0 cm in Figure 5.51 (a). The nondimensional plot of Figure 5.51 (b) shows excellent similarity. To confirm that the analysis using plane jet theory is valid, Figure 5.52 compares u/U_m using (a) classical wall jet and (b) free mixing region (classic plane jet) definitions. Equations [2.9] and [2.16] are plotted for reference, and there is no great difference between the two. The deviation from theory at approximately $\eta = -1$ is a direct effect of the inbound eddy of counter-clockwise rotation. Figure 5.53 shows that v does not collapse at all well to similarity, most likely because the profiles do not all pass through the centre of the inbound eddy, and the δ_{2-} values are not coincident. Still, it is interesting to note that the magnitude of v increases regularly with s.

Figure 5.54 (a) supports the observations of mean Reynolds stress per unit mass given in §5.1.3, that τ/ρ is approximately zero (slightly higher) at the jet centreline, increases to a maximum magnitude somewhere inside the jet body and then decreases again to a relatively small value in region of the large inbound eddy. Figure 5.54 (b) shows that $-\tau/\rho U_m^2 \times 100$ collapses well to similarity and has the same general distribution (although stretched an skewed in the negative η direction) as reported by Heskestad (1965). Figure 5.55 (a) also supports the observations of KE variation in §5.1.2, with KE_{max} occurring at the jet centreline and decreasing with s. Figure 5.55 (b) shows that KE/U_m^2 collapses well and displays excellent similarity; $KE/U_m^2 \approx 0.5$ at the centreline in the WJL region.

As noted in §5.1.4, the mean turbulent kinetic energy increases relatively quickly to some maximum value and then more slowly decreases to a background k value with increasing distance from the centreline. This is clearly shown in Figure 5.56 (a). Not only does k decrease with negative n, but k_{max} decreases and the peak also shifts inward with s, indicating that the true centreline trajectory near the end of the WJL region may be more inbound than the trajectory employed. Figure 5.56 (b) shows that $k/U_m^2 \times 100$ does collapses somewhat, although not to the degree of either u or τ/ρ. Figure 5.57 shows that the mean dissipation has the same general distribution with n and s as do both mean Reynolds stress and mean turbulent kinetic energy. The sensitivity of d to the gradients and the susceptibility of the computed values to edge dislocation errors are evident in the figure, at approximately n = –15 cm (the location of a tessera edge) A number of non-dimensionalizations of d were attempted, however no appreciable similarity was noted and the plots are not presented.

The distributions of vorticity and strain along the profiles of the WJL region are presented in Figure 5.58 and also support the assertions in §5.1.6 and §5.1.7. Both ω and ε are approximately zero at the jet centreline and increase to a maximum somewhere inside the body of the jet (usually within the first few centimeters). Both parameters then decrease to a background value in eddy region. The variation of the mean Kolmogorov length and velocity scales also support the qualitative observations from §5.1.8. As was the case for d, the susceptibility of l_k and v_k to tessera edge dislocation errors is also evident in Figure 5.59. The length scale is smallest at the jet centreline and increases with distance in the inbound direction, while the velocity scale exhibits the opposite trend.

5.2.6.2 Plane Jet-Like Flow

The PJL region provides very interesting profile plots. Figure 5.60 (a) dramatically shows both the effects of the inbound eddy on the negative profile stem and the growth of the jet on the positive stem. U_m clearly decays from approximately 100 cm/s at s = 55.59 cm to approximately 50 cm/s at s = 95.09 cm. Additionally, the steady growth of both δ_{1+} and δ_{2+} from almost zero downstream of the baffle tip to increasingly larger values is clearly evident. Figure 5.60 (b) shows that the profiles in the PJL region collapse very well, especially on the outbound side. The profiles furthest away from the baffle appear to lie closest to the theoretical line of equation [2.9], as shown in Figure 5.61. This shows that the local effects of the large inbound eddy of counter-clockwise rotation lessen with distance away from the eddy. The furthest upstream profiles exhibit the same deviation from equation [2.9] as do the WJL profiles, while further downstream the profiles become more and more plane jet-like.

Figure 5.62 shows that the v profiles on the inbound side of the trajectory behave very much like their WJL counterparts, showing the same lack of similarity. However, the outbound side exhibits a greater degree of similarity. It is interesting to note that the outbound side is least similar at the downstream end of the PJL region, where the effects of the impingement with the water surface are most manifest.

Figure 5.63 (a) also supports the qualitative observations of mean Reynolds stress per unit mass given in §5.1.3; the locus of maximum τ/ρ is located on the outbound side of the jet centreline, with the distance between the two increasing with s. Figure 5.63 (b) shows that although the $-\tau/\rho U_m^2 \times 100$ profiles do not really collapse to similarity, that the majority of the stress is found within the outbound profile stem, in the $0 \le \eta \le 2$ range. This stress is directly related to the shear layer that propagates in the outbound direction, which is generally absent from the inbound side due to the inbound eddy. Figure 5.64 (a) shows that KE_{max} is located at the jet centreline and decreases with s, as in the WJL region. Figure 5.64 (b) shows that KE/U_m^2 collapses well and displays excellent similarity; again, $KE/U_m^2 \approx 0.5$ at the centreline in the PJL region.

The mean turbulent kinetic energy exhibits comparable variation as the mean Reynolds stress. Figure 5.65 (a) clearly shows that k_{max} is located nearest the baffle and decreases in magnitude with distance downstream. The bulk of k is found on the outbound side of the jet, within the mixing region, and the locus of k_{max} is always below that of the jet centreline., the $k/U_m^2 \times 100$ profiles do not collapse well, as made evident by Figure 5.65 (b). However, the figure does further illustrate how the peak in the mean turbulent kinetic energy shifts away from the centreline with distance along the centreline, and shows that the nondimensional distribution is somewhat symmetrical about the peaks. As was the case for the WJL region, Figure 5.66 shows that the mean dissipation in the PJL region has the same general distribution with n and s as the mean turbulent kinetic energy.

The distributions of mean vorticity along the profiles of the PJL region are presented in Figure 5.58 (a) and confirm the more qualitative observations made in §5.1.6. ω is approximately zero at the jet centreline and increases to a different positive and negative maxima inside the body of the jet, along the inbound and outbound sides of the profiles, respectively. The mean vorticity increases to a generally low positive background value on the inbound side of the trajectory, indicative of the solid body rotation of the large inbound eddy of counter-clockwise rotation. On the outbound side, ω quickly increases to a much higher negative value and then decreases more slowly to a negative background value that is of the same order as the vorticity found on the inbound side. The maximum negative vorticity is highest directly downstream of the baffle and then quickly falls with s. The variation of mean strain mirrors that of the vorticity, except that ε is positive on the inbound side of the centreline and negative on the outbound side. The mean Kolmogorov length and velocity scales also support the qualitative observations from §5.1.8, as shown in Figure 5.68. The length scale is smallest on the outbound side of the jet centreline and decreases quite symmetrically on either side. The velocity scale exhibits the opposite trend. The variation in range between the maximum and minimum extremes of both Kolmogorov scales is greatest near the baffle, and decreases with distance along s.

5.2.6.3 Surface Jet-Like Flow

Figure 5.69 shows that the axial u velocities of the SJL region, like the those of the WJL region, collapse well and exhibit a good degree of similarity. Figure 5.69 (a) shows that the Um increases with s instead of decays, indicating that either the surface jet-like flow is not fully developed or the defined trajectory is lower than the true jet centreline. However, the nondimensional plot of Figure 5.69 (b) still exhibits good similarity. In Figure 5.70 equation [2.9] is plotted along with u/U_m: in addition to the similarity, it is obvious that as the profiles move away from the TZ2 region and further downstream, the nondimensional data between $\eta = 1$ and $\eta = 2$ becomes closer to the theoretical line. This occurs as the profiles move away from the upper-left corner of the large outbound eddy of clockwise rotation and into a region where the surrounding flow is dominated more by the v-component of velocity. As was the case with both the WJL and PJL data, profiles of v do not collapse at all well to similarity, as shown in Figure 5.71. Once again, this may be attributable to the existence of the backwards flow of the eddy below the SJL flow. It is interesting to note that the magnitude of v decreases regularly with s.

Figure 5.72 (a) shows that the mean Reynolds stress per unit distribution changes from the beginning to the end of the SJL region. Near the beginning, τ/ρ is highly negative near the centreline, and decreases in magnitude with n; near the end, τ/ρ is closer to zero at the centreline and increases in magnitude with n. Note that τ/ρ data is not available within approximately 2 cm of the centreline, as this area falls within the water surface reflection exclusion zone; only u, v, ω and ε were calculated in the region. Figure 5.72 (b) indicates that $-\tau/\rho U_m^2 \times 100$ does not collapse to similarity. As was the case in Figure 5.71, the profiles closest to the TZ2 region and the zone of stagnation exhibit the least amount of similarity. Figure 5.73 (a) supports the observations of u variation in the SJL region, with KE_{max} occurring near the jet centreline but increasing with s. Figure 5.73 (b) shows that KE/U_m^2 collapses only moderately well and displays only a moderate degree of similarity; as in the WJL region, $KE/U_m^2 \approx 0.5$ closest to the centreline in the SJL region.

As noted for the profiles in the WJL region, the mean turbulent kinetic energy in the SJL profiles increases relatively quickly to some maximum value and then more slowly decreases to a background k value with increasing distance from the centreline. This is clearly shown in Figure 5.74 (a). Figure 5.74 (b) shows that mean dissipation behaves in a similar manner. The sensitivity of d to the gradients and the susceptibility of the computed values to edge dislocation errors are evident in the figure, at approximately n = 2 cm and n = 7 cm.

The distributions of mean vorticity and strain along the profiles of the SJL region are presented in Figure 5.75. Both ω and ε trend to approximately zero at the jet centreline and then increase with n. As noted in §5.1.6 and §5.1.7, the range of the parameters is less than in either the WJL or PJL regions, and the background levels are relatively low. The variation of the mean Kolmogorov length and velocity scales in the SJL are consistent with the observation made in the other flow regions. The length scale is smallest near the jet centreline and increases with distance in the outbound direction, while the velocity scale exhibits the opposite trend, as shown in Figure 5.76.

5.2.6.4 Return Surface Jet-Like Flow

Figure 5.77 presents both the (a) u and (b) u/U_m mean velocity profiles for the return flow SJL region, while Figure 5.78 plots u/U_m against η with equation [2.9] provided for reference and comparison. To facilitate comparison with the main flow SJL region, the profiles have been plotted against positive n and h, although the flow is technically contained on the inbound side of the return flow jet trajectory. It is clear that the return flow SJL region varied almost identically as the main flow SJL region. U_m increases with s (in this case upstream distance, away from the zone of stagnation) as well as decreases with distance away from the centreline. The profiles collapse well, and exhibit the same type of variation past $\eta = 1$ as does the main flow SJL region: namely, that the profiles trend closer towards the theoretical line with increasing distance away from the TZ2 region. Figure were generated for the other parameters discussed in §5.2.6.1 to §5.2.6.3 and are presented in §8.

5.2.6.5 Transition Flows

Figures 5.79, 5.80 and 5.81 present the variations of both u and u/U_m for the TZ1, TZ2 and return flow TZ2 flow regions, respectively. Figures plotting the other parameters are presented in §8 for completeness. It has been suggested previously that the trajectory identified in the transition regions may not truly represent the actual jet centreline: that definition of the centreline by the $\omega = 0$ criterion may be flawed in the transition regions. Supporting this assertion is the awkward decay (and sometimes growth) of U_m and the non-tangential variation of θ_c upstream of the baffle and in the vicinity of the general stagnation zone, near the point of impingement. Further support is given by the figures introduced in this section. It is evident, especially in both TZ2 regions, that the maximum velocity along each profile does not always occur at the identified centreline. Although U_m consistently decays with s, the peak also shifts away from n = 0 cm.

For example, Figure 5.80 show that at s = 109.87 cm (the TZ2 profile nearest the stagnation zone) the peak mean u velocity does not occur at n = 0 cm, but at approximately n = 6 cm. However, at s = 117.43 cm (the TZ2 profile nearest the SJL flow) the peak has shifted upwards, to approximately n = 0 cm. This indicates that at s = 109.87 cm, the identified trajectory is not coincident with the locus of the true U_m filament. This potential flaw is evident in all three figures, but because there has not been any significant amount of research conducted on the transition regions of the plane deflected wall jet, it is not known whether this the divergence from complete similarity is normal.

5.2.7 Discharge Intensity Variation

The entrainment of surrounding fluid in to the expanding jet body is a well-studied phenomenon in plane jets. In addition the being simplified with entrainment coefficients and velocities as presented in §2, the variation of volume flux is also employed in the study plane jets (Rajaratnam 1976). Because plane jets are two-dimensional flows, mean discharge intensity can best describe the volume flux along the trajectory. It is defined as q and is given by the following equation:

$$q = \int_{\delta_{2-}}^{\delta_{2+}} u \, dn \qquad [5.2]$$

where u is the velocity component perpendicular to the profile section and n is the ordinate along the profile. The variation of discharge intensity was used by Wu and Rajaratnam (1995a) in their study of the plane deflected wall jet and by and Ead and Rajaratnam (2001) in their study of plane turbulent surface jets in shallow tailwater.

In the present study, the computation of discharge intensity is a straightforward matter. Using the u velocity data extant for each of the defined profiles, a numerical integration was performed using the local δ_2 values as integration limits. Note that the decision to compute ordinates every 0.05 cm along the profiles provides a good resolution for the trapezoidal numerical integration method employed. The value of discharge intensity at the gate is $q_o = 0.0335$ m^2/s.

Figure 5.82 presents the variation of q with s over (a) the full jet trajectory and over (b-d) the sections of the baffle, between the baffle and the point of impingement and downstream of the point of impingement, respectively. The discharge intensity for both the inbound (q_-) and outbound (q_+) sections of the jet have been plotted separately, as well as the total discharge intensity ($q = q_- + q_+$).

Consider first the variation of q on the inbound side of the jet trajectory. At s = 35.50 cm, $q_- = 0.1$ m^2/s and it declines at an increasing rate until the point of impingement at s = 109.87 cm, where $q_-$is approximately 0.005 m^2/s. In the WJL region, q_- remains relatively constant. In the TZ1 region, there exists a small defect or q_- deficit, directly upstream of the baffle. This is a false decrease, attributable to the entire negative n-stem profile not being defined in this region. θ_c for theses profiles is such that the negative stems of the profiles extend past the upstream edge of the assembled mosaic. As a result, the u velocity component at the defined δ_2 location has not yet decreased to zero, and the integration is not complete. The discharge intensity s artificially low. This phenomenon was previously noted in §5.2.6.4 for the TZ1 region. The decrease of q_- in the PJL region is very smooth, and it decreases more rapidly as s increases. This decrease continues until the point of impingement in the TZ2 region, after which q_- remains constant and effectively negligible at 0.005 m^2/s. The mean discharge intensity is not zero because there is still flow between the water surface and the jet centreline.

Consider second the variation of q on the outbound side of the jet trajectory. As was the case for q_- in the SJL region, q_+ in the WJL region is approximately 0.005 m^2/s and can be considered negligible. In the TZ1 region, the jet diverges from the horizontal deflects over the baffle and towards the water surface. In this region, and throughout the PJL region, the outbound side of the jet grows relatively freely. As a result, q_+ increases almost linearly from 0.005 m^2/s at s = 43.00 cm to approximately 0.055 m^2/s at s = 95.09 cm. In the TZ2 region, the discharge intensity remains relatively constant, decreasing by 0.01 m^2/s downstream of the point of impingement, at approximately s = 115.00 cm. Downstream of this point, throughout the remainder of the TZ2 region and through the entire SJL region, the discharge intensity increases linearly to q_+ =0.05 m^2/s at s = 128.90 cm.

The total discharge intensity is the sum of the inbound and outbound values. The variation of q in the WJL region is dominated by q_- while in the SJL region it is dominated by q_+. In the TZ1 region, there is a local and temporary increase in q in the region of the small eddy of clockwise rotation immediately upstream of the baffle. The temporary increase is a function of the eddy circulation. In the PJL region, the total discharge intensity remains relatively constant, peaking at $q = 0.115\ m^2/s$. At the end of the PJL region and throughout the TZ2 region, the jet effectively splits into the SJL main and return flows; hence q decreases to $0.055\ m^2/s$ at the point of impingement, where the surface jet-like flow begins to dominate.

Figure 5.83 (a) presents the variation of the nondimensional parameter q/q_o with ξ over the full jet trajectory, while Figure 5.83 (b) presents q/q_o with $\xi^{0.5}$. As discussed in §2, the growth rate of q/q_o has been found by precious investigators to be linear with respect to ξ for classic wall jets, and linear with respect to $\xi^{0.5}$ for classic plane jets. The relationship expressed in equations [2.12] and [2.19] employs the coefficient C_3. The coefficient was not calculated for the WJL region, as it is obvious that q/q_o decays instead of grows. Employing equation [2.19] and the assumptions of a classic wall jet, q/q_o would equal approximately 3.5; in fact q/q_o equal approximately 3.2.The decay is most likely an effect of the large inbound eddy of counter-clockwise rotation that so completely dominates the inbound flow. In the PJL region, there is effectively no growth in discharge intensity, mostly due to the decay of q_-. However, the growth rate for q_+ alone was calculated and then multiplied by two to obtain a theoretical estimate of C_3 if the plane jet-like region was symmetrical abut the centreline. Additionally, C_3 was calculated for the SJL region using the total discharge intensity. Table 5.9 presents the variation of C_3 along the full jet trajectory, for the PJL and SJL flow regions. The modified C_3 coefficient in the PJL region was 1.55, compared to 0.44 for classic plane jets. Although there are no reported C_3 values for classic surface jets, C_3 in the SJL region was 0.036, compared to 0.248 for a classic plane wall jet.

Figure 5.84 presents the variation of (a) q with s and of (b) q/q_o with ξ along the full return flow jet trajectory. Discharge intensities for both the inbound and outbound flows, as well as the total discharge intensity, are plotted separately. The variation is very similar to that in the TZ2 and SJL regions of the main flow, with q increasing along s. Figure 5.85 presents the variation of both (a) q and (b) q/q_o along the full main flow jet trajectory. To compare the division of the main flow into the two SJL flows, the return flow discharge intensity has been numerically added to that of the main flow (after the point of impingement) and also plotted. Theoretically, the sum of the main and return SJL flows should equal the flow in the PJL region. It is interesting to note that at the end of the SJL region, the combined q is approximately equal to the peak total q in the PJL region, indicating that the flow truly divides into two surface jet-like flows.

5.2.8 Momentum Flux Variation

The variation of momentum flux in plane jets has also been studied in great detail by previous investigators. As outlined in §2.1, it was initially theorized that momentum flux for a classic plane jet (M_o) was preserved, and equal to M_o. Heskestad (1968) reported that his experimental results indicated that the momentum flux decayed; this was confirmed by Kotsovinos (1978), who noted a loss of $0.2M_o$ at a distance of $100b_o$ downstream of the gate. This decay was confirmed by Wu and Rajaratnam (1995a) for deflected wall jets. As for discharge intensity, the computation of momentum flux per unit mass (m) is straightforward using the following equation:

$$m = \int_{\delta_{2+}}^{\delta_{2-}} u^2 \, dn \qquad [5.3]$$

The value of momentum flux per unit mass at the gate is $m_o = 0.0443\ m^3/s^2$. Figure 5.86 presents the variation of m with s over (a) the full jet trajectory and over (b-d) the sections of the baffle, between the baffle and the point of impingement and downstream of the point of impingement, respectively; m_-, m_+ and m (the total momentum flux) are plotted separately. Figure 5.87 presents the nondimensional parameter m/m_o versus (a) ξ and (b) $\xi^{0.5}$ over the full jet trajectory.

The variation closely resembles that of discharge intensity. In the WJL region, m/m_o decreases from approximately 1.4 to 1.2 and then remains constant until the TZ1 region. The increase is most likely due to the circulation of both of the eddies upstream of the baffle. At the baffle, the total momentum flux per unit mass quickly increases to approximately 1.4 and then steadily decreases to $m/m_o = 0.35$ at the point of impingement. The loss of m/m_o through the PJL region is $0.6m_o$, with a further loss to the point of impingement of $0.45m_o$. Throughout the remainder of the TZ2 region and through the entire SJL region, m/m_o increases linearly to approximately 0.46. The inbound and outbound components of momentum flux per unit mass also behave similarly to those of discharge intensity. From s = 35.50 cm to the point of impingement at s = 109.87 cm, m_-/m_o decreases from 1.3 to less than 0.05; m_+/m_o increases from approximately 0.05 at the end of the WJL region to 0.45 at the end of the PJL region., m_+/m_o undergoes a loss of 0.15 up until the point of impingement and then recovers that loss through the remainder of the TZ2 and SJL regions.

Figure 5.88 presents the variation of (a) m with s and of (b) m/m_o with ξ along the full return flow jet trajectory. The momentum flux per unit mass increases from $m/m_o = 0.14$ at the beginning of the return flow TZ2 region to 0.20 at the beginning of the return flow SJL region. Through the return flow SJL region, m/m_o increases linearly to approximately 0.42. This increase is directly related to the increase of Um in the region and the effects of the large inbound eddy of counter-clockwise rotation.

Figure 5.89 (a-b) presents the variation of both m and m/m_o along the full main flow jet trajectory. To compare the division of the main and return flows, the return flow momentum per unit mass has been numerically added to that of the main flow (after the point of impingement) and also plotted. The combined m is approximately equal to the peak total m at the end of the PJL region, again showing that the flow division into two surface jet-like flows.

5.2.9 Entrainment Velocities

The v component of velocity at the edges of the jet is defined as v_e, the entrainment velocity. Figure 5.90 presents the variation of (a) v_e with s and of (b) v_e/U_m with ξ along the full jet trajectory. Because the determination of both δ_{2-} and δ_{2+} was somewhat imprecise in certain locations (as described in §5.2.5), the values of v_e are reliable only where the jet widths are reliable. In all the transition regions, the entrainment inbound velocity component, v_{e-}, is unreliable. In both the WJL and PJL regions, v_{e-} linearly decreases with s. In the SJL region, v_{e-} exhibits a general (neglecting the peaking deviations) decline from 0.0 cm/s to –3.0 cm/s. Note that v_{e-} is primarily negative, indicating not entrainment, but detrainment. Once again, the domination of the inbound flow pattern by the large eddy is evident, as classical wall jet theory indicates entrainment. The variation of v_{e+} is reliable only downstream of the baffle and in the first part of the PJL region, before the onset of the unreliable δ_{2+} values, between $s = 51.80$ cm and $s = 75.00$ cm. In this region, the average value of v_e/U_m is –0.07, which compares well with the value of $\alpha_e = -0.058$ given in equation [2.13] for classic plane jets. It should be noted that the derivative of discharge intensity with s was also computed, and both v_e and α_e were obtained using the arguments of equation [2.5]. However, the resulting plots were extremely noisy, primarily because the flux of q using all of the profiles was both positive and negative.

tessera	u_{min} (cm/s)	u_{max} (cm/s)	v_{min} (cm/s)	v_{max} (cm/s)	V_{min} (cm/s)	V_{max} (cm/s)
1	-5.8	30.9	1.1	25.9	1.3	37.6
2	0	122.0	-6.1	66.0	0	122.0
3	-11.2	79.9	-3.7	68.6	0	104.0
4	2.6	53.6	22.2	68.4	22.4	86.9
5	-33.4	21.0	4.6	56.4	18.6	60.2
6	-52.7	0	-1.9	27.2	0	52.7
7	-21.4	29.0	0	34.4	0	35.8
8	-7.9	27.0	13.1	60.7	13.3	64.8
9	-11.3	36.7	1.7	65.0	6.0	73.4
10	-13.1	12.3	-0.7	19.2	5.8	22.8
11	-12.8	0.6	2.6	10.7	6.3	13.4
12	-4.7	34.2	-0.8	21.5	2.9	34.3
13	0	49.9	0	19.0	0	49.9
14	-44.8	1.7	-0.3	21.7	7.8	44.8

Table 5.1: Minimum and maximum mean velocities in each tessera.

parameter	minimum	maximum
u (cm/s)	-52.7	122.0
v (cm/s)	-6.1	68.6
V (cm/s)	0.6	172.6
KE (cm^2/s^2)	0.1	7445.6
τ/ρ (cm^2/s^2)	-392.2	49.2
k (cm^2/s^2)	5.6	990.5
d (cm^3/s^2)	0	229.4
ω (s^{-1})	-157.8	19.2
ε (s^{-1})	-53.8	9.3
l_k (cm)	0.009	0.036
v_k (cm/s)	0	1.3
t_k (s)	0.007	0.112

Table 5.2: Minimum and maximum mean flow properties in the full data mosaic.

tessera	u_{min} (cm/s)	u_{max} (cm/s)	v_{min} (cm/s)	v_{max} (cm/s)	V_{min} (cm/s)	V_{max} (cm/s)
1	-5.8	30.9	1.1	25.9	1.3	37.6
2	0	122.0	-6.1	66.0	0	122.0
3	-11.2	79.9	-3.7	68.6	0	104.0
4	2.6	53.6	22.2	68.4	22.4	86.9
5	-33.4	21.0	4.6	56.4	18.6	60.2
6	-52.7	0	-1.9	27.2	0	52.7
7	-21.4	29.0	0	34.4	0	35.8
8	-7.9	27.0	13.1	60.7	13.3	64.8
9	-11.3	36.7	1.7	65.0	6.0	73.4
10	-13.1	12.3	-0.7	19.2	5.8	22.8
11	-12.8	0.6	2.6	10.7	6.3	13.4
12	-4.7	34.2	-0.8	21.5	2.9	34.3
13	0.0	49.9	0	19.0	0	49.9
14	-44.8	1.7	-0.3	21.7	7.8	44.8

Table 5.3: Minimum and maximum mean flow properties in each tessera.

tessera	KE_{min} (cm^2/s^2)	KE_{max} (cm^2/s^2)	τ/ρ_{min} (cm^2/s^2)	τ/ρ_{max} (cm^2/s^2)	k_{min} (cm^2/s^2)	k_{max} (cm^2/s^2)
1	0.9	706.1	-26.9	-2.8	46.5	108.7
2	0	7445.6	-133.8	20.1	0.0	481.8
3	0	5403.1	-392.2	17.2	0.0	990.5
4	250.6	3775.0	-262.2	7.0	39.8	796.5
5	172.9	1813.7	-42.9	18.8	45.6	256.4
6	0	1388.7	-60.7	0	0	303.8
7	0	639.8	-82.1	0	0	398.2
8	89.1	2102.1	-250.3	7.0	221.2	625.8
9	18.3	2693.3	-257.6	6.4	40.3	763.5
10	17.0	260.5	-86.0	7.0	12.6	543.9
11	19.6	89.9	-33.0	16.2	40.9	220.8
12	4.1	586.6	-134.7	49.2	63.6	419.1
13	0	1244.4	-71.1	34.3	0.0	400.0
14	30.5	1001.7	-45.4	-10.8	46.1	131.1

Table 5.3 continued.

tessera	d_{min} (cm^2/s^3)	d_{max} (cm^2/s^3)	ω_{min} (s^{-1})	ω_{max} (s^{-1})	ε_{min} (s^{-1})	ε_{max} (s^{-1})
1	2.7	7.0	1.8	5.5	-0.3	1.1
2	0	158.0	-49.1	19.2	-26.9	9.3
3	0	229.4	-157.8	16.4	-53.8	5.6
4	3.1	81.5	-13.9	11.9	-1.9	4.3
5	2.6	26.9	-5.0	10.5	-3.2	4.6
6	0	27.2	0	6.4	-0.5	2.2
7	0	35.7	-3.4	5.3	-0.5	1.5
8	11.6	42.3	-6.5	6.4	-1.4	2.7
9	2.0	70.2	-13.3	6.7	-0.9	4.0
10	0.9	53.5	-10.7	2.4	-2.4	2.2
11	1.4	13.1	-2.9	0.3	-1.0	0.8
12	2.6	30.4	-11.4	1.4	-2.8	3.4
13	0	33.4	-5.4	0.1	-1.8	0.9
14	2.4	12.4	2.4	4.5	0.2	1.5

Table 5.3 continued.

tessera	$l_{k\,min}$ (cm)	$l_{k\,max}$ (cm)	$v_{k\,min}$ (cm/s)	$v_{k\,max}$ (cm/s)	$t_{k\,min}$ (s)	$t_{k\,max}$ (s)
1	0.023	0.029	0.4	0.5	0.042	0.068
2	0.010	0.026	0	1.2	0.009	0.055
3	0.009	0.035	0	1.3	0.007	0.102
4	0.012	0.027	0.4	1.0	0.012	0.062
5	0.015	0.027	0.4	0.7	0.020	0.066
6	0.015	0.022	0	0.7	0.021	0.041
7	0.014	0.019	0	0.8	0.018	0.030
8	0.014	0.019	0.6	0.8	0.017	0.032
9	0.012	0.030	0.4	0.9	0.013	0.076
10	0.013	0.036	0.3	0.9	0.015	0.112
11	0.018	0.032	0.4	0.6	0.030	0.091
12	0.015	0.028	0.4	0.8	0.019	0.066
13	0.015	0.018	0	0.8	0.019	0.029
14	0.020	0.031	0.4	0.6	0.032	0.074

Table 5.3 continued.

description	data points	profile no.	s (cm)	ξ	$\xi^{0.5}$	$\xi^{-0.5}$
WJL	30	1	35.50	13.98	3.74	0.267
		30	42.75	16.83	4.10	0.244
TZ1	40	31	43.00	16.93	4.11	0.243
		70	55.24	21.75	4.66	0.214
PJL	130	71	55.59	21.89	4.68	0.214
		200	95.09	37.44	6.12	0.163
TZ2	80	201	95.34	37.54	6.13	0.163
		280	118.19	46.53	6.82	0.147
SJL	52	281	118.44	46.63	6.83	0.146
		322	128.90	50.75	7.12	0.140
B	baffle location		51.80	20.39	4.52	0.221
I	impingement location		109.87	43.26	6.58	0.152

Table 5.4: Flow regime extents and boundary ordinates for the main jet flow.

description	data points	profile no.	s (cm)	ξ	$\xi^{0.5}$	$\xi^{-0.5}$
TZ2	30	1	109.87	43.26	6.58	0.152
		30	117.18	46.13	6.79	0.147
SJL	40	31	117.43	46.23	6.80	0.147
		70	127.95	50.37	7.10	0.141

Table 5.5: Flow regime extents and boundary ordinates for the return jet flow.

regime description	profile no.	s (cm)	$\xi^{-0.5}$	C_1
WJL	1 16	35.50 39.25	0.267 0.254	3.26
	16 30	39.25 42.75	0.254 0.244	9.05
TZ1	30 44	42.75 46.56	0.244 0.234	12.77
	44 50	46.56 48.37	0.234 0.229	2.15
	50 60	48.37 51.80	0.229 0.221	-18.73
	60 70	51.80 55.24	0.221 0.214	-0.72
PJL	70 200	55.24 95.09	0.214 0.163	7.46
TZ2 and SJL	200 250	95.09 109.87	0.163 0.152	21.84
	250 322	109.87 128.90	0.152 0.140	-20.93

Table 5.6: Variation of the C_1 coefficient along the full jet trajectory.

regime description	profile no.	s (cm)	ξ	C_2
WJL	1	35.50	13.98	-0.08
	16	39.25	15.45	
	16	39.25	15.45	-0.20
	30	42.75	16.83	
TZ1	30	42.75	16.83	-0.36
	44	46.56	18.33	
	44	46.56	18.33	0.01
	50	48.37	19.04	
	50	48.37	19.04	0.51
	60	51.80	20.39	
	60	51.80	20.39	0.00
	80	58.67	23.10	
PJL	80	58.67	23.10	-0.12
	168	86.16	33.92	
	168	86.16	33.92	0.00
	213	98.65	38.84	
TZ2	213	98.65	38.84	0.32
	283	118.94	46.83	

Table 5.7: Variation of the C_2 coefficient for the negative profile stem (δ_1) along the full jet trajectory.

regime description	profile no.	s (cm)	ξ	C_2
PJL	60	51.80	20.39	0.19
	213	98.65	38.84	
TZ2	213	98.65	38.84	0.70
	250	109.87	43.25	
	250	109.87	43.25	-0.54
	283	118.94	46.83	
SJL	283	118.94	46.83	-0.21
	322	128.90	50.75	

Table 5.8: Variation of the C_2 coefficient for the positive profile stem (δ_{1+}) along the full jet trajectory.

regime description	profile no.	s (cm)	ξ	$\xi^{0.5}$	C_3
PJL	60	51.80	20.39	4.52	1.55
	200	95.09	37.44	6.12	
SJL	283	118.94	46.83	6.84	0.036
	322	128.90	50.75	7.12	

Table 5.9: Variation of the C_3 coefficient along the full jet trajectory.

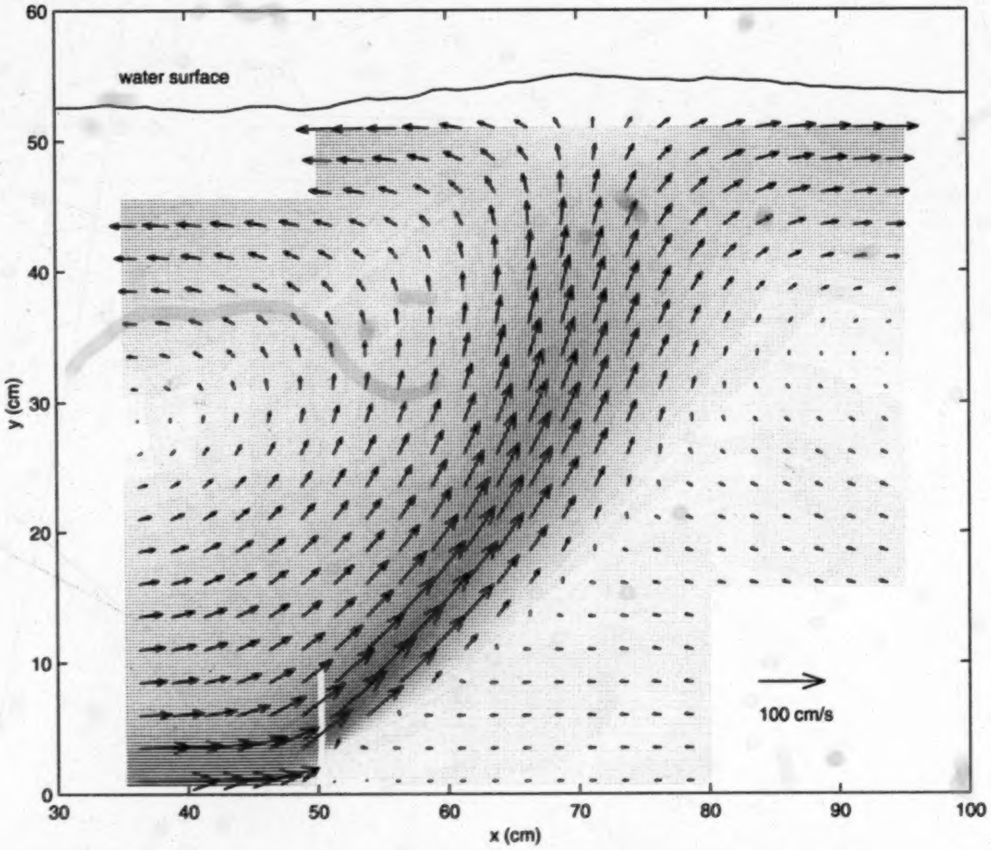

Figure 5.1: Full mean velocity vector field with additional superposed field showing every tenth vector at a larger scale.

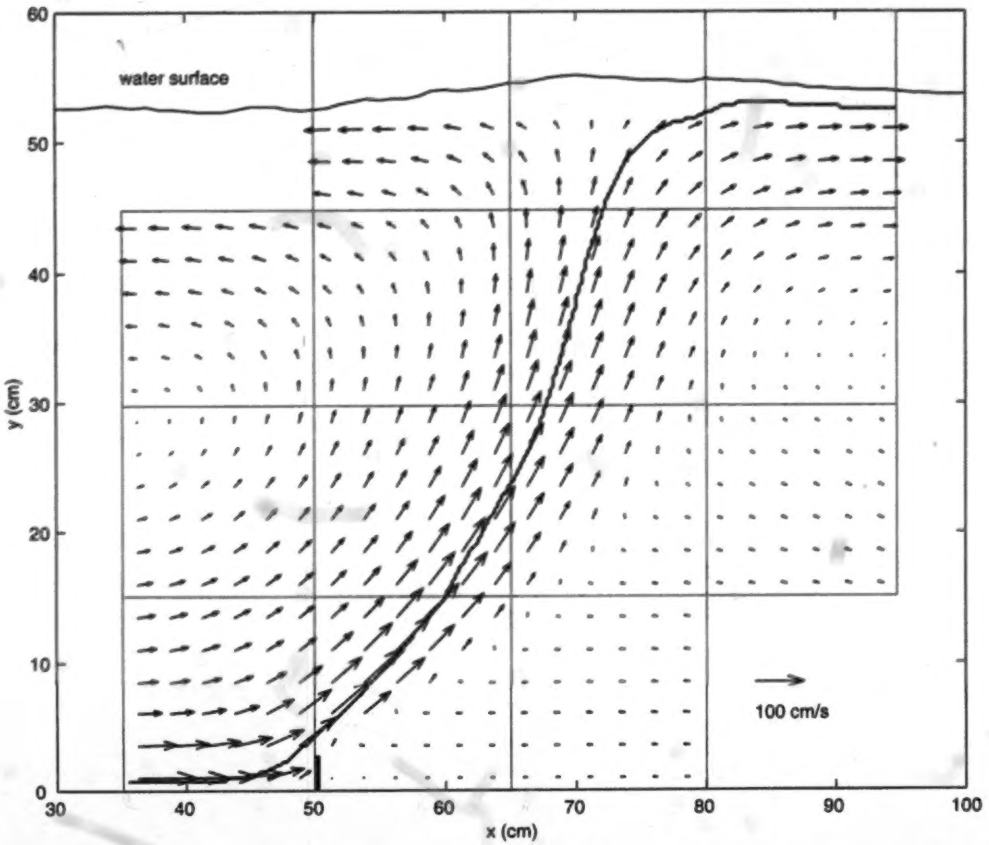

Figure 5.2: Mean velocity vector field for full mosaic showing every tenth velocity vector at scale and jet centreline trajectory.

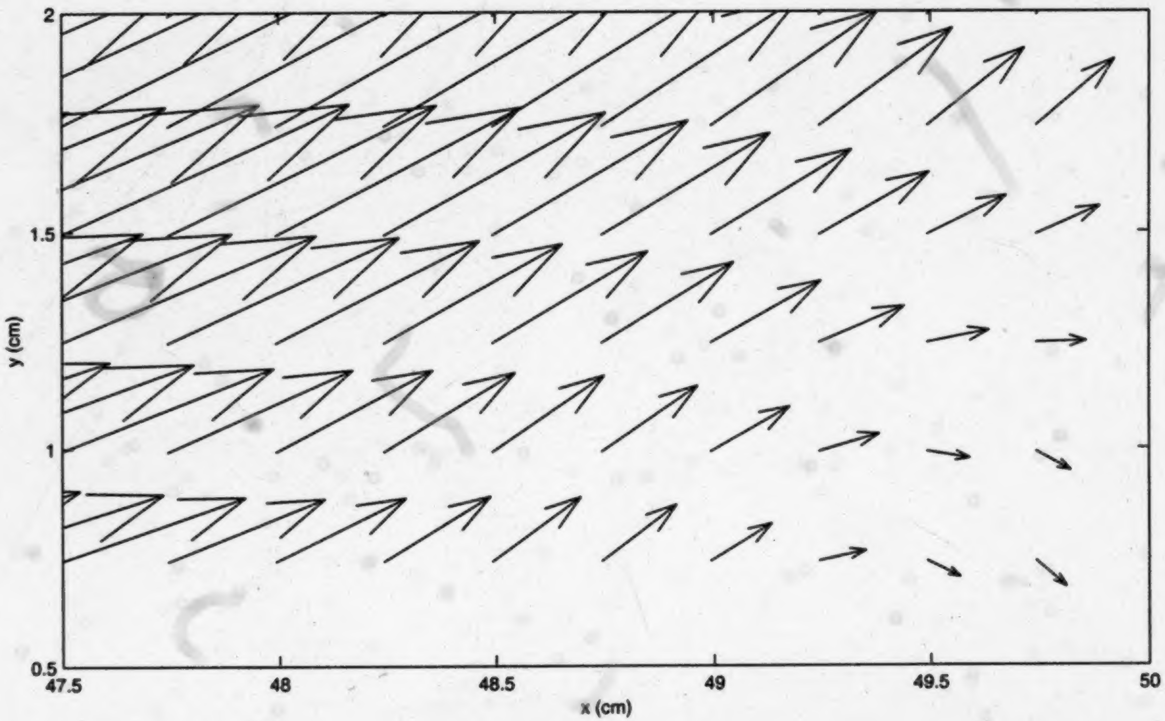

Figure 5.3: Mean velocity vector field of the area encompassing the small eddy of clockwise rotation.

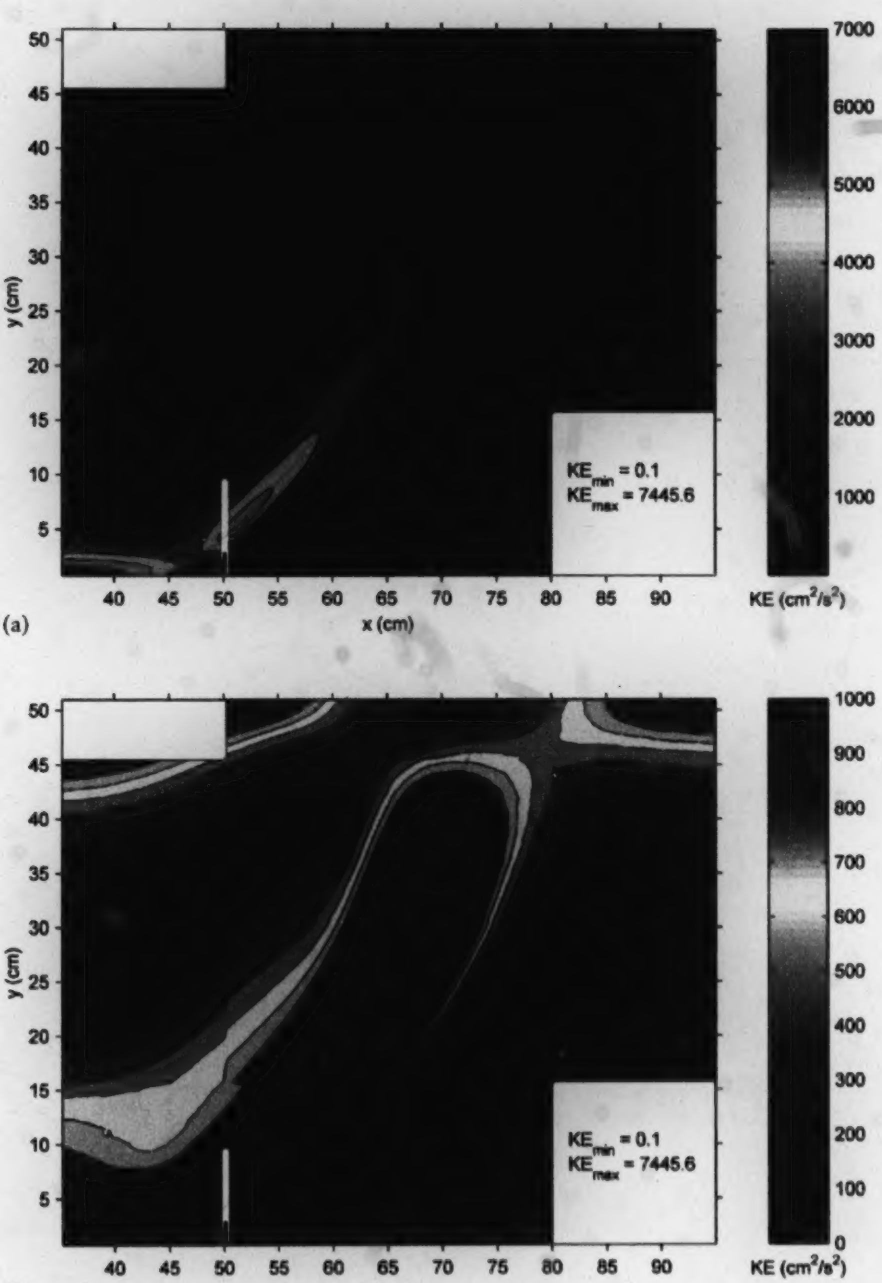

Figure 5.4: (a-b) Mean kinetic energy per unit mass (KE) contour maps describing full data mosaic with jet centreline trajectory.

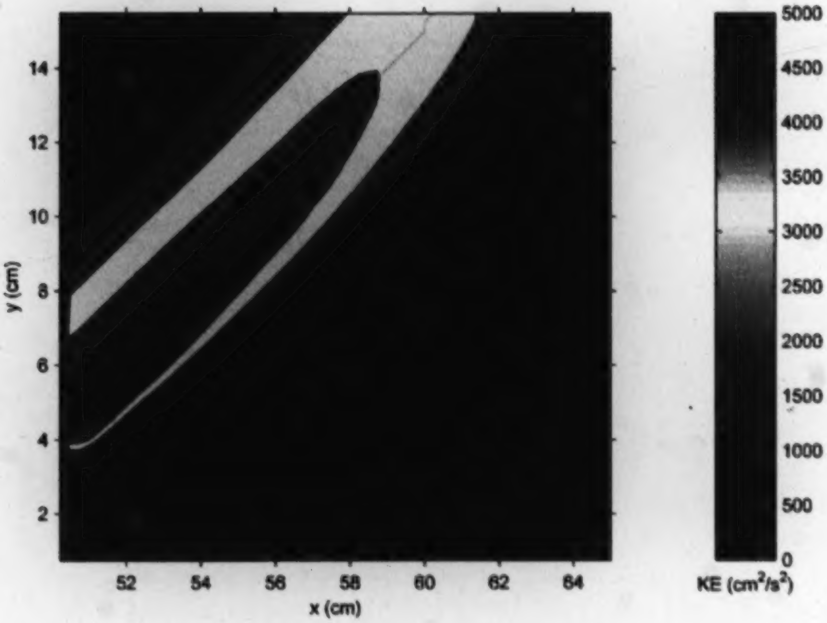

Figure 5.5: Mean kinetic energy per unit mass (KE) contour map for tessera 3 with jet centreline trajectory.

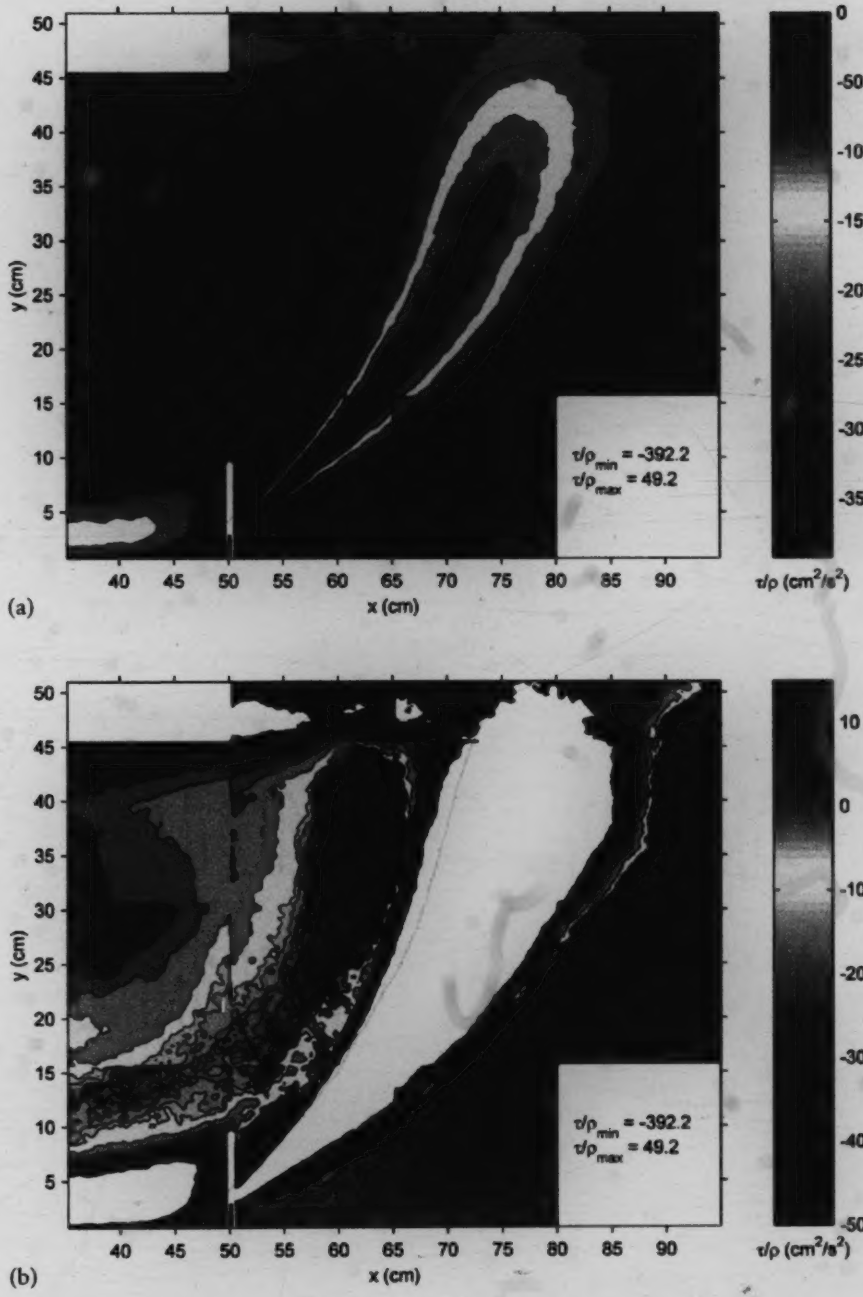

Figure 5.6: (a-b) Mean Reynolds stress per unit mass (τ/ρ) contour maps describing full data mosaic with jet centreline trajectory.

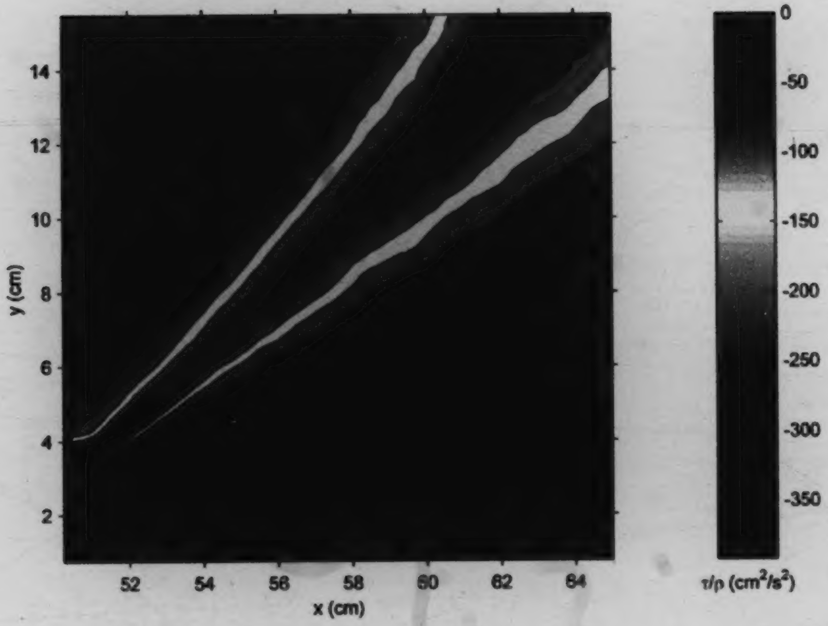

Figure 5.7: Mean Reynolds stress per unit mass (τ/ρ) contour map for tessera 3 with jet centreline trajectory.

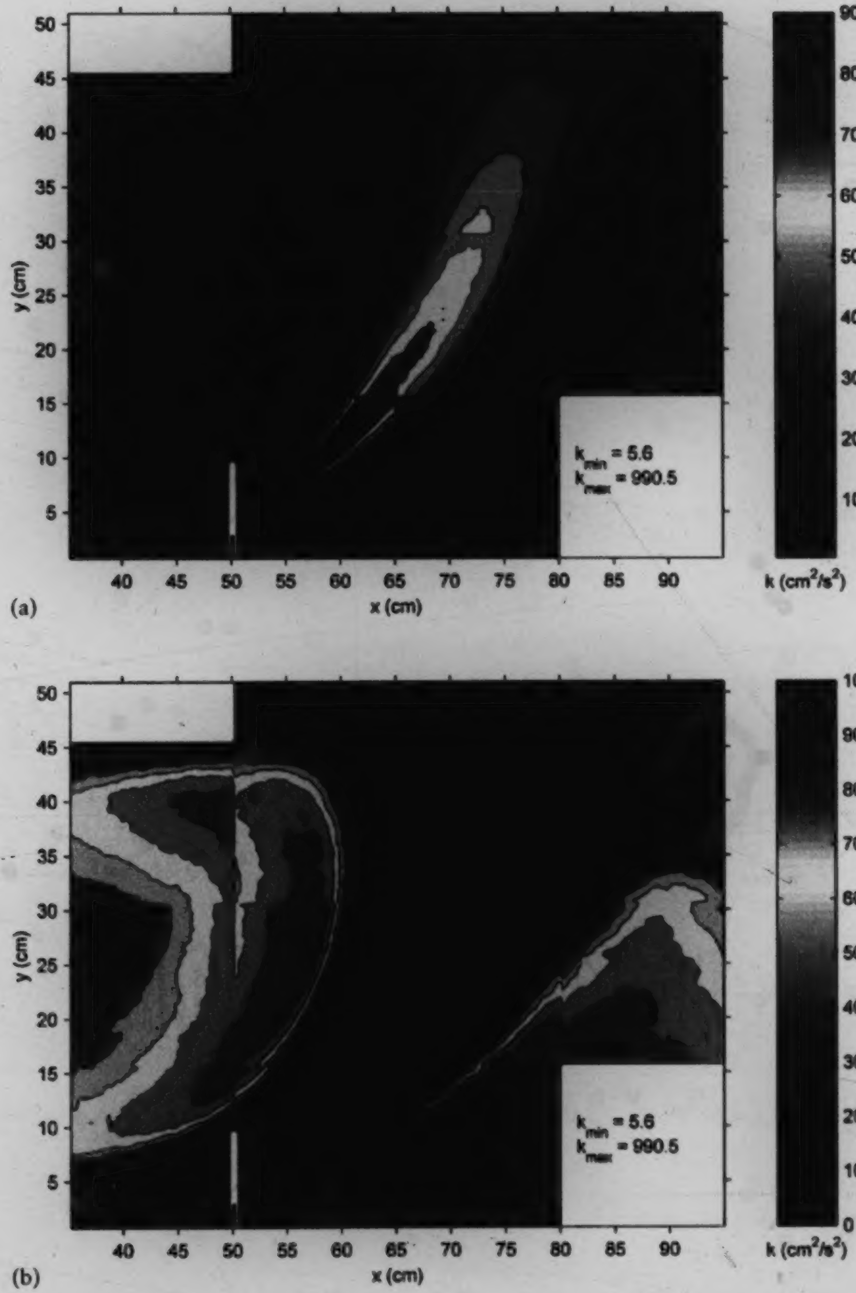

Figure 5.8: (a-b) Mean turbulent kinetic energy per unit mass (k) contour maps describing full data mosaic with jet centreline trajectory.

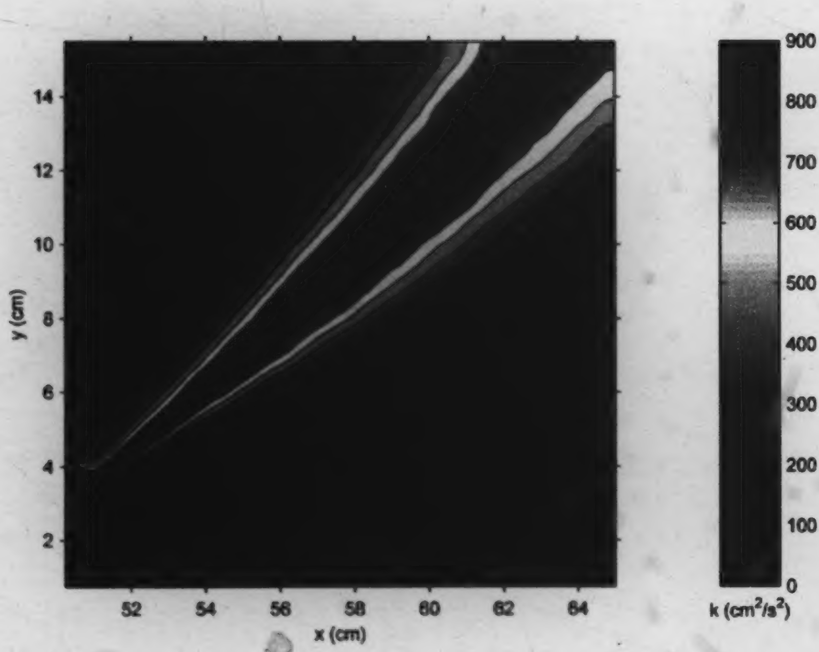

Figure 5.9: Mean turbulent kinetic energy per unit mass (k) contour map for tessera 3 with jet centreline trajectory.

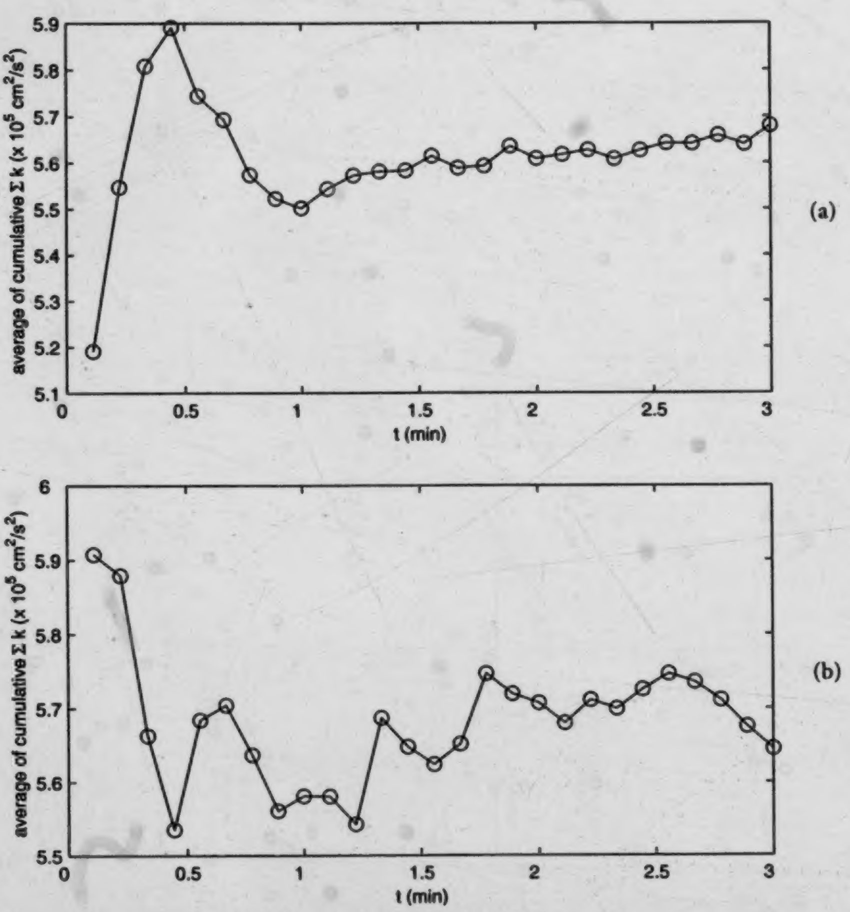

Figure 5.10: The cumulative average, plotted over increasing periods of time and averaging larger batches of PIV data files, of the sum of all turbulent kinetic energy (k) measurements in a tessera, presented for (a) tessera 2 and (b) tessera 4; showing that a sufficient amount of data was collected at each tessera for representative mean turbulent flow characteristics to be calculated. Note the stabilization by 2.5 minutes.

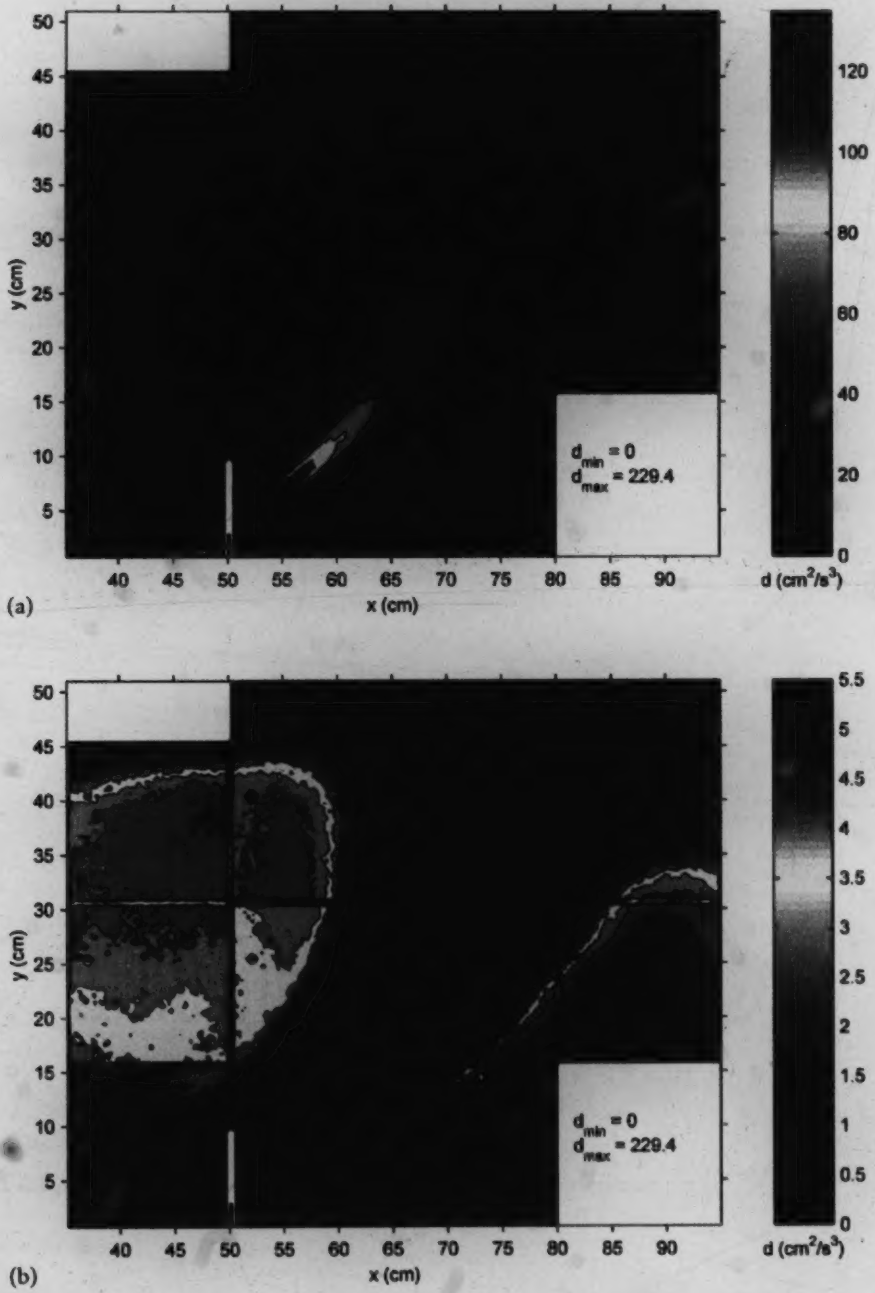

Figure 5.11: (a-b) Mean dissipation per unit mass (d) contour maps describing full data mosaic with jet centreline trajectory.

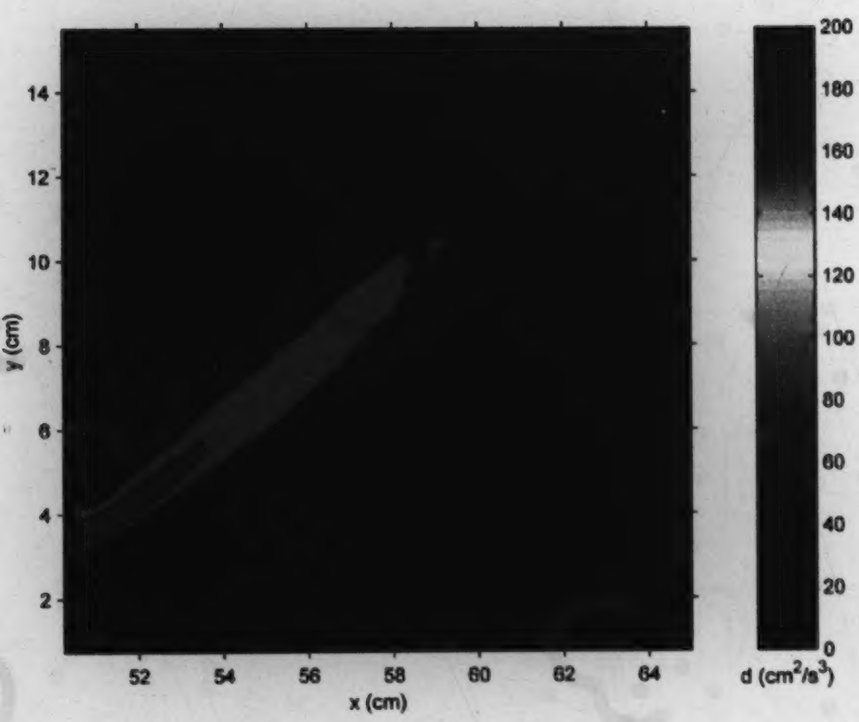

Figure 5.12: Mean dissipation per unit mass (d) contour map for tessera 3 with jet centreline trajectory.

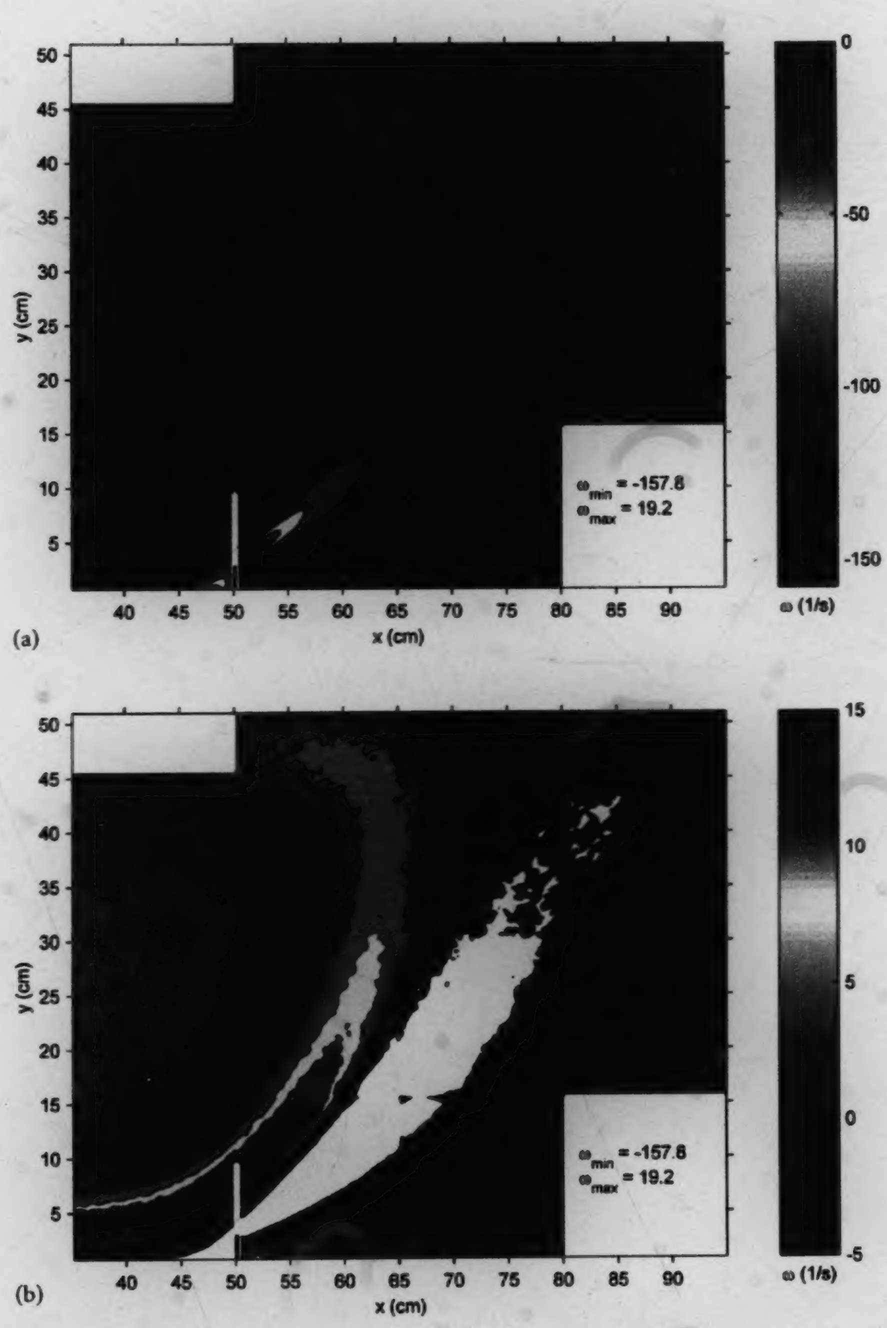

Figure 5.13: (a-d) Mean vorticity (ω) contour maps describing full data mosaic with jet centreline trajectory.

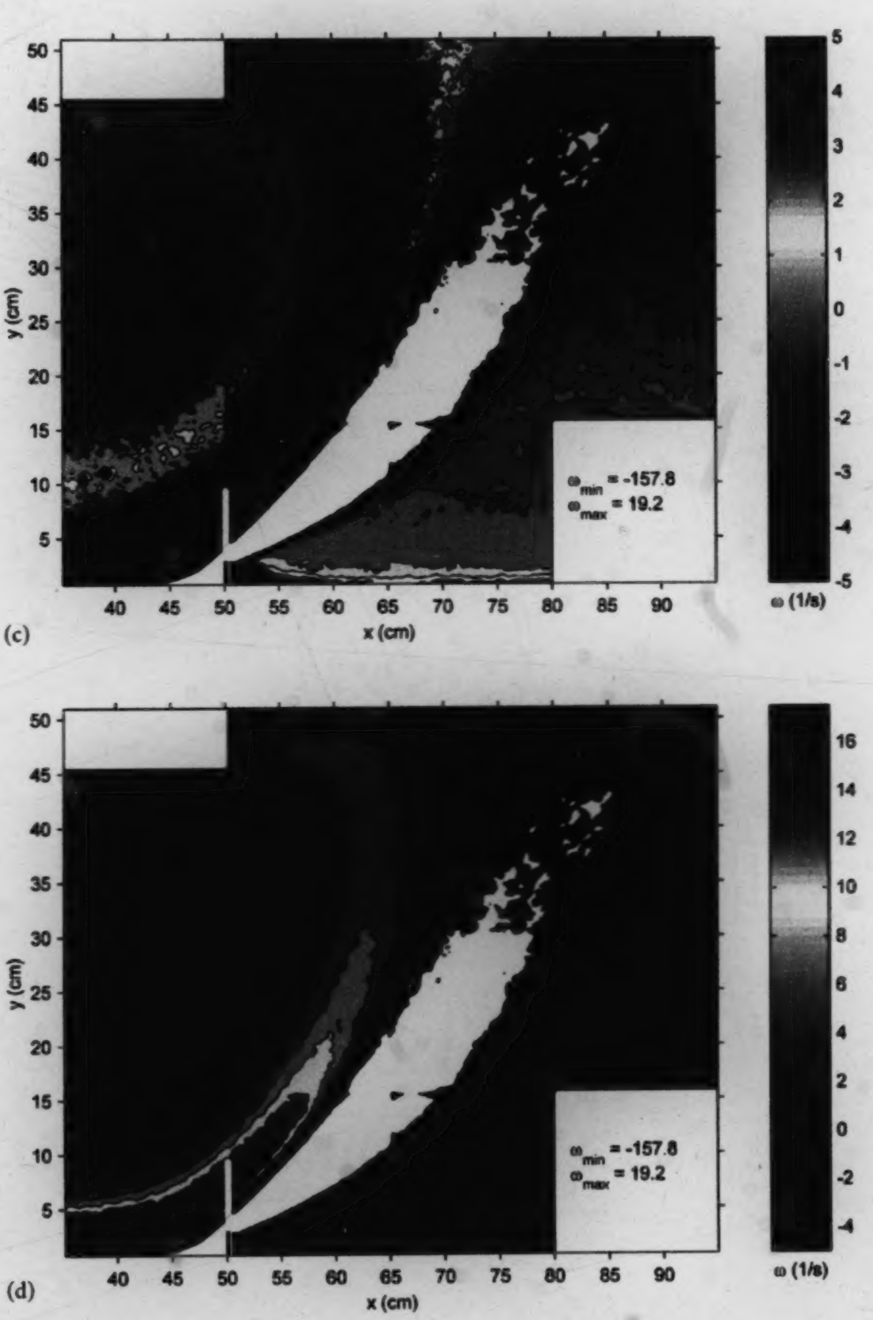

Figure 5.13: (a-d) Mean vorticity (ω) contour maps describing full data mosaic with jet centreline trajectory.

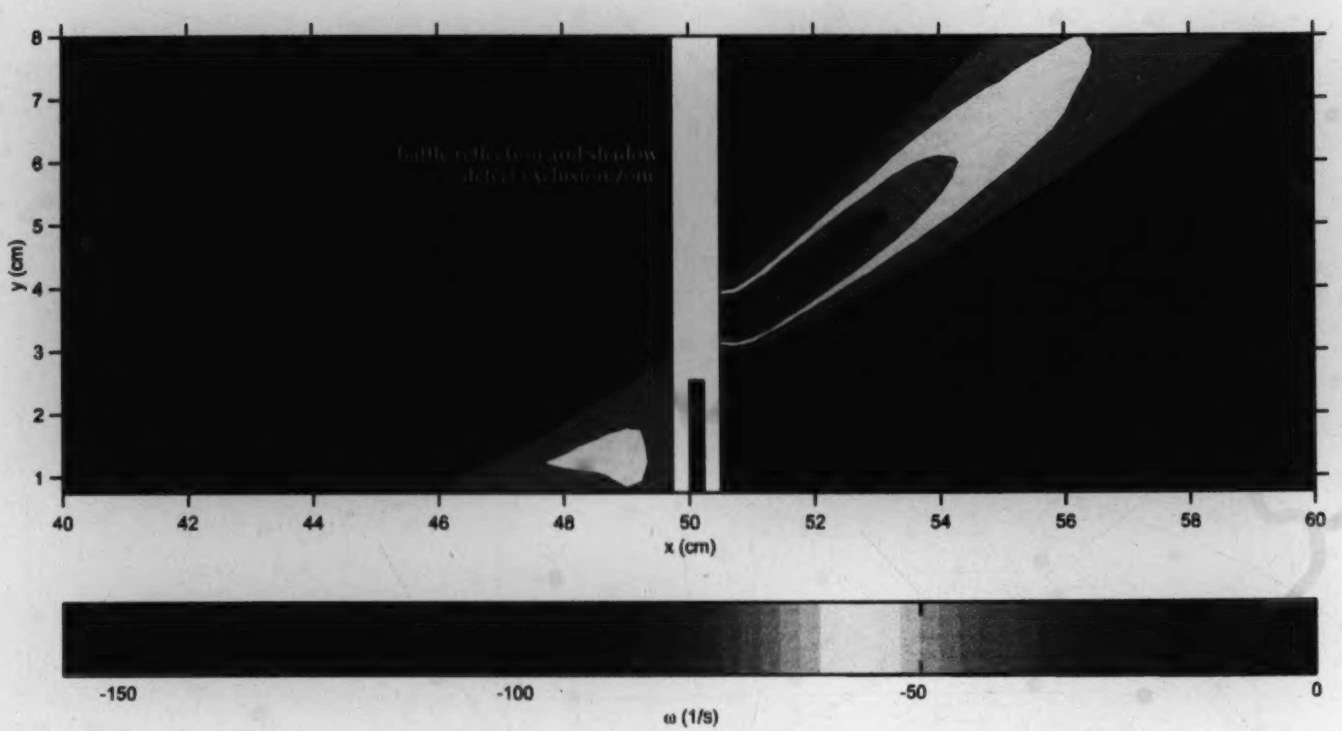

Figure 5.14: Mean vorticity (ω) contour map of mosaic area surrounding the baffle.

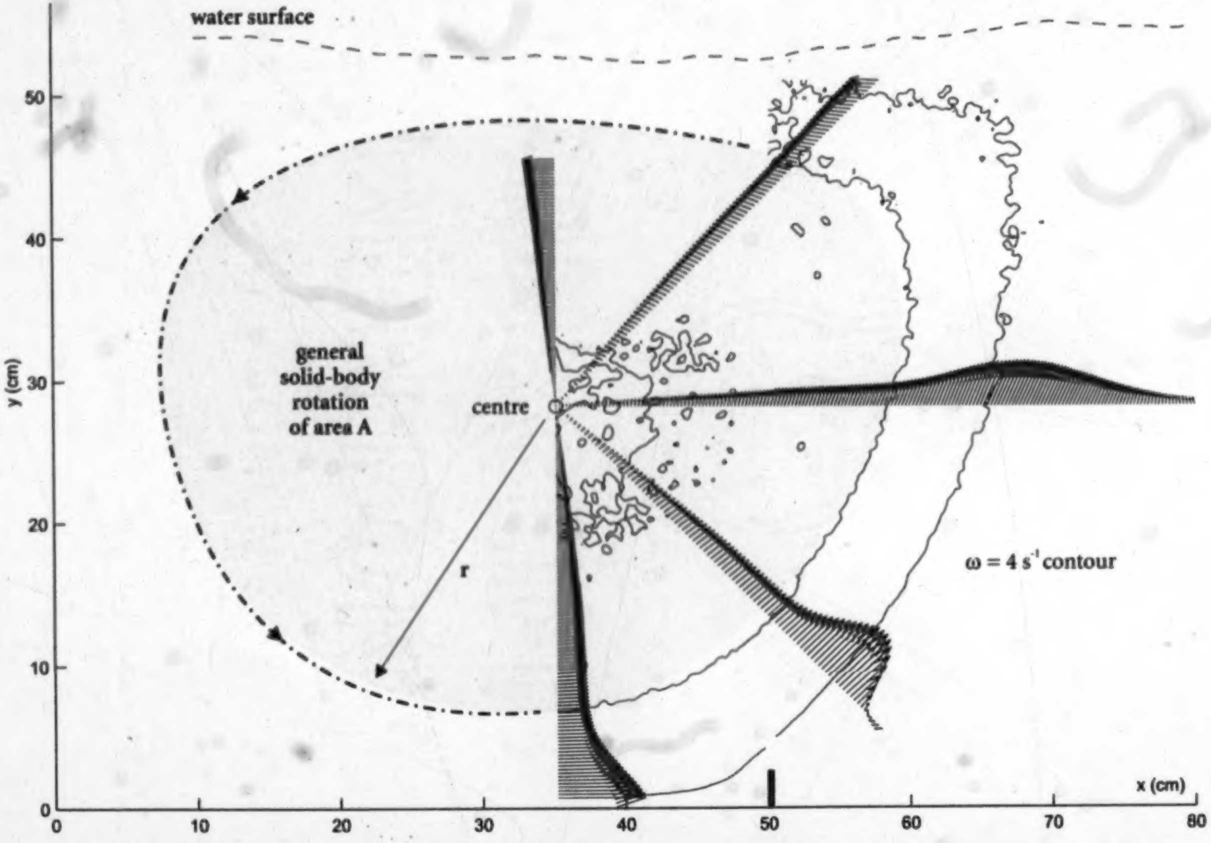

Figure 5.15: Velocity, vorticity and circulation in the large elliptical eddy found on the inbound side of the jet centreline trajectory .

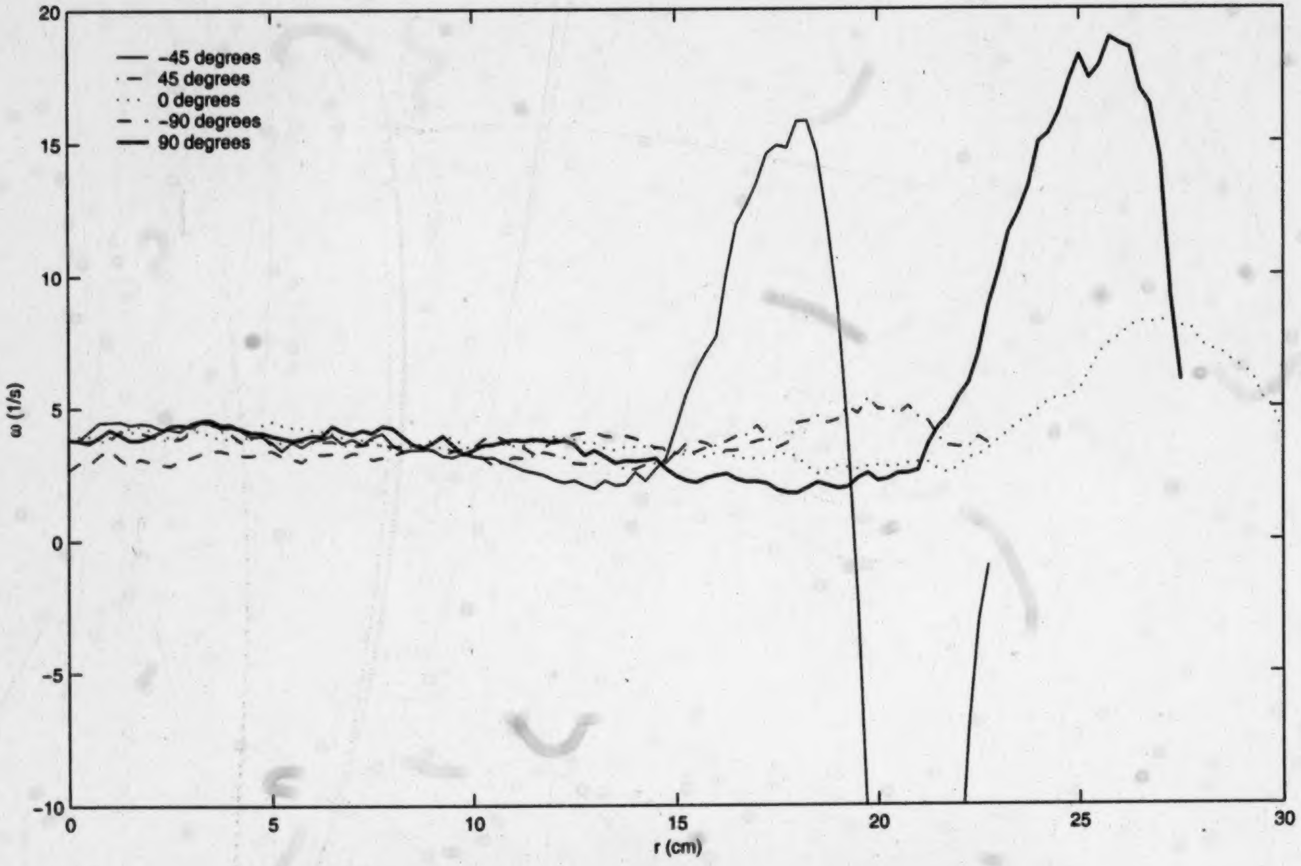

Figure 5.16: Vorticity distribution along the radius of the large elliptical eddy found on the inbound side of the jet centreline trajectory .

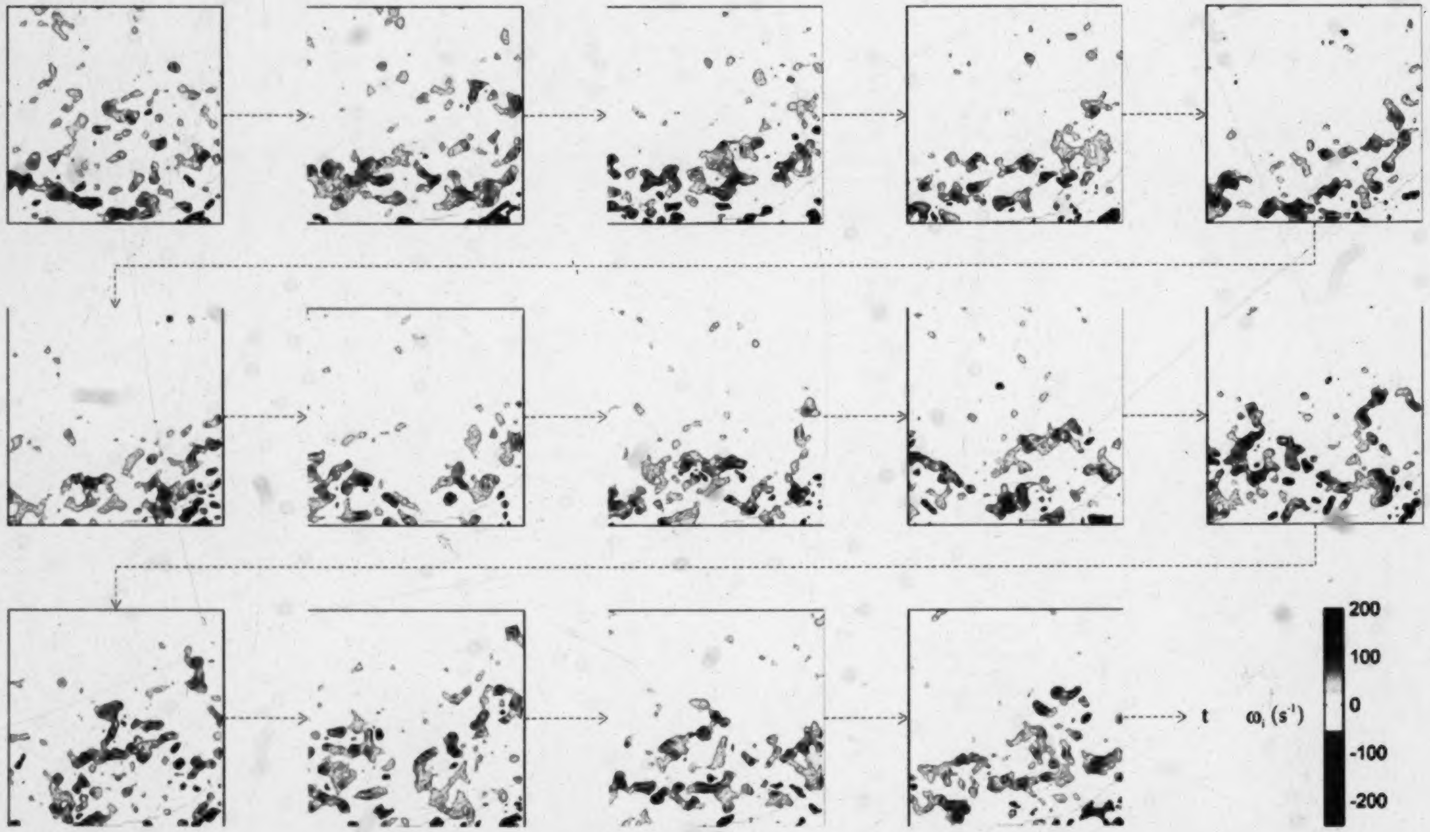

Figure 5.17: Instantaneous vorticity (ω_i) contour maps for tessera 2; consecutive 15 Hz frames with the background vorticity plotted in white to accentuate the coherent vortical structures and with the jet centreline trajectory as reference.

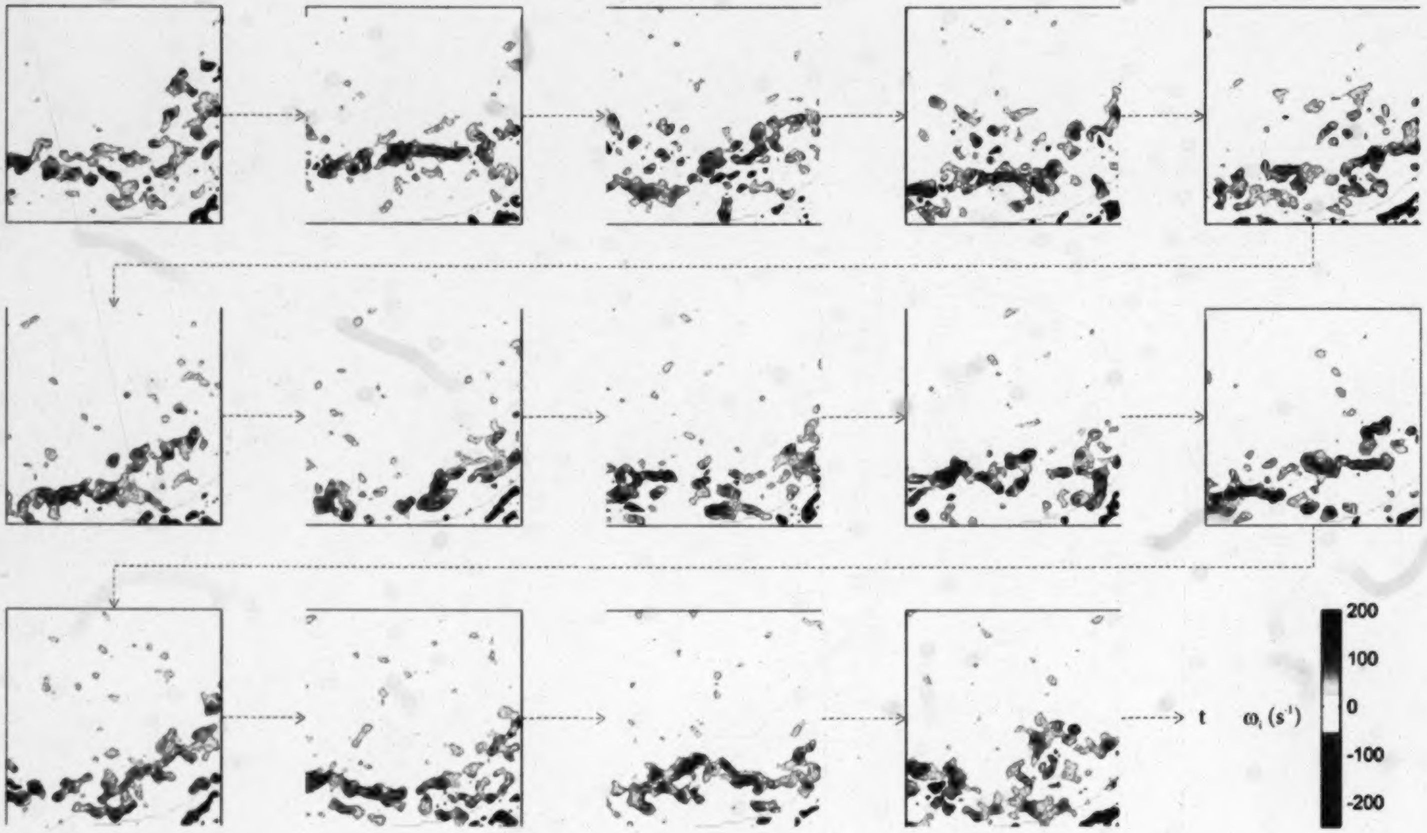

Figure 5.17 continued.

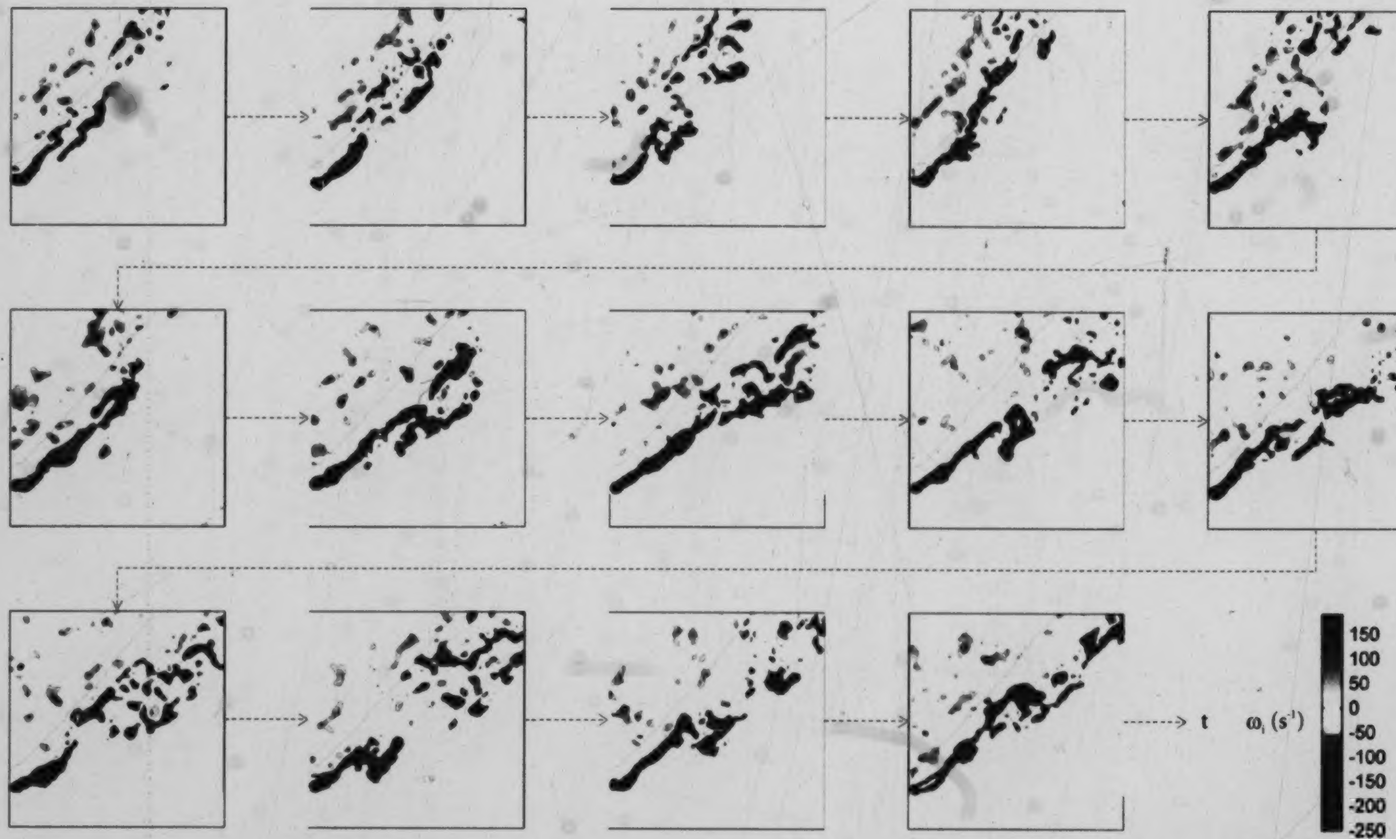

Figure 5.18: Instantaneous vorticity (ω_i) contour maps for tessera 3; consecutive 15 Hz frames with the background vorticity plotted in white to accentuate the coherent vortical structures and with the jet centreline trajectory as reference.

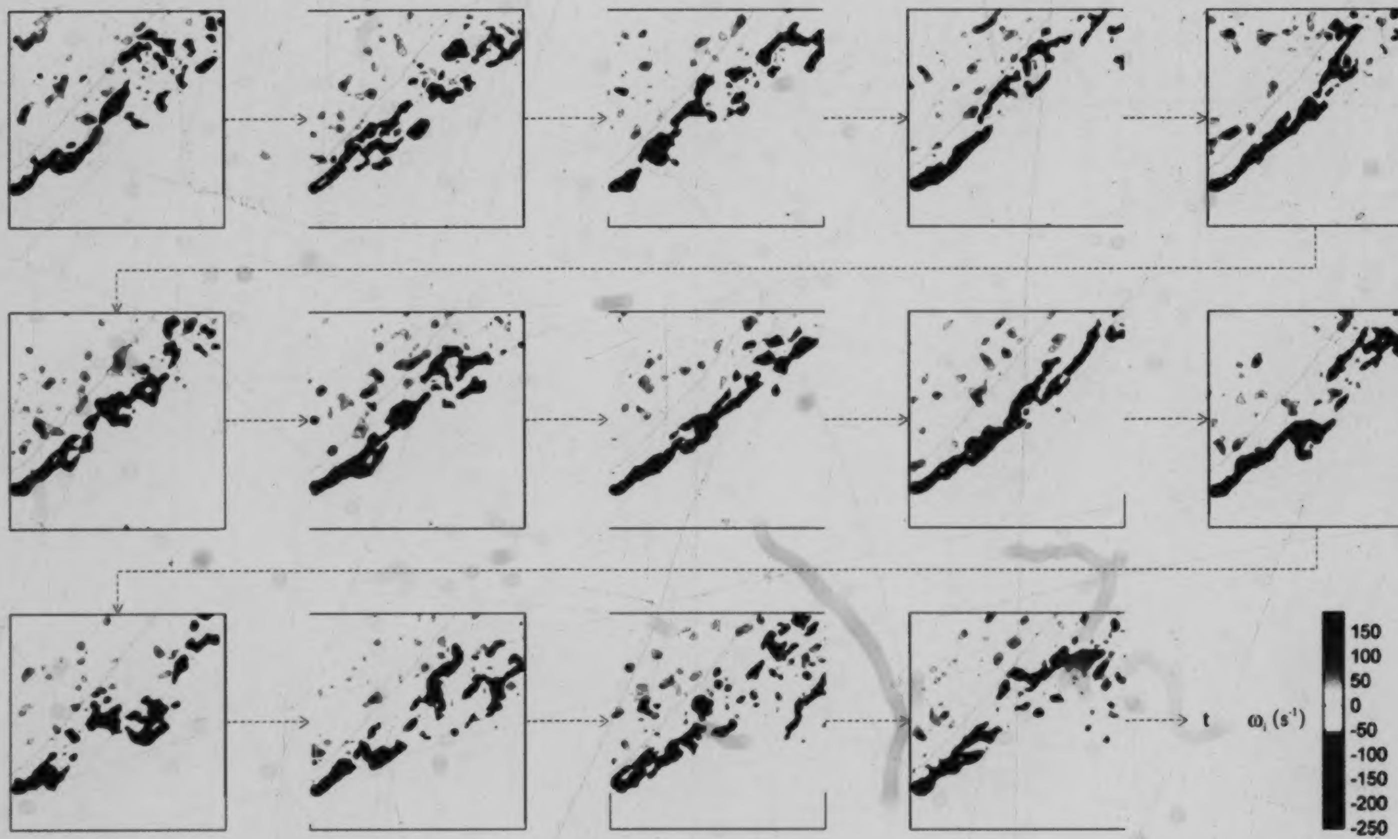

Figure 5.18 continued.

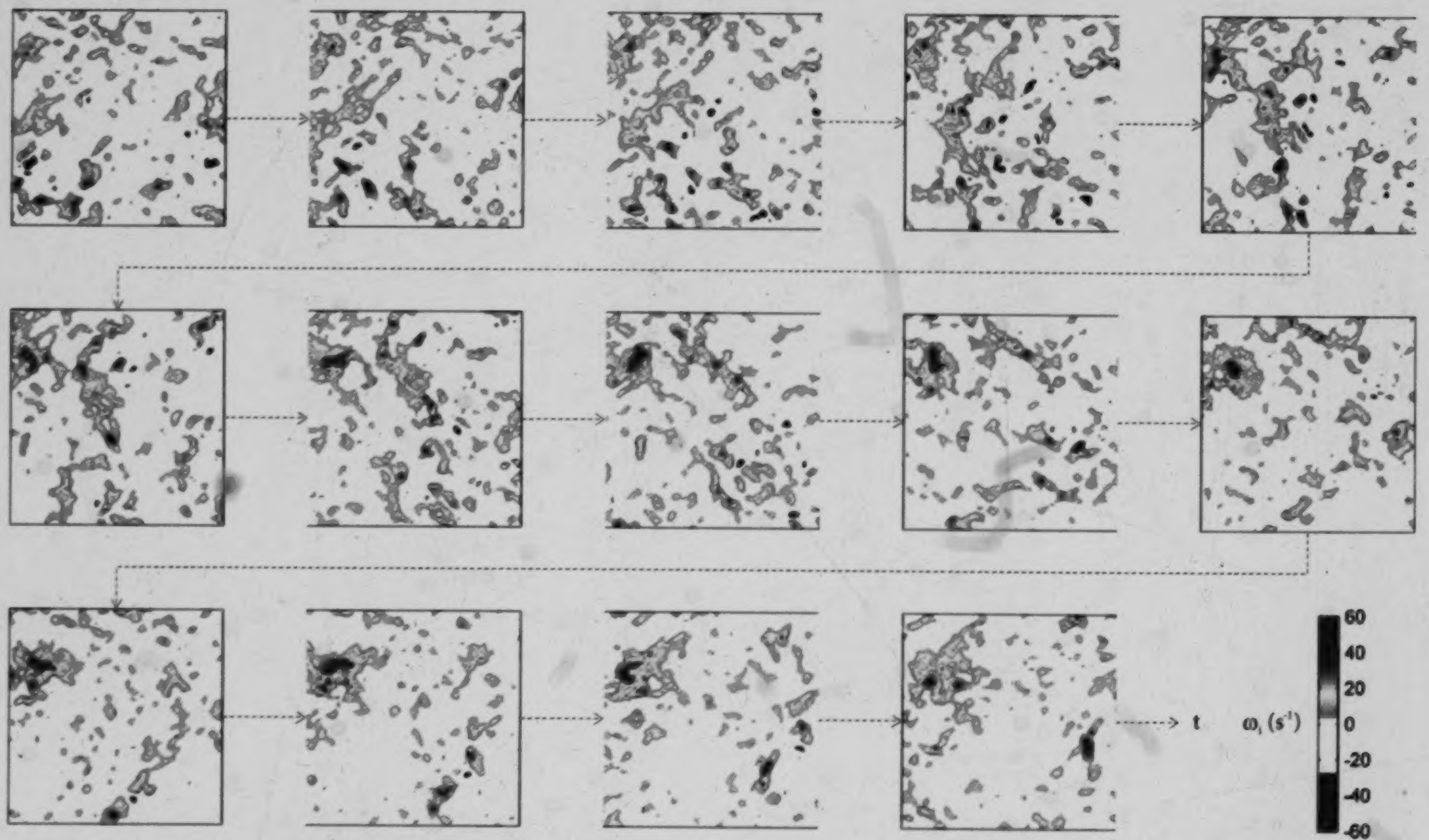

Figure 5.19: Instantaneous vorticity (ω_i) contour maps for tessera 1; consecutive 15 Hz frames with the background vorticity plotted in white to accentuate the coherent vortical structures.

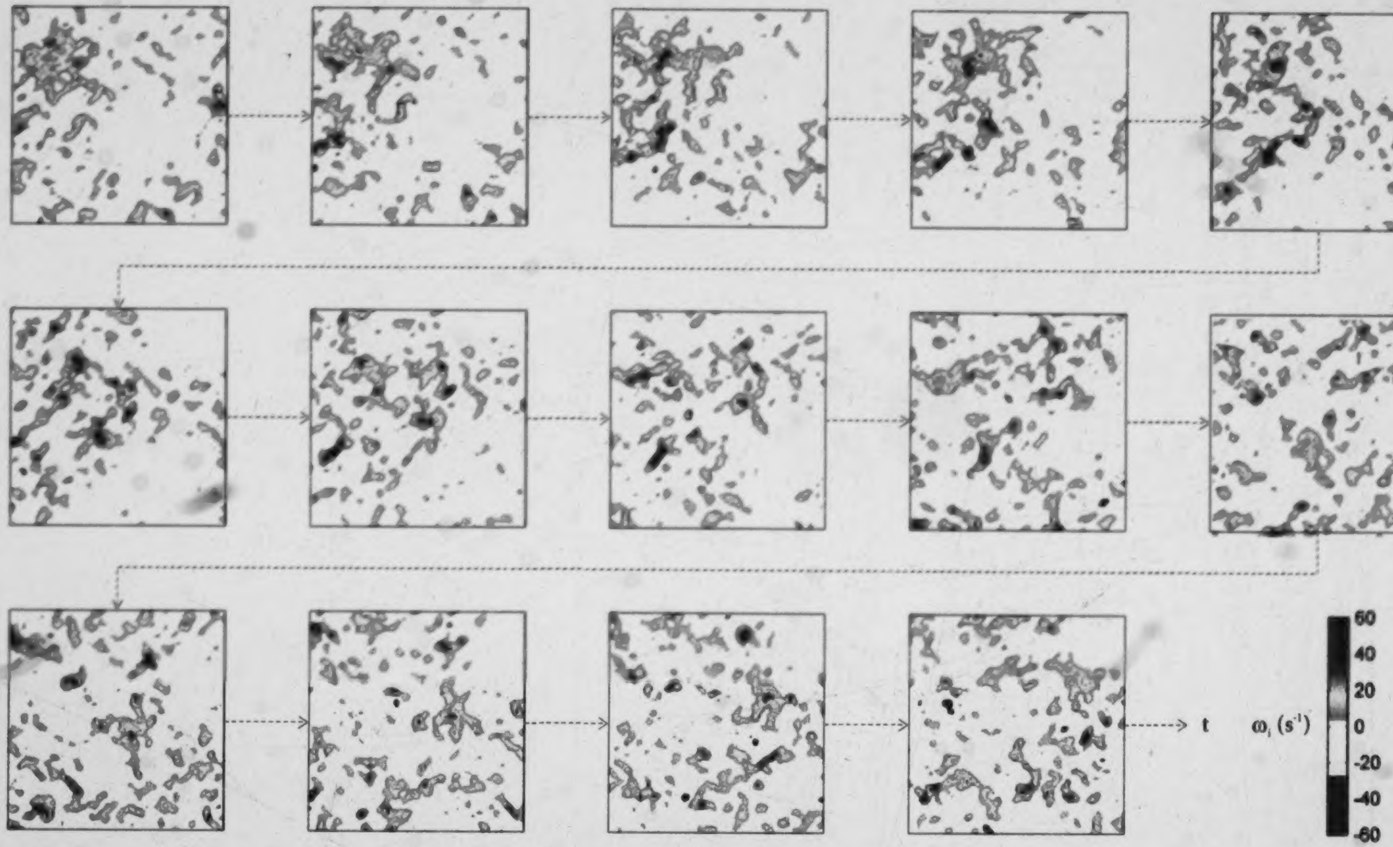

Figure 5.19 continued.

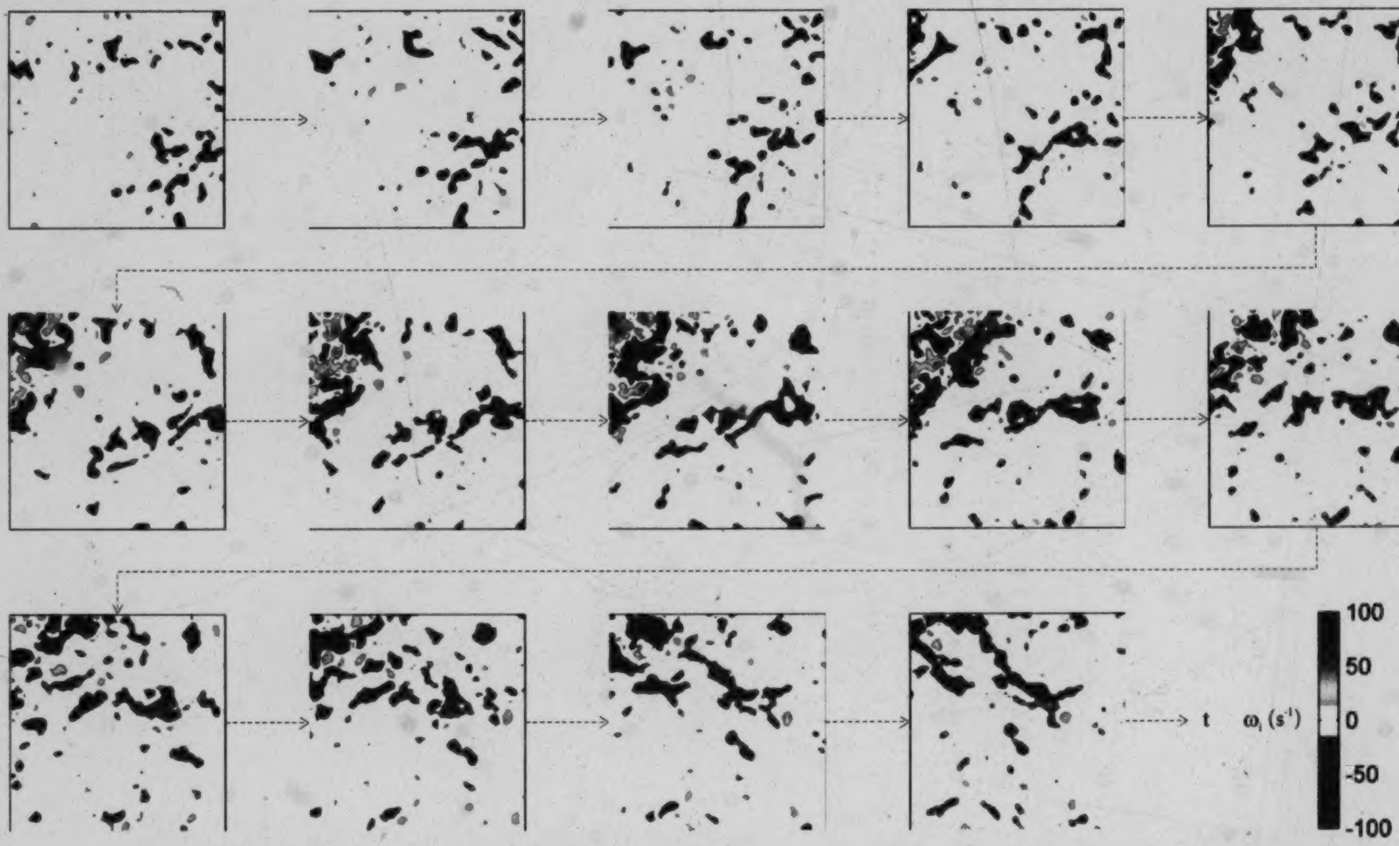

Figure 5.20: Instantaneous vorticity (ω_i) contour maps for tessera 11; consecutive 15 Hz frames with the background vorticity plotted in white to accentuate the coherent vortical structures.

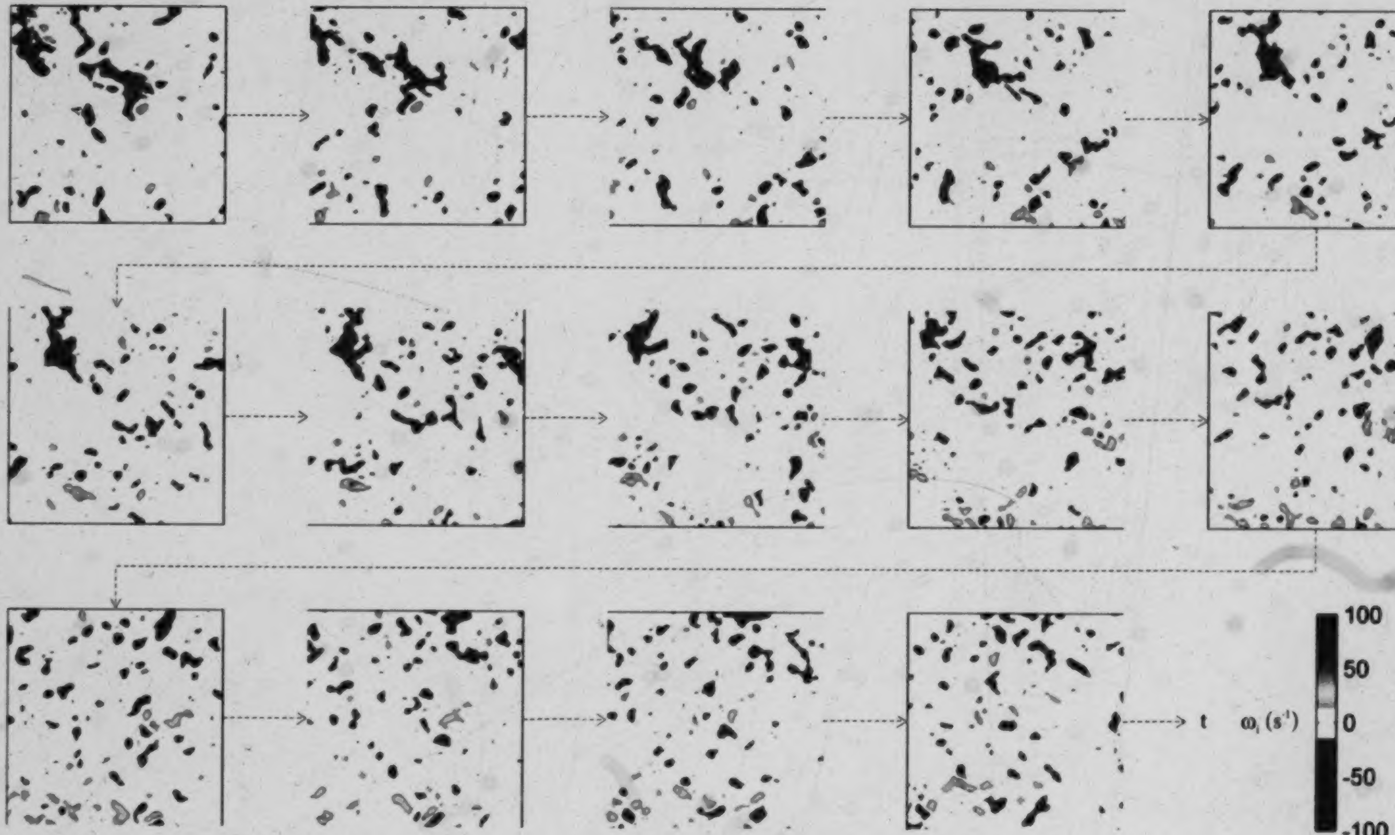

Figure 5.20 continued.

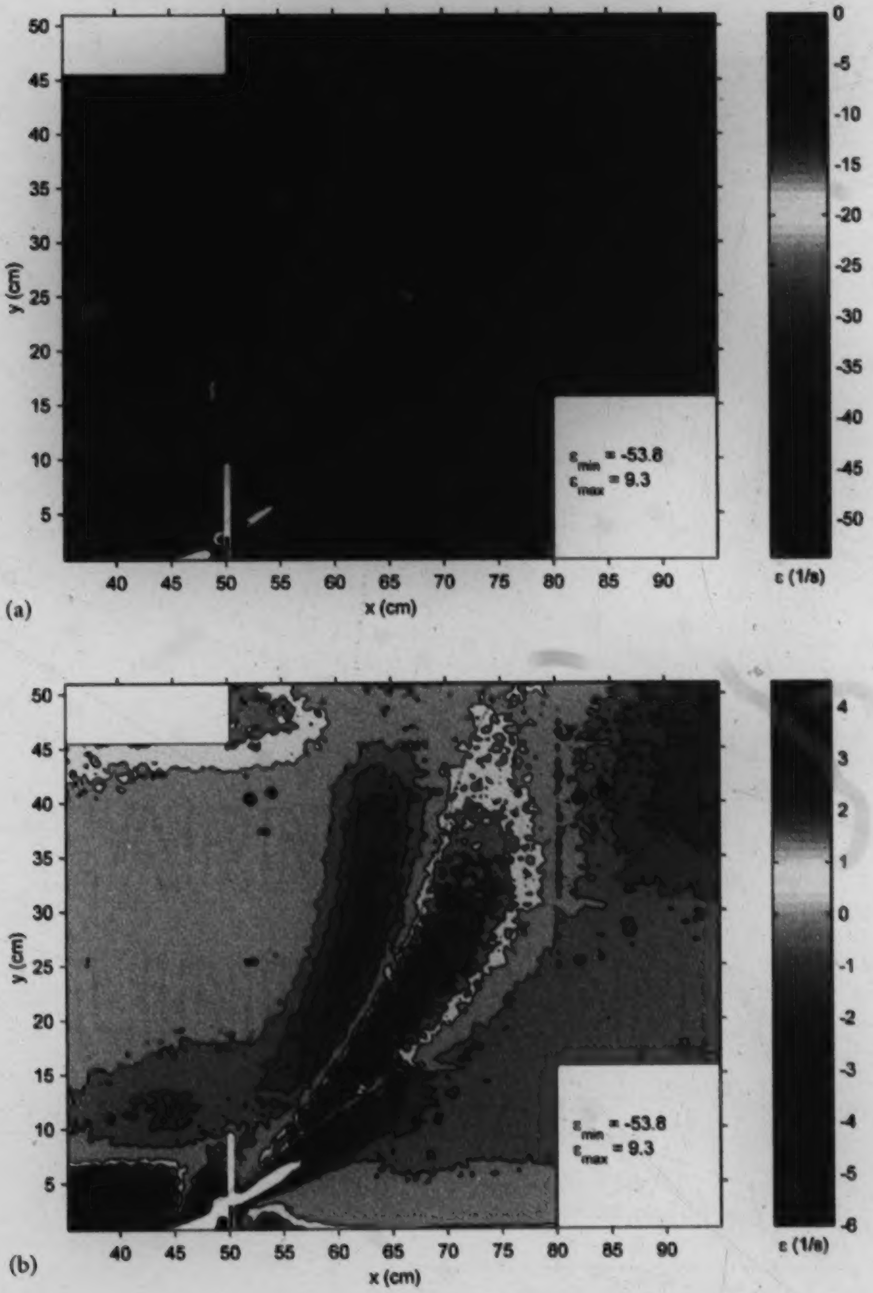

Figure 5.21: (a-b) Mean strain (ε) contour maps describing full data mosaic with jet centreline trajectory.

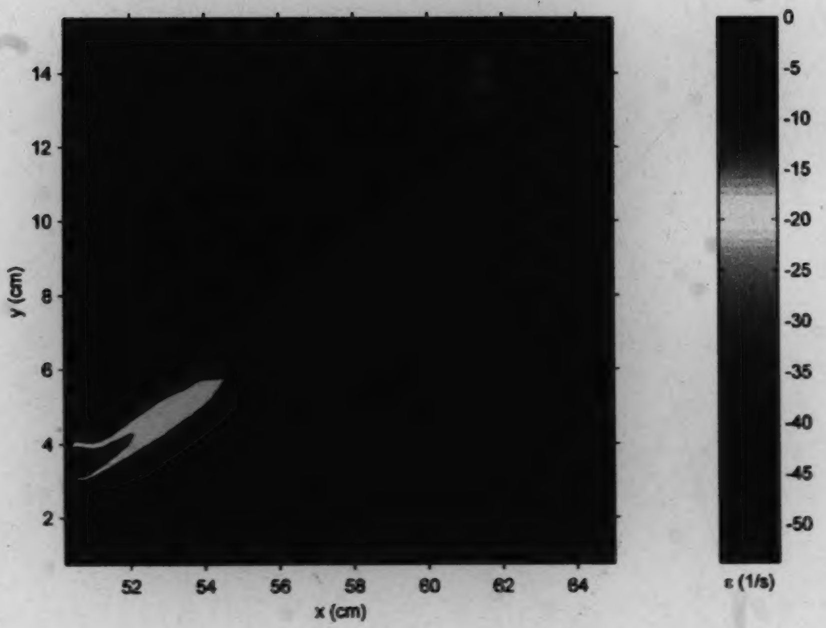

Figure 5.22: Mean strain (ε) contour map for tessera 3 with jet centreline trajectory.

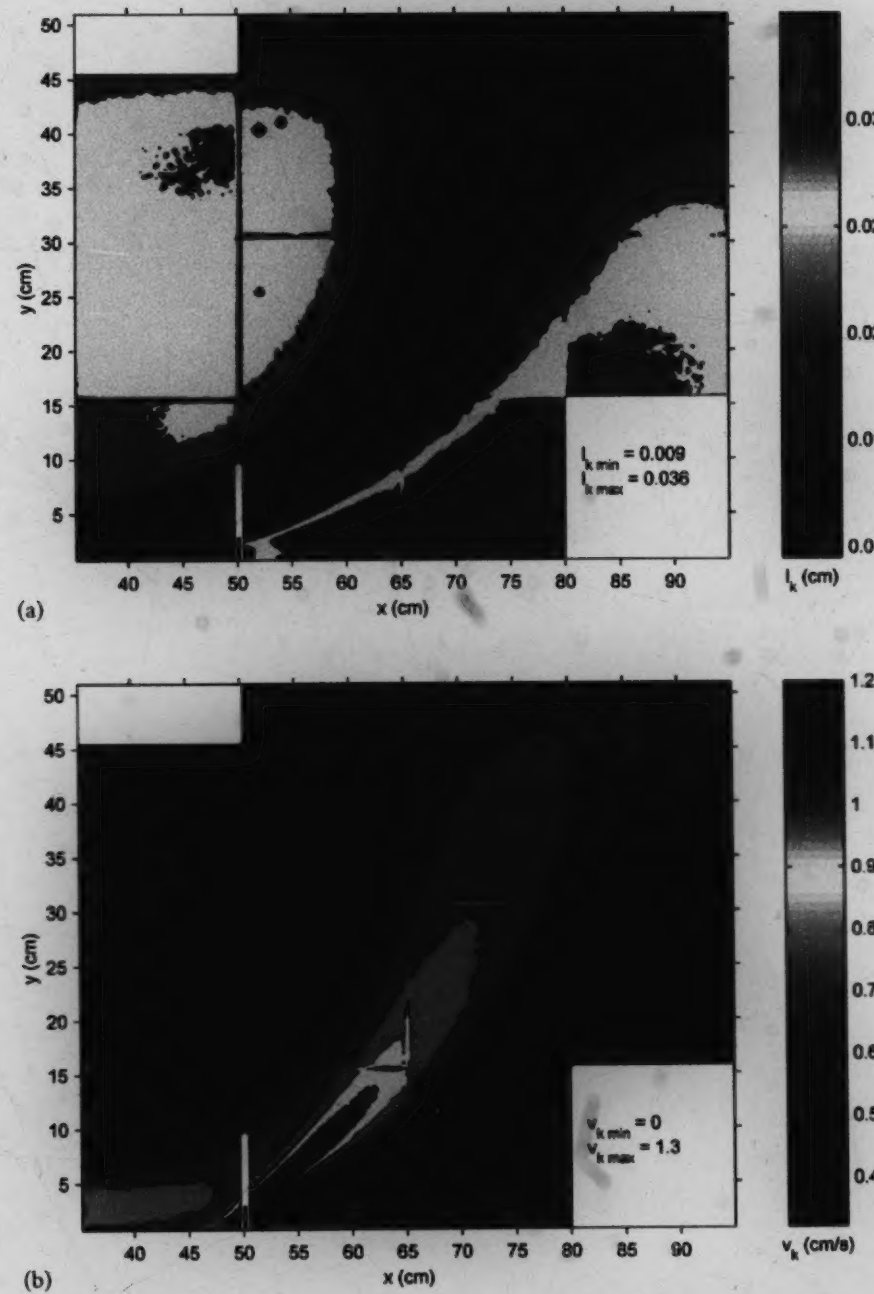

Figure 5.23: Mean Kolmogorov (a) length scale (l_k) and (b) velocity scale (v_k) contour maps describing full data mosaic with jet centreline trajectory.

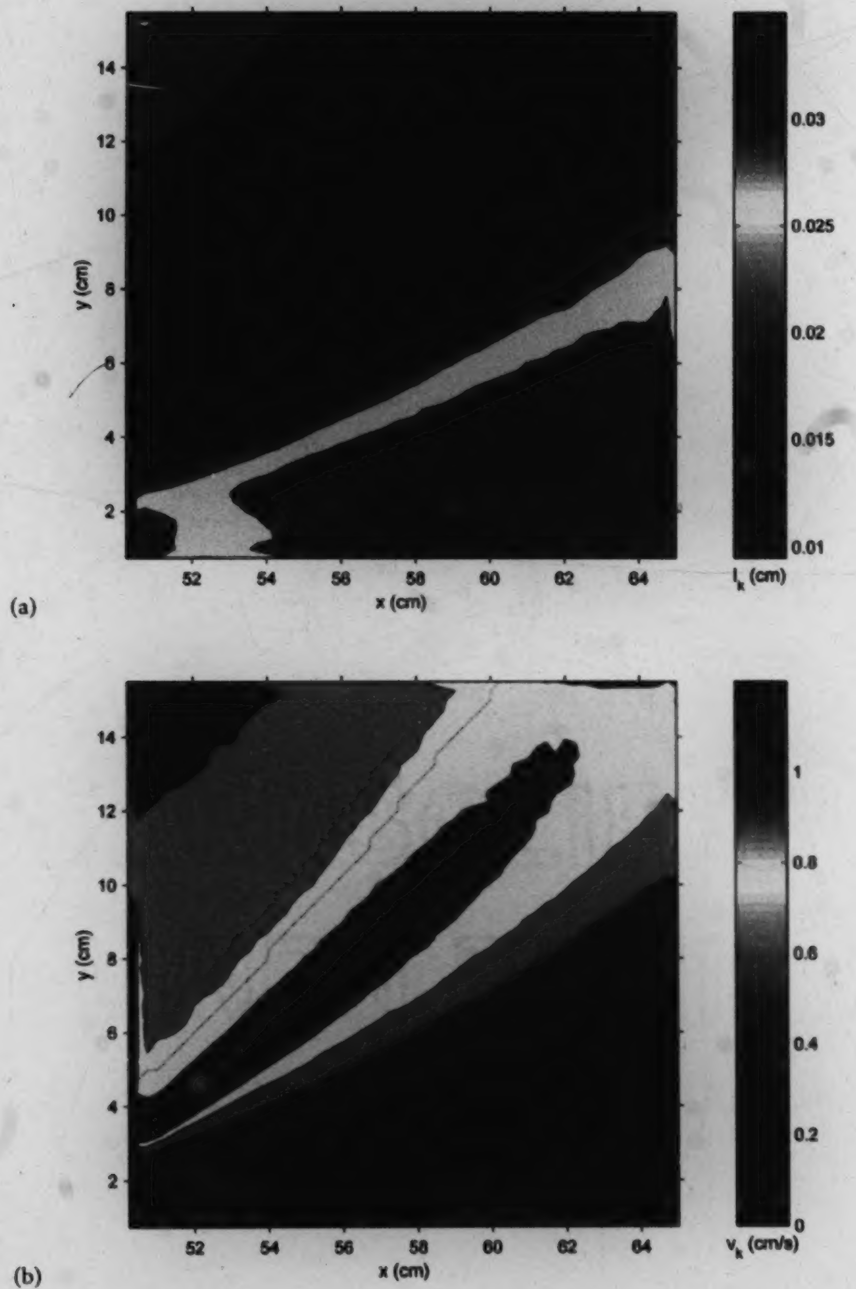

Figure 5.24: Mean Kolmogorov (a) length scale (l_k) and (b) velocity scale (v_k) contour maps for tessera 3 with jet centreline trajectory.

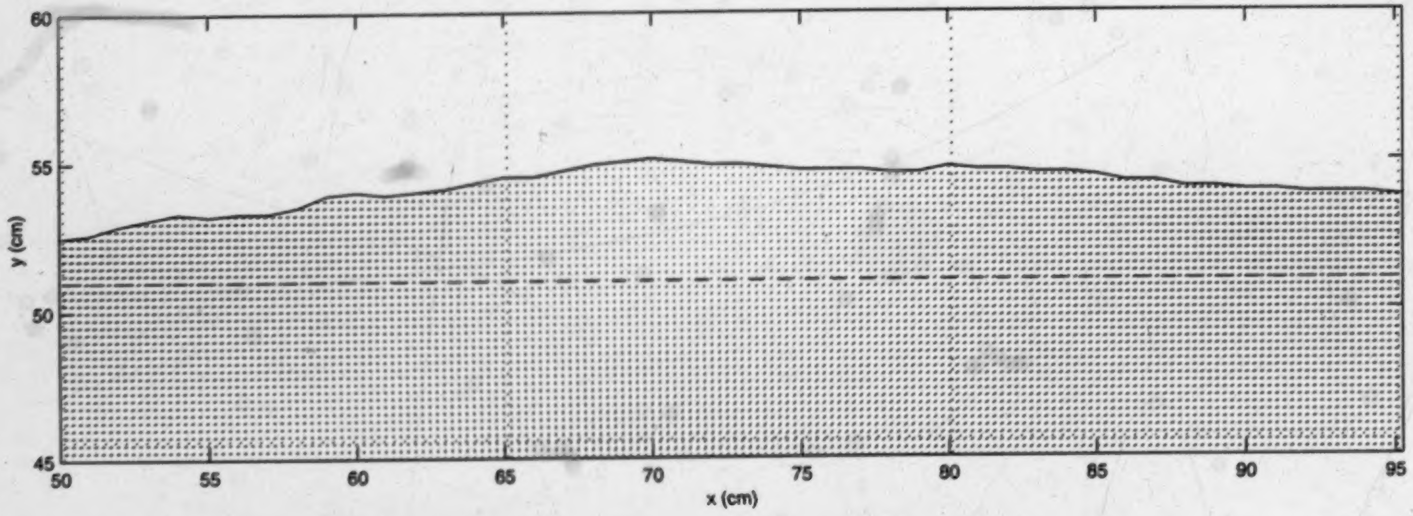

Figure 5.25: Replacement of mean velocity vectors in water surface reflection defect exclusion zone with mean raw corrected and scaled velocity vectors.

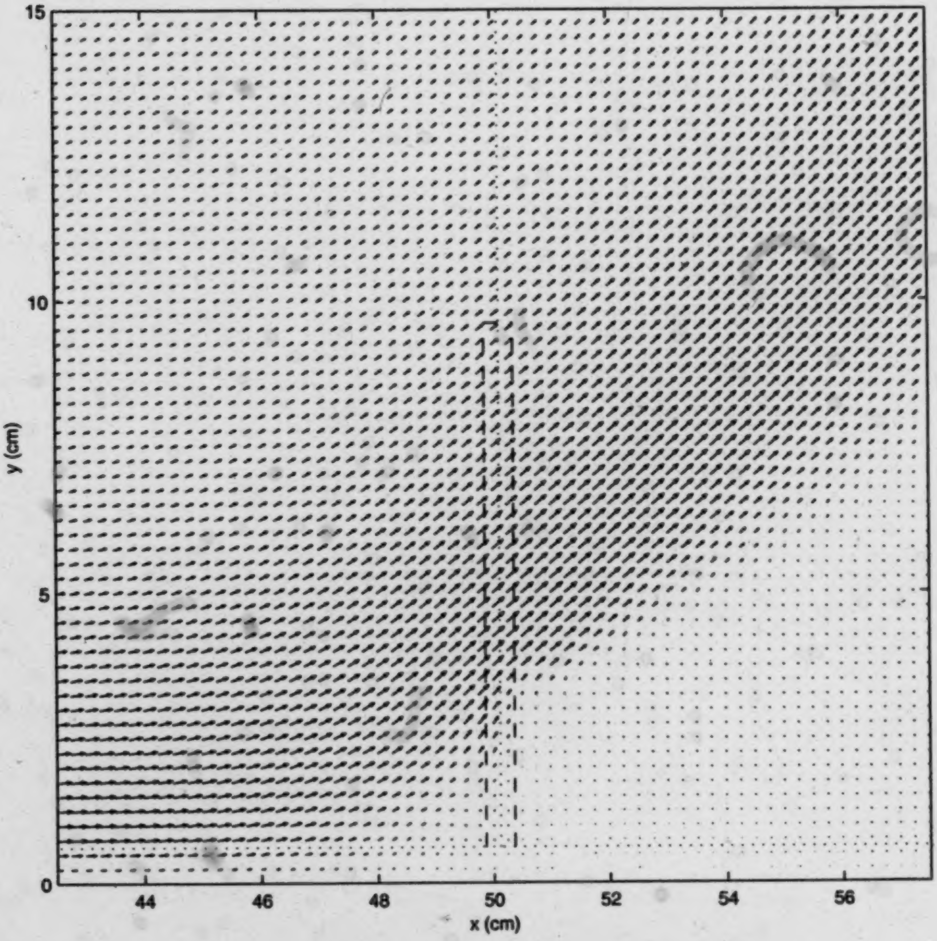

Figure 5.26: Interpolated mean velocity vectors in baffle reflection and baffle shadow defect exclusion zone.

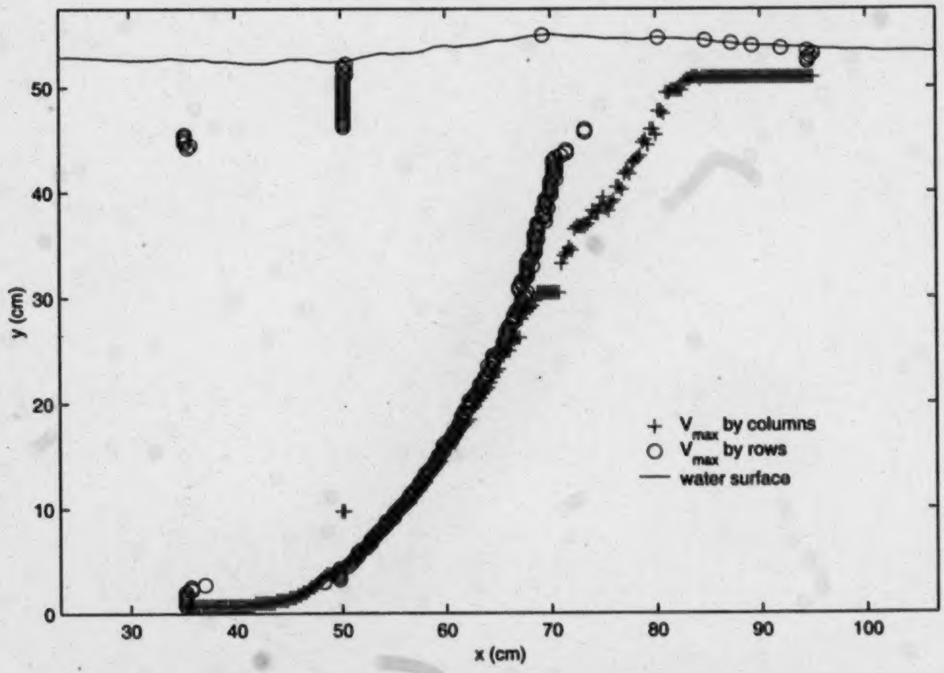

Figure 5.27: Locations of the maximum mean velocity magnitudes found in each column and each row of the full data mosaic.

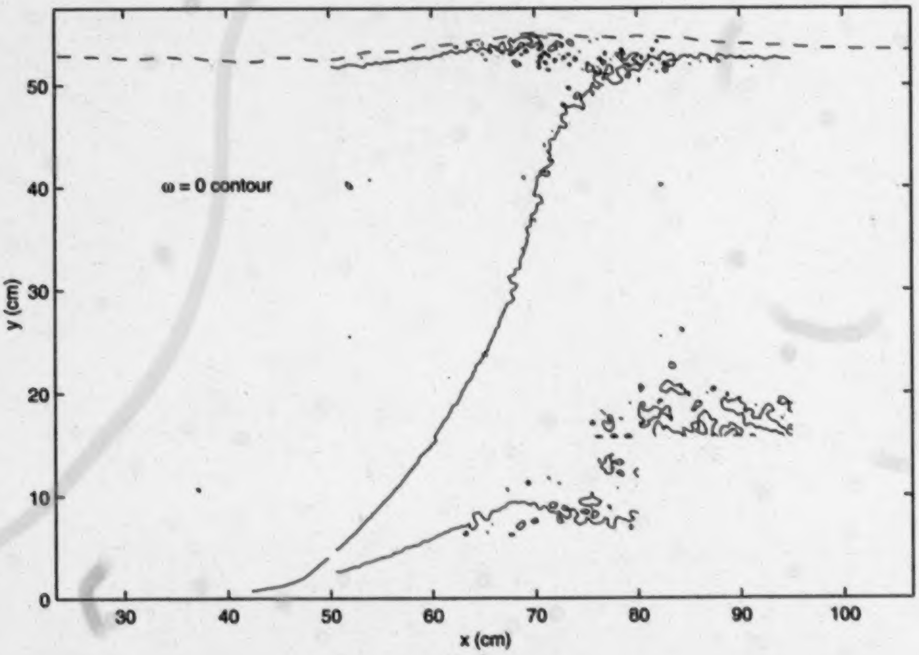

Figure 5.28: The contour line showing where the mean vorticity (ω) is equal to zero in the full data mosaic, including the replacement vectors in the water surface reflection defect exclusion zone.

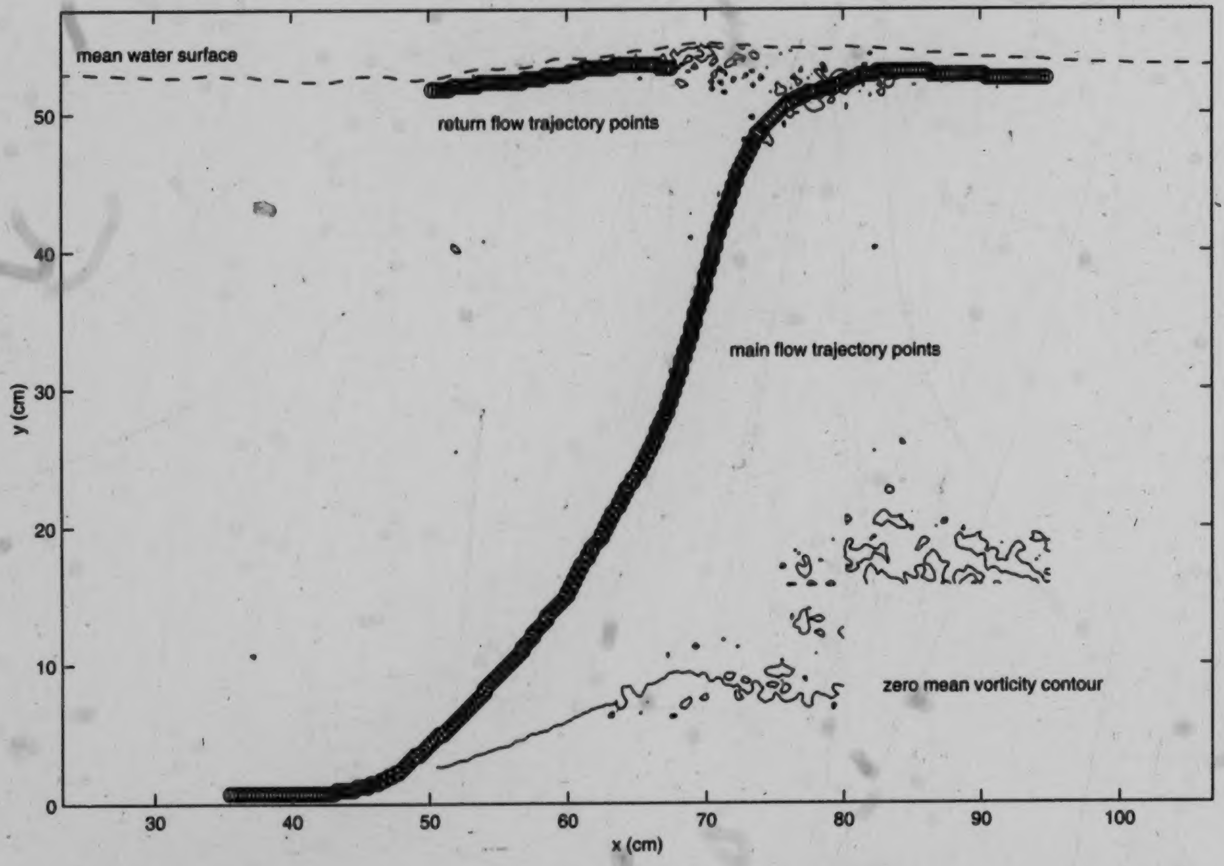

Figure 5.29: Final deflected wall jet trajectory for both the main jet and the return flow section.

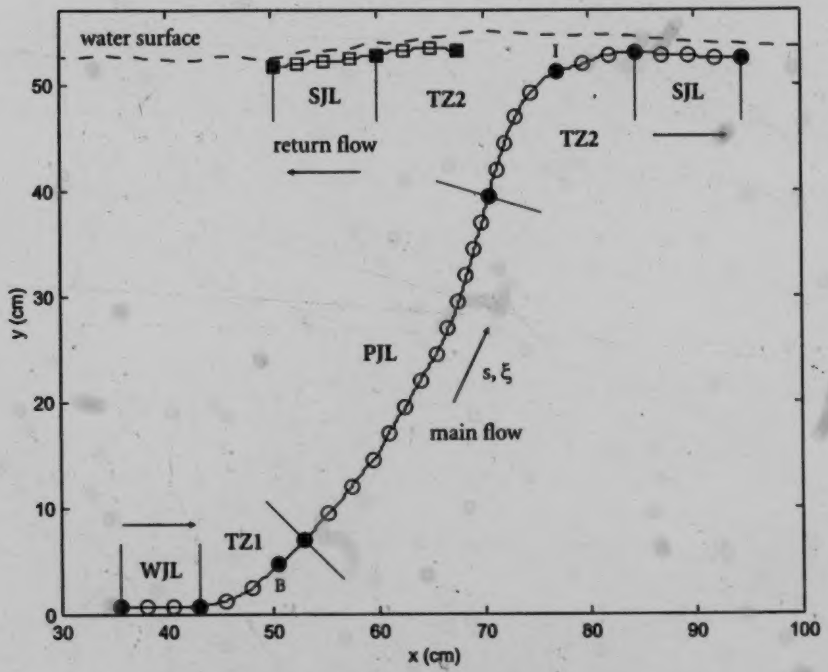

legend		
	WJL	wall jet-like flow regime
	PJL	plane jet-like flow regime
	SJL	surface jet-like flow regime
	TZ1	transition zone between WJL and PJL regimes
	TZ2	transition zone between PJL and SJL regimes
	●B	baffle location
	●I	impingement location
	●■	transition zone boundary
	s, ξ	axial ordinates along jet centreline trajectory

Figure 5.30: Flow regimes within the plane deflected wall jet.

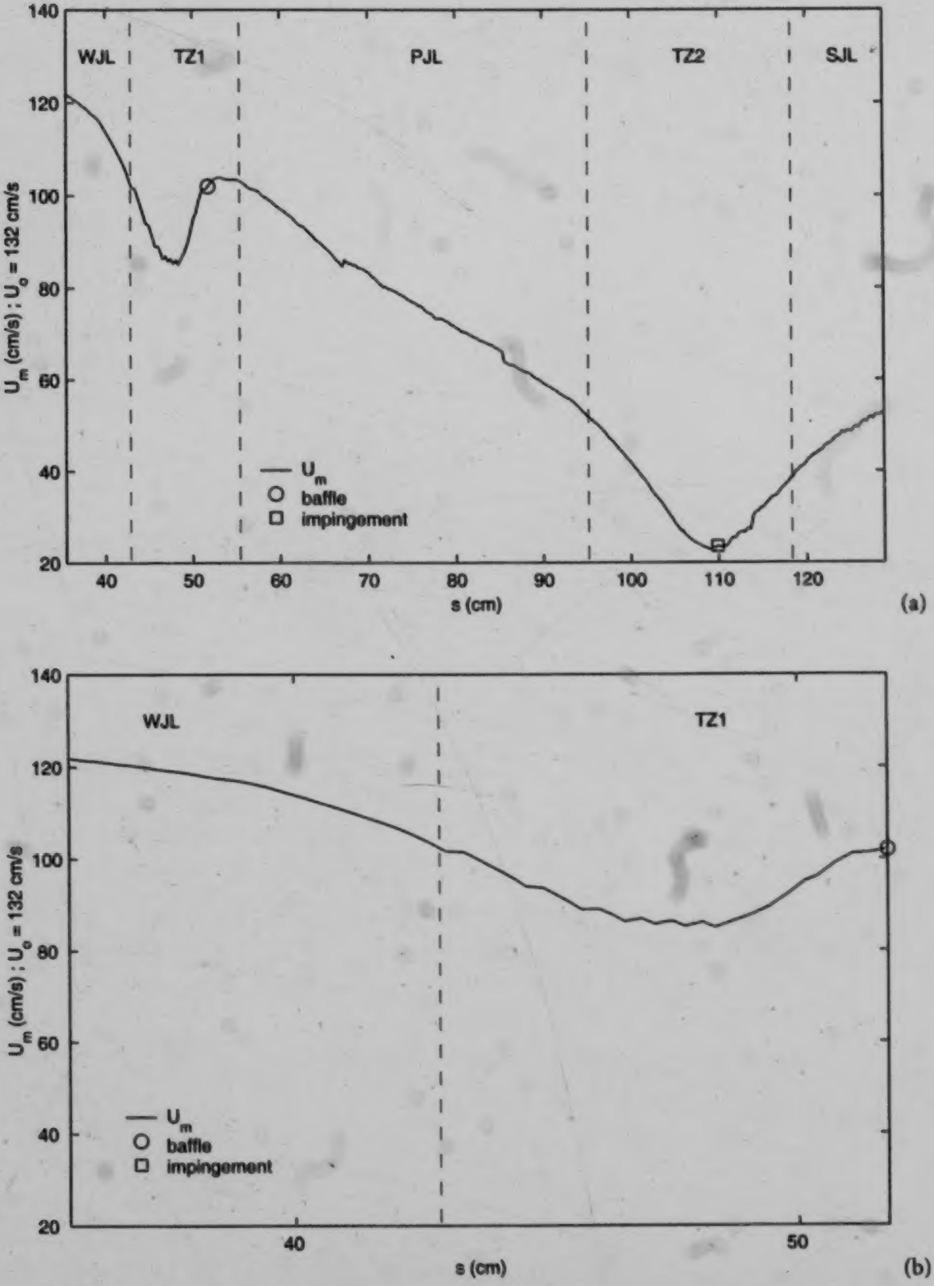

Figure 5.31: Variation of U_m with s over (a) the full jet trajectory and over (b-d) the sections upstream of the baffle, between the baffle and the point of impingement and downstream of the point of impingement, respectively.

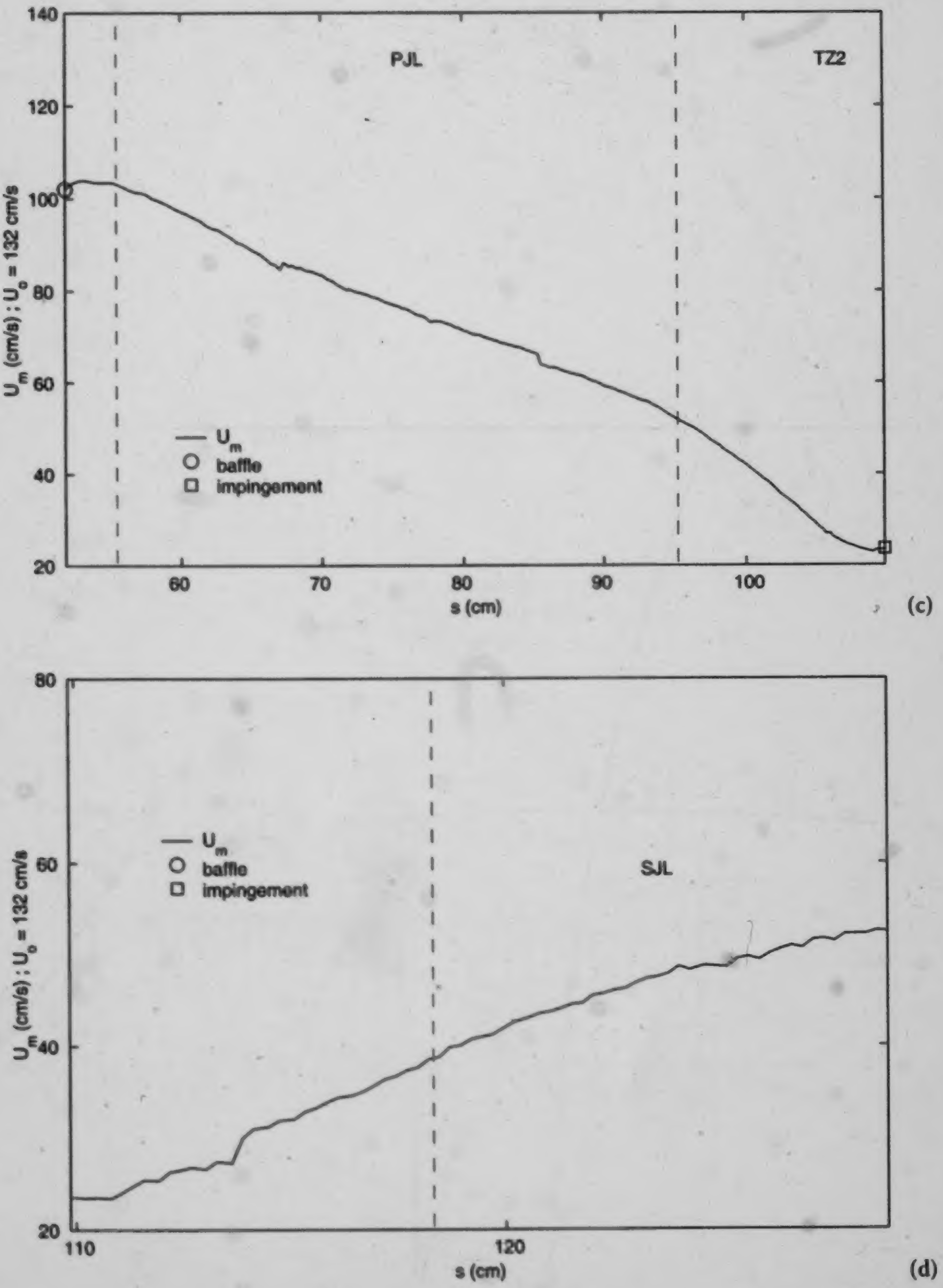

Figure 5.31: Variation of U_m with s over (a) the full jet trajectory and over (b-d) the sections upstream of the baffle, between the baffle and the point of impingement and downstream of the point of impingement, respectively.

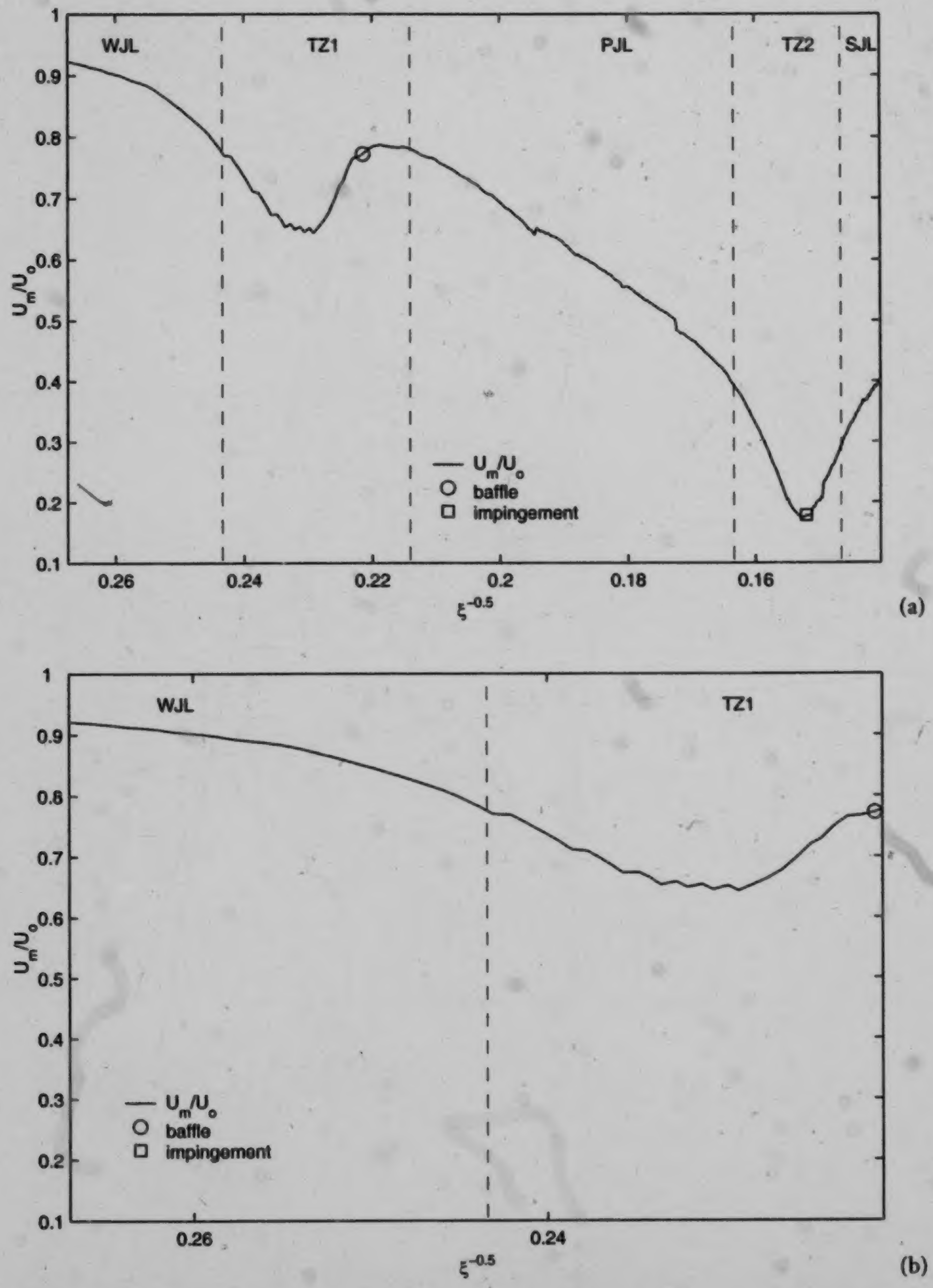

Figure 5.32: Variation of U_m/U_o with $\xi^{-0.5}$ over (a) the full jet trajectory and over (b-d) the sections upstream of the baffle, between the baffle and the point of impingement and downstream of the point of impingement, respectively.

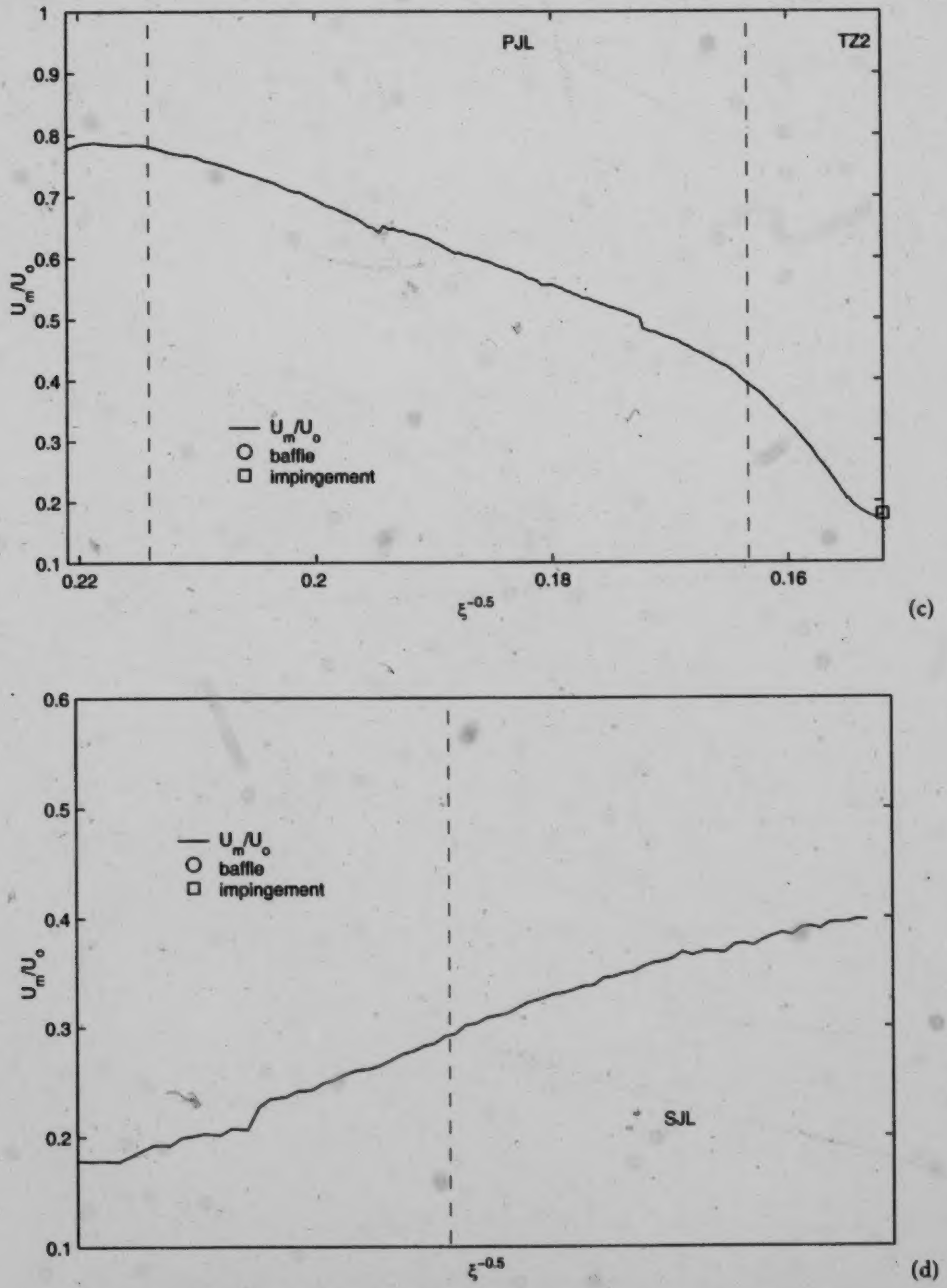

Figure 5.32: Variation of U_m/U_o with $\xi^{-0.5}$ over (a) the full jet trajectory and over (b-d) the sections upstream of the baffle, between the baffle and the point of impingement and downstream of the point of impingement, respectively.

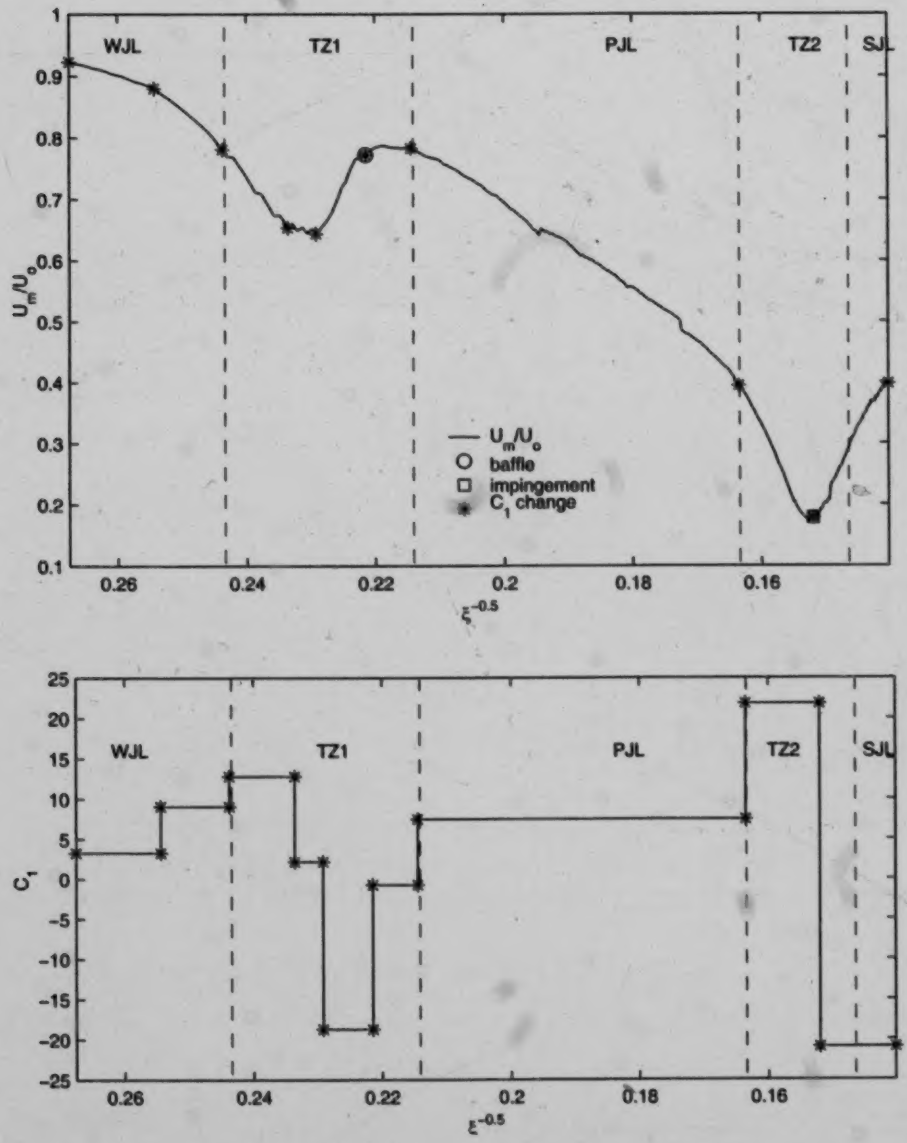

Figure 5.33: Variation of the C_1 coefficient along the full jet centreline trajectory.

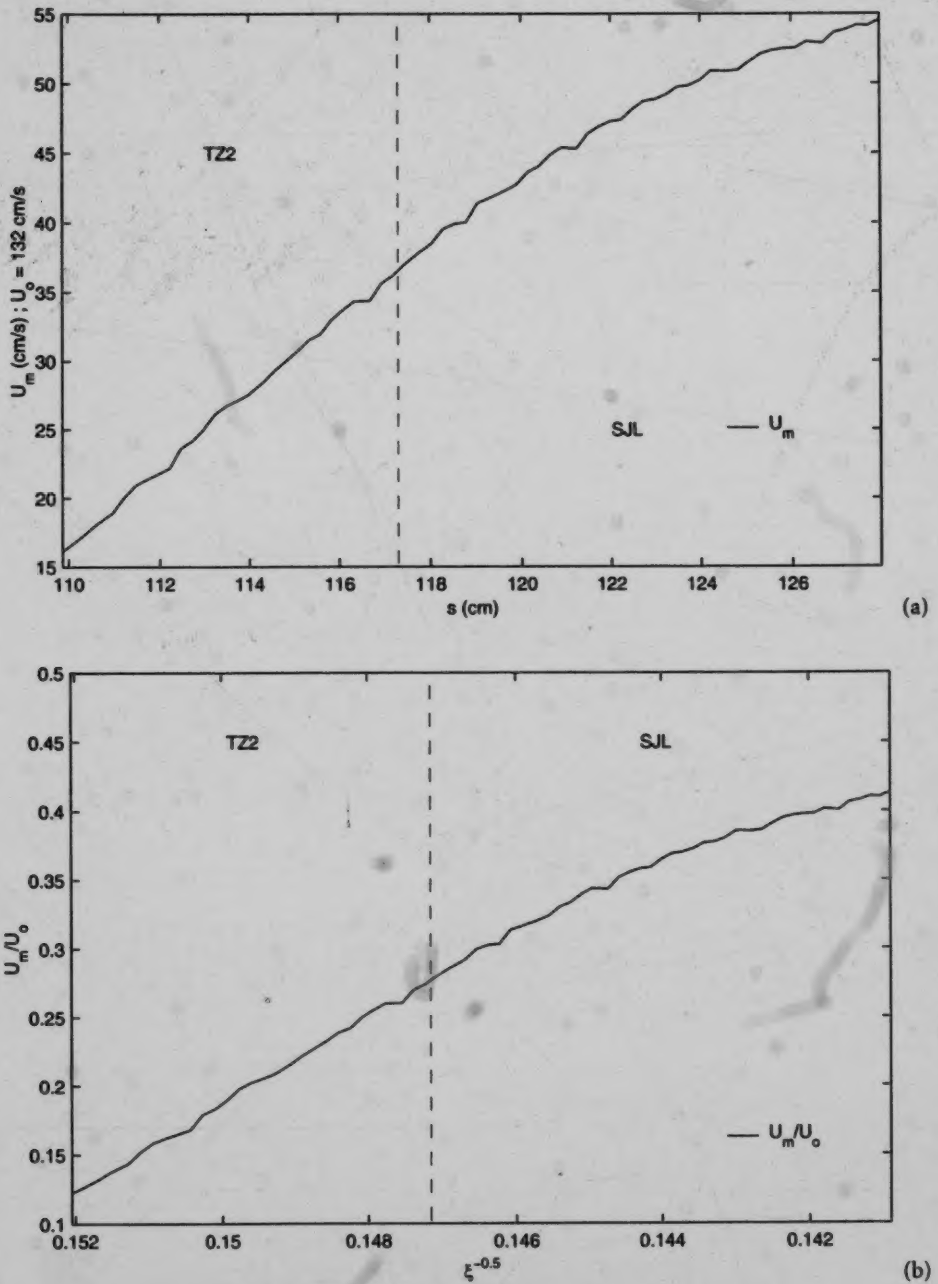

Figure 5.34: Variation of (a) U_m with s and of (b) U_m/U_o with $\xi^{-0.5}$ along the full return flow jet centreline trajectory.

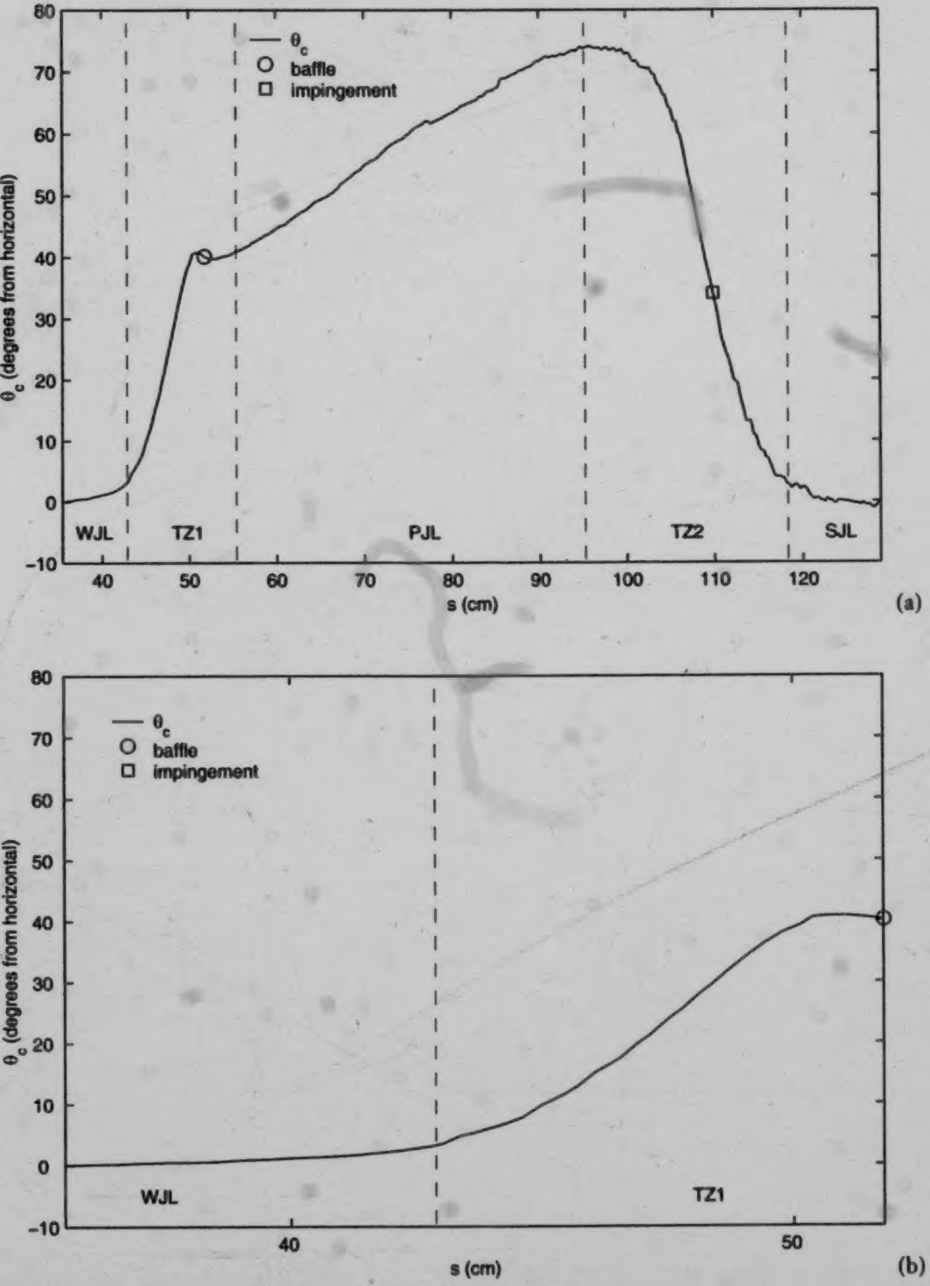

Figure 5.35: Variation of θ_c with s over (a) the full jet trajectory and over (b-d) the sections upstream of the baffle, between the baffle and the point of impingement and downstream of the point of impingement, respectively.

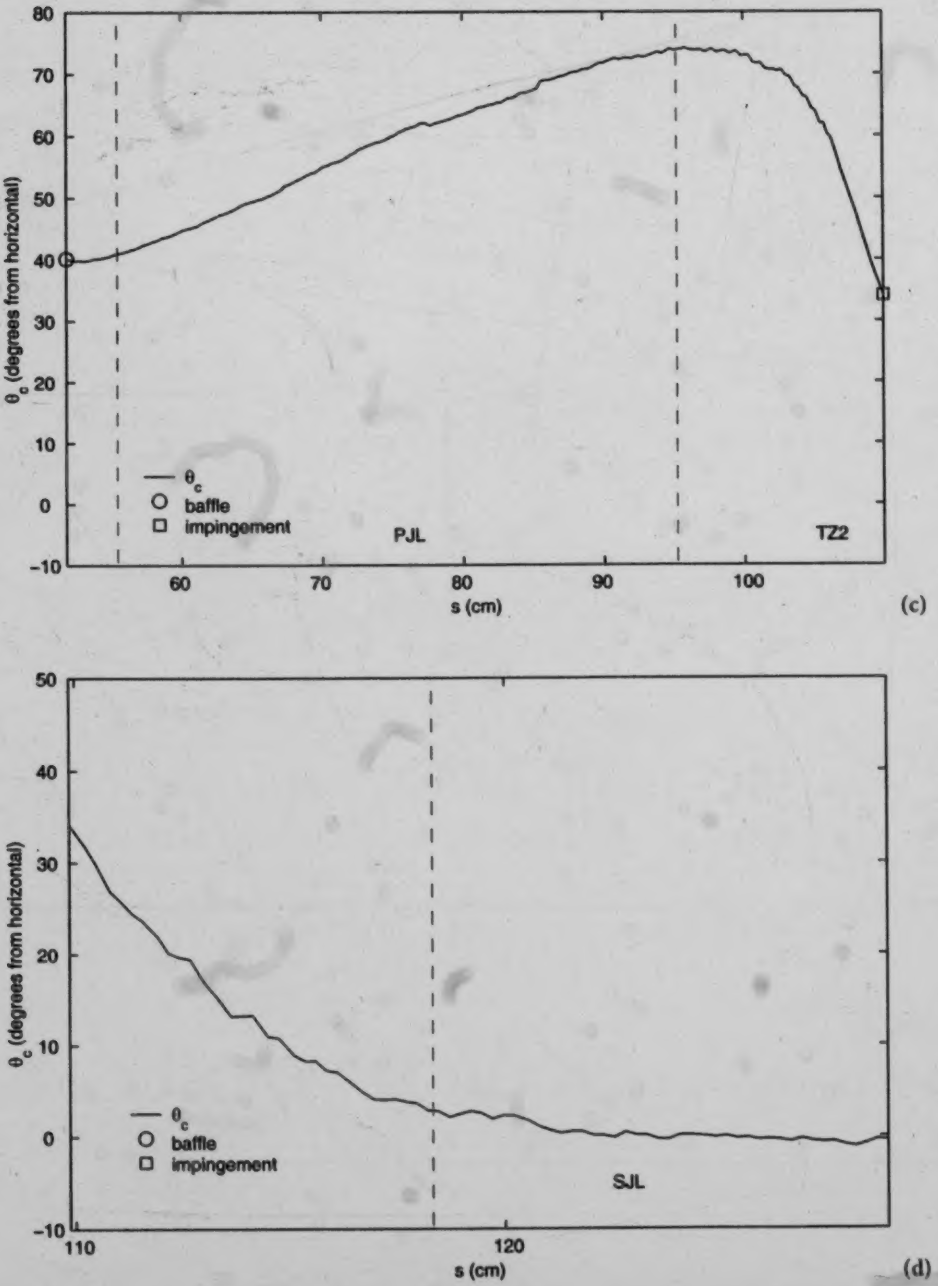

Figure 5.35: Variation of θ_c with s over (a) the full jet trajectory and over (b-d) the sections upstream of the baffle, between the baffle and the point of impingement and downstream of the point of impingement, respectively.

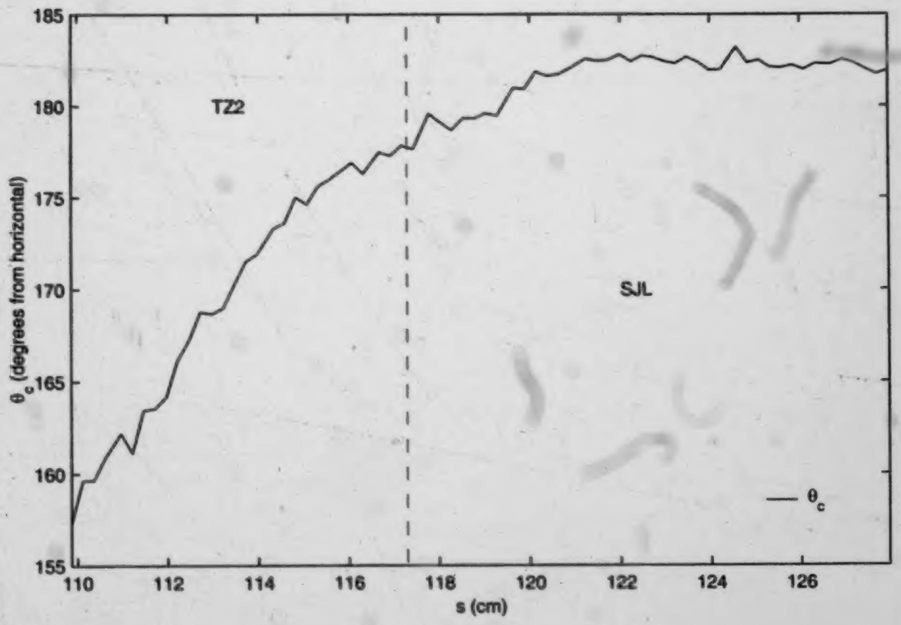

Figure 5.36: Variation of θ_c with s along the full return flow jet trajectory.

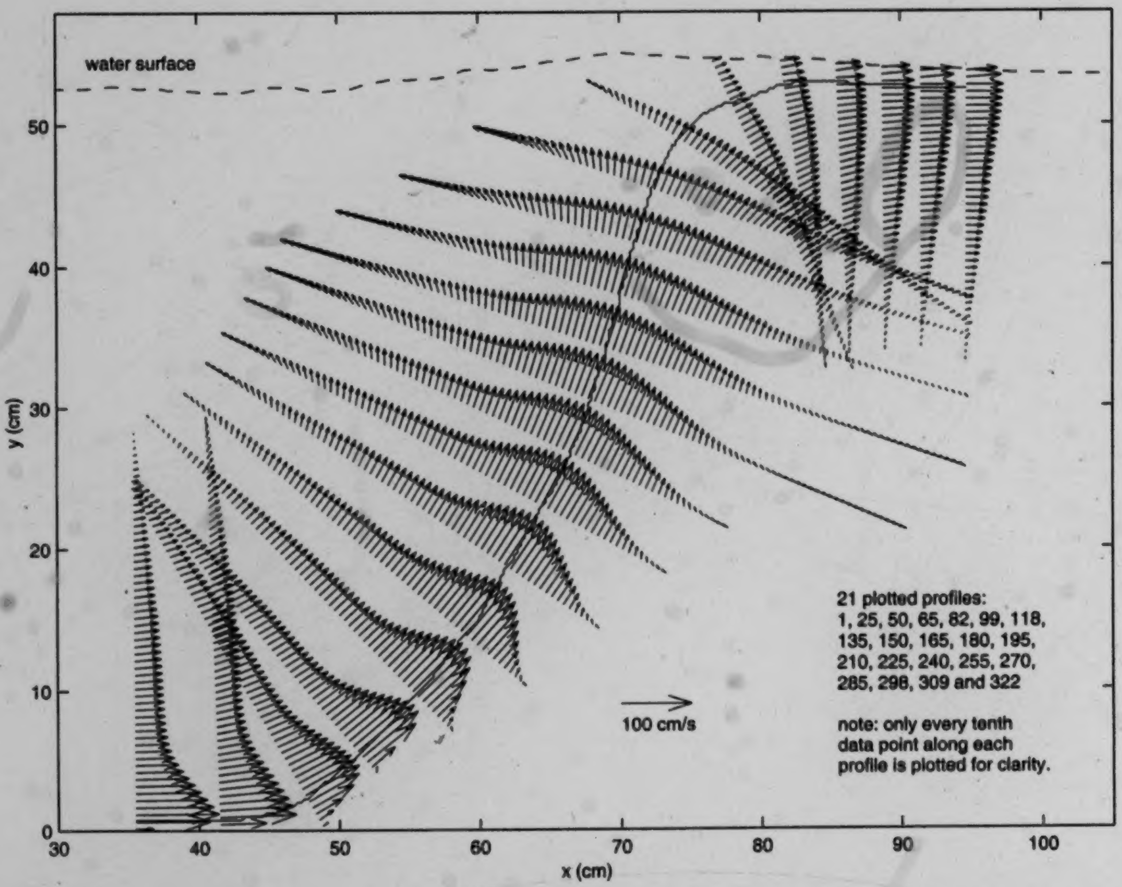

Figure 5.37: Select mean velocity vector profiles showing the development of the plane deflected wall jet with a provided velocity scale; only every tenth mean velocity data point along each profile section is plotted for clarity .

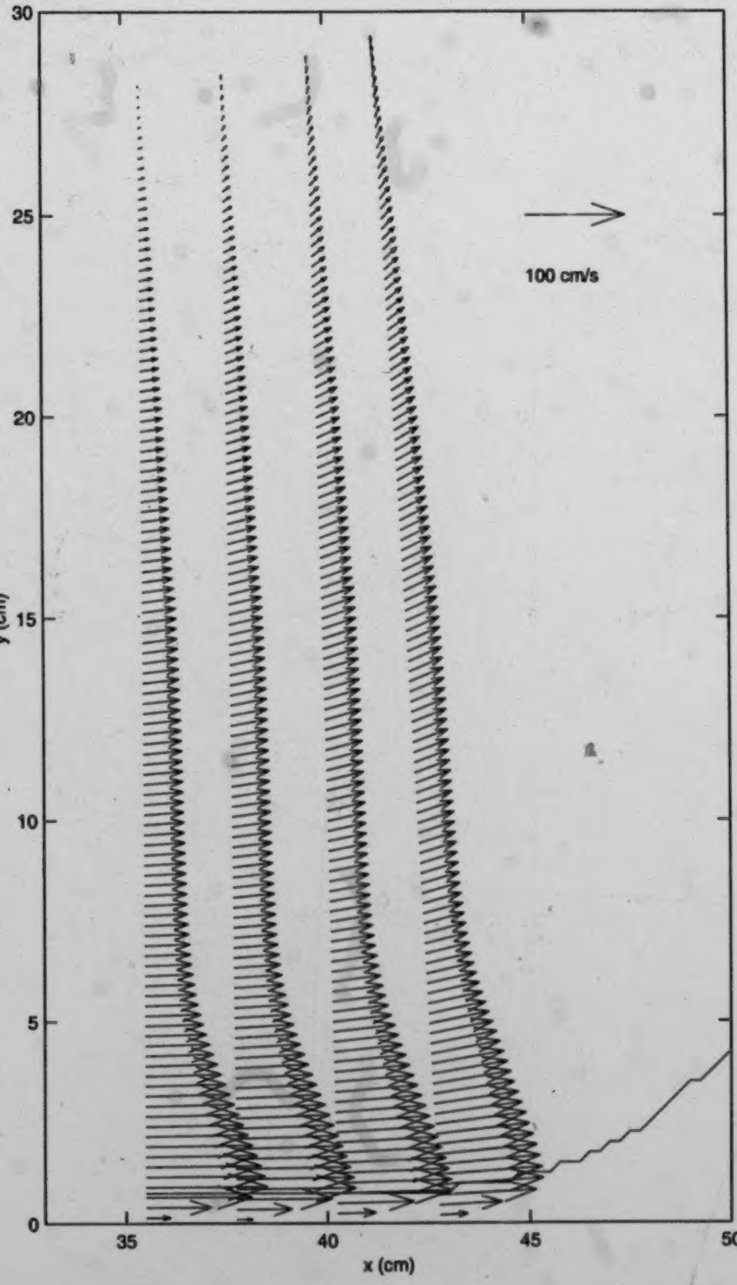

Figure 5.38: Select mean velocity profiles showing the development of the plane deflected wall jet in the wall jet-like (WJL) region .

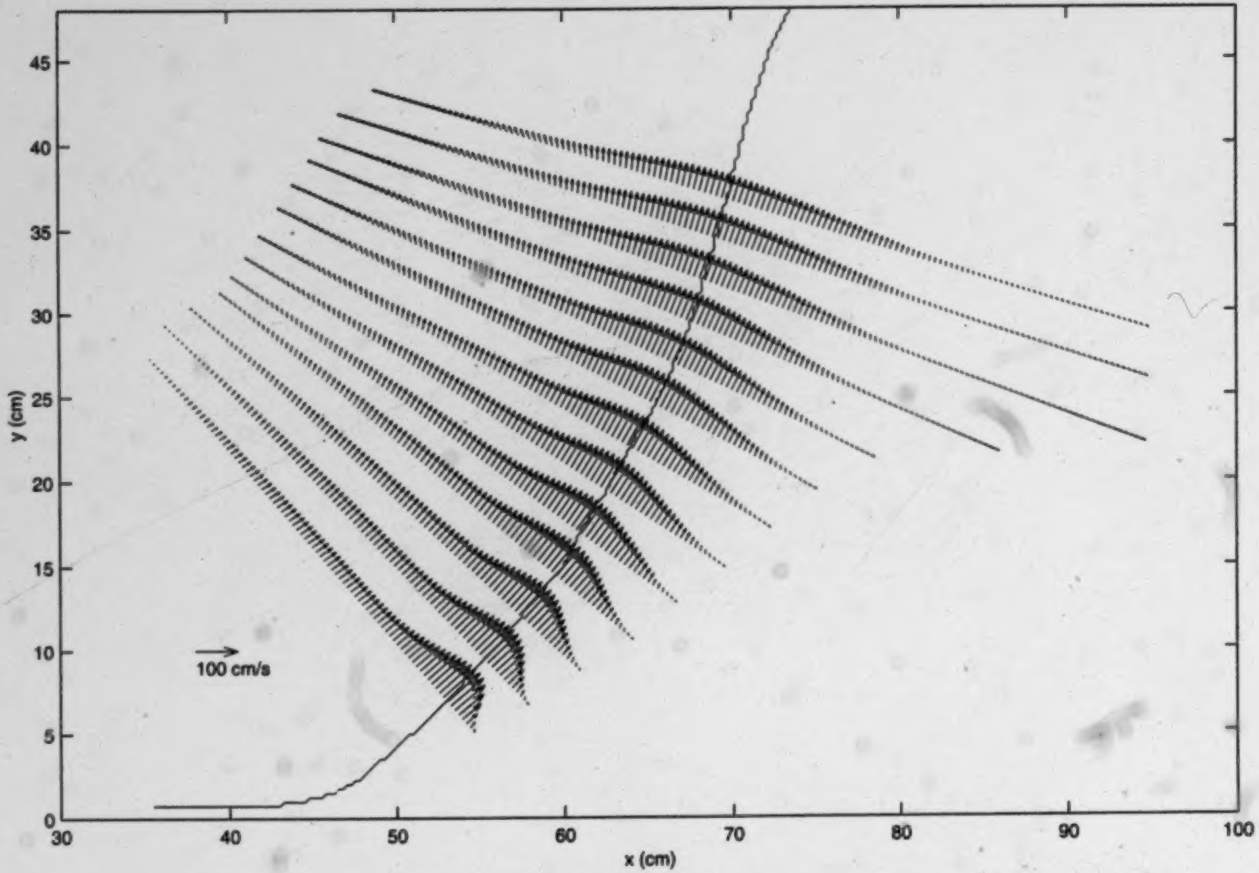

Figure 5.39: Select mean velocity profiles showing the development of the plane deflected wall jet in the plane jet-like (PJL) region .

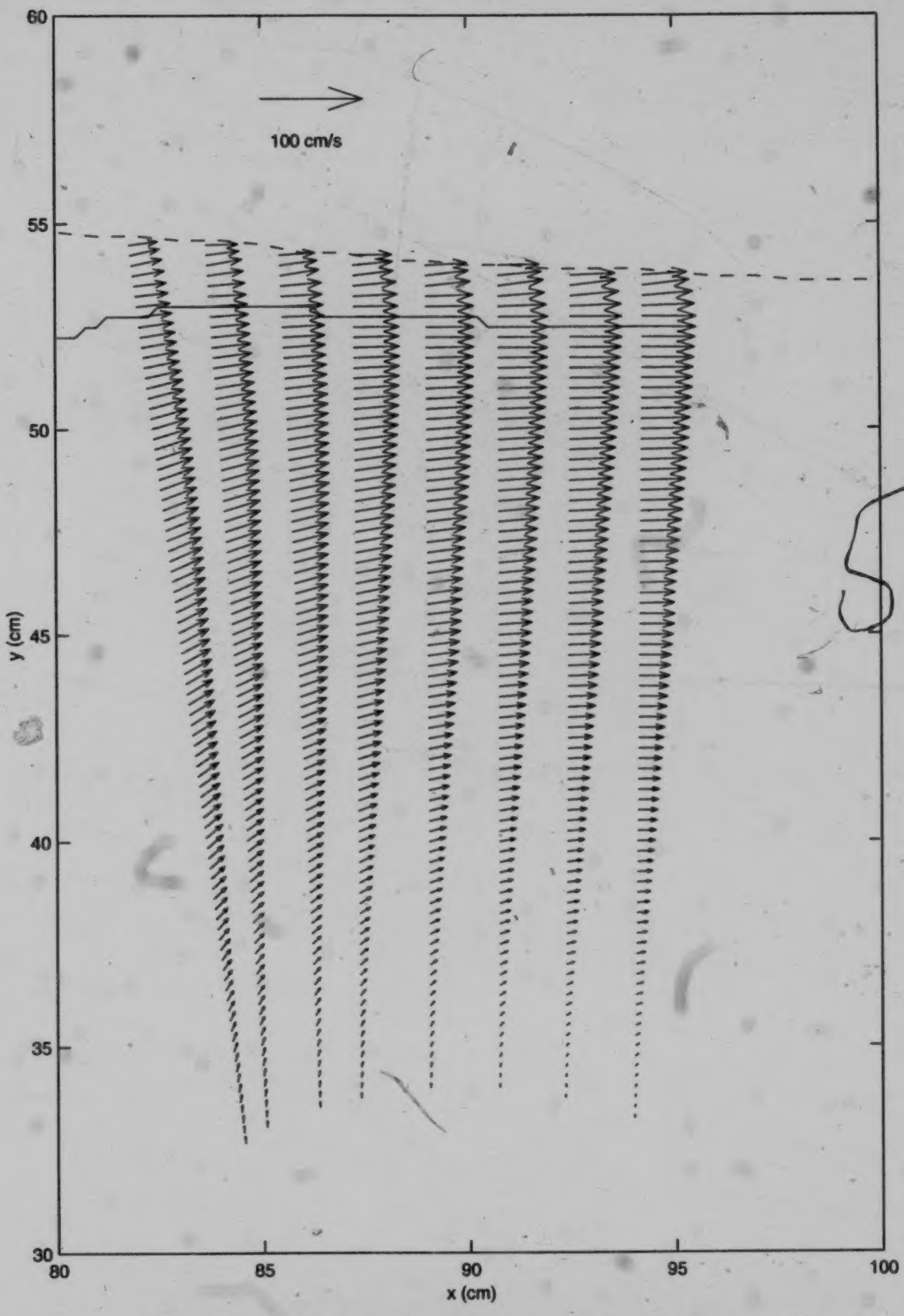

Figure 5.40: Select mean velocity profiles showing the development of the plane deflected wall jet in the surface jet-like (SJL) region .

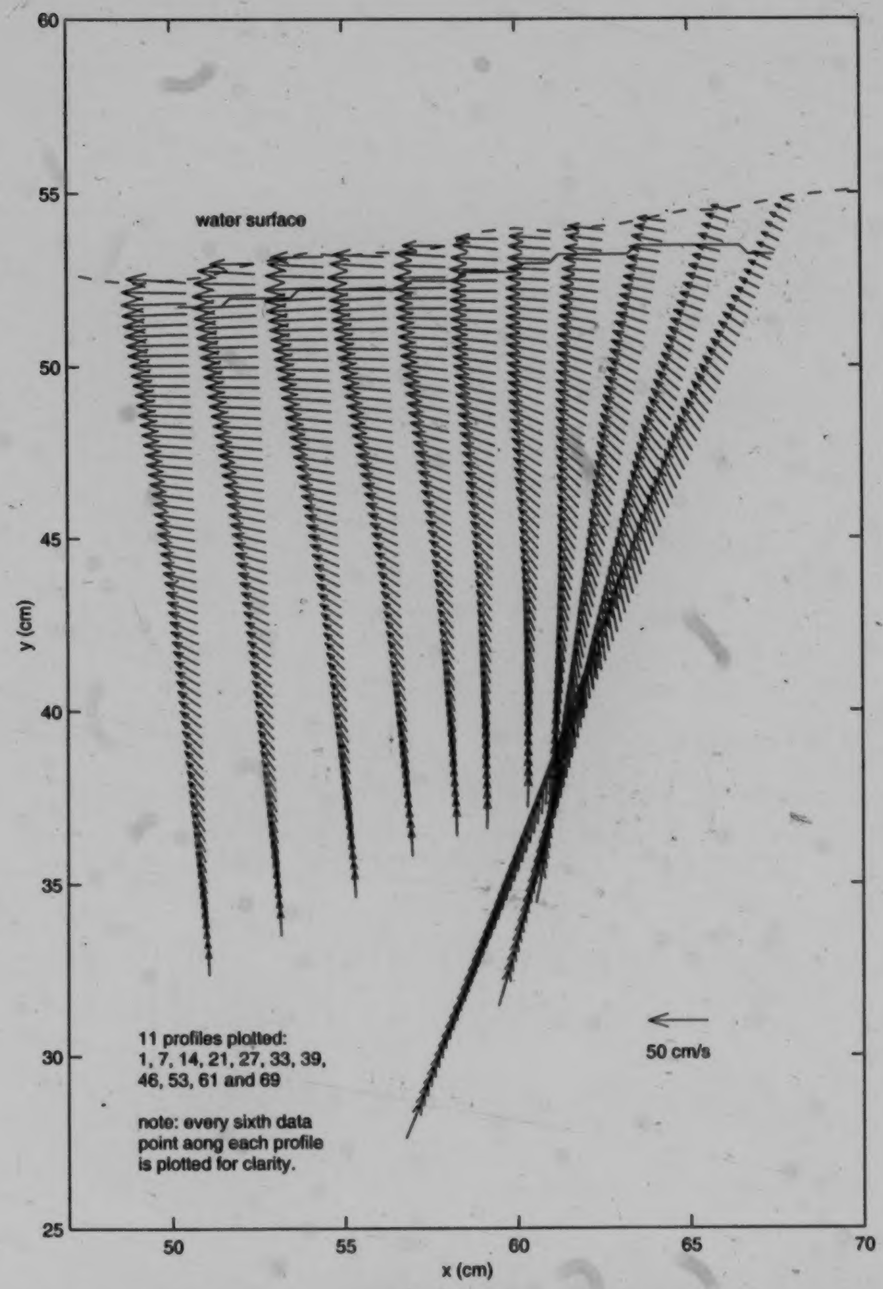

Figure 5.41: Select mean velocity profiles showing the development of the plane deflected wall jet in the return flow surface jet-like (SJL) region; only every tenth mean velocity data point along each profile section is plotted for clarity .

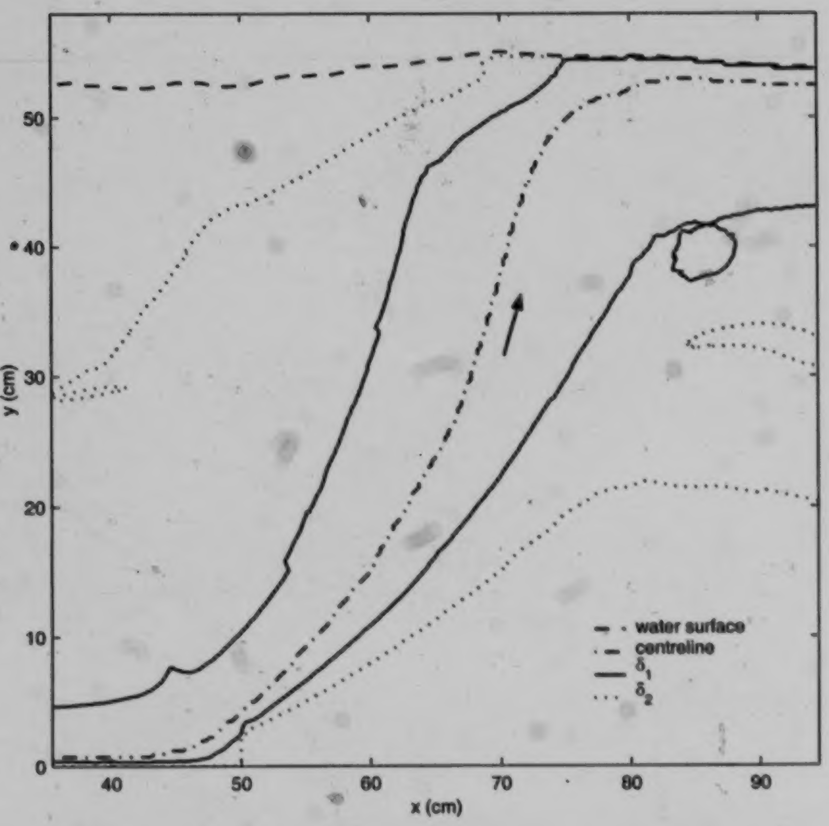

Figure 5.42: Loci of the jet centreline trajectory, the jet half-width (δ_1), the jet width (δ_2) and the water surface in the global Cartesian coordinate system .

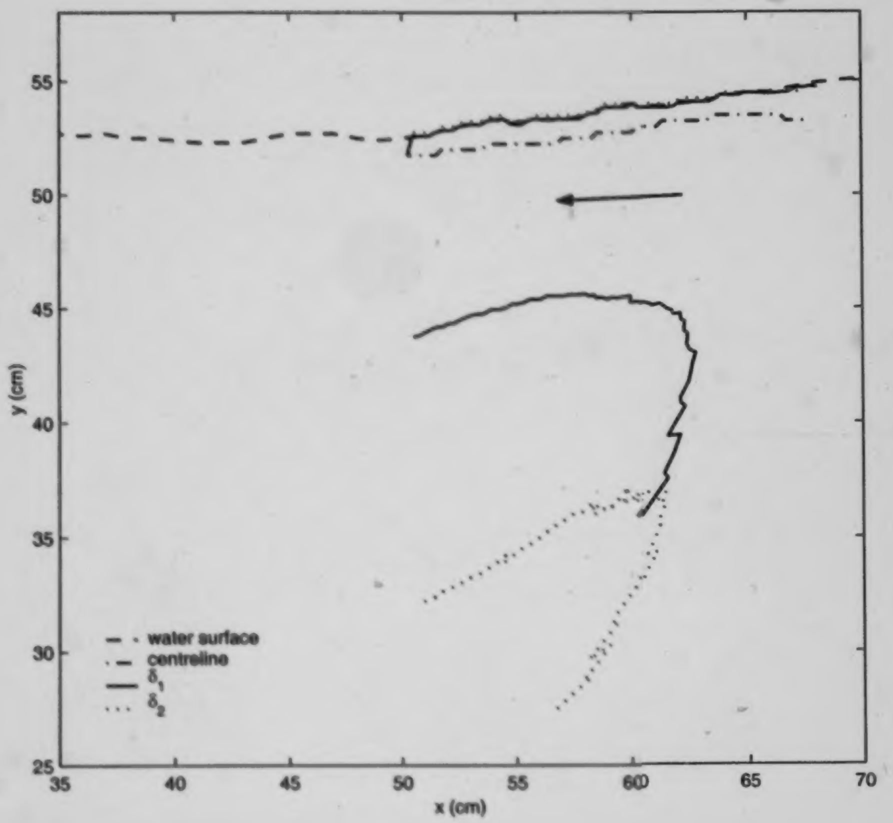

Figure 5.43: Loci of the return flow jet centreline trajectory, the jet half-width (δ_1), the jet width (δ_2) and the water surface in the global Cartesian coordinate system .

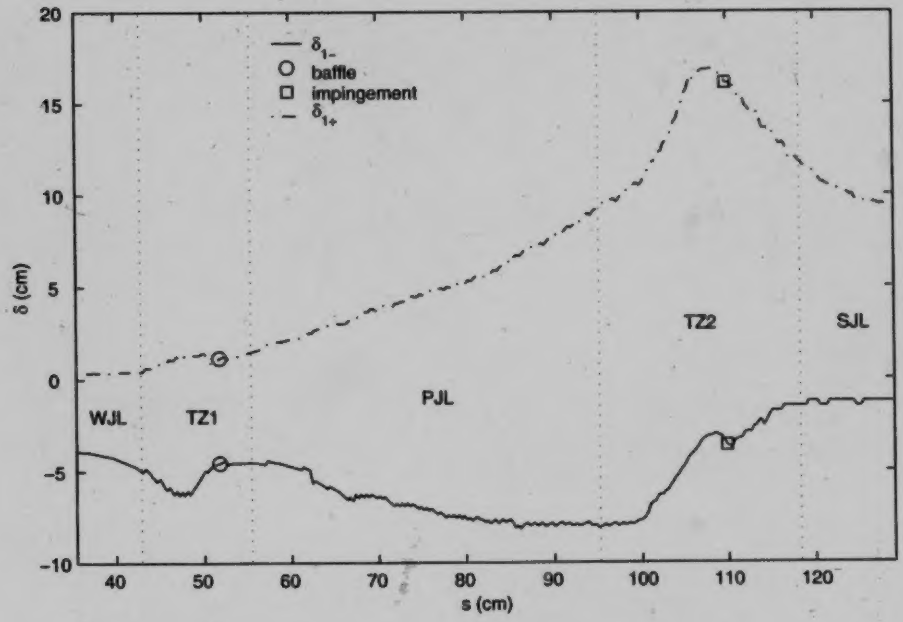

Figure 5.44: Variation of δ_1 with s over the full jet trajectory.

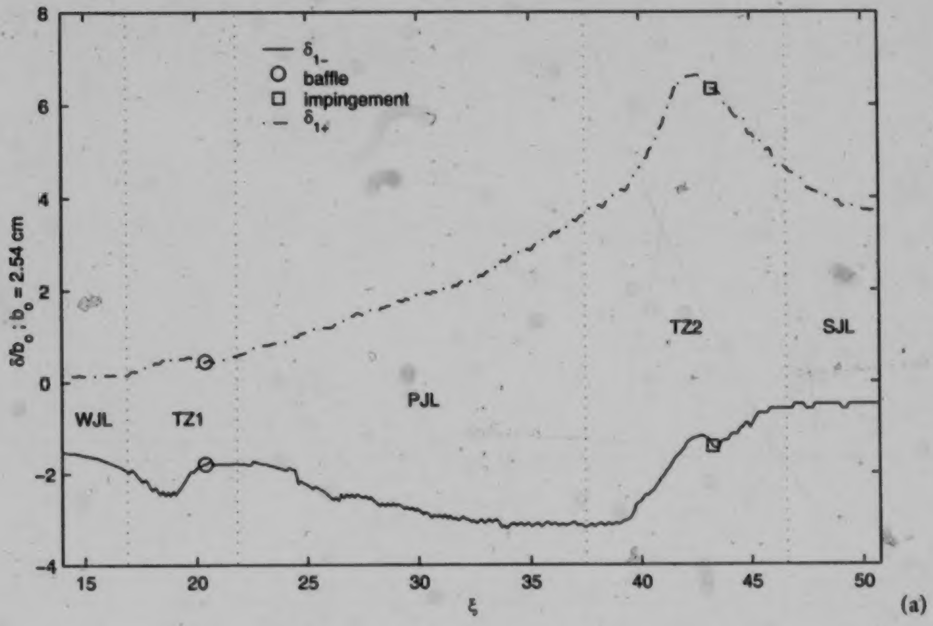

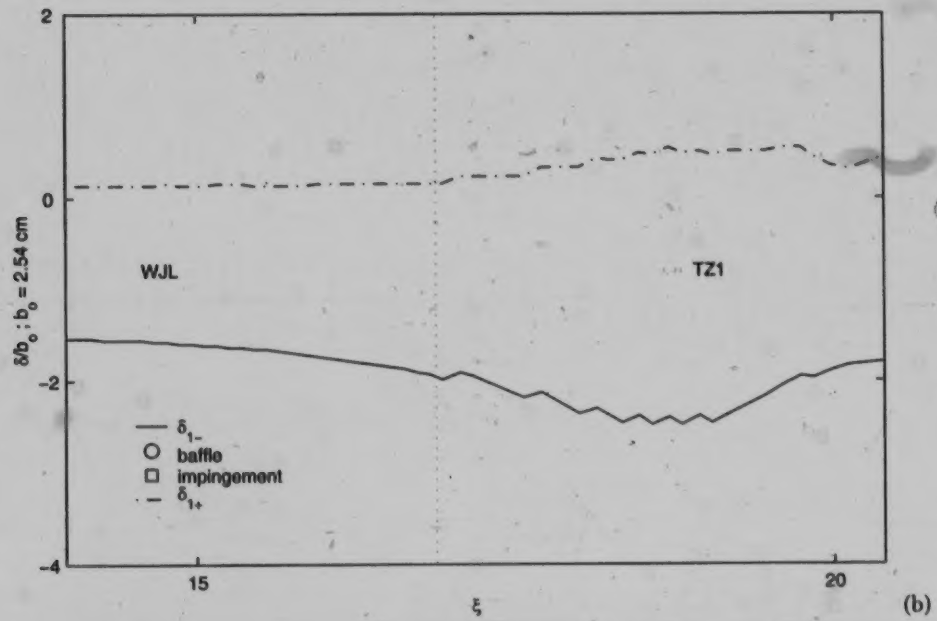

Figure 5.45: Variation of δ_l/b_o with ξ over (a) the full jet trajectory and over (b-d) the sections upstream of the baffle, between the baffle and the point of impingement and downstream of the point of impingement, respectively.

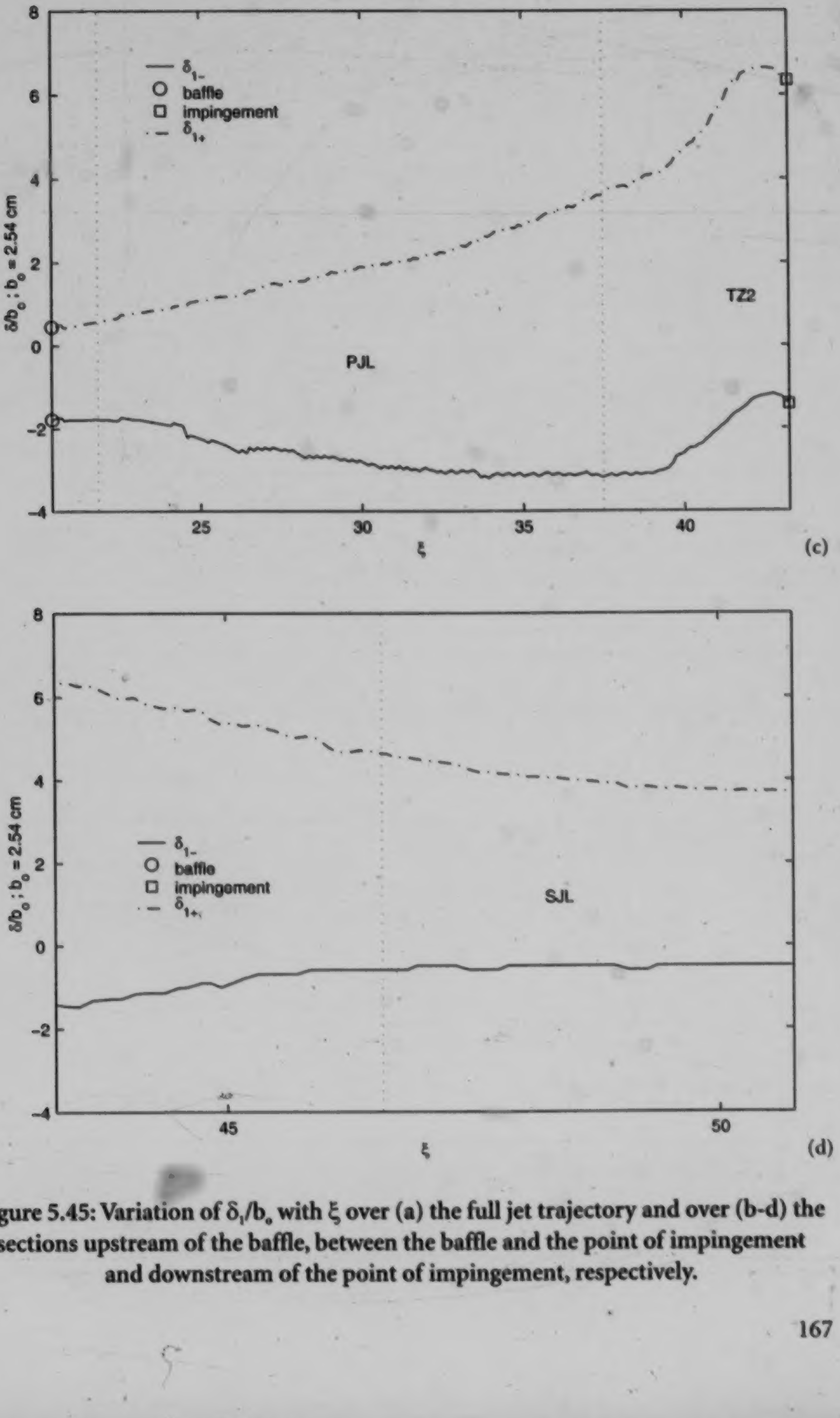

Figure 5.45: Variation of δ_l/b_o with ξ over (a) the full jet trajectory and over (b-d) the sections upstream of the baffle, between the baffle and the point of impingement and downstream of the point of impingement, respectively.

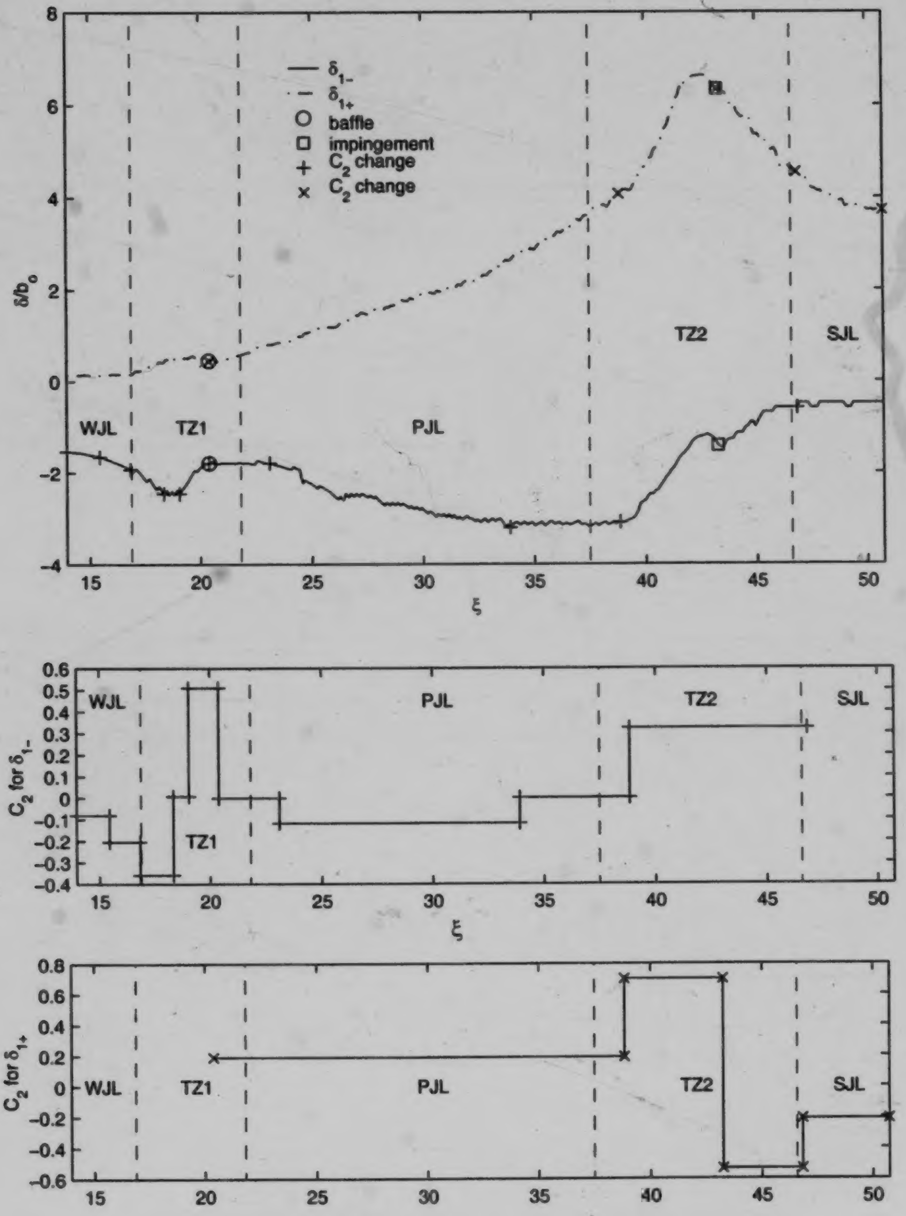

Figure 5.46: Variation of the C_2 coefficients for both δ_{1-} and δ_{1+} along the full jet centreline trajectory.

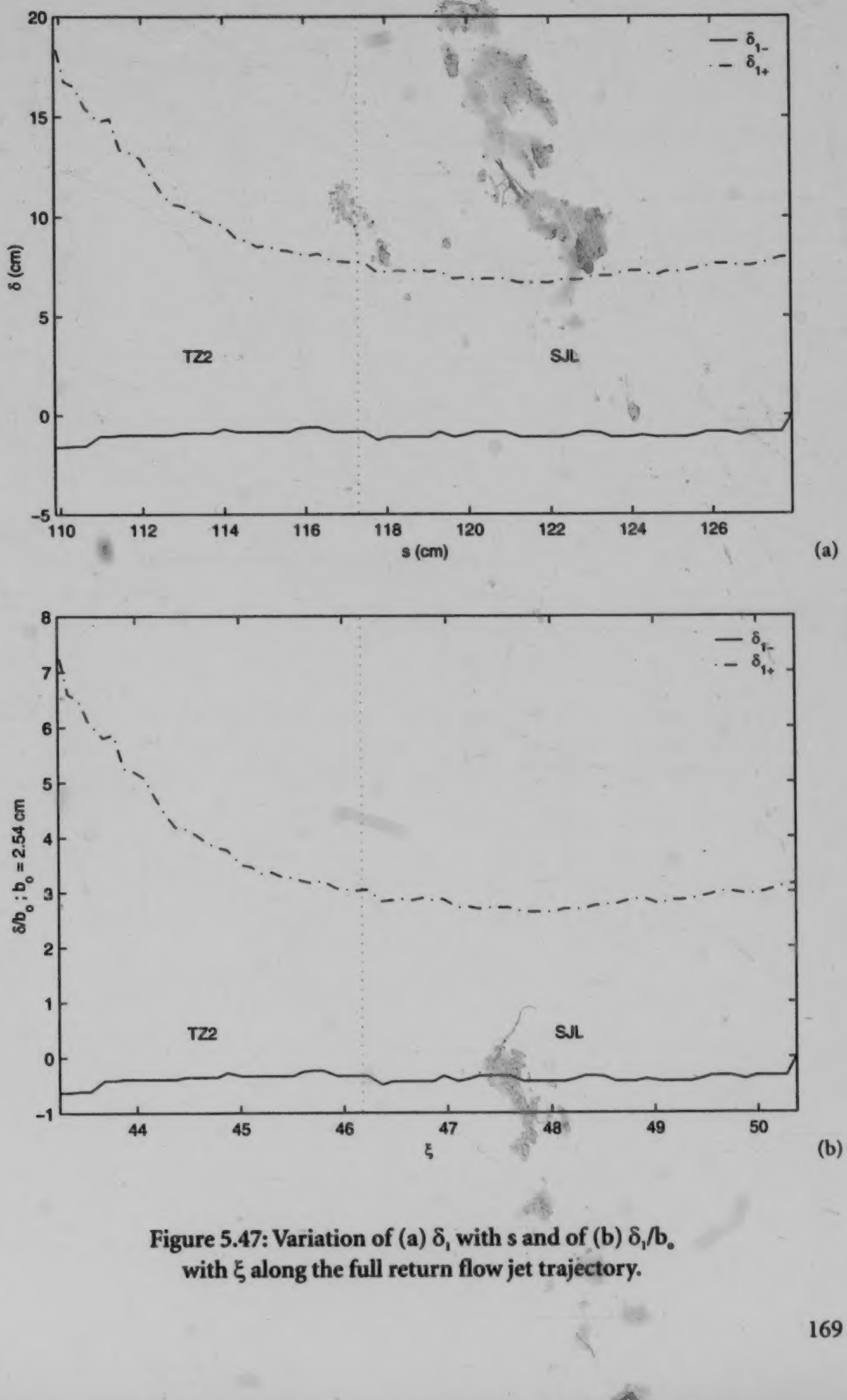

Figure 5.47: Variation of (a) δ_1 with s and of (b) δ_1/b_o with ξ along the full return flow jet trajectory.

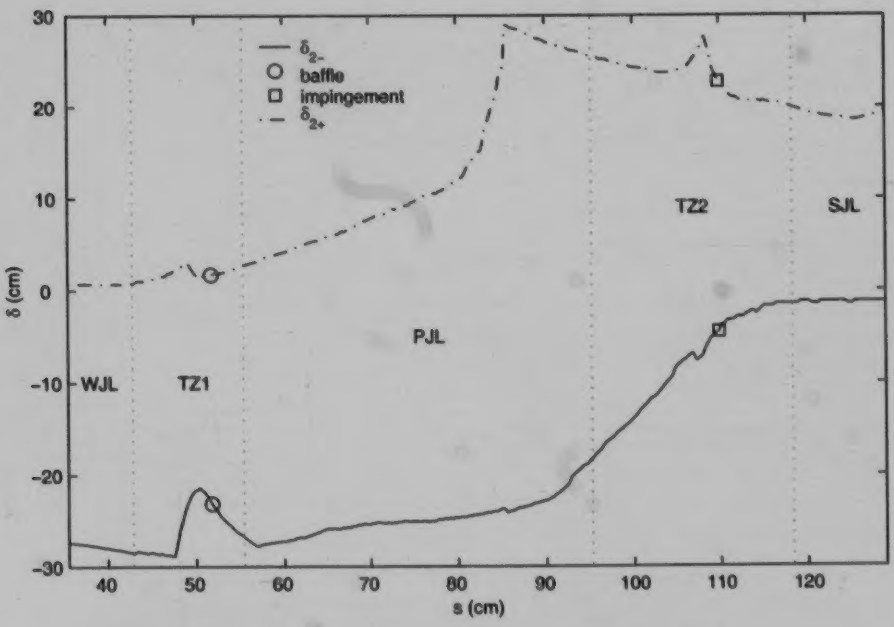

Figure 5.48: Variation of δ_2 with s over the full jet trajectory.

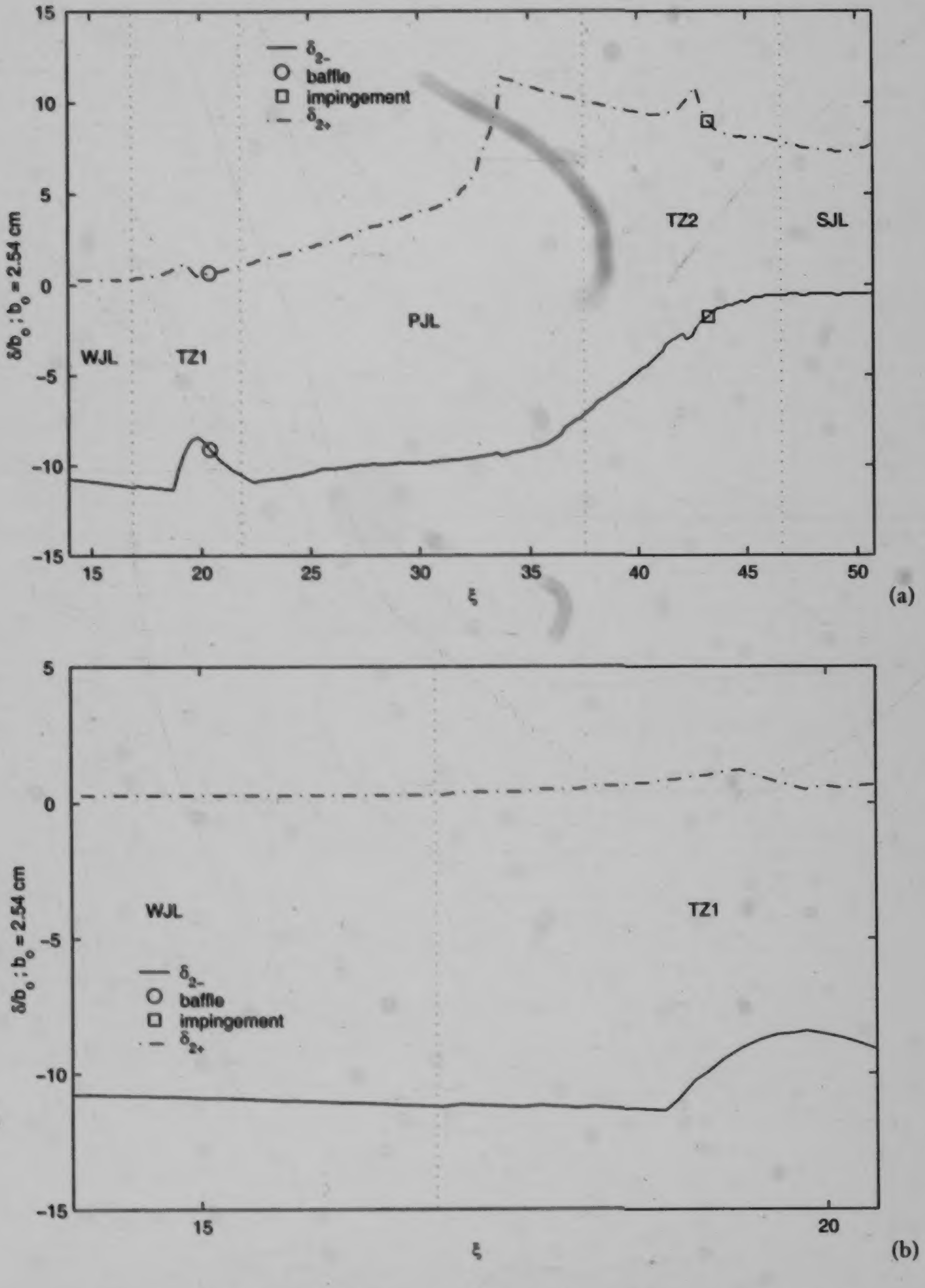

Figure 5.49: Variation of δ_2/b_o with ξ over (a) the full jet trajectory and over (b-d) the sections upstream of the baffle, between the baffle and the point of impingement and downstream of the point of impingement, respectively.

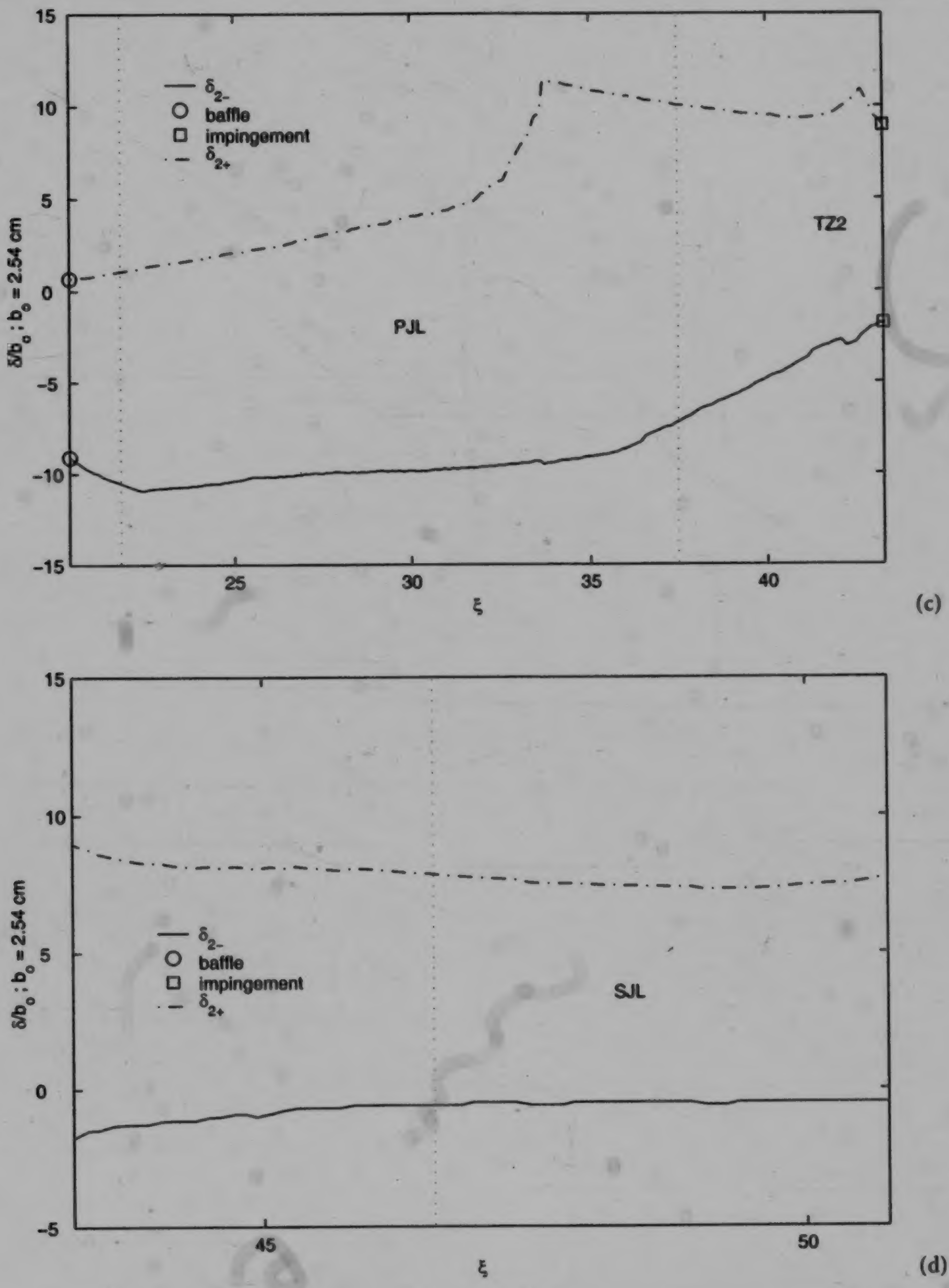

Figure 5.49 Variation of δ_2/b_o with ξ over (a) the full jet trajectory and over (b-d) the sections upstream of the baffle, between the baffle and the point of impingement and downstream of the point of impingement, respectively.

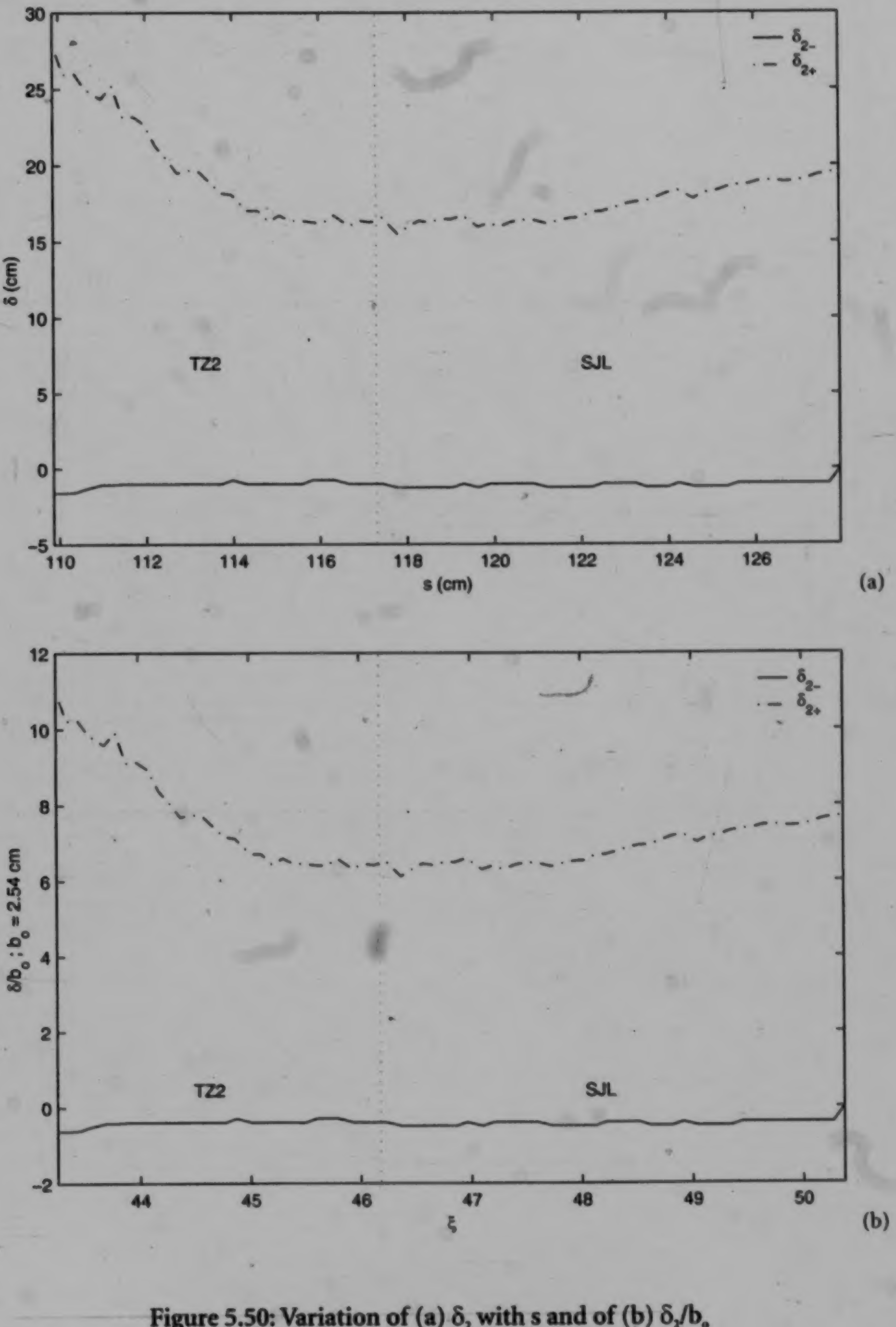

Figure 5.50: Variation of (a) δ_2 with s and of (b) δ_2/b_o with ξ along the full return flow jet trajectory.

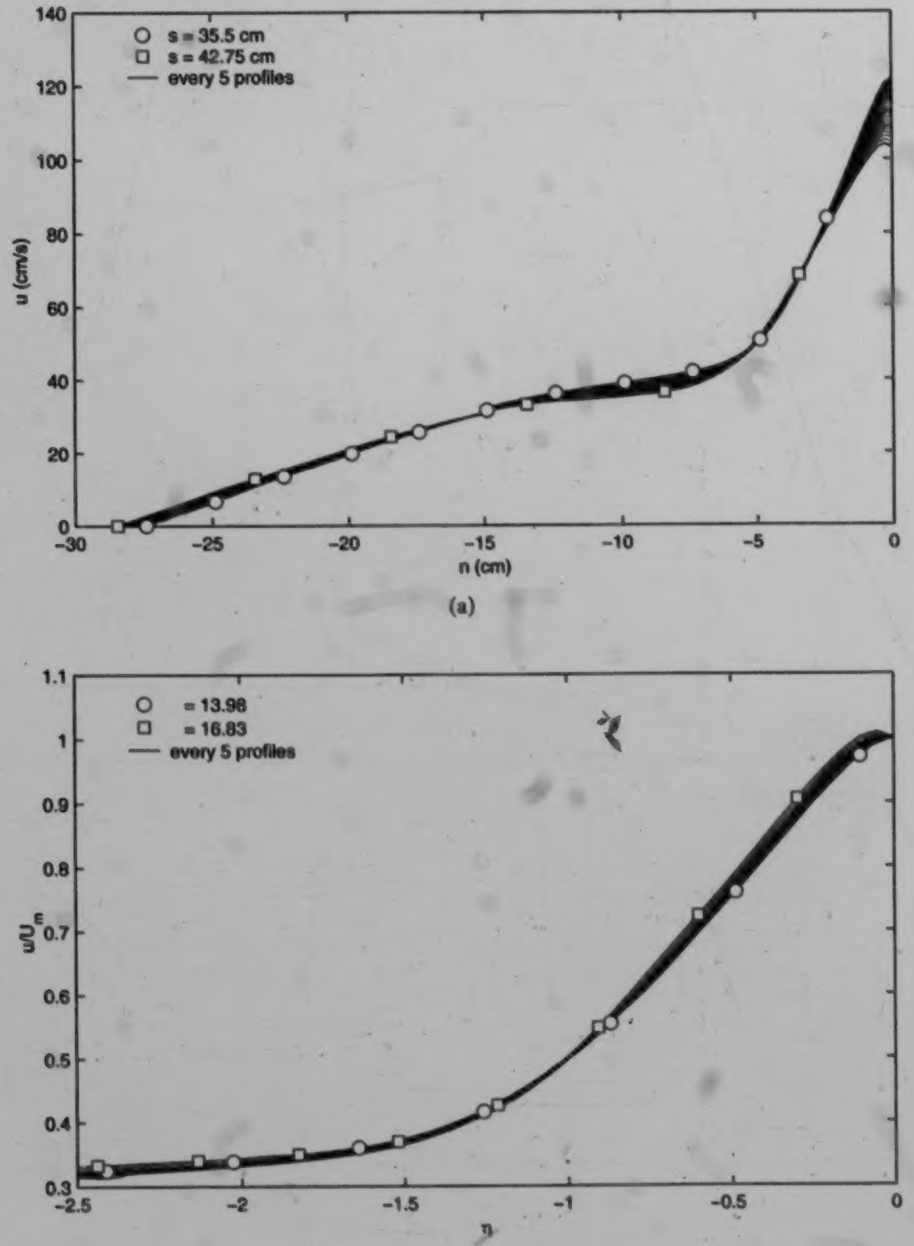

(a)

(b)

Figure 5.51: (a) Dimensional and (b) nondimensional u mean velocities for wall jet-like (WJL) profiles.

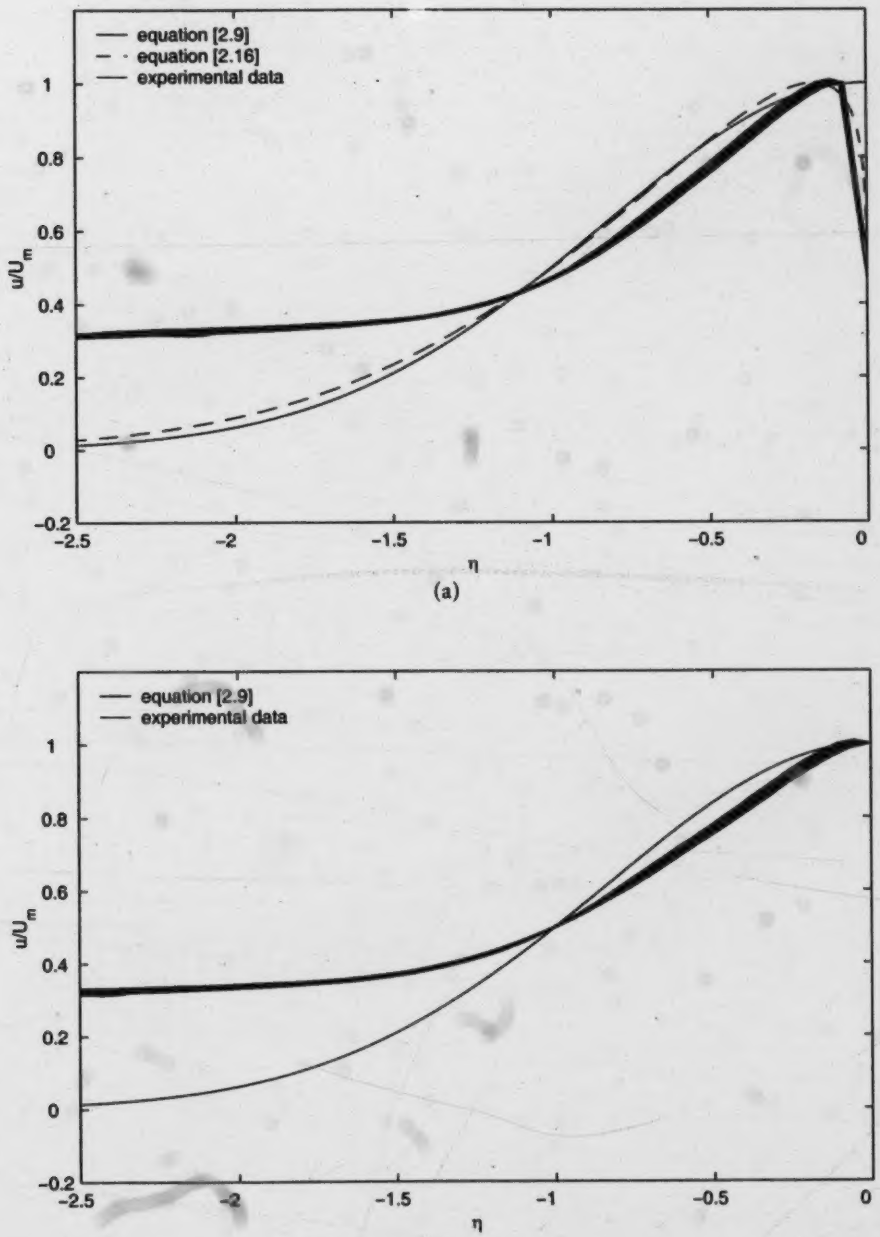

(a)

(b)

Figure 5.52: Comparison of theoretical curves describing the variation of u/U_m with η for wall jet-like (WJL) profiles using (a) classical wall jet and (b) free mixing region definitions.

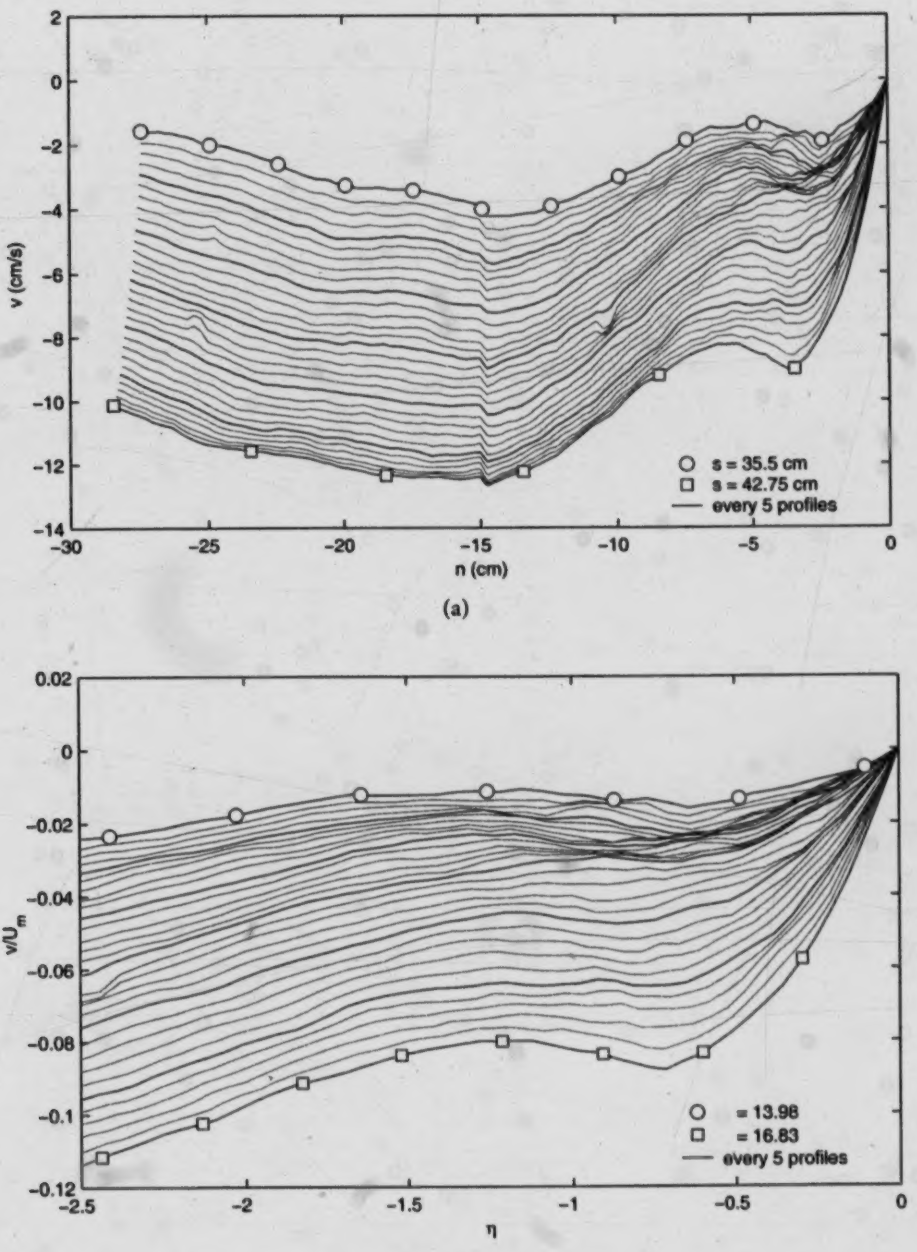

(a)

(b)

Figure 5.53: (a) Dimensional and (b) nondimensional v mean velocities for wall jet-like (WJL) profiles.

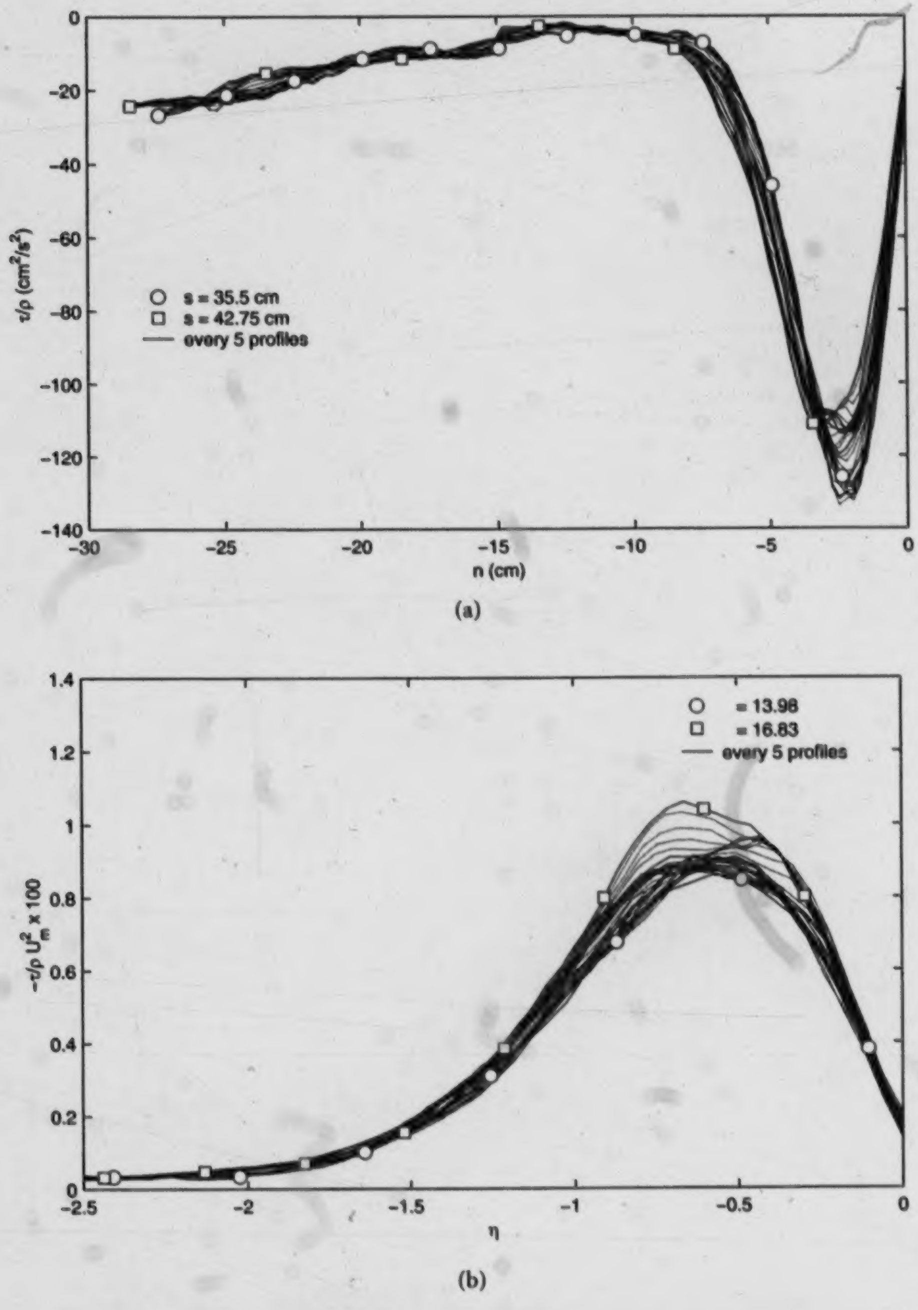

(a)

(b)

Figure 5.54: (a) Dimensional and (b) nondimensional mean Reynolds stress per unit mass (τ/ρ) for wall jet-like (WJL) profiles.

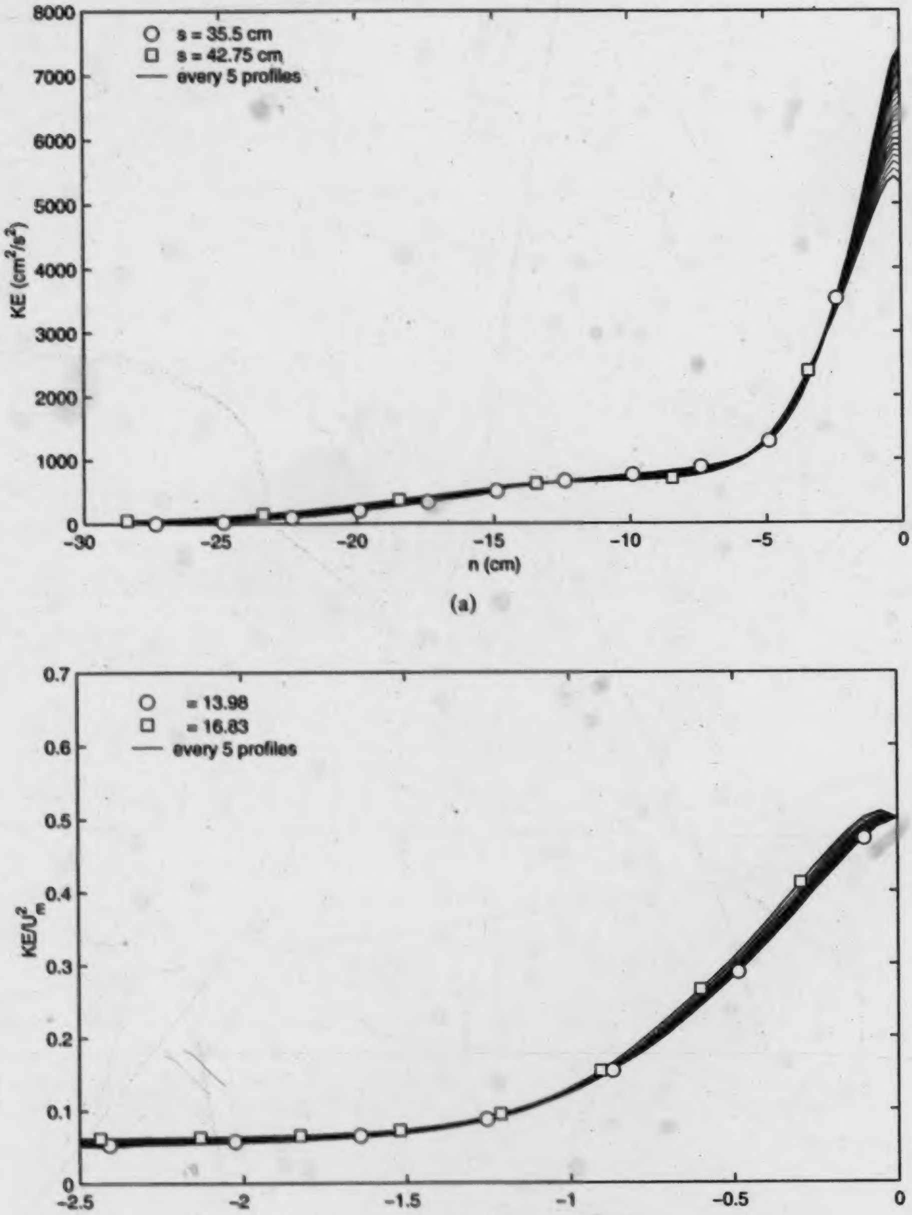

(a)

(b)

Figure 5.55: (a) Dimensional and (b) nondimensional mean kinetic energy per unit mass (KE) for wall jet-like (WJL) profiles.

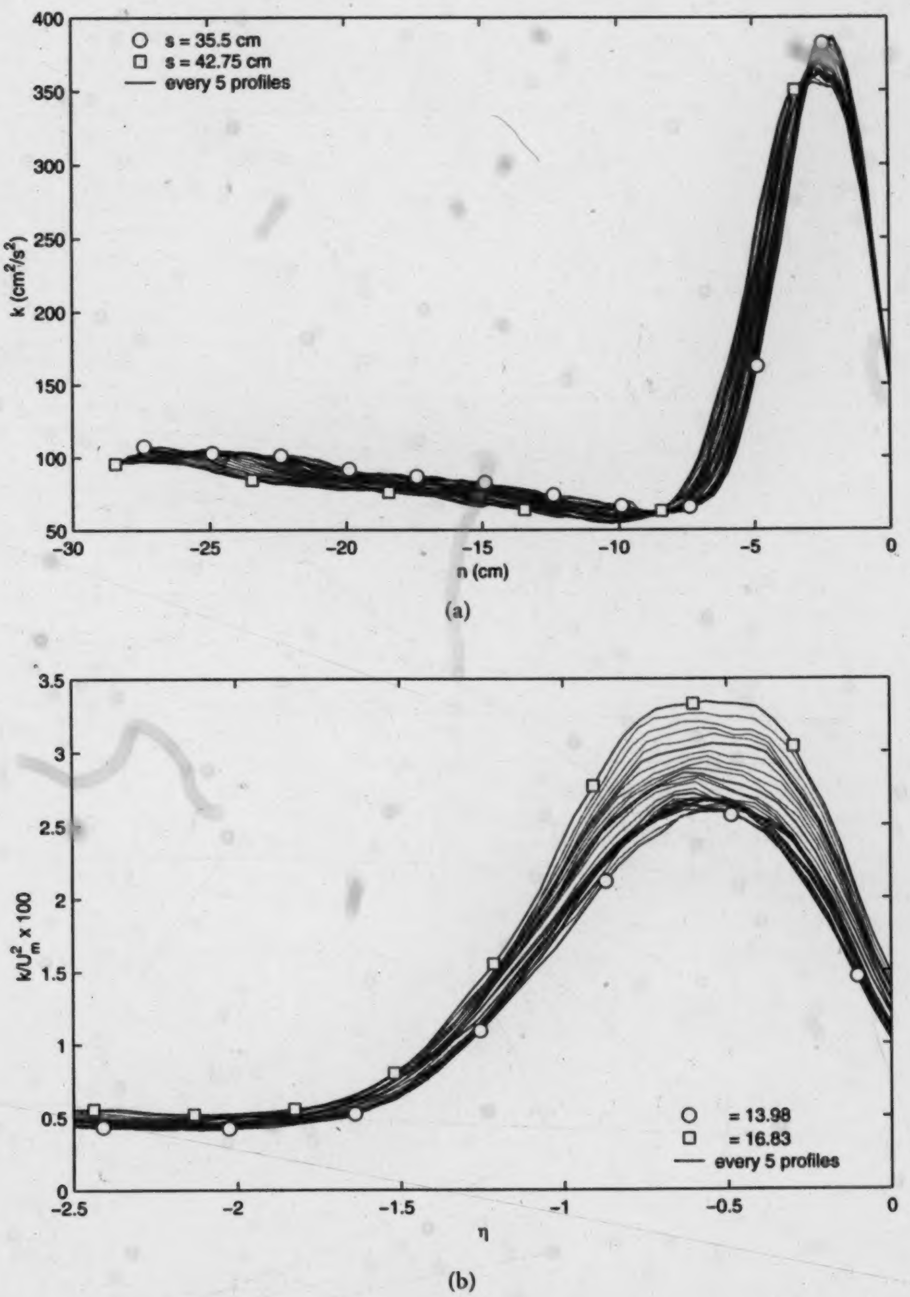

Figure 5.56: (a) Dimensional and (b) nondimensional mean turbulent kinetic energy per unit mass (k) for wall jet-like (WJL) profiles.

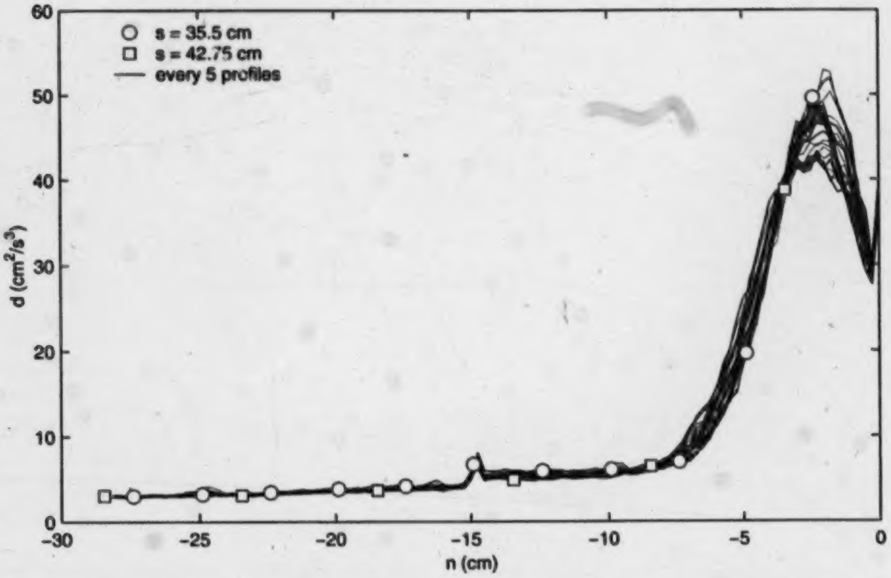

Figure 5.57: Mean dissipation per unit mass (d) for wall jet-like (WJL) profiles.

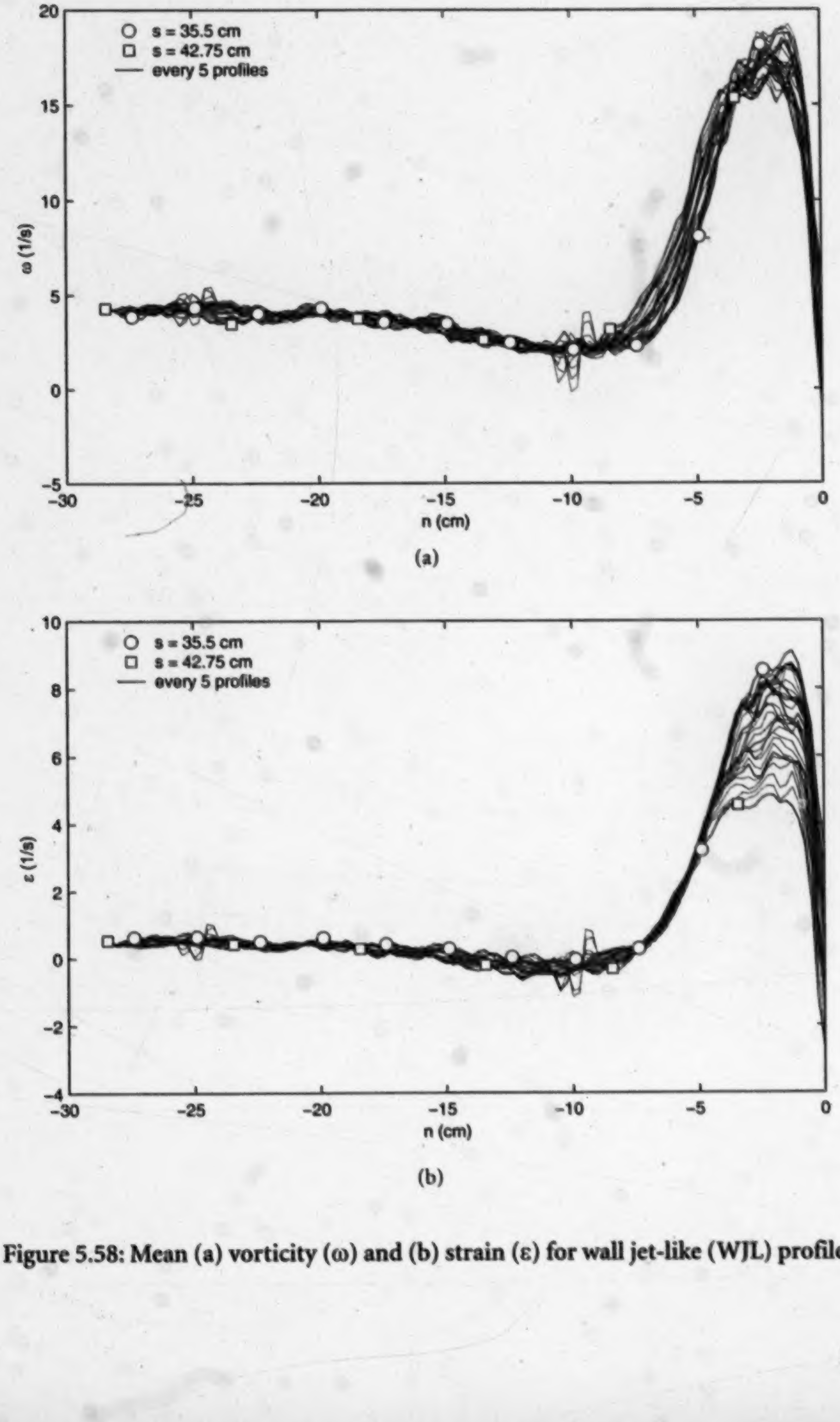

Figure 5.58: Mean (a) vorticity (ω) and (b) strain (ε) for wall jet-like (WJL) profiles.

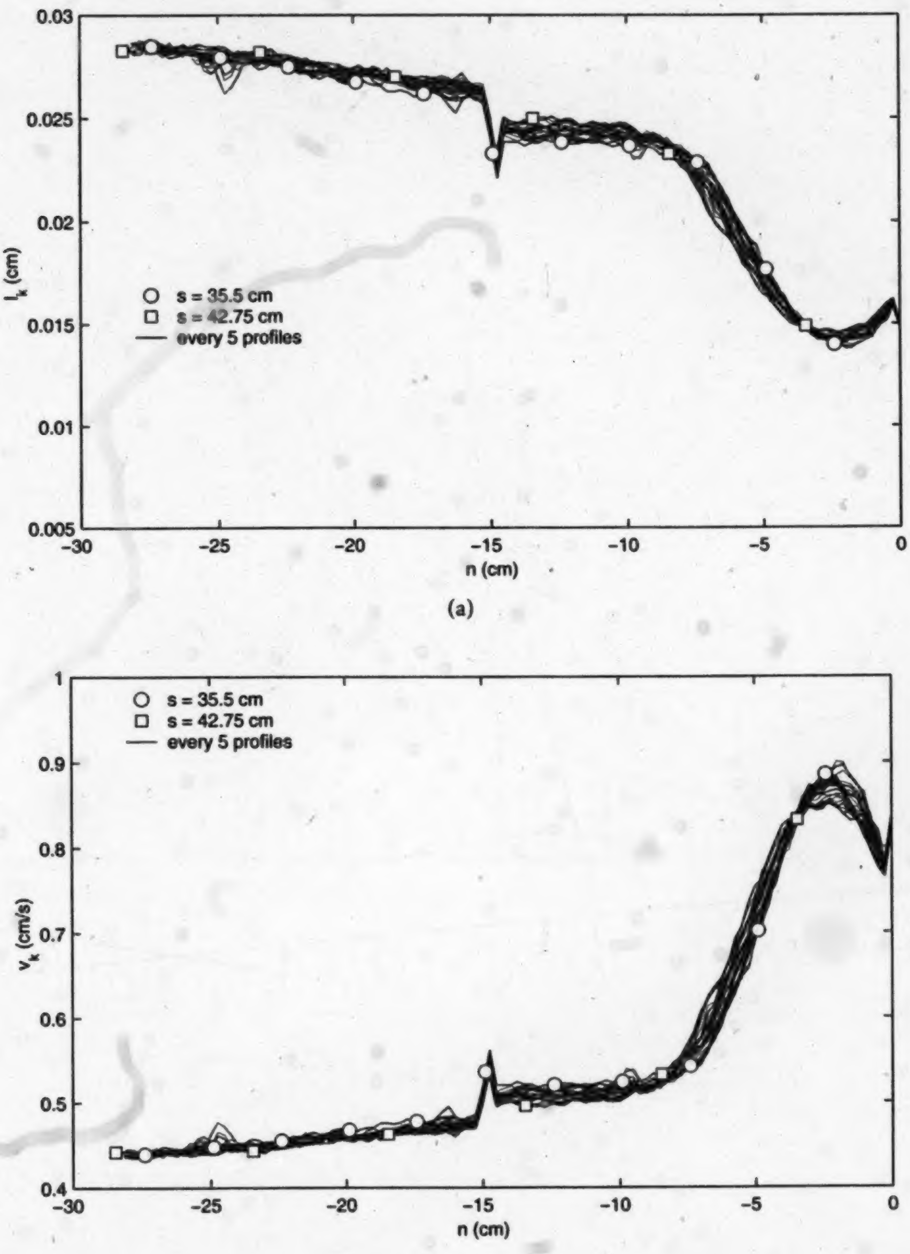

(a)

(b)

Figure 5.59: Mean Kolmogorov (a) length scales (l_k) and (b) velocity scales (v_k) for wall jet-like (WJL) profiles.

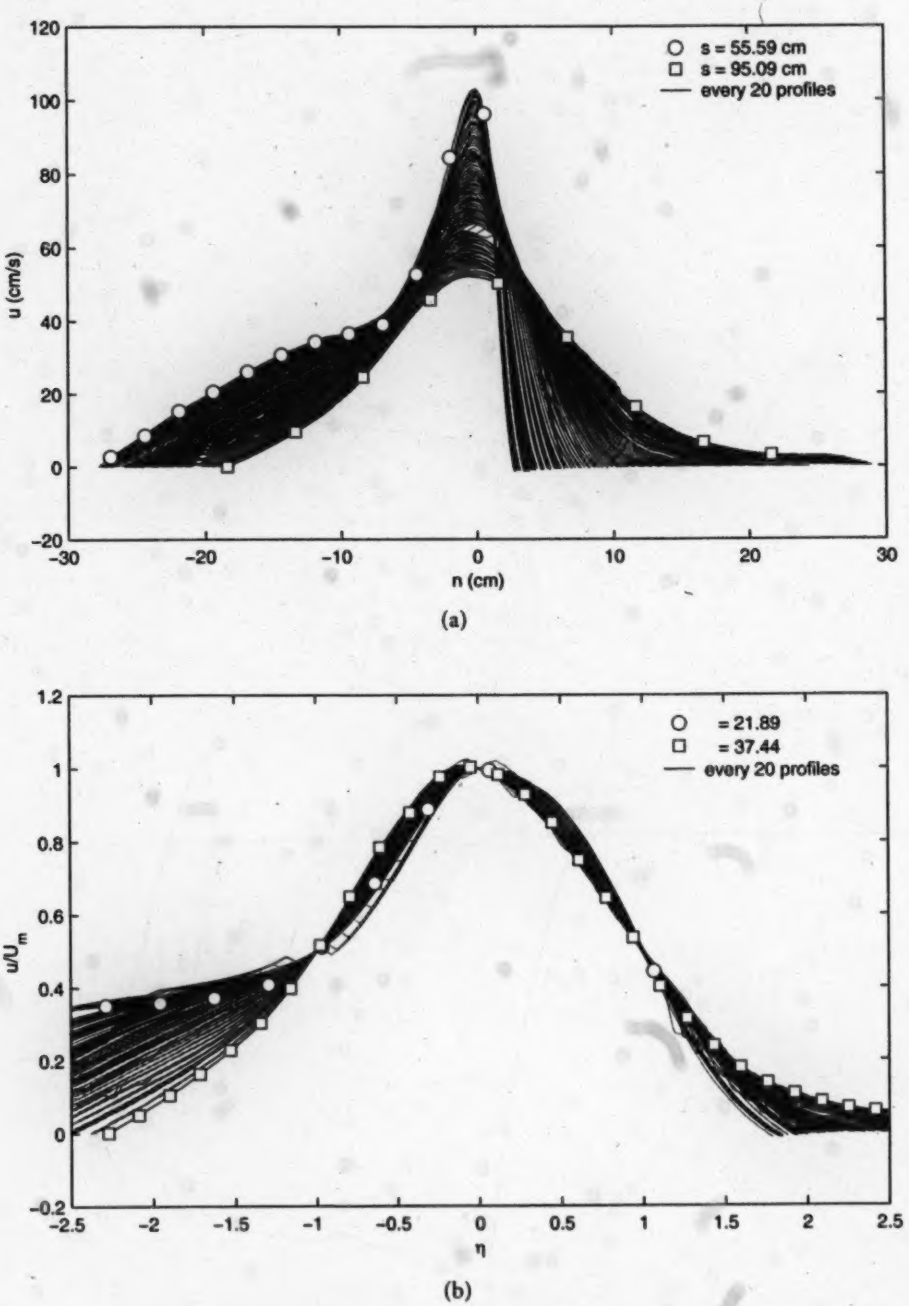

Figure 5.60: (a) Dimensional and (b) nondimensional u mean velocities for plane jet-like (PJL) profiles.

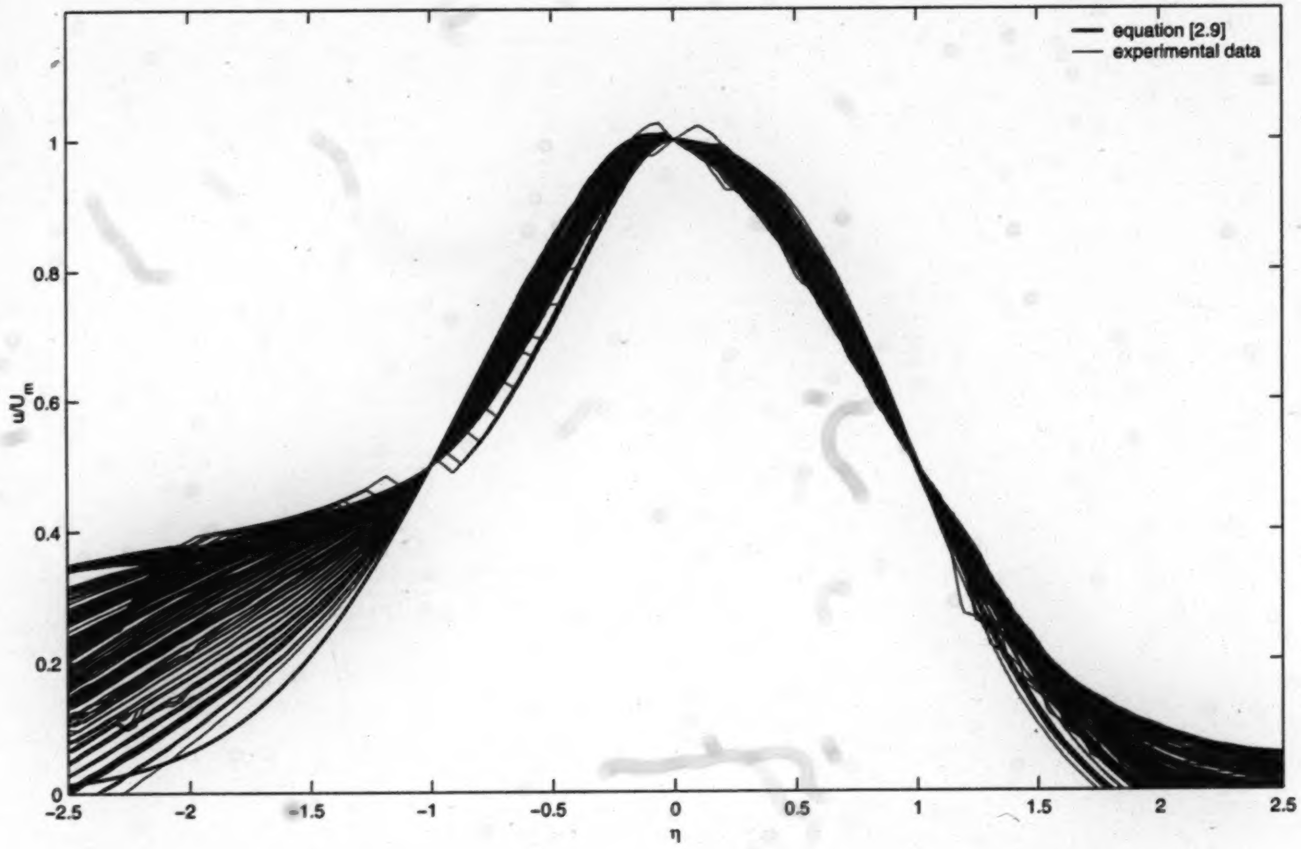

Figure 5.61: Variation of u/U_m with η for plane jet-like (PJL) profiles with equation [2.9] plotted for reference.

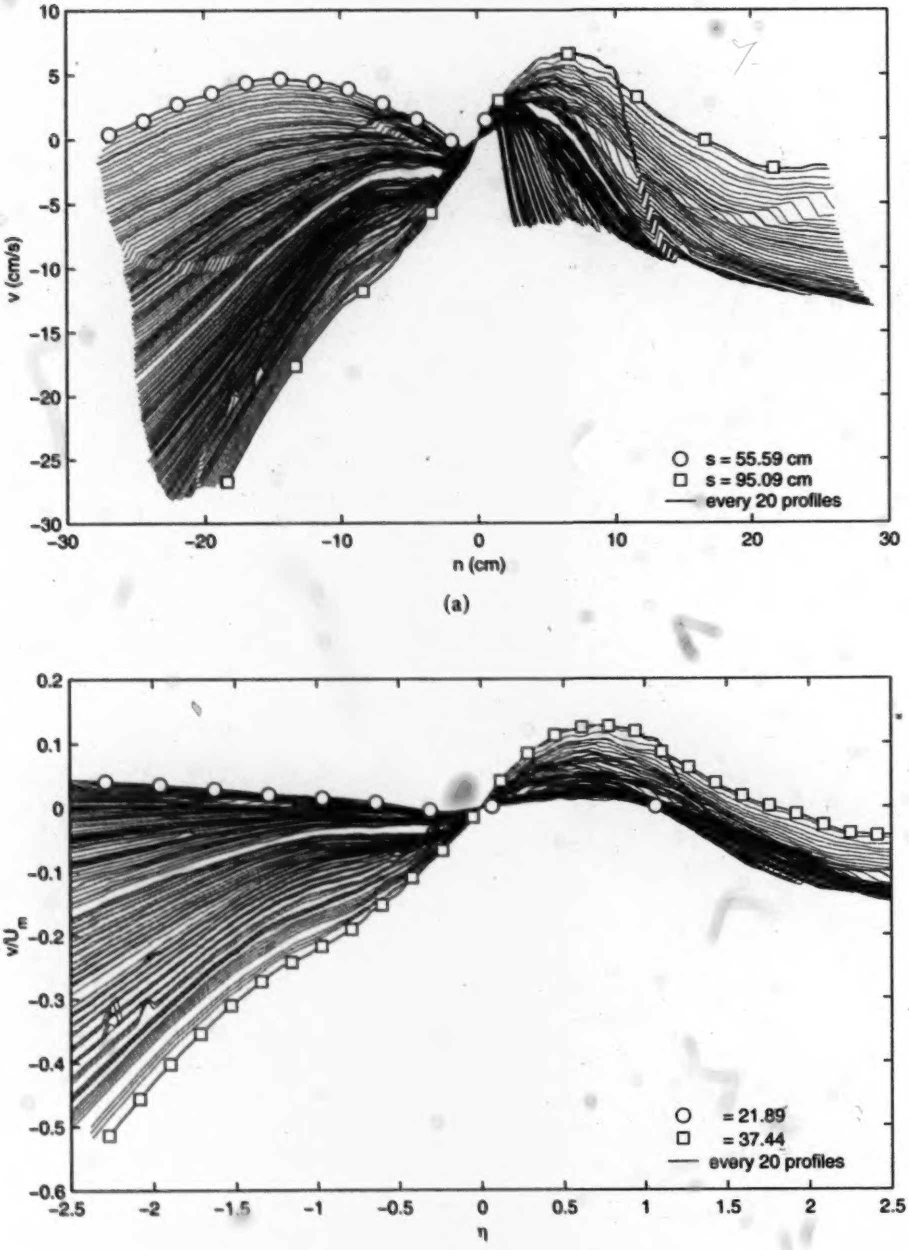

(a)

(b)

Figure 5.62: (a) Dimensional and (b) nondimensional v mean velocities for plane jet-like (PJL) profiles.

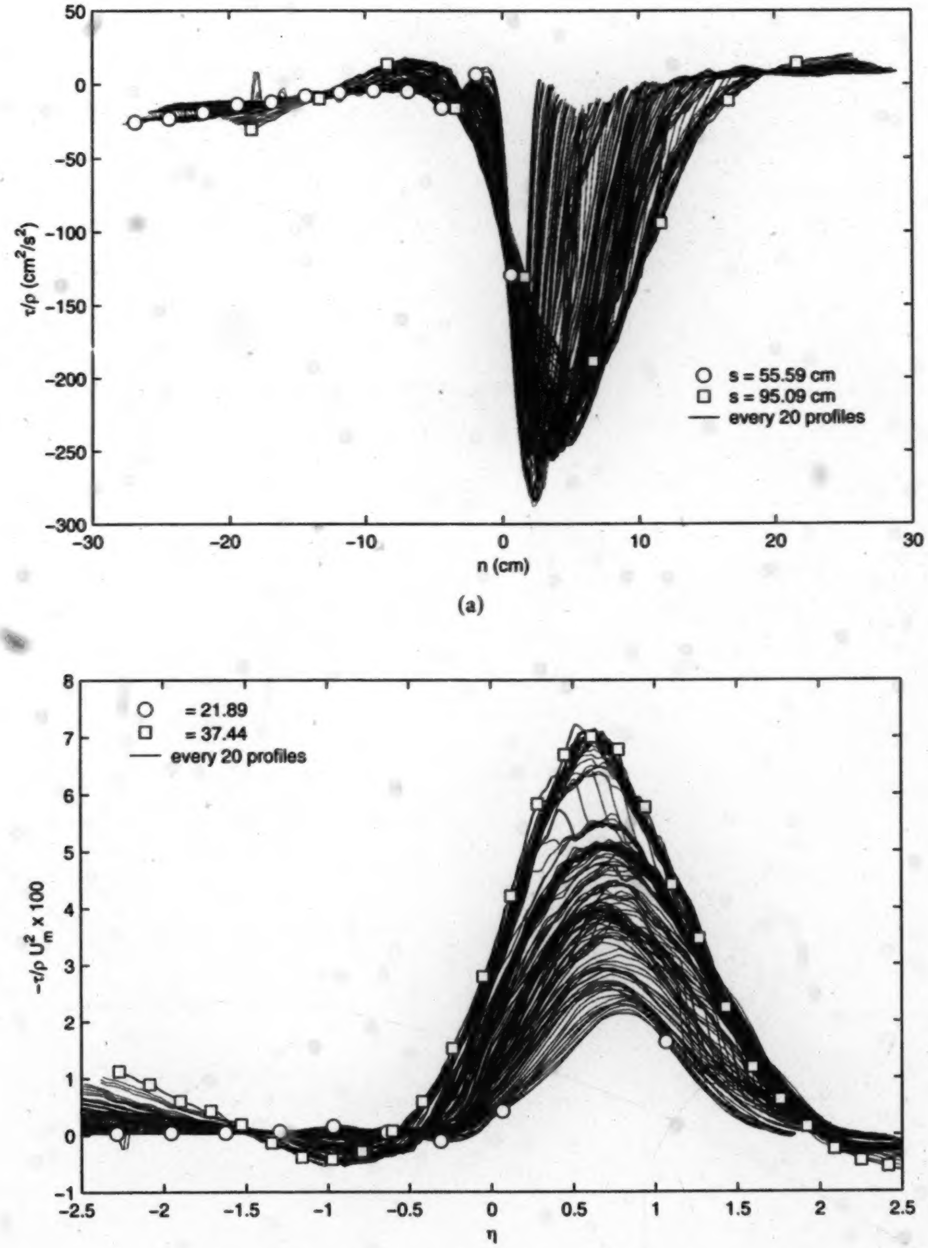

(a)

(b)

Figure 5.63: (a) Dimensional and (b) nondimensional mean Reynolds stress per unit mass (τ/ρ) for plane jet-like (PJL) profiles.

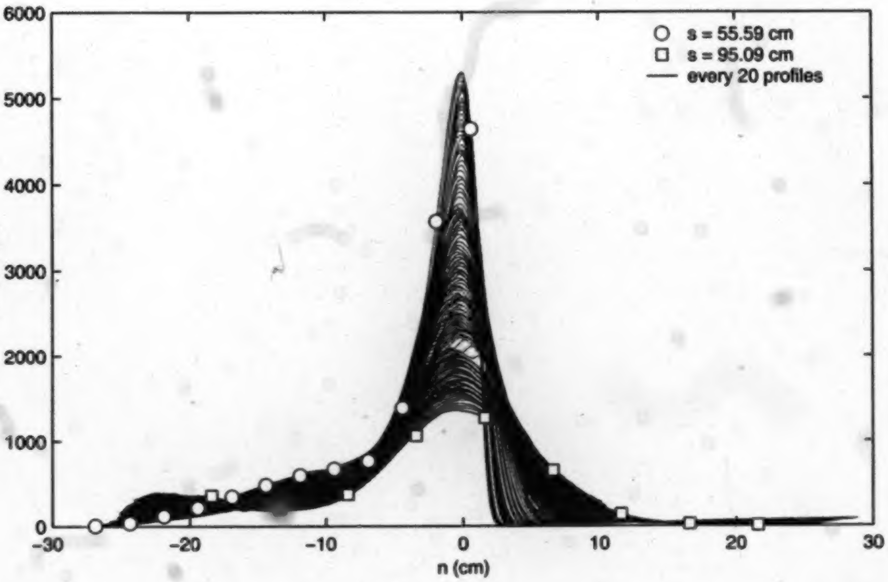

(a)

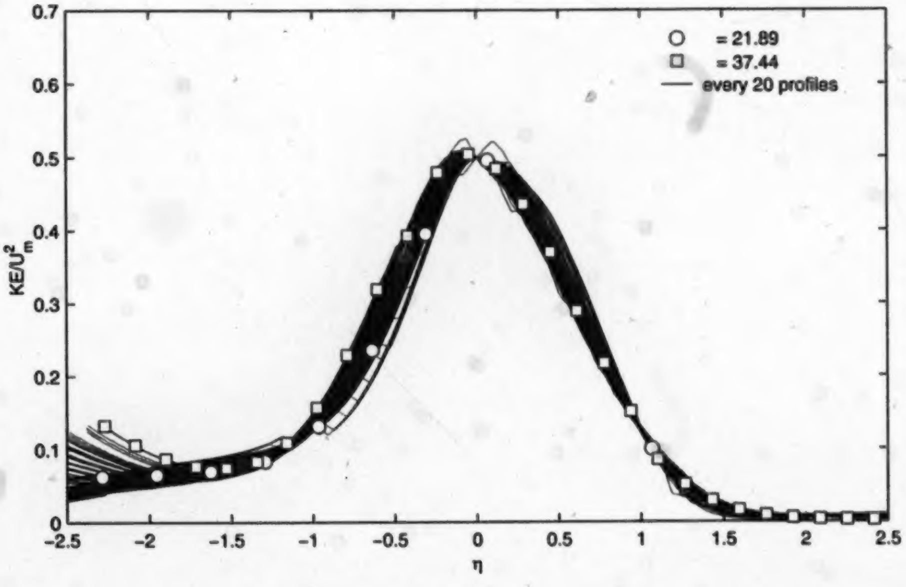

(b)

Figure 5.64: (a) Dimensional and (b) nondimensional mean kinetic energy per unit mass (KE) for plane jet-like (PJL) profiles.

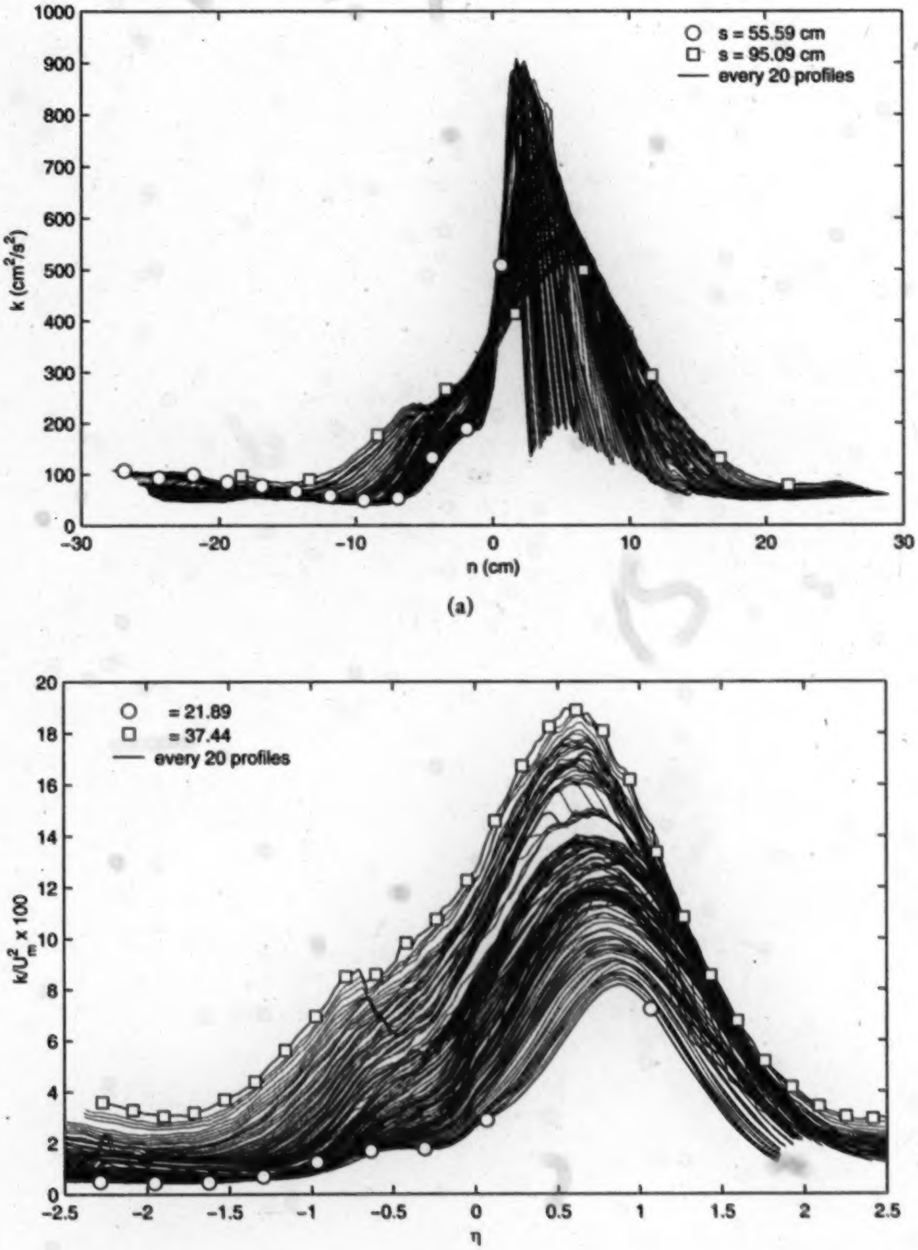

(a)

(b)

Figure 5.65: (a) Dimensional and (b) nondimensional mean turbulent kinetic energy per unit mass (k) for plane jet-like (PJL) profiles.

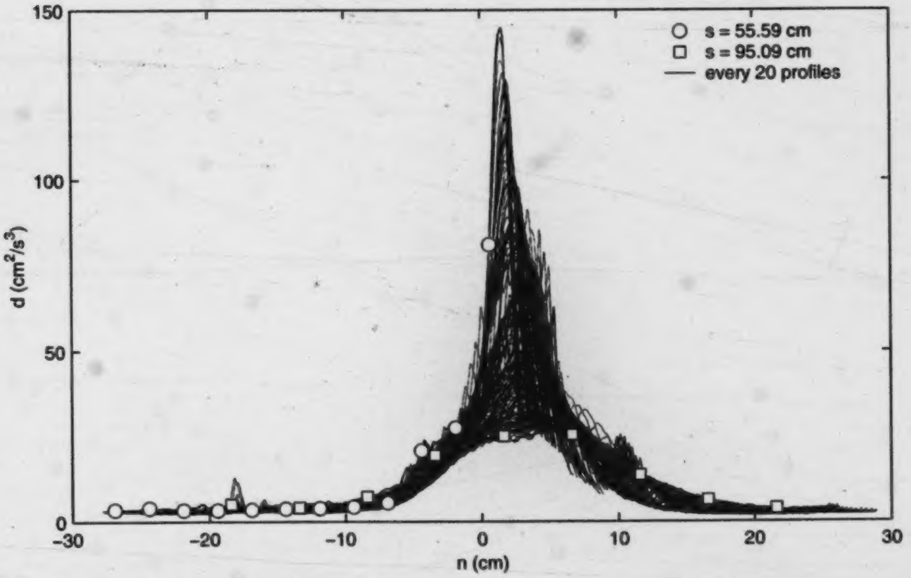

Figure 5.66: Mean dissipation per unit mass (d) for plane jet-like (PJL) profiles.

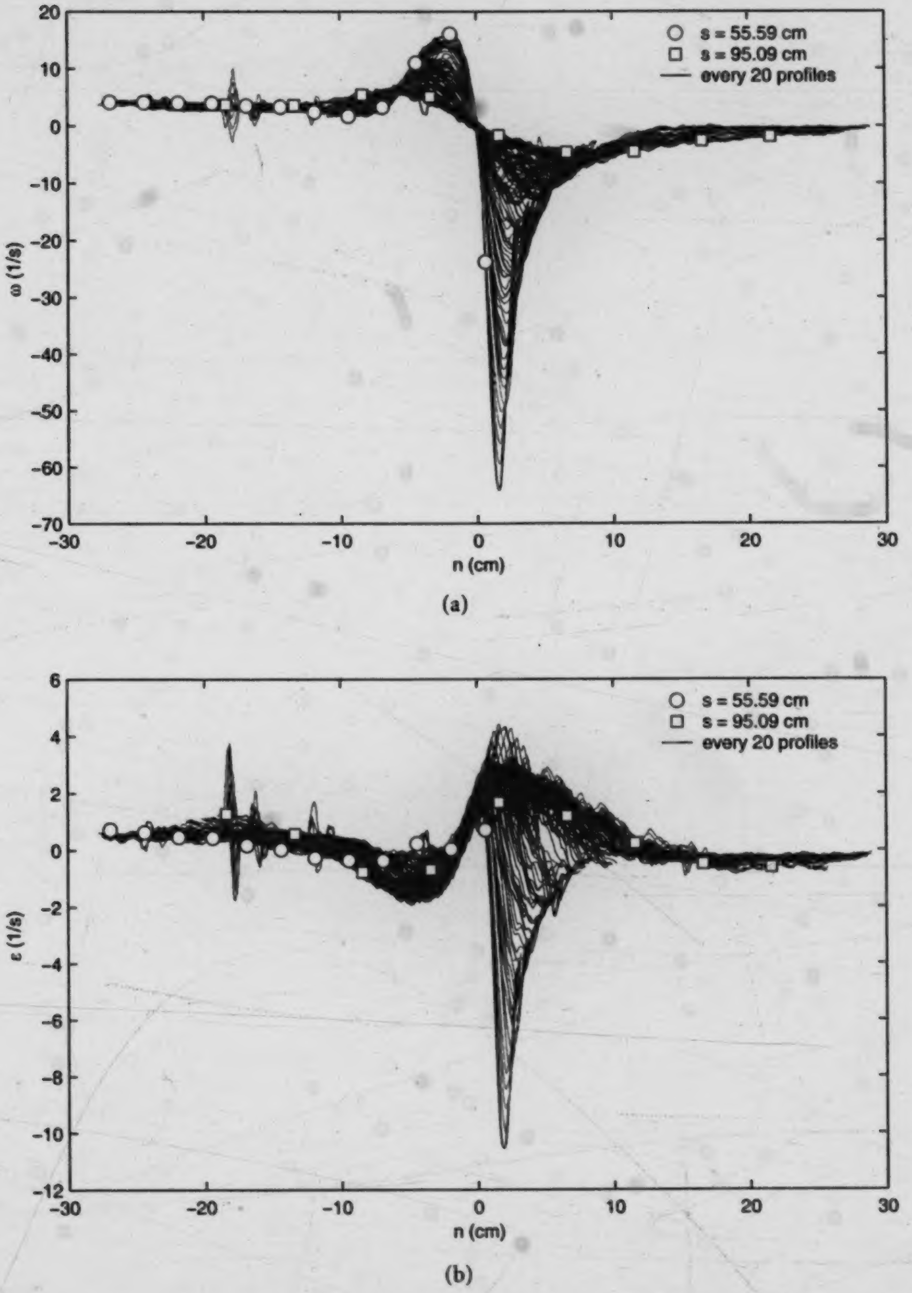

Figure 5.67: Mean (a) vorticity (ω) and (b) strain (ε) for plane jet-like (PJL) profiles.

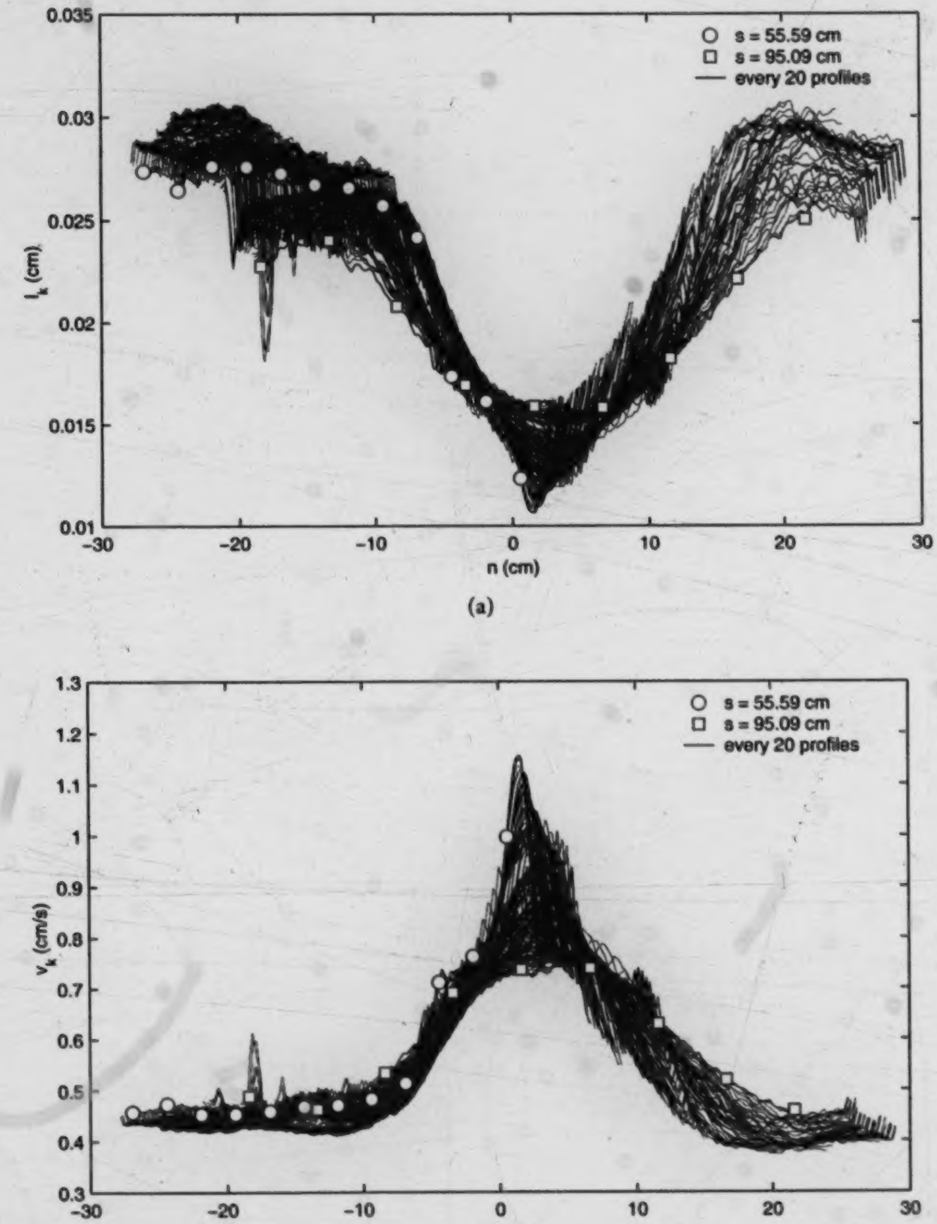

(a)

(b)

Figure 5.68: Mean Kolmogorov (a) length scales (l_k) and (b) velocity scales (v_k) for plane jet-like (PJL) profiles.

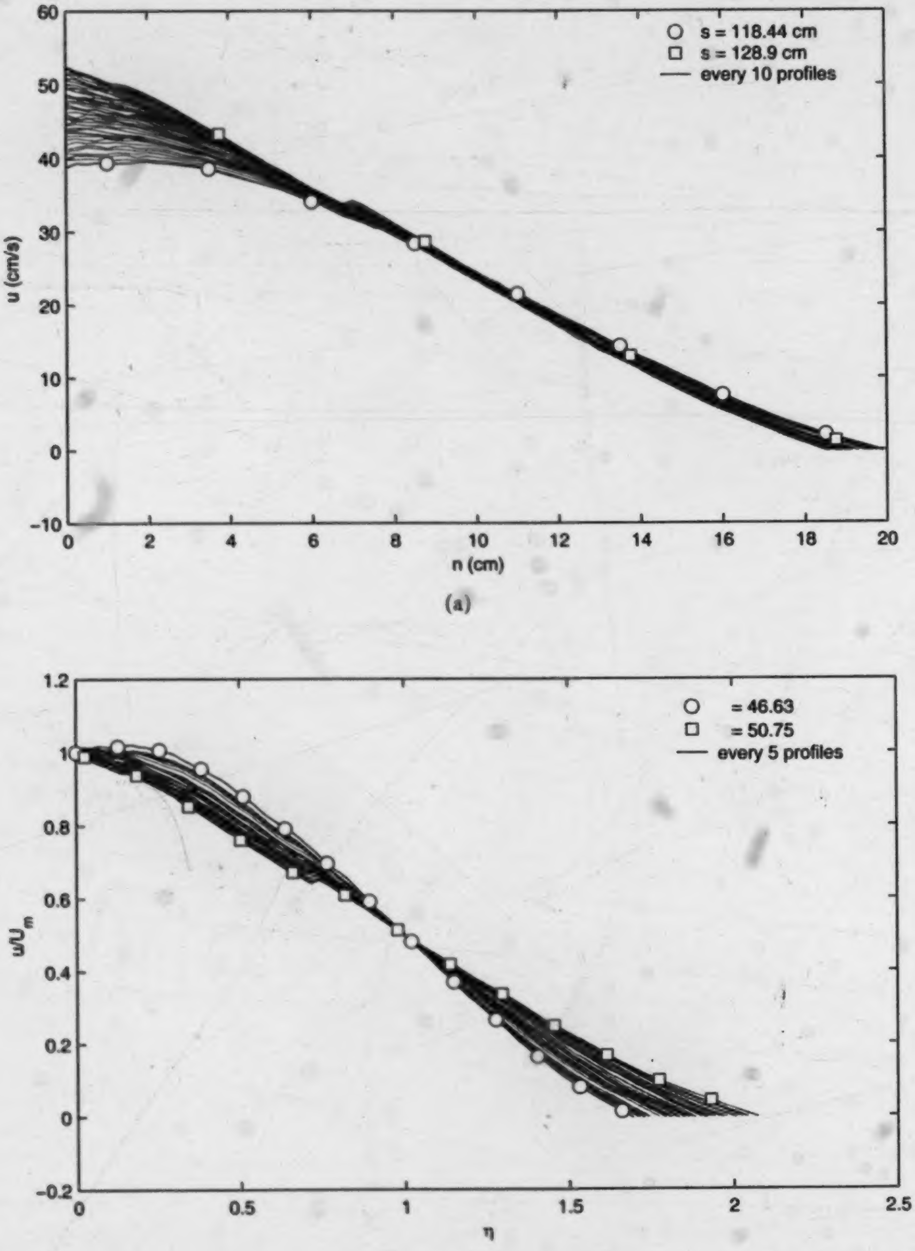

(a)

(b)

Figure 5.69: (a) Dimensional and (b) nondimensional u mean velocities for surface jet-like (SJL) profiles.

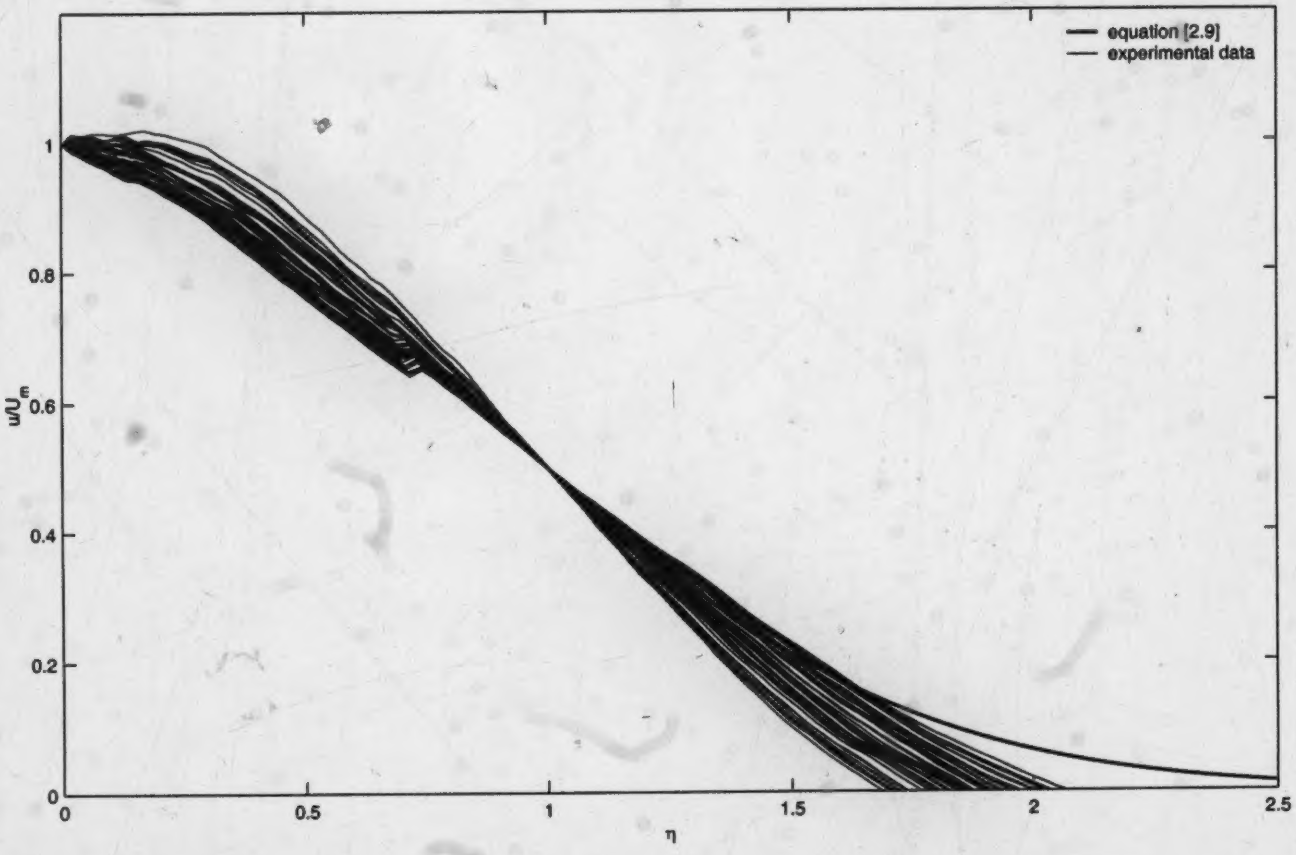

Figure 5.70: Variation of u/U_m with η for surface jet-like (SJL) profiles with equation [2.9] plotted for reference.

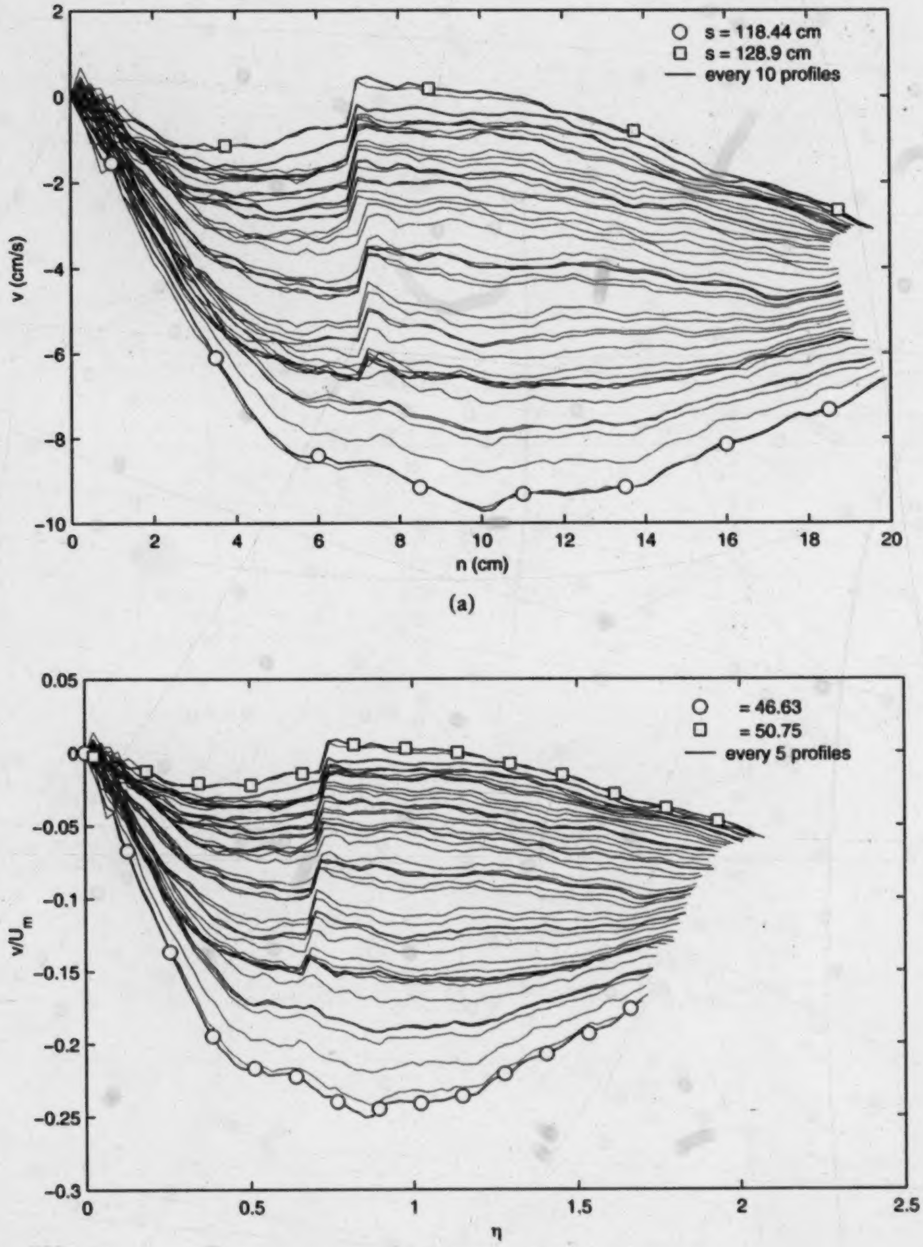

(a)

(b)

Figure 5.71: (a) Dimensional and (b) nondimensional v mean velocities for surface jet-like (SJL) profiles.

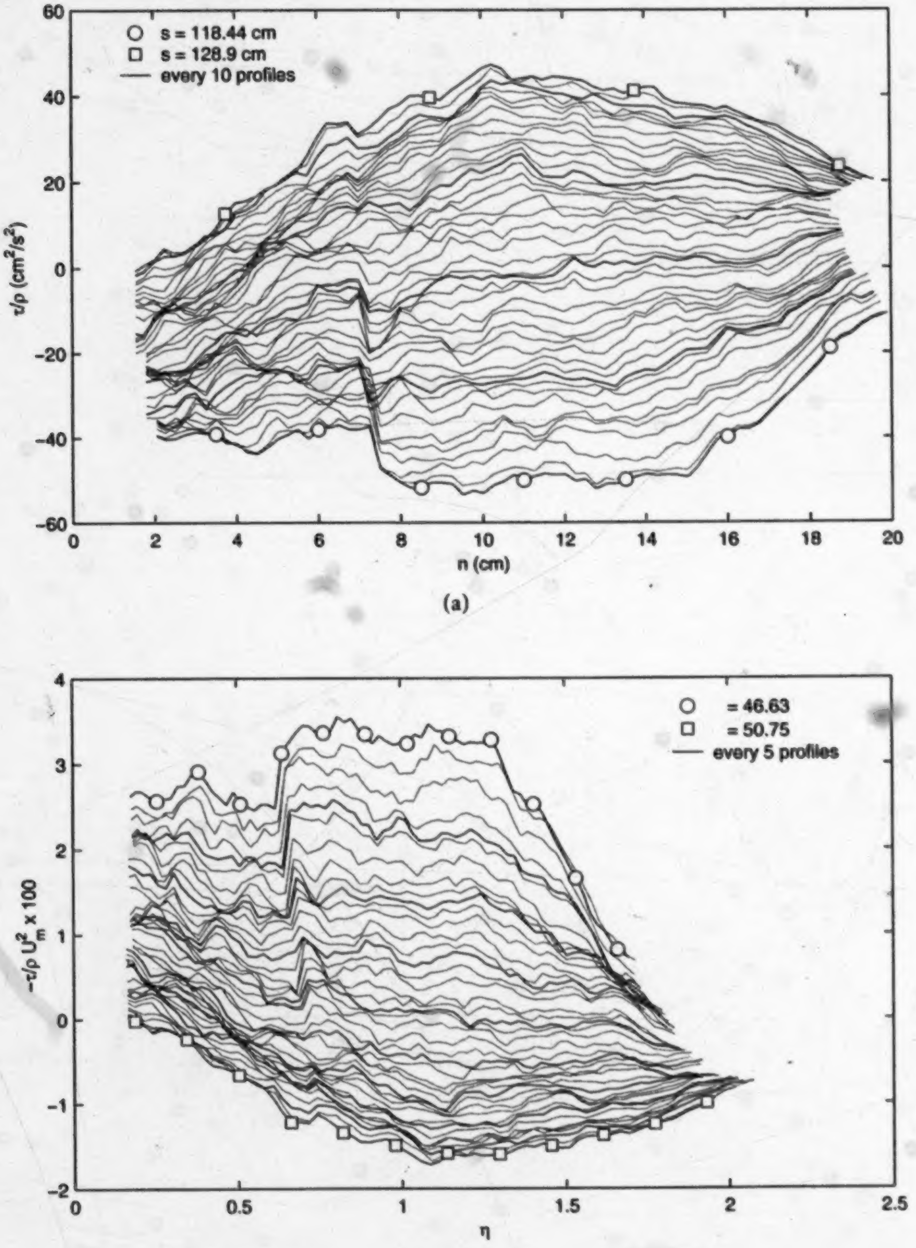

(a)

(b)

Figure 5.72: (a) Dimensional and (b) nondimensional mean Reynolds stress per unit mass (τ/ρ) for surface jet-like (SJL) profiles.

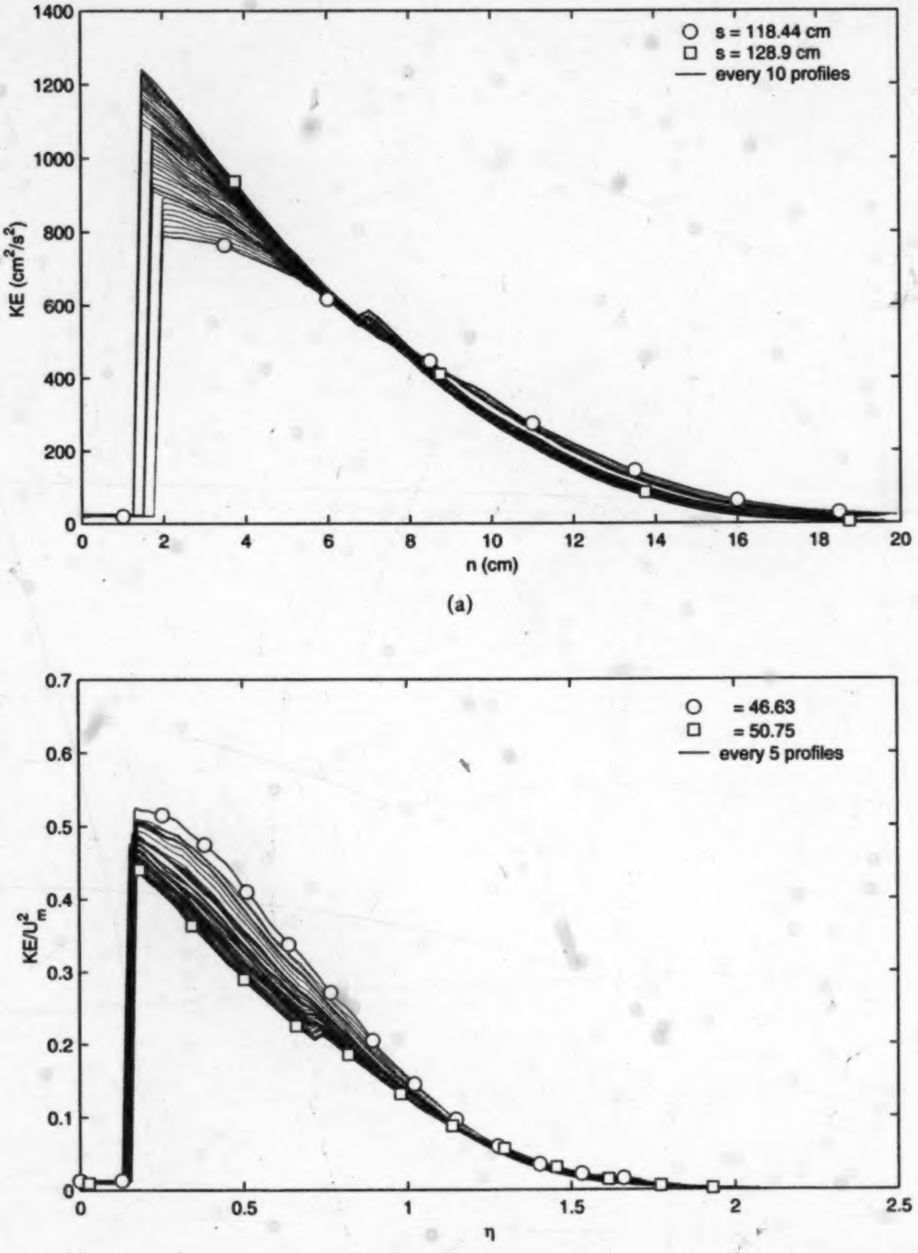

(b)

Figure 5.73: (a) Dimensional and (b) nondimensional mean kinetic energy per unit mass (KE) for surface jet-like (SJL) profiles.

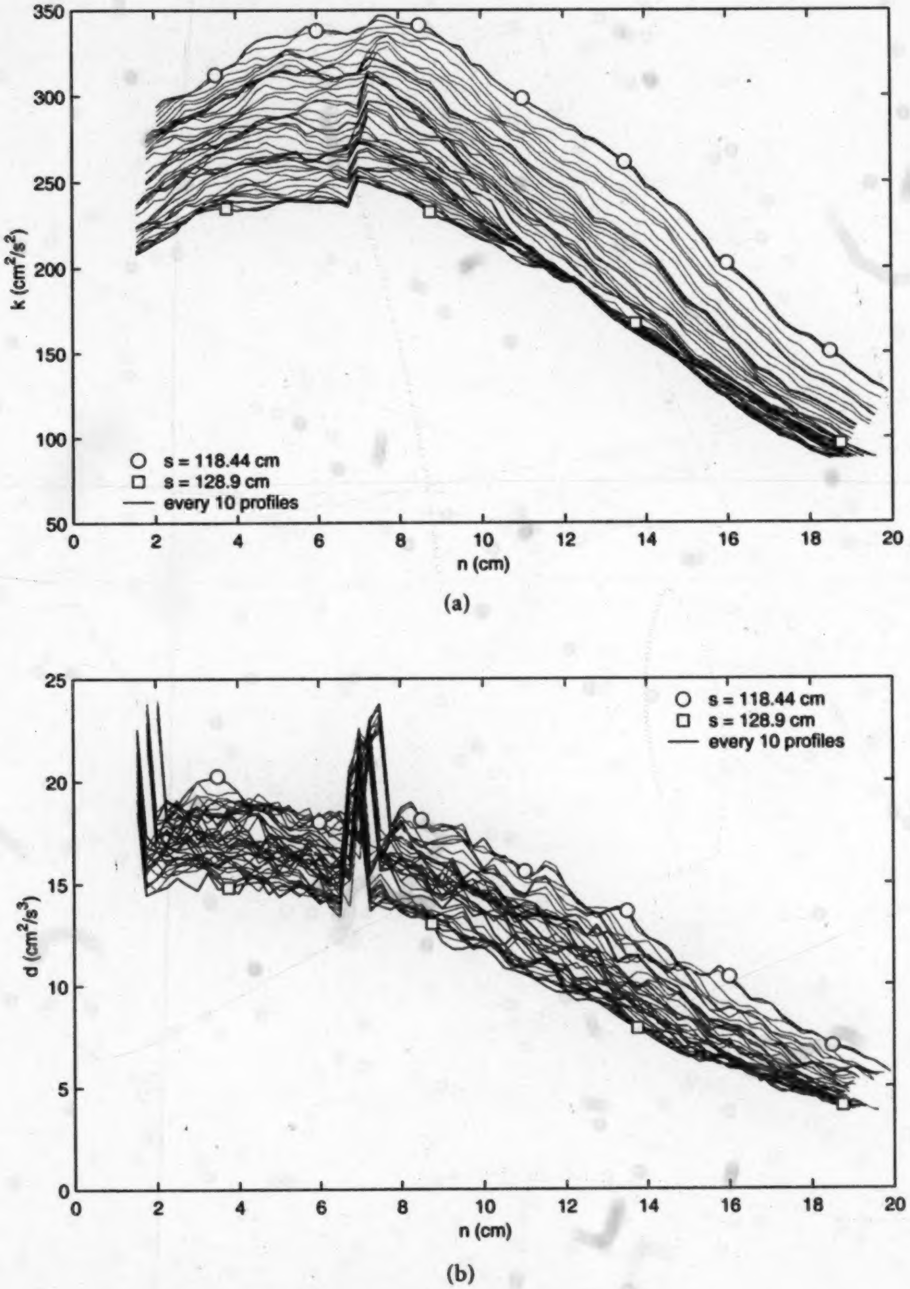

(a)

(b)

Figure 5.74: Mean (a) turbulent kinetic energy per unit mass (k) and (b) dissipation per unit mass (d) for surface jet-like (SJL) profiles.

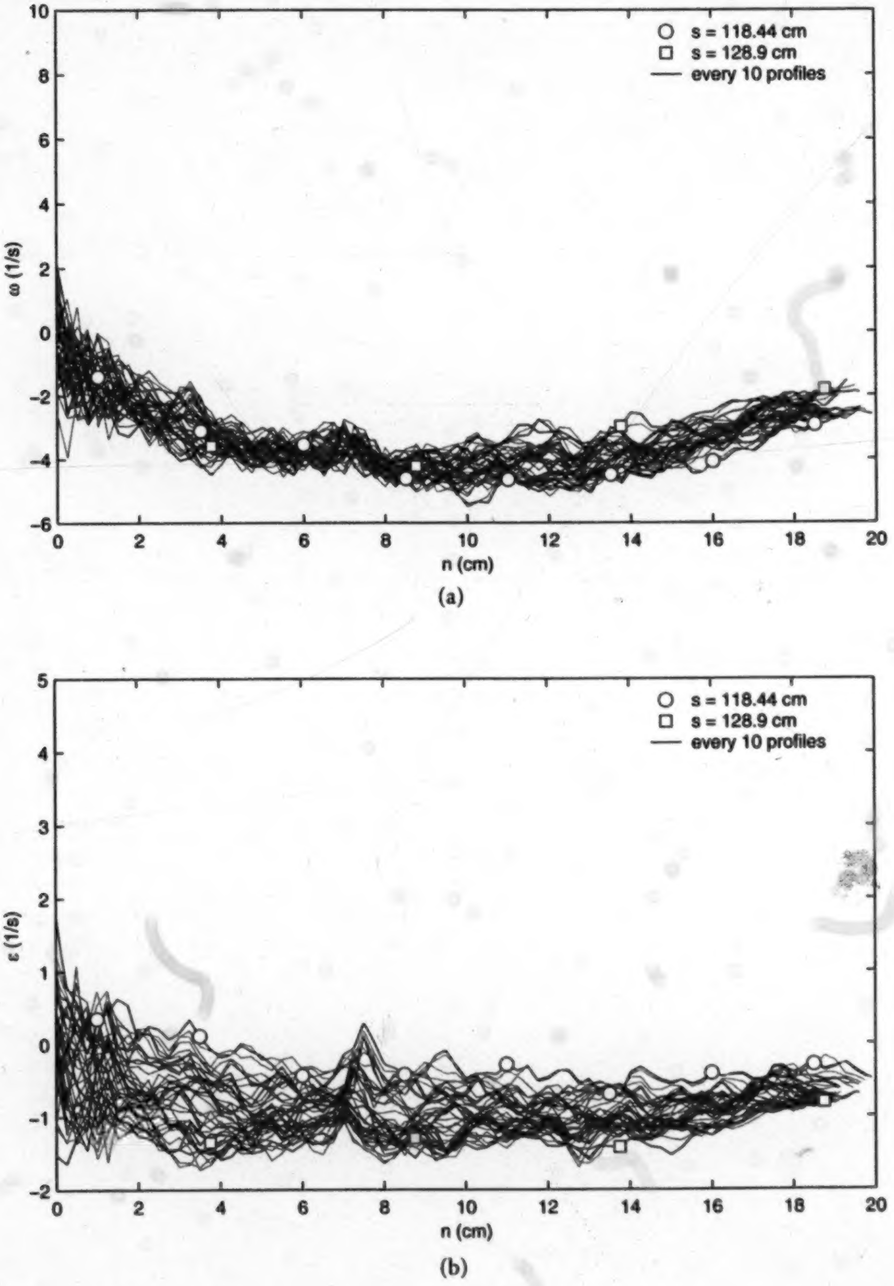

(a)

(b)

Figure 5.75: Mean (a) vorticity (ω) and (b) strain (ε) for surface jet-like (SJL) profiles.

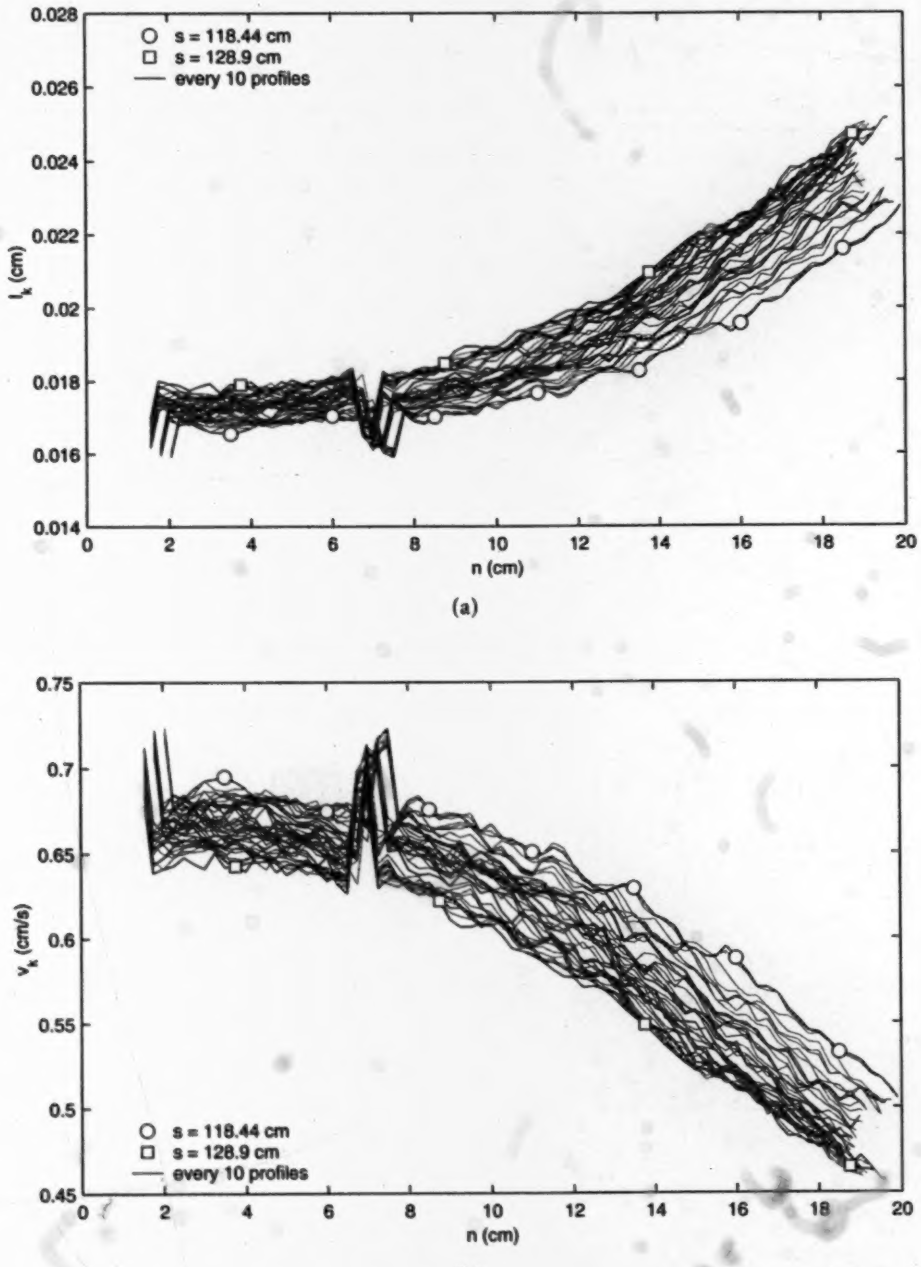

(a)

(b)

Figure 5.76: Mean Kolmogorov (a) length scales (l_k) and (b) velocity scales (v_k) for surface jet-like (SJL) profiles.

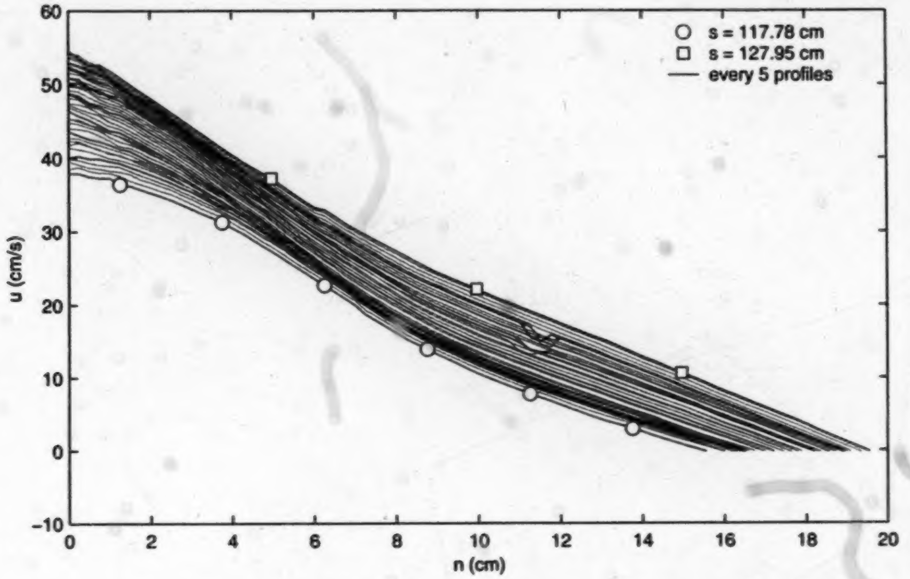

(a)

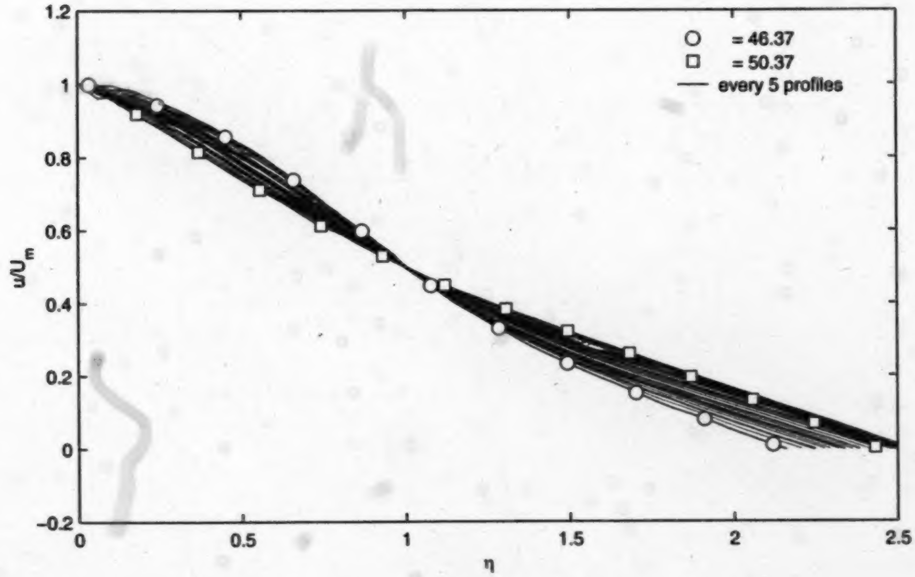

(b)

Figure 5.77: (a) Dimensional and (b) nondimensional u mean velocities for return flow surface jet-like (SJL) profiles.

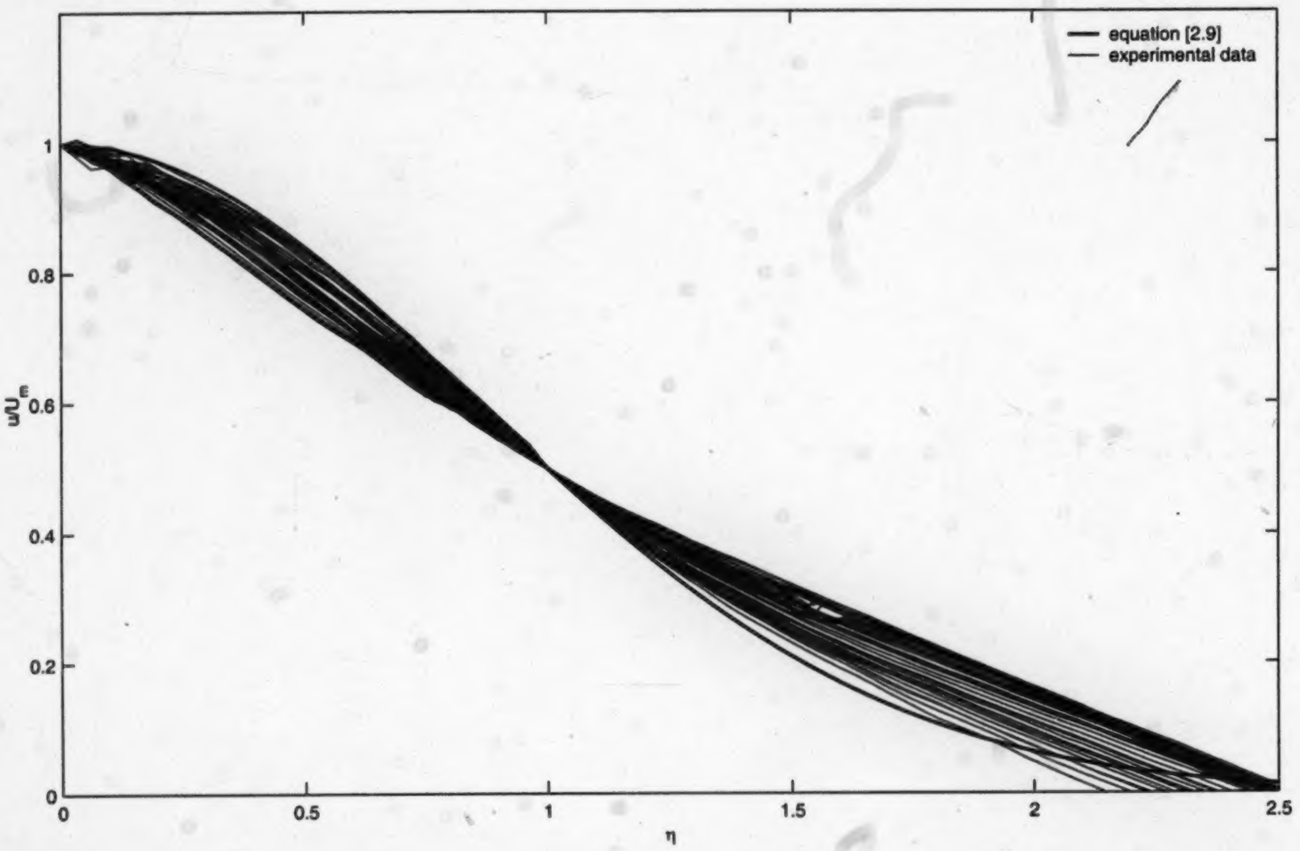

Figure 5.78: Variation of u/U_m with η for return flow surface jet-like (SJL) profiles with equation [2.9] plotted for reference.

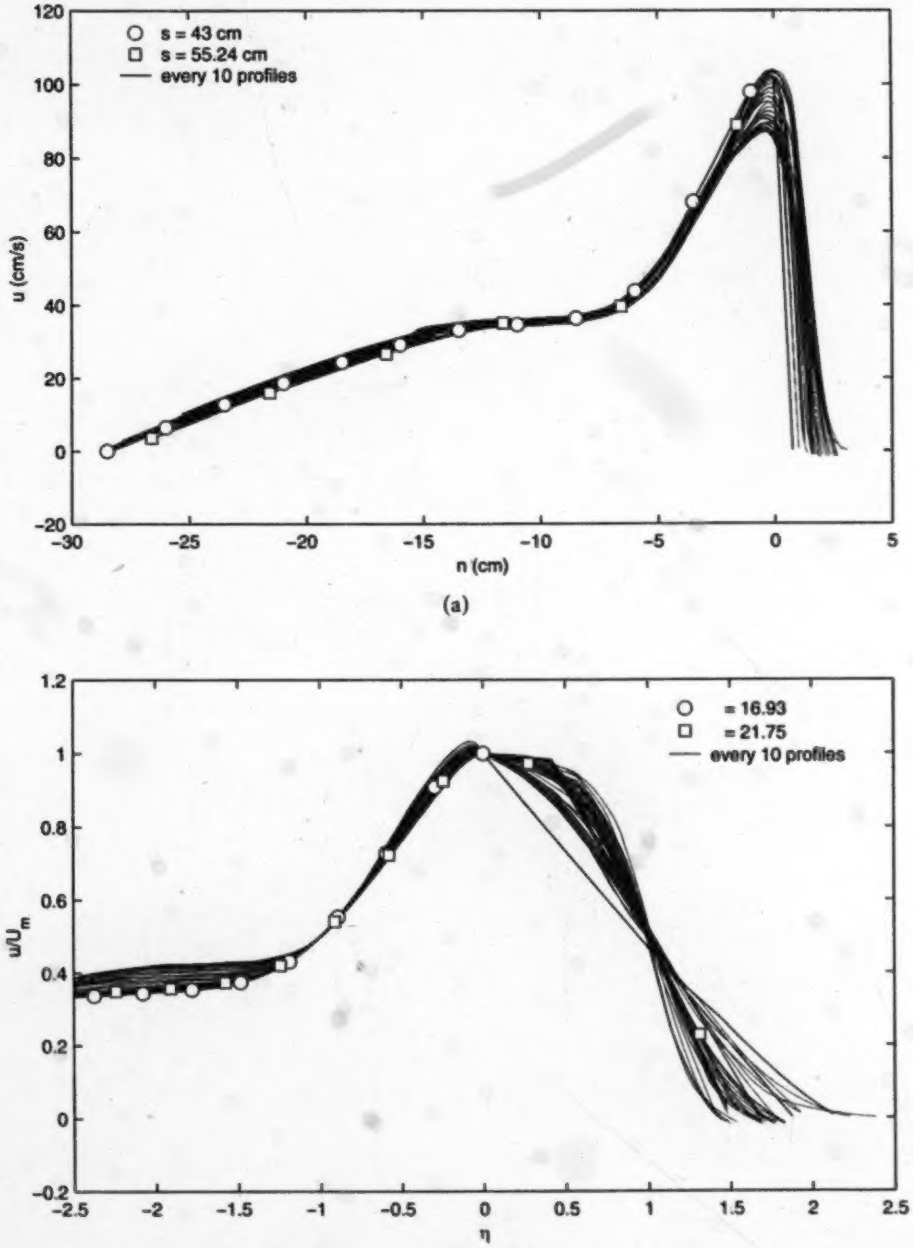

(a)

(b)

Figure 5.79: (a) Dimensional and (b) nondimensional u mean velocities for the first transition zone (TZ1) profiles.

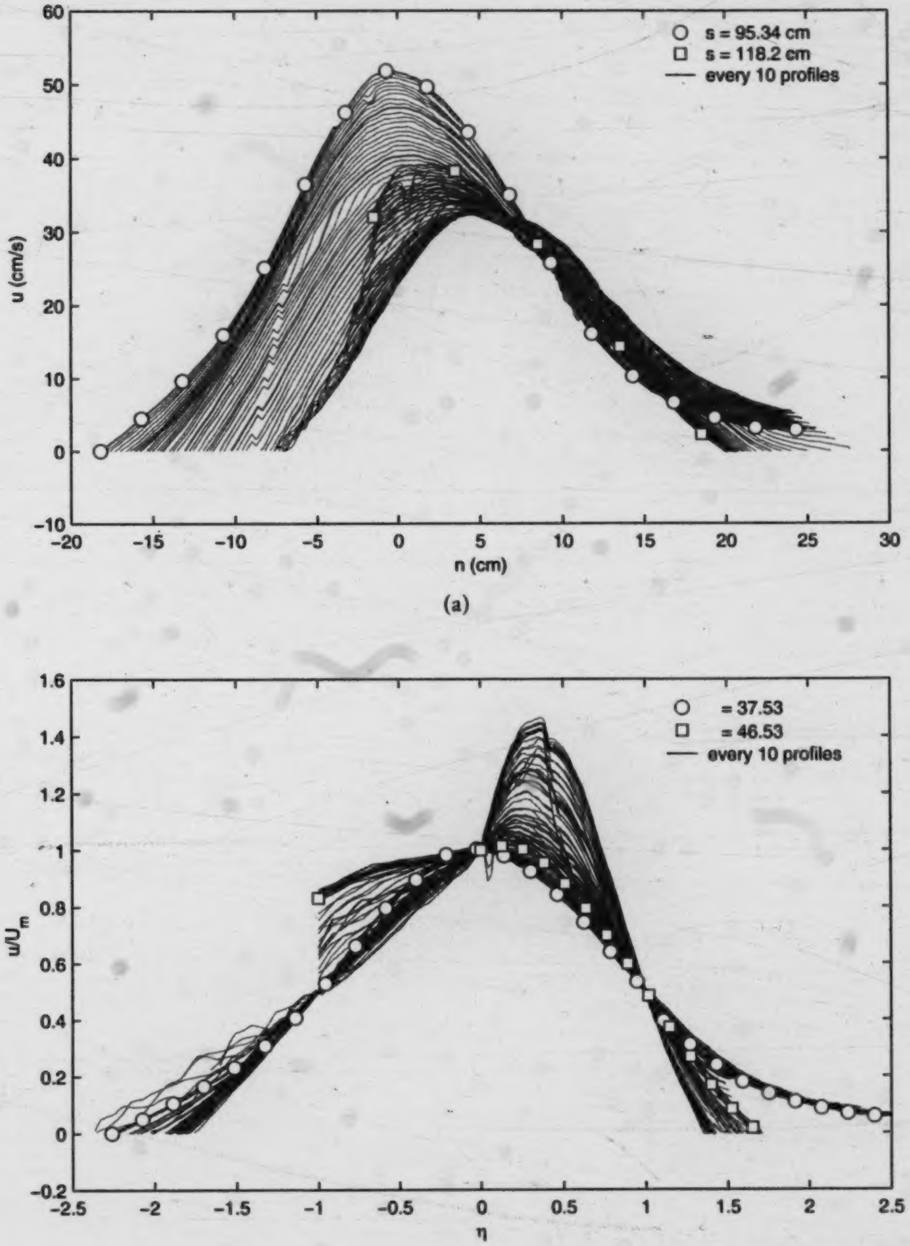

(a)

(b)

Figure 5.80: (a) Dimensional and (b) nondimensional u mean velocities for the second transition zone (TZ2) profiles.

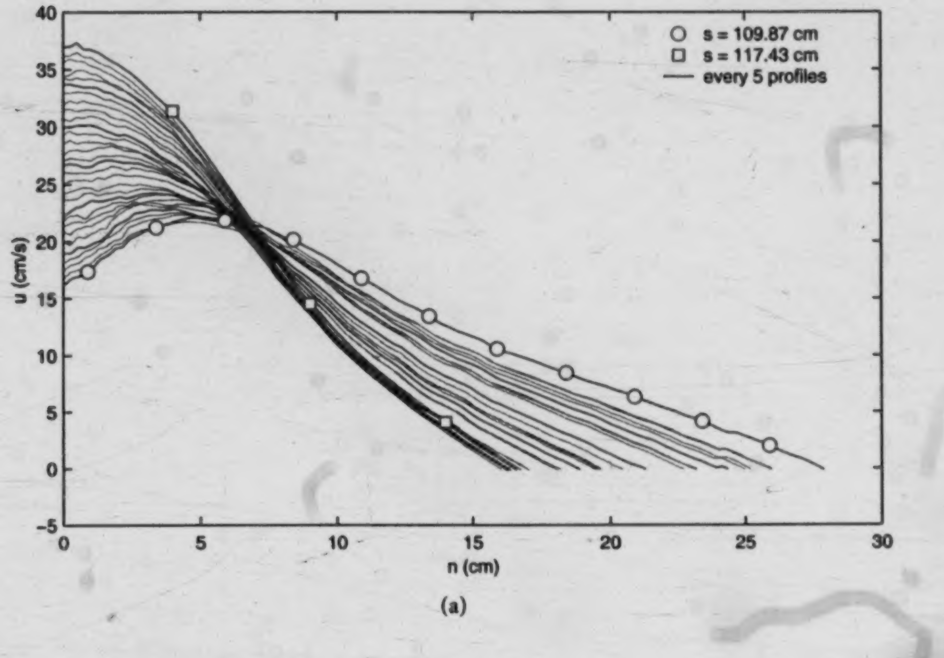

Figure 5.81: (a) Dimensional and (b) nondimensional u mean velocities for the return flow second transition zone (TZ2) profiles.

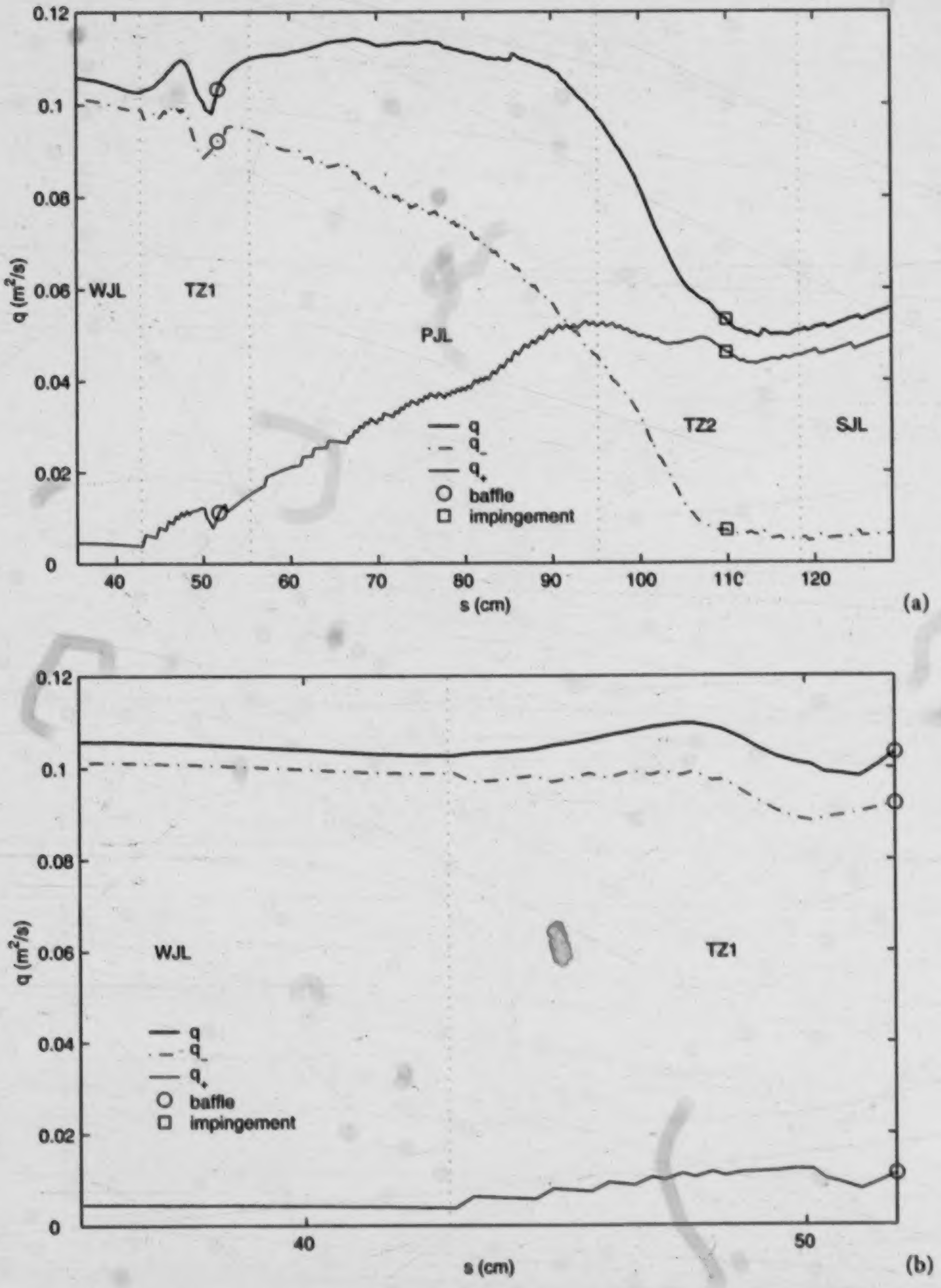

Figure 5.82: Variation of q with s over (a) the full jet trajectory and over (b-d) the sections upstream of the baffle, between the baffle and the point of impingement and downstream of the point of impingement, respectively.

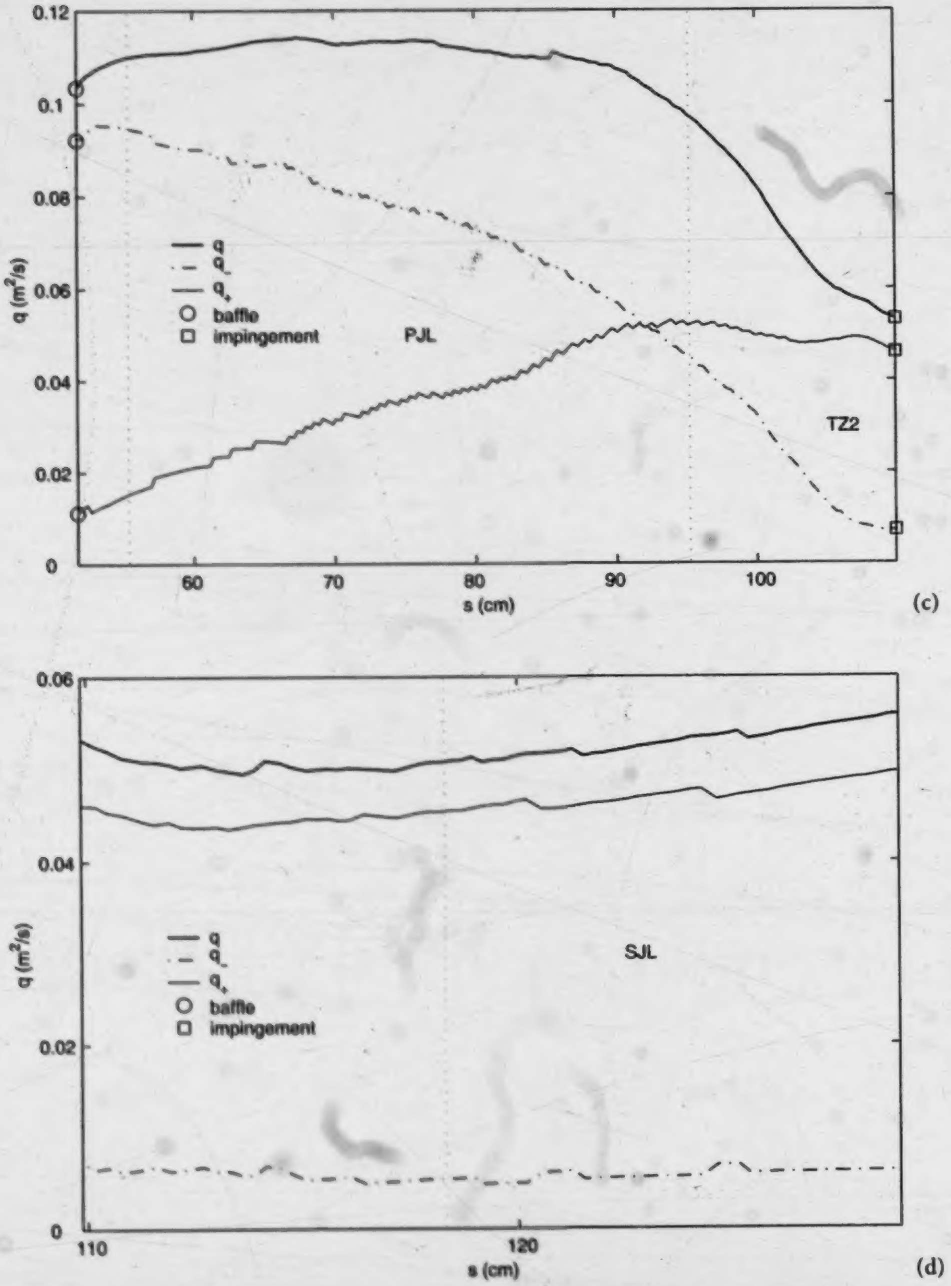

Figure 5.82: Variation of q with s over (a) the full jet trajectory and over (b-d) the sections upstream of the baffle, between the baffle and the point of impingement and downstream of the point of impingement, respectively.

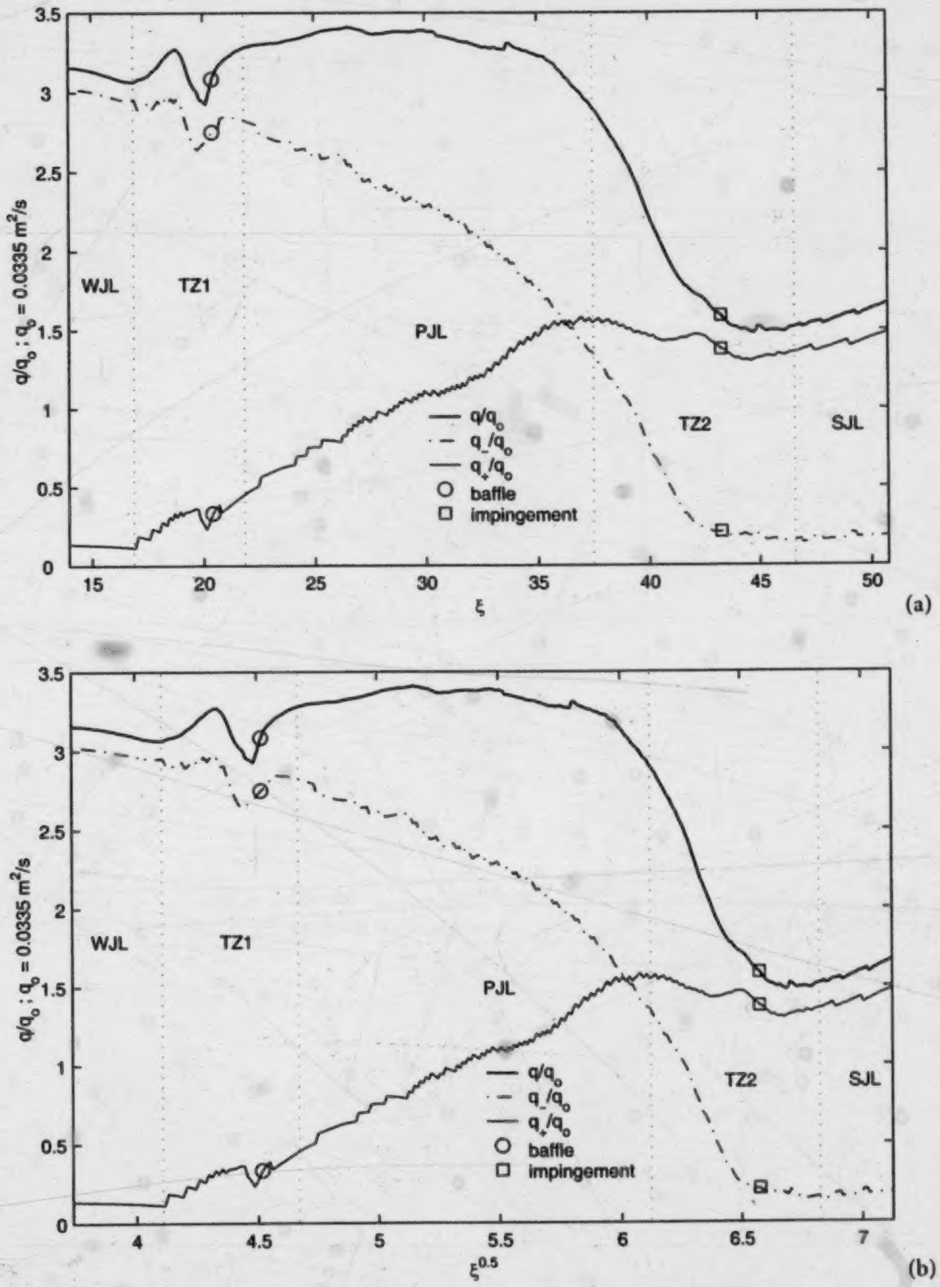

Figure 5.83: Variation of (a) q/q_o with ξ and of (b) q/q_o with $\xi^{0.5}$ along the full jet trajectory.

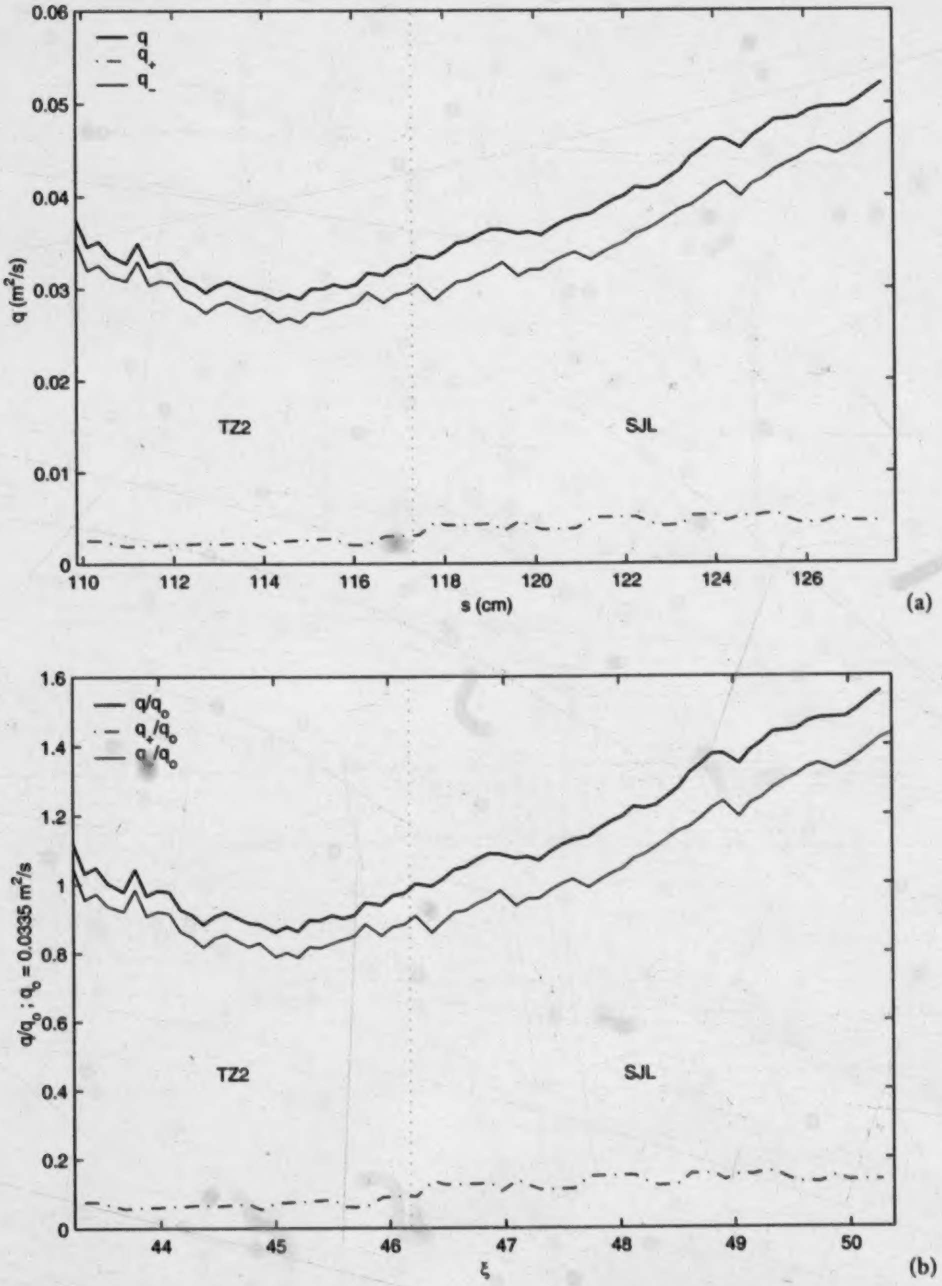

Figure 5.84: Variation of (a) q with s and of (b) q/q_o with ξ along the full return flow jet trajectory.

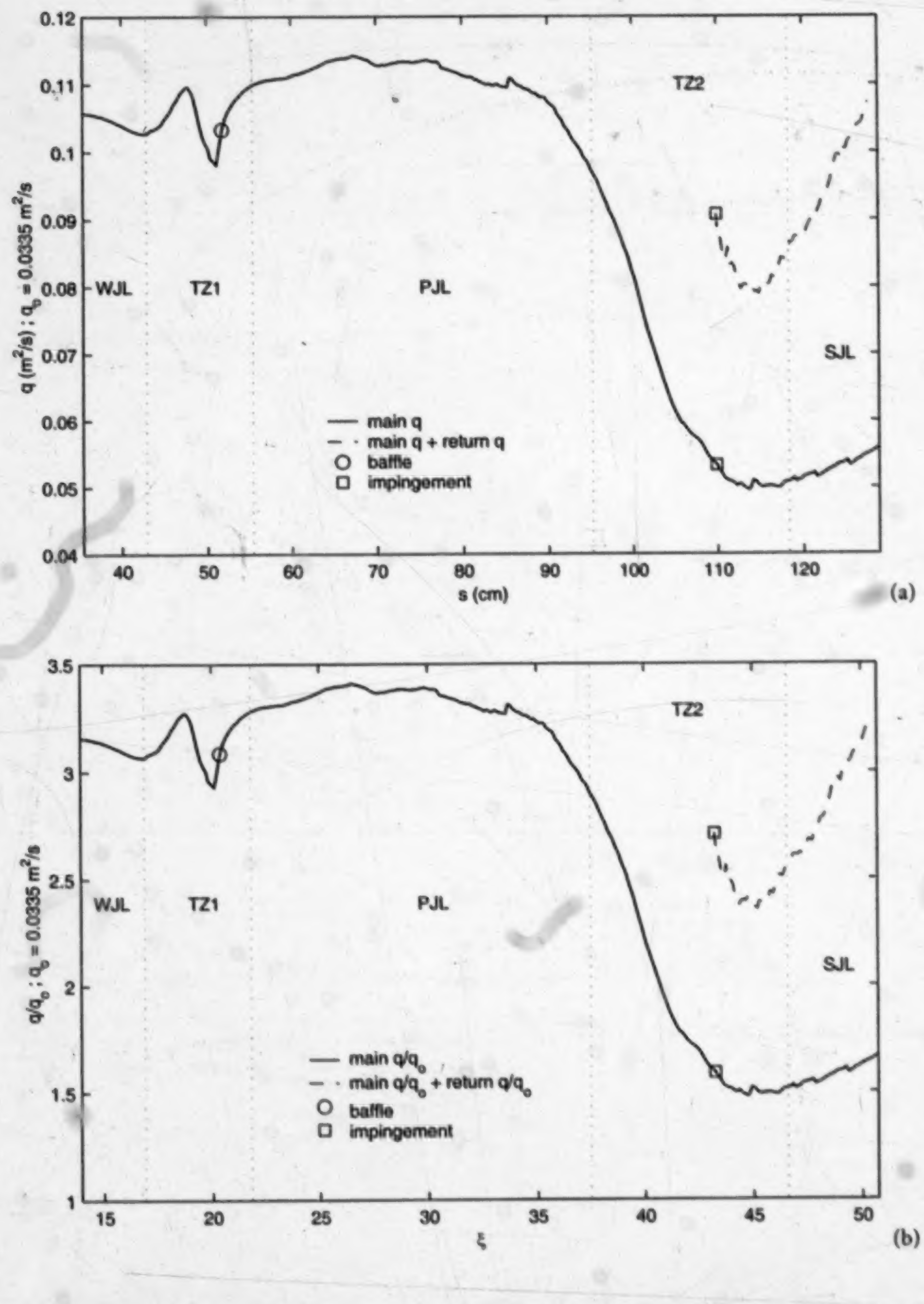

Figure 5.85: Variation of (a) q with s and of (b) q/q_o with ξ along the full jet trajectory for both the main flow and the return flow components of the jet.

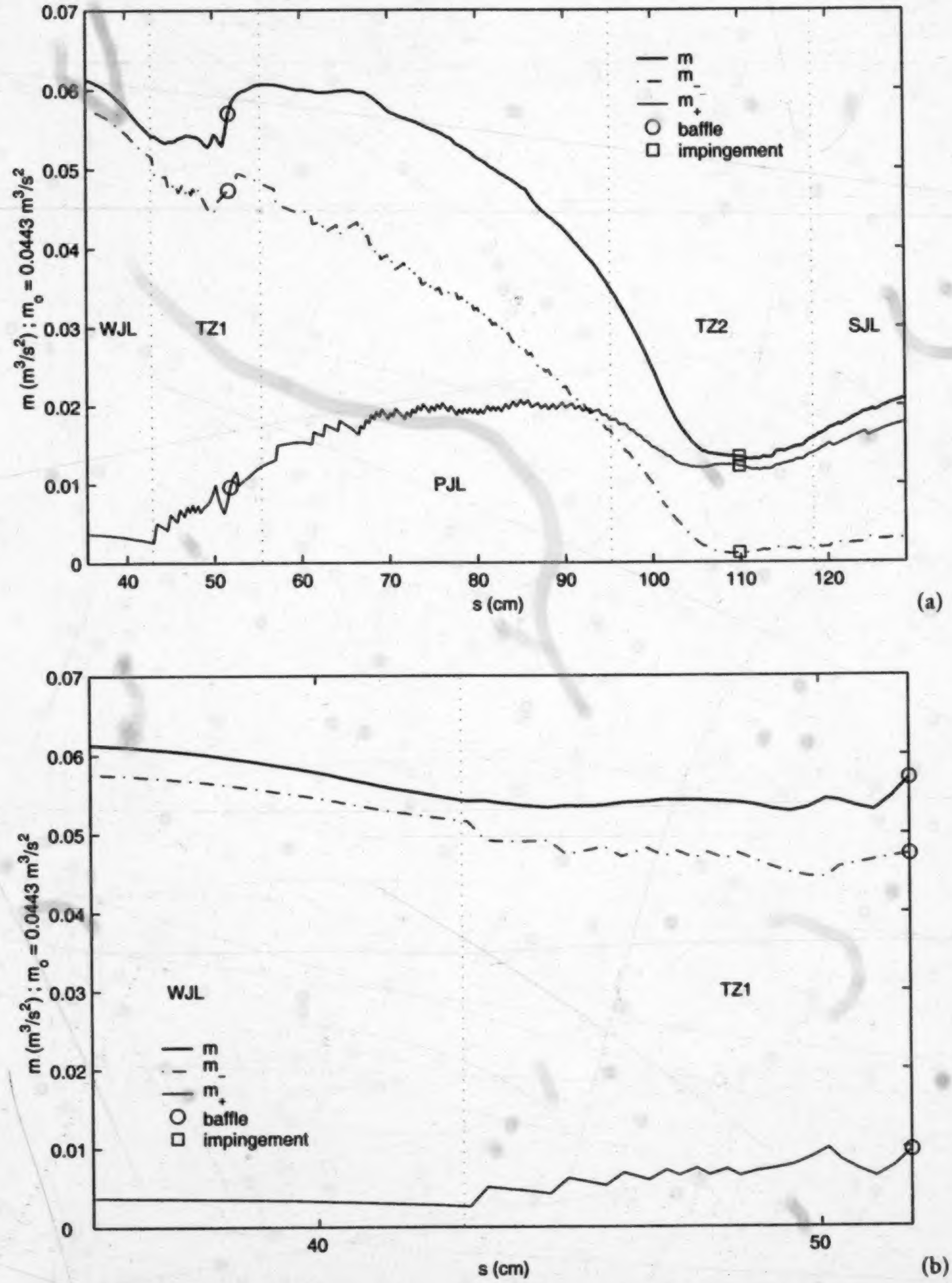

Figure 5.86: Variation of m with s over (a) the full jet trajectory and over (b-d) the sections upstream of the baffle, between the baffle and the point of impingement and downstream of the point of impingement, respectively.

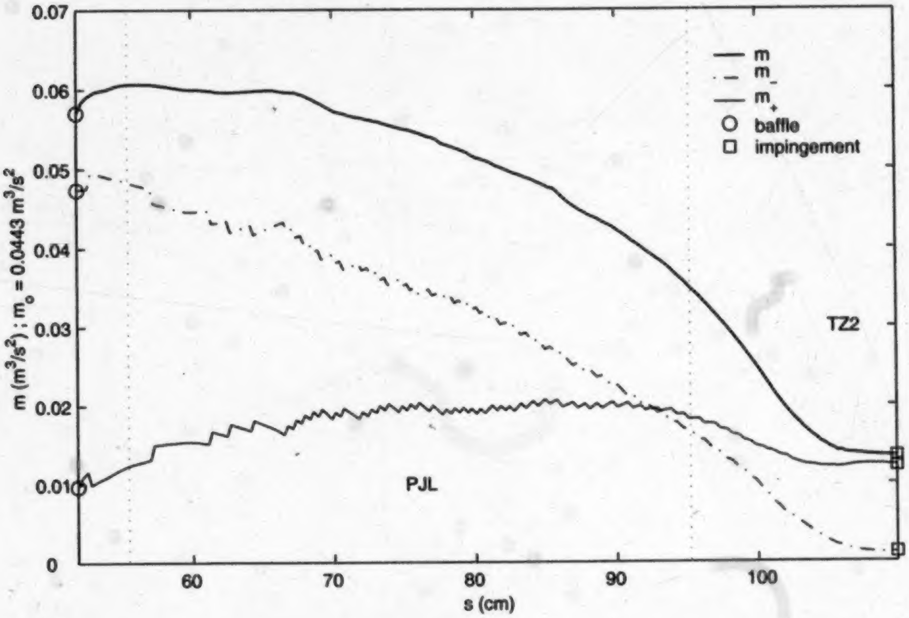

(c)

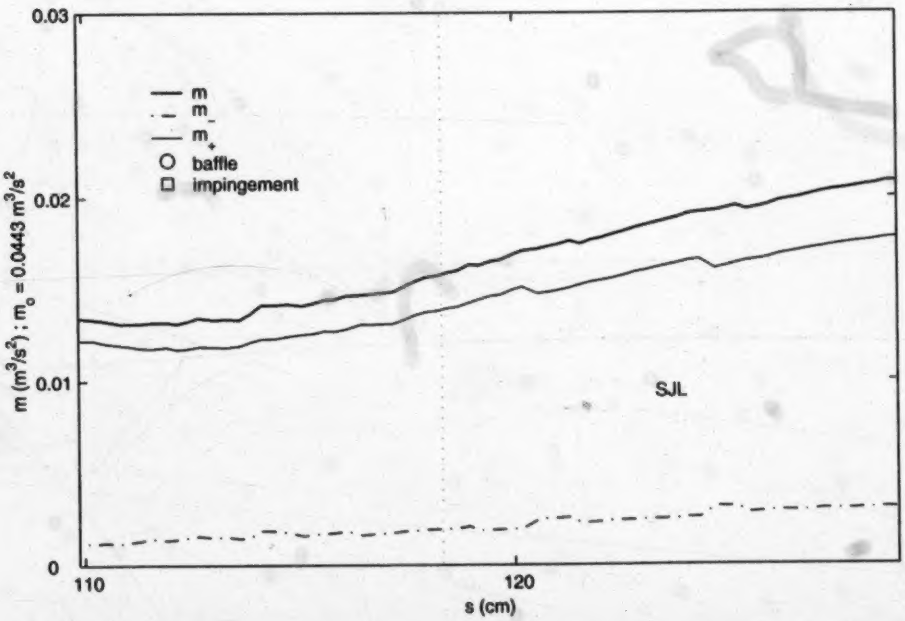

(d)

Figure 5.86: Variation of m with s over (a) the full jet trajectory and over (b-d) the sections upstream of the baffle, between the baffle and the point of impingement and downstream of the point of impingement, respectively.

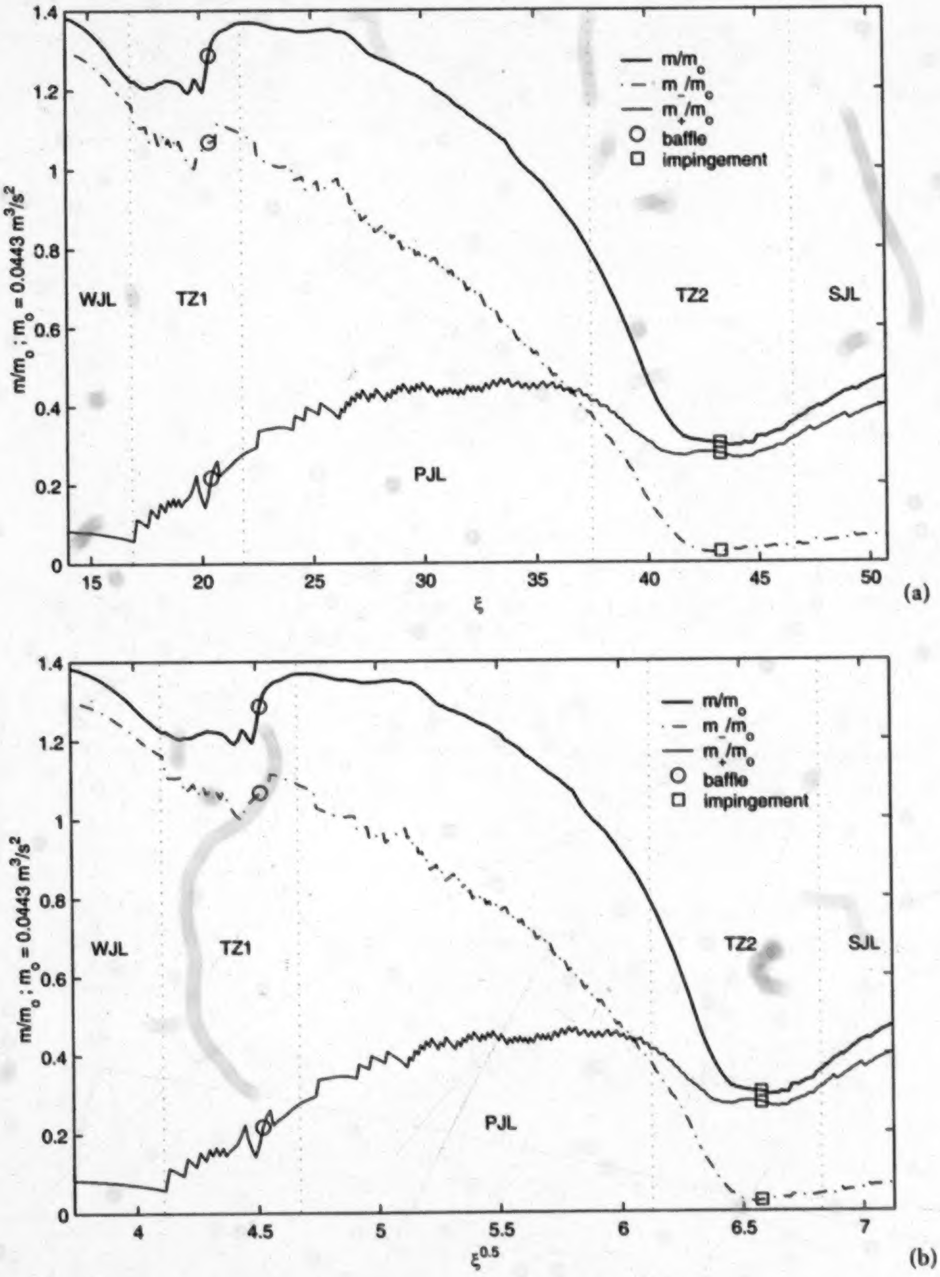

Figure 5.87: Variation of (a) m/m_o with ξ and of (b) m/m_o with $\xi^{0.5}$ along the full jet trajectory.

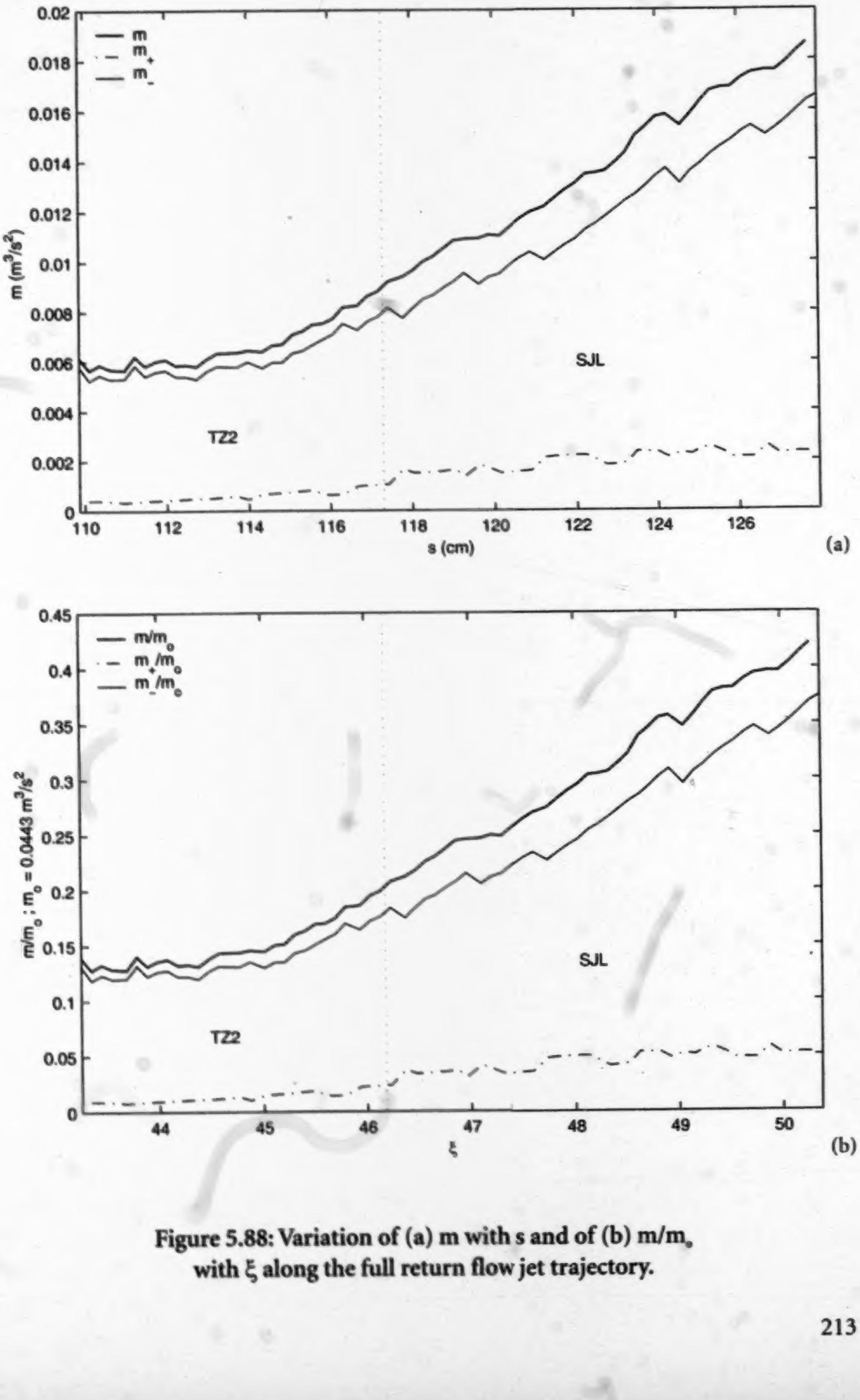

Figure 5.88: Variation of (a) m with s and of (b) m/m_o with ξ along the full return flow jet trajectory.

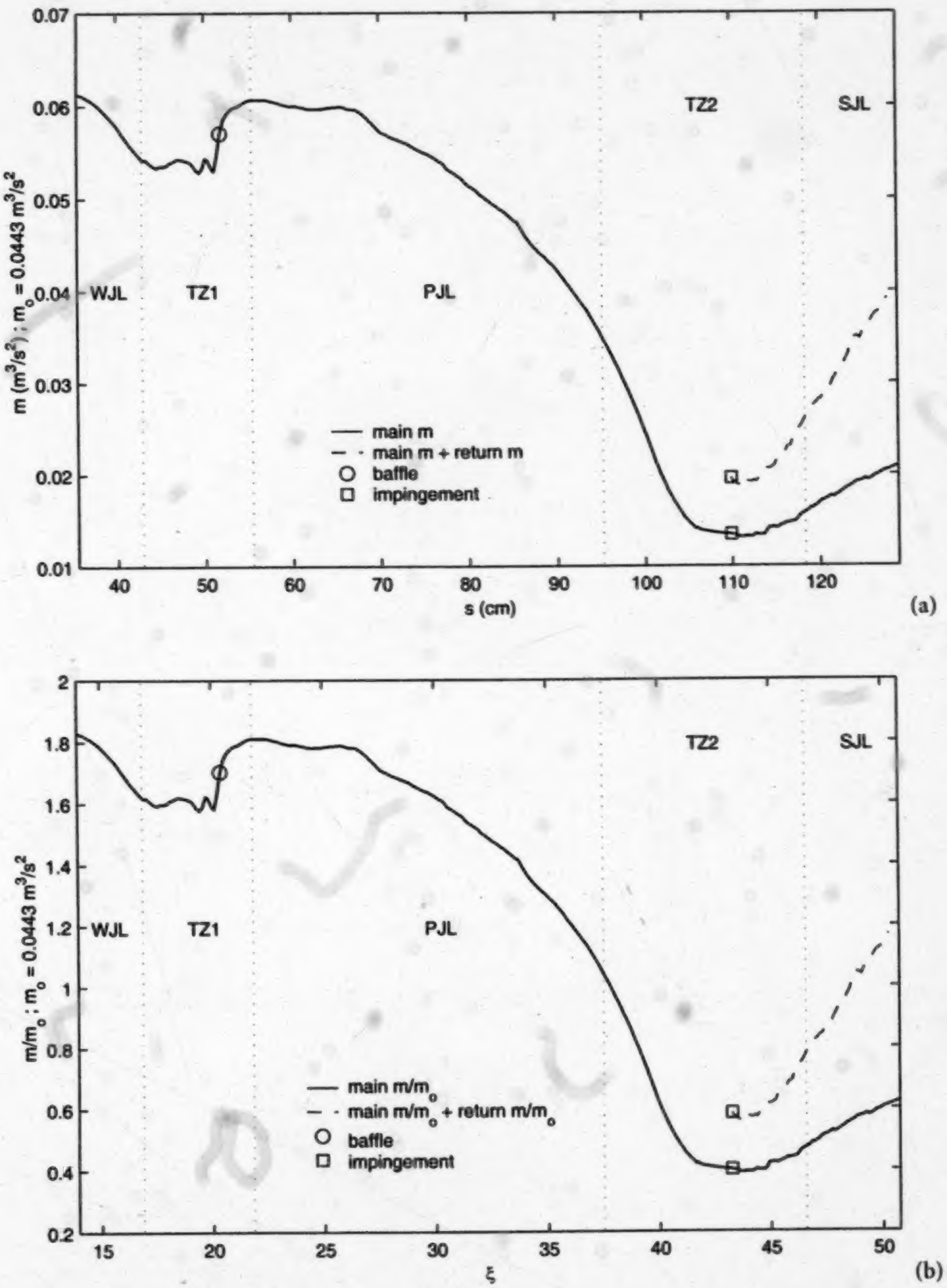

Figure 5.89: Variation of (a) m with s and of (b) m/m$_o$ with ξ along the full jet trajectory for both the main flow and the return flow components of the jet.

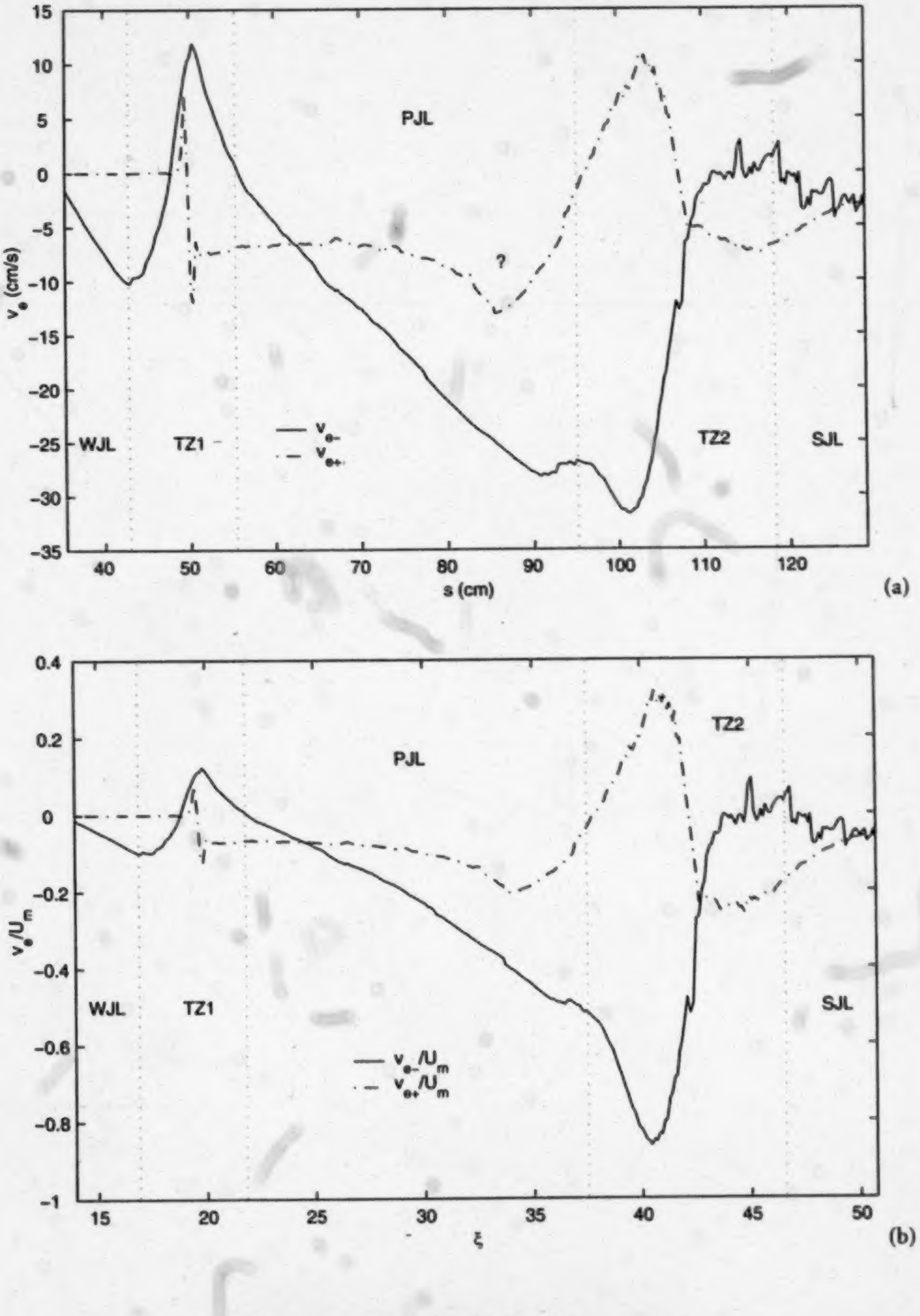

Figure 5.90: Variation of (a) v_e with s and of (b) v_e/U_m with ξ along the full jet trajectory.

6 Conclusion

A plane deflected wall jet is defined by Wu and Rajaratnam (1995a) as the flow structure in which a baffle wall is employed to deflect a plane wall jet in such a way that it travels upward as a plane turbulent jet to eventually become a plane surface jet at the free surface. Preceding this current work, the only investigation of this phenomenon was conducted by Wu and Rajaratnam (1995a); time averaged velocity and pressure data were collected using standard point measurement techniques. The purpose of this work was to conduct further research and to collect more detailed mean and turbulent experimental data using the particle image velocimetry (PIV) technique. The following flow parameters were calculated: instantaneous, mean and turbulent flow properties including: u and v velocities, kinetic energy per unit mass, Reynolds stress per unit mass, turbulent kinetic energy per unit mass, dissipation rate per unit mass, vorticity, strain, Kolmogorov length scales and Kolmogorov velocity scales. The division of a large area of interest into smaller fields of view, and the unusual procedure of assembling the individual PIV tesserae into one large mosaic is also discussed.

6.1 Experimental Observations

The description of the mean flow pattern of the deflected wall jet provided by Wu and Rajaratnam was confirmed by the whole-field mean velocity vector maps and the colour contour maps of the calculated flow parameters. A wall jet-like (WJL) flow closely follows along the wall before reaching the baffle. After the baffle, the flow deflects becomes plane jet-like (PJL) and is deflected along a curvilinear trajectory toward the water surface. The vector maps show that the jet divides into two surface jet-like (SJL) flows, one continuing downstream along the water surface and one returning upstream. The strength of the jet decays with distance along the trajectory and three eddies were identified. The large eddy of counter-clockwise rotation, found on the inbound side of the trajectory, dominates the flow in the inbound region and acts as a region of solid-body rotation with a generally constant mean vorticity and circulation. A small eddy of clockwise rotation lies directly upstream of the baffle and has a diameter on the same order as the baffle height. The third eddy is weaker than the others, and is found on the outbound side of the jet trajectory.

The mean kinetic energy per unit mass decays along the trajectory and decreases with distance from the centreline on both sides of the jet. A zone of high KE occurs along the flume bed and upstream of the baffle. The locus of highest mean Reynolds stress per unit mass is not coincident with the jet centreline trajectory; although the two are generally parallel, the $(\tau/\rho)_{max}$ locus is found on the outbound side of the trajectory. The largest positive mean Reynolds stress values can be found in four concentrated pockets, located where the deflected jet transitions between constitutive jet flow regimes. The magnitude of the mean turbulent kinetic per unit mass generally decreases as the jet progresses downstream; the location of maximum k occurs directly downstream of the baffle tip. The bulk of largest values of the rate of turbulent energy dissipation occur on the outbound side of the jet centreline trajectory, primarily in the curved plane jet-like region of flow. There is also significant dissipation concentrated in the wall-jet-like region of flow, directly upstream of the baffle.

The entire inbound region of flow has a relatively constant and small counter-clockwise rotation, while the outbound region of flow has a larger (by approximately two orders) and more varied clockwise rotation. Separating the two is the jet centreline, which is based on the locus of zero mean vorticity. The mean vorticity increases with distance from the centreline on either side, to a maximum somewhere inside the jet body, before decreasing to background levels. The most intense zone of positive mean vorticity lies along the jet trajectory in the WJL region and the adjacent TZ1 region. There is a constant production of counter-clockwise vorticity at the wall, which convects away from the jet axis towards the centre of the eddy. Almost all of the highly negative vorticity is generated directly at the tip of the baffle. Full sets of instantaneous vorticity data were converted into real-time movies for individual tesserae. The movies allowed for observation of vortex creation, advection, interaction, evolution and decay within a single FOV through time and clearly show the effects of the eddies on the vortical structures.

The jet centreline trajectory was identified via a zero vorticity criterion. The variation of parameters along the centreline was studied. U_m was observed to decay along the trajectory, except in the transition zones. U_m experienced temporary increases directly upstream of the baffle and in the TZ2 and SJL regions. The rate of decay in the WJL region was similar to the value observed by previous investigators, however, in the PJL region it was much larger. Discharge intensity and momentum flux varied similarly and confirmed both division of the main flow into two surface jet-like flows and the decay of momentum flux.

Profiles were extracted from the PIV data set for all previously calculated flow parameters, and taken perpendicular to U_m using the angle θ_c. The data was non-dimensionalized using the standard scales of jet half-width (δ_1) and the centreline velocity component (U_m). Similarity was observed for u in the WJL, PJL and SJL regions. The effect of the large inbound eddy skewed the u velocity profiles in the WJL and SJL regions and the nondimensional curves diverged from theory and previous experimental results. The v velocity component did not display a great degree of similarity, especially in the inbound flow region. The other flow parameters displayed varying degrees of similarity, however there exists no other turbulent plane deflected wall jet data to use for comparison. Generally, turbulent kinetic energy, dissipation and vorticity were concentrated inside the jet body or mixing region and decayed with distance along the trajectory. Results in the transition zones did not display a great degree of similarity, and exposed potential flaws in the centreline definition and identification scheme.

6.2 Future Considerations

The present study has shown that the PIV technique can be successfully applied to the plane deflected wall jet; the analyses developed for this thesis can and should be applied to future studies of the plane deflected wall jet. Comparing the data for experiments employing different baffle heights, slot widths, tailwaters and Froude numbers may reveal if the phenomenon exhibits its own unique similarity and if the flow can be further simplified. The energy dissipating potential of the plane deflected wall jet can only be generalized through the study of more cases and under varying conditions.

Both the quality and the efficiency of the analyses can also be improved for future work. It is recommended that the overlap between tesserae be increased if more experiments are conducted, so that the effects of edge dislocations are minimized. A more accurate alignment apparatus (perhaps one that is mechanized and automated) is required for increased spatial accuracy, as well as better quality camera lenses to avoid optical distortion at the corners of the individual PIV images. Although the mosaic method introduced in this study has proven to be successful, it would be beneficial to use cameras with larger fields of view, or multiple cameras working in tandem. The experimental programme would require less time to complete, and instantaneous properties could be studied over larger areas with the same resolution.

Planar illumination from different angles should be further investigated so that the shadow defect at the baffle can be minimized. It was inconvenient to wrestle with data exclusion zones. More rigorous investigation of the flow area directly below the water surface, with algorithms to identify and disregard individual surface reflections would also aid in future experiments. It would be beneficial to spend more effort in developing procedures to determine the optimum laser timing separations. This would lessen the necessity for multiple preliminary experiments, as well as maximize the available dynamic ranges of each of the tesserae and reduce potential peak locking and dislocation error.

Faster processing schemes would greatly benefit future PIV investigations of the plane deflected wall jet. It would be convenient if data quality could be validated immediately and if the processing itself was less time consuming. An iterative process to identify the jet centreline is also recommended for future work, as the potential flaws in the trajectory were directly responsible for the lack of confidence in the transition flow region centreline and profile data. It may be helpful to start with the zero vorticity criterion, extract profile data and then redefine the trajectory using the locus of maximum velocities in the local profile coordinate axes.

7 References

Agüí, J.C. and Jiménez, J. 1987 On the performance of particle tracking. *Journal of Fluid Mechanics*, 185, 447-468.

Albertson, M.L., Dai, Y.B., Jensen, R.A. and Rouse, H. 1950 Diffusion of submerged jets. *Transactions of the American Society of Civil Engineers*, 115, 639-664.

Chang, K.A. and Liu, P.L. 2000 Pseudo turbulence in PIV breaking-wave measurements. *Experiments in Fluids*, 29, 331-338.

Corrsin, S. 1943 Investigation of flow in an axially symmetrical heated jet or air. National Advisory Committee for Aeronautics, Washington, Wartime Report no. W-94.

Cowen, E.A. and Monismith, S.G 1997 A hybrid digital particle tracking velocimetry technique. *Experiments in Fluids*, 22, 199-211.

Dabiri, D. and Gharib, M. 1997 Experimental investigation of the vorticity generation within a spilling water wave. *Journal of Fluid Mechanics*, 330, 113-139.

Doron, P., Bertuccioli, L., Katz, J. and Osborn, T.R. 2001 Turbulence characteristics and dissipation estimates in the coastal ocean bottom boundary layer from PIV data. *Journal of Physical Oceanography*, 31, 2108-2134.

Ead, S.A. 1999 Plane turbulent jets in shallow tailwater and their application to energy dissipation. Ph.D. Thesis, University of Alberta.

Ead, S.A. and Rajaratnam, N. 2001 Plane turbulent surface jets in shallow tailwater. *Journal of Fluids Engineering*, 123 (March), 121-127.

Fincham, A. and Delerce, G. 2000 Advanced optimization of correlation imaging velocimetry algorithms. *Experiments in Fluids* (Supplement), S13-S22.

Fincham, A.M. and Spedding, G.R. 1997 Low cost, high resolution DPIV measurement of turbulent fluid flow. *Experiments in Fluids*, 23, 449-462.

Förthmann, E. 1934 Über turbulente strahlausbreitung. *Ingenieur-Archiv*, 5, 42-54.

Glauert, M.B. 1956 The wall jet. *Journal of Fluid Mechanics*, 1, 625-643.

Goldschmidt, V. and Eskinazi, S. 1966 Two-phase turbulent flow in a plane jet. *Journal of Applied Mechanics*, 33 (4), 735-747.

Görtler, H. 1942 Berechnung von aufgaben der freien turbulenz auf grund eines neuen naherungsansatzes. *Zeitschrift für anngewandte Mathematik und Mechanik*, 22, 244-254.

Govinda Rao, N.S. and Rajaratnam, N. 1963 The submerged hydraulic jump. *Journal of the Hydraulics Division*, Proceedings of the American Society of Civil Engineers, 89 (1), 139-162.

Hasselbrink, E.F. and Mungal, M.G. 2001a Transverse jets and jet flames. Part 1. Scaling laws for strong transverse jets. *Journal of Fluid Mechanics*, 443, 1-25.

Hasselbrink, E.F. and Mungal, M.G. 2001b Transverse jets and jet flames. Part 2. Velocity and OH field imaging. *Journal of Fluid Mechanics*, **443**, 27-68.

Heskestad, G. 1965 Hot-wire measurements in a plane turbulent jet. *Journal of Applied Mechanics*, 32 (4), 721-734.

Kotsovinos, N.E. 1978 A note on the conservation on axial momentum of turbulent jets. *Journal of Fluid Mechanics*, 87 (7), 55-63.

Kotsovinos, N.E. 1975 A study of the entrainment and turbulence in plane bouyant jet. W.M. Keck Laboratory of Hydraulics and Water Resources, California Institute of Technology, Technical Report no. KH R-32.

Lourenço, L.M. 1996 Particle image velocimetry. *Particle Image Velocimetry*. von Karman Institute for Fluid Dynamics, Lecture series 1996-03.

Marxen, M. 1998 Particle Image Velocimetry in Strömungen mit starken Geschwindigkeitsgradienten. Diplomarbeit, Fakultät für Physik und Astronomie, Ruprecht-Karls-Universität Heidelberg.

Miller, D.R. and Comings, E.W. 1957 Static pressure distribution in the free turbulent jet. *Journal of Fluid Mechanics*, 3 (10), 1-16.

Myers, G.E., Schauer, J.J. and Eustis R.H. 1963 Plane turbulent wall jet flow development and friction factor. *Journal of Basic Engineering*, Proceedings of the American Society of Mechanical Engineers, March, 47-53.

Naib, S.K.A. 1992 Diffusion of the sluice way jet. Jet Mechanics and Hydraulic Structures. Ashmead Press, London, 108-114.

Nogueira, J., Lecuona, A. and Rodríguez, P.A. 2001 Identification of a new source of peak locking, analysis and its removal in conventional and super-resolution PIV techniques. *Experiments in Fluids*, 30, 309-316.

Prasad, A.K., Adrian, R.J., Landreth, C.C. and Offutt, P.W. 1992 Effect of resolution on the speed and accuracy of particle image velocimetry interrogation. *Experiments in Fluids*, 13, 105-116.

Raffel, M., Willert, C.E. and Kompenhans, J. 1998 *Particle Image Velocimetry: A Practical Guide*. Springer-Verlag, Berlin.

Rajaratnam, N. 1995 Almanac of energy dissipation mechanisms. *Energy Dissipators*. A.A. Balkema, Rotterdam, 23-41. editors D.L. Vischer and W.H. Hager.

Rajaratnam, N. 1976 *Turbulent Jets*. Elsevier Scientific Publishing Company, The Netherlands.

Rajaratnam, N. 1965a Flow below a submerged sluice gate as a wall jet problem. *Proceedings of the Second Australasian Conference of Hydraulics and Fluid Mechanics*, Auckland.

Rajaratnam, N. 1965b Submerged hydraulic jump. *Journal of the Hydraulics Division*, Proceedings of the American Society of Civil Engineers, 91 (4), 71-96.

Rajaratnam, N. 1965c The hydraulic jump as a wall jet. *Journal of the Hydraulics Division*, Proceedings of the American Society of Civil Engineers, 91 (5), 107-132.

Rajaratnam, N. and Humphries, J. A. 1984 Turbulent non-bouyant surface jet. *Journal of Hydraulic Research*, 22 (2), 103-114.

Rajaratnam, N. and Subramanya, K. 1968 Plane turbulent reattached wall jets. *Journal of the Hydraulics Division*, Proceedings of the American Society of Civil Engineers, 94 (1), 95-112.

Rajaratnam, N. and Subramanya, K. 1967 Flow immediately below submerged sluice gate. *Journal of the Hydraulics Division*, Proceedings of the American Society of Civil Engineers, 93 (4), 57-77.

Reichardt, H. 1941 Uber eine neue theorie der freien turbulenz. *Zeitschrift für angewandte Mathematik und Mechanik*, 21, 257-264.

Schlichting, H. 1960 *Boundary Layer Theory*. 7th Edition. McGraw-Hill, New York.

Schnieder, W. 1985 Decay of momentum flux in submerged jets. *Journal of Fluid Mechanics*, 154 (5), 91-110.

Schwarz, W.H. and Cosart, W.P. 1960 The two-dimensional turbulent wall-jet. *Journal of Fluid Mechanics*, 10, 481-495.

Sigalla, A. 1958 Measurement of skin friction in a plane turbulent wall jet. *Journal of the Royal Aeronautical Society*, 62, 872-877.

Spedding, G.R. and Rignot, E.J.M. 1993 Performance analysis and application of grid interpolation techniques for fluid flows. *Experiments in Fluids*, 15, 417-430.

Siddiqui, M.H. 2002 Laboratory measurements of the flow beneath microscale breaking waves. Ph.D. Thesis, University of Toronto.

Siddiqui, M.H., Loewen, M.R., Richardson, C., Asher, W.E. and Jessup, A.T. 2001 Simultaneous particle image velocimetry and infrared imagery of microscale breaking waves. *Physics of Fluids*, 13 (7), 1891-1903.

Swean, T.F., Ramberg, S.E., Plesniak, M.W. and Stewart, M.B 1989 Turbulent surface jet in channel of limited depth. *Journal of Hydraulic Engineering*, 115 (12), 1587-1606.

Tennekes, H. and Lumley, J.L. 1972 *A First Course in Turbulence*. MIT Press, Cambridge.

Tollmien, W. 1926 Berechnung turbulenter ausbreitungsvorgänge. *Zeitschrift für angewandte Mathematik und Mechanik*, 6, 468-478.

Vanvari, M.R. and Chu, V.H. 1974 Two-dimensional turbulent surface jets of low Richardson number. Fluid Mechanics Laboratory, McGill University, Technical Report no. 74-2.

Verhoff, A. 1963 The two-dimensional turbulent wall jet with and without and external stream. Princeton University, Report no. 626.

Westerweel, J. 1994 Efficient detection of spurious vectors in particle image velocimetry data. *Experiments in Fluids*, 16, 236-247.

Wu, S. 1994 Four contributions to the application of turbulent jet theory in hydraulic engineering. Ph.D. Thesis, University of Alberta.

Wu, S. and Rajaratnam, N. 1995a Effect of baffles on submerged jumps. *Journal of Hydraulic Engineering*, 121 (9), 644-652.

Wu, S. and Rajaratnam, N. 1995b Free jumps, submerged jumps and wall jets. *Journal of Hydraulic Research*, 33 (2), 197-212.

Yu-Leuk, C. and Wood, I.R. 1966 Momentum diffusion from a two-dimensional jet. Water Research Laboratory, University of New South Wales, Report no. 99.

Zijnen, B.G. Van der Hegge 1958 Measurements of the velocity distribution in a plane turbulent jet of air. *Applied Scientific Research, A.*, 7, 256-276.

8 Appendix

The appendix of this thesis contains one table and many figures that were not considered necessary for the main body of the work, but included for completeness. Table 8.1 presents a full list of the contents of the included compact disc, found on the back sleeve of this thesis. Figures 8.1 though 8.14 present the complete set of sample instantaneous (a) raw and (b) corrected and interpolated pixel displacement vector fields for all the tesserae. Figures 8.15 though 8.21 present mean velocity vector fields for all the tesserae at individual scales. Figures 8.22 though 8.35 present the individual tessera component fields of the assembled mean velocity vector field mosaic, plotted separately for manual assembly. It is recommended that these figures be duplicated and assembled to provide a large-scale vector field for personal observation. Figures 8.36 though 8.49 present the peak locking error (derived from the raw pixel displacement data) in all the tesserae. Figures 8.50 (a-n) presents the cumulative averages, plotted over increasing periods of time and averaging larger batches of PIV data files, of the sums of all turbulent kinetic energy (k) measurements in all the tesserae. Figures 8.51 through 8.78 present the various dimensional and nondimensional parameters plotted for the figures in §5.2.6 for the return flow SJL regions and the main flow TZ1 and TZ2 regions.

filename	description
thesis.pdf	thesis (portable document format)
vort_t01.avi	tessera 1 ω_i movie (AVI format)
vort_t02.avi	tessera 2 ω_i movie (AVI format)
vort_t03.avi	tessera 3 ω_i movie (AVI format)
vort_t04.avi	tessera 4 ω_i movie (AVI format)
vort_t05.avi	tessera 5 ω_i movie (AVI format)
vort_t06.avi	tessera 6 ω_i movie (AVI format)
vort_t07.avi	tessera 7 ω_i movie (AVI format)
vort_t08.avi	tessera 8 ω_i movie (AVI format)
vort_t09.avi	tessera 9 ω_i movie (AVI format)
vort_t10.avi	tessera 10 ω_i movie (AVI format)
vort_t11.avi	tessera 11 ω_i movie (AVI format)
vort_t12.avi	tessera 12 ω_i movie (AVI format)
vort_t13.avi	tessera 13 ω_i movie (AVI format)
vort_t14.avi	tessera 14 ω_i movie (AVI format)

Table 8.1: Contents of accompanying compact disc.

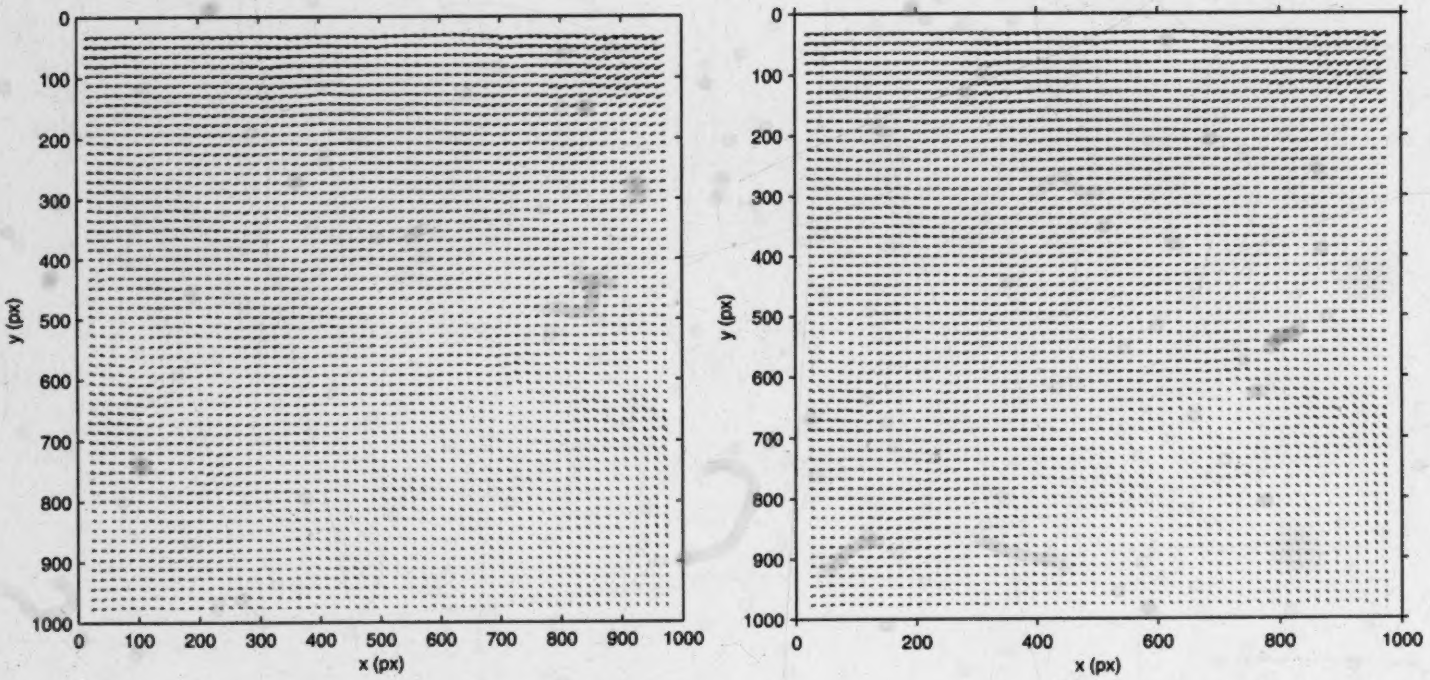

(a)

(b)

Figure 8.1: Sample instantaneous (a) raw and (b) corrected and interpolated pixel displacement vector fields for tessera 14.

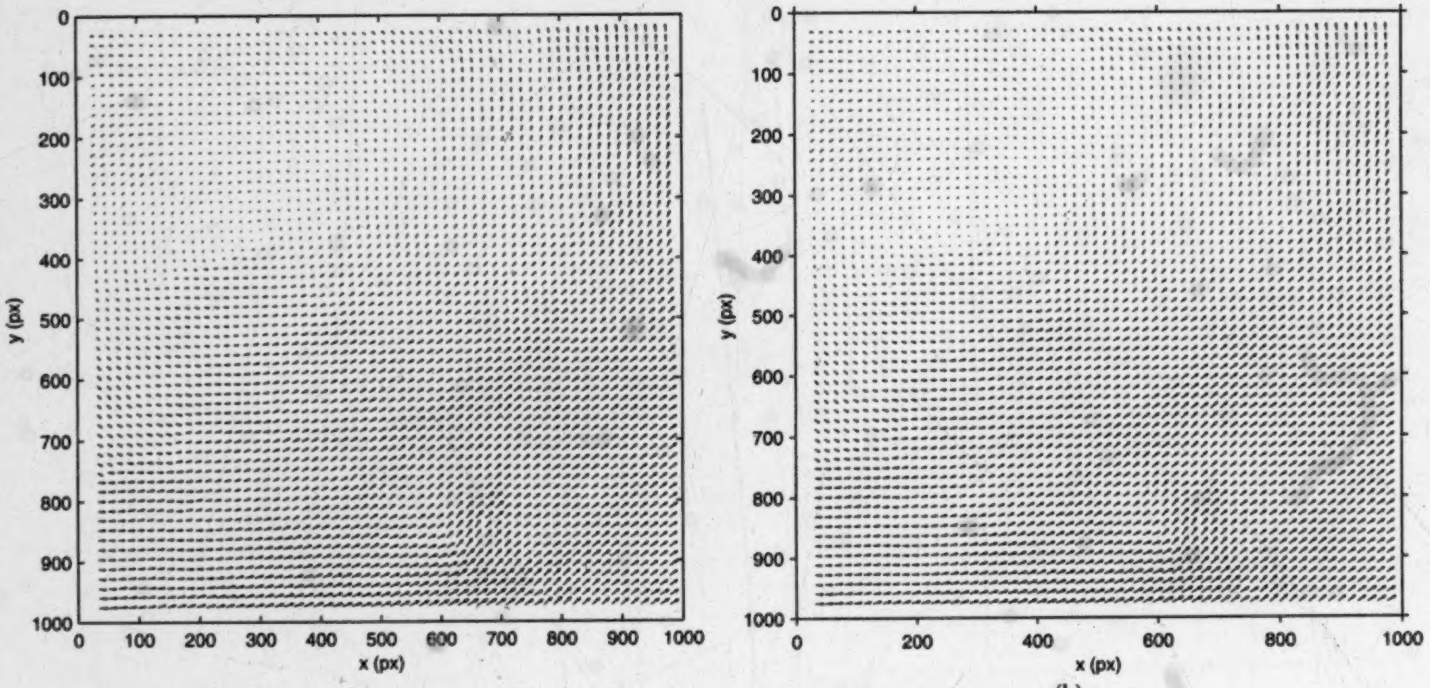

(a)

(b)

Figure 8.2: Sample instantaneous (a) raw and (b) corrected and interpolated pixel displacement vector fields for tessera 1.

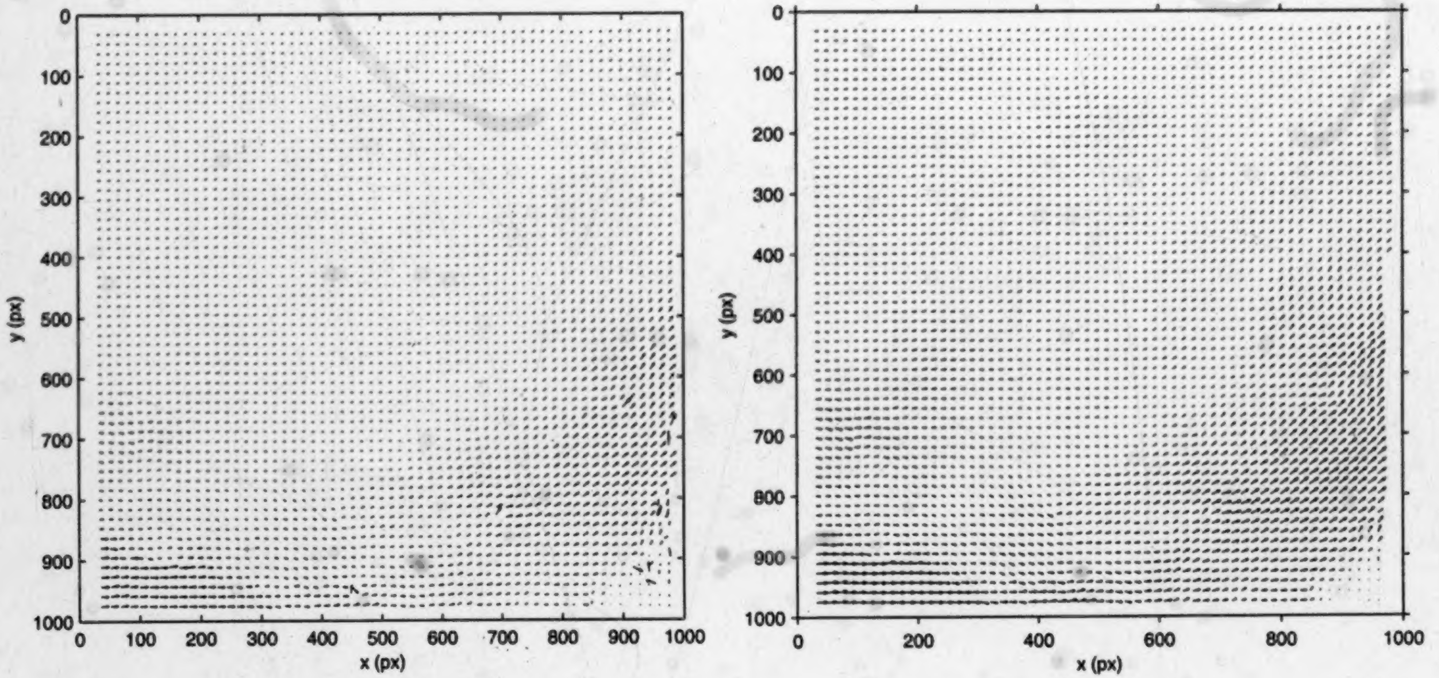

(a)

(b)

Figure 8.3: Sample instantaneous (a) raw and (b) corrected and interpolated pixel displacement vector fields for tessera 2.

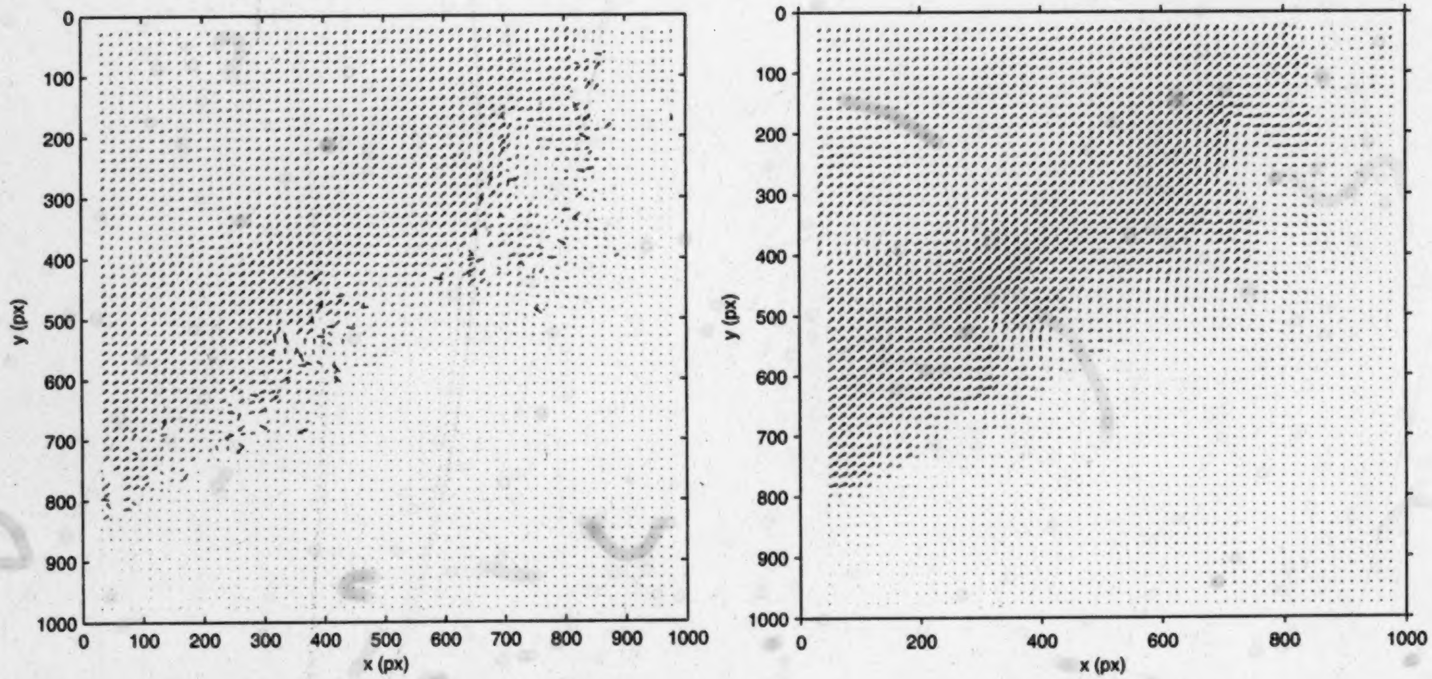

(a)

(b)

Figure 8.4: Sample instantaneous (a) raw and (b) corrected and interpolated pixel displacement vector fields for tessera 3.

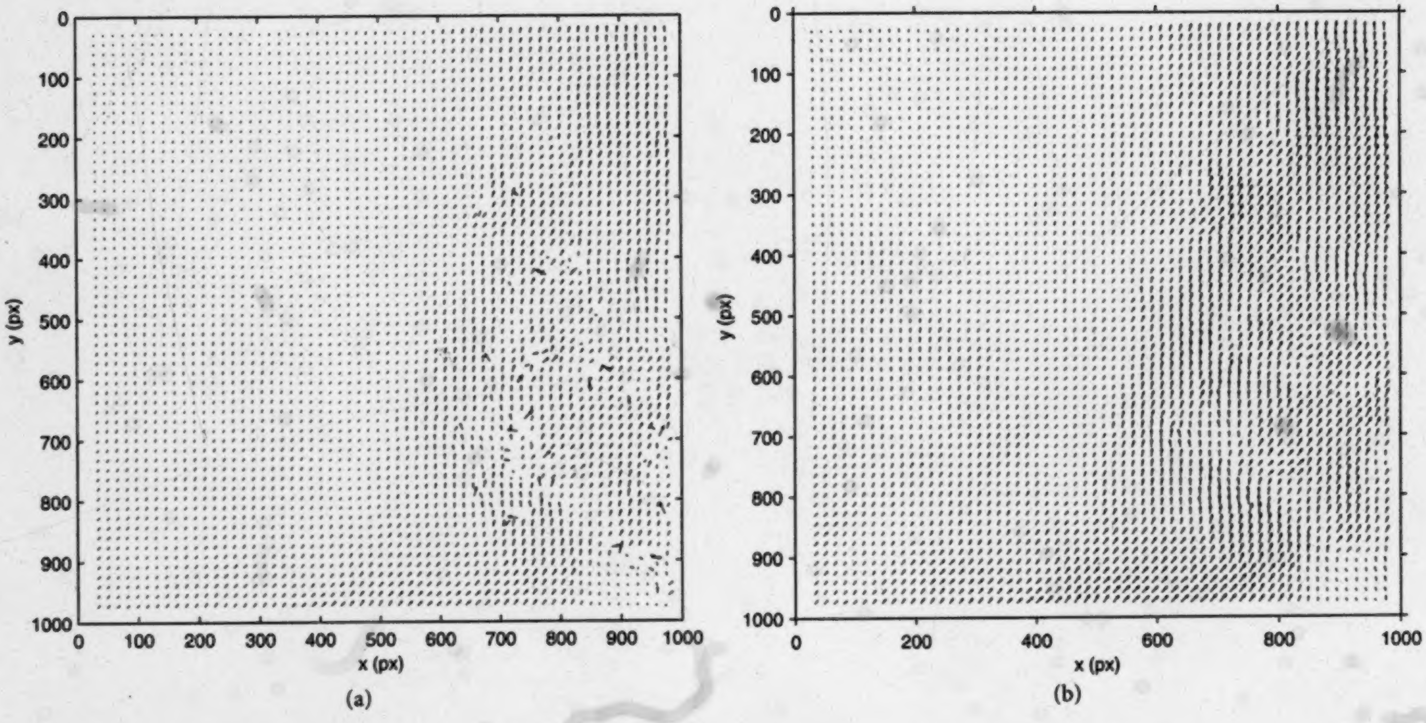

Figure 8.5: Sample instantaneous (a) raw and (b) corrected and interpolated pixel displacement vector fields for tessera 4.

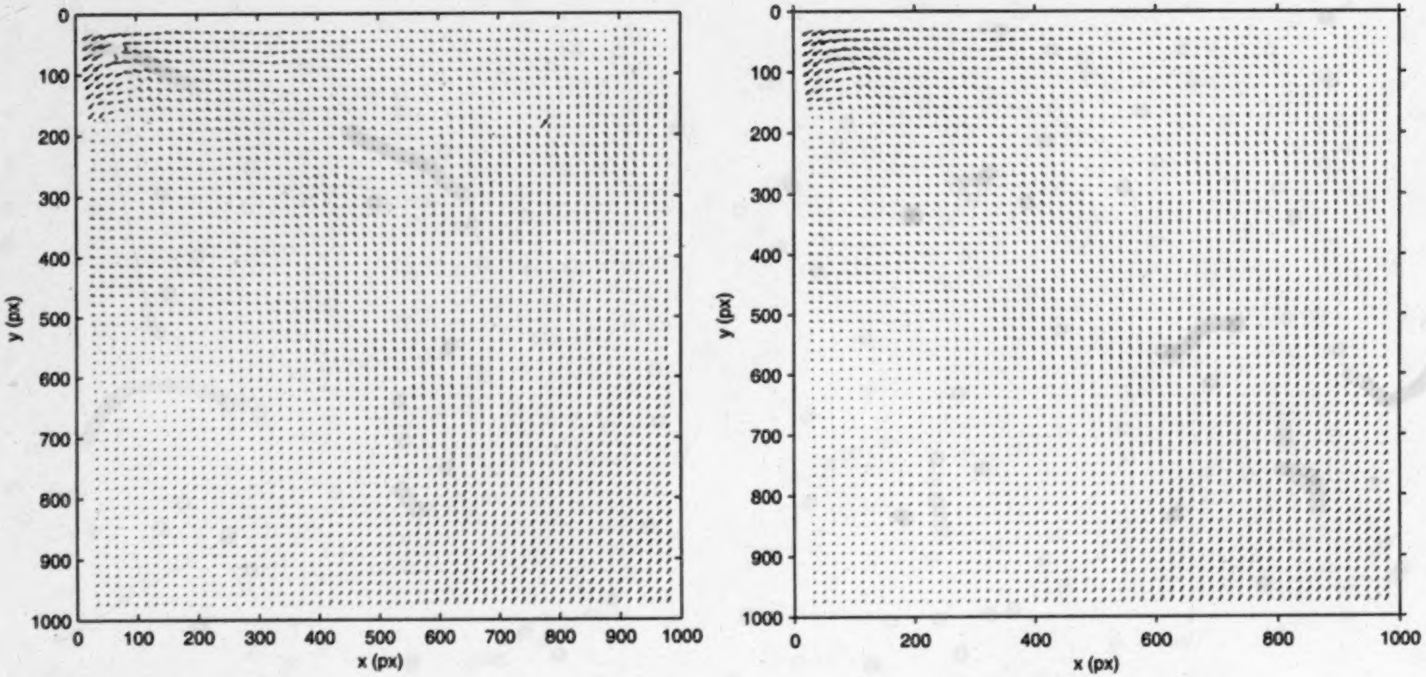

(a)

(b)

Figure 8.6: Sample instantaneous (a) raw and (b) corrected and interpolated pixel displacement vector fields for tessera 5.

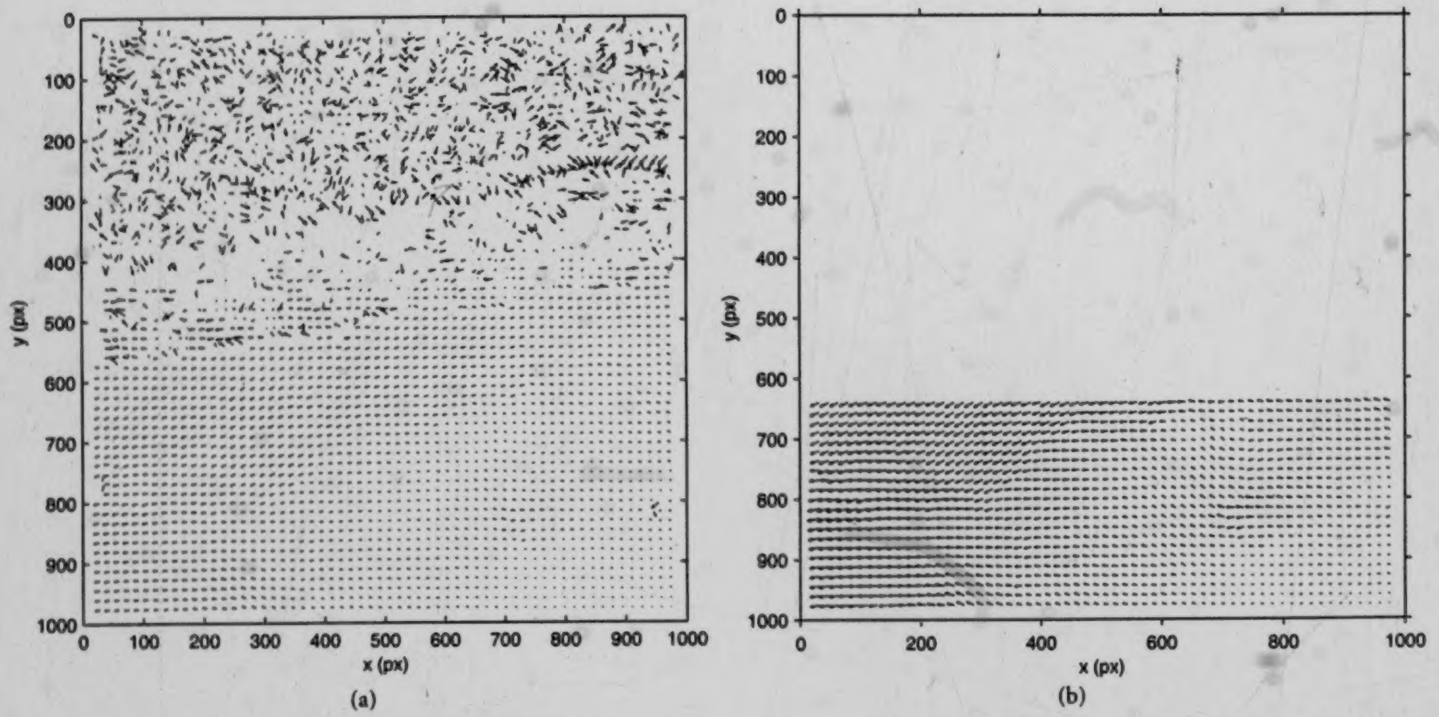

(a)

(b)

Figure 8.7: Sample instantaneous (a) raw and (b) corrected and interpolated pixel displacement vector fields for tessera 6.

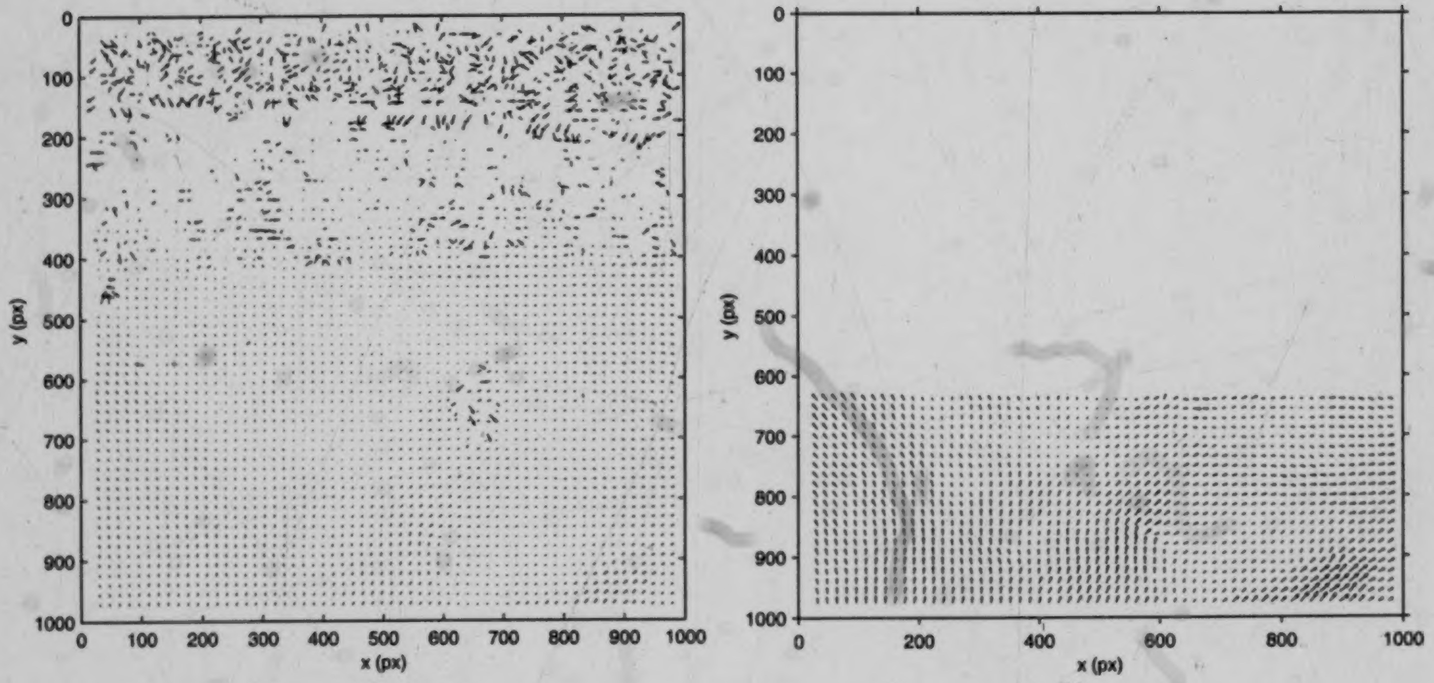

(a)

(b)

Figure 8.8: Sample instantaneous (a) raw and (b) corrected and interpolated pixel displacement vector fields for tessera 7.

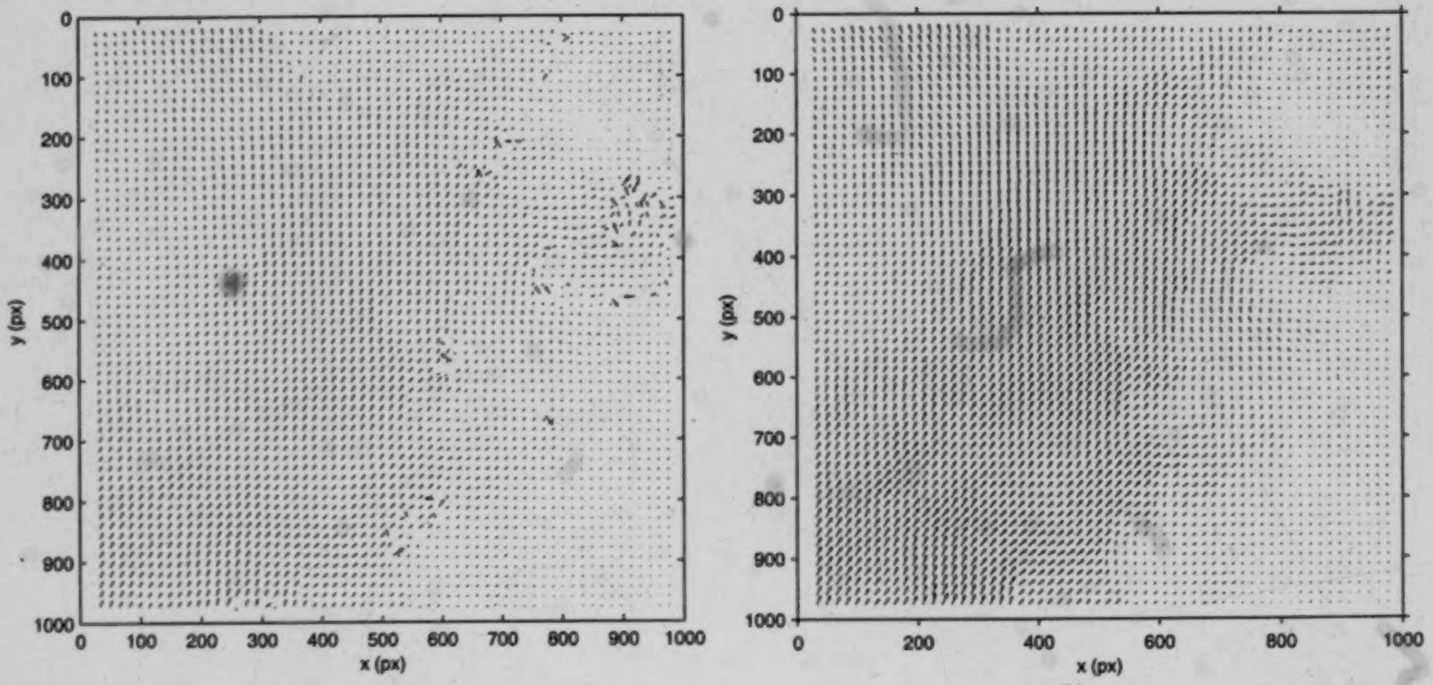

(a)

(b)

Figure 8.9: Sample instantaneous (a) raw and (b) corrected and interpolated pixel displacement vector fields for tessera 8.

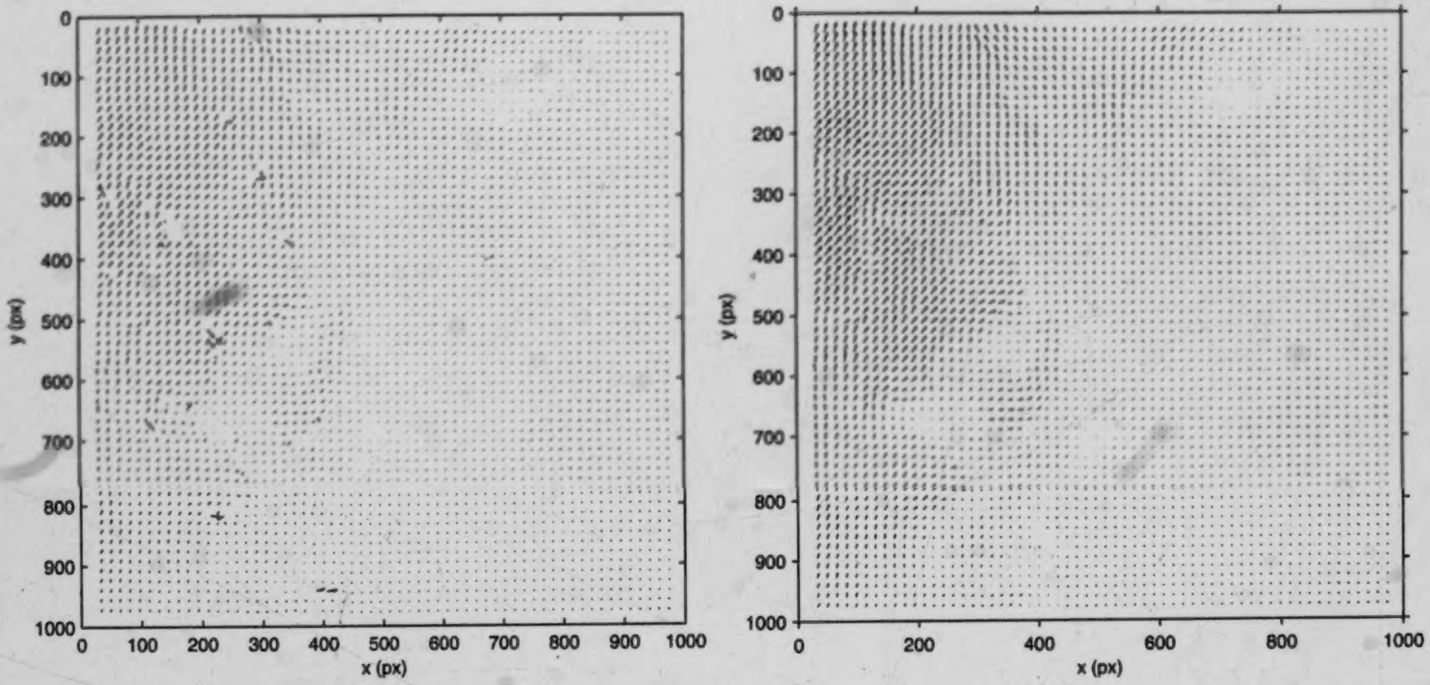

(a)

(b)

Figure 8.10: Sample instantaneous (a) raw and (b) corrected and interpolated pixel displacement vector fields for tessera 9.

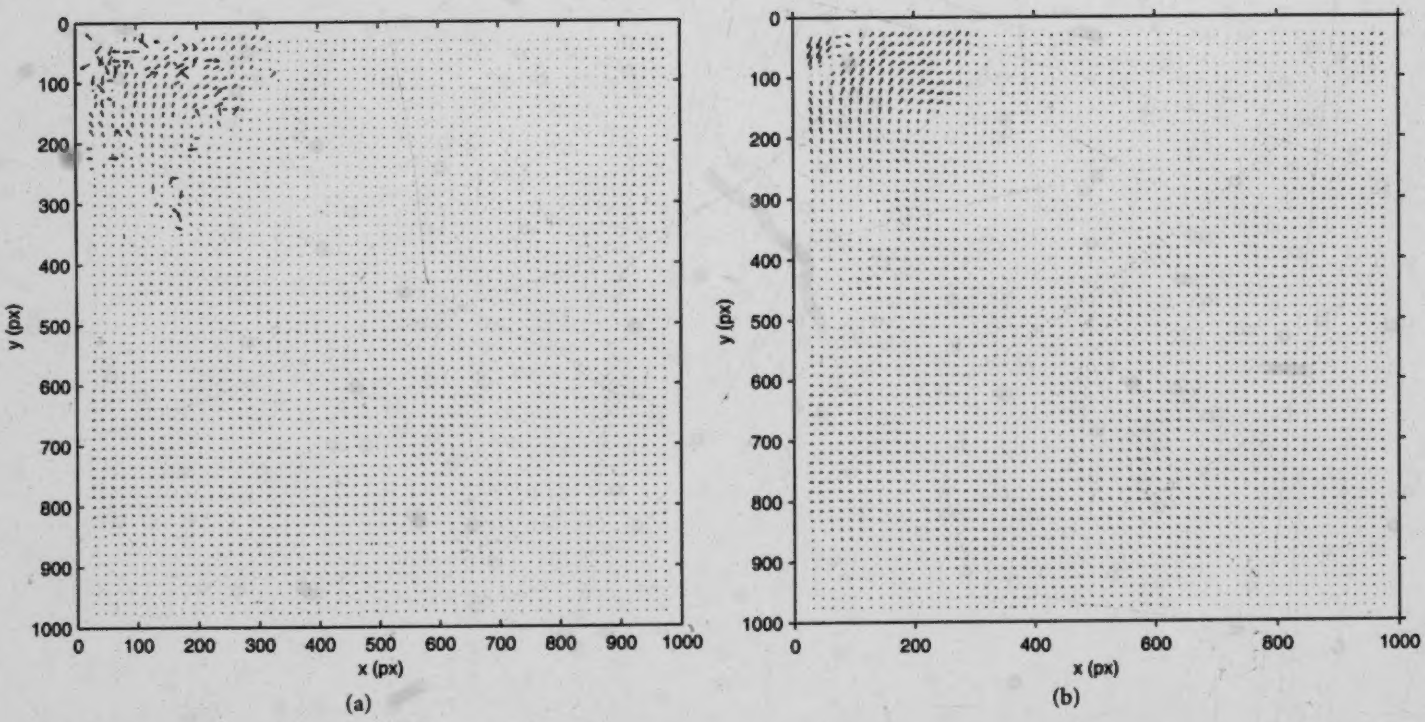

(a)

(b)

Figure 8.11: Sample instantaneous (a) raw and (b) corrected and interpolated pixel displacement vector fields for tessera 10.

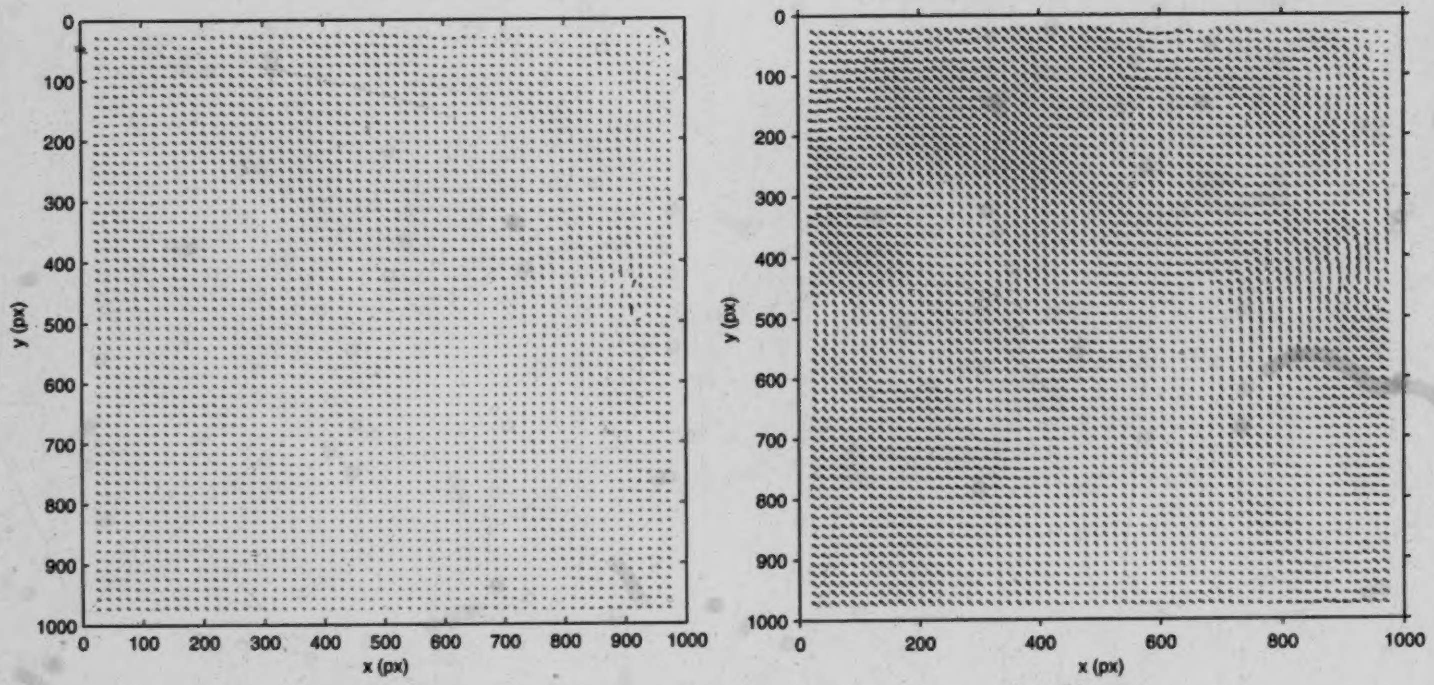

(a) (b)

Figure 8.12: Sample instantaneous (a) raw and (b) corrected and interpolated pixel displacement vector fields for tessera 11.

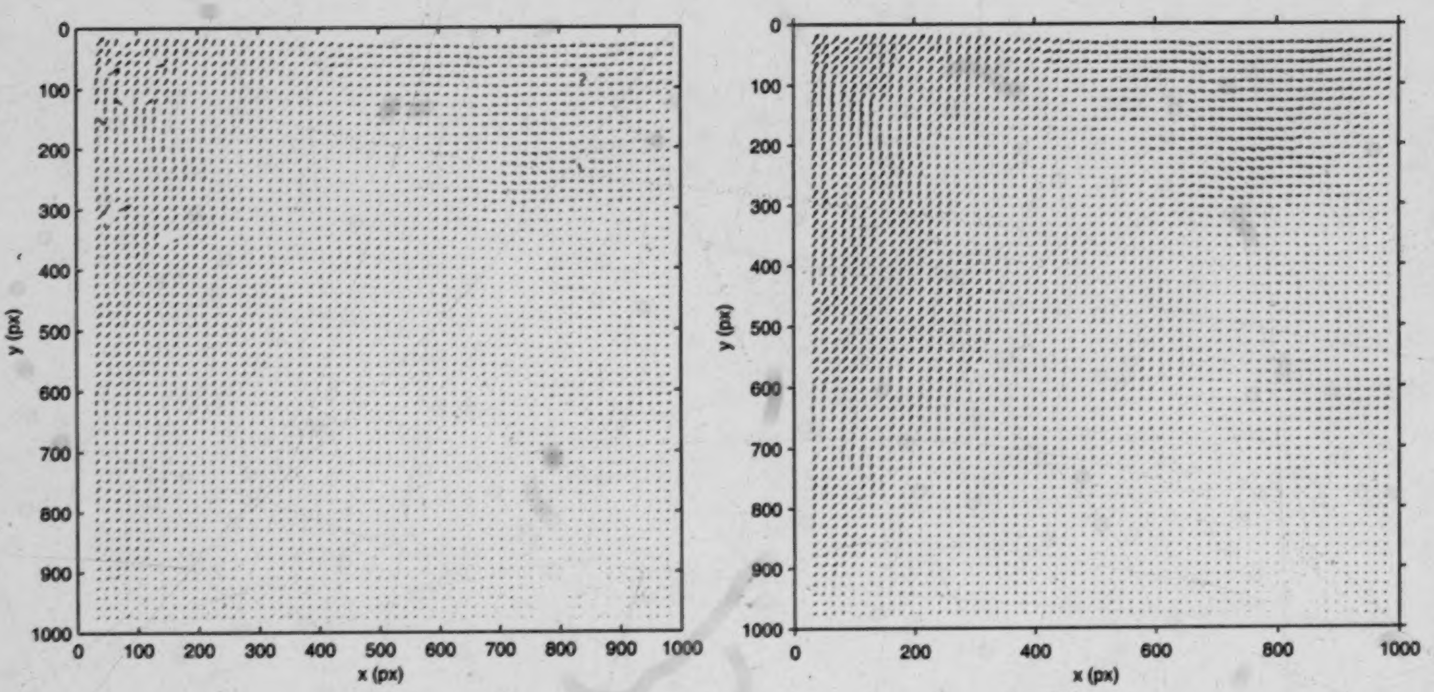

(a)

(b)

Figure 8.13: Sample instantaneous (a) raw and (b) corrected and interpolated pixel displacement vector fields for tessera 12.

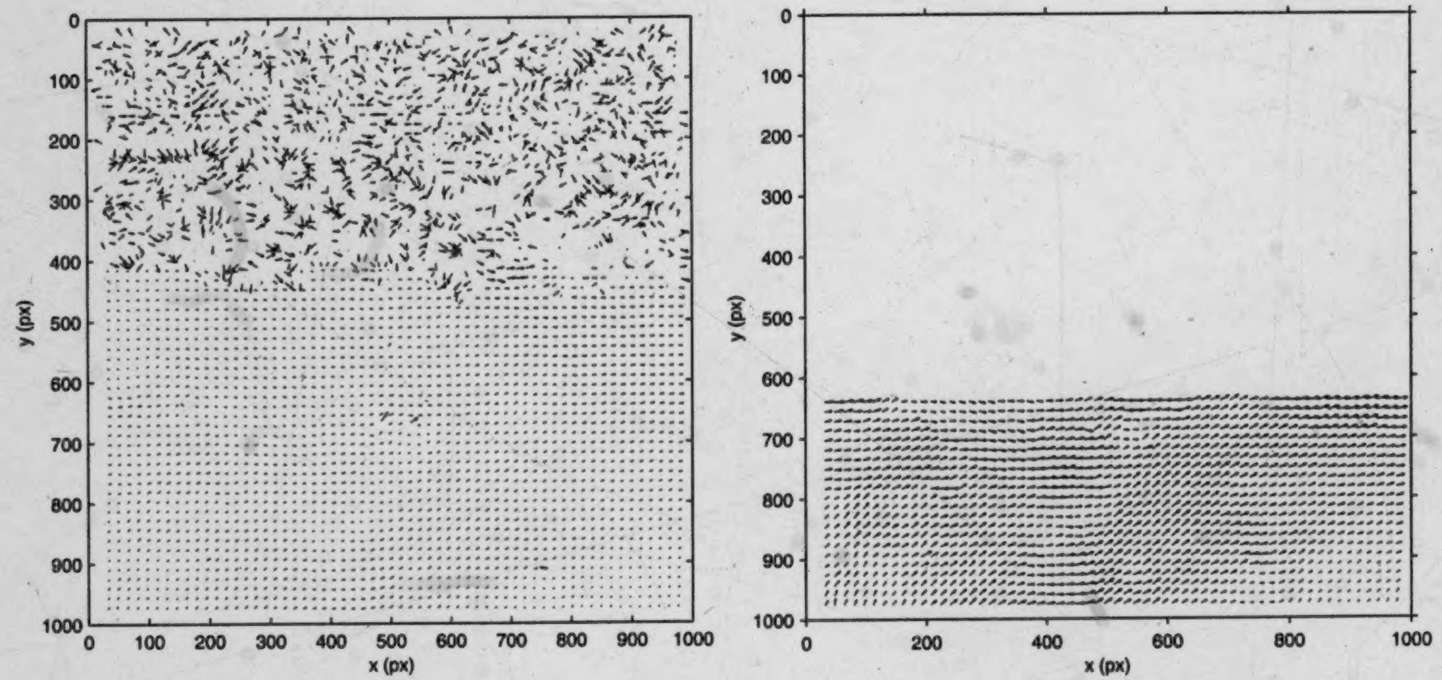

(a)

(b)

Figure 8.14: Sample instantaneous (a) raw and (b) corrected and interpolated pixel displacement vector fields for tessera 13.

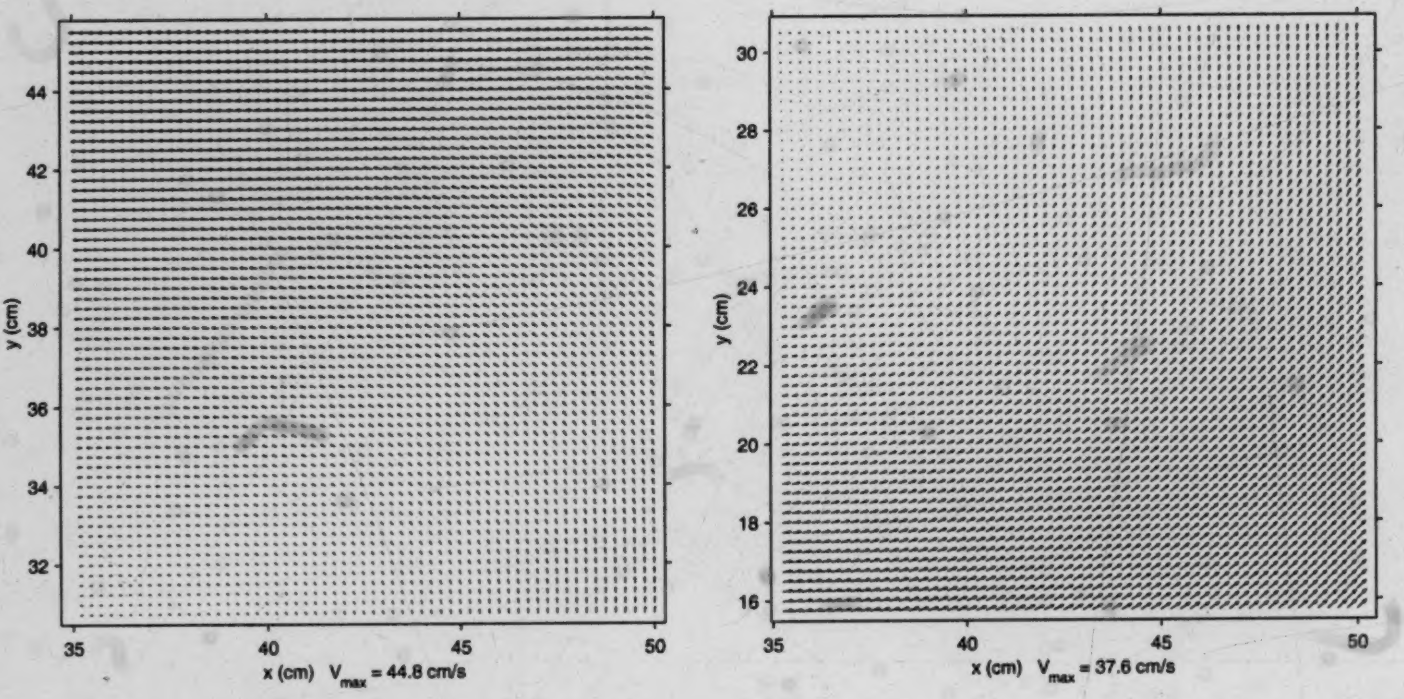

(a) (b)

Figure 8.15: Mean velocity vector fields for (a) tessera 14 and (b) tessera 1; individual scale.

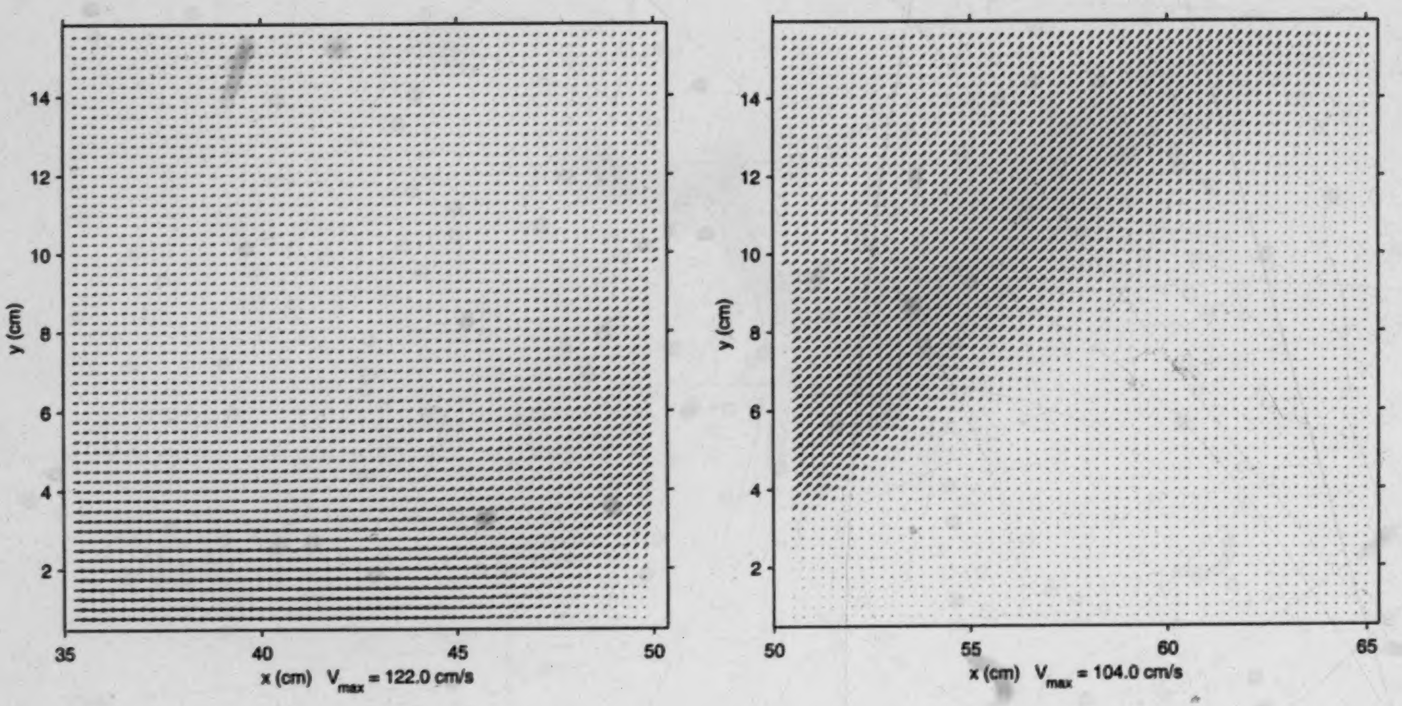

(a)

(b)

Figure 8.16: Mean velocity vector fields for (a) tessera 2 and (b) tessera 3; individual scale.

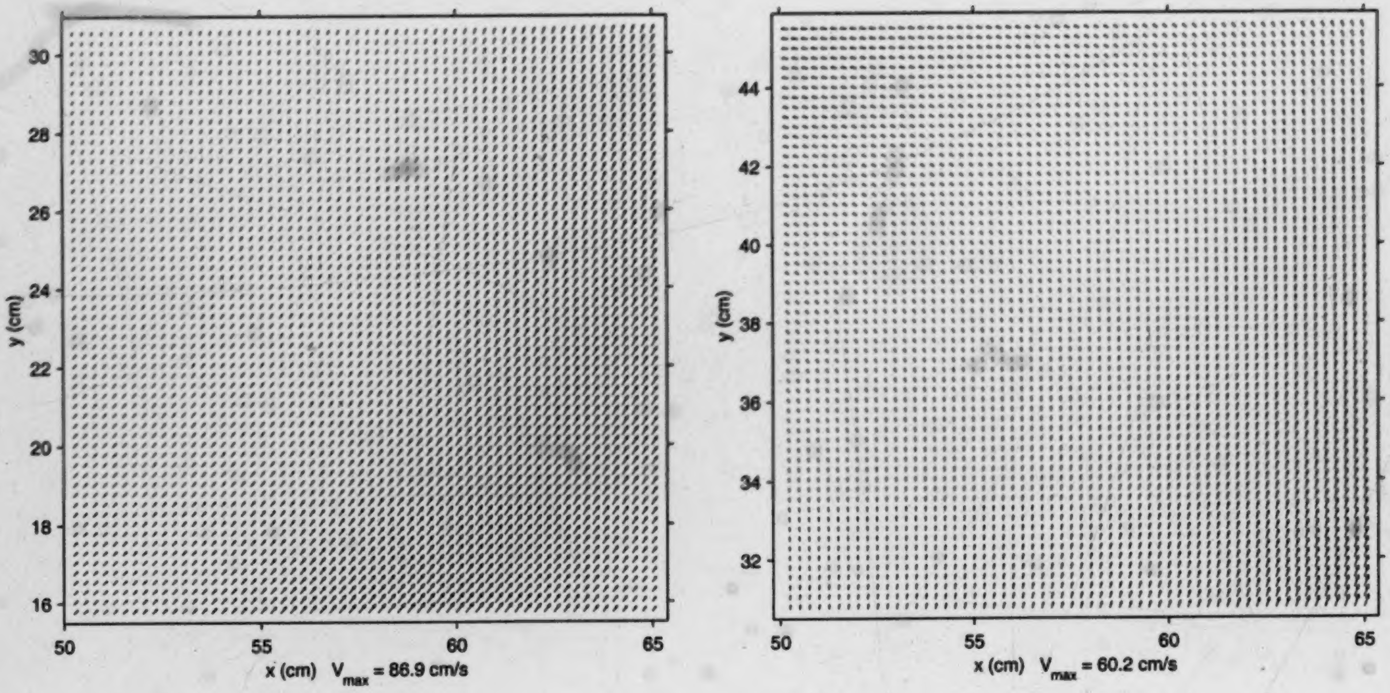

(a)

(b)

Figure 8.17: Mean velocity vector fields for (a) tessera 4 and (b) tessera 5; individual scale.

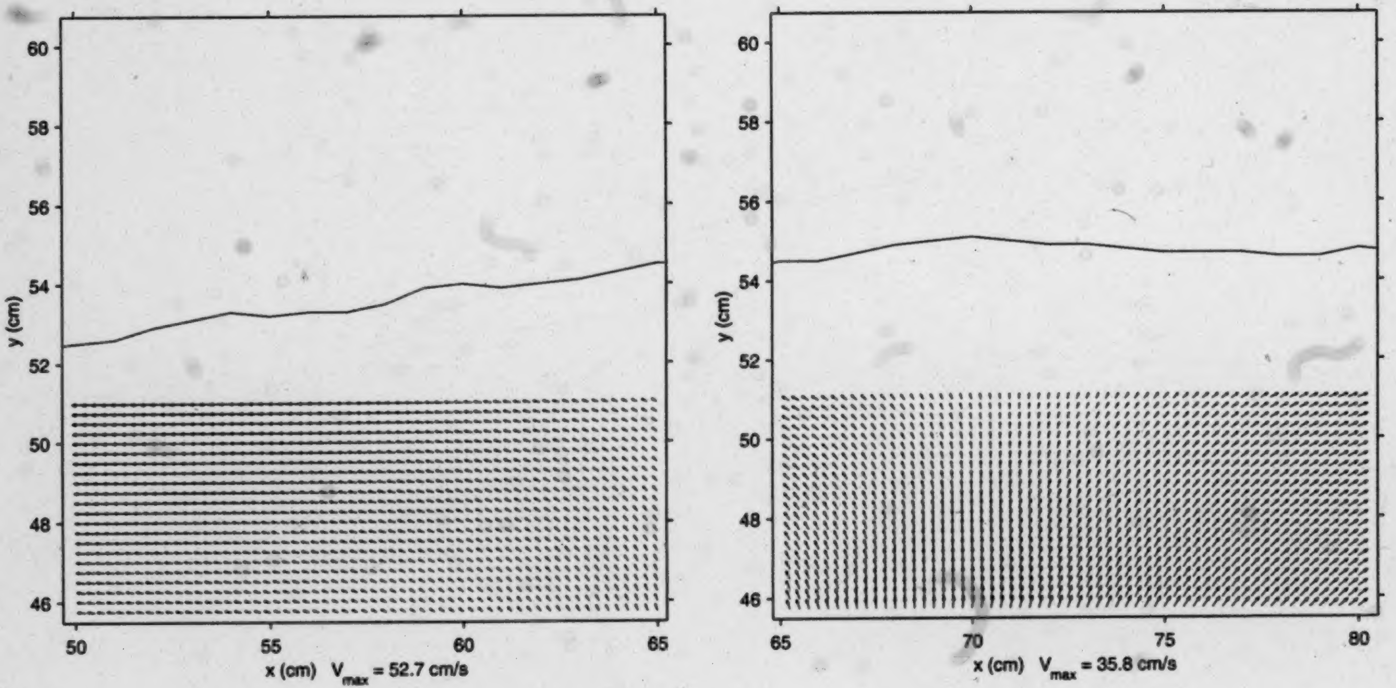

(a)

(b)

Figure 8.18: Mean velocity vector fields for (a) tessera 6 and (b) tessera 7; individual scale.

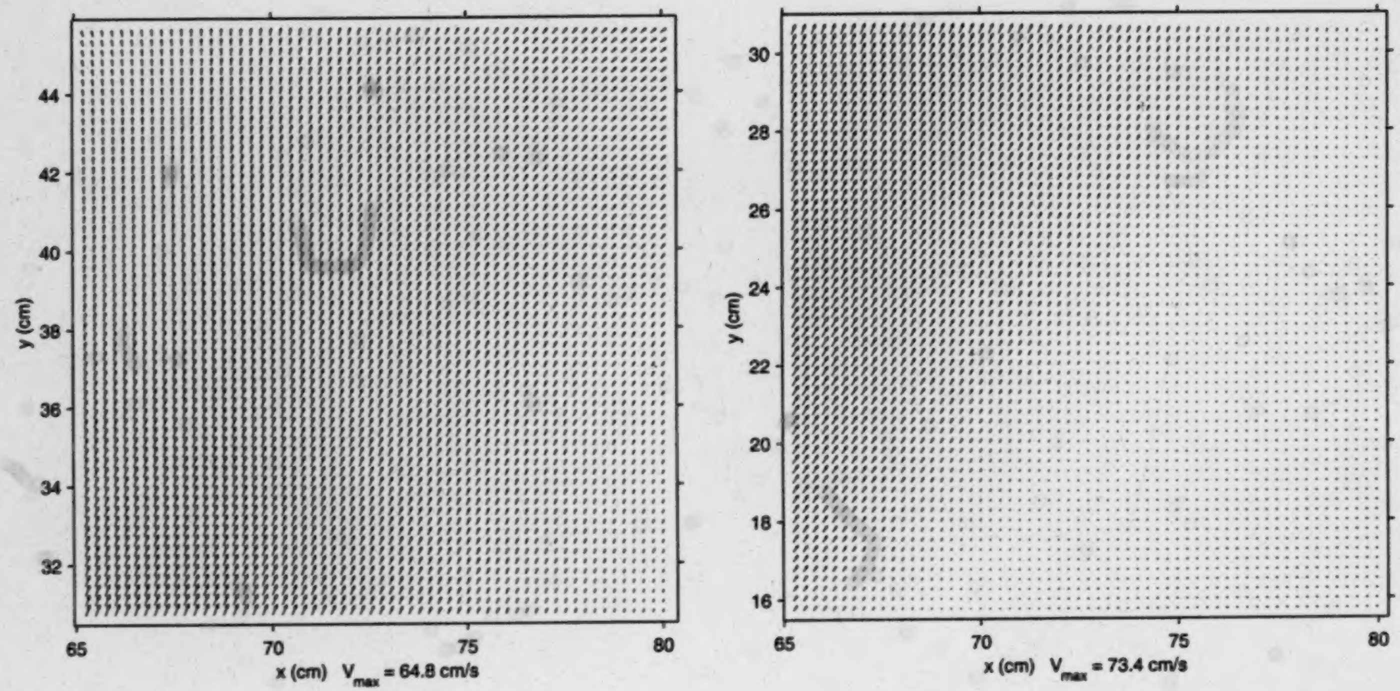

(a)

(b)

Figure 8.19: Mean velocity vector fields for (a) tessera 8 and (b) tessera 9; individual scale.

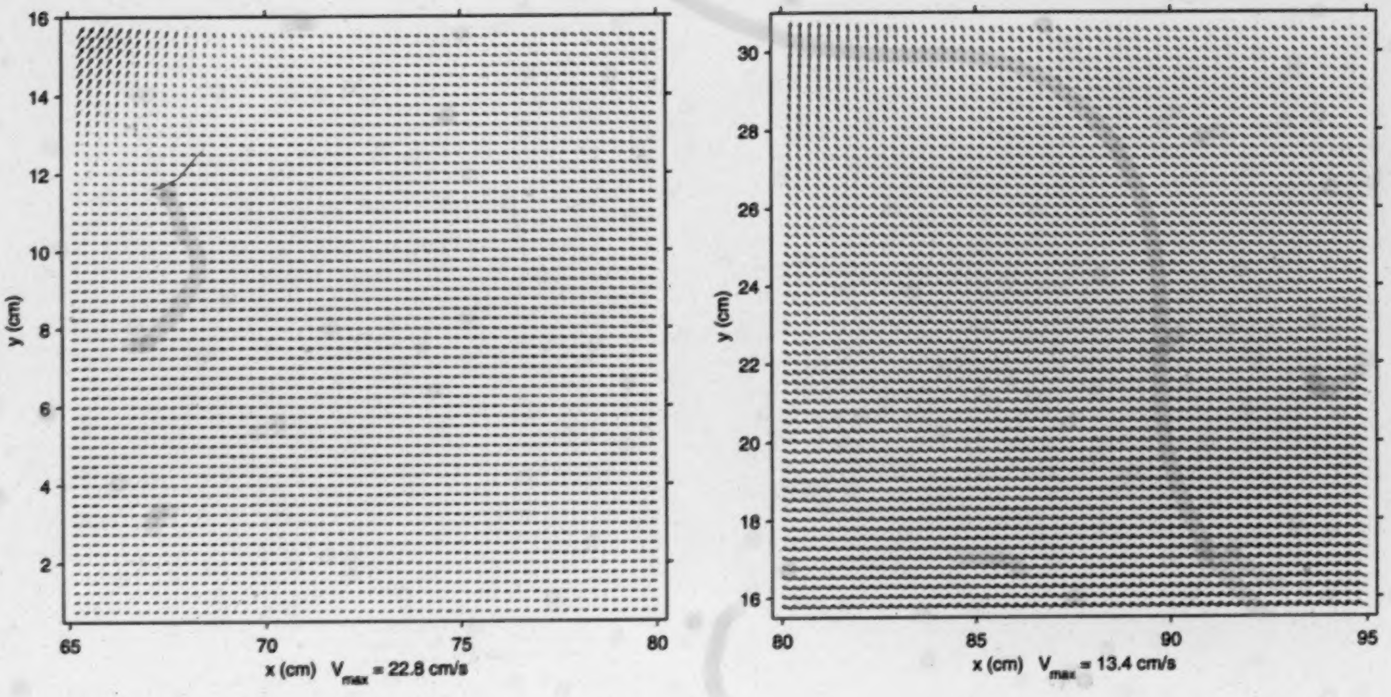

(a)

(b)

Figure 8.20: Mean velocity vector fields for (a) tessera 10 and (b) tessera 11; individual scale.

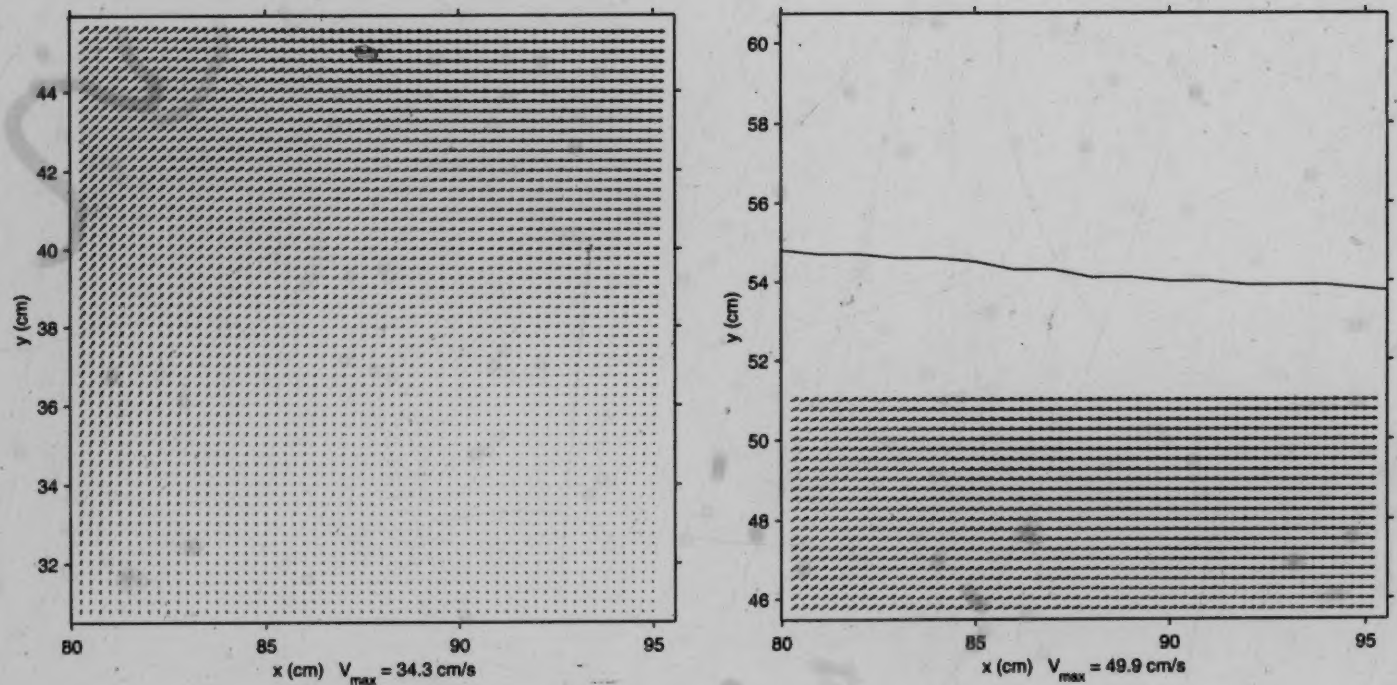

(a)

(b)

Figure 8.21: Mean velocity vector fields for (a) tessera 12 and (b) tessera 13; individual scale.

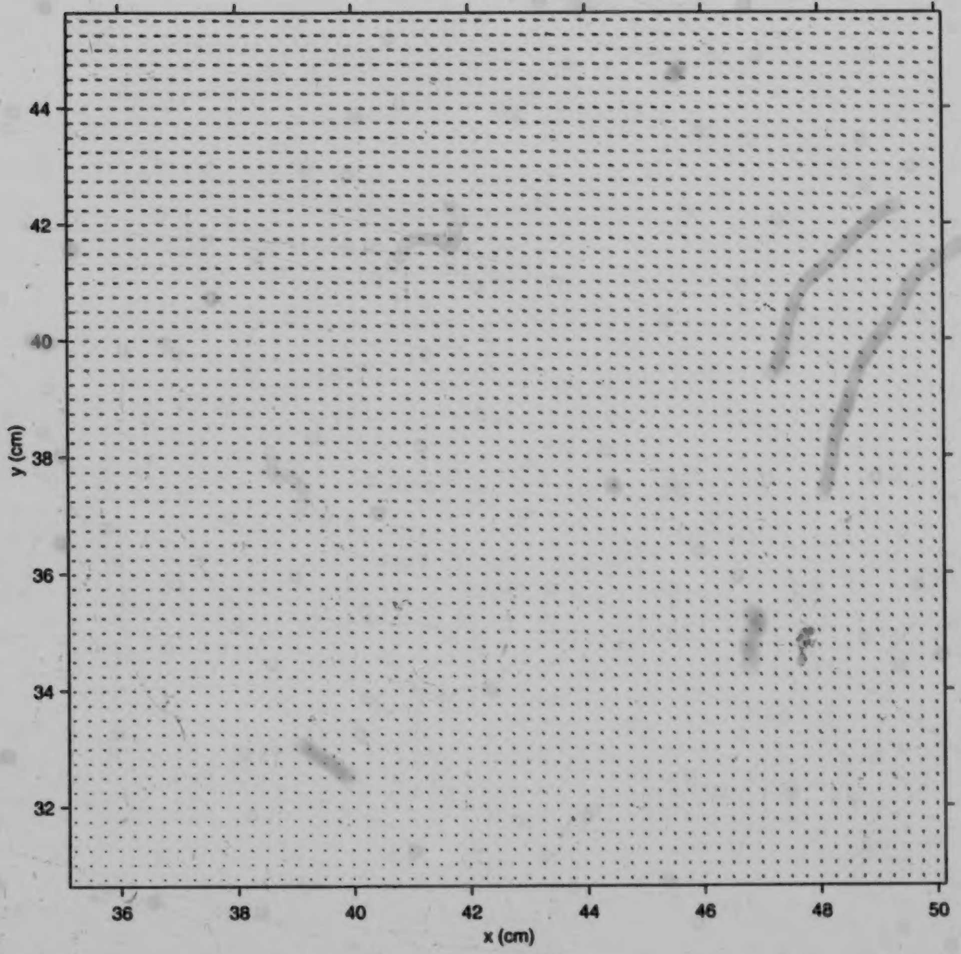

Figure 8.22: Tessera 14 component of assembled mean velocity vector field mosaic.

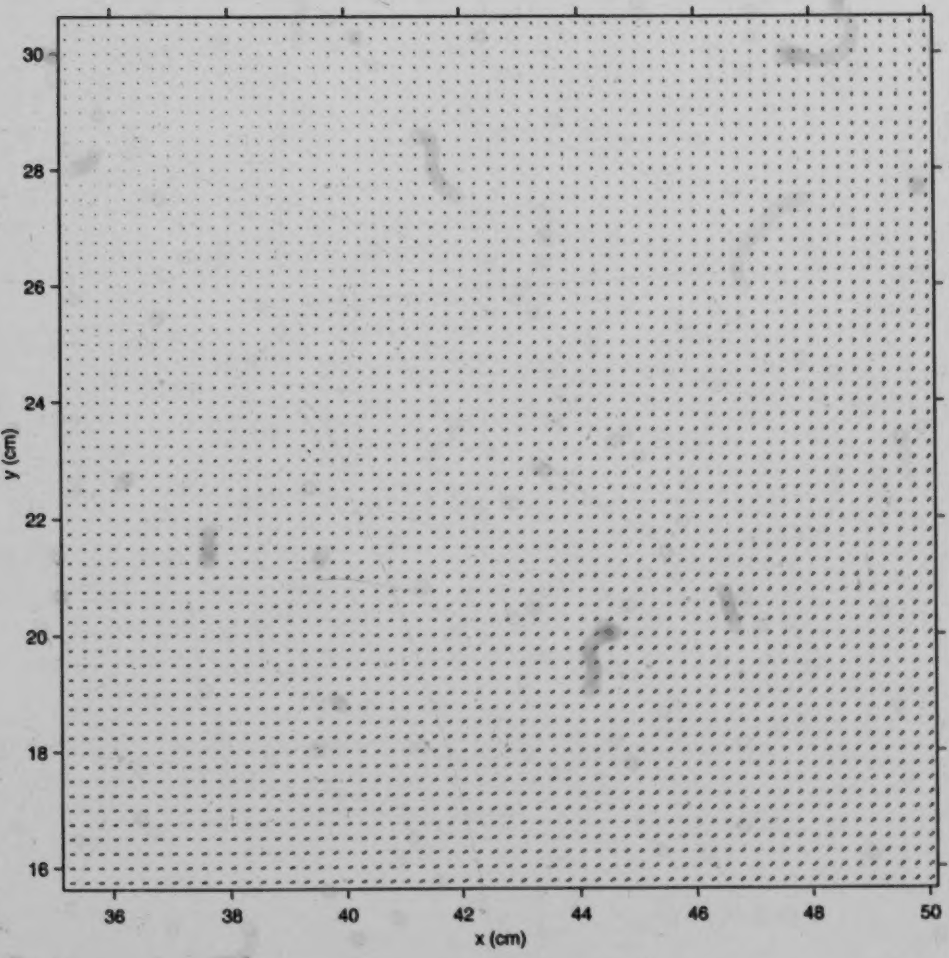

Figure 8.23: Tessera 1 component of assembled mean velocity vector field mosaic.

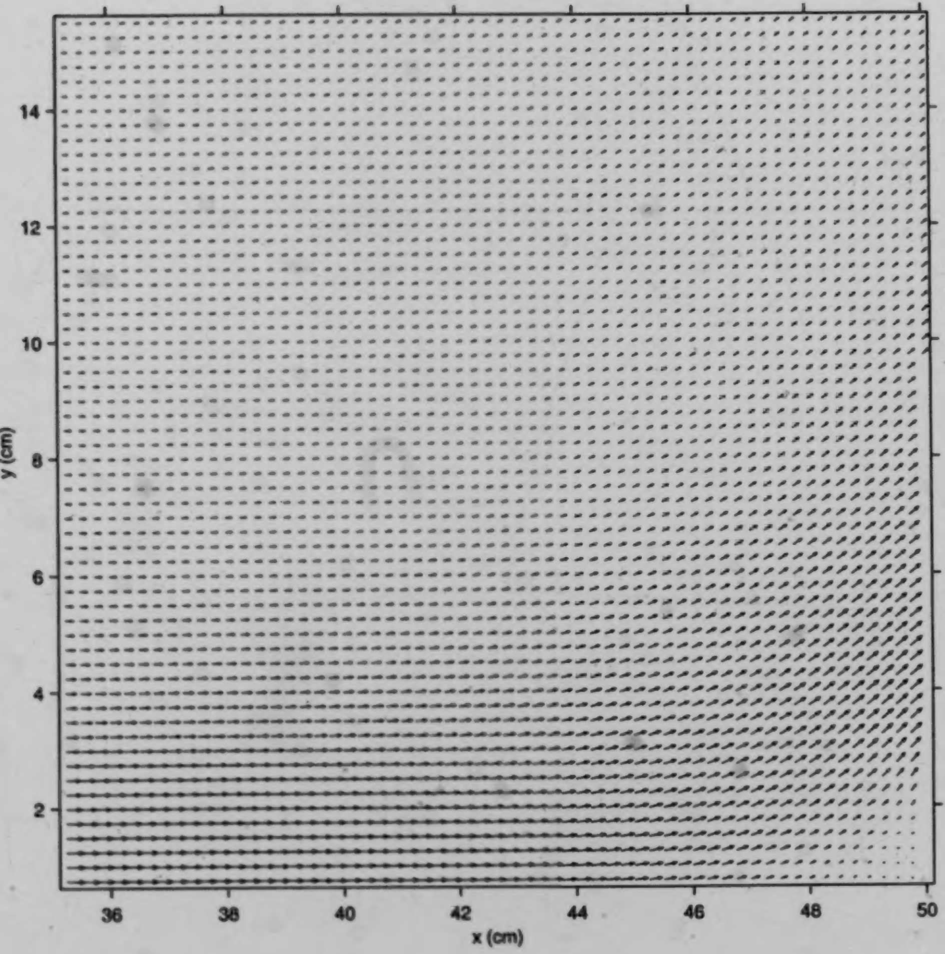

Figure 8.24: Tessera 2 component of assembled mean velocity vector field mosaic.

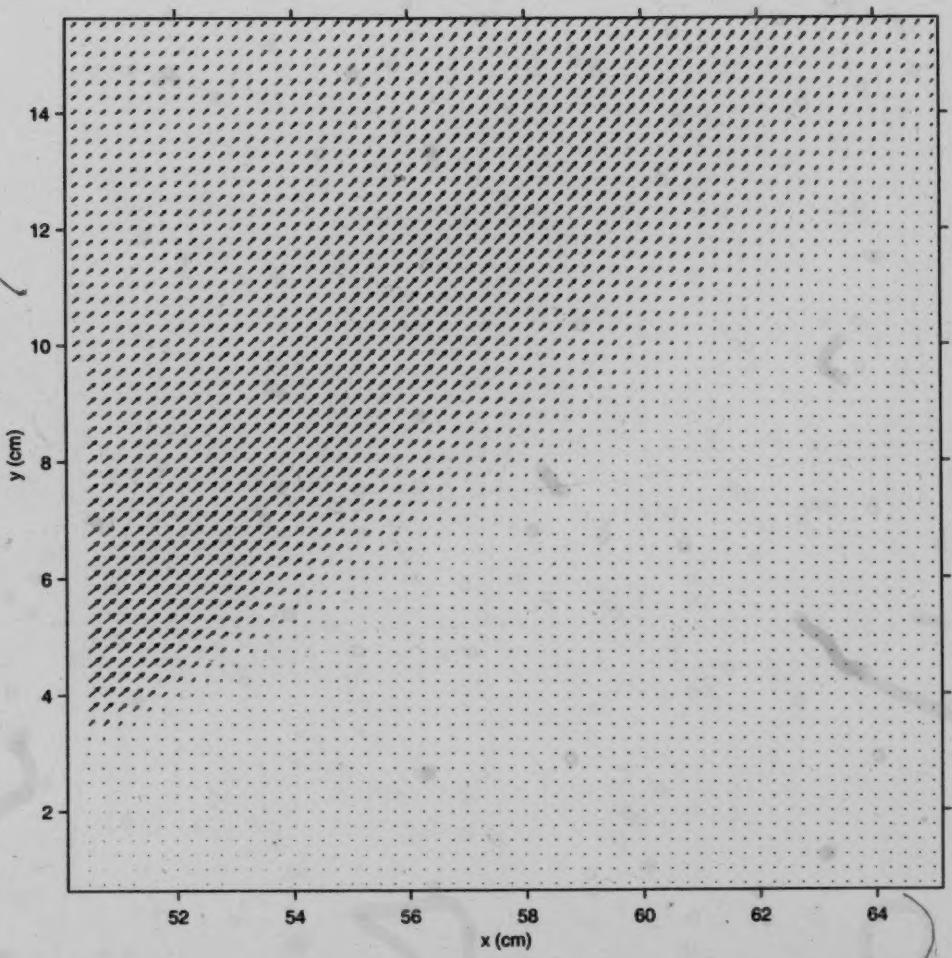

Figure 8.25: Tessera 3 component of assembled mean velocity vector field mosaic.

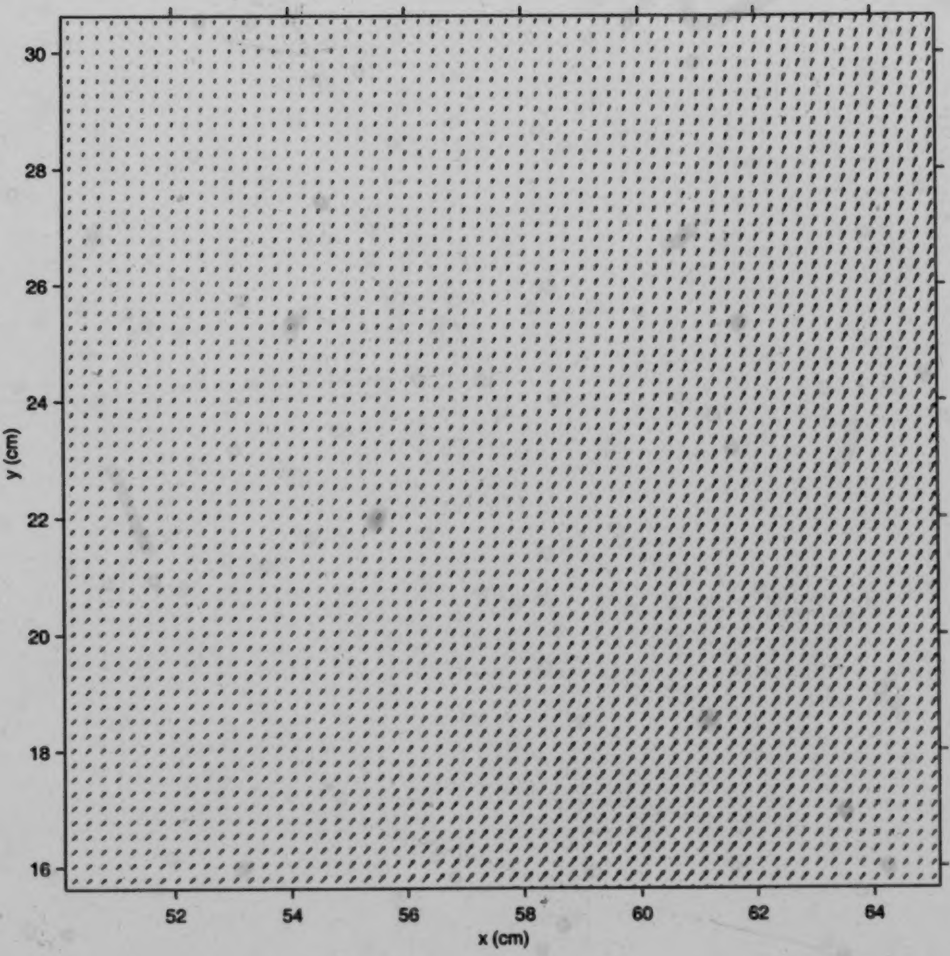

Figure 8.26: Tessera 4 component of assembled mean velocity vector field mosaic.

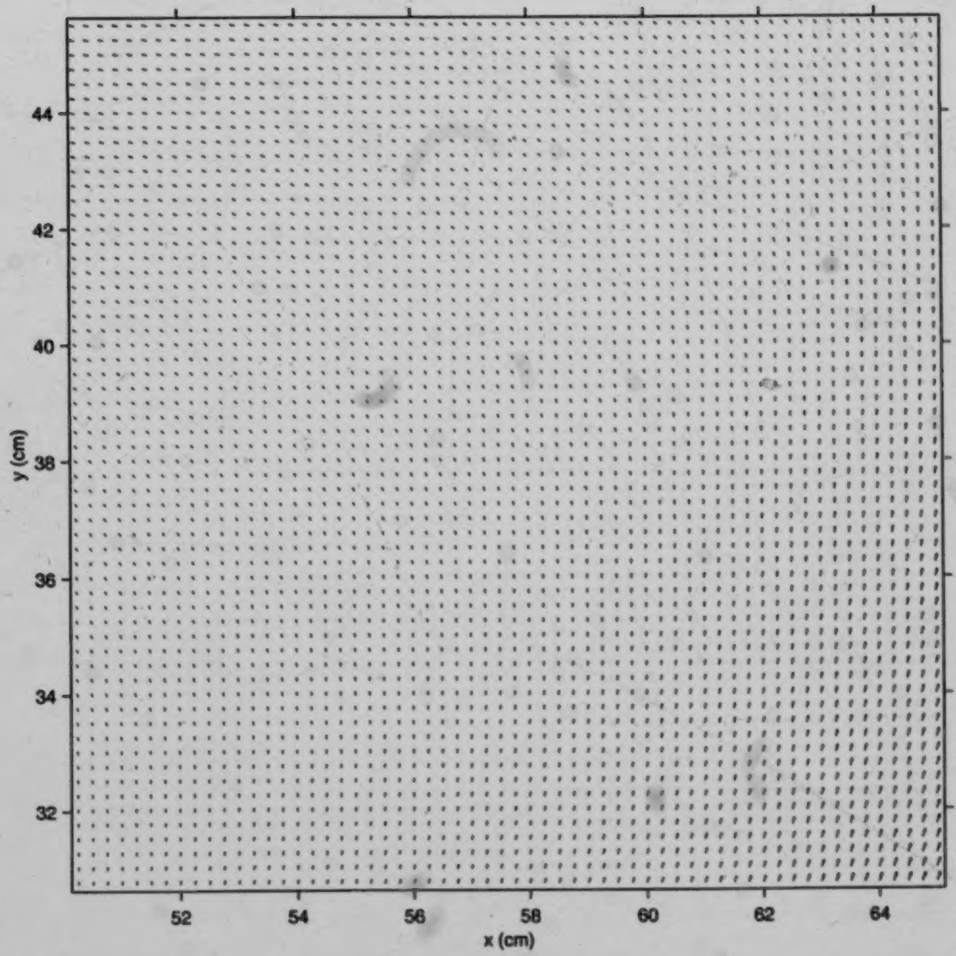

Figure 8.27: Tessera 5 component of assembled mean velocity vector field mosaic.

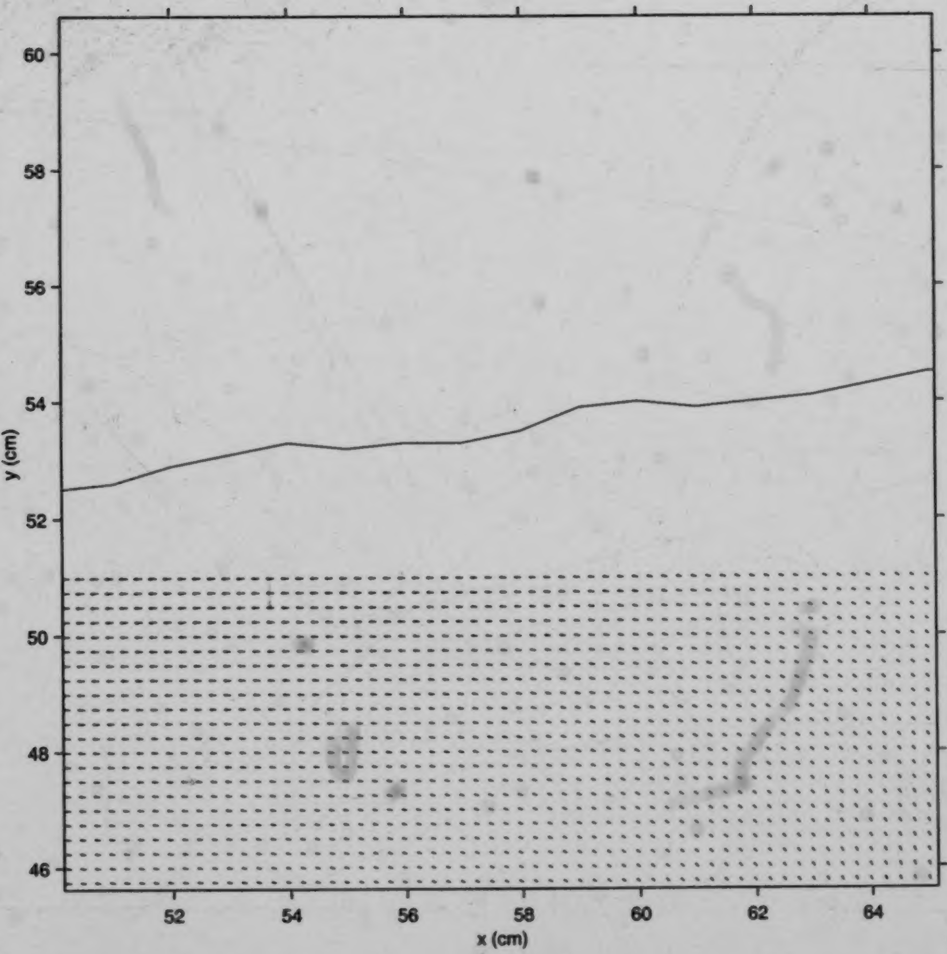

Figure 8.28: Tessera 6 component of assembled mean velocity vector field mosaic.

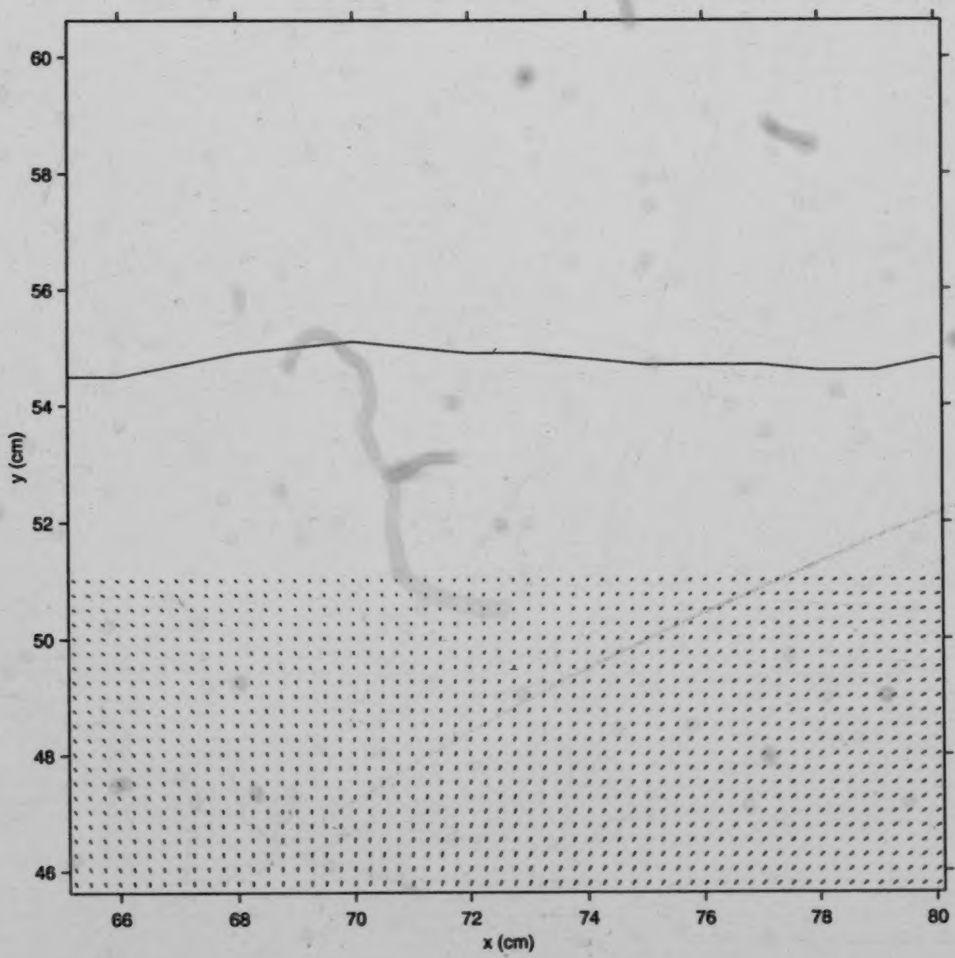

Figure 8.29: Tessera 7 component of assembled mean velocity vector field mosaic.

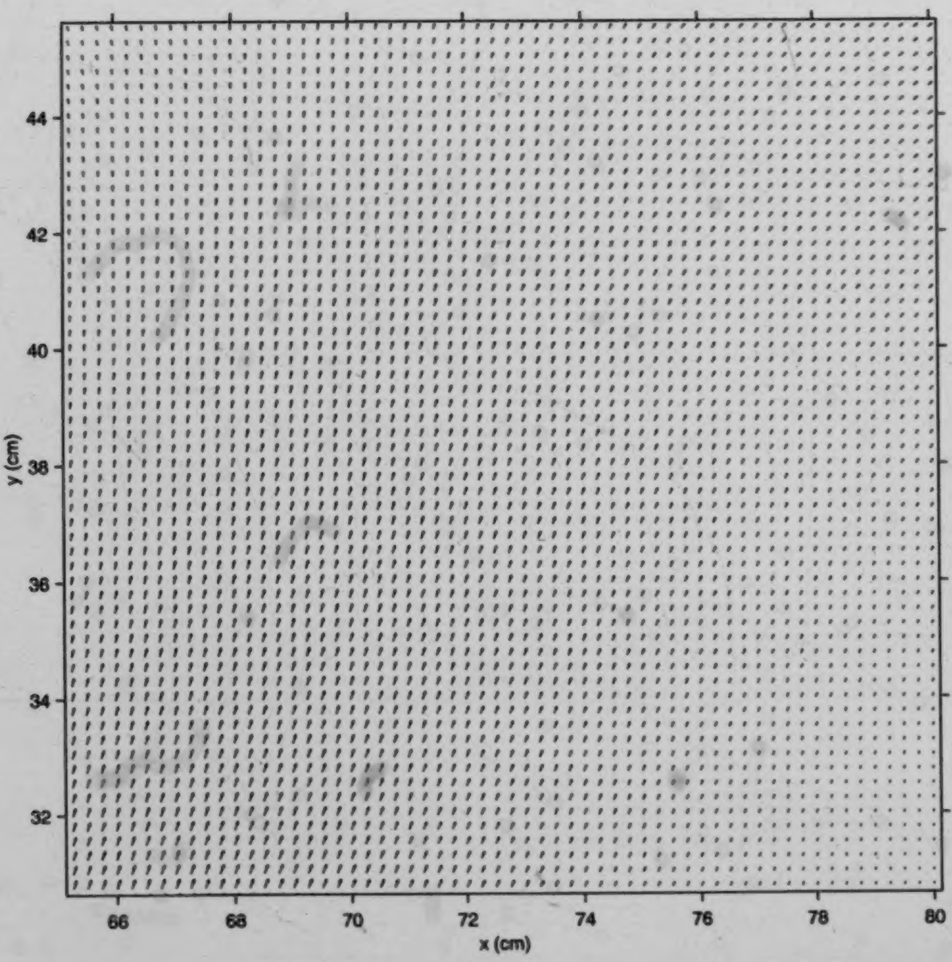

Figure 8.30: Tessera 8 component of assembled mean velocity vector field mosaic.

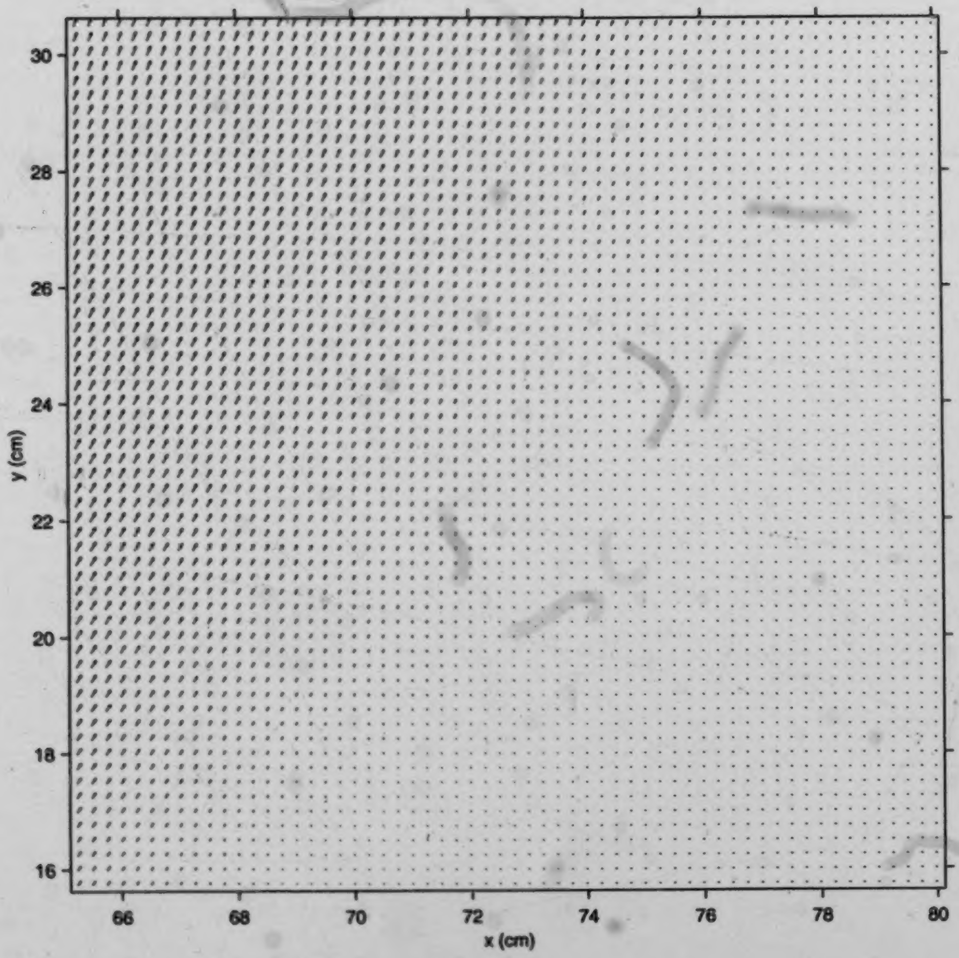

Figure 8.31: Tessera 9 component of assembled mean velocity vector field mosaic.

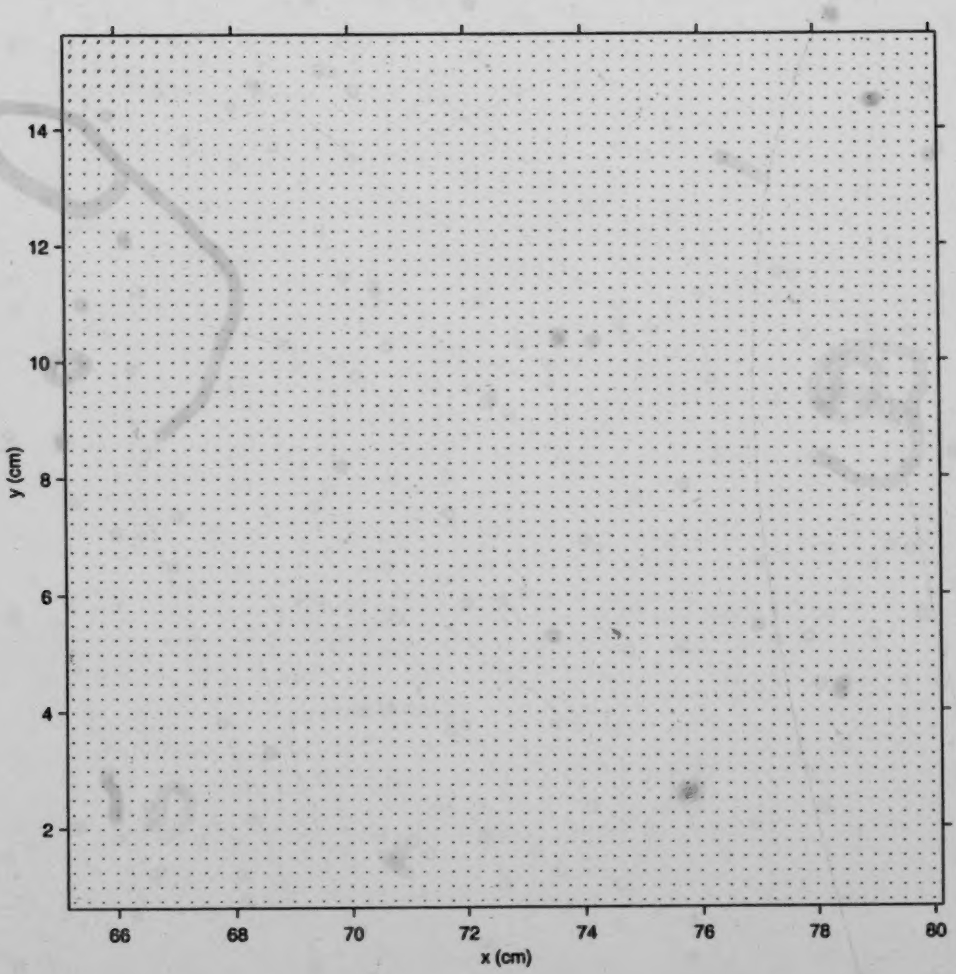

Figure 8.32: Tessera 10 component of assembled mean velocity vector field mosaic.

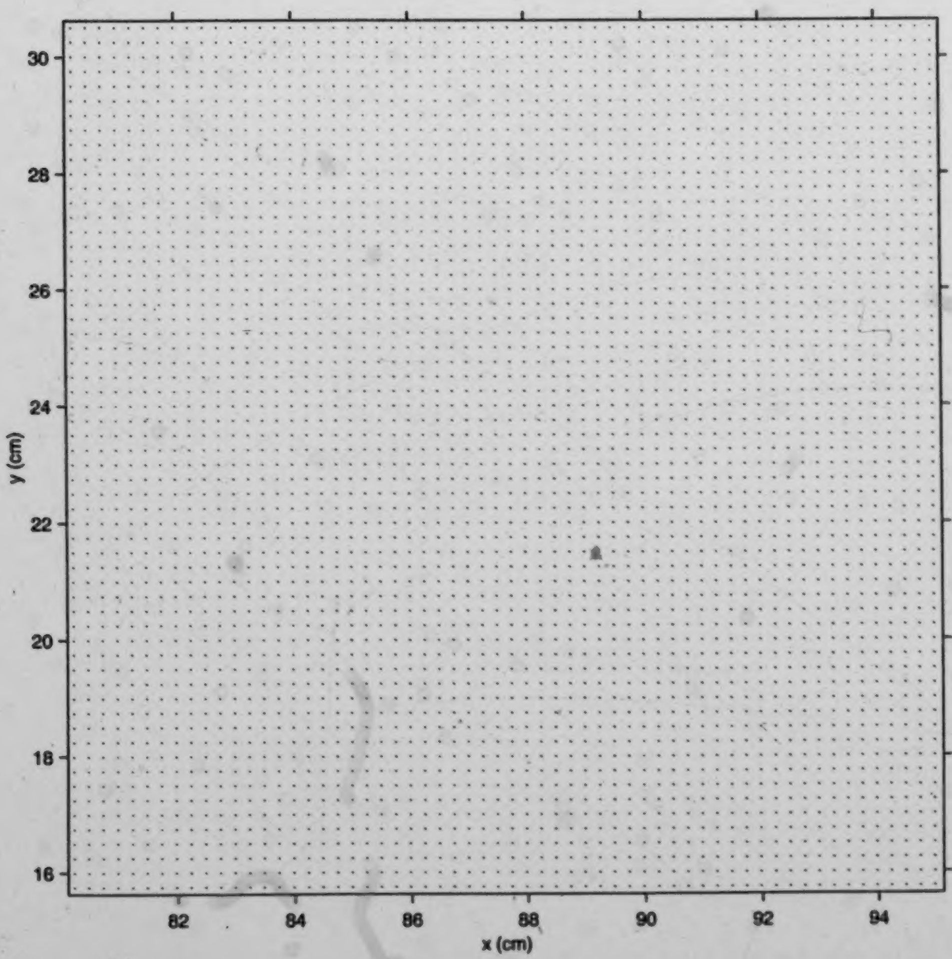

Figure 8.33: Tessera 11 component of assembled mean velocity vector field mosaic.

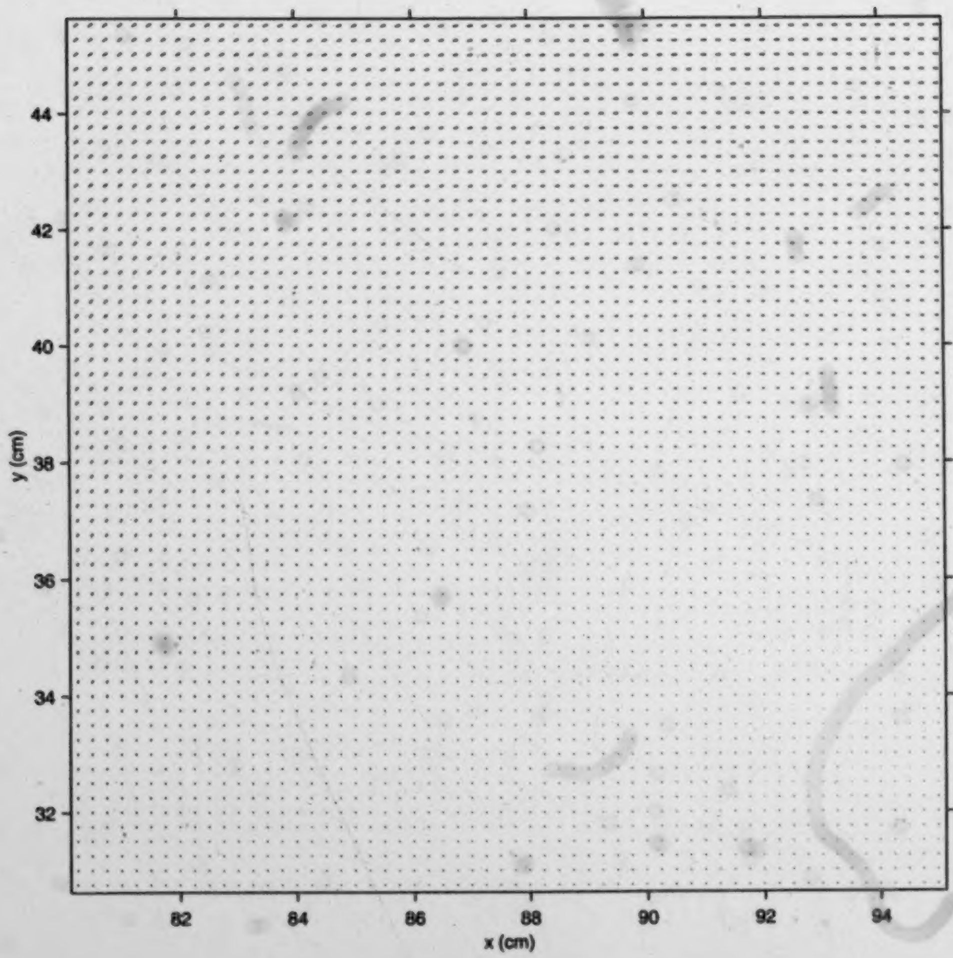

Figure 8.34: Tessera 12 component of assembled mean velocity vector field mosaic.

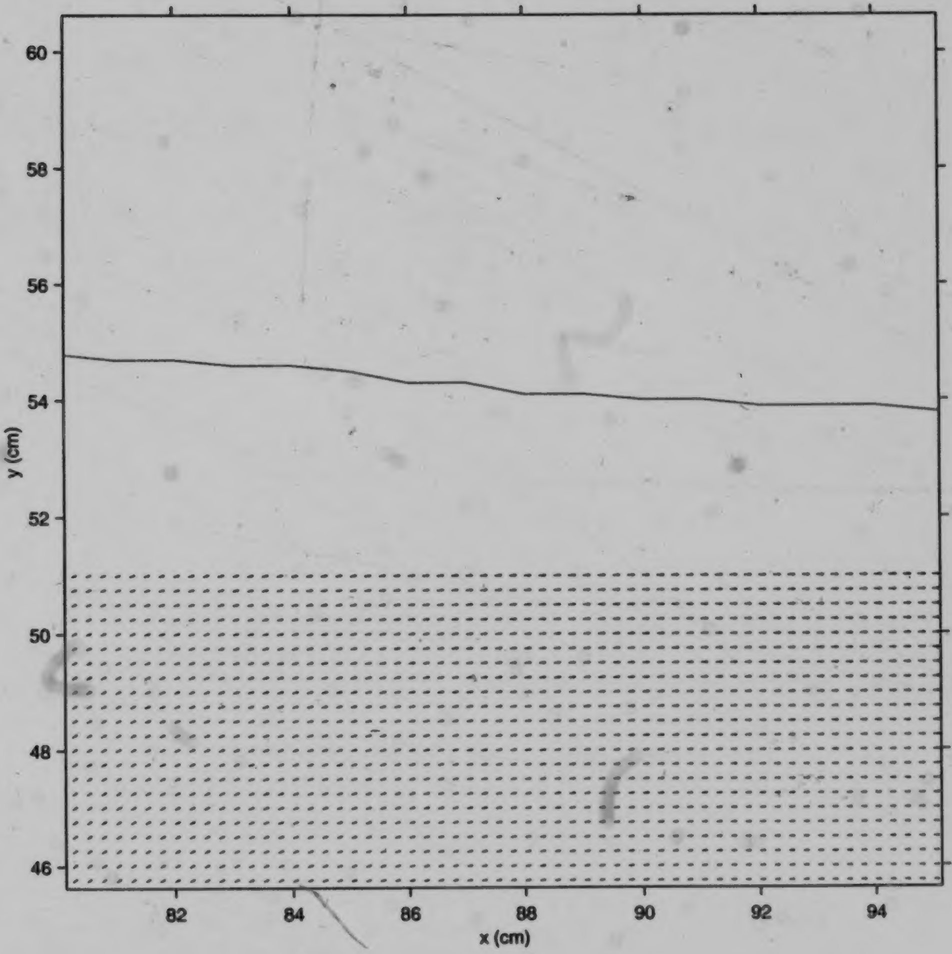

Figure 8.35: Tessera 13 component of assembled mean velocity vector field mosaic.

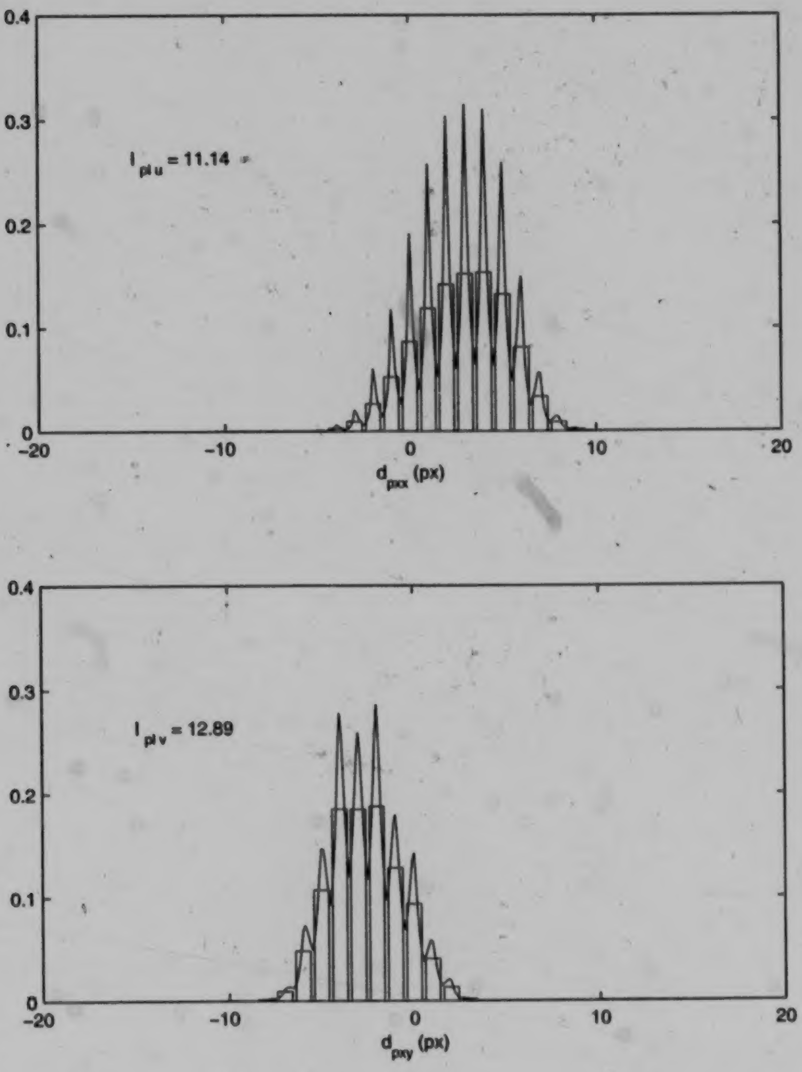

Figure 8.36: Peak locking error in tessera 1 raw pixel displacement data.

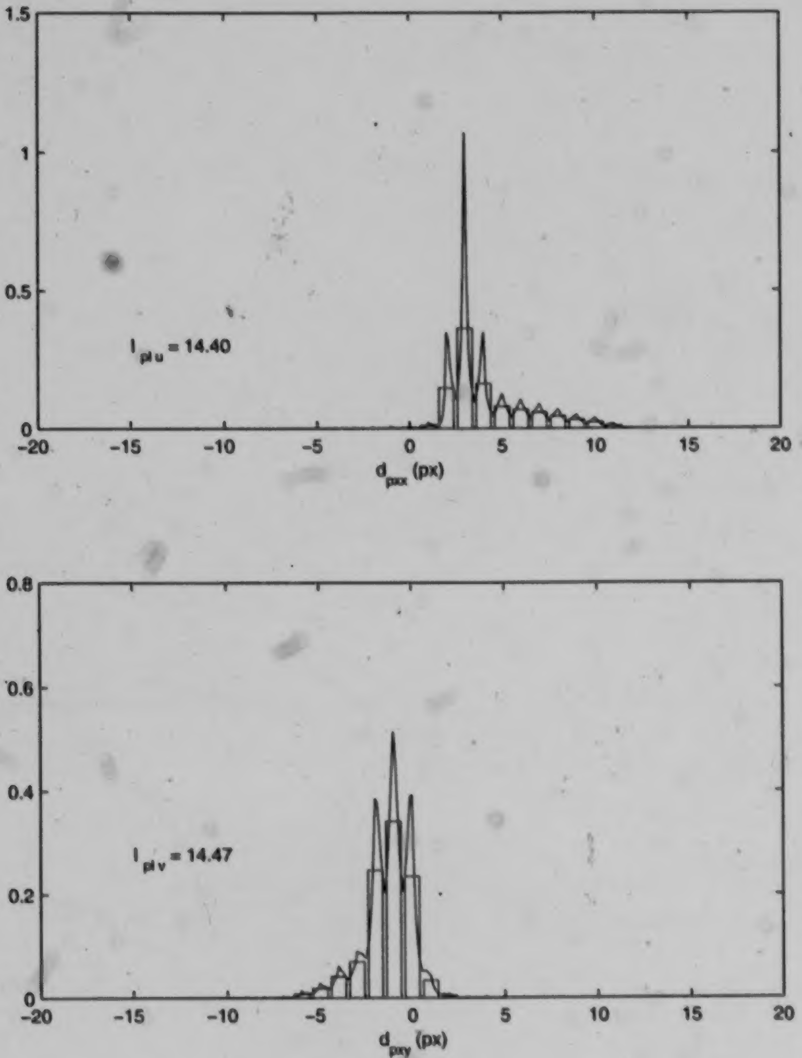

Figure 8.37: Peak locking error in tessera 2 raw pixel displacement data.

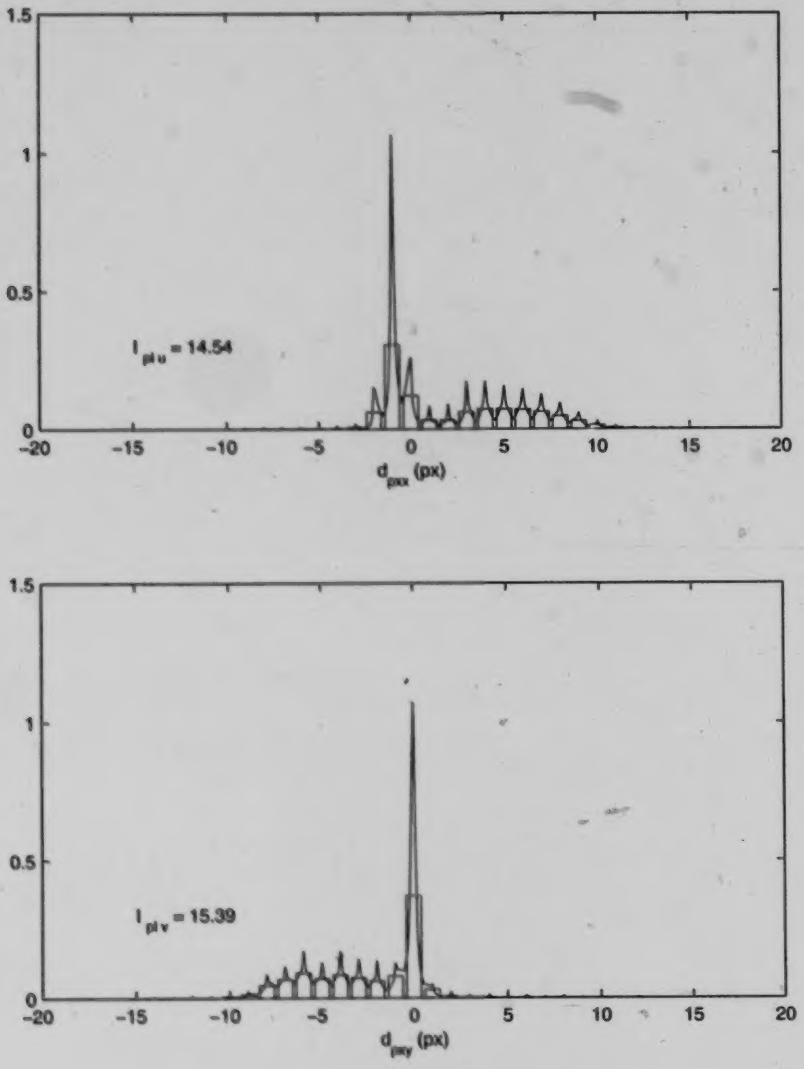

Figure 8.38: Peak locking error in tessera 3 raw pixel displacement data.

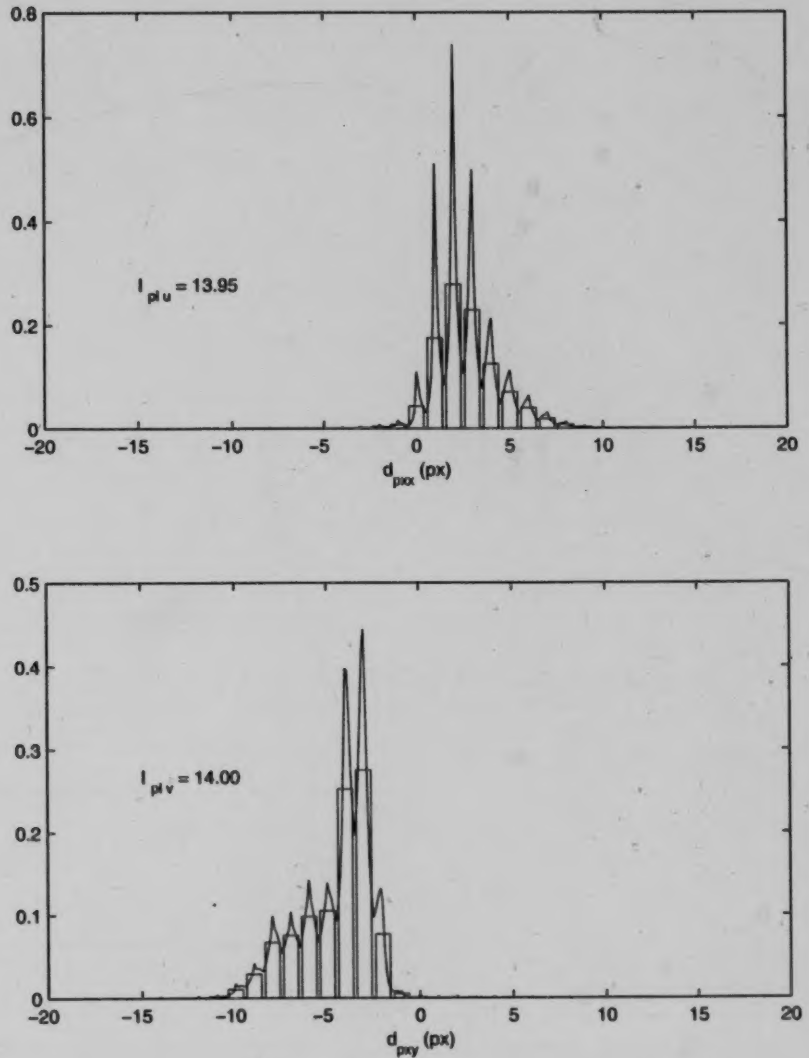

Figure 8.39: Peak locking error in tessera 4 raw pixel displacement data.

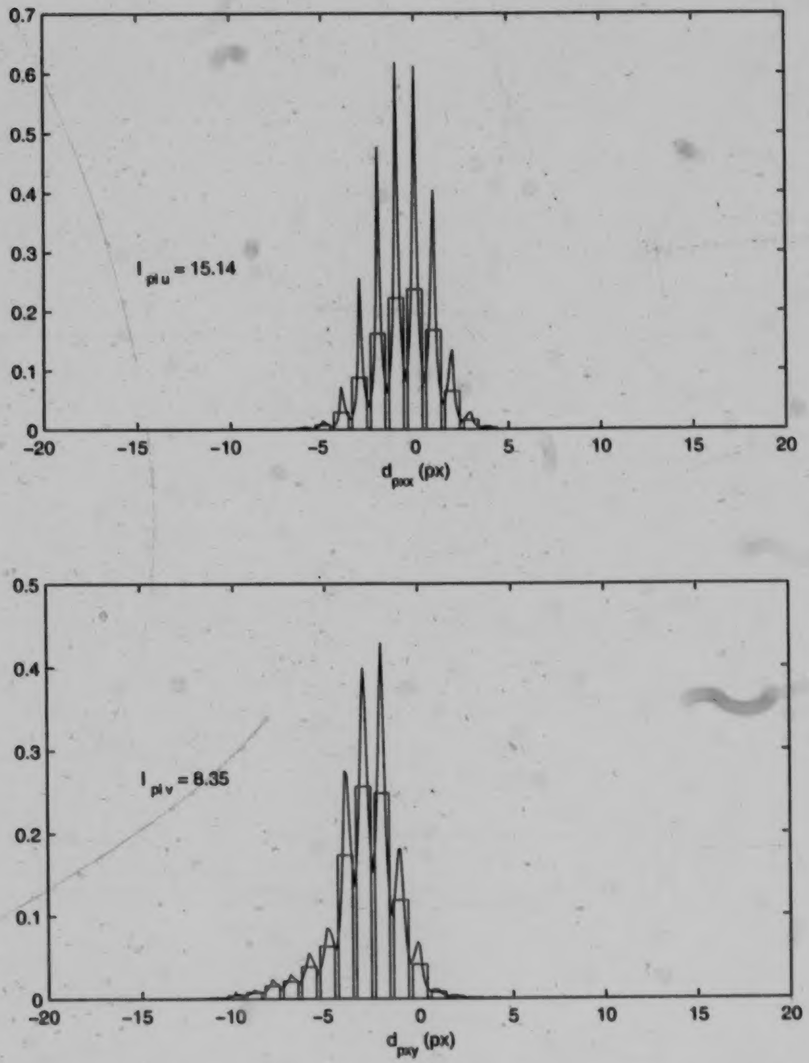

Figure 8.40: Peak locking error in tessera 5 raw pixel displacement data.

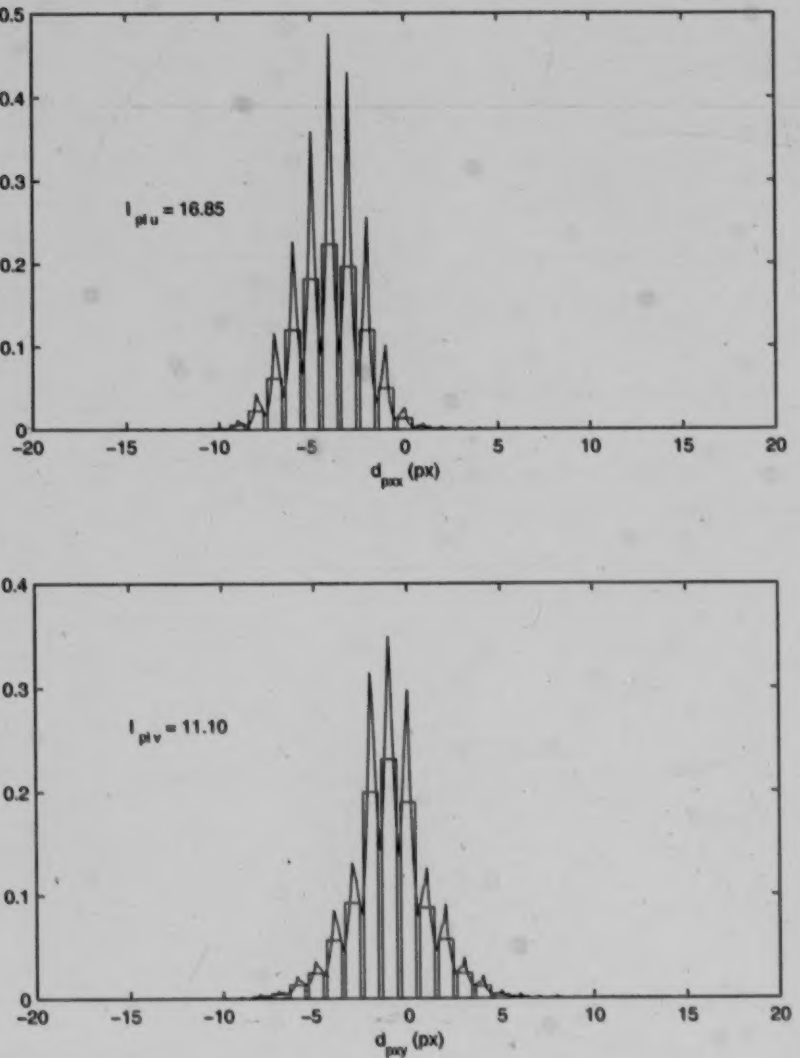

Figure 8.41: Peak locking error in tessera 6 raw pixel displacement data.

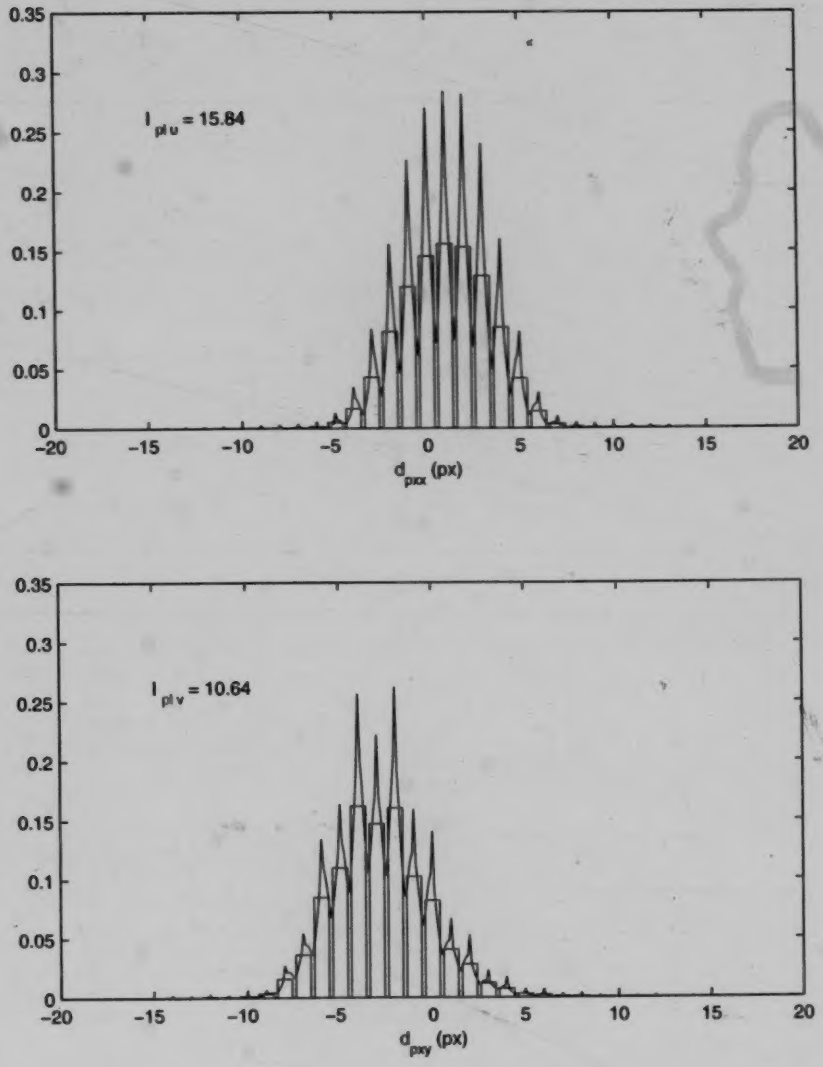

Figure 8.42: Peak locking error in tessera 7 raw pixel displacement data.

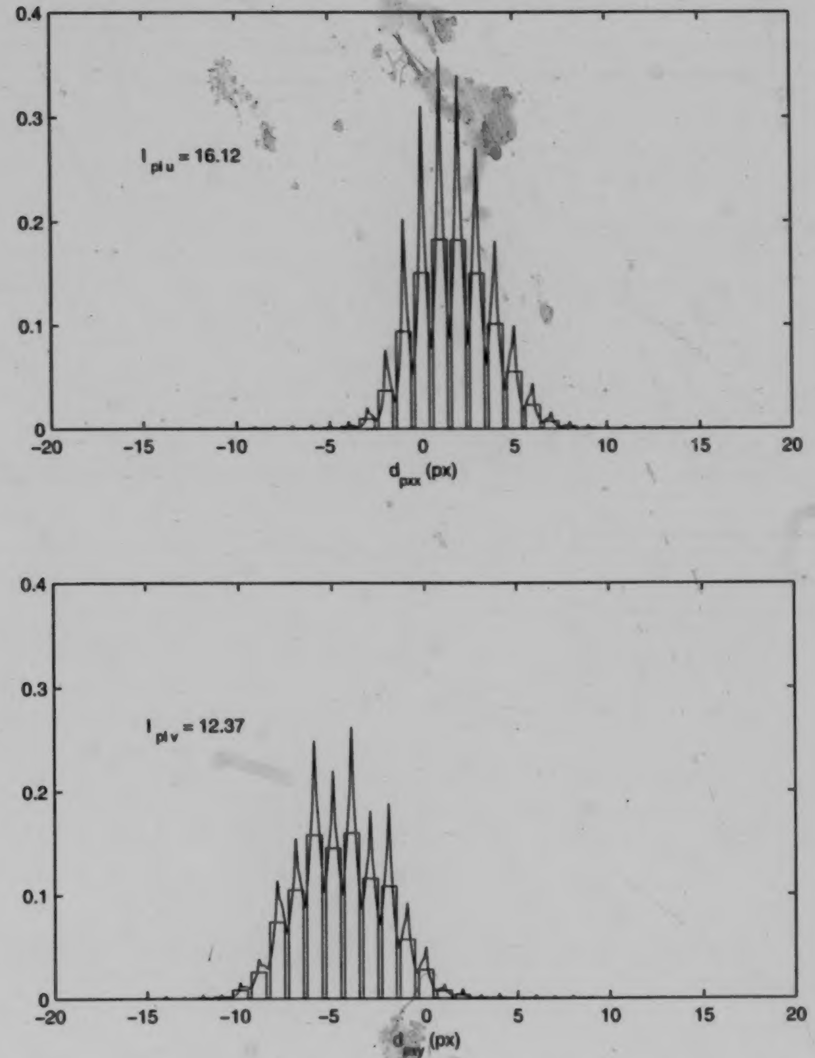

Figure 8.43: Peak locking error in tessera 8 raw pixel displacement data.

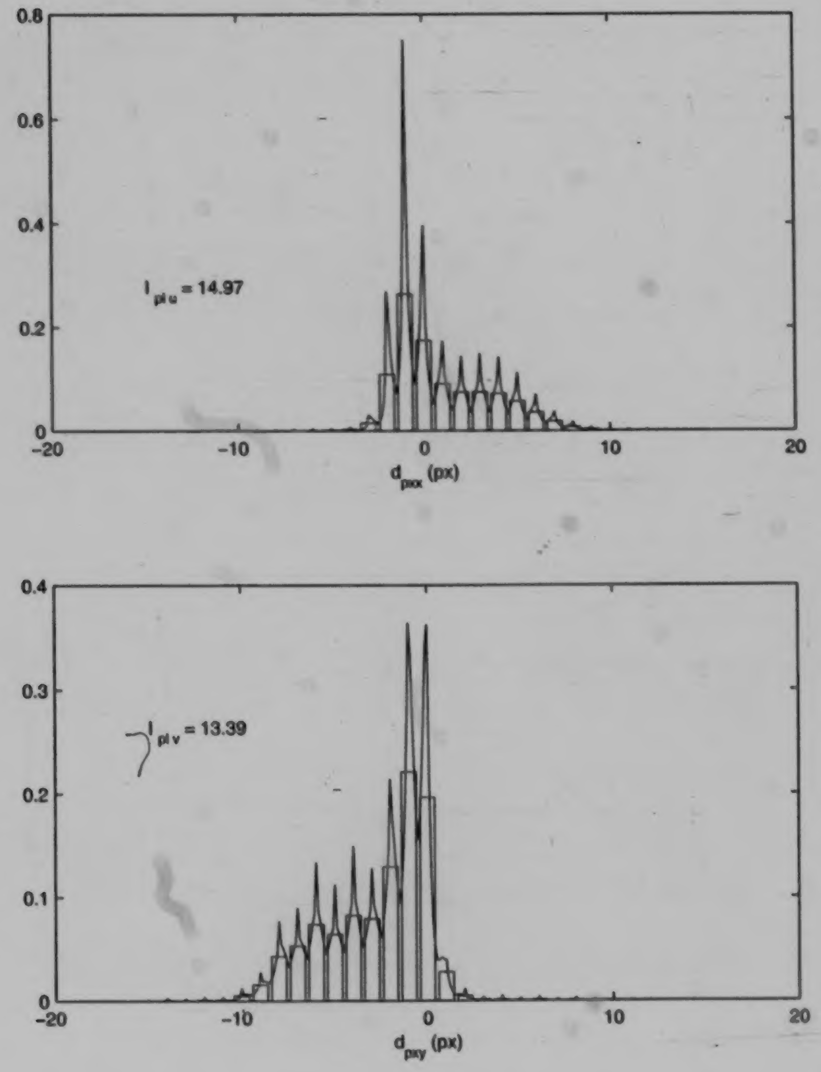

Figure 8.44: Peak locking error in tessera 9 raw pixel displacement data.

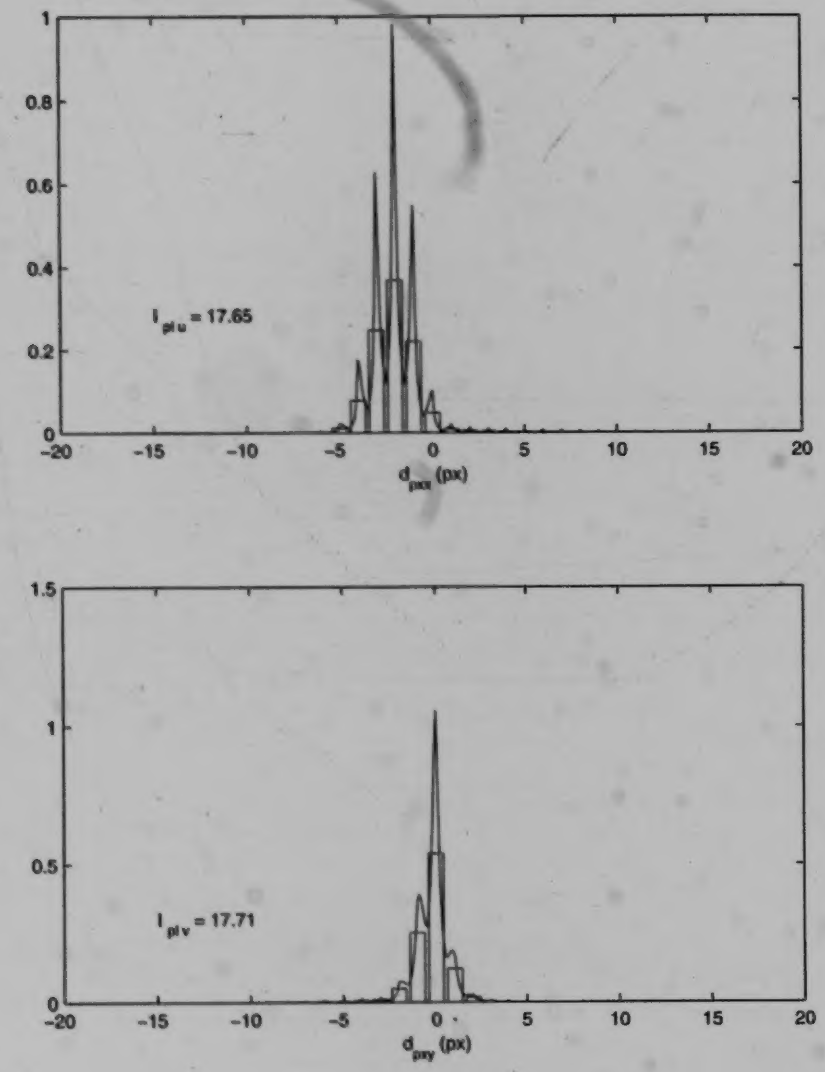

Figure 8.45: Peak locking error in tessera 10 raw pixel displacement data.

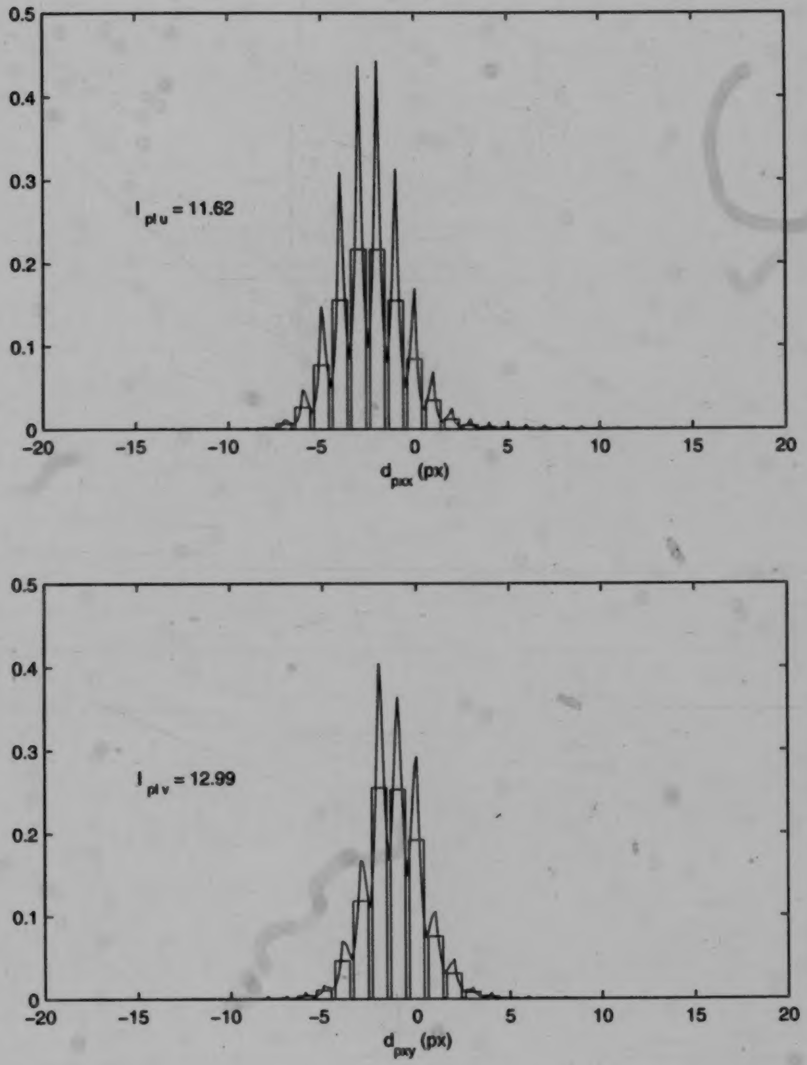

Figure 8.46: Peak locking error in tessera 11 raw pixel displacement data.

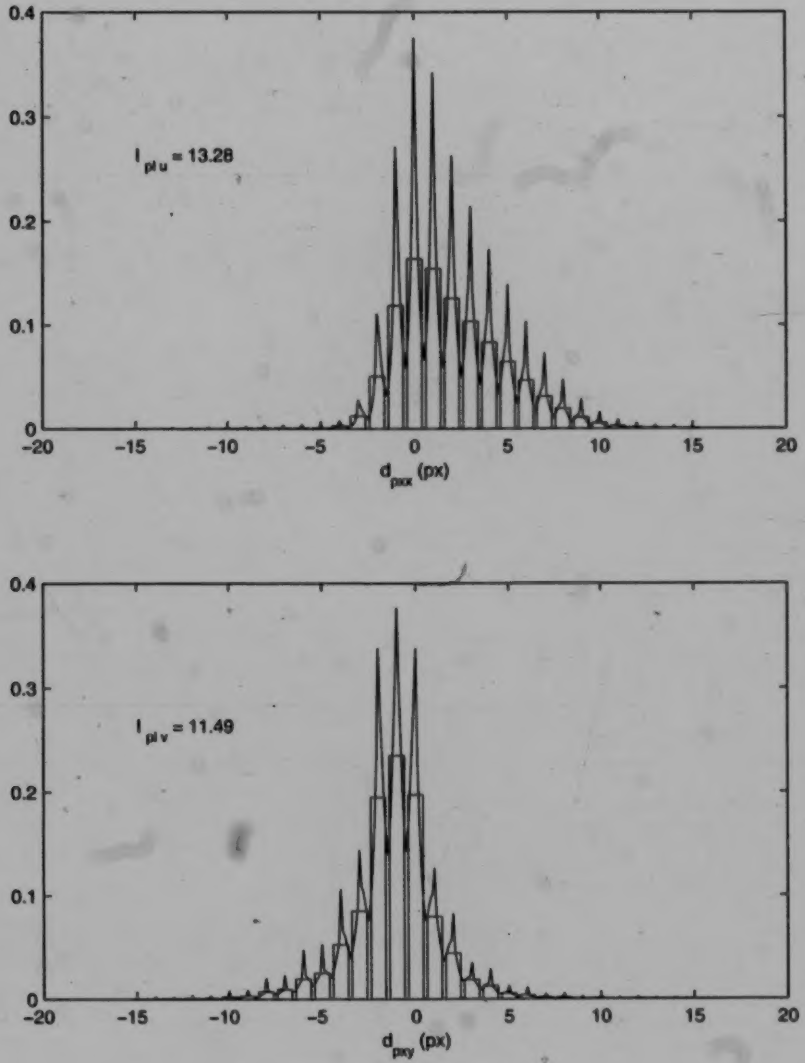

Figure 8.47: Peak locking error in tessera 12 raw pixel displacement data.

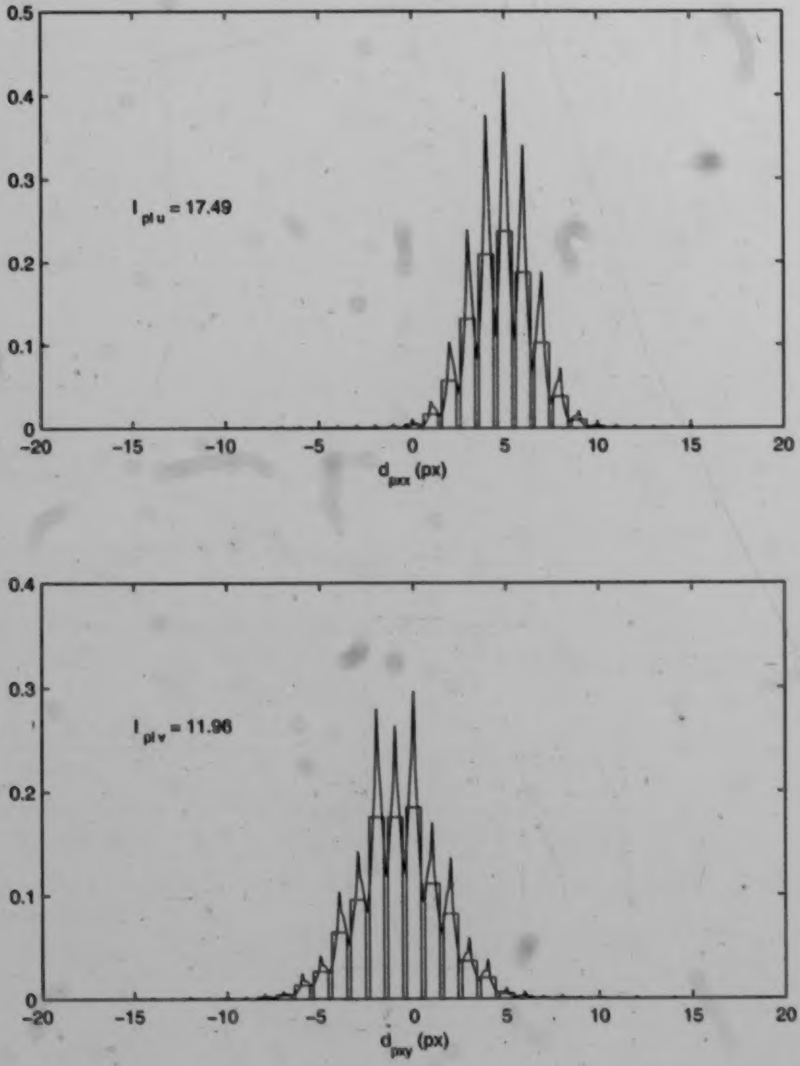

Figure 8.48: Peak locking error in tessera 13 raw pixel displacement data.

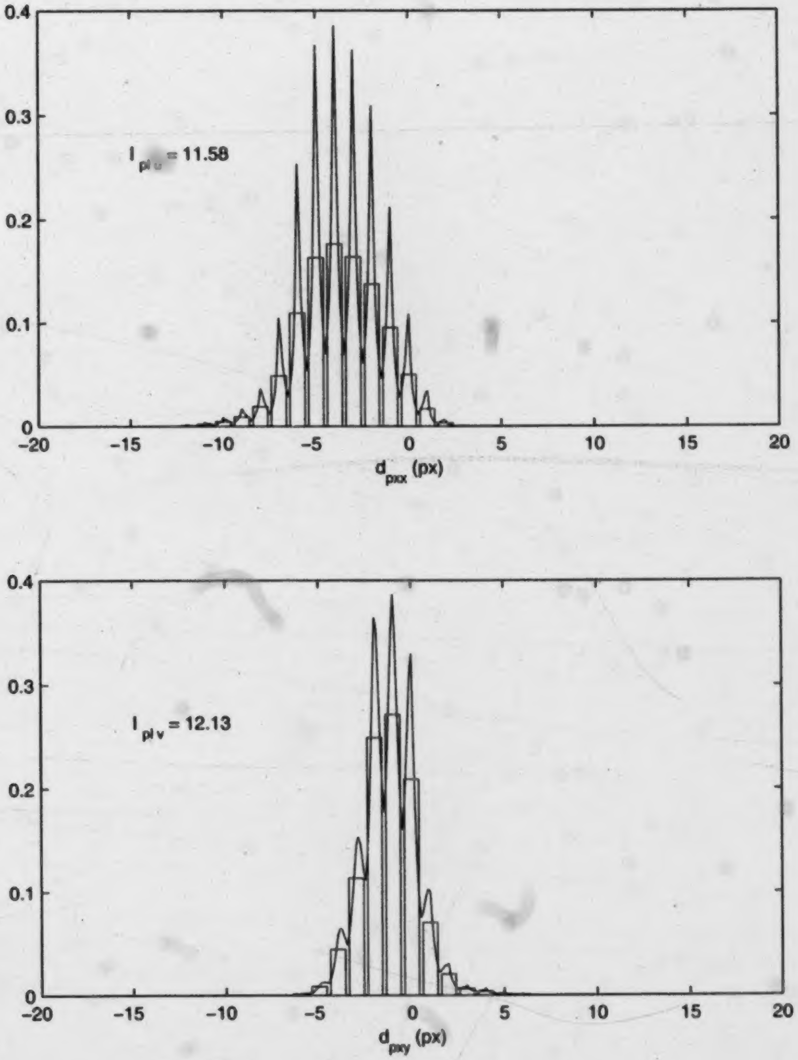

Figure 8.49: Peak locking error in tessera 14 raw pixel displacement data.

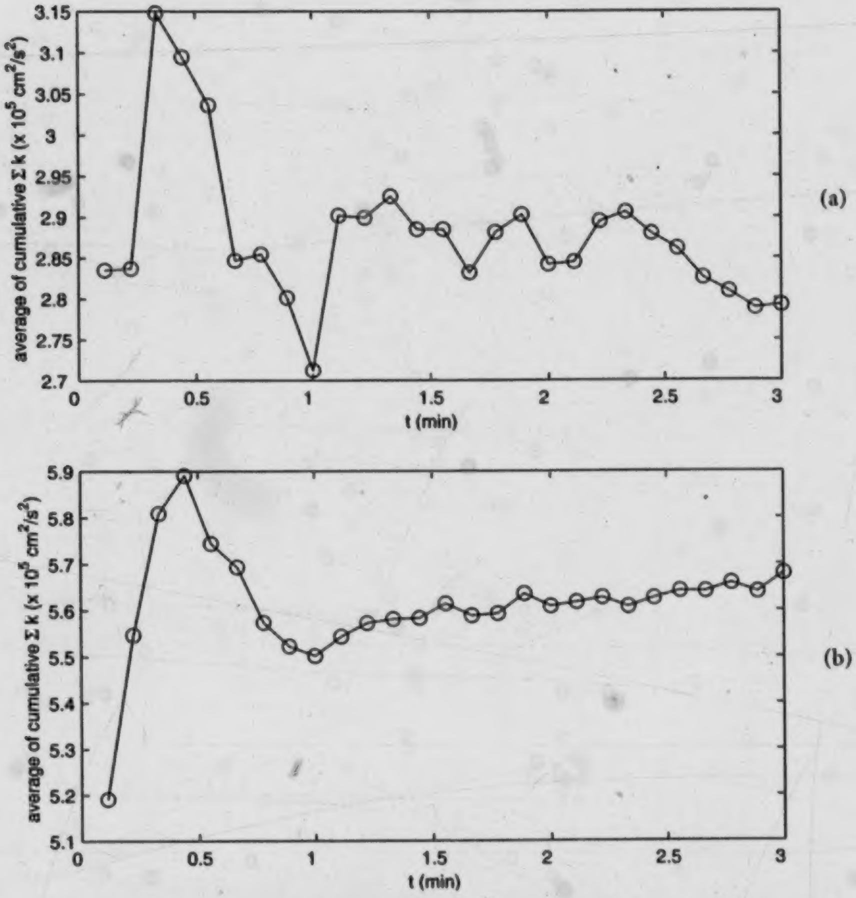

Figure 8.50: (a-n) The cumulative average, plotted over increasing periods of time and averaging larger batches of PIV data files, of the sum of all turbulent kinetic energy (k) measurements in a tessera, presented for (a) tessera 1 through (n) tessera 14; showing that a sufficient amount of data was collected at each tessera for representative mean turbulent flow characteristics to be calculated.

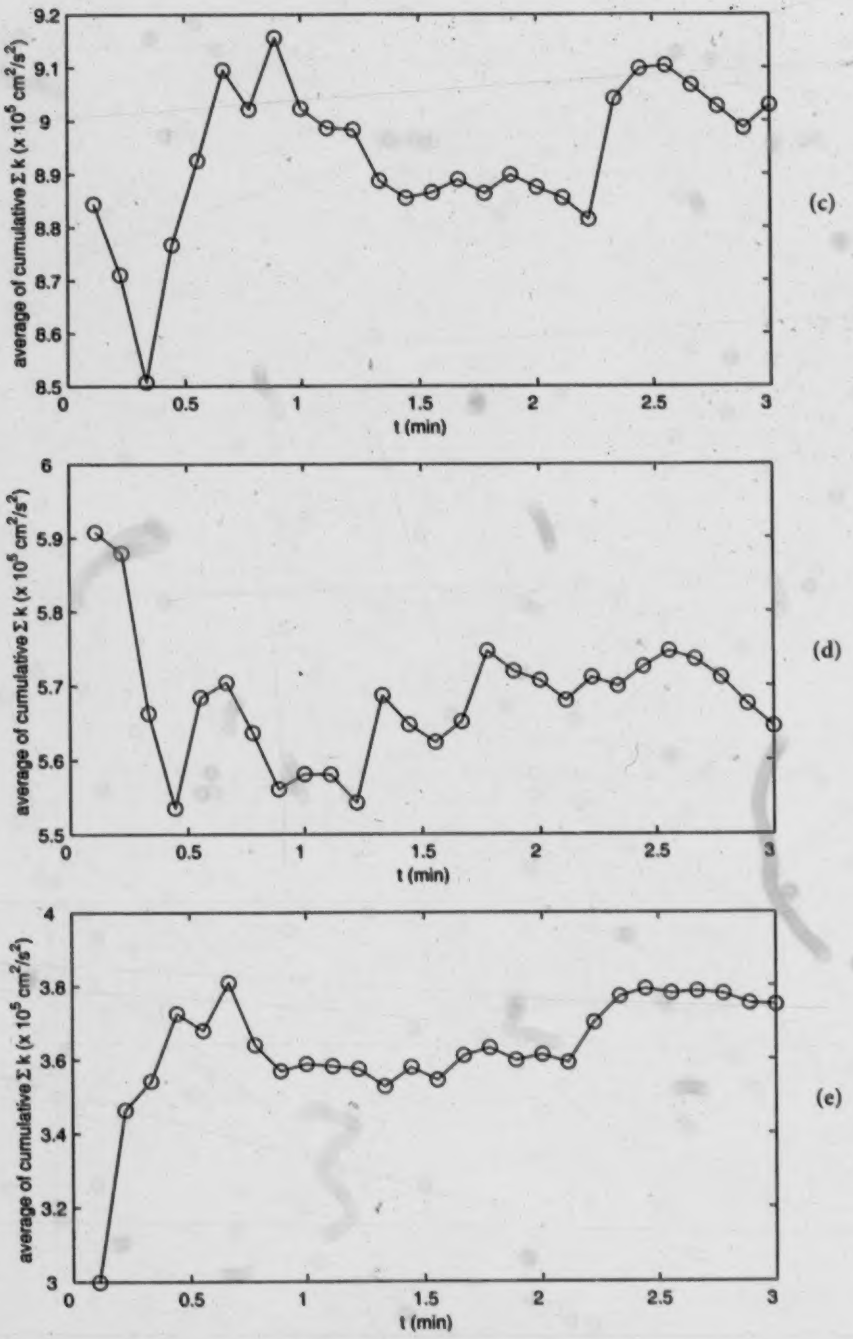

Figure 8.50 continued.

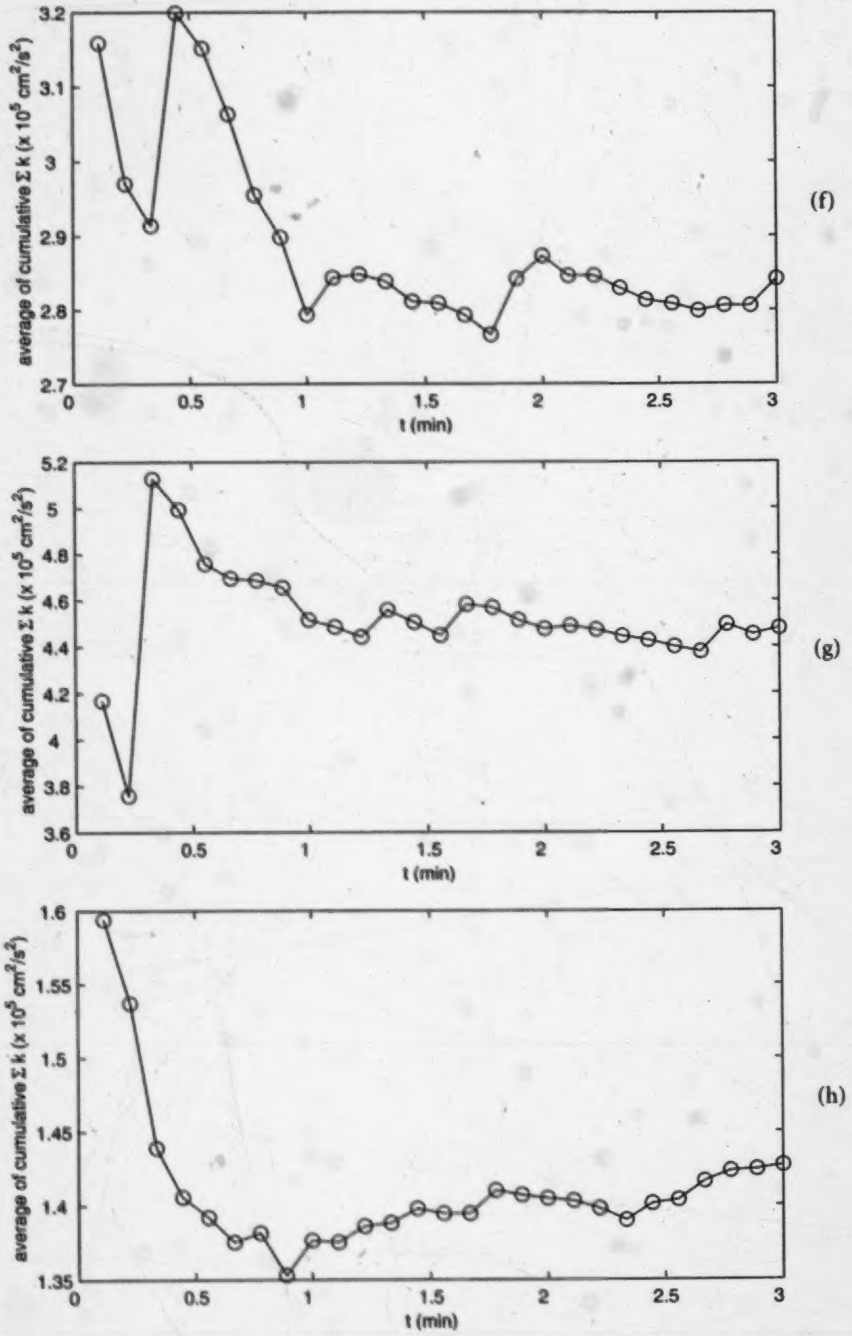

Figure 8.50 continued.

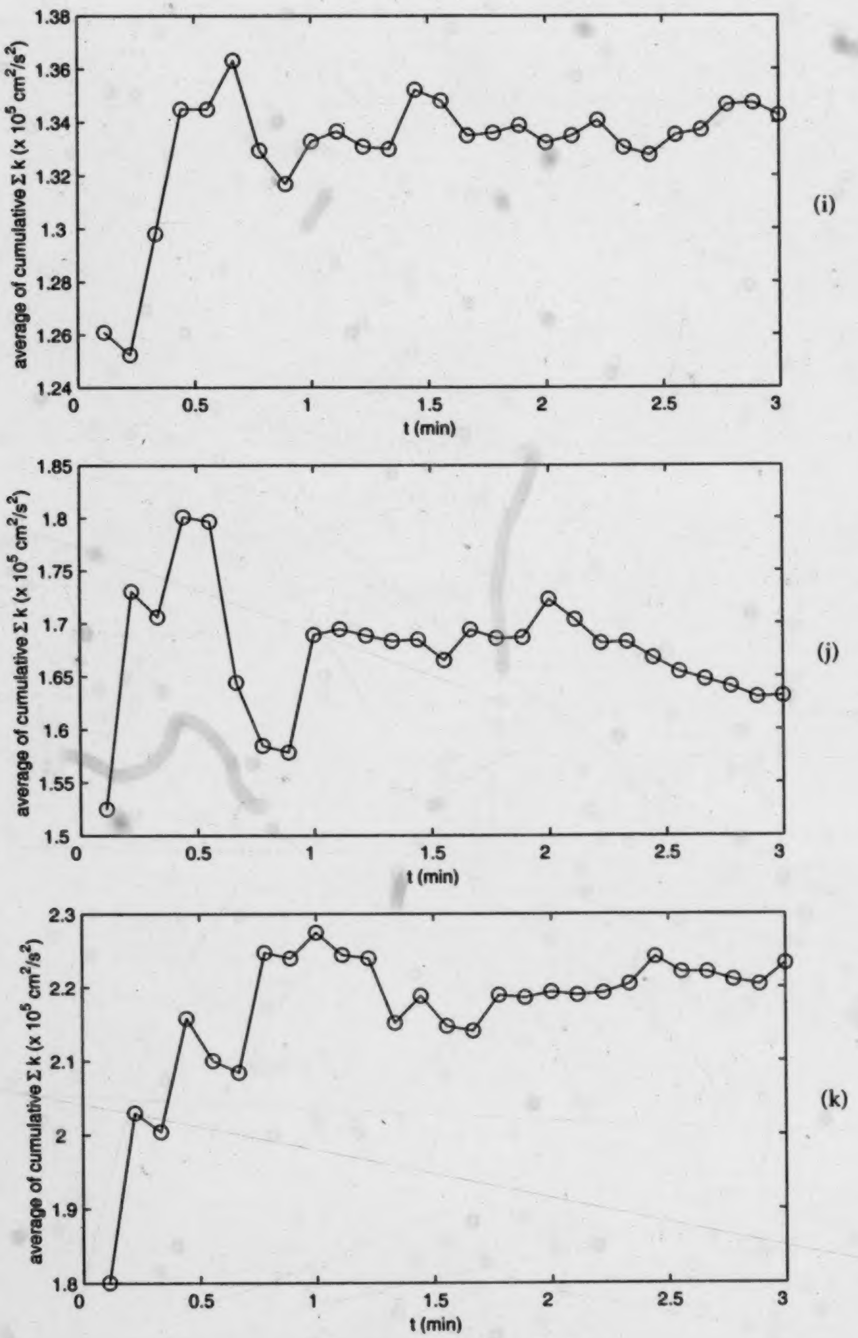

Figure 8.50 continued.

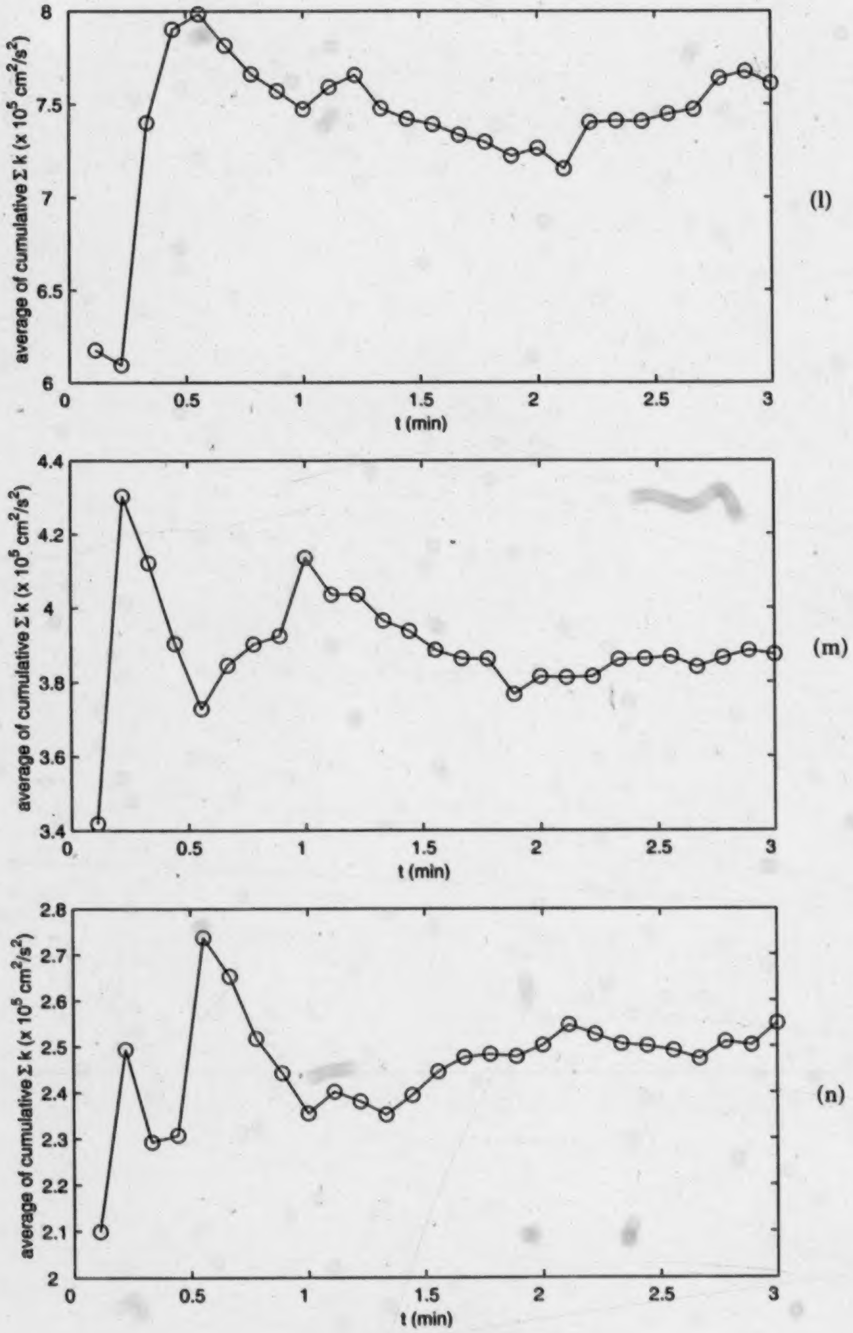

Figure 8.50 continued.

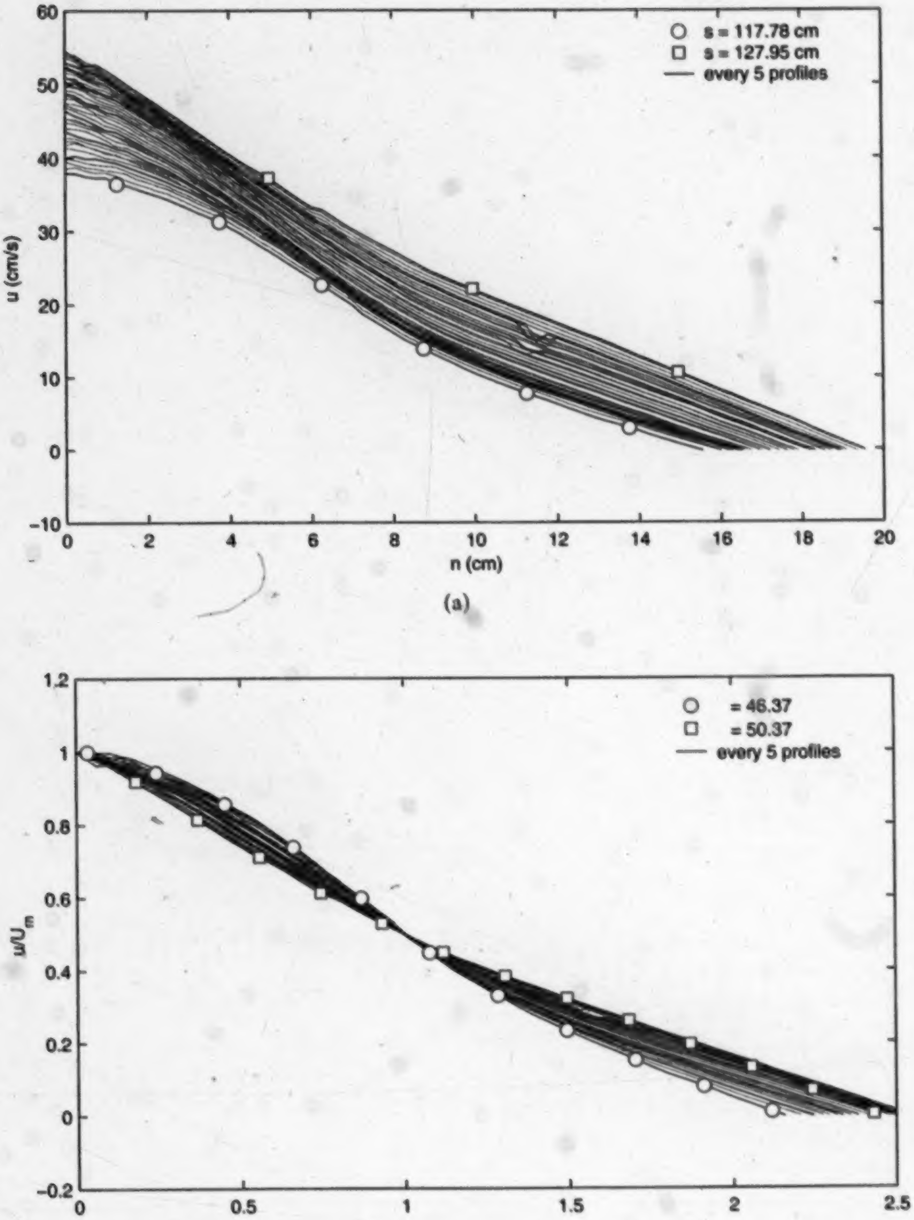

(a)

(b)

Figure 8.51: (a) Dimensional and (b) nondimensional u mean velocities for return flow surface jet-like (SJL) profiles.

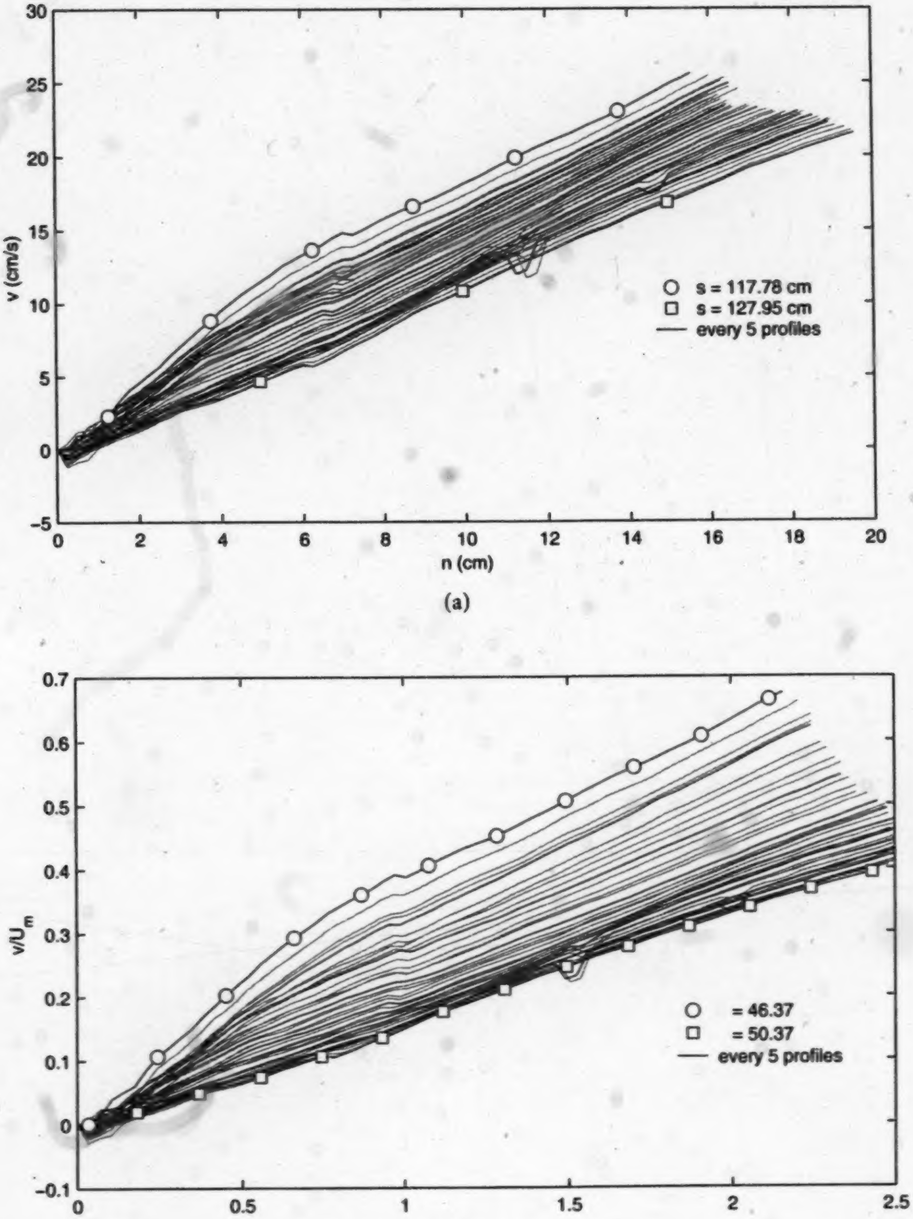

(a)

(b)

Figure 8.52: (a) Dimensional and (b) nondimensional v mean velocities for return flow surface jet-like (SJL) profiles.

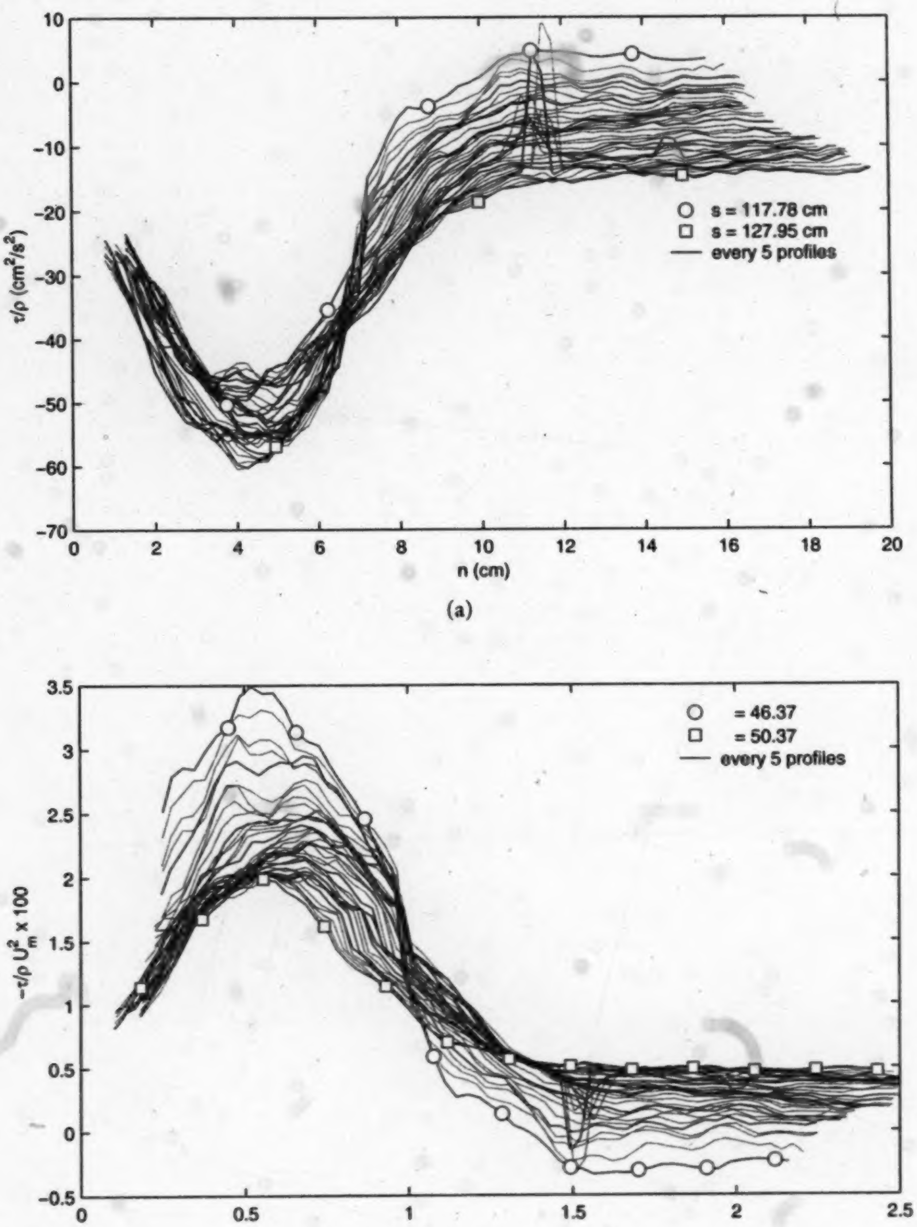

(a)

(b)

Figure 8.53: (a) Dimensional and (b) nondimensional mean Reynolds stress per unit mass (τ/ρ) for return flow surface jet-like (SJL) profiles.

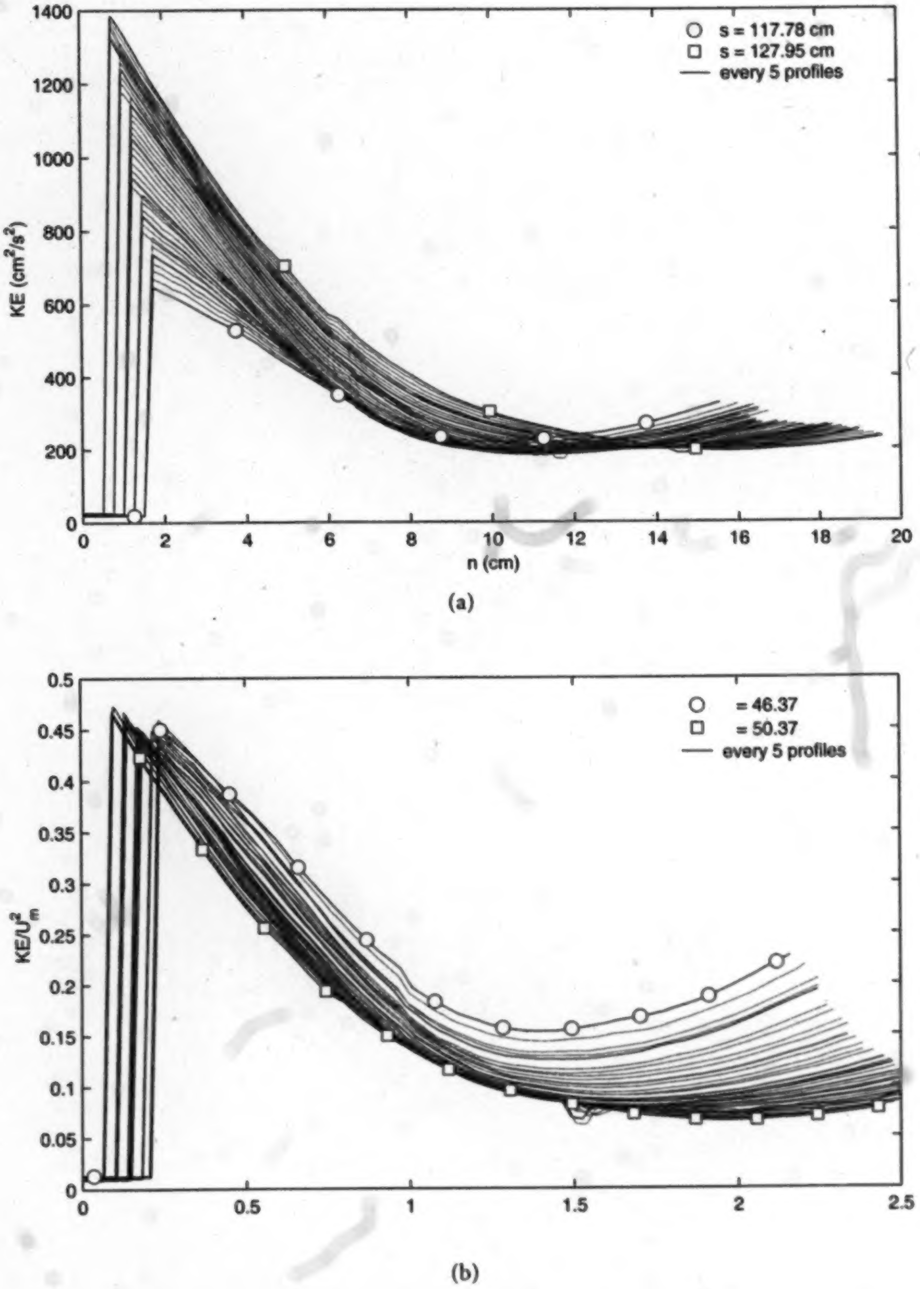

Figure 8.54: (a) Dimensional and (b) nondimensional mean kinetic energy per unit mass (KE) for return flow surface jet-like (SJL) profiles.

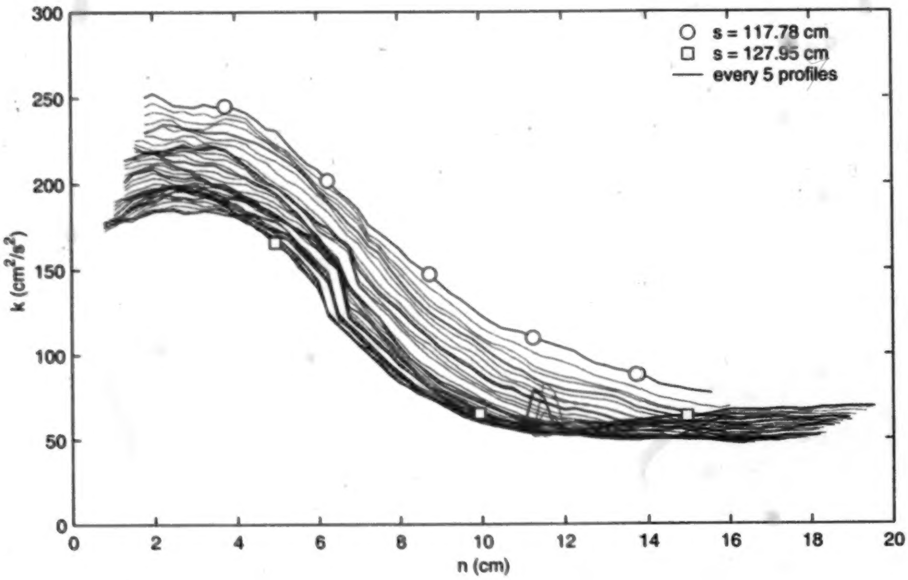

(a)

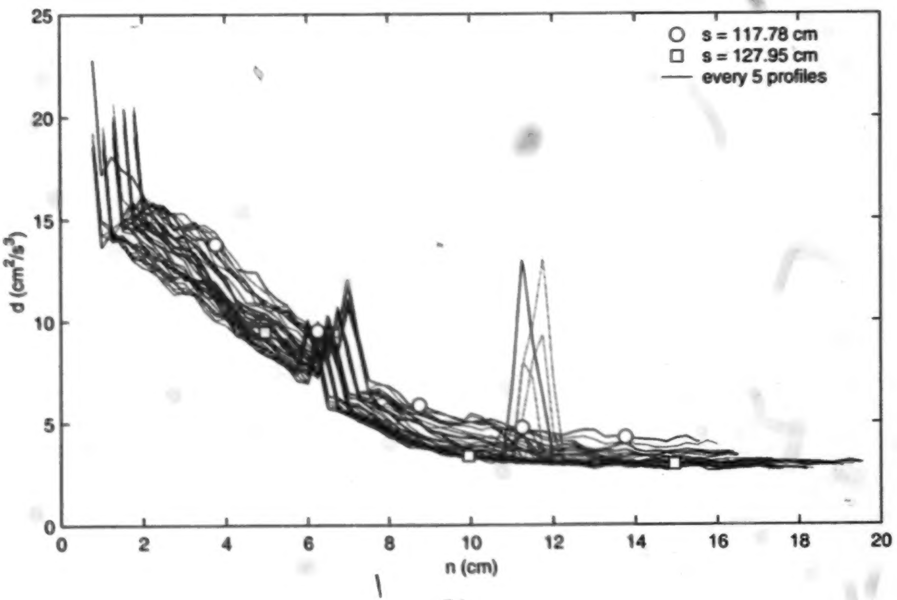

(b)

Figure 8.55: Mean (a) turbulent kinetic energy per unit mass (k) and (b) dissipation per unit mass (d) for return surface jet-like (SJL) profiles.

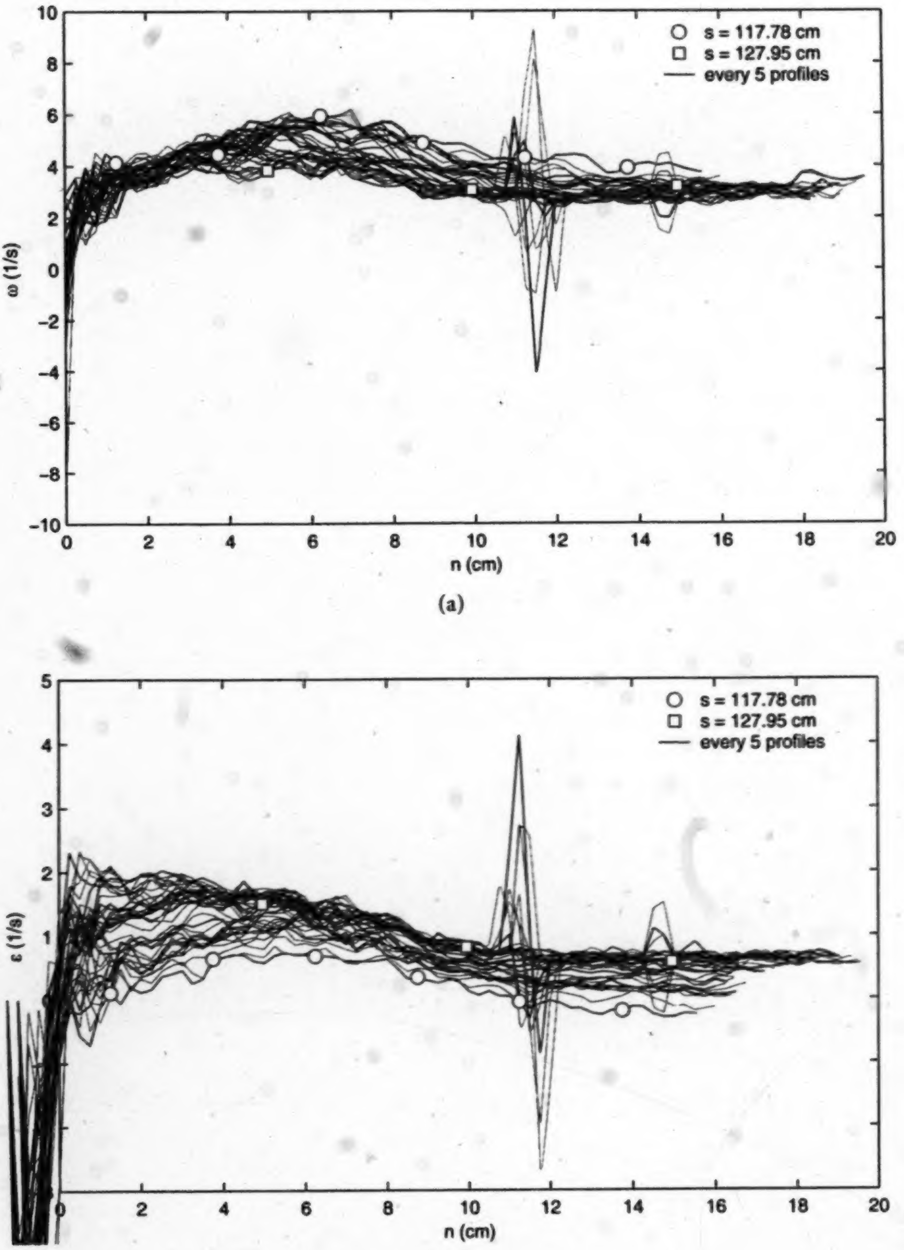

(a)

(b)

Figure 8.56: Mean (a) vorticity (ω) and (b) strain (ε) for return surface jet-like (SJL) profiles.

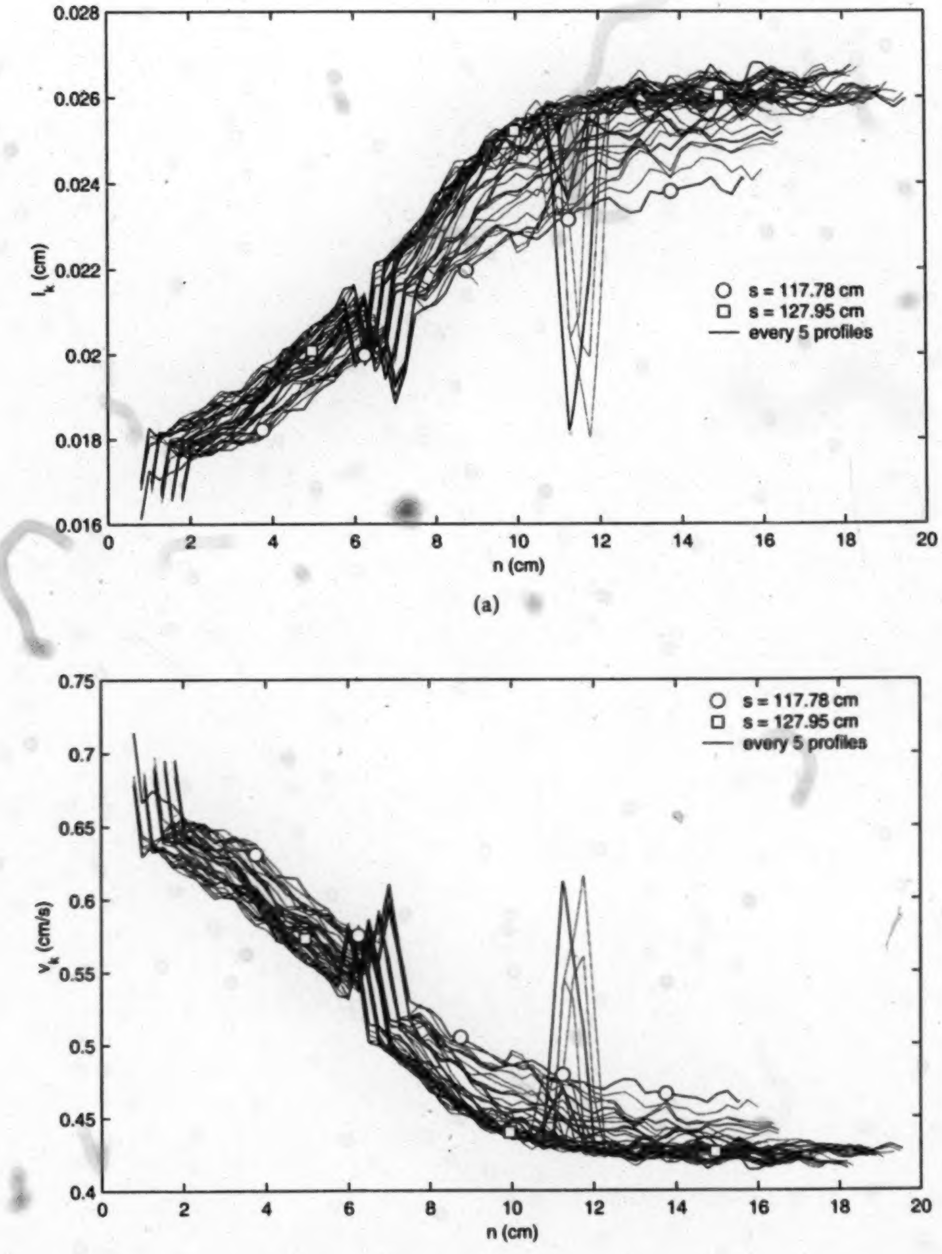

(a)

(b)

Figure 8.57: Mean Kolmogorov (a) length scales (l_k) and (b) velocity scales (v_k) for return surface jet-like (SJL) profiles.

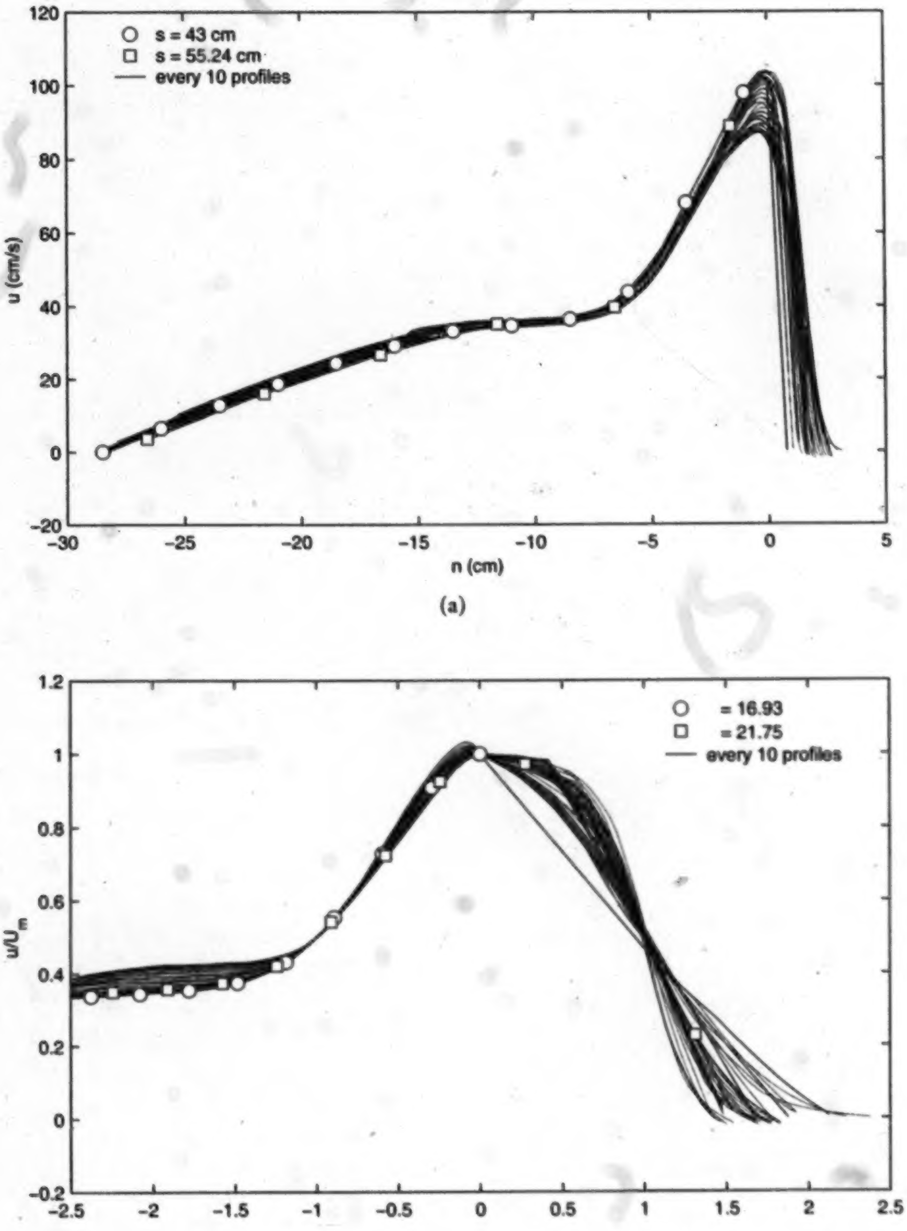

(a)

(b)

Figure 8.58: (a) Dimensional and (b) nondimensional u mean velocities for first transition zone (TZ1) profiles.

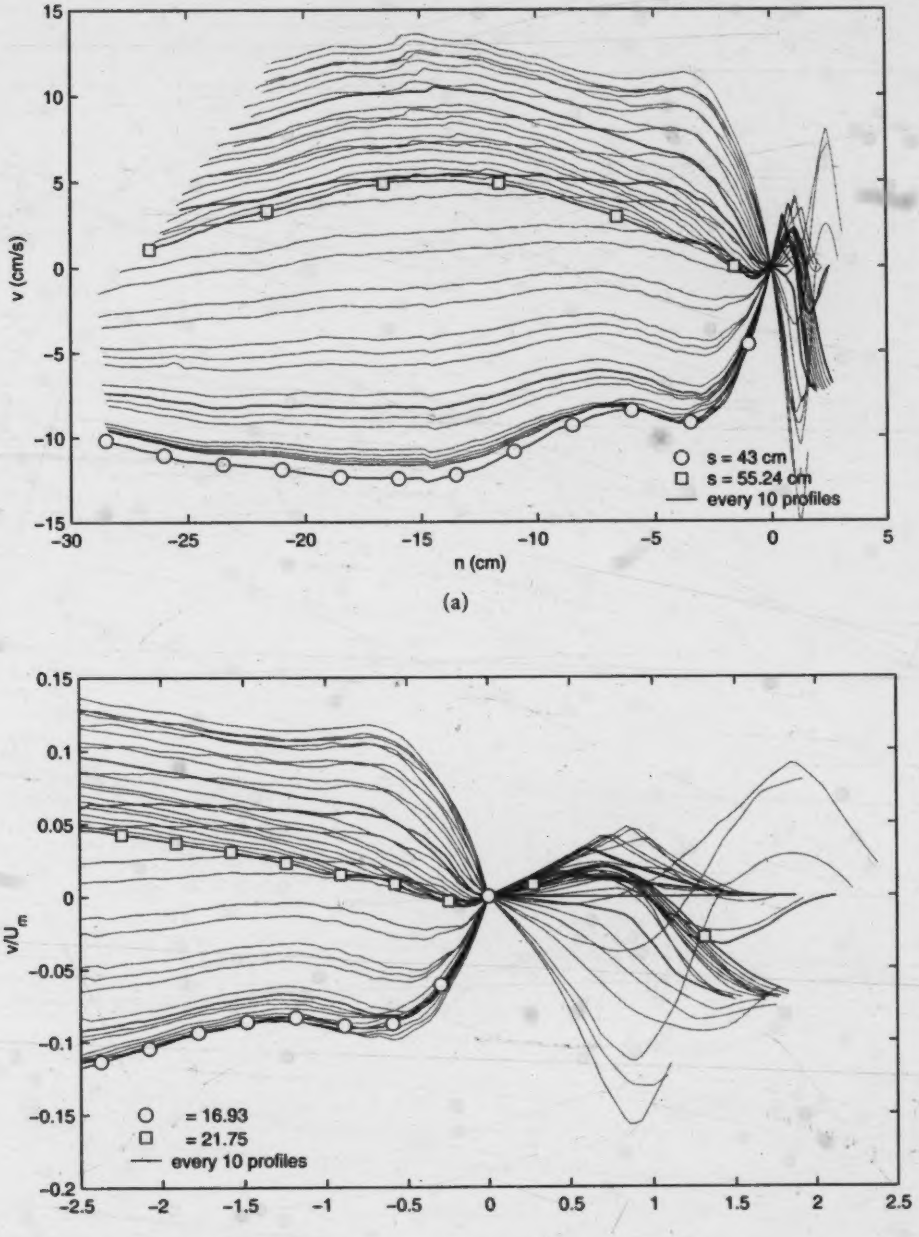

(a)

(b)

Figure 8.59: (a) Dimensional and (b) nondimensional v mean velocities for first transition zone (TZ1) profiles.

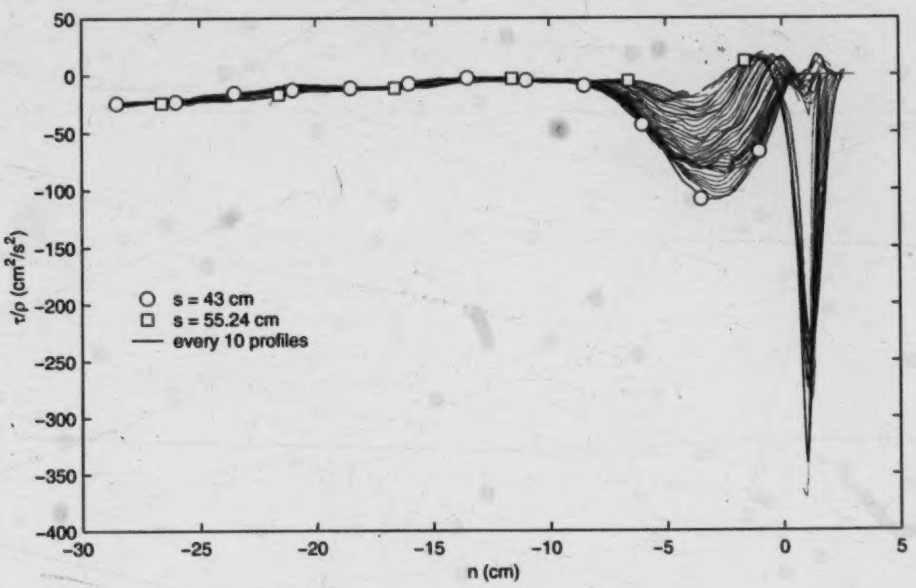

(a)

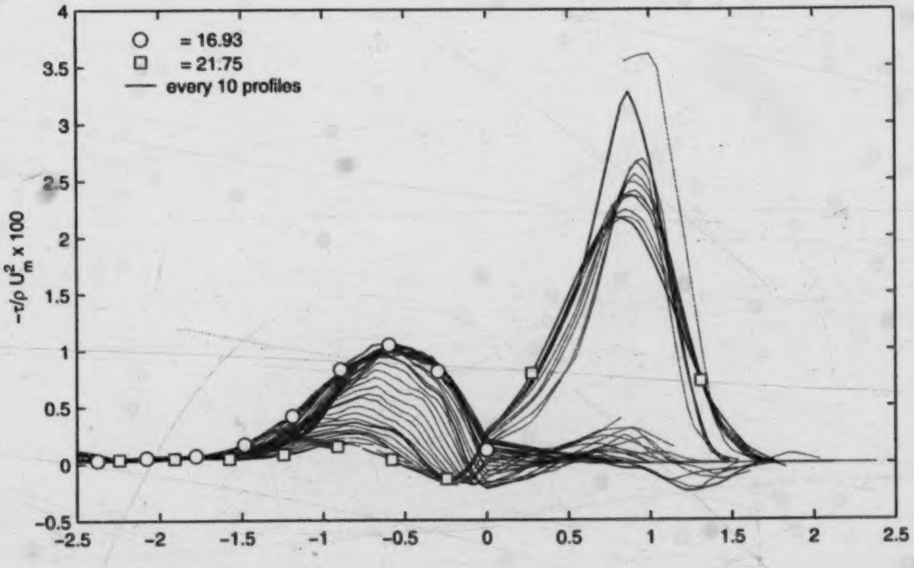

(b)

Figure 8.60: (a) Dimensional and (b) nondimensional mean Reynolds stress per unit mass (τ/ρ) for first transition zone (TZ1) profiles.

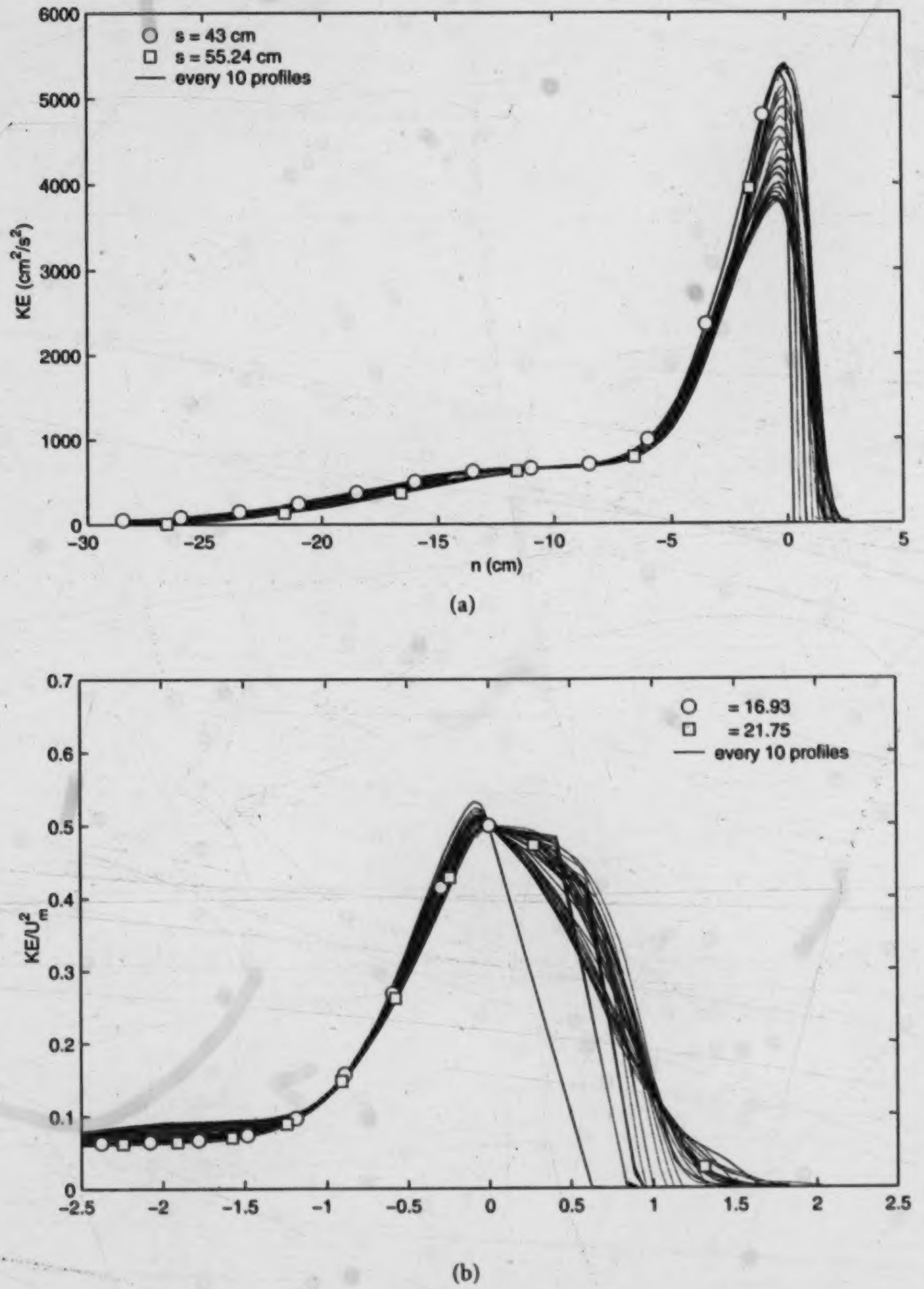

Figure 8.61: (a) Dimensional and (b) nondimensional mean kinetic energy (KE) for first transition zone (TZ1) profiles.

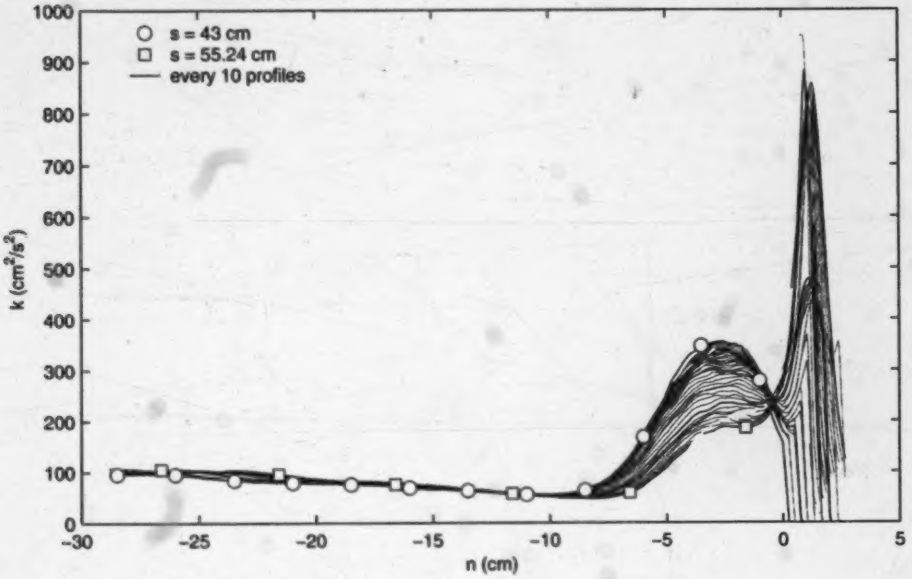

(a)

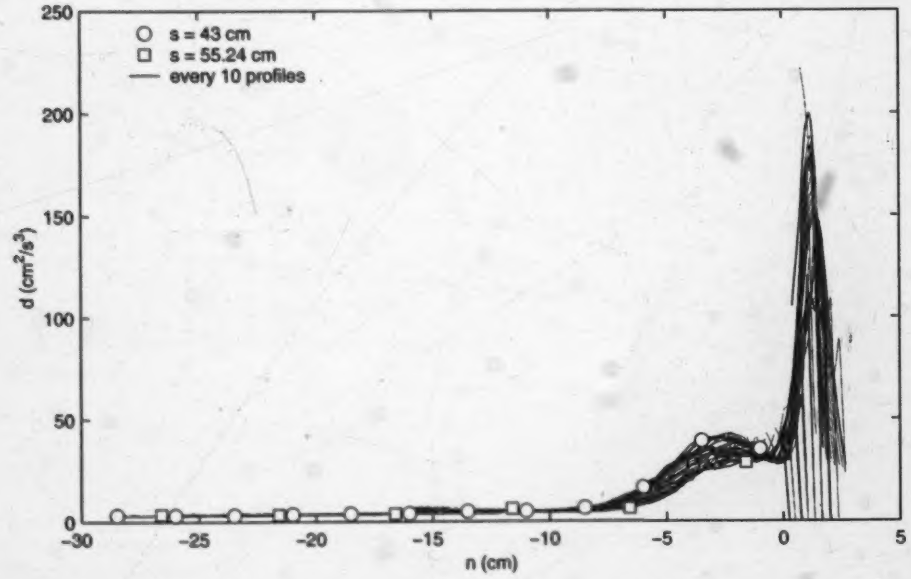

(b)

Figure 8.62: Mean (a) turbulent kinetic energy per unit mass (k) and (b) dissipation per unit mass (d) for the first transition zone (TZ1) profiles.

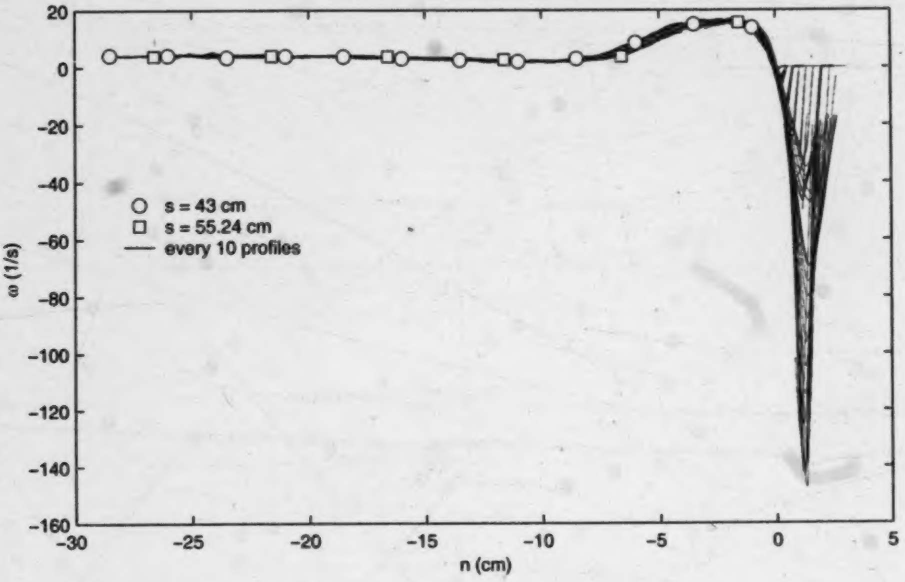

(a)

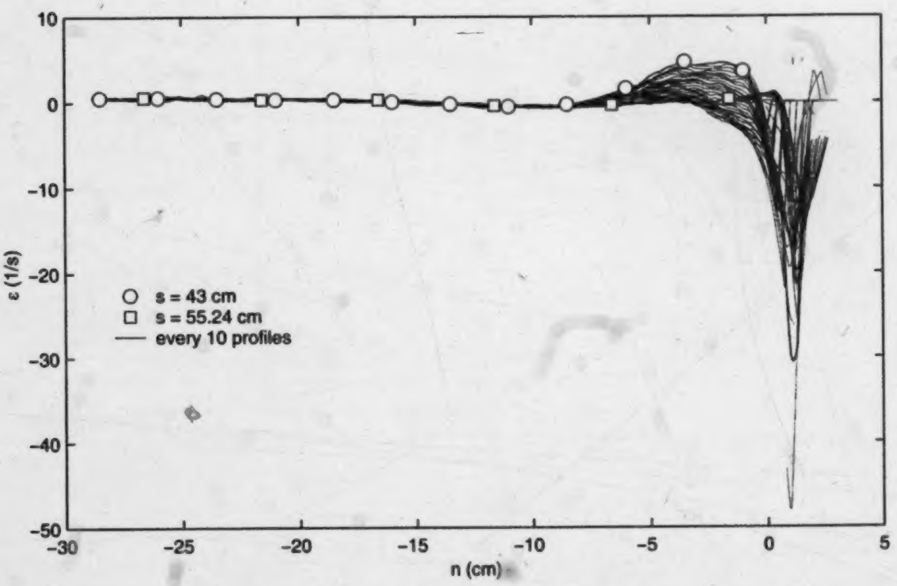

(b)

Figure 8.63: Mean (a) vorticity (ω) and (b) strain (ε) for the first transition zone (TZ1) profiles.

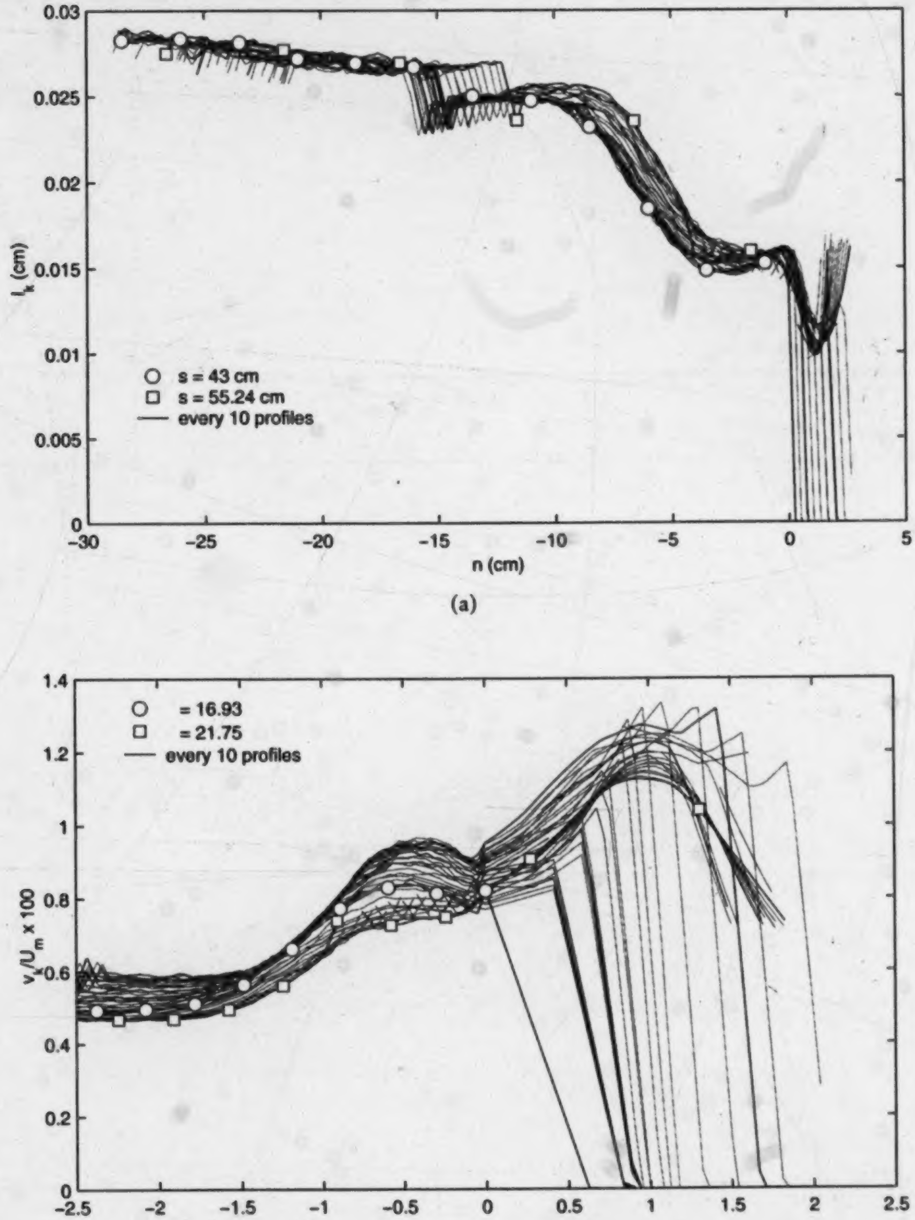

(a)

(b)

Figure 8.64: Mean Kolmogorov (a) length scales (l_k) and (b) velocity scales (v_k) for the first transition zone (TZ1) profiles.

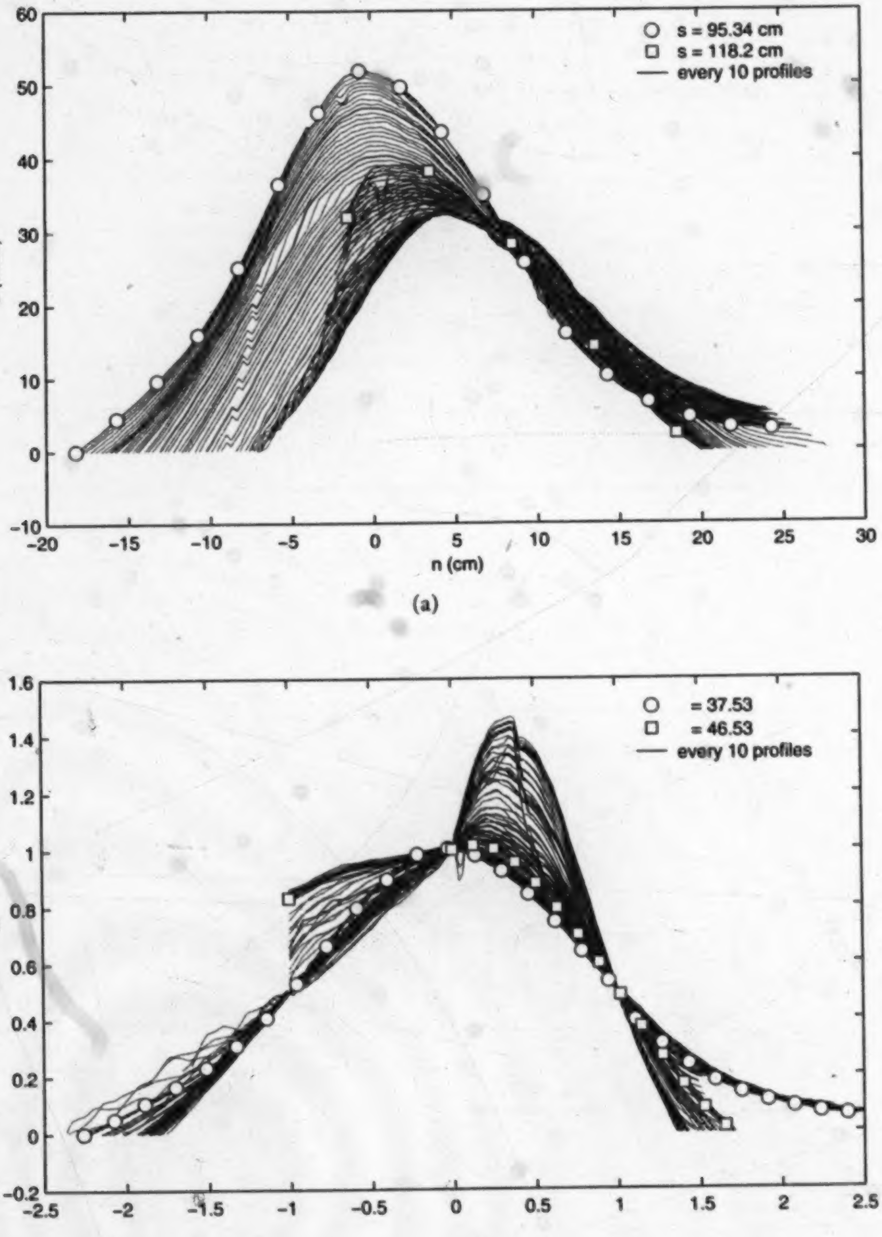

Figure 8.65: (a) Dimensional and (b) nondimensional u mean velocities for second transition zone (TZ2) profiles.

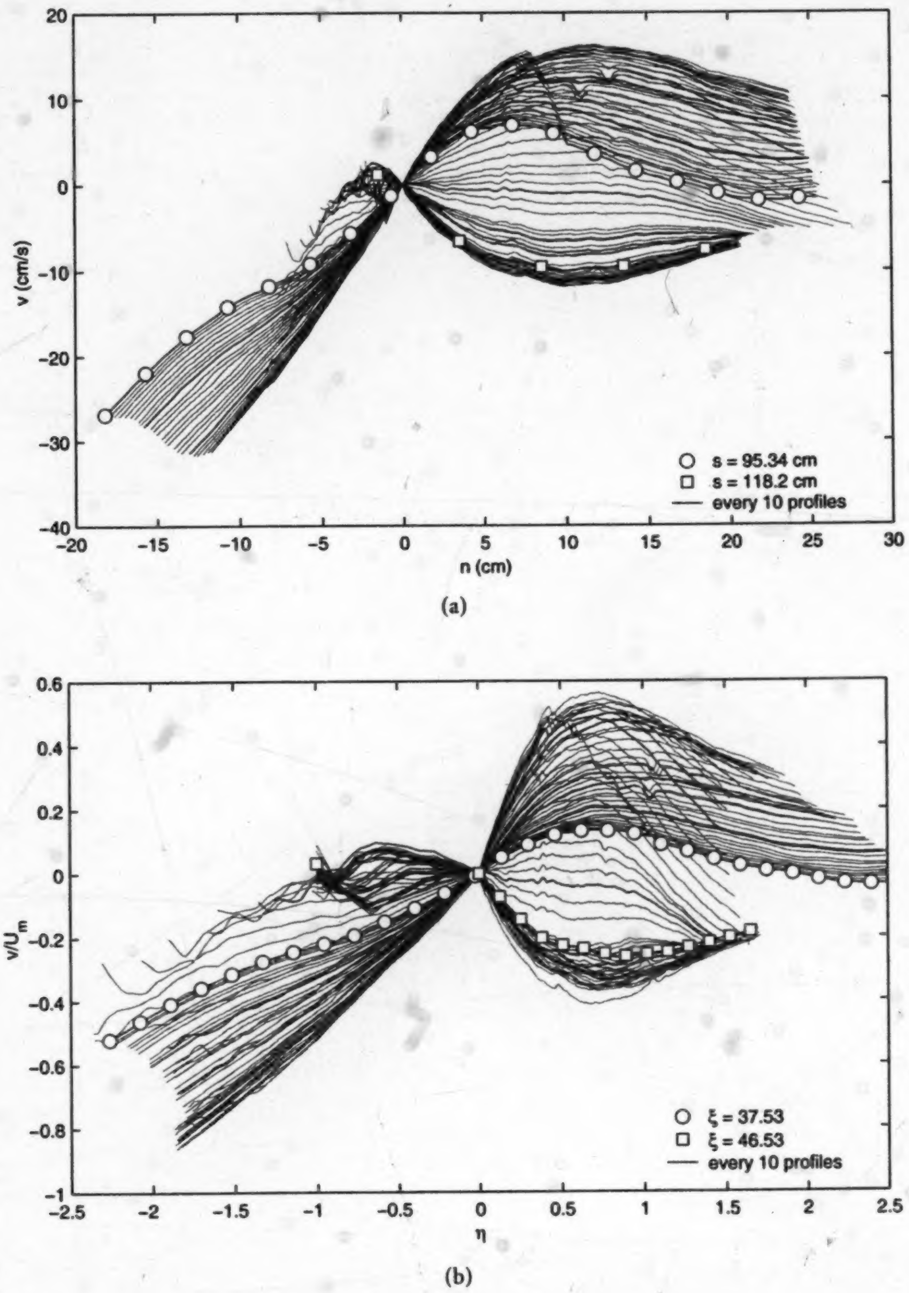

(a)

(b)

Figure 8.66: (a) Dimensional and (b) nondimensional v mean velocities for second transition zone (TZ2) profiles.

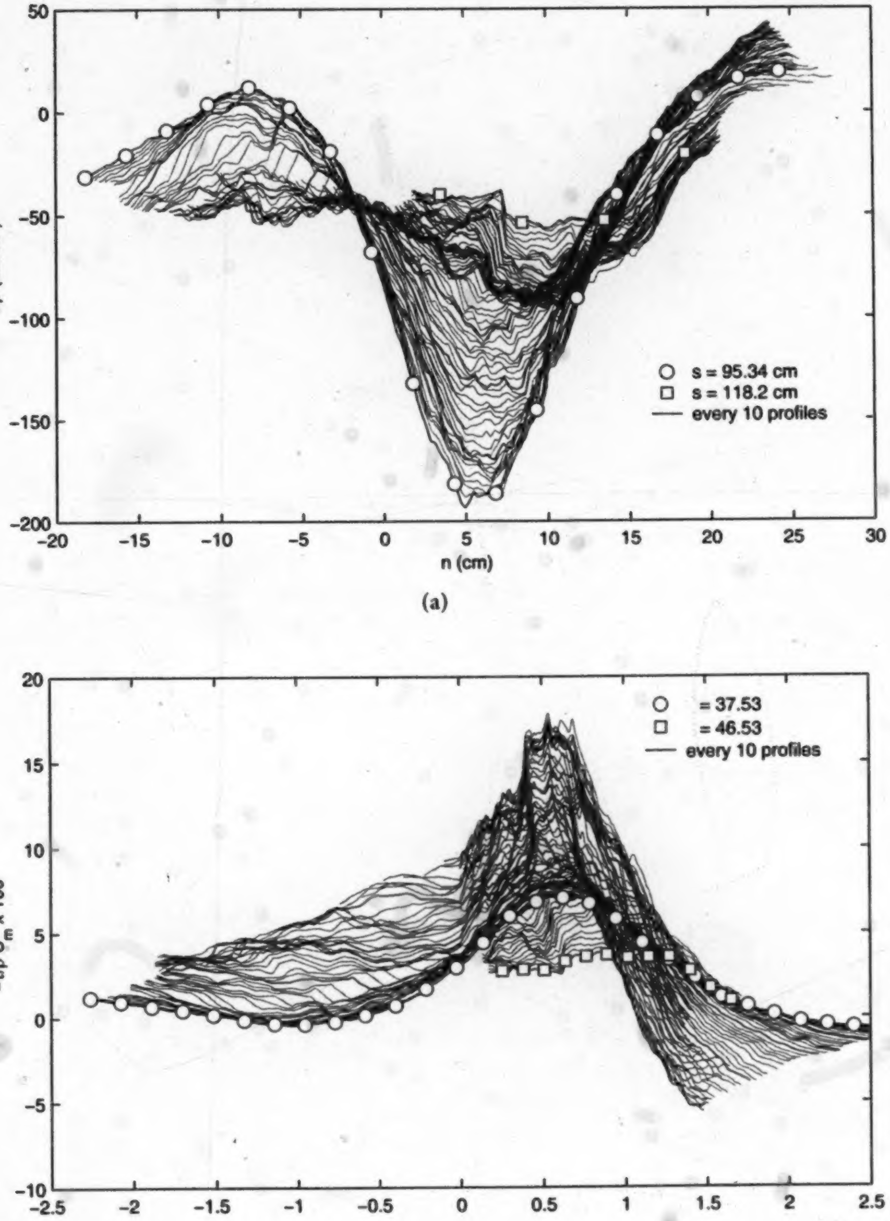

(a)

(b)

Figure 8.67: (a) Dimensional and (b) nondimensional mean Reynolds stress per unit mass (τ/ρ) for second transition zone (TZ2) profiles.

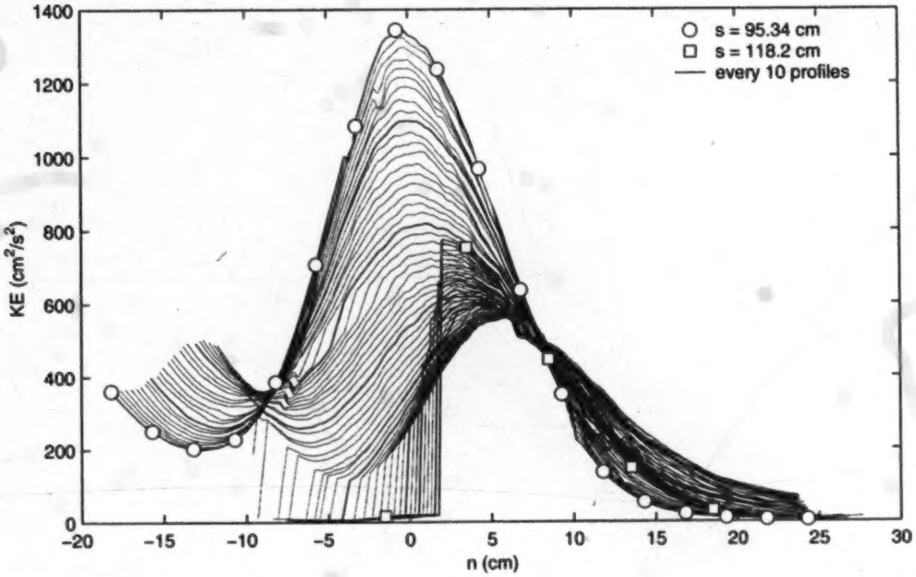

(a)

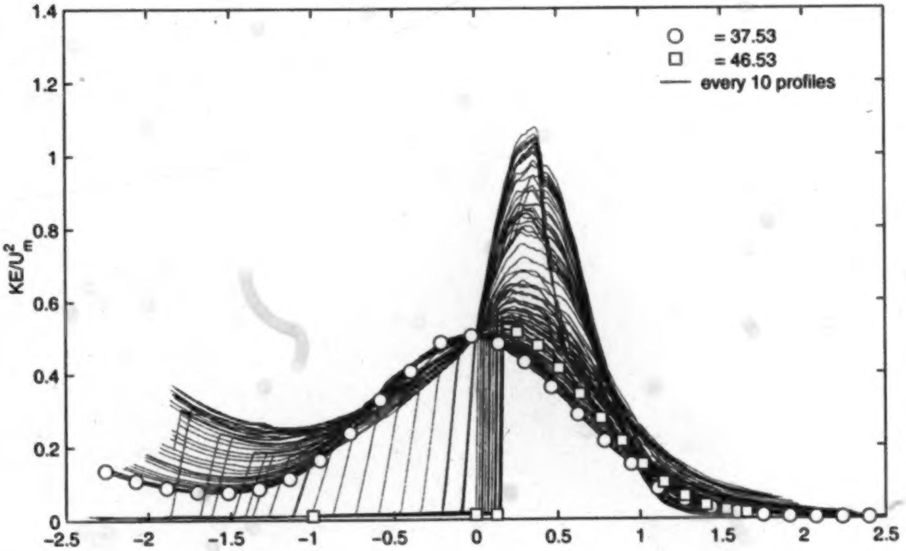

(b)

Figure 8.68: (a) Dimensional and (b) nondimensional mean kinetic energy (KE) for second transition zone (TZ2) profiles.

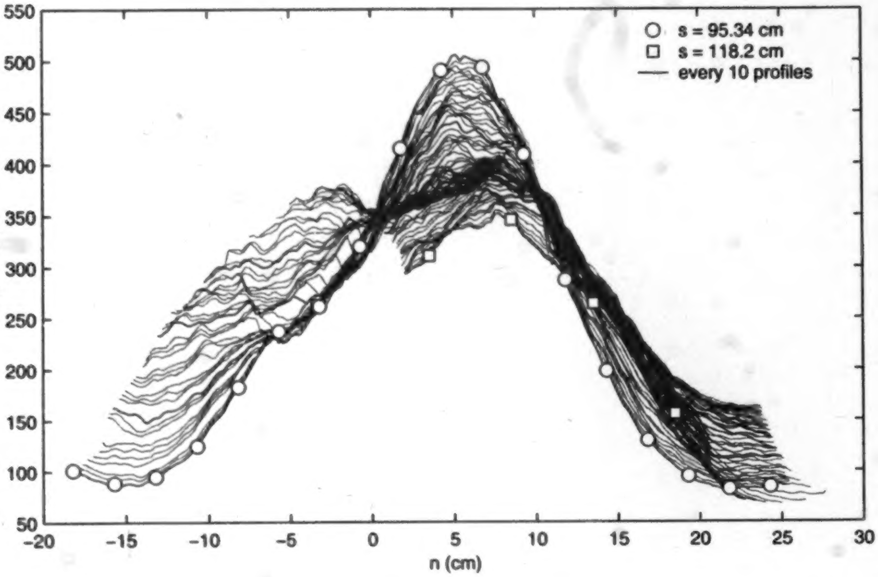

(a)

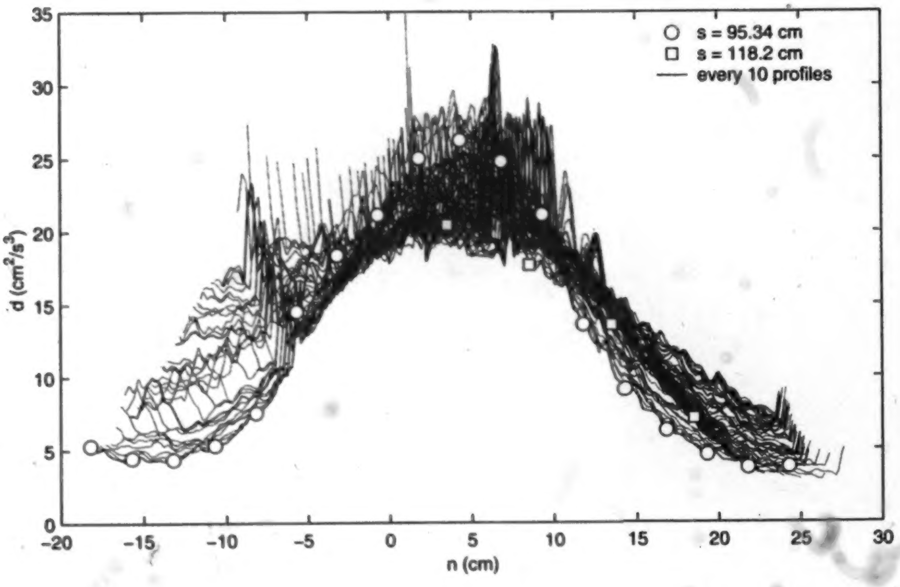

(b)

Figure 8.69: Mean (a) turbulent kinetic energy per unit mass (k) and (b) dissipation per unit mass (d) for the second transition zone (TZ2) profiles.

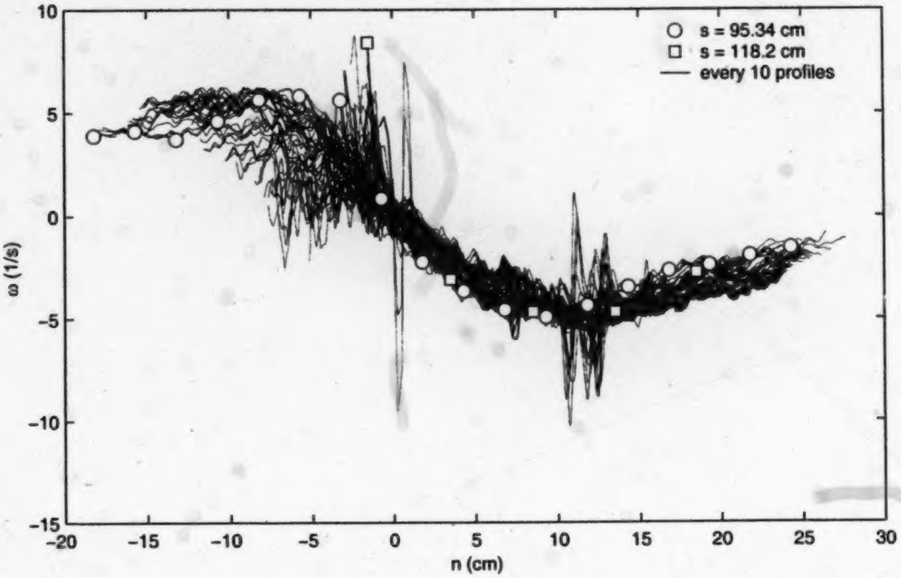

(a)

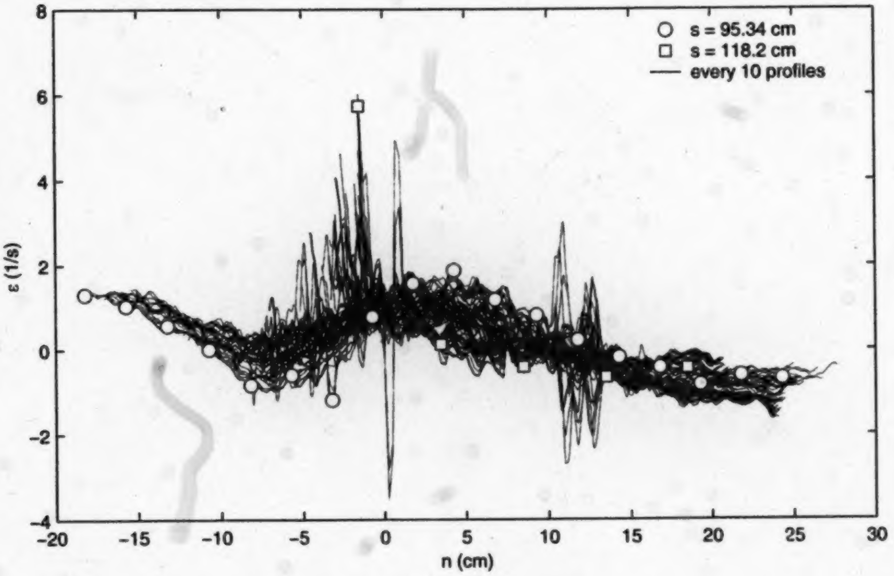

(b)

Figure 8.70: Mean (a) vorticity (ω) and (b) strain (ε) for the second transition zone (TZ2) profiles.

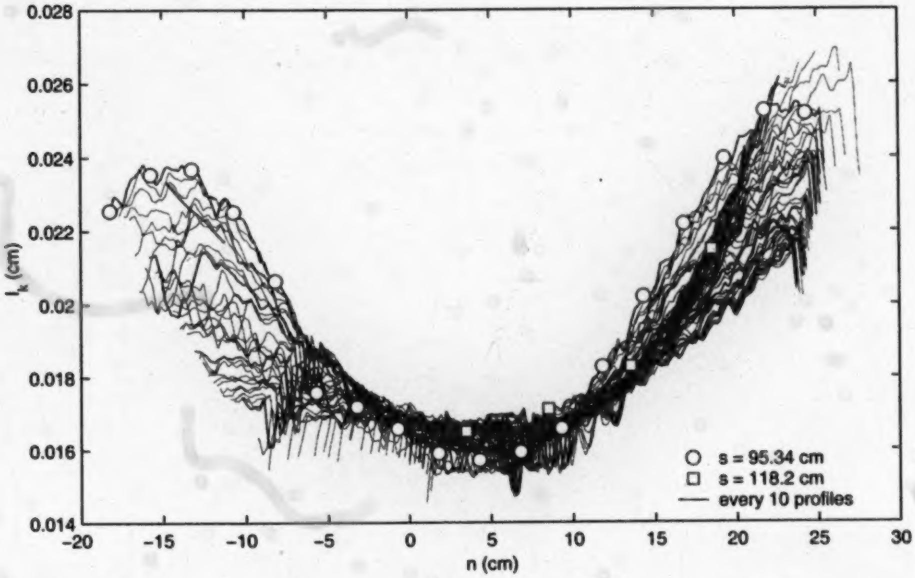

(a)

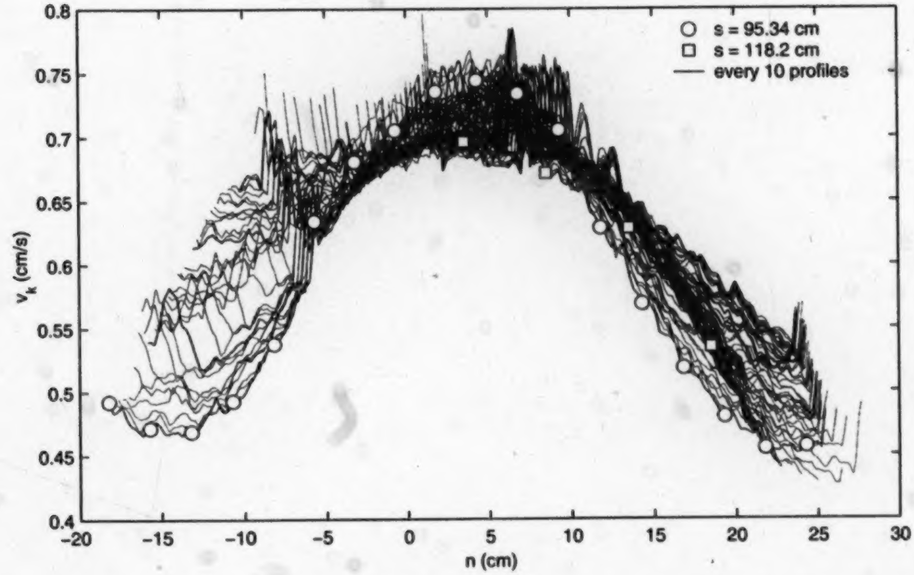

(b)

Figure 8.71: Mean Kolmogorov (a) length scales (l_k) and (b) velocity scales (v_k) for the second transition zone (TZ2) profiles.

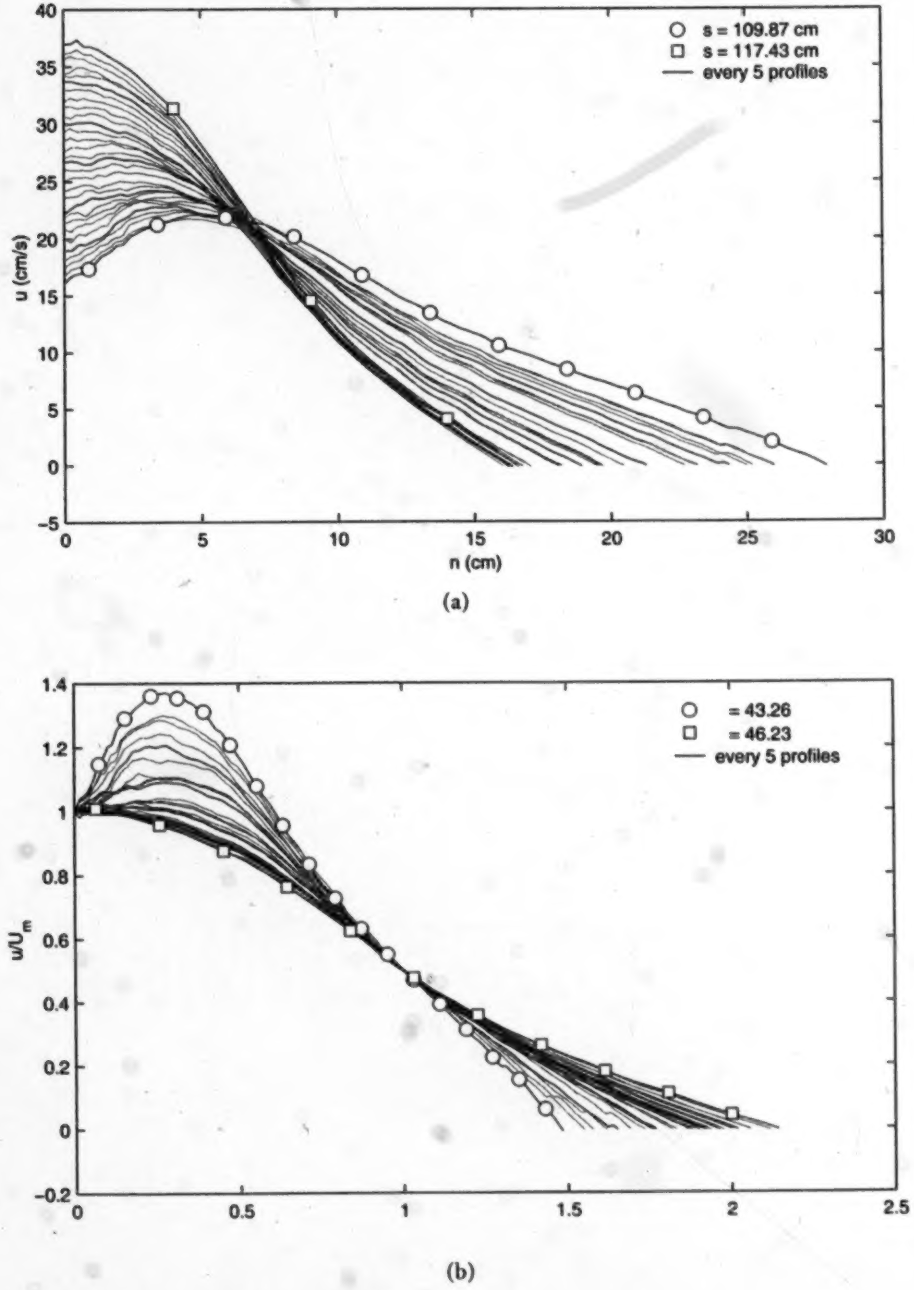

Figure 8.72: (a) Dimensional and (b) nondimensional u mean velocities for return flow second transition zone (TZ2) profiles.

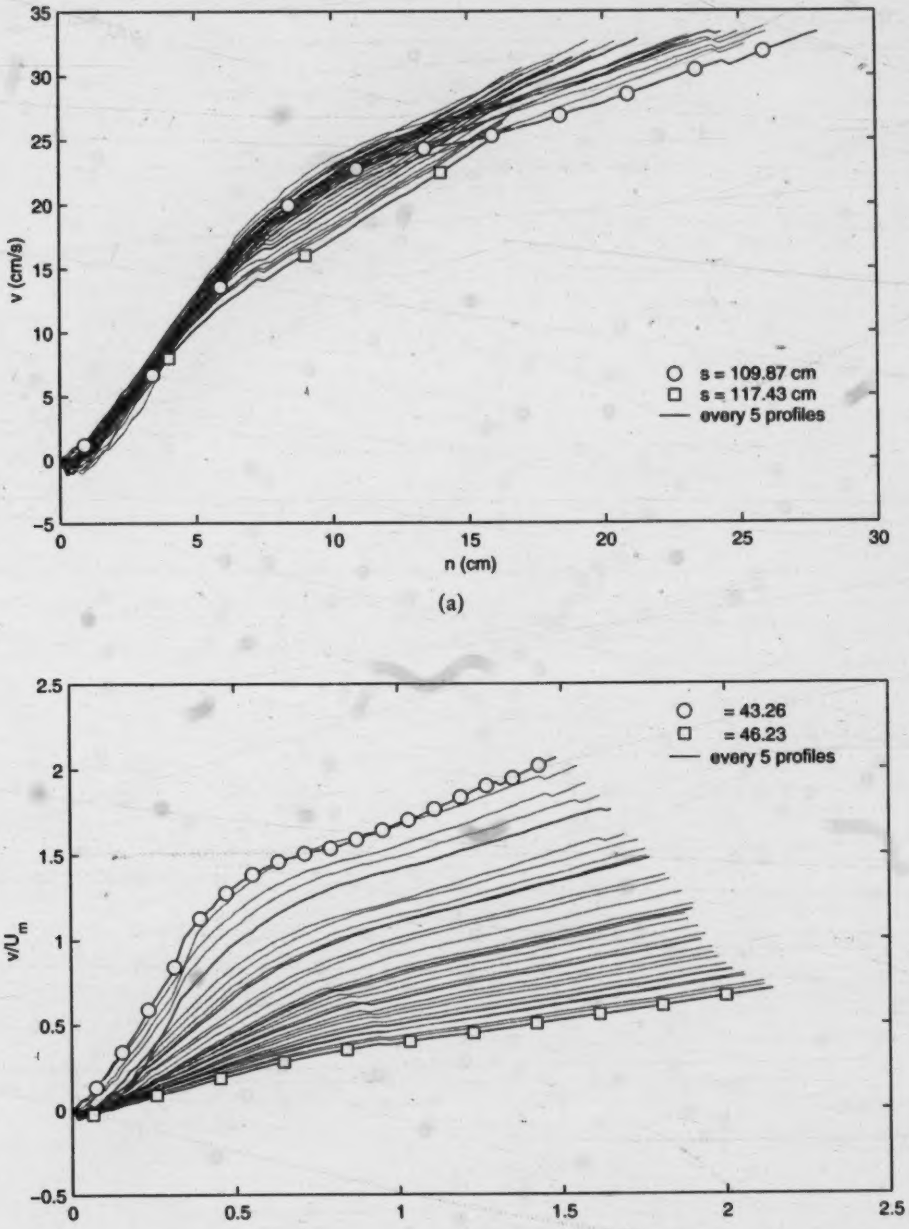

(a)

(b)

Figure 8.73: (a) Dimensional and (b) nondimensional v mean velocities for return flow second transition zone (TZ2) profiles.

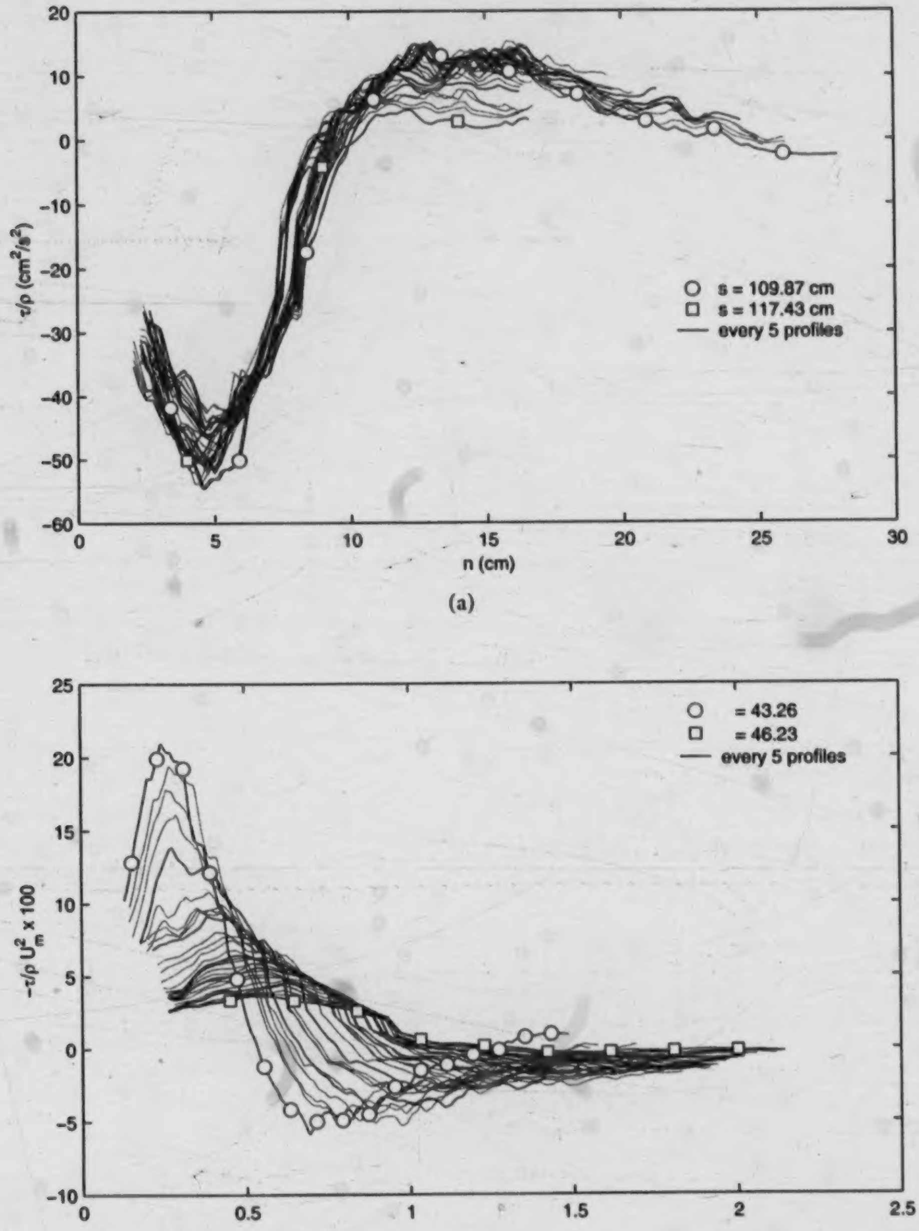

(a)

(b)

Figure 8.74: (a) Dimensional and (b) nondimensional mean Reynolds stress per unit mass (τ/ρ) for return flow second transition zone (TZ2) profiles.

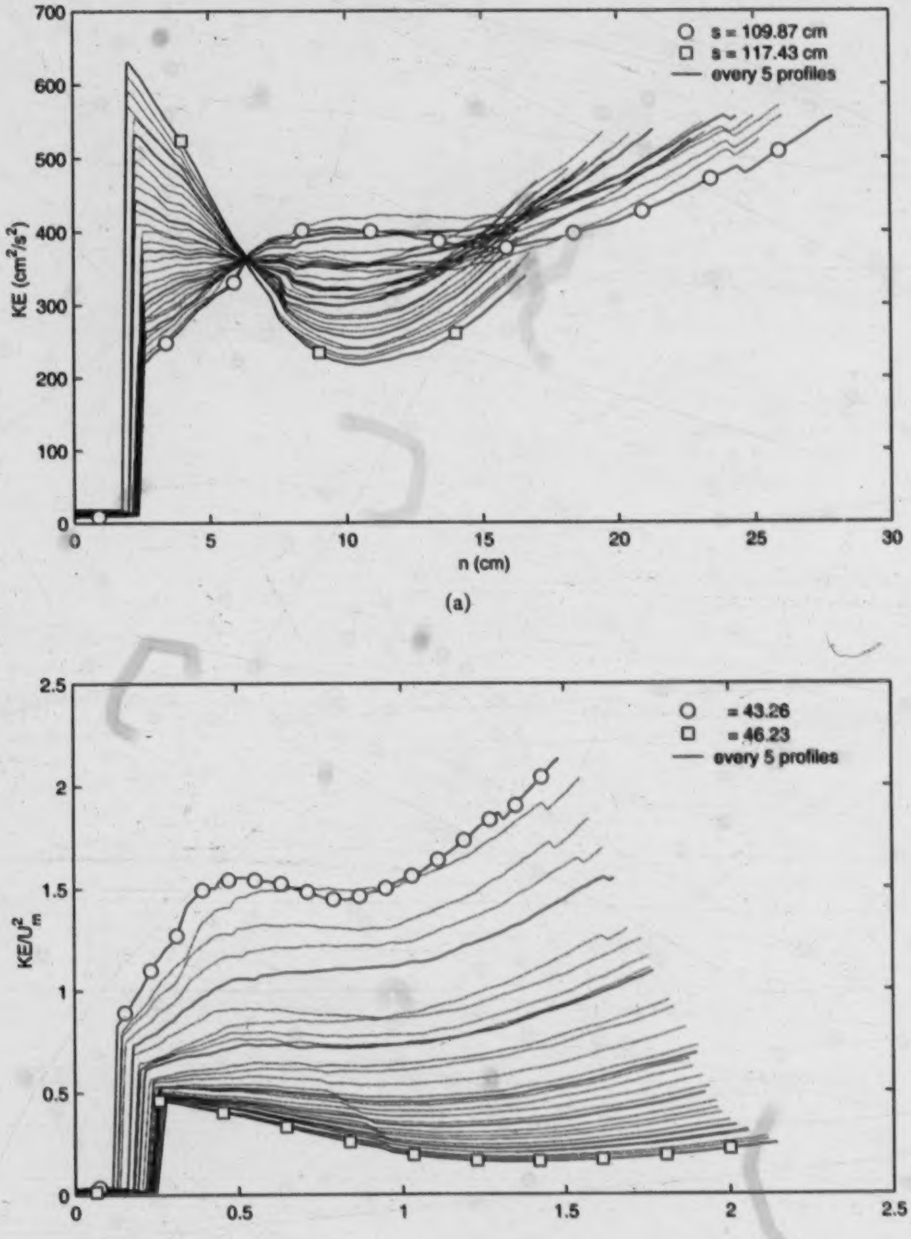

Figure 8.75: (a) Dimensional and (b) nondimensional mean kinetic energy (KE) for return flow second transition zone (TZ2) profiles.

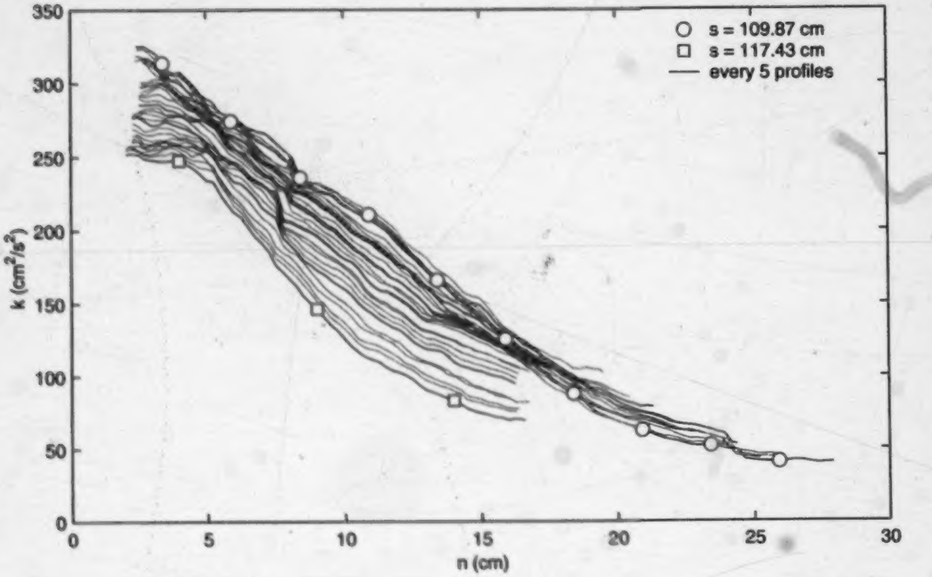

(a)

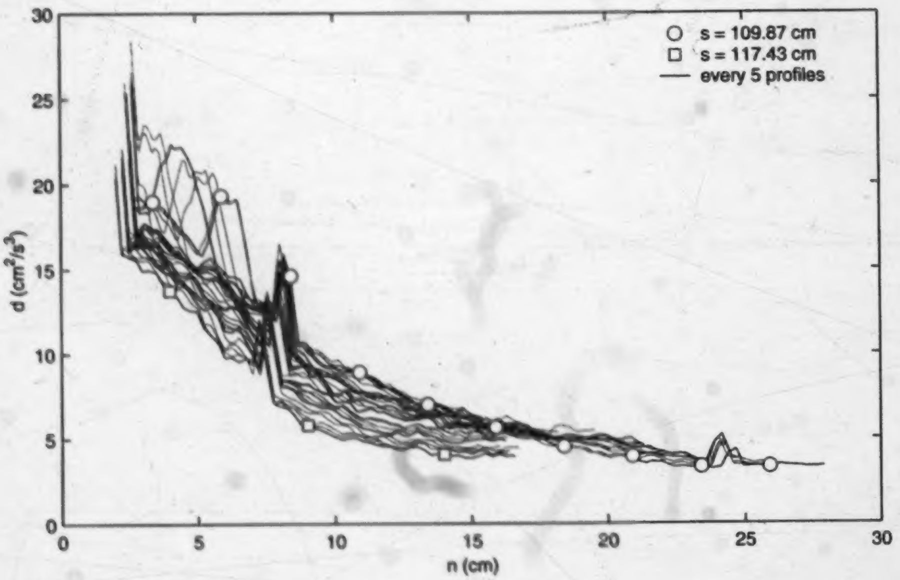

(b)

Figure 8.76: Mean (a) turbulent kinetic energy per unit mass (k) and (b) dissipation per unit mass (d) for the return flow second transition zone (TZ2) profiles.

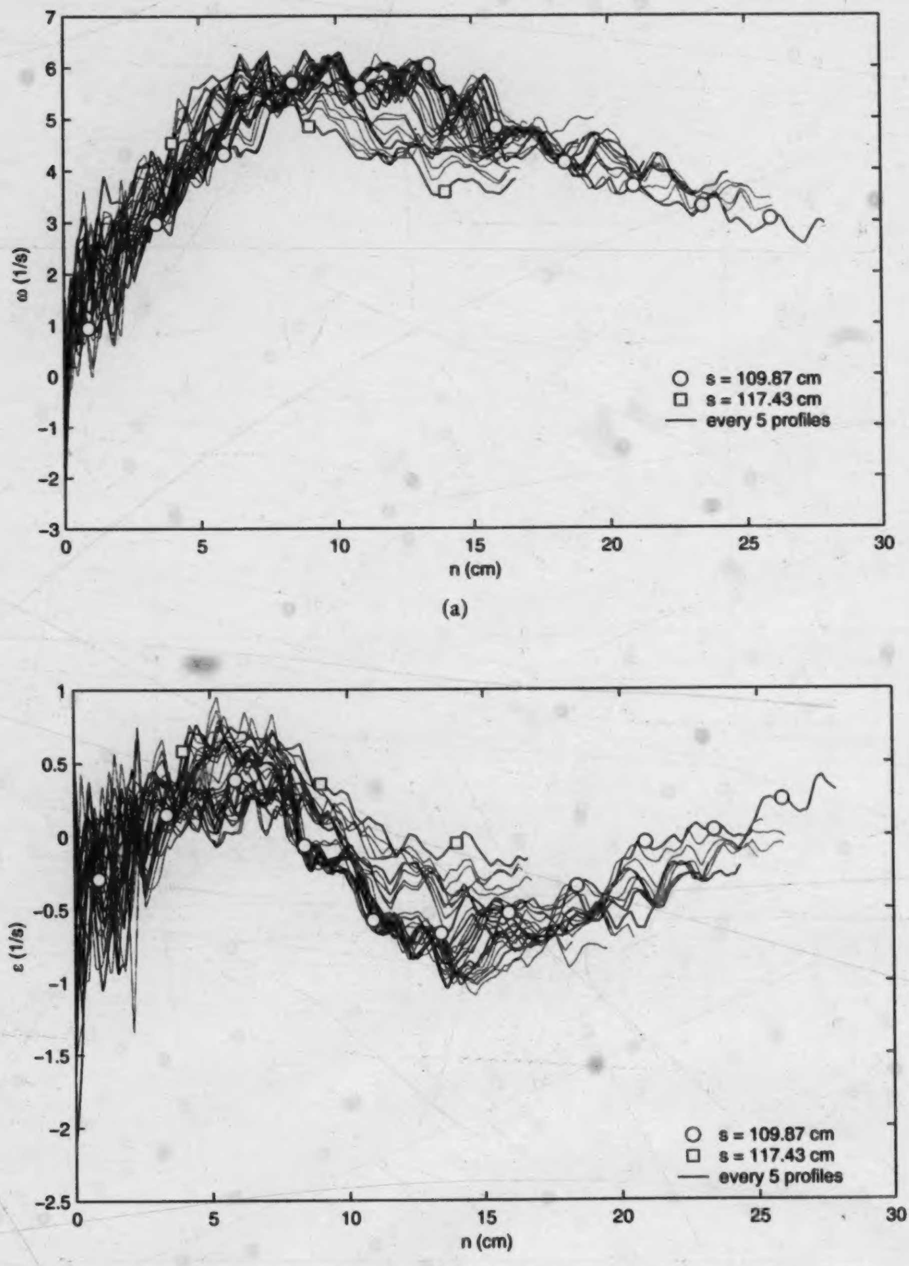

(a)

(b)

Figure 8.77: Mean (a) vorticity (ω) and (b) strain (ε) for the return flow second transition zone (TZ2) profiles.

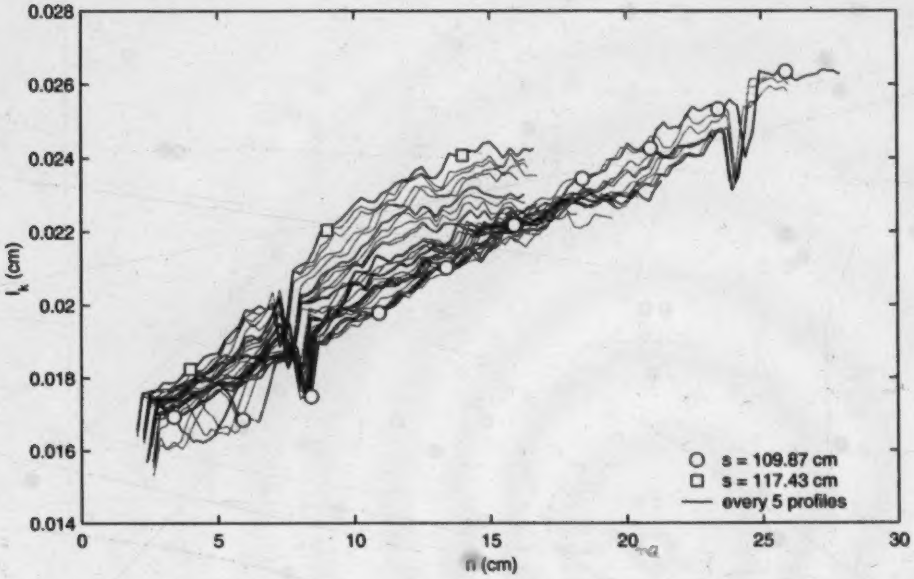

(a)

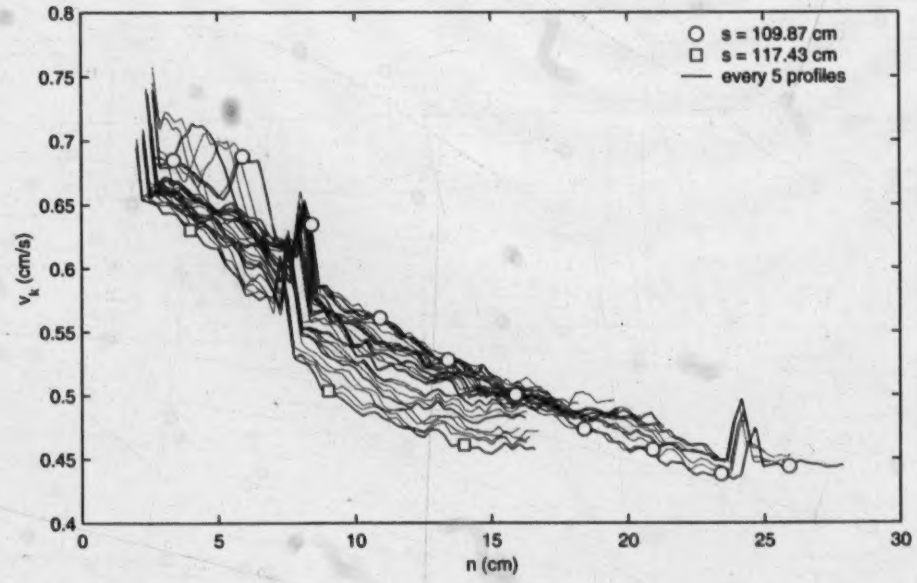

(b)

Figure 8.78: Mean Kolmogorov (a) length scales (l_k) and (b) velocity scales (v_k) for the return flow second transition zone (TZ2) profiles.